PROGRAMA UNIVERSITARIO DE DOCTORADO EN TECNOLOGÍAS DE LA INFORMACIÓN Y COMUNICACIONES EN REDES MÓVILES / MOBILE NETWORK INFORMATION AND COMMUNICATION TECHNOLOGIES – UNIVERSIDAD DE CANTABRIA, UNIVERSIDADE DA CORUÑA, UNIVERSIDAD DE OVIEDO, UNIVERSIDAD DE ZARAGOZA, Y UNIVERSIDAD DE PAÍS VASCO

FUSION OF OPTICAL IMAGING TECHNIQUES FOR THE CHARACTERIZATION OF MUSCULAR DYSTROPHIES

VERÓNICA MIEITES ALONSO

Under the supervision of
OLGA MARÍA CONDE PORTILLA

A thesis submitted for the degree of
Doctor of Philosophy

Santander, Cantabria, 2025

UNIVERSIDAD DE CANTABRIA

Publisher
Final version, March 2025. First printed in May 2025 by Universidad de Cantabria.

To my dad, mom, brother, and sister.
Thank you for guiding me to this
point and giving me the strength
to continue.

Abstract

Muscular dystrophies are a group of inherited myopathies characterized by progressive muscle weakness and degeneration, leading to significant physical disability and reduced quality of life. Current diagnostic methods often rely on invasive procedures like muscle biopsies, which can be painful, carry risks, and may not be readily accessible. This PhD dissertation explores the potential of advanced optical imaging techniques as non-invasive tools for the diagnosis and monitoring of muscular dystrophies, aiming to provide detailed information about muscle structure, composition, and function. This research utilizes a unique dataset of ex-vivo mice skeletal muscle tissue, both healthy and dystrophic, to comprehensively investigate the optical properties associated with the disease.

The primary objective of this thesis is to evaluate the feasibility and efficacy of several optical imaging modalities to aid in muscular dystrophy diagnosis and evaluation: intensity and polarization-sensitive optical coherence tomography (OCT/PS-OCT), hyperspectral imaging in the visible-near infrared (HSI-VISNIR) and short-wave infrared (HSI-SWIR) ranges, spatial frequency domain imaging (SFDI), and multispectral Mueller matrix imaging (MMI). Each technique offers unique capabilities for visualizing different aspects of muscle tissue. OCT and PS-OCT provide high-resolution microstructural information, with PS-OCT being particularly useful in the assessment of birefringence, a key indicator of muscle fiber organization. HSI in both spectral ranges allows for the identification and quantification of tissue components based on their spectral signatures. At the same time, SFDI provides similar information to that of HSI, with the advantage of being able to decouple scattering and absorption. MMI offers a comprehensive characterization of the polarization properties of muscle tissue, providing insights into retardance, diattenuation, and depolarization.

The findings of this thesis demonstrate the significant potential of these optical techniques for characterizing muscle pathology in muscular dystrophies. PS-OCT analysis revealed that birefringence is a more sensitive marker to dystrophy-related changes than attenuation, likely due to the disruption of muscle fiber organization occurring at a small enough scale to not be detectable as intensity variations but at phase variations instead. HSI and SFDI measurements indicated distinct spectral characteristics and differences in scattering and absorption properties between healthy and dystrophic samples, which suggests fat accumulation and altered chromophore content in diseased tissue. MMI analysis highlighted depolarization as a key parameter for distinguishing healthy muscle from damaged tissue and fat, with the additional benefit of simplified polarimetric classifiers achieving comparable accuracy to full Mueller matrix analysis, opening the doors to partial Mueller polarimetry for achieving fast muscle diagnosis.

Multimodal data analysis, while presenting challenges due to inter-sample variability and to the random sampling approach, offered a richer understanding of muscle pathology by considering both structural and chemical aspects. While a direct combination of all features for classification did not consistently outperform individual modalities, treating each imaging technique as an independent source of information yielded promising results, suggesting the potential for specialized diagnostic devices tailored to specific optical modalities. Visualization techniques effectively highlighted key differences in birefringence and tissue organization between healthy and dystrophic tissues, making these techniques useful to aid in pinpointing damaged areas in the muscle.

In conclusion, this dissertation demonstrates that optical imaging methodologies hold significant promise for aiding in the diagnosis and monitoring of muscular dystrophies. By providing non-invasive, label-free, and potentially real-time assessment of muscle tissue structure and composition, these techniques can complement existing diagnostic methods, potentially leading to earlier detection, improved understanding of disease progression, and the development of more effective therapeutic strategies for individuals living with muscular dystrophies. Future efforts should focus on refining these techniques, validating their clinical utility through larger studies, and developing practical tools for in vivo applications to reach their full potential in managing this debilitating group of diseases.

Resumen

Las distrofias musculares son un grupo de miopatías hereditarias caracterizadas por debilidad y degeneración muscular progresiva, lo que conlleva una discapacidad física significativa y una reducción de la calidad de vida. Los métodos de diagnóstico actuales a menudo se basan en procedimientos invasivos como las biopsias musculares, que pueden ser dolorosas, acarrear riesgos y no ser fácilmente accesibles. Esta tesis doctoral explora el potencial de las técnicas avanzadas de imagen óptica como herramientas no invasivas para el diagnóstico y el seguimiento de las distrofias musculares, con el objetivo de proporcionar información detallada sobre la estructura, composición y función muscular de músculos sanos y distróficos. Esta investigación utiliza un conjunto de datos único de tejido muscular esquelético ex vivo de ratones para investigar exhaustivamente las propiedades ópticas asociadas con la enfermedad.

El objetivo principal de esta tesis es evaluar la viabilidad y la eficacia de varias modalidades de imagen óptica para ayudar en el diagnóstico y la evaluación de la distrofia muscular. Entre las técnicas seleccionadas se incluyen: tomografía de coherencia óptica sensible a la intensidad y la polarización (OCT/PS-OCT), imagen hiperespectral en los rangos visible-infrarrojo cercano (HSI-VISNIR) e infrarrojo de onda corta (HSI-SWIR), imagen de dominio de las frecuencias espaciales (SFDI) e imagen de matriz de Mueller multiespectral (MMI). Cada técnica ofrece capacidades únicas para visualizar diferentes aspectos del tejido muscular. OCT y PS-OCT proporcionan información microestructural de alta resolución, siendo PS-OCT particularmente útil en la evaluación de la birrefringencia, un indicador clave de la organización de las fibras musculares. HSI en ambos rangos espectrales permite la identificación y cuantificación de los componentes del tejido en función de sus firmas espectrales. De la misma manera, SFDI proporciona información similar a la de HSI, con la ventaja de poder desacoplar el esparcimiento y la absorción. MMI ofrece una caracterización exhaustiva de las propiedades de polarización del tejido muscular, proporcionando información sobre el retardo, la diatenuación y la despolarización.

Los hallazgos de esta tesis demuestran el potencial significativo de estas técnicas ópticas para caracterizar la patología muscular en las distrofias musculares. El análisis PS-OCT reveló que la birrefringencia es un marcador más sensible a los cambios relacionados con la distrofia que la atenuación, probablemente debido a la alteración de la organización de las fibras musculares que ocurre a una escala lo suficientemente pequeña como para no ser detectable como variaciones de intensidad, sino como variaciones de fase. Las medidas HSI y SFDI indicaron características espectrales distintas y diferencias en las propiedades de esparcimiento y absorción entre las muestras sanas y distróficas, lo que sugiere acumulación de grasa y contenido alterado de cromóforos en el tejido enfermo. El análisis MMI destacó la despolarización como un parámetro clave para distinguir el músculo sano del tejido dañado y de la grasa, con el beneficio adicional de que los clasificadores polarimétricos simplificados logran una precisión comparable al análisis completo de la matriz de Mueller, lo que abre las puertas a la polarimetría parcial de Mueller para lograr un diagnóstico muscular rápido.

El análisis de datos multimodales, a pesar de presentar desafíos debido a la variabilidad entre muestras y al enfoque de muestreo aleatorio, ofreció una comprensión más rica de la patología muscular al considerar tanto los aspectos estructurales como los químicos. Si bien una combinación directa de todas las características para la clasificación no superó consistentemente a las modalidades individuales, el tratamiento de cada técnica de imagen como una fuente de información independiente mostró resultados prometedores, lo que sugiere el potencial de dispositivos de diagnóstico especializados adaptados a modalidades ópticas específicas. Las técnicas de visualización resaltaron eficazmente las diferencias clave en la birrefringencia y la organización del tejido entre los tejidos sanos y distróficos, lo que hace que estas técnicas sean útiles para ayudar a identificar las áreas dañadas en el músculo.

En conclusión, esta tesis demuestra que las metodologías de imagen óptica son muy prometedoras para ayudar en el diagnóstico y el seguimiento de las distrofias musculares. Al proporcionar una evaluación no invasiva, sin marcadores y potencialmente en tiempo real de la estructura y composición del tejido muscular, estas técnicas pueden complementar los métodos de diagnóstico existentes, lo que podría conducir a una detección más temprana, una mejor comprensión de la progresión de la enfermedad y el desarrollo de

estrategias terapéuticas más eficaces para las personas que viven con distrofias musculares. Los esfuerzos futuros deberían centrarse en refinar estas técnicas, validar su utilidad clínica a través de estudios más amplios y desarrollar herramientas prácticas para aplicaciones in vivo para alcanzar su máximo potencial en el manejo de este grupo de enfermedades debilitantes.

Resumo

As distrofias musculares son un grupo de miopatías hereditarias caracterizadas por debilidade e dexeneración muscular progresiva, o que causa unha discapacidade física significativa e unha redución da calidade de vida. Os métodos de diagnóstico actuais baséanse a miúdo en procedementos invasivos como as biopsias musculares, que poden ser dolorosas, carrexar riscos e non ser facilmente accesibles. Esta tese de doutoramento explora o potencial das técnicas avanzadas de imaxe óptica como ferramentas non invasivas para o diagnóstico e o seguimento das distrofias musculares, co obxectivo de proporcionar información detallada sobre a estrutura, composición e función muscular. Esta investigación utiliza un conxunto de datos único de tecido muscular esquelético ex vivo de ratos, tanto sans como distróficos, para investigar exhaustivamente as propiedades ópticas asociadas coa enfermidade.

O obxectivo principal desta tese é avaliar a viabilidade e a eficacia de varias modalidades de imaxe óptica para axudar no diagnóstico e na avaliación da distrofia muscular. Entre as técnicas seleccionadas inclúense: tomografía de coherencia óptica sensible á intensidade e a polarización (OCT/PS-OCT), imaxe hiperespectral nos rangos visible-infravermello próximo (HSI-VISNIR) e infravermello de onda curta (HSI-SWIR), imaxe no dominio das frecuencias espaciais (SFDI) e imaxe de matriz de Mueller multiespectral (MMI). Cada técnica ofrece capacidades únicas para visualizar diferentes aspectos do tecido muscular. OCT e PS-OCT proporcionan información microestrutural de alta resolución, sendo PS-OCT particularmente útil na avaliación da birrefrinxencia, un indicador clave da organización das fibras musculares. HSI en ambos rangos espectrais permite a identificación e cuantificación dos compoñentes do tecido en función das súas sinaturas espectrais. Ao mesmo tempo, SFDI proporciona información similar á de HSI, coa vantaxe de poder desacoplar o esparexemento e a absorción. MMI ofrece unha caracterización exhaustiva das propiedades de polarización do tecido muscular, proporcionando información sobre o retardo, a diatenuación e a despolarización.

Os achados desta tese demostran o potencial significativo destas técnicas ópticas para caracterizar a patoloxía muscular nas distrofias musculares. A análise PS-OCT revelou que a birrefrinxencia é un marcador máis sensible aos cambios relacionados coa distrofia que a atenuación, probablemente debido á alteración da organización das fibras musculares que ocorre a unha escala o suficientemente pequena como para non ser detectable como variacións de intensidade, senón como variacións de fase. As medicións HSI e SFDI indicaron características espectrais distintas e diferenzas nas propiedades de esparexemento e absorción entre as mostras sans e distróficas, o que suxire acumulación de graxa e contido alterado de cromóforos no tecido enfermo. A análise MMI destacou a despolarización como un parámetro clave para distinguir o músculo san do tecido danado e da graxa, co beneficio adicional de que os clasificadores polarimétricos simplificados acadan unha precisión comparable á análise completa da matriz de Mueller, o que abre as portas á polarimetría parcial de Mueller para lograr un diagnóstico muscular rápido.

A análise de datos multimodais, aínda que presentou desafíos debido á variabilidade entre mostras e ó enfoque de mostraxe aleatorio, ofreceu unha comprensión máis rica da patoloxía muscular ao considerar tanto os aspectos estruturais como os químicos. Aínda que unha combinación directa de todas as características para a clasificación non superou consistentemente as modalidades individuais, o tratamento de cada técnica de imaxe como unha fonte de información independente arroxou resultados prometedores, o que suxire o potencial de dispositivos de diagnóstico especializados adaptados a modalidades ópticas específicas. As técnicas de visualización resaltaron eficazmente as diferenzas clave na birrefrinxencia e a organización do tecido entre os tecidos sans e distróficos, o que fai que estas técnicas sexan útiles para axudar a identificar as áreas danadas no músculo.

En conclusión, esta tese demostra que as metodoloxías de imaxe óptica son moi prometedoras para axudar no diagnóstico e o seguimento das distrofias musculares. Ao proporcionar unha avaliación non invasiva, sen marcadores e potencialmente en tempo real da estrutura e composición do tecido muscular, estas técnicas poden complementar os métodos de diagnóstico existentes, o que podería conducir a unha detección máis temperá, unha mellor comprensión da progresión da enfermidade e o desenvolvemento de estratexias terapéuticas máis eficaces para as persoas que viven con distrofias musculares. Os esforzos futuros deberían

centrarse en refinar estas técnicas, validar a súa utilidade clínica a través de estudos máis amplos e desenvolver ferramentas prácticas para aplicacións in vivo para alcanzar o seu máximo potencial na xestión deste grupo de enfermidades debilitantes.

Acknowledgements

They say that doctoral theses are very personal documents, and indeed, only one person has written this text. However, this document would not exist without the constant moral and scientific support of many people who have been kind (and patient) enough to accompany me during this process.

Firstly, I want to express my profound gratitude to my doctoral thesis advisor, Olga, for always fostering my intellectual growth and challenging me to think critically, despite not always agreeing. The numerous discussions and reflections throughout these years have shaped this research and have instilled in me a deeper understanding of biomedical optics. I am truly grateful for her constant dedication to my academic development.

Throughout this process, I have had the opportunity to work with a large number of scientists from whom I have been able to learn enormously. Especially, I want to thank José for his incessant collaboration and goodwill when assembling devices together, which is never a simple task, and to Fran for helping every time I needed it. Furthermore, I want to thank Giulio, Maria, Vadzim, Kaizhong, Ziyan, Zepeng, and Dan for having welcomed me with open arms into their laboratory. Without their knowledge and (especially) without the lunchtime conversations, a large part of this thesis could not have been developed. Additionally, I want to thank Mónica and Irene for the valuable polarimetric help they have given me, which has allowed me to solidify the knowledge discussed throughout this document.

A large part of the merit of this thesis also belongs to my friends Aida, Alberto, Celia, Efrén, Esteban, Fabián, Manuel, and Pablo, who, although we only see each other once a year, it always brightens my day to be able to write to them at any time and know that they will bring a smile to my face. I especially want to thank my friend Andrea, who has accompanied me throughout this time, in the good times and bad, and from whom I have learned that attitude is everything to bring a work like this forward. What electronics-physics united, let life not separate!

I also want to thank the constant support of my family, including my grandfather, my aunts and uncles and cousins, Manny and Txell, and my long-time friend Olga. I also want to thank my nephew Pol, who will go as far in life as he wants to, for his encouragement all this time. I especially want to thank my father, Saturnino, and my mother, María José, for always encouraging me to do what fulfills me and for having raised three such different children. Without the incessant support of my brother Anxo and my sister Goretti, neither would the science written in this document have been so extensive, nor would my stubbornness in defending it.

Finally, I want to thank my partner Arturo for his character, his humor, his knowledge, and his passion for science, all of which are particularly contagious, for helping me to be a better person and a better scientist.

This book's merit belongs to all of you!

Agradecimientos

Dicen que las tesis doctorales son un documento muy personal y, ciertamente, sólo una persona ha escrito este texto. Sin embargo, este documento no existiría sin el apoyo constante, moral y científico, de muchas personas que han tenido la amabilidad (y la paciencia) de prestármelo durante este proceso.

En primer lugar, quiero expresar mi profundo agradecimiento a mi directora de tesis doctoral, Olga, por fomentar siempre mi crecimiento intelectual y desafiarme a pensar críticamente, a pesar de no estar siempre de acuerdo. Las numerosas discusiones y reflexiones a lo largo de estos años han moldeado esta investigación y me han inculcado una comprensión más profunda de la óptica biomédica. Estoy verdaderamente agradecida por su dedicación constante a mi desarrollo como académica.

Durante este proceso, he tenido la oportunidad de trabajar con un gran número de científicos de quienes he podido aprender enormemente. Especialmente, le quiero agradecer a José su colaboración incesante y buena voluntad a la hora de montar dispositivos juntos, lo cual nunca es una tarea sencilla, y a Fran por siempre ayudar cuando hacía falta. Por otra parte, quiero agradecerle a Giulio, Maria, Vadzim, Kaizhong, Ziyan, Zepeng y Dan por haberme recibido con los brazos abiertos en su laboratorio. Sin su conocimiento y (especialmente) sin las conversaciones a la hora de comer, una gran parte de esta tesis no se habría podido desarrollar. Además, quiero agradecerle a Mónica e Irene la valiosa ayuda polarimétrica que me han prestado, la cual me ha permitido afianzar los conocimientos discutidos a lo largo de este documento.

Gran parte del mérito de esta tesis se lo merecen también mis amigos Aida, Alberto, Celia, Efrén, Esteban, Fabián, Manuel y Pablo, que aunque nos veamos una vez al año siempre me alegra el día poder escribirles en cualquier momento y saber que me sacarán una sonrisa. Especialmente quiero agradecérselo a mi amiga Andrea, quien me ha acompañado durante todo este tiempo, en las temporadas buenas y malas, y de quien he aprendido que la actitud lo es todo para sacar un trabajo como este adelante. Que lo que unió la electrónica-física no lo separe la vida!

Quiero agradecer también el apoyo constante de mi familia, incluyendo a mi abuelo, mis tíos y primos, de Manny y de Txell, y de mi amiga Olga. También quiero agradecerle a mi sobrino Pol, quien llegará tan lejos como él quiera, los ánimos que me ha dado todo este tiempo. Especialmente quiero agradecerle a mi padre Saturnino y a mi madre María José, por haberme animado siempre a hacer aquello que me llena, y por haber criado a tres hijos tan diferentes. Sin el apoyo incesante de mi hermano Anxo y de mi hermana Goretti, la ciencia escrita en este documento no habría sido tanta, como tampoco lo habría sido mi cabezonerío a la hora de defenderla.

Finalmente, quiero agradecerle a mi pareja Arturo su carácter, su humor, su conocimiento y su pasión por la ciencia, siendo todo ello particularmente contagioso, por ayudarme a ser una mejor persona y una mejor científica.

¡El mérito de este libro es vuestro!

Agradecementos

Din que as teses de doutoramento son documentos moi persoais e, certamente, só unha persoa escribiu este texto. Porén, este documento non existiría sen o apoio constante, moral e científico de moitas persoas que tiveron a amabilidade (e a paciencia) de mo prestar durante este proceso.

En primeiro lugar, quero expresar o meu profundo agradecemento á miña directora de tese de doutoramento, Olga, por fomentar sempre o meu crecemento intelectual e desafiarme a pensar criticamente, a pesar de non estar sempre de acordo. As numerosas discusións e reflexións ao longo destes anos moldearon esta investigación e inculcáronme unha comprensión máis profunda da óptica biomédica. Estou verdadeiramente agradecida pola súa dedicación constante ao meu desenvolvemento como académica.

Ao longo deste proceso, tiven a oportunidade de traballar cun gran número de científicos dos que puiden aprender enormemente. Especialmente, quero agradecerlle a José a súa colaboración incesante e boa vontade á hora de montar dispositivos xuntos, o cal nunca é unha tarefa sinxela, e a Fran por axudar sempre que fixo falta. Por outra banda, quero agradecerlle a Giulio, Maria, Vadzim, Kaizhong, Ziyan, Zepeng e Dan por me teren recibido cos brazos abertos no seu laboratorio. Sen o seu coñecemento e (especialmente) sen as conversas á hora de comer, unha gran parte desta tese non se tería podido desenvolver. Ademais, quero agradecerlle a Mónica e Irene a valiosa axuda polarimétrica que me prestaron, a cal me permitiu afianzar os coñecementos discutidos ao longo deste documento.

Gran parte do mérito desta tese tamén o teñen os meus amigos Aida, Alberto, Celia, Efrén, Esteban, Fabián, Manuel e Pablo, que aínda que nos vexamos unha vez ao ano sempre me alegra o día poder escribirlles en calquera momento e saber que me sacarán un sorriso. Especialmente quero agradecerllo á miña amiga Andrea, quen me acompañou durante todo este tempo, nas tempadas boas e malas, e de quen aprendín que a actitude o é todo para sacar un traballo coma este adiante. Que o que uniu a electrónica-física non o separe a vida!

Quero agradecer tamén o apoio constante da miña familia, incluíndo o meu avó, os meus tíos e primos, de Manny e de Txell, e da miña amiga Olga. Tamén quero agradecerlle ó meu sobriño Pol, quen chegará tan lonxe como él queira, os ánimos que me mandou todo este tempo. Especialmente quero agradecerlle ao meu pai, Saturnino, e á miña nai, María José, por me teren animado sempre a facer aquilo que me enche, e por teren criado tres fillos tan diferentes. Sen o apoio incesante do meu irmán Anxo e da miña irmá Goretti, nin a ciencia escrita neste documento tería sido tanta, nin a miña teimosía á hora de defendela.

Finalmente, quero agradecerlle á miña parella Arturo o seu carácter, o seu humor, o seu coñecemento e a súa paixón pola ciencia, sendo todo isto particularmente contaxioso, por me axudar a ser unha mellor persoa e unha mellor científica.

O mérito deste libro é voso!

Institutional acknowledgements

This research was conducted with the facilities and resources provided by different institutions, projects, and grants, including:

- All mice samples examined in this document were provided and prepared by the Neuromuscular Diseases Unit at the Hospital de la Santa Creu I Sant Pau, Universidad Autónoma de Barcelona, under the supervision and collaboration with Jordi Diaz Manera (John Walton Muscular Dystrophy Research Centre, University of Newcastle, UK) and Xavier Suárez-Calvet (Hospital de la Santa Creu I Sant Pau).
- Predoctoral grant PREVAL21/07 (FUSIOMUSCLE), financed by Valdecilla Health Research Institute (IDIVAL).
- HyperMuscle, Hyperspectral and OCT imaging of muscle for assessing muscle degeneration and dystrophy in Duchenne disease" (Proyecto CI128). Intermural project CIBER-BBN (Bioingeniería, Biomateriales y Nanomedicina – Grupo Ingeniería Fotónica, CB16/01/00430) y CIBER-ER (Enfermedades Raras - Unidad de Enfermedades Neuromusculares del Hospital de la Santa Creu i Sant Pau, CB06/05/0030). Consorcio CIBER (Centro de Investigación Biomédica en Red). Instituto de Salud Carlos III.
- Custom camera for the automated diagnosis of tissue perfusion in surgical environments DTS22/00127 (hyPERfusioCAM), financed by Carlos III Health Institute (ISCIII), the Spanish Ministry of Science and Innovation, and co-financed by the European Union (EU).
- Transference of the hyperspectral imaging systems for the active monitoring of tissue perfusion SUBVTC-2021-0038 (HYPERfusionTRANS), financed by the Government of Cantabria.
- High-resolution, polarization-sensitive optical coherence tomography system 2019-006589-P (ETCOSPAR), financed by the ISCIII, IDIVAL, FEDER funds, and the Spanish Ministry of Science, Innovation and Universities.
- Project DTS17-00055 (INTRACARDIO), financed by the ISCIII, Valdecilla Health Research Institute, and the Spanish Ministry of Science, Innovation and Universities, co-financed with FEDER funds.
- Project PID2019-107270RB-C21/AEI/10.13039/501100011033 (DISFOS), financed by the ISCIII, Valdecilla Health Research Institute, and the Spanish Ministry of Science, Innovation and Universities, co-financed with FEDER funds.
- Project TED2021-130378B-C21 (PALACE), funded by MICIU/AEI/10.13039/501100011033 and the European Union NextGenerationEU/PRTR.
- Project PID2022-137269OB-C22 (PERFORMANCE), financed by MCIN/AEI/10.13039/501100011033/ and by the European Regional Development Fund (FEDER), EU.
- Project PID2022-136898OB-I00 (Neanderthal History), financed by MICIU/AEI/10.13039/501100011033 and by the European Regional Development Fund (FEDER), EU.
- Additional funds were received from the Carlos III Health Institute (ISCIII), Valdecilla Health Research Institute (IDIVAL), the Bioengineering, Biomaterials and Nanomedicine Research Network (CIBER-BBN), and FEDER funds.

Contents

List of Figures

List of Tables

Part I

Introduction and clinical context

Introduction

The human body is a complex and dynamic system, and muscle tissue is no exception. Its intricate network of fibers and proteins, essential for movement and strength, is also susceptible to devastating disruptions, as seen in muscular dystrophies. These disorders affect not only the physical body but also have profound psychological, social, and economic consequences.

Muscular dystrophy (MD) is a term that encompasses a specific type of gene-related, inherited myopathy characterized by muscle weakness [1]. It is the inherited genetic nature of MD that helps differentiate it from other muscle problems. The many types of MD are related to different genetic alterations with a specific phenotype and are present in various populations. Blaszczyk *et al.* [2] summarize those diseases included under the umbrella of "muscular dystrophy" as having three main characteristics in common: weakness and disability caused by muscular disorders, young onset age (5-30 years), and a high probability of heart failure due to cardiac involvement. Nonetheless, the symptoms and consequences of each MD can be vastly different.

The impact of muscular dystrophies extends beyond physical symptoms. For individuals living with MD, their daily lives are often marked by a progressive loss of independence. Simple tasks such as walking, climbing stairs, or even reaching objects from high shelves become increasingly difficult. As the disease progresses, many individuals become dependent on assistive devices like wheelchairs or ventilators, impacting their mobility and overall quality of life. The emotional burden of living with a progressive, debilitating disease can be quite considerable, leading to frustration, anxiety, and depression. Social isolation is also common, as participation in activities with friends and family becomes restricted. Furthermore, the economic costs associated with MD can be substantial, including medical expenses and the need for long-term care. MDs also places a heavy burden on caregivers, whose commitment throughout the patient's remaining time needs to increase as the disease becomes more debilitating. Thus, caregivers may risk unemployment while potentially needing to hire specialized medical professionals. This escalating level of involvement, coupled with the potential for a shortened patient lifespan, often becomes an unbearable reality for both patients and their loved ones.

Early diagnosis of muscular dystrophy is crucial. When detected early, physical therapy, medication, and assistive devices can help slow down the progression of muscle weakness, maintain function, and improve quality of life. On the other hand, a delayed diagnosis can lead to missed opportunities for intervention, resulting in more rapid muscle deterioration, worsening disability, and a poorer prognosis. Unfortunately, current diagnostic methods often rely on invasive procedures like muscle biopsies, which can be painful, carry complication risks, and may not be readily available in all healthcare settings. These biopsies can also be expensive and time-consuming, leading to delays in diagnosis and treatment. The limitations of current diagnostic approaches highlight the urgent need for alternative methods that are non-invasive, accurate,

and accessible to all. Although there exist less-invasive procedures for diagnosis, these can still cause distress to the patient. Thus, having alternative diagnostic methods that could be used regularly might improve physicians' ability to monitor disease progression while minimizing patients' suffering.

The definition of a rare disease varies across regions. According to the European Commission, a rare disease is defined as a chronically debilitating, life-threatening disease, with low prevalence (no more than 5 per 10 000 inhabitants, or 1 per 2000)[1], while the United States National Institutes of Health (NIH) indicates a prevalence of no more than 1 in 1625 people[2]. MDs with an estimated global prevalence of 1 in 5000 individuals (Fig. 1), are considered as rare diseases [3].

Numerous organizations are committed to rare disease research, including muscular dystrophies. Major examples include the Muscular Dystrophy Association (MDA) in the US and, in Europe, the European Reference Network of Neuromuscular Diseases (EURO-NDM) and the European Neuromuscular Centre (ENMC). However, the ongoing discovery of new muscular dystrophy-causing mutations -each with unique diagnostic and treatment needs- coupled with the additional challenge of muscular dystrophy samples' scarcity and overall low number of studies, highlights the critical importance of integrating alternative monitoring and diagnostic approaches in the clinical environment.

The field of optical imaging remains largely unexplored in the diagnosis, evaluation, and monitoring of muscular dystrophies, as well as in the search for any optical biomarkers that might represent these diseases. To address this gap, this thesis aims to explore the potential of optical imaging technologies to assess muscle tissue composition, both chemically and structurally, and to evaluate their potential as tools for aiding in the understanding and managing of complex pathologies like muscular dystrophies through the development of disease-specific optical equipment and dedicated software analysis tools. With its ability to provide non-invasive, real-time assessment of muscle tissue, optical imaging has the potential to provide earlier and more accurate diagnoses and to monitor pharmacological development and efficacy, facilitating timely intervention and improving patient outcomes. For instance, *optical coherence tomography* (OCT), a technique analogous to ultrasound but using light, along with its polarization-sensitive variant (PS-OCT), could provide high-resolution images of muscle structure, allowing for the visualization of changes in muscle fiber size and organization associated with different stages of muscular dystrophy. *Hyperspectral imaging* (HSI), which captures images across a wide range of wavelengths, may detect subtle alterations in muscle tissue composition, such as changes in the concentration of specific proteins or the accumulation of fatty deposits, which are hallmarks of muscular dystrophy progression. Additionally, *polarization imaging* can assess the birefringence of muscle fibers, providing information about the organization of contractile proteins and the degree of muscle damage, potentially aiding in identifying and characterizing different muscular dystrophies. These techniques, among others, will be explored throughout this thesis to evaluate their potential for improving the diagnosis and follow-up of muscular dystrophies, leading to earlier diagnosis and more effective disease monitoring.

[1] The complete definition of a rare disease according to the European Commission is available here.

[2] Specifically, the NIH states that a rare disease must not affect over 200000 people in the US, and the calculation was estimated with 325 million inhabitants. More information on the NIH's definition is available here.

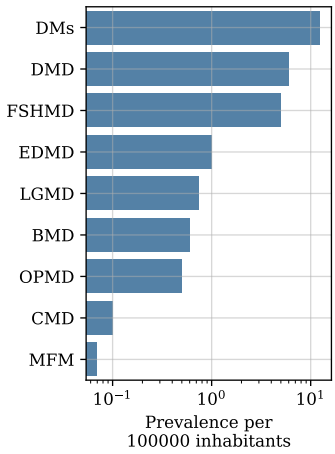

Figure 1: Prevalence of the most common dystrophies per 100000 inhabitants. DMs = Myotonic dystrophies. DMD = Duchenne muscular dystrophy. FSHMD = Fascioscapulohumeral muscular dystrophy. EDMD = Emery-Dreifuss muscular dystrophy. LGMD = Limb-girdle muscular dystrophy. BMD = Becker muscular dystrophy. OPMD = Oculopharyngeal muscular dystrophy. CMD = Congenital muscular dystrophy. MFM = Myofibrillar myopathy.

Objectives of this work

This PhD dissertation aims to explore the potential of advanced optical imaging techniques for the diagnosis and monitoring of muscular dystrophies. As previously introduced, these diseases encompass a group of inherited disorders characterized by progressive muscle weakness and degeneration, leading to significant physical disabilities and reduced quality of life. Current diagnostic methods often rely on invasive procedures or have limitations in terms of sensitivity and specificity. This research seeks to address these limitations by investigating the capabilities of non-invasive optical imaging modalities to provide detailed information about muscle structure, composition, and function.

While some individual optical techniques have shown promise in various biomedical applications, others, along with their combined use for characterizing muscle pathology in muscular dystrophies, represent a novel approach in this field. This research will utilize a unique dataset of ex vivo mice skeletal muscle tissue with and without muscular dystrophies, allowing for a detailed investigation of the optical properties associated with healthy and diseased muscle, contributing to both the field of optical imaging and muscular dystrophy research.

The primary objective of this work is to evaluate the feasibility and efficacy of four specific optical imaging techniques – intensity and polarization-sensitive optical coherence tomography (OCT/PS-OCT), hyperspectral Imaging in two different spectral ranges, visible-near infrared (HSI-VISNIR) and short-wave infrared (HSI-SWIR), spatial frequency domain imaging (SFDI), and multispectral Mueller matrix imaging MMI – for characterizing muscle pathology in muscular dystrophies. Each of these techniques offers unique advantages in terms of visualizing different aspects of muscle tissue.

By combining these complementary imaging modalities, this research aims to develop a comprehensive approach for assessing muscle health in muscular dystrophies. This involves not only visualizing the structural and compositional changes associated with the disease but also extracting quantitative parameters that can serve as potential biomarkers for diagnosis and disease monitoring. A final aspect of this work will be to develop a methodology for integrating the measurements obtained from the different techniques. This will involve creating visualizations that effectively represent the combined data and performing statistical analyses to evaluate the correlations and interdependency between the various parameters derived from each method. Furthermore, this work will explore the application of advanced image analysis techniques, including classification and machine learning algorithms, to enhance the diagnostic capabilities of these optical imaging methods. Ultimately, this research seeks to contribute to the development of non-invasive, accurate, and accessible diagnostic tools for muscular dystrophies, with the potential to improve early detection, personalized treatment strategies, and patient outcomes.

Document structure

This thesis uses optical imaging to improve the diagnosis of muscular dystrophies with the aim of providing new insights into muscle structure. Organized into six parts, it covers the clinical context, theory, methodology, results, and broader applications.

Part I: Introduction and Clinical Context

This part introduces the topic of muscular dystrophies and lays the groundwork for the research presented in the thesis. It provides essential background information on the clinical aspects of muscular dystrophies and the current state of diagnostic methods.

- Chapter 1: Muscular Dystrophies: A Cellular and Clinical Overview: This chapter provides a comprehensive overview of muscular dystrophies, starting with the cellular anatomy of different muscle types. It then focuses on the classification and characteristics of various dystrophies. The chapter follows with a discussion of the current gold-standard diagnostic methods and biomarkers used in clinical practice. Finally, it introduces the concept of using optical imaging techniques for MD diagnosis, providing a brief overview of different optical methods, categorized by their underlying principles: intensity-based, spectrum-based, and phase-based.

Part II: The Behavior of Light

This part provides the necessary theoretical background on the physics of light and its interaction with matter. All the content in this part conforms to a comprehensive summary of the fundamentals of electromagnetism and light-matter interactions and was included based on the content already existing in reference textbooks. Readers familiar with these concepts may choose to skip this part and proceed directly to the description of the optical imaging techniques.

- Chapter 2: Light propagation in uniform and non-uniform media: This chapter covers the fundamental principles of light propagation, including Maxwell's equations, wave behavior in different media, and light-matter interactions. It discusses concepts such as refractive index, reflection, refraction, and absorption.
- Chapter 3: Light polarization: This chapter delves into the concept of light polarization, explaining different polarization states and how they can be represented using Jones and Mueller matrix formalisms. It also discusses the polarization properties of various optical elements, as well as multiple matrix decomposition methods.

Part III: Materials and Methods

This part details the experimental setups, imaging techniques, and analysis methods used and developed in this research. It provides a comprehensive description of how the data was acquired, processed, and analyzed.

- Chapter 4: Optical Imaging Technologies: This chapter describes the optical imaging techniques employed in the study: OCT, PS-OCT, HSI, SFDI and MMI. For each technique, the chapter covers the fundamental principles, instrumentation, and relevant optical properties.
- Chapter 5: Analysis of Optical Imaging Measurements: This chapter outlines the methods used to analyze the acquired optical imaging data. It covers signal denoising, spectral data compression, Monte Carlo simulations for deriving optical properties, visualization, and classification methods.

Part IV: Results and Discussion

This part presents the main findings of the research, including experimental results, data analysis, and interpretation. It focuses on the application of the used optical imaging techniques to dystrophic mice muscles and the insights gained from analyzing the data.

- Chapter 6: OCT and PS-OCT measurements of dystrophic mice muscles: This chapter presents the results obtained from OCT and PS-OCT imaging of muscle tissue in dystrophic mice. It includes a description of the samples and an overview of the measurements. It further analyzes specific parameters derived from the images, such as attenuation and birefringence.
- Chapter 7: HSI and SFDI measurements of dystrophic mice muscles: This chapter focuses on the results from HSI and SFDI imaging of the same muscle tissues. It analyzes HSI reflectance, color reconstruction, scattering and absorption properties, and chromophore concentrations. It also examines SFDI reflectance, scattering, and absorption characteristics decoupled with this technique.
- Chapter 8: Multispectral Mueller-matrix imaging of dystrophic mice muscles: This chapter presents the results from multispectral Mueller-matrix imaging. It describes the sample preparation and dataset used for this technique, analyzes the Mueller matrices, and discusses matrix decomposition methods. It further explores the importance of specific Mueller matrix elements through different methods for feature extraction and tissue identification.
- Chapter 9: Combination of optical imaging data from different modalities: This chapter explores the integration of data from the different optical imaging techniques. It presents visualization methods to represent the combined data effectively and discusses the statistical evaluation of the parameters derived from each method. The chapter also introduces a first approach to the created dataset's performance on classification tasks. This integrated analysis aims to provide a more comprehensive understanding of muscle pathology in muscular dystrophies.

Part V: Related Work

This part explores the application of optical imaging techniques in fields beyond muscular dystrophy. It highlights the versatility of these methods and their potential for broader impact in different research areas.

- Chapter 10: Optical imaging in other fields of research: This chapter provides a brief overview of how optical imaging is being used in other fields, including ophthalmology, archaeology, bioengineering, and neuroscience. It discusses specific examples and key findings from each field, demonstrating the diverse applications of these technologies.

Part 6: Final remarks

This concluding section synthesizes the findings from each chapter, connecting them to the fundamental aspects of the disease. The aim is to provide a comprehensive understanding of the presented optical technologies and their usage in muscular dystrophies, as well as to highlight their potential applications in the future.

Remaining document

After introducing the general conclusions of this work, the document finishes with a comprehensive summary of the thesis in Spanish and Galician, including the introduction, optical imaging techniques, and main results. It is followed by a list of publications produced during this PhD research, showcasing the dissemination of the findings to the scientific community.

References

[1] D. Verhaert et al.: "Cardiac Involvement in Patients With Muscular Dystrophies", *Circulation: Cardiovascular Imaging* **4**(1), 67–76 (2011). DOI: 10.1161/CIRCIMAGING.110.960740.

[2] E. Blaszczyk, J. Gröschel, and J. Schulz-Menger: "Role of CMR Imaging in Diagnostics and Evaluation of Cardiac Involvement in Muscle Dystrophies", *Current Heart Failure Reports* **18**(4), 211–224 (2021). DOI: 10.1007/s11897-021-00521-2.

[3] A. LaPelusa, R. M. D. Asuncion, and M. Kentris: "Muscular Dystrophy. [Updated 2024 Feb 26]. In: StatPearls [Internet]. Treasure Island (FL): StatPearls Publishing", https://www.ncbi.nlm.nih.gov/books/NBK560582/. Accessed: 20 March 2025. 2004.

Muscular Dystrophies: A Cellular and Clinical Overview

1

1.1 Muscular cell anatomy

Muscular dystrophies cause damage to various muscle cell types in different locations, resulting in diverse clinical presentations. While the symptoms of muscular dystrophies are evident on a larger scale, understanding muscle cell anatomy is crucial for visualizing the specific structures that may be damaged, replaced, or undergo necrosis when a patient develops a muscular dystrophy. This subsection provides a concise overview of each muscle cell type, detailing its structure, key chemical components, and physiological function.

Muscle cells, also known as *myocytes*, are classified into three distinct types: skeletal, cardiac, and smooth. Each type possesses unique structural, functional, and compositional characteristics that will be summarized in this section.

1.1.1 Skeletal muscle cells

Skeletal muscle cells (Fig. 1.1) form the muscular groups responsible for movement, posture, and breathing, including those in the limbs, back, chest, neck, and face. These highly anisotropic cells are composed of smaller, elongated structures called *myofibrils*, consisting of individual contractile units known as *sarcomeres*. Cellular organelles and multiple nuclei are located in the *sarcoplasm*, the cytoplasm of the muscle fiber surrounding the myofibrils [1].

Skeletal muscle fibers consist primarily of water (approximately 75%), distributed throughout the sarcoplasm, myofibrils, and organelles. Water plays essential roles in maintaining cellular structure, facilitating protein interactions, and serving as a medium for the transport and storage of various molecules [2]. The dry mass of skeletal muscle fibers is primarily composed of proteins, which are essential for their contractile, regulatory, and structural activities (Fig. 1.2). *Actin* and *myosin* are the main proteins of the sarcomere, enabling muscular contraction. Regulatory proteins, such as *troponin* and *tropomyosin*, control the interaction between actin and myosin. Structural proteins, including titin and nebulin, provide a framework that supports and aligns the contractile and regulatory proteins essential for muscle contraction. Skeletal muscle cells store energy primarily as *glycogen* (a complex carbohydrate), while ions like calcium, sodium, and potassium play crucial roles in regulating muscle contraction [3]. Skeletal muscle fibers are wrapped in a protective layer called the sarcolemma. Many fibers bundle together into larger groups called *fascicles*. These fascicles, along with blood vessels and nerves, combine to form the muscle itself. Each level of organization - the fiber, fascicle, and whole muscle - is encased in a rugged, flexible connective tissue sheath made primarily of collagen and elastin [4].

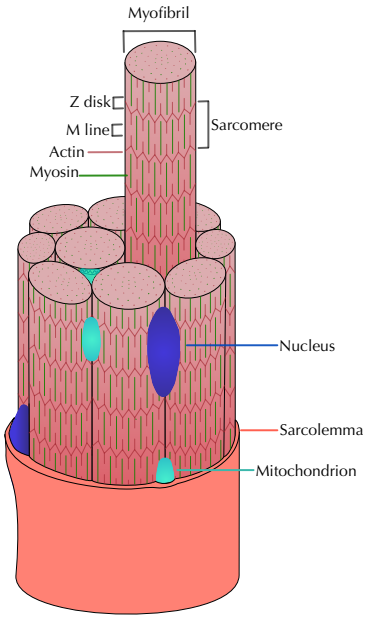

Figure 1.1: Schematic of a skeletal muscle cell (myocyte).

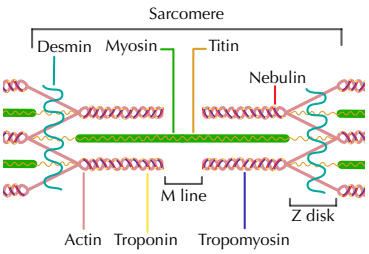

Figure 1.2: Structure of a sarcomere (individual contractile unit of a striated muscle cell) and its main proteins.

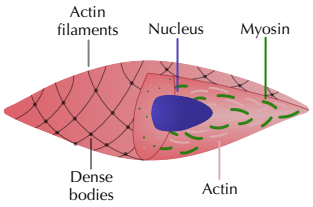

Figure 1.3: Structure of a smooth muscle cell (SMC) and its main proteins.

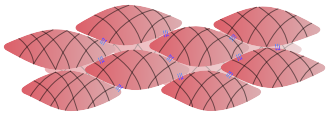

Figure 1.4: Connection between multiple SMCs. The junctions are illustrated in blue.

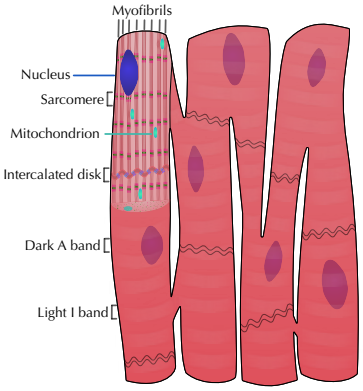

Figure 1.5: Structure of a cardiomyocyte. Multiple cardiomyocytes connect through the intercalated disk, which contains gap junctions. The dark A band corresponds with the protein regions of sarcomeres (Fig. 1.2), while the light I band corresponds with the areas where the Z disks align (Fig. 1.2).

1.1.2 Smooth muscle cells (SMCs)

Smooth muscle cells (SMCs) surround blood vessels and hollow organs, such as the intestines and stomach, to facilitate essential functions like blood circulation, digestion, and nutrient absorption [5]. Their main function is to contract, which enables the movement of substances through the structures they are attached to, ensuring proper physiological function [6]. As such, their contraction is involuntary and continuous.

Similarly to the skeletal muscle cells, SMCs are formed of filaments, including actin, tropomyosin, or myosin [6], that stabilize the cell during contraction. However, the structure of skeletal muscle cells is vastly different from that of skeletal muscle cells in that they are not arranged via sarcomeres. Instead, SMCs are surrounded by actin networks that contract the whole cell in all directions when needed (Fig. 1.3). *Dense bodies* are anchoring points within each cell, allowing the forces generated by the actin network to be transmitted efficiently and uniformly throughout the cell body. These forces are also anchored to the cell's exterior through dense plaques [7], which contain *desmin*—another protein that helps maintain the structural and mechanical integrity of the cells and that is also present in the *Z disk* of skeletal muscle cells [8], depicted in Figs. 1.1 and 1.2. Multiple cells connect to each other primarily through *adherens junctions* and *gap junctions*, both of which anchor the cells together, enable coordinated contractions across smooth muscle tissue [9, 10], and form the three-dimensional structures that surround vessels and organs (Fig. 1.4).

1.1.3 Cardiac muscle cells (cardiomyocytes)

Cardiac muscle cells, also known as cardiomyocytes (Fig. 1.5), form the walls of the heart and are responsible for generating the contractions that pump blood throughout the body. The contraction of these branched, anisotropic cardiomyocytes allows for the coordinated propagation of electrical waves, which initiate and synchronize the heart's movements [11].

The structure of cardiomyocytes shares similarities with skeletal myocytes, especially in the presence of actin and myosin filaments organized into myofibrils and sarcomeres. However, cardiomyocytes also have unique features. They are branched and interconnected, forming a complex network. Desmin is also present in cardiomyocytes, and it provides structural support by linking myofibrils and other cellular components within the cardiomyocyte. The entire cell is enveloped by the sarcolemma, which interacts with the extracellular matrix through a specialized group of proteins [12].

Calcium ions play a central role in triggering cardiomyocyte contraction. An electrical signal initiates calcium influx across the cell membrane, further amplified by calcium release from the sarcoplasmic reticulum, the network of interconnected membrane-bound sacs and tubules that extends throughout the sarcoplasm. This increment in intracellular calcium binds to troponin, allowing myosin to interact with actin and generate the power stroke that shortens the sarcomere, resulting in

contraction. Active removal of calcium from the cytoplasm leads to relaxation, resetting the cell for the next beat [13].

1.2 Types of Muscular dystrophies

Muscular dystrophies encompass a range of inherited diseases causing progressive muscle weakness and disability. These disorders share common pathological features, including muscle fiber necrosis and regeneration, variations in fiber size, and, in some cases, fiber splitting. The ongoing cycle of muscle damage and attempted repair ultimately leads to irreversible muscle loss, replaced by fatty and fibrous tissue [14].

This section explores various types of muscular dystrophy, their characteristic symptoms, and underlying causes. The specific *genes*[1] involved, *inheritance patterns*[2], and the impact of these genetic *mutations*[3] on muscle proteins are examined here as well. The observable changes in muscle tissue, as well as distinct biomarkers associated with each type, are also covered by this section. Furthermore, the typical age of onset and life expectancy for individuals with different forms of muscular dystrophy are also covered.

[1] Gene: a segment of DNA that carries the instructions for building and maintaining an organism, often by encoding for a specific protein [15].

[2] Inheritance pattern: describes how genes, and their different versions (alleles), are passed from parents to offspring, influencing the likelihood of inheriting specific traits [15].

[3] Mutation: a permanent change in the DNA sequence of a gene, which can alter the instructions it carries and potentially affect the resulting [15].

1.2.1 Duchenne (DMD) and Becker muscular dystrophies (BMD).

Duchenne and Becker muscular dystrophies (DMD and BMD, respectively) are both *X-linked*[4], *recessive*[5] disorders caused by mutations in a gene, the `DMD` *gene* that encodes dystrophin (i.e., dystrophinopathies). Dystrophin is a protein located in the sarcolemma which stabilizes the cell wall during muscular contraction and expansion by linking the cells to the extracellular matrix [16, 17]. The lack (DMD) or a reduced amount (BMD) of dystrophin leads to the cell's inability to keep up with muscular movements. As a consequence, the sarcolemma goes through consistent microfractures that contribute to the muscular fiber's replacement with adipose tissue (i.e., fat infiltration) or fibrotic tissue (i.e., collagen and elastin increment) [18, 19].

[4] X-linked: genetic condition caused by a mutation in a gene on the X chromosome. Males, having only one X chromosome, are more likely to be affected by the condition if they inherit this mutation [15].

[5] Recessive inheritance: defines genetic traits that only appear if an individual inherits two copies of a gene, one from each parent [15].

Dystrophin is also present in brain tissue. Although its presence is only 1% of that in muscles, mutations in the DMD gene also lead to slight cognitive impairment [20]. Aside from muscle cells, a lower background level of dystrophin is also present in most tissues [20], specifically in vascular smooth cells, which can, in turn, lead to a deficiency in vascularization that makes muscular recovery after fibrous fractures even less effective [21]. The sarcolemma fractures lead to first inflammation, then fatty replacement, and finally fibrosis in DMD that transforms healthy muscle into larger (hypertrophy) but less functional muscle mass, especially in the lower limbs [17]. These deficiencies lead to loss of strength and ambulation capabilities at first and later evolve into respiratory and cardiac insufficiency [22], the main causes of death in DMD patients [23]. In BMD, the clinical pattern is similar but usually less severe and appears later in life [22].

Given that DMD and BMD are both X-linked dystrophies, they are mainly present in the male population. Specifically, DMD is the most common

type of early-onset MD [20] as affects 1 in 3000-5000 male births with a prevalence of 6 in 100000 [18, 22–25], while BMD is approximately 10 times less common [18]. DMD patients' life expectancy has been recently estimated to be over 25 years [23], with a median of 24 years [18], while BMD patients live longer, even without symptoms until middle age [22]. Although rare, there have been a small number of female cases reported, and female DMD carriers might have symptoms similar to those of BMD [26] or present cardiomyopathy-related issues [18]. These numbers[6] set DMD as the most studied MD[7] , with over 4600 journal articles focusing on it and just over 700 for Becker's.

[6] This chapter includes multiple side notes with links to Web of Science searches. Said searches were last accessed in December 2024. Direct access through the links requires institutional access.

[7] Web of Science searches **TI=(Duchenne muscular dystrophy) AND DT=(Article)** and **TI=(Becker muscular dystrophy) AND DT=(Article)**, available here and here, respectively.

1.2.2 Emery-Dreifuss muscular dystrophy (EDMD)

Another kind of MD is Emery-Dreifuss muscular dystrophy (EDMD), typically inherited as an X-linked recessive trait (EDMD1 or X-EDMD) or as a rarer *autosomal*[8] *dominant*[9] (EDMD2 or AD-EDMD) form [18, 22, 27]. However, there are other less common variants [28]. The recessive variant is caused by a mutation in the gene that codes for emerin (`EMD`), while the AD variant affects the gene that codes for lamins A and C (`LMNA`)[22]. Unlike dystrophin, emerin is a protein of the nuclear membrane that stabilizes the nucleus inside skeletal muscle cells and acts as extra support during muscle contraction [29, 30]. Lamins A and C are also involved in nuclear positioning by modifying the contractile properties of the nucleus under mechanical strain [29].

[8] Autosomal: refers to traits or genes located in the non-sex chromosomes [15].

[9] Dominant inheritance: defines genetic traits that appear if an individual inherits at least one copy of a gene [15].

EDMD presents itself initially as contractures, typically in the Achilles tendons and the elbows, with variable intensity levels that increase in severity in the second decade [31]. In AD-EDMD, the biceps and quadriceps are more affected and weak than in X-EDMD in the early years, and contractures start appearing later in life [32]. Muscular problems often lead to cardiac issues, which are more predictable in the case of X-EDMD than in AD-EDMD[31], and to loss of ambulation in the case of AD-EDMD[32].

EDMD is less common than DMD[10], with a prevalence of 1 in 100000 [22], although AD-EDMD's exact prevalence is unknown due to the few cases reported [33]. X-EDMD is present mainly in the male population, but female carriers have been identified with a similar cardiac pattern to that of X-EDMD patients [27].

[10] 267 articles identified through the Web of Science search **(TI=(Emery Dreifuss muscular dystrophy) OR TI=(Emery Dreifuss)) AND DT=(Article)**, available here.

1.2.3 Fascioscapulohumeral muscular dystrophy (FSHMD)

The gene affected in Fascioscapulohumeral muscular dystrophy (FSHMD) is the `DUX4` gene, which encodes for the double homeobox 4 protein, a *transcription factor*[11] [34]. The `DUX4` gene is present during embryonic development and gets silenced in most tissues, including muscle cells, after this early stage. However, in patients with FSHMD, the `DUX4` gene is over-expressed in muscle cells, leading to transcription irregularities, cell toxicity, myocyte death, or immune responses [35, 36].

[11] Transcription factor: protein that controls the rate of gene transcription, the process of copying a DNA sequence into an RNA molecule, by binding to DNA [15].

Physiologically, FSHMD is subject to loss of muscle mass and strength, muscular replacement with fat and fibrotic tissues, and inflammation

[36]. Specifically, FSHMD initially affects the facial muscles, along with the shoulder and upper arm, and progresses to the abdomen, lower limb, and pelvic girdle muscle weakness [34]. Although FSHMD can cause different levels of loss of ambulation, it has been established that this disease does not affect the life expectancy of the patients [22, 34, 37].

In Europe, FSHMD prevalence has been established to be between 5 to 12 per 100000 inhabitants [34], and 5 in 100000 worldwide [38], making one of the most frequent MDs[12]. The onset age for this disease is variable, but usually within the second decade of life [34]. While there are variations in prevalence and genetic subtypes, the overall impact of FSHMD is not restricted to any specific population [37].

[12] 698 articles identified in Web of Science through the search **(TI=(facioscapulohumeral muscular dystrophy) OR TI=(facioscapulohumeral)) AND DT=(Article)**, available here.

1.2.4 Limb-girdle muscular dystrophy (LGMD)

Limb-girdle muscular dystrophies (LGMD) comprise a diverse group of inherited muscle disorders primarily impacting the shoulder and hip muscles[13] . These diseases lead to progressive weakening of proximal limb muscles, with potential involvement of the heart and respiratory system. The clinical presentations of LGMD vary widely, reflecting the broad genetic and phenotypic heterogeneity of these conditions [39, 40].

[13] 1068 articles identified in Web of Science through the search **(TI=(limb-girdle muscular dystrophy) OR TI=(limb-girdle)) AND DT=(Article)**, available here.

The inheritance patterns of LGMD are diverse and include autosomal dominant and recessive variants, further contributing to clinical heterogeneity of limb-girdle muscular dystrophies. As of 2016, 31 distinct *genetic loci*[14] have been identified [39], with eight autosomal dominant and 23 autosomal recessive, each impacting a different gene and its corresponding protein product.

[14] Genetic locus: the specific physical location of a gene or other DNA sequence on a chromosome [15].

Autosomal dominant LGMDs typically disrupt structural and support proteins like myotilin, lamin A/C, and desmin, crucial for muscle integrity. In contrast, autosomal recessive AR-LGMDs impact a wider range of proteins essential for muscle function, including calpain, dysferlin, sarcoglycans, titin, and desmin [39]. These recessive forms encompass diverse subtypes like calpainopathies, dysferlinopathies, and sarcoglycanopathies, affecting components like the contractile apparatus, nuclear lamina, and sarcolemma [40].

Limb-girdle muscular dystrophies manifest diversely, with possible distal or proximal weakness, muscle inflammation, cardiomyopathy, and respiratory issues. Additional symptoms can include calf changes, scapular winging, limb weakness, dysphagia, and limited finger/toe flexion. Some cases exhibit brain, eye, or spinal anomalies, alongside intellectual disability [39, 40].

The onset and progression of LGMD vary widely, from severe and fatal to mild with near-normal lifespans, with onset ranging from early childhood to late adulthood depending on the type [39]. AR-LGMD is far more common than AD-LGMD, with a prevalence of 1:15000 for the autosomal recessive variant, compared to only 10% of all LGMD cases for the autosomal dominant one [39, 41], which implies a prevalence of 1:135000 cases. Some types are globally distributed, while others are concentrated in specific regions [40].

1.2.5 Congenital muscular dystrophy (CMD)

Similarly to LGMDs, *congenital*[15] muscular dystrophies (CMDs) encompass a spectrum of diverse phenotypes unified by their early onset of muscular weakness, neonatal low muscle tone (hypotonia), and characteristic dystrophic lesions on muscle biopsies [42]. The main difference between CMDs and other childhood-onset MDs like Duchenne's is that CMDs traits are visible even before the first year of life, with symptoms showing almost immediately after birth. Although its presence in the population is not precisely known, it has been estimated at a prevalence of 1 per 1000000 [42, 43], and the inheritance pattern is primarily autosomal recessive [44].

The expanding list of CMDs[16] has led to a proposed classification based on the types of genes affected: those encoding structural proteins of the basal lamina or extracellular matrix (including collagen), those involved in *glycosylation*[17], those causing abnormalities in nuclear envelope proteins, in proteins of the endoplasmic reticulum, or the mitochondrial envelope structure [45].

The gene-related defects of CMDs lead to a deficiency of the involved proteins, which macroscopically manifest as muscular weakness, intellectual disability, along with contractures of shoulders, elbows, or knees [43, 45]. However, the symptoms of a CMD do not tend to evolve fast [43]. It has been found that in CMD muscles tend to show abnormal variations in fiber size when biopsied, and MRI findings of the brain indicate white matter involvement through an increment on the T2-weighted modality signal with respect to healthy brain[18] [43].

[15] Congenital: present at birth.

[16] 1040 articles identified in Web of Science through the search **(TI=(congenital muscular dystrophy) OR TI=(congenital dystrophy)) AND DT=(Article)**, available here.

[17] Glycosylation: the process of attaching sugars to proteins or lipids.

[18] Details on T2-weighted imaging are included in section 1.3.

1.2.6 Myotonic dystrophies types I (DM1) and II (DM2).

Myotonic dystrophies (DMs) are particularly interesting due to their genetic origin. Contrary to most dystrophies, myotonic dystrophies are not related to protein-encoding regions of genes [46], meaning that, while related to protein genes, DMs are not directly affecting how the protein is created, but instead they deregulate how RNA behaves. There are two types of myotonic dystrophies, namely DM1 and DM2, that are associated with mutations at two different non-coding regions of RNA, both caused by the repetition of unstable RNA sequences [47]. While inherited in an autosomal dominant fashion[48], the size of the repetition determines if the symptoms are visible at birth (congenital), in childhood, as an adult, or later in life [49]. DM1 is caused by an expansion in the CTG *nucleotide pattern*[19] of the `DMPK` gene (involved in intercellular communication), while DM2 is originated by an expansion of the `CCTG` nucleotide pattern of the CNBP gene (related to *DNA-RNA binding*[20]) [47, 48, 50]. As the proteins themselves are not affected by the length increment of the affected RNA, it is believed that the remaining multiplied RNA forms clumps inside of the cell that induce cell toxicity, leading to the different symptoms of DM1 and DM2 [46].

There are several symptoms related to DMs, including muscular weakness and atrophy, myotonia, pain or myalgia, respiratory and cardiac deficiencies, overall fatigue, hearing loss, early-onset cataracts, endocrine disorders, elevated serum creatine kinase[21], and even higher predisposi-

[19] Nucleotide pattern: refers to a specific sequence of nucleotides in DNA or RNA.

[20] DNA-RNA binding: refers to the interaction between DNA and RNA molecules, often facilitated by proteins that can bind to both types of nucleic acids.

[21] Creatine kinase: an enzyme found in muscles that enables muscular energy production.

tion for cancer [47–50]. Those symptoms have been found in patients with a prevalence of over 1 in 8000 [50], with variable geographical presence [48].

The fact that these diseases are the most commonly inherited form of muscle disorders [48] and that are not immediately lethal might have contributed to the increment of studies published regarding MDs in recent years. Specifically, studies published on these diseases per year between 2017 and 2023 (average of 132 studies/year) are almost twice those that were published between 2001 and 2007 (average of 69 studies/year)[22].

[22] 4675 articles identified in Web of Science through the search **(TI=(myotonic dystrophy) OR TI=(myotonic dystrophies) or TI=(dystrophia myotonica)) AND DT=(Article)**, available here.

1.2.7 Oculopharyngeal muscular dystrophy (OPMD)

As occurred with DMs, oculopharyngeal muscular dystrophy (OPMD) is caused by mutations in the `PABPN1` gene due to short *repeats*[23] of GCN nucleotide triplets, where N could be any of the bases [51]. The repeat also leads to the accumulation of clumps inside the nucleus of muscle cells, named intranuclear inclusions, that result in cell death [52].

[23] Nucleotide repeats: short DNA sequences that are repeated a number of times in a row.

Although OPMD shows similar traits to other muscular dystrophies, the first characteristic these patients present is *ptosis*, a weakness of the upper eyelid causing them to drop, followed by *dysphagia*, which is trouble swallowing [51–53]. These symptoms start showing later in life, mainly during the fifth or sixth decade [53]. In diagnosis, these symptoms are complemented with high serum creatine kinase, with the amount being dependent on the severity of the case, and with fatty replacement of muscles, specifically the tongue and lower leg muscles [54].

OPMD is present[24] in multiple populations of the world with variable prevalence, being less common in the European population (0.13 per 100000 inhabitants in Northern England [55] and 1 in 100000-1000000 in Europe [54]), and more common in Israel (1 in 600 [54]) or in French-Canadians (1 in 1000 inhabitants [54]), with both autosomal dominant and recessive pathways being possible.

[24] 410 articles identified in Web of Science through the search **(TI=(oculopharyngeal muscular dystrophy) OR TI=(oculopharyngeal dystrophy) or TI=(oculopharyngeal) or TI=(oculo-pharyngeal)) AND DT=(Article)**, available here.

1.2.8 Myofibrillar myopathy (MFM)

Myofibrillar myopathy is a disease caused by alterations in proteins of the Z disk (Fig. 1.2) that lead to myofibril deterioration [56]. Many mutations in genes encoding proteins have been found to cause MFM, including those in desmin, lamin A/C, $\alpha\beta$-crystalin, titin, sarcoglycans, or dystrophin, among others [57]. Given the overlap in gene mutations between MFM and other dystrophies, MFM can also appear accompanied by other MDs. The field of MFMs is not extensive and continues to grow[25]. Therefore, the exact prevalence of MFM is not known and varies with the population (0.07 per 100000 inhabitants in Northern England [55]). However, it appears that most forms of MFM are transmitted in an autosomal dominant manner, although there are autosomal-recessive or X-linked forms as well [58].

[25] 137 articles identified in Web of Science through the search **(TI=(Myofibrillar myopathy)) AND DT=(Article)**, available here.

The similarity of MFM with other MDs in terms of genetic mutations also implies similar symptoms, and the onset age varies between early childhood and late adulthood [58]. This overlap leads to a complicated

diagnosis, and the main way to detect the destruction caused to the Z disk (Fig. 1.2), characteristic of MFM, is based on muscle biopsy [59].

1.3 The gold standard: Diagnostic methods and biomarkers

Genetically induced sub-cellular defects in muscular dystrophies manifest in two primary macroscopic changes. First, structural proteins in skeletal, cardiac, or smooth muscle, or even the brain, are disrupted, leading to alterations in those tissues. Some structures may become enlarged (hypertrophy), while others shrink (atrophy) with impaired function. Both scenarios can result in cell death and necrosis. Second, these structural changes often coincide with chemical imbalances throughout the body. These might stem directly from the mutation (altered protein production) or arise from the breakdown of healthy and necrotic tissue, often accompanied by increased fat or extracellular matrix deposition.

Consequently, diagnosing MDs involves more than just genetic testing or histopathology. Functional testing, electromyography (EMG), electrocardiography (ECG), and imaging techniques often play a crucial complementary role. This section outlines the most common diagnostic methods utilized for MDs.

1.3.1 Observational diagnosis

All muscular dystrophies lead to some degree of movement impairment, whether it is evident at birth or emerging later. Thus, a simple physical examination can sometimes reveal signs of MDs. Specifically, enlarged calf muscles (hypertrophy) are common in DMD, BMD or some subtypes of LGMD, whereas reduced muscle mass (hypotonia) is seen in CMD, EDMD or FSHMD patients. Lower limb muscle involvement is also typical in FSHMD and OPMD, while FSHMD may also affect the upper limbs. Even facial muscles can exhibit symptoms. All these muscular issues result in weakness during walking, standing, lifting arms, or general movement, all of which can be assessed with a basic clinical assessment. For example, Gower's sign, characterized by difficulty rising from a sitting or squatting position, indicates weakness in the lower limbs and pelvic girdle and has been observed in nearly every type of MD [60]. Additional symptoms, such as respiratory or cardiac insufficiency, may be initially detected using a stethoscope.

1.3.2 Diagnosis from samples

Beyond physical examinations, blood and muscle tissue samples offer crucial information for definitively diagnosing muscular dystrophy.

Serum creatine kinase Blood samples can be utilized two-fold for the diagnosis of MDs. Specifically, serum creatine kinase levels (CK) can provide information about the stage of the disease. One indicator standard in many muscular dystrophies is the presence of elevated values of CK in blood serum. Creatine kinase is a protein present in high amounts in muscle, especially in the myocardium, but also in skeletal muscle and even in the brain [61]. Therefore, any process that breaks the sarcolemma may induce the travel of CK to the bloodstream, leading to an increase with respect to normal levels. Although normal processes like heavy exercise, trauma, or surgery may increase serum CK [61–63], it is well known that the disruption of muscular and neural tissue caused by MDs can be detected by screening blood samples for high CK levels [64].

Genetic testing The other use for blood samples in MDs is genetic testing. Due to the high amount of overlap between symptoms of the different MDs, the only way to tell for sure which pathology the patient has is through genetic testing. Single- or multiple-gene *sequencing*[26] can be applied to the diagnosis of muscular dystrophies to confirm the suspicions of one specific dystrophy or to know if there is more than one gene involved in the patient's phenotype. The most commonly used ones are Sanger sequencing, next-generation sequencing (NGS), and multiplex ligation-dependent probe amplification (MLPA) [66].

[26] Gene sequencing: the method used to determine the order of the DNA nucleotides [65].

Sanger sequencing involves cutting a *template*[27] DNA and using modified bases (ddNTPs) to identify individual base positions on the template DNA of interest [68]. Although this method is highly accurate for small sections, it is slow and costly for larger ones. MLPA, on the other hand, can examine multiple DNA sections simultaneously, using probes to detect extra or missing DNA pieces [69]. Next-Generation Sequencing (NGS) technologies, like Nanopore [70, 71], Pacific Biosciences [72], and Illumina [73], have improved sequencing speeds. Nanopore utilizes nanopores and electrical currents for direct, long-read sequencing [70], while Pacific Biosciences employs fluorescently labeled bases for real-time analysis by copying the DNA strand with a DNA *polymerase*[28] [72]. Illumina uses a complex preparation phase involving proprietary, surface-modified flow cells and clusters of DNA copies performed on said cells via thermally induced unions. Its imaging-based approach allows parallel processing of billions of templates, significantly accelerating sequencing [74]. The human genome project, which used exclusively Sanger sequencing due to it being the only method available, took almost 15 years to sequence the entire human DNA [75], while using Illumina's method could provide whole genome sequencing in a day.

[27] Template: A strand of RNA or DNA used for replication of new RNA/DNA strands [67].

[28] DNA Polymerase: the enzyme capable of synthesizing DNA [65].

Muscular biopsies Although genetic testing remains the only possible way to precisely identify what gene has the mutation related to one of the many dystrophies, it is worth noting that overlapping phenotypes still pose a challenge for accurate muscular dystrophy identification, especially in those with many variants, like LGMDs or CMDs [76]. Additionally, serum CK levels can tell that there is some muscular degeneration, but not where in the body it is happening or whether it definitely comes from a muscular disorder since it can also be caused by muscular strain and it varies significantly between populations and ethnicities [63, 77].

As an alternative, muscle biopsies can be valuable for identifying specific muscular dystrophy subtypes, assessing muscle damage severity, and even conducting genetic testing as well.

Given the highly structured morphology of muscle tissue, skeletal muscular biopsies of healthy individuals look like uniform patterns of fibers with the nuclei on the periphery [78]. On the contrary, dystrophinopathies (DMD, BMD, MFMs...) tend to show uneven fiber size and an increase in internal nuclei, as well as the presence of necrotic or regenerated patches [79, 80]. Nuclear envelope disorders (X-EDMD, FSHMD) show loss of some nuclear membranes and channel formation inside the nuclear matrix [81], and hindered interaction with nuclear-related proteins [82, 83], or even intranuclear inclusions like in the case of OPMD [52].

Minimally invasive biopsies (needle- or punch-based) offer reduced patient discomfort but can be trickier in terms of sample orientation and size. Open biopsies, while providing more control over the sampled area, are more invasive and less suitable for frequent use [78].

1.3.3 Specialized diagnosis

The diagnosis of MDs can be complemented and better understood with the use of specialized tools that provide insight into the stage of the disease. More precisely, several diagnostic methods based on muscular electrical performance or imaging are often applied to the diagnosis and the follow-up of MD patients.

Electromyography (EMG) Neuromuscular disorders change how muscles work, and their structural differences and effects can be seen, for example, in electromyography (EMG) signals. EMG operation is based on inserting needles into the muscles under study. Then, by instructing the patients on a series of relaxation-contraction movements, muscles release their electrical currents, captured in terms of the sample rate chosen a priori. EMG measures a magnitude called *motor unit potential* or MUP that defines the amplitude and phase of the electrical currents that make muscles contract and relax.

Thus, the analysis of EMG data can discern if a muscle is healthy or affected by a disorder. Nonetheless, it is worth noting that the choice of analysis method can drastically impact its diagnostic value [84]. When assessing muscle damage, the quantitative variant of EMG has been proven helpful to distinguish between different stages of the disease and even its progression throughout the various muscle groups involved in FSHMD, LGMD and BMD [85]. Specifically, it has been shown that the MUP signal can be more complex at the early stages of the disease due to the existence of multiple changes in fiber size caused by degeneration/regeneration patterns, while the loss of amplitude in MUP at later stages could be an indicator of muscular fiber loss [85].

Even when the diagnosis is already known, EMG can also be used to provide an objective metric to common muscular dystrophy symptoms, like the quantification of the degree of dysphagia, although further research has been suggested to confirm these claims [86]. A significant difference between EMG results was also found when studying DM1 and

DM2 patients, at least for an initial diagnosis [87]. While EMG needles penetrate only about 1 cm, surface EMG, using taped electrodes, offers a non-invasive alternative with promising results in assessing DMD presence and severity [88].

Electrocardiography (ECG) More often than not, the heart's musculature is also damaged by muscular dystrophies, which makes ventricular failure one of the principal causes of death in MD patients [22]. When cardiac involvement is present or suspected, conventional electrocardiograms (ECG) are the main tool of choice for fast and periodic evaluation. Less invasive than EMG, ECG is performed by placing electrodes on the skin near the heart to record the electrical signals it generates. In a recent review by L. Tang *et al.* [89], several common features were found in DMDs patients of different ages and ethnicities. For example, the authors found that multiple articles reported unusual *Q waves* and increased amplitude on the *R waves*[29], both involved in describing the electrical behavior of the heart's ventricles [89]. They also report the common *sinus tachycardia* and shortened *PR interval*[30] in DMD patients, meaning that the heart was often beating faster than in healthy individuals and that the electrical signals between the atria and the ventricles were also traveling faster [89].

Atrial and ventricular arrhythmias, electrical conduction abnormalities, and ventricular hypertrophy have also been found across multiple studies of myotonic dystrophies, as reported by D. McBride *et al.* [91]. Specifically, DM1 patients are more prone to ECG abnormalities than DM2 [91]. Other muscular dystrophies have also been assessed with ECG, like the limb-girdle type, which showcased a low prevalence of conduction delays, or the fascioscapulohumeral type, whose patients had ECG parameters within normal limits [92].

Ultrasound (US) Imaging technologies provide an additional point of view that can complement the previously described diagnostic technologies by indicating the extent of muscle damage in the studied areas. Ultrasound (US) modalities are basic staples of muscular dystrophy diagnosis, specifically when focusing on skeletal muscle (echomyography) or the heart (echocardiography) (Fig. 1.6). In general, the core principle of ultrasound lies in the varying ways that different tissues interact with the sound waves the USs devices produce. Some tissues reflect the waves strongly, creating bright areas in the resulting image, while others allow the waves to pass through, resulting in darker areas [93].

US: Echomyography Two main approaches in muscle ultrasound, namely the grayscale level (GSL) and quantitative backscattering analysis (QBA), have been proven helpful for DMD diagnosis [94]. GSL measures the intensity of the recorded US image, and an increment in brightness[31] can be an indicator of muscle damage and inflammation [95]. On the other hand, QBA focuses on obtaining tissue parameters from the backscattered US signal by analyzing it according to the sound waves-tissue interactions. Both magnitudes have been monitored over time in healthy and DMD skeletal muscles and have been found to increase faster in the latter, leading to earlier deterioration detection when compared to using only

[29] QRS Wave complex: represents the electrical depolarization behavior of the heart's ventricles. The Q and R waves relate to the depolarization of specific areas in the ventricles [90].

[30] PR interval: time interval between atrial depolarization and the first step of the QRS complex [90].

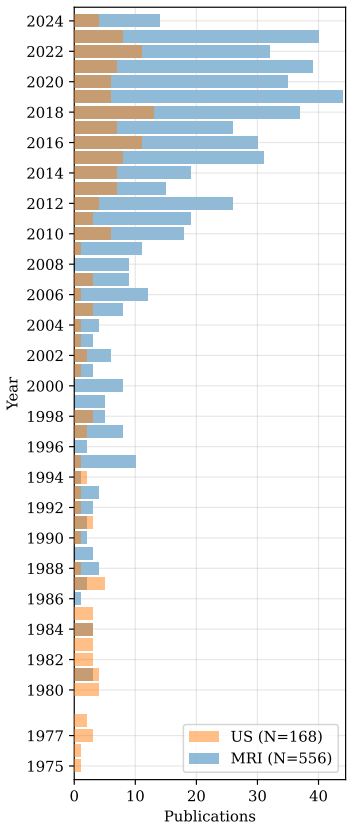

Figure 1.6: Number of indexed publications per year in Web of Science dedicated specifically to MD evaluation through either US or MRI. US: Ultrasound (Web of Science search available here); MRI: Magnetic resonance imaging (Web of Science search available here).

[31] Also known as *echogenicity*.

functional assessments [94]. However, in the same study, US was not able to detect corticosteroid effects related to dystrophy treatments. In OPMD, absolute echo intensity (AEI) was used to effectively detect muscle abnormalities through higher AEI values than those captured for healthy muscles, and to relate AEI increment over time to muscular deterioration [96]. Muscle ultrasound has also been proven useful for detecting characteristic imaging patterns in collagen 6-related muscular dystrophies from an early age [97]. A similar result was found in FSHMD [98] and DM1 patients [99], who showcased widespread echogenicity, even in asymptomatic patients and disease carriers.

US: Echocardiography Echocardiography was used in multiple studies as well, as compiled in the review by G. Song *et al.*, where they provided a meta-analysis about the usefulness of speckle-tracking echocardiography (STE) in DMD [100]. STE can be used to measure the strain the heart suffers by measuring the stretch and contraction properties in US images through the analysis of the same speckle points over time [101]. The review showed that several measures of myocardial strain were significantly decreased in children with DMD compared to healthy controls, indicating impaired heart function in DMD patients. Their findings suggest that STE can detect early signs of cardiac dysfunction in DMD, even before symptoms or other imaging techniques show abnormalities [100]. STE was also used to explain further the processes of cardiac involvement of some of the most common LGMD, revealing that not all sub-types of the limb-girdle affecting dystrophies deteriorate the heart in the same way [102]. Using echocardiography, ventricular geometry was found to be larger than usual in both types of EDMD with respect to healthy individuals, and often with lower capacity to pump blood than the latter as well [103].

Magnetic resonance imaging (MRI) Ultrasound plays a valuable role in evaluating muscular dystrophies, but magnetic resonance imaging (MRI) remains the preferred imaging technique for these conditions (Fig. 1.6). As previously introduced, many types of muscular dystrophies lead to enough muscular degeneration to cause inflammation, muscular replacement, and necrosis, all of which can be assessed with MRI [104]. Magnetic resonance imaging is based on the application of strong magnetic fields and radio frequencies to the patient's tissue. By analyzing the changes in molecular orientation caused by the strong magnets, different tissue types can be discerned, leading to three-dimensional images of the body with tissue-specific responses [105]. T1- or T2-weighted imaging, magnetic resonance spectroscopy (MRS), diffusion-weighted (DWI) and diffusion tensor imaging (DTI), or Dixon sequences are some of the MRI-based modalities that have been applied to MD evaluation [104].

MRI: T1- and T2-weighted imaging After being excited by the magnet, the molecules turn to their basal states. Specifically, the time required for protons to become aligned with the magnetic field, which is also the time they need to return to equilibrium, is known as the T1 or longitudinal relaxation time [106]. This type of imaging has been able to detect the level of cardiac involvement in DMD patients via higher T1 than for the controls, even with normal ventricular function [107], and to indicate

myocardial fibrosis as short T1 times in myotonic dystrophy patients [108]. T1 was also used for evaluating the progression of fatty infiltrations over a two-year period of FSHMD patients [109]. However, T1-weighted MRI needs to be referenced to the patient's bone marrow intensity in each frame, which is also subject to image inhomogeneities, making it not the ideal way to measure fat infiltrations [110].

Similarly to T1, T2-weighted imaging measures a relaxation time. Still, instead of referring to a single proton, T2 is the time a whole section of tissue takes to return to equilibrium after taking into account both the interaction with the excitation field and also between the molecules themselves[32] [106]. The T2 time of water is useful for the identification of inflammation or edema [110] and has been previously used to monitor disease progression in FSHMD through textural analysis [111]. Similarly, edema was also found in DMD patients, as well as a correlation between T2 fat values and actual fat fractions, indicating that T2-weighted imaging can also detect fatty infiltrations in muscle tissue [112].

[32] Also known as spin-spin relaxation time

MRI: Dixon sequences MRI's Dixon sequences are some of the established ways to quantify fatty infiltrations in muscular tissue. These types of sequences are based on evaluating the phase of the received signals instead of the intensity values. Each Dixon sequence requires capturing two or three images in order to quantify fat infiltration as a biomarker of muscular degradation. In one of the images, fat and water are captured in phase, meaning tissues with high water and fat content will appear bright in the MRI images. In the next capture, fat and water are captured in opposing phases, meaning they will have opposing intensities as well. This procedure is known as the 2-point Dixon sequence, and it can retrieve individual fat and water images by adding or subtracting the in-phase and out-of-phase images [104]. A third image can be used to avoid the effects of inhomogeneities of the magnetic field, according to the 3-point Dixon sequence protocol [110]. Recently performed analyses indicate that the Dixon sequences correlation with clinical DMD and BMD measures could potentially perform well as non-invasive biomarkers of muscular dystrophy [113, 114].

MRI: Magnetic resonance spectroscopy Magnetic resonance spectroscopy (MRS) is a particularly interesting modality of MRI that looks at the whole spectrum of magnetic energy bands emitted by the different molecules (^{1}H, ^{23}Na, ^{31}P...) in the specimen for tissue identification or to create molecule-specific images [104]. MRS provides an alternative way to measure edema and fat infiltrations as main biomarkers of MDs that can be enhanced by combining it with T1, T2, or Dixon sequences to detect DMD accurately, FSHMD, or potentially other dystrophies, sometimes even before fat infiltration occurs [115–117]. Nonetheless, the need for spectral references and voxel-wise calculations might limit the applicability of MRS to specific muscle groups only with well-known spectroscopic properties [110].

MRI: Diffusion-weighted and diffusion tensor imaging Diffusion-weighted imaging (DWI) and diffusion tensor imaging (DTI) are two modalities based on measuring the diffusivity of water through tissue

either from T2-images or voxel-wise calculations [116]. Given that muscular dystrophy-affected muscles are prone to inflammation, tracking water through muscles can lead to edema foci. Specifically, fractional anisotropy, which measures the degree of isotropy in water diffusion, has been found to be a promising biomarker to assess the severity of DMD [118]. Another recently developed model, known as the random permeable barrier model, which models skeletal muscular tissue as randomly oriented barriers to estimate fiber diameter, provided good agreement with the increased diameter visible in histological results of BMD patients [119]. In LGMD, the apparent diffusion coefficient (ADC) obtained through DTI was a good indicator of connective tissue infiltration in muscle [120], and specific cases reported the possible existence of edema in white matter tissue in the brain of congenital MD patients, thanks to the detection of increased ADC [121].

1.4 Optical methods and their potential for MD diagnosis

So far, we have explored the most commonly used diagnostic methods for the identification and evaluation of MDs over time. Optical techniques are not among them, and yet they can bring new opportunities and points of view into this field. Due to only using wavelengths between the ultraviolet (UV) and infrared (IR), most optical technologies are considered non-invasive, as they can provide chemical and/or structural information without damaging the patient, specimen, or sample. Additionally, they do not need any kind of sample preparation, although there are specific modalities that can benefit from some specific prior procedures.

A broad classification of methods can be done in terms of the properties of light being studied by each system: intensity-based, spectrum-based, or phase-based methods. We will provide an overview of each of them in the following sections.

1.4.1 Intensity based

This section includes the main optical technologies that focus on the intensity of light returned by the samples, i.e., in the amount of light they transmit or reflect. Generally, these methods can be performed with monochrome light sources or detectors, and the information they provide is derived from the interaction between light at specific wavelengths (λ) and the sample. Said interaction is modulated by the refractive index (n) of the sample and its interaction properties, namely the absorption (μ_a), scattering (μ_s), and anisotropy (g) coefficients.

Microscopy As one of the staples in biopsy evaluation, microscopy is commonly used for MD diagnosis. Although the technique itself is non-invasive for the samples, the slide preparation protocol must be thoroughly followed for optimal image results [122]. First, the biopsy is taken, typically from skeletal muscle tissue, and later on, it can be quickly frozen using liquid nitrogen to avoid freezing artifacts [122]. The next step involves cutting the biopsy into 8-10 μm slices by using a cryostat

to keep the sample frozen [122]. Finally, each slice can be tinted using hematoxylin and eosin (H&E stain) and evaluated in the microscope, one by one, in search for MD biomarkers such as non-uniform tissue, nuclei migration, or nuclear inclusions [122]. The whole protocol, from extraction to diagnosis, can take from two to three days to over a week. Nonetheless, the high-resolution images (≈200 nm/px) that optical microscopy provides remain undisputed to understand the extent of the damage caused to muscle tissue, even with the limited sampling options.

Optical Coherence Tomography (OCT) Optical Coherence Tomography (OCT) uses light interferometry to obtain 3D images of the sample [123]. Although resolution is lower than that of microscopy (in the range of a few μm/px), the field of view analyzed in each image is much greater (tens of millimeters), allowing for fast evaluation of the whole biopsy at once. At the core of each OCT system lies an interferometer that splits a laser beam, typically in the IR range, into two independent rays. One of them bounces on a mirror and returns to the detector unperturbed (reference beam). The other (sample beam) reaches the sample and recombines with the reference beam in the detector by creating an interference pattern. This pattern contains intensity variations that are specific to each sample, thanks to the different ways light decays inside different tissues. This decay is related to the attenuation coefficient of the samples (μ_t), which can act as a marker of structural uniformity [123]. Some preliminary studies assessed the viability of OCT to successfully distinguish between healthy and damaged or regenerated muscle fibers [124], which later on led to accurately determining necrotic lesions in fresh ex vivo samples of DMD mouse models [125].

Spatial Domain Frequency Imaging (SFDI) Muscular damage caused by muscular dystrophies is not uniform and depends on the different muscle groups. OCT can be used to guide microscopy in the sense that it can give a fast, 3D evaluation of a region of tens of millimeters, but microscopy is still needed for the in-depth analysis of sub-micron structures. Nonetheless, when the damage is not widely spread, Spectral Domain Frequency Imaging (SFDI) can potentially help broadly identify areas in the tens of centimeters as healthy or damaged. Some of the already established MRI modalities are used for this task. However, if surgery is needed, none of them can be used while operating, whereas SFDI can potentially be implemented. SFDI works by projecting patterns of light using a 2D projector in order to obtain the decoupled μ_a and μ_s characteristic of each tissue [126]. To the author's knowledge, SFDI has never been applied to MD evaluation outside of this thesis (see chapters 4 and 7 and reference [127]). Still, it has been used to measure real-time oxygenation levels [128], to distinguish between stromal and epithelial breast tissue [129], and for breast surgical margin delineation [130]. All of this highlights the potential of SFDI to provide similar information to MRI data while performing surgery if it is ever needed.

1.4.2 Spectrum-based

The optical methods introduced in the previous section are based on wavelength-dependent properties, meaning tissues are not going to provide the same responses if the images are taken at different wavelengths. As such, there is an extensive field of research focusing on obtaining the absorption, attenuation, or scattering properties at various wavelengths and using the whole spectral information for tissue identification. Contrary to the intensity-based devices, these systems must have the capability to capture images at multiple wavelengths, which can be done by using spectrally tunable sources or wavelength filters[33] at light emission or capture. To be considered "optical", the wavelength range must roughly be between 200 nm (UV) and 1800 nm (IR).

[33] Or filter-like optical elements.

Optical spectroscopy The most fundamental technique of optical spectroscopy is based on punctual measurements of UV or visible (VIS) to near-infrared absorption of light. These systems typically use some form of focusing optics to illuminate a sample in a single point with a light source with a known emission spectrum, whether by design or because it was measured. Then, similar optics are used to capture the light that is either reflected by or transmitted through the sample. When light enters and travels through the sample according to its absorption and scattering properties, some of the initial intensity will be absorbed at specific wavelengths. This leads to a modification of the emission spectrum of the light source that will be specific to the chemical composition of the sample. Similarly to magnetic resonance spectroscopy, optical spectroscopy can be used to identify specific compounds that can act as MD biomarkers, like water (edema/inflammation) [131–133], fats (fatty infiltrations) [134], and elastin and collagen (fibrosis) [135, 136]. Thin samples would be required for transmission spectroscopy, while any kind of sample can be used in reflectance configurations. Although typically optical spectroscopy is not the main focus of MD articles, it is used as a tool to aid in specific tasks like treatment monitoring [137].

Vibrational spectroscopy Vibrational spectroscopy is a variant of optical spectroscopy that returns a spectrum generated by the vibration of the molecules after absorbing the incident light. The molecules that constitute the sample vibrate in multiple ways by stretching or contracting, rotating, or bending in multiple planes, leading to a spectrum of molecule-specific infrared peaks, also known as the *molecular fingerprint* of the sample. Two main modalities stand out in this field: Raman spectroscopy and Fourier transform infrared spectroscopy (FTIR). Raman spectroscopy involves a light conversion process where, typically, a visible-range laser excites the sample, and some of that excitation turns into heat, i.e., infrared radiation or vibrations [138]. On the other hand, FTIR uses an interferometer setup and a broadband infrared light source to capture the infrared interferogram caused by the molecular vibrations [139]. Both Raman and FTIR have been applied to muscular dystrophies in different aspects. For example, Raman has been found useful for evaluating exercise-induced necrosis in DMD mice models [140], while FTIR shows promise in aiding the biochemical characterization of DM1 [141]. The main drawback of Raman is that it requires high power sources to deal

with the low efficiency of the wavelength conversion process, and trying to compensate with long exposure times might lead to autofluorescence signals or photobleaching of the samples. FTIR does not have the same issues, but the spectra recorded are subject to low signal regions due to water absorption.

Multispectral (MSI) and hyperspectral (HSI) imaging Sometimes, especially when doing a first exploration, it is convenient to have a way to evaluate a large area to pinpoint regions where damage is more prominent [142]. Multispectral (MSI) and hyperspectral (HSI) imaging provide a way to do precisely so by obtaining pixel-wide spectral information over a wide[34] field of view (FoV). The main difference between MSI and HSI systems lies in the number of wavelengths used. Usually, an MSI system can resolve between 4 and 10 wavelengths, while a higher number can be considered HSI. There are several possible configurations for spectral imaging devices in terms of the wavelength-capturing method. Since camera sensors are two-dimensional and spectral imaging captures three dimensions, one spectral and two spatial, either spatial or spectral scanning is commonly used [143]. Spatial scanning involves capturing the whole spectrum in a single point (whiskbroom scanning) or line (pushbroom scanning) and using either a moving stage for the sample or a moving system to scan the remaining spatial dimensions. Spectral scanning, on the other hand, captures the 2D image at one wavelength at a time by using wavelength filters or using tunable light sources. Snapshot systems are non-scanning alternatives of MSI/HSI devices that capture the spectral information by adding wavelength filters on top of the sensor's pixel, allowing for faster capture than the scanning alternatives at the cost of worse spatial resolution [143]. The biomarkers detectable by spectral imaging are usually the same as those detected with optical spectroscopy, but with the added benefit of having 2D maps of the biomarker distribution throughout the whole sample [142–144].

[34] Tens of centimeters.

Fluorescence imaging Fluorescence is a non-linear effect caused when photons at some wavelengths interact with the sample's electrons by exciting them and then getting re-emitted when the electrons return to the basal state [145]. However, before re-emission, some of the photon's initial energy is lost when electrons shift to lower vibrational states before returning to the starting orbital. This phenomenon causes the emitted photon to be lower energy (i.e., red-shifted in wavelength) than the absorbed one [145]. Endogenous fluorescence exists in some tissues, making them easily detectable by using fluorescence-specific wavelength filters. In other cases, molecule-specific fluorescent markers can be introduced in the sample or patient to create images of the distribution of specific compounds. Fluorescence is often combined with microscopy by adding specific sources for excitation and specific filters for detection, and its use in MD detection is commonly linked to the use of Illumina's gene-sequencing method, where images of the nitrogenous bases are taken to identify the genetic sequence under study. However, fluorescent markers can also be used directly attached to RNA molecules, through the method called RNA fluorescence in situ hybridization, to accurately diagnose DM1 with no false positives [146]

Multi-photon imaging Multi-photon imaging is an optical microscopy technique utilizing the simultaneous absorption of multiple photons to generate an image. Second harmonic generation (SHG) and third harmonic generation (THG) are label-free processes where the sample itself adsorbs two or three photons and generates a signal at twice or three times the excitation frequency, respectively. There are non-linear analogs to SHG and THG, where the two or three photons absorbed are not emitted right away, but instead, some energy is lost before returning to the basal state, similar to what occurs in fluorescent tissues. The methods that exploit this phenomenon are called two or three-photon fluorescent microscopy[35] in terms of the number of photons absorbed each time. Multi-photon luminescence can also be used with exogenous fluorophores. The main advantage that multi-photon imaging or luminescence provides versus conventional microscopy is that by using lower-energy photons for excitation, mainly in the IR, light can penetrate deeper inside tissues without getting absorbed, aiding in in-vivo sub-superficial imaging. Some research groups have applied two-photon fluorescent microscopy to visualize the delivery of immunotherapy medicine in animal models of DMD [147], and to locate specific protein in healthy muscle fibers and its absence in a mouse model for LGMD, suggesting its potential involvement in the disease [148]. Interestingly, two-photon microscopes can also be used to induce controlled laser damage due to their confocal properties. This method was applied to damage precise areas of muscle cells in healthy and dysferlin-deficient muscle samples (like LGMD) to confirm the reduced repair properties of the latter [149]. More recent experiments in mouse models indicate that SHG can be used to visualize and evaluate the 3D collagen network at different stages of cardiac fibrosis of DMD [150] thanks to collagen's autofluorescence.

[35] Or two or three photon luminescence.

1.4.3 Phase-based

The optical methods explained so far are based on the analysis of single or multi-wavelength intensity of light. Instead, its phase can also be used to analyze the polarization of light produced or disturbed by the sample. Samples with low structural anisotropy will tend to depolarize the incident light, while anisotropic tissues like healthy muscle fibers will keep some of the polarization. To analyze the phase, polarization techniques need to have optical elements with known polarization properties, i.e., polarizers and waveplates, and all-optical paths must keep the polarization of the light without modifying it, either by using volume optics or polarization-maintaining fibers.

Polarized light microscopy Polarized light microscopy can be used to enhance anisotropic structures of tissues. This technique is typically performed in transmission microscopy with the aid of two linear polarizers - one before and another after the sample. Anisotropic samples can showcase birefringence (Δn), which is an optical property that indicates how much faster light travels through the sample when parallel to the main anisotropy axis versus perpendicular to it. The more anisotropic a tissue is, the higher its birefringence. In this sense, birefringence can act

as a marker of healthy skeletal muscle tissue without the need for external staining, aiding in fast diagnosis. It can also help identify the main direction of fibers or crystals in the sample [151]. It is worth noting that there are polarized light microscopes that do not have phase elements like waveplates, meaning that only the linear properties of the samples can be measured, but not the circular ones like circular dichroism and optical rotation, which are good indicators of molecular chirality.

Polarization Sensitive OCT Similarly to polarized light microscopy, polarization-sensitive OCT (PS-OCT) is a functional variant of conventional OCT that enables measurements of the phase of light by adding polarizers and waveplates. Most PS-OCT excite the sample with polarized light with one specific state (circular) to excite all the orientations of the sample in a similar way. This allows for the measurement of the Stokes parameters at every point inside the sample, which describe precisely the polarization state of light. Stokes parameters can also be used to retrieve the birefringence of the sample by evaluating how the phase changes when traveling through it. Different tissue types will lead to different birefringence properties that can be identified with this methodology, which can later on be used as a marker of disease [152].

Mueller imaging Light with some specific polarization will suffer changes after interacting with a sample, and the induced changes will be a function of the polarization properties of the sample. The Stokes parameters are useful for describing the polarization properties of light but not of the samples. Instead, the Mueller matrix is used for this purpose, which acts as a transference matrix between an input and output Stokes vectors. To measure the full Mueller matrix of a sample, it is necessary to excite the sample with multiple different and controlled polarization states, which can only be done by using a combination of polarization optics that can be modified either in position, rotation, or phase. Although more cumbersome than other methodologies, Mueller imaging can reconstruct images of the polarization properties of tissues, like their depolarization, retardance, or diattenuation [153]. It can also be adapted to any other kind of imaging technique, whether it is wide-field imaging or transmission microscopy.

References

[1] M. A. Wallace, D. C. Hughes, and K. Baar: "mTORC1 in the Control of Myogenesis and Adult Skeletal Muscle Mass", in: *Molecules to Medicine with mTOR: Translating Critical Pathways into Novel Therapeutic Strategies*. Elsevier Inc., 2016 37–56. ISBN: 9780128027332. DOI: 10.1016/B978-0-12-802733-2.00025-6.

[2] S. R. Ward and R. L. Lieber: "Density and hydration of fresh and fixed human skeletal muscle", *Journal of Biomechanics* **38**(11), 2317–2320 (2005). DOI: 10.1016/j.jbiomech.2004.10.001.

[3] K. Mukund and S. Subramaniam: "Skeletal muscle: A review of molecular structure and function, in health and disease", *Wiley Interdisciplinary Reviews: Systems Biology and Medicine* **12**(1), e1462 (2020). DOI: 10.1002/wsbm.1462.

[4] R. Lieber: "Skeletal Muscle Structure, Function, and Plasticity: the physiological basis of rehabilitation", Lippincott Williams & Wilkins, 2002. ISBN: 9780781730617.

[5] M. Barany: "Biochemistry of Smooth Muscle Contraction", Academic Press, 1996. ISBN: 9780080527895.

[6] J. Chamley-Campbell, G. R. Campbell, and R. Ross: "The smooth muscle cell in culture", *Physiological Reviews* **59**(1), 1–61 (1979). DOI: 10.1152/physrev.1979.59.1.1.

[7] B. Sit, D. Gutmann, and T. Iskratsch: "Costameres, dense plaques and podosomes: the cell matrix adhesions in cardiovascular mechanosensing", *Journal of Muscle Research and Cell Motility* **40**(2), 197–209 (2019). DOI: 10.1007/s10974-019-09529-7.

[8] D. Paulin and Z. Li: "Desmin: A major intermediate filament protein essential for the structural integrity and function of muscle", *Experimental Cell Research* **301**(1), 1–7 (2004). DOI: 10.1016/j.yexcr.2004.08.004.

[9] G. J. Christ et al.: "Gap Junctions in Vascular Tissues. Evaluating the Role of Intercellular Communication in the Modulation of Vasomotor Tone.", *Circulation Research* **79**(4), 631–646 (1996). DOI: 10.1161/01.RES.79.4.631.

[10] T. J. Eddinger, J. D. Schiebout, and D. R. Swartz: "Smooth muscle adherens junctions associated proteins are stable at the cell periphery during relaxation and activation", *American Journal of Physiology-Cell Physiology* **289**(6), C1379–C1387 (2005). DOI: 10.1152/ajpcell.00193.2005.

[11] C. A. Walker and F. G. Spinale: "The structure and function of the cardiac myocyte: A review of fundamental concepts", *The Journal of Thoracic and Cardiovascular Surgery* **118**(2), 375–382 (1999). DOI: 10.1016/S0022-5223(99)70233-3.

[12] N. J. Severs: "The cardiac muscle cell", *BioEssays* **22**, 188–199 (2000). DOI: 10.1002/(SICI)1521-1878(200002)22:2%3C188::AID-BIES10%3E3.0.CO;2-T.

[13] A. Ghigo et al.: "PI3K and Calcium Signaling in Cardiovascular Disease", *Circulation Research* **121**(3), 282–292 (2017). DOI: 10.1161/CIRCRESAHA.117.310183.

[14] S. H. Laval and K. M. Bushby: "Limb-girdle muscular dystrophies - From genetics to molecular pathology", *Neuropathology and Applied Neurobiology* **30**(2), 91–105 (2004). DOI: 10.1111/j.1365-2990.2004.00555.x.

[15] W. Klug et al.: "Concepts of Genetics", Pearson Education, 2014. ISBN: 9780133887099.

[16] E. M. Yiu and A. J. Kornberg: "Duchenne muscular dystrophy", *Journal of Paediatrics and Child Health* **51**(8), 759–764 (2015). DOI: 10.1111/jpc.12868.

[17] S. M. Chrzanowski, B. T. Darras, and S. B. Rutkove: "The Value of Imaging and Composition-Based Biomarkers in Duchenne Muscular Dystrophy Clinical Trials", *Neurotherapeutics* **17**(1), 142–152 (2020). DOI: 10.1007/S13311-019-00825-1.

[18] C. Rochitte, G. Liberato, and M. Silva: "Comprehensive Assessment of Cardiac Involvement in Muscular Dystrophies by Cardiac MR Imaging", *Magnetic Resonance Imaging Clinics of North America* **27**(3), 521–531 (2019). DOI: 10.1016/j.mric.2019.04.009.

[19] C. Senesac et al.: "Magnetic resonance imaging studies in duchenne muscular dystrophy: Linking findings to the physical therapy clinic", *Physical Therapy* **100**(11), 2035–2048 (2020). DOI: 10.1093/ptj/pzaa140.

[20] I. Benga and O. Benga: "Implications of water channel proteins in selected neurological disorders: Epilepsies, muscular dystrophies, amyotrophic lateral sclerosis, neuromyelitis optica, Parkinson's disease, and spongiform encephalopathies", *Molecular Aspects of Medicine* **33**(5-6), 590–604 (2012). DOI: 10.1016/j.mam.2012.03.003.

[21] P. Podkalicka et al.: "Targeting angiogenesis in Duchenne muscular dystrophy", 2019. DOI: 10.1007/s00018-019-03006-7.

[22] D. Verhaert et al.: "Cardiac Involvement in Patients With Muscular Dystrophies", *Circulation: Cardiovascular Imaging* **4**(1), 67–76 (2011). DOI: 10.1161/CIRCIMAGING.110.960740.

[23] L. Power et al.: "Imaging the heart to detect cardiomyopathy in Duchenne muscular dystrophy: A review", *Neuromuscular Disorders* **28**(9), 717–730 (2018). DOI: 10.1016/j.nmd.2018.05.011.

[24] F. Roller, S. Harth, and G. Krombach: "Value of Cardiac T1-Mapping and ECV Quantification in Duchenne Muscular Dystrophy (DMD): Case Report, Typical Imaging Findings and Review of the Literature", *RoFo Fortschritte auf dem Gebiet der Rontgenstrahlen und der Bildgebenden Verfahren* **189**(1), 75–77 (2017). DOI: 10.1055/s-0042-116685.

[25] S. Mavrogeni et al.: "Oedema-fibrosis in Duchenne Muscular Dystrophy: Role of cardiovascular magnetic resonance imaging", *European Journal of Clinical Investigation* **47**(12) (2017). DOI: 10.1111/eci.12843.

[26] D. Duan et al.: "Duchenne muscular dystrophy", *Nature Reviews Disease Primers* **7**(1), 13 (2021). DOI: 10.1038/s41572-021-00248-3.

[27] S. C. Brown et al.: "Investigating the pathology of Emery-Dreifuss muscular dystrophy", in: *Biochemical Society Transactions*. **36**. (6). 2008 1335–1338. DOI: 10.1042/BST0361335.

[28] C. Panicucci et al.: "Early Muscle MRI Findings in a Pediatric Case of Emery-Dreifuss Muscular Dystrophy Type 1", *Neuropediatrics* **54**(6), 426–429 (2022). DOI: 10.1055/s-0043-1768989.

[29] V. Cenni et al.: "Desmin and Plectin Recruitment to the Nucleus and Nuclei Orientation Are Lost in Emery-Dreifuss Muscular Dystrophy Myoblasts Subjected to Mechanical Stimulation", *Cells* **13**(2), 162 (2024). DOI: 10.3390/cells13020162.

[30] S. Manilal et al.: "The Emery-Dreifuss Muscular Dystrophy Protein, Emerin, is a Nuclear Membrane Protein", *Human Molecular Genetics* **5**(6), 801–808 (1996). DOI: 10.1093/hmg/5.6.801.

[31] A. Madej-Pilarczyk: "Clinical aspects of Emery-Dreifuss muscular dystrophy", *Nucleus* **9**(1), 314–320 (2018).

[32] G. Bonne et al.: "Clinical and molecular genetic spectrum of autosomal dominant Emery-Dreifuss muscular dystrophy due to mutations of the lamin A/C gene", *Annals of Neurology* **48**(2), 170–180 (2000). DOI: 10.1002/1531-8249(200008)48:2<170::AID-ANA6>3.0.CO;2-J.

[33] S. Cesar et al.: "Characterization of cardiac involvement in children with LMNA-related muscular dystrophy", *Frontiers in Cell and Developmental Biology* **11**, 1–19 (2023). DOI: 10.3389/fcell.2023.1142937.

[34] M. M. McNiff et al.: "Facioscapulohumeral Muscular Dystrophy European Patient Survey: Assessing Patient Reported Disease Burden and Preferences in Clinical Trial Participation", *Journal of Neuromuscular Diseases* **11**(2), 459–472 (2024). DOI: 10.3233/JND-230171.

[35] E. Mocciaro et al.: "DUX4 role in normal physiology and in FSHD muscular dystrophy", *Cells* **10**(12), 3322 (2021). DOI: 10.3390/cells10123322.

[36] A. M. DeSimone et al.: "Facioscapulohumeral muscular dystrophy", *Comprehensive Physiology* **7**(4), 1229–1279 (2017). DOI: 10.1002/cphy.c160039.

[37] A. Varma et al.: "A longitudinal study of disease progression in facioscapulohumeral muscular dystrophy (FSHD)", *Muscle and Nerve* **69**(3), 362–367 (2024). DOI: 10.1002/mus.28031.

[38] A. Fischmann and D. Fischer: "Neuromuscular imaging in muscular dystrophies and other muscle diseases", *Imaging in Medicine* **5**(3), 237–248 (2013). DOI: 10.2217/iim.13.26.

[39] V. Nigro and M. Savarese: "Genetic basis of limb-girdle muscular dystrophies: the 2014 update", *Acta Myologica* **33**(1), 1–12 (2014).

[40] M. Guglieri et al.: "Limb-girdle muscular dystrophies", *Current Opinion in Neurology* **21**(5), 576–584 (2008). DOI: 10.1097/WCO.0b013e32830efdc2.

[41] M. Zatz, M. Vainzof, and M. R. Passos-Bueno: "Limb-girdle muscular dystrophy: one gene with different phenotypes, one phenotype with different genes", *Current Opinion in Neurology* **13**(5), 511–517 (2000). DOI: 10.1097/00019052-200010000-00002.

[42] R. Falsaperla et al.: "Congenital muscular dystrophy: From muscle to brain", *Italian Journal of Pediatrics* **42**(1), 1–11 (2016). DOI: 10.1186/s13052-016-0289-9.

[43] E. Bertini et al.: "Congenital Muscular Dystrophies: A Brief Review", *Seminars in Pediatric Neurology* **18**(4), 277–288 (2011). DOI: 10.1016/j.spen.2011.10.010.

[44] U. C. Reed: "Congenital Muscular Dystrophy Part I: a review of phenotypical and diagnostic aspects", *Arquivos de Neuro-Psiquiatria* **67**(1), 144–168 (2009). DOI: 10.1590/S0004-282X2009000100038.

[45] E. Mercuri and F. Muntoni: "The ever-expanding spectrum of congenital muscular dystrophies", *Annals of Neurology* **72**(1), 9–17 (2012). DOI: 10.1002/ana.23548.

[46] C. A. Thornton: "Myotonic dystrophy", *Neurologic Clinics* **32**(3), 705–719 (2014). DOI: 10.1016/j.ncl.2014.04.011.

[47] G. Meola and R. Cardani: "Myotonic dystrophies: An update on clinical aspects, genetic, pathology, and molecular pathomechanisms", *Biochimica et Biophysica Acta - Molecular Basis of Disease* **1852**(4), 594–606 (2015). DOI: 10.1016/j.bbadis.2014.05.019.

[48] S. Wenninger, F. Montagnese, and B. Schoser: "Core clinical phenotypes in Myotonic Dystrophies", *Frontiers in Neurology* **9** (2018). DOI: 10.3389/fneur.2018.00303.

[49] C. Turner and D. Hilton-Jones: "Myotonic dystrophy: Diagnosis, management and new therapies", *Current Opinion in Neurology* **27**(5), 599–606 (2014). DOI: 10.1097/WCO.0000000000000128.

[50] K. Yum, E. T. Wang, and A. Kalsotra: "Myotonic dystrophy: disease repeat range, penetrance, age of onset, and relationship between repeat size and phenotypes", *Current Opinion in Genetics and Development* **44**, 30–37 (2017). DOI: 10.1016/j.gde.2017.01.007.

[51] B. Brais: "Oculopharyngeal muscular dystrophy", in: *Handbook of Clinical Neurology*. **101**. Elsevier B.V., 2011 181–192. DOI: 10.1016/B978-0-08-045031-5.00014-1.

[52] B. Brais et al.: "Oculopharyngeal Muscular Dystrophy", *Seminars in Neurology* **19**(1), 59–66 (1999). DOI: 10.1055/s-2008-1040826.

[53] B. Brais: "Oculopharyngeal muscular dystrophy: A late-onset polyalanine disease", *Cytogenetic and Genome Research* **100**(1-4), 252–260 (2003). DOI: 10.1159/000072861.

[54] S. Yamashita: "Recent progress in oculopharyngeal muscular dystrophy", *Journal of Clinical Medicine* **10**(7), 1375 (2021). DOI: 10.3390/jcm10071375.

[55] F. L. M. Norwood et al.: "Prevalence of genetic muscle disease in Northern England: in-depth analysis of a muscle clinic population", *Brain* **132**(11), 3175–3186 (2009). DOI: 10.1093/brain/awp236.

[56] Y. Akaba et al.: "Wide Spectrum of Cardiac Phenotype in Myofibrillar Myopathy Associated With a Bcl-2-Associated Athanogene 3 Mutation: A Case Report and Literature Review", *Journal of clinical neuromuscular disease* **24**(1), 49–54 (2022). DOI: 10.1097/CND.0000000000000392.

[57] D. Selcen, K. Ohno, and A. G. Engel: "Myofibrillar myopathy: Clinical, morphological and genetic studies in 63 patients", *Brain* **127**(2), 439–451 (2004). DOI: 10.1093/brain/awh052.

[58] J. P. Fichna, A. Maruszak, and C. Żekanowski: "Myofibrillar myopathy in the genomic context", *Journal of Applied Genetics* **59**(4), 431–439 (2018). DOI: 10.1007/s13353-018-0463-4.

[59] D. Avila-Smirnow et al.: "Cardiac arrhythmia and late-onset muscle weakness caused by a myofibrillar myopathy with unusual histopathological features due to a novel missense mutation in FLNC", *Revue Neurologique* **172**(10), 594–606 (2016). DOI: 10.1016/j.neurol.2016.07.017.

[60] R. F. Chang and S. J. Mubarak: "Pathomechanics of Gowers' Sign: A Video Analysis of a Spectrum of Gowers' Maneuvers", *Clinical Orthopaedics & Related Research* **470**(7), 1987–1991 (2012). DOI: 10.1007/s11999-011-2210-6.

[61] H. Walker, W. Hall, and J. Hurst: "Clinical Methods: The History, Physical, and Laboratory Examinations", NCBI Bookshelf. Butterworths, 1990. ISBN: 9780409900774.

[62] P. Brancaccio, N. Maffulli, and F. M. Limongelli: "Creatine kinase monitoring in sport medicine", *British Medical Bulletin* **81-82**(1), 209–230 (2007). DOI: 10.1093/bmb/ldm014.

[63] R. C. Neal et al.: "Relationship of Ethnic Origin, Gender, and Age to Blood Creatine Kinase Levels", *American Journal of Medicine* **122**(1), 73–78 (2009). DOI: 10.1016/j.amjmed.2008.08.033.

[64] F. Vassella, R. Richterich, and E. Rossi: "The diagnostic value of serum creatine kinase in neuromuscular and muscular disease", *Pediatrics* **35**(2), 322–330 (1965). DOI: 10.1542/peds.35.2.322.

[65] T. Brown: "Genomes. 2nd edition. Oxford: Wiley-Liss; 2002. Chapter 6, Sequencing Genomes.", https://www.ncbi.nlm.nih.gov/books/NBK21117/. Accessed: 20 March 2025. 2002.

[66] D. Narasimhaiah, M. S. Uppin, and P. Ranganath: "Genetics and muscle pathology in the diagnosis of muscular dystrophies: An update.", *Indian journal of pathology & microbiology* **65**(Suppl 1), S259–S270 (2022).

[67] B. Alberts et al.: "Molecular Biology of the Cell. 4th edition. New York: Garland Science; 2002. From DNA to RNA.", https://www.ncbi.nlm.nih.gov/books/NBK26887/. Accessed: 20 March 2025. 2002.

[68] F. Sanger, S. Nicklen, and A. R. Coulson: "DNA sequencing with chain-terminating inhibitors", *Proceedings of the National Academy of Sciences* **74**(12), 5463–5467 (1977). DOI: 10.1073/pnas.74.12.5463.

[69] L. Stuppia et al.: "Use of the MLPA assay in the molecular diagnosis of gene copy number alterations in human genetic diseases.", *International journal of molecular sciences* **13**(3), 3245–3276 (2012). DOI: 10.3390/ijms13033245.

[70] A. Meller et al.: "Rapid nanopore discrimination between single polynucleotide molecules", *Proceedings of the National Academy of Sciences (PNAS)* **97**(3), 1079–1084 (2000). DOI: 10.1073/pnas.97.3.1079.

[71] J. J. Kasianowicz et al.: "Characterization of individual polynucleotide molecules using a membrane channel", *Proceedings of the National Academy of Sciences* **93**(24), 13770–13773 (1996). DOI: 10.1073/pnas.93.24.13770.

[72] J. Eid et al.: "Real-Time DNA Sequencing from Single Polimerase Molecukles", *Science* **323**(5910), 133–138 (2009). DOI: 10.1126/science.1162986.

[73] M. L. Metzker: "Sequencing technologies the next generation", *Nature Reviews Genetics* **11**(1), 31–46 (2010). DOI: 10.1038/nrg2626.

[74] D. R. Bentley et al.: "Accurate whole human genome sequencing using reversible terminator chemistry", *Nature* **456**(7218), 53–59 (2008). DOI: 10.1038/nature07517.

[75] S. Behjati and P. S. Tarpey: "What is next generation sequencing?", *Archives of Disease in Childhood: Education and Practice Edition* **98**(6), 236–238 (2013). DOI: 10.1136/archdischild-2013-304340.

[76] H. Pikó et al.: "Muscular dystrophies: Diagnostic approaches in Hungary", *Acta Physiologica Hungarica* **95**(4), 405–418 (2008). DOI: 10.1556/APhysiol.95.2008.4.7.

[77] L. M. Brewster et al.: "Ethnic differences in tissue creatine kinase activity: an observational study.", *PloS one* **7**(3), e32471 (2012). DOI: 10.1371/journal.pone.0032471.

[78] J. Walters and A. Baborie: "Muscle biopsy: what and why and when?", *Practical Neurology* **20**(5), 385–395 (2020). DOI: 10.1136/practneurol-2019-002465.

[79] G. A. Gronert et al.: "Absence of Malignant Hyperthermia Contractures in Becker-Duchenne Dystrophy at Age-2", *Muscle and Nerve* **15**(1), 52–56 (1992). DOI: 10.1002/mus.880150110.

[80] H. F. Jones et al.: "Importance of muscle biopsy to establish pathogenicity of DMD missense and splice variants", *Neuromuscular Disorders* **29**(12), 913–919 (2019). DOI: 10.1016/j.nmd.2019.09.013.

[81] A. Fidziańska and I. Hausmanowa-Petrusewicz: "Architectural abnormalities in muscle nuclei. Ultrastructural differences between X-linked and autosomal dominant forms of EDMD", *Journal of the Neurological Sciences* **210**(1-2), 47–51 (2003). DOI: 10.1016/S0022-510X(03)00012-1.

[82] P. S. Masny et al.: "Localization of 4q35.2 to the nuclear periphery: Is FSHD a nuclear envelope disease?", *Human Molecular Genetics* **13**(17), 1857–1871 (2004). DOI: 10.1093/hmg/ddh205.

[83] M. Bakay et al.: "Nuclear envelope dystrophies show a transcriptional fingerprint suggesting disruption of Rb-MyoD pathways in muscle regeneration", *Brain* **129**(4), 996–1013 (2006). DOI: 10.1093/brain/awl023.

[84] L. J. Pino, D. W. Stashuk, and S. Podnar: "Probabilistic muscle characterization using quantitative electromyography: Application to facioscapulohumeral muscular dystrophy", *Muscle and Nerve* **42**(4), 563–569 (2010). DOI: 10.1002/mus.21742.

[85] K. L. Derry, S. L. Venance, and T. J. Doherty: "Decomposition-based quantitative electromyography in the evaluation of muscular dystrophy severity", *Muscle and Nerve* **45**(4), 507–513 (2012). DOI: 10.1002/mus.22341.

[86] S. K. Archer et al.: "Dysphagia in Duchenne muscular dystrophy assessed objectively by surface electromyography", *Dysphagia* **28**(2), 188–198 (2013). DOI: 10.1007/s00455-012-9429-6.

[87] E. Szmidt-Salkowska et al.: "Does quantitative EMG differ myotonic dystrophy type 2 and type 1?", *Journal of Electromyography and Kinesiology* **24**(5), 755–761 (2014). DOI: 10.1016/j.jelekin.2014.05.012.

[88] M. Bora et al.: "Investigation of surface electromyography amplitude values during stair climbing task in children with Duchenne muscular dystrophy", *Neurological Sciences* **43**(4), 2791–2801 (2022). DOI: 10.1007/s10072-021-05643-y.

[89] L. Tang, S. Shao, and C. Wang: "Electrocardiographic features of children with Duchenne muscular dystrophy", *Orphanet Journal of Rare Diseases* **17**(1) (2022). DOI: 10.1186/s13023-022-02473-9.

[90] E. Ashley and N. J.: "Cardiology Explained. London: Remedica; 2004. Chapter 3, Conquering the ECG.", https://www.ncbi.nlm.nih.gov/books/NBK2214/. Accessed: 20 March 2025. 2002.

[91] D. McBride et al.: "Cardiac Involvement and Arrhythmias Associated with Myotonic Dystrophy", *Reviews in Cardiovascular Medicine* **23**(4) (2022). DOI: 10.31083/j.rcm2304126.

[92] A. Nikhanj et al.: "Clinical utility of 12-lead electrocardiogram in evaluating heart disease in patients with muscular dystrophy: Assessment of left ventricular hypertrophy, conduction disease, and cardiomyopathy", *Annals of Noninvasive Electrocardiology* **26**(6), e12876 (2021). DOI: 10.1111/anec.12876.

[93] K. Erikson, F. Fry, and J. Jones: "Ultrasound in Medicine - A Review", *IEEE Transactions on Sonics and Ultrasonics* **SU21**(3), 144–170 (1974). DOI: 10.1109/T-SU.1974.29810.

[94] C. M. Zaidman et al.: "Quantitative muscle ultrasound detects disease progression in Duchenne muscular dystrophy", *Annals of Neurology* **81**(5), 633–640 (2017). DOI: 10.1002/ana.24904.

[95] M. C. Moreta et al.: "Reliability and Validity of the Modified Heckmatt Scale in Evaluating Muscle Changes With Ultrasound in Spasticity", *Archives of Rehabilitation Research and Clinical Translation* **2**(4), 100071 (2020). DOI: 10.1016/j.arrct.2020.100071.

[96] R. Kroon et al.: "Imaging: EP.339 Longitudinal assessment of muscle ultrasound in oculopharyngeal muscular dystrophy", *Neuromuscular Disorders* **31**, S152–S153 (2021). DOI: 10.1016/j.nmd.2021.07.364.

[97] S. Syeda et al.: "Collagen Related Muscle Diseases: EP.60 Muscle ultrasound in COL6-related muscular dystrophy: patterns and progression", *Neuromuscular Disorders* **31**, S67 (2021). DOI: 10.1016/j.nmd.2021.07.085.

[98] S. C. Vincenten et al.: "Establishing the role of muscle ultrasound as an imaging biomarker in facioscapulohumeral muscular dystrophy", *Neuromuscular Disorders* **33**(12), 936–944 (2023). DOI: 10.1016/j.nmd.2023.10.015.

[99] A. Mori et al.: "Characteristic involvement of muscle ultrasound in myotonic dystrophy type 1", *Journal of the Neurological Sciences* **381**, 1088–1089 (2017). DOI: 10.1016/j.jns.2017.08.3072.

[100] G. Song et al.: "Usefulness of speckle-tracking echocardiography for early detection in children with Duchenne muscular dystrophy: a meta-analysis and trial sequential analysis", *Cardiovascular Ultrasound* **18**(1) (2020). DOI: 10.1186/s12947-020-00209-y.

[101] B. Leśniak-Plewińska et al.: "Novel measurement setup for evaluation of left ventricle motion and strain tracking methods", in: *Medical Imaging 2017: Ultrasonic Imaging and Tomography*. **10139**. SPIE, 2017 1013919. ISBN: 9781510607231. DOI: 10.1117/12.2254539.

[102] A. Akyüz et al.: "Evaluation of cardiomyopathy with two-dimensional speckle tracking echocardiography in limb-girdle muscular dystrophy type 2A and 2B", *Journal of Clinical Ultrasound* **50**(9), 1242–1248 (2022). DOI: 10.1002/jcu.23323.

[103] M. Marchel et al.: "Echocardiographic Features of Cardiomyopathy in Emery-Dreifuss Muscular Dystrophy", *Cardiology Research and Practice* **2021**, 1–7 (2021). DOI: 10.1155/2021/8812044.

[104] D. Leung: "Advancements in magnetic resonance imaging-based biomarkers for muscular dystrophy", *Muscle and Nerve* **60**(4), 347–360 (2019). DOI: 10.1002/mus.26497.

[105] W. P. Rothwell: "Nuclear magnetic resonance imaging", *Applied Optics* **24**(3), 3958–3968 (1985). DOI: 10.1364/AO.24.003958.

[106] C. M. Mills et al.: "Cerebral abnormalities: use of calculated T1 and T2 magnetic resonance images for diagnosis.", *Radiology* **150**(1), 87–94 (1984). DOI: 10.1148/radiology.150.1.6689792.

[107] C. Grigoratos et al.: "Cardiac magnetic resonance in patients with muscular dystrophies", *European Journal of Preventive Cardiology* **28**(14), 1526–1535 (2021). DOI: 10.1177/2047487320923052.

[108] E. B. Turkbey et al.: "Assessment of cardiac involvement in myotonic muscular dystrophy by T1 mapping on magnetic resonance imaging", *Heart Rhythm* **9**(10), 1691–1697 (2012). DOI: 10.1016/j.hrthm.2012.06.032.

[109] S. D. Friedman et al.: "Longitudinal features of stir bright signal in FSHD", *Muscle & Nerve* **49**(2), 257–260 (2014). DOI: 10.1002/mus.23911.

[110] J. Burakiewicz et al.: "Quantifying fat replacement of muscle by quantitative MRI in muscular dystrophy", *Journal of Neurology* **264**(10), 2053–2067 (2017). DOI: 10.1007/s00415-017-8547-3.

[111] P. F. Felisaz et al.: "Texture analysis and machine learning to predict water T2 and fat fraction from non-quantitative MRI of thigh muscles in Facioscapulohumeral muscular dystrophy", *European Journal of Radiology* **134**, 109460 (2021). DOI: 10.1016/j.ejrad.2020.109460.

[112] H. K. Kim et al.: "Quantitative Skeletal Muscle MRI: Part 2, MR Spectroscopy and T2 Relaxation Time Mapping - Comparison Between Boys With Duchenne Muscular Dystrophy and Healthy Boys", *American Journal of Roentgenology* **205**(2), W216–W223 (2015). DOI: 10.2214/AJR.14.13755.

[113] M. Mohanty et al.: "Fat-fraction quantification using Dixon technique in Duchenne muscular dystrophy and its correlation with clinical progression and genotypic characteristics", *Neuromuscular Disorders* **33**, S79 (2023). DOI: 10.1016/j.nmd.2023.07.062.

[114] U. Bonati et al.: "Longitudinal 2-point dixon muscle magnetic resonance imaging in becker muscular dystrophy", *Muscle & Nerve* **51**(6), 918–921 (2015). DOI: 10.1002/mus.24629.

[115] T. Xu et al.: "High-Speed T2-Corrected Multiecho Magnetic Resonance Spectroscopy for Quantitatively Detecting Skeletal Muscle Fatty Infiltration and Predicting the Loss of Ambulation in Patients With Duchenne Muscular Dystrophy", *Journal of Magnetic Resonance Imaging* **58**(4), 1270–1278 (2023). DOI: 10.1002/jmri.28641.

[116] D. G. Leung et al.: "Multivoxel proton magnetic resonance spectroscopy in facioscapulohumeral muscular dystrophy", *Muscle and Nerve* **57**(6), 958–963 (2018). DOI: 10.1002/mus.26048.

[117] W. Cui et al.: "Early detection of myocardial bioenergetic deficits: A 9.4 tesla complete non invasive 31P MR spectroscopy study in mice with muscular dystrophy", *PLoS ONE* **10**(8), 1–8 (2015). DOI: 10.1371/journal.pone.0135000.

[118] H. Sane et al.: "Severity of muscle impairment and its progression assessed using musculoskeletal magnetic resonance imaging and diffusion tension imaging in 78 boys with Duchenne muscular dystrophy: a retrospective study", *Polish Journal of Radiology* **89**(1), e88–e105 (2024). DOI: 10.5114/pjr.2024.135718.

[119] D. Cameron et al.: "Diffusion-tensor magnetic resonance imaging captures increased skeletal muscle fibre diameters in Becker muscular dystrophy", *Journal of Cachexia, Sarcopenia and Muscle* **14**(3), 1546–1557 (2023). DOI: 10.1002/jcsm.13242.

[120] G. Hernández-Salazar et al.: "Diffusion and ideal MRI techniques to characterize limb-girdle muscular dystrophy", in: *AIP Conference Proceedings*. **1494**. 2012 103–105. ISBN: 9780735411067. DOI: 10.1063/1.4764612.

[121] P. E. Sijens et al.: "MR spectroscopy and diffusion tensor imaging of the brain in congenital muscular dystrophy with merosin deficiency: Metabolite level decreases, fractional anisotropy decreases, and apparent diffusion coefficient increases in the white matter", *Brain and Development* **29**(5), 317–321 (2007). DOI: 10.1016/j.braindev.2006.10.004.

[122] A. Cotta et al.: "Muscle biopsy essential diagnostic advice for pathologists", *Surgical and Experimental Pathology* **4**(1) (2021). DOI: 10.1186/s42047-020-00085-w.

[123] D. Huang et al.: "Optical Coherence Tomography", *Science* **254**(5035), 1178–1181 (1991). DOI: 10.1126/science.1957169.

[124] B. R. Klyen et al.: "Three-dimensional optical coherence tomography of whole-muscle autografts as a precursor to morphological assessment of muscular dystrophy in mice", *Journal of Biomedical Optics* **13**(1), 011003 (2008). DOI: 10.1117/1.2870170.

[125] B. R. Klyen et al.: "Identification of muscle necrosis in the mdx mouse model of Duchenne muscular dystrophy using three-dimensional optical coherence tomography", *Journal of Biomedical Optics* **16**(7), 076013 (2011). DOI: 10.1117/1.3598842.

[126] D. J. Cuccia et al.: "Modulated Imaging: Quantitative Analysis and Tomography of Turbid Media in the Spatial-Frequency Domain", *Optics Letters* **30**(11), 1354 (2005). DOI: 10.1364/OL.30.001354.

[127] V. Mieites et al.: "Wide-field optical properties estimation of whole limbs in muscle dystrophy murine models via SFDI: a case study", in: *Translational Biophotonics: Diagnostics and Therapeutics III*. Ed. by Z. Huang and L. D. Lilge. **12627**. International Society for Optics and Photonics. SPIE, 2023 1262731. DOI: 10.1117/12.2670573.

[128] M. Schmidt et al.: "Real-time, wide-field, and quantitative oxygenation imaging using spatiotemporal modulation of light", *Journal of Biomedical Optics* **24**(07), 1 (2019). DOI: 10.1117/1.jbo.24.7.071610.

[129] D. M. McClatchy et al.: "Light scattering measured with spatial frequency domain imaging can predict stromal versus epithelial proportions in surgically resected breast tissue", *Journal of Biomedical Optics* **24**(07), 1 (2018). DOI: 10.1117/1.jbo.24.7.071605.

[130] A. Pardo et al.: "Scatter signatures in SFDI data enable breast surgical margin delineation via ensemble learning", in: *Biomedical Applications of Light Scattering X*. International Society for Optics and Photonics SPIE, 2020 112530K. ISBN: 9781510632691. DOI: 10.1117/12.2546945.

[131] R. M. Pope and E. S. Fry: "Absorption spectrum (380–700 nm) of pure water II Integrating cavity measurements", *Applied Optics* **36**(33), 8710 (1997). DOI: 10.1364/AO.36.008710.

[132] H. Buiteveld, J. H. M. Hakvoort, and M. Donze: "Optical properties of pure water", in: *Ocean Optics XII*. Ed. by J. S. Jaffe. **2258**. International Society for Optics and Photonics. SPIE, 1994 174–183. DOI: 10.1117/12.190060.

[133] L. Kou, D. Labrie, and P. Chylek: "Refractive indices of water and ice in the 065- to 25-μm spectral range", *Applied Optics* **32**(19), 3531 (1993). DOI: 10.1364/AO.32.003531.

[134] R. L. P. Van Veen et al.: "Determination of VIS-NIR absorption coefficients of mammalian fat, with time-and spatially resolved diffuse reflectance and transmission spectroscopy", in: *Biomedical Topical Meeting, OSA technical Digest*. Optica Publishing Group, 2004 SF4. DOI: 10.1364/BIO.2004.SF4.

[135] S. Konugolu Venkata Sekar et al.: "Broadband diffuse optical characterization of elastin for biomedical applications", *Biophysical Chemistry* **229**, 130–134 (2017). DOI: 10.1016/j.bpc.2017.07.004.

[136] S. K. V. Sekar et al.: "Diffuse optical characterization of collagen absorption from 500 to 1700 nm", *Journal of Biomedical Optics* **22**(1), 015006 (2017). DOI: 10.1117/1.jbo.22.1.015006.

[137] D. P. d. S. Haupenthal et al.: "Effects of chronic treatment with gold nanoparticles on inflammatory responses and oxidative stress in Mdx mice", *Journal of Drug Targeting* **28**(1), 46–54 (2020). DOI: 10.1080/1061186X.2019.1613408.

[138] D. Long: "The Raman Effect: A Unified Treatment of the Theory of Raman Scattering by Molecules", Wiley, 2002. ISBN: 9780471490289.

[139] P. Griffiths, J. De Haseth, and J. Winefordner: "Fourier Transform Infrared Spectrometry", Chemical Analysis: A Series of Monographs on Analytical Chemistry and Its Applications. Wiley, 2007. ISBN: 9780470106297.

[140] J. J. P. Alix et al.: "Fiber optic Raman spectroscopy for the evaluation of disease state in Duchenne muscular dystrophy: An assessment using the mdx model and human muscle", *Muscle & Nerve* **66**(3), 362–369 (2022). DOI: 10.1002/mus.27671.

[141] T. Mateus et al.: "Fourier-Transform Infrared Spectroscopy as a Discriminatory Tool for Myotonic Dystrophy Type 1 Metabolism: A Pilot Study", *International Journal of Environmental Research and Public Health* **18**(7), 3800 (2021). DOI: 10.3390/ijerph18073800.

[142] G. Lu and B. Fei: "Medical hyperspectral imaging: a review", *Journal of Biomedical Optics* **19**(1), 010901 (2014). DOI: 10.1117/1.JBO.19.1.010901.

[143] A. Bhargava et al.: "Hyperspectral imaging and its applications: A review", *Heliyon* **10**(12), e33208 (2024). DOI: 10.1016/j.heliyon.2024.e33208.

[144] M. J. Khan et al.: "Modern Trends in Hyperspectral Image Analysis: A Review", *IEEE Access* **6**, 14118–14129 (2018). DOI: 10.1109/ACCESS.2018.2812999.

[145] J. Albani: "Principles and Applications of Fluorescence Spectroscopy", Wiley, 2008. ISBN: 9780470691335.

[146] E. Bonifazi et al.: "Use of RNA Fluorescence In Situ Hybridization in the Prenatal Molecular Diagnosis of Myotonic Dystrophy Type I", *Clinical Chemistry* **52**(2), 319–322 (2006). DOI: 10.1373/clinchem.2005.056283.

[147] W. H. Kong et al.: "Self-adjuvanted hyaluronate - antigenic peptide conjugate for transdermal treatment of muscular dystrophy", *Biomaterials* **81**, 93–103 (2016). DOI: 10.1016/j.biomaterials.2015.12.007.

[148] A. K. Peter et al.: "Nanospan, an alternatively spliced isoform of sarcospan, localizes to the sarcoplasmic reticulum in skeletal muscle and is absent in limb girdle muscular dystrophy 2F", *Skeletal Muscle* **7**(1), 11 (2017). DOI: 10.1186/s13395-017-0127-9.

[149] D. Bansal et al.: "Defective membrane repair in dysferlin-deficient muscular dystrophy", *Nature* **423**(6936), 168–172 (2003). DOI: 10.1038/nature01573.

[150] J. Pichon et al.: "Label-free 3D characterization of cardiac fibrosis in muscular dystrophy using SHG imaging of cleared tissue", *Biology of the Cell* **114**(3), 91–103 (2022). DOI: 10.1111/boc.202100056.

[151] T. W. Sawyer et al.: "Evaluation of segmentation algorithms for optical coherence tomography images of ovarian tissue", *Journal of Medical Imaging* **6**(01), 1 (2019). DOI: 10.1117/1.jmi.6.1.014002.

[152] E. Real et al.: "Collagen birefringence assessment in heart chordae tendineae through PS-OCT", in: *Optical Coherence Tomography and Coherence Domain Optical Methods in Biomedicine XXI*. Ed. by J. G. Fujimoto, J. A. Izatt, and V. V. Tuchin. **10053**. International Society for Optics and Photonics. SPIE, 2017 1005334. DOI: 10.1117/12.2254303.

[153] J. J. Gil and R. Ossikovski: "Polarized Light and the Mueller Matrix Approach", Series in Optics and Optoelectronics. CRC Press, 2022 215–228. ISBN: 9781000568660.

Part II

The behavior of light

Light propagation in uniform and non-uniform media

2

The corpus of this chapter is focused on providing the fundamentals required to understand the optical diagnostic methods that will be explored throughout this document. To ensure a clear and consistent foundation, this chapter will establish a uniform mathematical description of light behavior that will be followed throughout the book. This framework will facilitate a deeper understanding of the principles underlying various optical imaging techniques and their applications in the study of muscular dystrophies. Therefore, this chapter synthesizes information from key references, notably Born and Wolf's *Principles of Optics* [1] and Hecht's *Optics* [2]. Any information not directly derived from these sources is explicitly referenced.

There are two main formalisms for describing the behavior of light: one that considers light as an electromagnetic wave and another that considers it as particles called photons. In this chapter, we will focus on the former, namely the electromagnetic theory of light, given that it provides a straightforward way of analyzing light in terms of its intensity, spectral properties, or phase, which will help relate the theory described here with the different optical modalities studied in this thesis. Readers familiar with this content can skip to the next chapter for polarization properties of light or to the next part for materials and methods.

In this chapter, scalars (and vector magnitudes) are introduced in italics (a), vectors are depicted with an arrow on top ($\vec{a}$), and unitary vectors are represented with a hat ($\hat{a}$). The dot product is introduced as a centered dot ($\cdot$), the vector product with a cross ($\times$), and the tensor product with a circled cross ($\otimes$). This notation will be used in subsequent theory chapters.

2.1 Maxwell's laws of electromagnetism

Light can be described as an electromagnetic field and, as such, its behavior is well described by Maxwell's electromagnetic equations, which we will derive in this section, based on [1] and [2].

2.1.1 Electromagnetic force

A way to understand an electromagnetic field is by its effect on punctual charges. If one punctual charge q is subject to an electromagnetic field, this field will impose a force on it so that it will start moving. When the field has only an electric component, $\vec{E}$, the force it applies on the charge q, namely $\vec{F}_E$, will be aligned with the field (Fig. 2.1) and proportional to the value of the charge,

$$\vec{F}_E = q \cdot \vec{E} \quad .$$

On the other hand, if only a magnetic induction[1] $\vec{B}$ is present, the charge

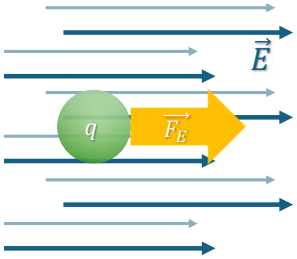

Figure 2.1: Representation of the electric force $\vec{F}_E$ that a charge q experiences under an electric field $\vec{E}$.

[1] Sometimes, in the literature, both the terms *magnetic induction* and *magnetic field* are used interchangeably to describe vector $\vec{B}$. However, we will keep the standard naming convention of *magnetic induction* for $\vec{B}$ and magnetic field for $\vec{H}$.

q will travel perpendicularly to $\vec{B}$ with a speed $\vec{v}$ (Fig. 2.2). Thus, the force a magnetic induction applies over a charge ($\vec{F_B}$) is defined as

$$\vec{F_B} = q \cdot \vec{v} \times \vec{B} \ .$$

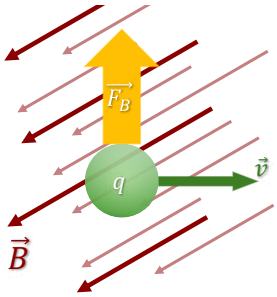

Figure 2.2: Representation of the magnetic force $\vec{F_B}$ that a charge q that moves with a speed $\vec{v}$ experiences under a magnetic induction $\vec{B}$.

Generally speaking, an electromagnetic field will have both components $\vec{E}$ and $\vec{B}$, and the force applied on a charge q for an electromagnetic field, $\vec{F}$, will include both $\vec{F_E}$ and $\vec{F_B}$ as follows:

$$\vec{F} = \vec{F_E} + \vec{F_B} = q \cdot \vec{E} + q \cdot \vec{v} \times \vec{B} \ . \tag{2.1}$$

2.1.2 Faraday's law of induction

When a closed, flat, conductive loop is introduced inside a magnetic inductance $\vec{B}$, a part of $\vec{B}$ will go through the area enclosed by the loop, A. The part that travels through A, i.e., the magnetic flux Φ_M, generates the movement of charges and, thus, an electromotive force[2] ε inside of the loop. The magnetic flux that travels through the area of the closed loop is described by

$$\Phi_M = \iint_A \vec{B} \cdot d\vec{S} \ ,$$

where $d\vec{S}$ is the surface differential that points perpendicularly to the surface of the area enclosed by the loop. The speed at which the loop is introduced in $\vec{B}$ will determine the magnitude of ε according to

$$\varepsilon = -\frac{d\Phi_M}{dt} = -\frac{d}{dt} \iint_A \vec{B} \cdot d\vec{S} \ . \tag{2.2}$$

The first equality of 2.2 is known as Lenz's Law, which states that the voltage induced by a changing magnetic flux will oppose (thus the minus sign) the rate of variation of said flux.

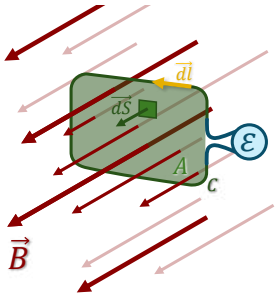

Figure 2.3: Representation of Faraday's law of induction. A closed loop C with line differential $\vec{dl}$ is inserted in a magnetic inductance $\vec{B}$. Part of the field goes through the area enclosed by the loop A with surface differential $\vec{dS}$. As a result, an electromotive force ε (and an electric field $\vec{E}$) travels in the loop C.

On the other hand, ε is a potential difference, which relates to an electric field through

$$\varepsilon = \oint_C \vec{E} \cdot d\vec{l} \ , \tag{2.3}$$

where C indicates an integral on the loop and $d\vec{l}$ is a line differential on the loop. Equation 2.3 indicates that the existence of ε is due to an electric field that is traveling inside of the closed loop. When we combine equations 2.2 and 2.3, we arrive at the Faraday induction law (Fig. 2.3),

$$\oint_C \vec{E} \cdot d\vec{l} \ = -\frac{d}{dt} \iint_A \vec{B} \cdot d\vec{S} \ , \tag{2.4}$$

which states that a time-varying magnetic induction $\vec{B}$ generates electric fields $\vec{E}$ that travel in closed loops in planes perpendicular to $\vec{B}$[3].

2.1.3 Gauss's law for electric fields

When an electric field is enclosed by a surface A, an electric flux Φ_E will travel, outwards or inwards, through the said surface (Fig. 2.4). The net

[2] In the electromagnetic context, the electromotive force ε is a voltage – a potential difference. When possible, the term *force* will not be used to avoid confusion.

[3] Often, $\vec{B}$ is not going to be uniform in space, and really be a function of the spatial point $\vec{r}$ and time ($\vec{B} = \vec{B}(\vec{r}, t)$). Therefore, the partial derivative $\partial/\partial t$ might be depicted instead of the total derivative d/dt.

electric flux is thus

$$\Phi_E = \oiint_A \vec{E} \cdot d\vec{S} \quad . \tag{2.5}$$

Now, if this field is generated by a single point charge q and we evaluate it on a spherical surface, $\vec{E}$ will be perpendicular to the surface and, therefore, $\vec{E}$ and $d\vec{S}$ will be parallel. Additionally, the magnitude of the electric field E would be uniform in any spherical surface with radius r (Fig. 2.5), thus

$$\Phi_E = E \oiint_A dS = E4\pi r^2 \quad . \tag{2.6}$$

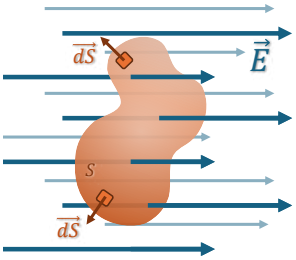

Figure 2.4: Electric field $\vec{E}$ traveling inside and outside of one closed arbitrary surface S with surface differential $d\vec{S}$.

On the other hand, Coulomb's law states that the magnitude of the electric field generated by a point charge is

$$E = \frac{1}{4\pi\epsilon_0}\frac{q}{r^2} \tag{2.7}$$

where, in this case, r represents the distance to the point charge and ϵ_0 the vacuum permittivity[4]. Combining equations 2.6 and 2.7 gives the electric flux caused by a point charge as

$$\Phi_E = \frac{q}{\epsilon_0} \quad ,$$

which can be extended to the electric flux caused by a group of N point charges as

$$\Phi_E = \frac{1}{\epsilon_0}\sum_n^N q_n \quad . \tag{2.8}$$

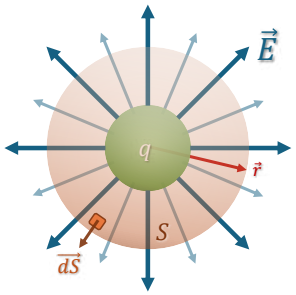

Figure 2.5: Electric field $\vec{E}$ created by a point charge q traveling through a spherical surface S of radius r with surface differential $d\vec{S}$.

[4] $\epsilon_0 = 8.854188 \times 10^{-12}\ F/m$

In the case where the charges are not individually considered but instead treated as a charge density ρ that occupies a volume V (Fig. 2.6), the Gauss law for electric fields is finally derived from the combination of equations 2.5 and 2.8, and transforming the charge sum by the volume integral of the charge density as

$$\oiint_A \vec{E} \cdot d\vec{S} = \frac{1}{\epsilon_0}\iiint_V \rho dV \quad , \tag{2.9}$$

where $\vec{E}$ is the electric field, A the closed integration area, $d\vec{S}$ the surface differential of A, ϵ_0 the vacuum permittivity[5], V the integration volume, and dV the volume differential of V.

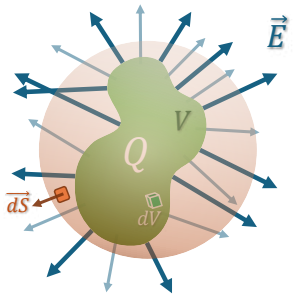

Figure 2.6: Electric field $\vec{E}$ created by a charge density ρ distributed over a volume V ($Q = \iiint_V \rho dV$) traveling through a spherical surface S of radius r with surface differential $d\vec{S}$.

2.1.4 Gauss's law for magnetic fields

There is no magnetic equivalent to the electric point charge, meaning that there are no known particles that act as sources or sinks of magnetic field lines. Instead, a point "magnet" can be considered as an equivalent to the electric point charge, but every field line that exits the north pole of this magnet will end up on its south pole (Fig. 2.7). As such, any closed, arbitrary surface that we could trace around the point magnet will have the same number of lines exiting the surface and entering it at another point. Therefore, the magnetic flux on said surface will always be null.

[5] In the case where the charges are not in vacuum but in a material medium, the electric permittivity of the medium (ϵ) should be used instead of that of vacuum (ϵ_0).

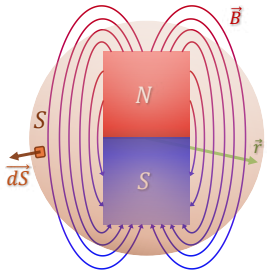

Figure 2.7: Magnetic induction $\vec{B}$ created by a magnet traveling through a spherical surface S of radius r with surface differential $\vec{dS}$.

The Gauss law for magnetic fields is then given by:

$$\Phi_M = \oiint_A \vec{B} \cdot d\vec{S} = 0 \quad . \tag{2.10}$$

2.1.5 Ampère's circuital law

When a straight, infinitesimally thin wire transports a uniform charge current[6] j, a magnetic induction $\vec{B}$ is generated around said wire by the moving current. Specifically, $\vec{B}$ is perpendicular to the travel direction of j, and its magnitude is given by

$$B = \frac{\mu_0 j}{2\pi r}$$

where r is the distance from the wire and μ_0 is the vacuum permeability[7]. Note that the total current j and the current density $\vec{J}$ are related through the integral

$$j = \iint_A \vec{J} \cdot d\vec{S} = \iint_A J \cdot dS \quad .$$

By tracing a closed, circular loop C in a perpendicular plane to j, the line differential on the loop $d\vec{l}$ and the magnetic induction $\vec{B}$ are parallel, giving

$$\vec{B} \cdot d\vec{l} = B \cdot dl = Br \cdot d\phi \quad ,$$

where r is the radius of C, and $d\phi \in [0, 2\pi]$ the angle differential (Fig. 2.8).

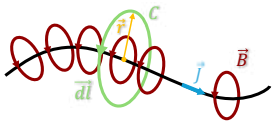

Figure 2.8: Representation of the enclosed loop of integration C to obtain the magnetic induction $\vec{B}$ created by an uniform current density $\vec{J}$ traveling through a thin wire with path differential of $d\vec{l}$.

Now, by integrating the field around the thin wire, we obtain Ampère's circuital law for a single, infinitesimally thin wire as

$$\oint_C \vec{B} \cdot d\vec{l} = \oint_C Br \cdot d\phi = \frac{\mu_0 j}{2\pi r} \cdot r \int_0^{2\pi} d\phi \quad ,$$

$$\oint_C \vec{B} \cdot d\vec{l} = \mu_0 \cdot j \quad . \tag{2.11}$$

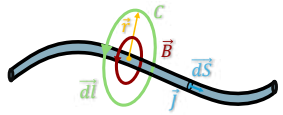

Figure 2.9: Representation of the enclosed loop of integration C to obtain the magnetic induction $\vec{B}$ created by a non-uniform current density $\vec{J}$ traveling through a wire with path differential of $d\vec{l}$ and differential cross section of $d\vec{S}$.

Following the same rationale applied to deriving Gauss's law for electric fields, we could assume that adding N infinitesimally thin wires inside of C would lead to changing j for $\sum_n^N j_n$ in equation 2.11. We could go further and explore what happens when the wire is not infinitesimally thin. In that case, the wire would have a non-zero cross-section, and the current j would no longer be uniform when traveling through the wire. In this case, a current density $\vec{J}$ would need to be evaluated in an area A with a surface differential[8] $d\vec{S}$, leading to the complete integral definition of Ampère's law[9] (Fig. 2.9):

$$\oint_C \vec{B} \cdot d\vec{l} = \mu_0 \iint_A \vec{J} \cdot d\vec{S} \tag{2.12}$$

This first version of Ampère's law is not complete and can lead to some inconsistencies. An example is provided in [2], which consists of evaluating Eq. 2.12 in the case of charging a capacitor with two wires.

[6] The notation for the current was taken from [2], where the current is indicated by a lowercase letter (i) and its density by an uppercase letter ($\vec{J}$). Here, we changed the lowercase from i to j to avoid confusion with the imaginary unit.

[7] $\mu_0 = 1.256637 \times 10^{-6}\ N/A^2$

[8] Note that, according to this first version of Ampère's law, the integration area does not need to be closed, since we are evaluating the current that travels through the area and not a net flux that needs to consider what enters and what exits a volume.

[9] Similarly to Eq. 2.9, if the current is embedded in a medium, the medium permeability (μ) should be used instead of that of the vacuum (μ_0).

In this example, each wire would be connected to each terminal of the capacitor, and, between both terminals, no current is able to travel through (the inside of a capacitor is filled with a non-conductive medium). According to Eq. 2.12, we can integrate the right side on any area A. If we choose A in one of the wires, a current will be traveling from the source to one of the capacitor plates, and the integral would be non-zero. However, by choosing A as one of the plates, no current is actually traveling *through* it, and the integral would now be zero, although nothing has physically changed, and we know sinks of $\vec{B}$ do not exist. This inconsistency is fixed by considering that a charging or discharging capacitor produces a magnetic field between its plates, even without moving charges, meaning that charges are not the only source of magnetic fields, as equation 2.12 suggests.

Specifically, an electric field $\vec{E}$ exists between the plates of area A of a capacitor with total charge Q (Fig. 2.10) given by

$$\epsilon E = \frac{Q}{A} \ .$$

When this field varies over time, the previous equation results

$$\epsilon \frac{\partial E}{\partial t} = \frac{\partial Q/\partial t}{A} = \frac{j}{A} \ ,$$

which is, by definition, a current density known as displacement current density $\vec{J_D} = \epsilon(\partial\vec{E}/\partial)t$, parallel to $\vec{E}$.

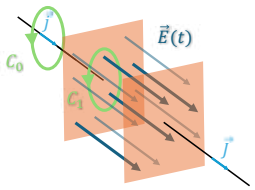

Figure 2.10: A time-variable electric field $\vec{E}$ exists between the plates of a capacitor in the presence of a moving current $\vec{H}$, so that the integrals of the magnetic field along C_1 and C_2 are both non-zero.

This addition to Eq. 2.12 leads to what today is known as Ampère's Law

$$\oint_C \vec{B} \cdot d\vec{l} = \mu \iint_A \left(\vec{J} + \epsilon \frac{\partial \vec{E}}{\partial t} \right) \cdot d\vec{S} \ , \tag{2.13}$$

which states that both moving currents and time-varying electric fields are sources of magnetic fields.

2.1.6 Maxwell's equations

The four previous sections introduced equations 2.4, 2.9, 2.10, and 2.13, which constitute the four Maxwell's laws for electromagnetic fields. In their simplest form, when no charges ($\rho = 0$) or currents ($\vec{J} = 0$) are present, and the field is evaluated in free space ($\epsilon = \epsilon_0$, $\mu = \mu_0$), the four equations are reduced to

$$\oiint_A \vec{E} \cdot d\vec{S} = 0 \ ,$$

$$\oiint_A \vec{B} \cdot d\vec{S} = 0 \ ,$$

$$\oint_C \vec{E} \cdot d\vec{l} = - \iint_A \frac{\partial \vec{B}}{\partial t} \cdot d\vec{S} \ , \text{ and}$$

$$\oint_C \vec{B} \cdot d\vec{l} = \mu_0 \epsilon_0 \iint_A \frac{\partial \vec{E}}{\partial t} \cdot d\vec{S} \ .$$

$\vec{E}$ and $\vec{B}$ are vector fields, which means that we can take their divergence[10] ($\vec{\nabla}\cdot$) and curl ($\vec{\nabla}\times$) to evaluate their behavior. By using these operators, alongside Gauss's divergence theorem for a vector field $\vec{F}$

$$\oiint_A \vec{F}\cdot d\vec{S} = \iiint_V \vec{\nabla}\cdot\vec{F}dV \quad , \tag{2.14}$$

and Stokes's theorem

$$\oint_C \vec{F}\cdot d\vec{l} = \iint_A \vec{\nabla}\times\vec{F}\cdot d\vec{S} \quad , \tag{2.15}$$

one can reach[11] the differential form of Maxwell's equations:

$$\vec{\nabla}\cdot\vec{E} = \frac{\rho}{\epsilon_0} \tag{2.16}$$

$$\vec{\nabla}\cdot\vec{B} = 0 \tag{2.17}$$

$$\vec{\nabla}\times\vec{E} = -\frac{\partial\vec{B}}{\partial t} \tag{2.18}$$

$$\vec{\nabla}\times\vec{B} = \mu_0\epsilon_0\frac{\partial\vec{E}}{\partial t} \tag{2.19}$$

[10] The *Nabla* operator $\vec{\nabla}$ is used to express the partial derivatives on the chosen coordinate space. For example, in Cartesian coordinates,

$$\vec{\nabla} = \hat{x}\frac{\partial}{\partial x} + \hat{y}\frac{\partial}{\partial y} + \hat{z}\frac{\partial}{\partial z} \quad ,$$

where $(\hat{x}, \hat{y}, \hat{z})$ are the Cartesian unit vectors.

[11] We refer to reference [2], section 3.1.5 for the full transformation from the integral to the differential Maxwell's equations

2.2 Material and wave equations

Maxwell's laws define entirely the electromagnetic field caused by a distribution of charges or currents. Still, when evaluated on a medium other than the vacuum, one must also consider the effect the field has on the medium and vice versa. This section will introduce the remaining equations that describe the impact of the effects mentioned above, which lead to the wave equation that describes how light moves through space. All the content in this section is included in references [2] and [1].

2.2.1 Material polarization and material equations

When a dielectric medium is subject to the effects of an electric field $\vec{E}$, the charges inside the medium will shift positions, leading to a different charge distribution than when $\vec{E}$ is absent. Specifically, the charges will tend to align with $\vec{E}$, leading to positively and negatively charged areas inside the material, i.e., a dipole is created inside the material. The separation between those areas will, in turn, create its own electric field that will overlap with the external field and that is characterized by the dipole moment per unit volume, defined as electric polarization $\vec{P}$. When the medium is isotropic, lineal and homogeneous, $\vec{P}$ is parallel and proportional to $\vec{E}$ and can be derived as

$$(\epsilon - \epsilon_0)\vec{E} = \vec{P} \tag{2.20}$$

When no medium is present ($\epsilon = \epsilon_0$), $\vec{P} = 0$.

The electric polarization $\vec{P}$ will alter the electric field inside the medium with respect to its value in the vacuum. The electric displacement $\vec{D}$,

defined as

$$\vec{D} = \epsilon_0 \vec{E} + \vec{P} \ ,$$

measures the change in the electric field given by the existence of $\vec{P}$. Including Eq. 2.20 to the previous one leads to

$$\vec{D} = \epsilon \vec{E} \ ; \tag{2.21}$$

while $\vec{P}$ exists only inside of the medium, $\vec{D}$ exists everywhere $\vec{E}$ exists.

Analogously, where a material is subject to a magnetic inductance $\vec{B}$, said field will induce a magnetic dipole moment per unit volume $\vec{M}$, that will alter the incident $\vec{B}$. The alteration can be characterized through the magnetic field intensity $\vec{H}$ as follows:

$$\vec{H} = \frac{1}{\mu_0}\vec{B} - \vec{M} \ .$$

Again, for an isotropic, linear, homogeneous, and non-ferromagnetic medium, $\vec{B}$ and $\vec{H}$ are related through

$$\vec{H} = \frac{1}{\mu}\vec{B} \ . \tag{2.22}$$

The last equation needed to describe the electromagnetic behavior of materials is Ohm's law

$$\vec{J} = \sigma \vec{E} \tag{2.23}$$

which states that the application of an electric field over a material with conductivity σ will lead to the creation of currents $\vec{J}$.

2.2.2 The wave equations for electromagnetic fields

By using the material equations (2.21, 2.22, and 2.23) to rewrite Maxwell's equations (2.16, 2.17, 2.18 and 2.19), one can derive[12] the following two equations[13]

$$\nabla^2 \vec{E} - \mu\epsilon \frac{\partial^2 \vec{E}}{\partial t^2} - \mu\sigma \frac{\partial \vec{E}}{\partial t} = \vec{\nabla}\left(\frac{\rho}{\epsilon}\right)$$

$$\nabla^2 \vec{B} - \mu\epsilon \frac{\partial^2 \vec{B}}{\partial t^2} - \mu\sigma \frac{\partial \vec{B}}{\partial t} = 0$$

When a medium is non-conducting ($\sigma = 0$) and has no charge ($\rho = 0$), the previous equations reduce to

$$\nabla^2 \vec{E} - \mu\epsilon \frac{\partial^2 \vec{E}}{\partial t^2} = 0 \ , \text{ and}$$

$$\nabla^2 \vec{B} - \mu\epsilon \frac{\partial^2 \vec{B}}{\partial t^2} = 0 \ ,$$

and, in free space ($\mu = \mu_0$ and $\epsilon = \epsilon_0$)

$$\nabla^2 \vec{E} - \mu_0\epsilon_0 \frac{\partial^2 \vec{E}}{\partial t^2} = 0 \ , \text{ and} \tag{2.24}$$

[12] We refer to references [2], appendix 1, and [1], section 1.2 for the full derivation of the vector expressions of Maxwell's equations.

[13] The *Laplacian* operator ∇^2 is a scalar operator defined in terms of the coordinate space of choice. In Cartesian coordinates, its definition is

$$\nabla^2 = \frac{\partial^2}{\partial x^2} + \frac{\partial^2}{\partial y^2} + \frac{\partial^2}{\partial z^2} \ ,$$

not to be confused with the *Nabla* operator $\vec{\nabla}$.

$$\nabla^2 \vec{B} - \mu_0 \epsilon_0 \frac{\partial^2 \vec{B}}{\partial t^2} = 0 \quad . \tag{2.25}$$

Given two fields $\vec{E} = (E_x, E_y, E_z)$ and $\vec{B} = (B_x, B_y, B_z)$, equations 2.24 and 2.25 are in fact a set of three equations each, one for each component of $\vec{E}$ and one for each element of $\vec{B}$, taking into account that the Laplacian ∇^2 acts for all directions of the vector field.

All these equations have the shape of a scalar wave equation

$$\frac{\partial^2 \psi}{\partial x^2} + \frac{\partial^2 \psi}{\partial y^2} + \frac{\partial^2 \psi}{\partial z^2} = \frac{1}{v^2} \frac{\partial^2 \psi}{\partial t^2} \tag{2.26}$$

under the condition that the propagation speed of said waves needs to be

$$v = \frac{1}{\sqrt{\mu_0 \epsilon_0}} \quad ,$$

which indeed leads to the speed of light in a vacuum

$$c = (\sqrt{\epsilon_0 \mu_0})^{-1} = 2.998926 \times 10^8 m/s \quad . \tag{2.27}$$

Thus, electromagnetic fields can be treated as energy-carrying waves moving through any medium.

2.2.3 The transverse nature of light waves

To evaluate the way light propagates through space, we will start considering a plane wave that is traveling in the z direction, with $\vec{E} = \vec{E}(z, t)$. In this case, Maxwell's equation 2.16 reduces to

$$\frac{\partial \vec{E}}{\partial z} = 0$$

which means that if the wave is not uniform across space, its variation is not going to be in the direction of propagation z but instead in the other components. This is the definition of a transverse wave. Light behaving as a transverse wave means that to have a complete definition of the wave, it is necessary to know the direction $\vec{E}$ is pointing to. The complete description in the plane perpendicular to z is known as *Polarization*, which will be explored further down this chapter.

Let us now consider an electric field such that

$$\vec{E} = E_x(z, t) \cdot \hat{x} \quad ,$$

i.e., a plane wave that travels in the z direction, and its oscillations are restricted to the x axis of the Cartesian coordinate space. By Maxwell's equation 2.18 we obtain

$$\frac{\partial E_x}{\partial z} = -\frac{\partial B_y}{\partial t} \quad , \tag{2.28}$$

with B_z being the component of $\vec{B}$ parallel to the z axis. This expression indicates that for a time-varying $\vec{E}$ to exist, with oscillations restricted to the x axis, the only time-varying $\vec{B}$ possible that follows Maxwell's laws

must have its oscillations parallel to the y axis. As such, the directions of $\vec{E}$ and $\vec{B}$ are restricted to a plane perpendicular to the propagation direction of the wave, meaning that the complete electromagnetic field behaves as a transverse wave.

If we apply the previous relationship to a harmonic field with angular frequency ω and phase ϕ, described by

$$E_x(z,t) = E_{0,x}\cos\left[\omega\left(\frac{z}{c}-t\right)+\phi\right] \quad , \tag{2.29}$$

it can be derived[14] that

$$E_x = cB_y \quad ,$$

which indicates that the amplitudes of the $\vec{E}$ and $\vec{B}$ fields are in phase, perpendicular to each other, and proportional through c. In dielectric (non-magnetic and non-conducting) media with light propagation speed v in the $\hat{k}$ direction, this expression can be generalized for the amplitudes $||\vec{E}|| = E$ and $||\vec{B}|| = B$, as

$$E = vB \quad , \tag{2.30}$$

and, for any general medium,

$$\begin{aligned} \vec{E} &= -\sqrt{\frac{\mu}{\epsilon}}\hat{k}\times\vec{H} \quad \text{, and} \\ \vec{H} &= \sqrt{\frac{\epsilon}{\mu}}\hat{k}\times\vec{E} \quad . \end{aligned} \tag{2.31}$$

[14] We refer to section 3.2.1 of reference [2], and section 1.4.1 of reference [1] for the full derivation of equations 2.30 and 2.31.

2.3 Energy and irradiance

An electromagnetic field carries energy with it, which allows us to measure the field and its properties with conventional detectors. This section aims to provide the necessary equations to describe energy propagation in electromagnetic fields. This section constitutes a summary of what is described in reference [1].

2.3.1 Poynting vector

The density of electric (u_E) and magnetic (u_H) energy are defined as

$$u_E = \frac{1}{2}\vec{E}\cdot\vec{D} \quad = \frac{\epsilon_0}{2}E^2, \text{and}$$

$$u_B = \frac{1}{2}\vec{H}\cdot\vec{B} \quad = \frac{1}{2\mu_0}B^2,$$

respectively. Then, the total electromagnetic energy contained in a region of space of volume V must be

$$U = U_E + U_B = \int_V (u_E + u_B)dV = \frac{1}{2}\int_V (\vec{E}\cdot\vec{D} + \vec{H}\cdot\vec{B})dV$$

This integral appears in the energy conservation law for electromagnetic fields, which is a continuity equation defined as

$$\int_V \left(\vec{E} \cdot \frac{\partial \vec{D}}{\partial t} + \vec{H} \cdot \frac{\partial \vec{B}}{\partial t} \right) dV + \int_V (\vec{E} \cdot \vec{J}) dV + \oint_A (\vec{E} \times \vec{H}) dS = 0 \quad , \quad (2.32)$$

that states that in order for the energy to be conserved inside a volume V enclosed by a surface A, three terms need to cancel each other. The first term corresponds to the temporal variation of total electromagnetic energy $\partial U / \partial t$, which, as previously indicated, is the total energy in the volume. The second term indicates that part of the variation of energy inside of V is due to the appearance of some currents $\vec{J}$. Specifically, $\vec{J}$ has two components: a displacement current caused by the movement of a charge density ρ with speed $\vec{v}$ inside of V, and another caused by the ohmic conductivity of the medium σ. Therefore:

$$\vec{J} = \sigma \vec{E} + \rho \vec{v} \quad .$$

Finally, the last term on equation 2.32 represents the amount of energy that leaves the volume V through the surface A, which leads to the definition of Poynting's vector:

$$\vec{S} = \vec{E} \times \vec{H} = \frac{1}{\mu_0} \vec{E} \times \vec{B} \quad = c^2 \epsilon_0 \vec{E} \times \vec{B}. \quad (2.33)$$

This vector indicates that the energy carried by an electromagnetic wave is perpendicular to $\vec{E}$ and $\vec{B}$, which means that the energy travels parallel to the propagation speed of the electromagnetic wave.

2.3.2 Irradiance

The amount of light that illuminates a surface is the average energy per unit area and unit time. It receives the name *irradiance* and is denoted by I. Electromagnetic waves have a periodic nature, and their period of variation, especially for those waves on the visible wavelength range ($\lambda \sim 10^{-7}$ m), is in the range of $\tau = 10^{-15}$ s. Therefore, any actual measurement of I with a conventional camera with minimum exposure speeds in the range of microseconds is going to take a minimum of $10^9 \tau$ to capture an image, leading to the impossibility of measuring the instantaneous state of the field.

As its definition suggests, the irradiance is related to the Poynting vector $\vec{S}$, but not to its instant value, but to its average behavior after a measurement time $T >> \tau$:

$$I = \langle \vec{S} \rangle_T = \langle \vec{E} \times \vec{H} \rangle$$

Let us now consider the specific case of a harmonic electromagnetic field with

$$\begin{aligned} \vec{E} &= \vec{E_0} \cos(\vec{k} \cdot \vec{r} - \omega t) \quad \text{and} \\ \vec{B} &= \vec{B_0} \cos(\vec{k} \cdot \vec{r} - \omega t) \quad , \end{aligned} \quad (2.34)$$

where $\vec{k}$ represents the propagation vector (i.e., parallel to the Poyting vector orientation), $\vec{r}$ represents a point in space, ω is the angular frequency[15]

[15] ω can be denoted in the literature as *angular frequency* or *angular speed*, and represents the number of radians per second. It is directly proportional to the frequency f by a factor 2π.

of the wave, t is time, and $\vec{E}_0$ and $\vec{B}_0$ are the real amplitudes of the fields. By considering a point with a constant phase and differentiating the phase with respect to time, one can relate the propagation vector $\vec{k}$ to the angular frequency ω and the propagation speed of the wave v through the following relationship:

$$v = \frac{\omega}{||\vec{k}||} = \frac{\omega}{k} \quad , \tag{2.35}$$

where the absolute value of the propagation vector, k, is defined as the *wavenumber* of the wave, and relates to its wavelength λ through

$$||\vec{k}|| = k = \frac{2\pi}{\lambda} \tag{2.36}$$

The time average of the Poynting vector for the field described in equations 2.34 is

$$\langle \vec{S}(r,t) \rangle_T = c^2 \epsilon_0 |\vec{E}_0 \times \vec{B}_0| \langle \cos^2(\vec{k} \cdot \vec{r} - \omega t) \rangle = \frac{c^2 \epsilon_0}{2} |\vec{E}_0 \times \vec{B}_0| \quad ,$$

which leads to an irradiance of

$$I = \frac{c\epsilon_0}{2} E_0^2 \quad . \tag{2.37}$$

The energy of an electromagnetic field is balanced between $\vec{E}$ and $\vec{B}$ so that its irradiance, which is the measurable magnitude of the energy the fields carry, is proportional to the square of the electric field.

2.4 Light-matter interactions in non-dispersive, continuous media

This section explores how light interacts with uniform biological tissues, such as those found in the cornea or vitreous humor, covering fundamental concepts like refraction, reflection, and transmission. Here, we'll examine Snell's Law, Fresnel's equations, and the behavior of evanescent waves.[16]. The contents of this section can be found in references [1] and [2].

[16] In this section, we will interchangeably use electromagnetic field and light. Usually, the latter often refers to the visible part of the electromagnetic spectrum. Still, for us, the term *light* or *radiation* will cover the whole electromagnetic range, given that there is no formal mathematical distinction between the two terms.

2.4.1 Refractive index

We have introduced in section 2.2.1 that when light travels inside a medium, the medium affects the electromagnetic field. We have also introduced the two principal magnitudes that help describe the changes the electromagnetic field suffers, namely the electric permittivity (ϵ) and magnetic permeability (μ) of the medium. We have also seen, in section 2.2.2, that electromagnetic fields travel as a wave with speed defined by the same two magnitudes in a vacuum, $c = (\sqrt{\epsilon_0 \mu_0})^{-1}$ (Eq. 2.27).

It is natural, then, to define that light moving inside a medium will travel with a speed given by

$$v = \frac{1}{\sqrt{\mu\epsilon}} \quad .$$

[17] Usually, by *refractive index*, the literature refers to the real part of the *complex refractive index*.

The index of refraction or refractive index[17] is the measurement of the speed of light inside a medium with respect to its speed in vacuum,

$$n = \frac{c}{v} = \sqrt{\frac{\epsilon\mu}{\epsilon_0\mu_0}} \geq 1 \ , \tag{2.38}$$

with the refractive index of the vacuum being $n_0 = 1$.

Even though we have not mathematically introduced ϵ and μ, it is worth noting that these are wavelength-dependent quantities, meaning that they are going to provide a different response in terms of the wavelength of the electromagnetic field, λ. This wavelength dependency of the refractive index is the reason why shining a white light at an angle onto a prism ($n = n(\lambda)$) is enough to split it into its different colors, given that each wavelength moves at a different speed (and angle, as we will see in the following sections). This phenomenon is known as dispersion.

In reality, the refractive index is the real part of the complex refractive index

$$\tilde{n}(\lambda) = n(\lambda) - i\kappa(\lambda) \tag{2.39}$$

where $\kappa(\lambda)$ contains the wavelength-dependent attenuation of light inside the medium, as we will introduce in the next sections.

2.4.2 Boundary effects

Light traveling in a vacuum has different properties (i.e., propagation speed) than when traveling inside a medium. Therefore, when an electromagnetic wave reaches a boundary that separates the vacuum from the inside of the medium, there must be a specific set of equations that describe the transition from the outside to the inside. We know that Maxwell's laws describe the behavior of the electromagnetic field in any medium, so it must be possible to derive a set of specific boundary conditions that relate the fields on both sides of the boundary.

Let $\hat{n}_1$ be a unitary vector normal to the boundary pointing to the inside of the first medium, and $\hat{n}_2$ be a unitary vector normal to the boundary pointing to the inside of the second medium, so that $\hat{n}_1 = -\hat{n}_2$. Let the sub-indexes 1 and 2 denote magnitudes on the first and second medium, respectively, on each side of the boundary. Then, the following four conditions can be derived[18] from Maxwell's equations by considering closed volumes or areas that cross the boundary:

[18] We refer to M. Born and E. Wolf's book, *Principles of Optics* [1], section 1.1.3 for the full derivation of the boundary conditions.

$$\hat{n}_2 \cdot (\vec{B}_2 - \vec{B}_1) = 0 \ , \tag{2.40}$$

$$\hat{n}_2 \cdot (\vec{D}_2 - \vec{D}_1) = 4\pi\rho \ , \tag{2.41}$$

$$\hat{n}_2 \times (\vec{E}_2 - \vec{E}_1) = 0 \ , \text{ and} \tag{2.42}$$

$$\hat{n}_2 \times (\vec{H}_2 - \vec{H}_1) = \frac{4\pi}{c}\vec{J} \ , \tag{2.43}$$

where ρ (Eq. 2.41) represents a possible charge density present on the boundary, and $\vec{J}$ (Eq. 2.43) is a current density flowing on the boundary's surface. Note that while ρ is a scalar quantity, $\vec{J}$ is a vector quantity, with direction pointing to the current movement.

These four equations are known as the boundary conditions of the electromagnetic field, and are interpreted as follows [1]:

- Eq. 2.40: The normal components of the magnetic inductance are continuous on the boundary.
- Eq. 2.41: The normal components of the electric displacement are modified in the presence of a surface charge density or otherwise continuous when $\rho = 0$.
- Eq. 2.42: The tangential components of the electric field are continuous on the boundary.
- Eq. 2.43: The tangential components of the amplitude of the magnetic field are modified in the presence of a surface current density or otherwise continuous when $\vec{J} = 0$.

Now that we know how the electromagnetic field behaves in a boundary between two media, we can use the boundary conditions to derive how a boundary modifies an incident field after their interaction. For the following steps, we will continue with the wave formalism to derive the equations that indicate how the electromagnetic field is modified after reaching a boundary between two media, starting with a monochromatic (λ = constant) plane wave. Let $\vec{E}_i$ be an incident wave onto a two-medium boundary, with a time-independent amplitude $\vec{E}_{0,i}$, propagation vector $\vec{k}_i$, propagation speed v, and angular frequency ω_i. Let $\vec{r} = (x, y, z)$ be the position vector and t be the point in time. According to this definition, $\vec{E}_i$ is given by

$$\begin{aligned}\vec{E}_i &= \vec{E}_{0,i}\cos\left(\vec{k}_i\cdot\vec{r}_i-\omega_i t\right) = \vec{E}_{0,i}\cos\left(k_i\hat{k}_i\cdot\vec{r}_i-\omega_i t\right) = \\ &= \vec{E}_{0,i}\cos\left(\frac{\omega_i}{v_i}\hat{k}_i\cdot\vec{r}_i-\omega_i t\right) = \vec{E}_{0,i}\cos\left[\omega_i\left(\frac{\hat{k}_i}{v_i}\cdot\vec{r}_i-t\right)\right] \quad .\end{aligned} \tag{2.44}$$

After reaching the boundary, part of the incident wave's energy will reach the second medium, while another part will stay on the first. Let $\vec{E}_r$ and $\vec{E}_t$ represent the part of $\vec{E}_i$ that is reflected to the first medium and transmitted into the second one, respectively. Then, their expressions are

$$\vec{E}_r = \vec{E}_{0,r}\cos\left[\omega_r\left(\frac{\hat{k}_r}{v_r}\cdot\vec{r}_r-t\right)\right] \quad ,$$
$$\vec{E}_t = \vec{E}_{0,t}\cos\left[\omega_t\left(\frac{\hat{k}_t}{v_t}\cdot\vec{r}_t-t\right)\right] \quad ,$$

where the sub-indices r and t refer to the same properties of the incident wave defined in Eq.2.44, but for the reflected and transmitted wave, respectively.

Let θ_i be the incidence angle of $\vec{E}_i$ on the surface that separates both media, with respect to the surface normal, that relates to $\hat{k}_i$ via

$$\hat{k}_i = (\sin\theta_i, 0, \cos\theta_i) \quad . \tag{2.45}$$

For the reflected and transmitted waves, their respective propagation

vectors would be

$$\begin{aligned} \vec{k}_r &= \frac{w_r}{v_r}(\hat{k}_{x,r}, \hat{k}_{y,r}, \hat{k}_{z,r}) \text{ and} \\ \vec{k}_t &= \frac{w_t}{v_t}(\hat{k}_{x,t}, \hat{k}_{y,t}, \hat{k}_{z,t}) \ , \end{aligned} \tag{2.46}$$

where $\hat{k}_{a,b}$ represents component a of the unitary propagation vector $\hat{k}_b$.

2.4.3 Phase of the electromagnetic field in a boundary: Reflection and Snell's laws

At the point $p = (p_x, p_y, p_z)$ in the surface where $\vec{E}_i$, $\vec{E}_r$ and $\vec{E}_t$ coincide, the phase of the three waves must be the same. Therefore, it must be fulfilled that

$$\omega_i \left(\frac{\hat{k}_i}{v_i} \cdot \vec{r}_i - t \right) = \omega_r \left(\frac{\hat{k}_r}{v_r} \cdot \vec{r}_r - t \right) = \omega_t \left(\frac{\hat{k}_t}{v_t} \cdot \vec{r}_t - t \right) \ .$$

If we consider the coordinate origin on the surface, the point p reduces to $(p_x, p_y, 0)$, which leads to:

$$\begin{aligned} \omega_i \left(\frac{\hat{k}_i}{v_i} \cdot (p_x, p_y, 0) - t \right) &= \omega_r \left(\frac{\hat{k}_r}{v_r} \cdot (p_x, p_y, 0) - t \right) = \\ &= \omega_t \left(\frac{\hat{k}_t}{v_t} \cdot (p_x, p_y, 0) - t \right) \ . \end{aligned}$$

We can modify the previous equation by considering the equations of the unitary propagation vectors 2.45 and 2.46, leading to

$$\begin{aligned} \omega_i \left(\frac{p_x \sin\theta_i}{v_i} - t \right) &= \omega_r \left(\frac{p_x \hat{k}_{x,r} + p_y \hat{k}_{y,r}}{v_r} - t \right) = \\ &= \omega_t \left(\frac{p_x \hat{k}_{x,t} + p_y \hat{k}_{y,t}}{v_t} - t \right) \ . \end{aligned} \tag{2.47}$$

Now, for the previous equation to be true, three rules must be obeyed. The first one is that the angular frequency of the three waves must be the same

$$w_i = w_r = w_t \ . \tag{2.48}$$

By Eqs. 2.35 and 2.36, we know that the angular frequency relates to the wavelength through

$$\omega = vk = \frac{2\pi v}{\lambda}$$

so, if ω is the same for the three waves and v is not, the wavelength λ must be modified to fulfill Eq. 2.48. The first relationship in equation 2.48

is

$$\begin{aligned} \omega_i &= \omega_t \\ \frac{2\pi v_i}{\lambda_i} &= \frac{2\pi v_t}{\lambda_t} \\ \frac{\lambda_t}{\lambda_i} &= \frac{v_t}{v_i} \\ \lambda_t &= \lambda_i \frac{n_i}{n_t} \end{aligned} \tag{2.49}$$

which states that light changing from one medium to another can lead to shorter ($n_i < n_t, \lambda_t < \lambda_i$) or longer ($n_i > n_t, \lambda_t > \lambda_i$) wavelengths. To consider the second relationship of equation 2.48 is sufficient to change all t by r in the previous derivation, and we would arrive at the same relationship for the wavelengths of the incident and reflected waves. However, given that the reflection is produced inside the first medium, $n_i = n_r$ and $\lambda_i = \lambda_r$.

The second relationship in the equation 2.47 that must be fulfilled to be true is

$$0 = p_y \hat{k}_{y,r} = p_y \hat{k}_{y,t}$$

which indicates that when a wave that only has components in the directions $\hat{x}$ and $\hat{z}$, the transmitted and reflected waves only have components in the same directions. Another way to say the same is that the three waves are constrained to the same plane, i.e., they are co-planar.

The last relationship to evaluate in Eq. 2.47 is

$$\frac{p_x \sin\theta_i}{v_i} = \frac{p_x \hat{k}_{x,r}}{v_r} = \frac{p_x \hat{k}_{x,t}}{v_t} \tag{2.50}$$

Let us evaluate the first equality of this equation. If we consider that $v_i = v_r$, due to $\vec{E}_i$ and $\vec{E}_r$ being in the same medium, and we know both waves are co-planar, we can define the unitary propagation vector of $\vec{E}_r$ as

$$\hat{k}_r = (\sin\theta_r, 0, -\cos\theta_r) \ ,$$

with θ_r being the angle between $\vec{k}_r$ and the normal to the interface surface inside the first medium. By adding this information to the first side of Eq. 2.50, we get

$$\frac{p_x \sin\theta_i}{v_i} = \frac{p_x \sin\theta_r}{v_i} \ , \text{ or}$$

$$\theta_i = \theta_r \ , \tag{2.51}$$

which is known as the law of reflection (Fig. 2.11). This relationship states that reflections are produced at the same angle θ_r as the incidence angle θ_i.

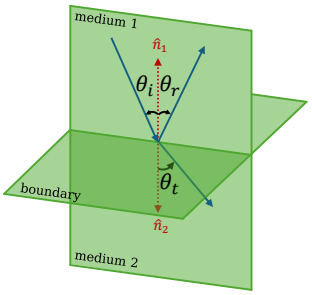

Figure 2.11: Schematics of the reflection and refraction laws given an incident wave (subindex i) that reaches a boundary between two media with different refractive indices, leading to a reflected (subindex r) and a transmitted (subindex t) wave.

Now, for the second equality of Eq. 2.50, we need to consider that the normal to the surface now points to the second medium, and the unitary propagation vector of $\vec{E}_t$ is

$$\hat{k}_t = (\sin\theta_t, 0, -\cos\theta_t) \ .$$

Following the same derivation as before, we arrive at

$$\frac{p_x \sin\theta_i}{v_i} = \frac{p_x \sin\theta_t}{v_t} \quad , \text{ or}$$

$$n_i \sin\theta_i = n_t \sin\theta_t \quad . \tag{2.52}$$

Eq. 2.52 is known as Snell's law of refraction (Fig. 2.11), or simply as Snell's law, which indicates that the change in angle due to refraction between the transmitted and incident beams is going to be caused by the difference in refractive indexes of the two media.

2.4.4 Amplitude of the magnetic field in a boundary: Fresnel's equations

The phase is not the only parameter that must coincide for waves $\vec{E}_i$, $\vec{E}_r$ and $\vec{E}_t$ at a point (p_x, p_y, p_z) in the surface between two media; their amplitudes $\vec{E}_{0,i}$, $\vec{E}_{0,r}$, and $\vec{E}_{0,t}$ must be the same as well.

Let the plane (x, z) be the *incidence plane*, defined as the plane that contains the unitary propagation vector of the incident wave, $\hat{k}_i$, and the normal to the boundary's surface. Let (x, y) be the plane parallel to the surface. We have derived in Sec. 2.2.3 that the electromagnetic field travels as a transverse wave, meaning that if the propagation is parallel to $\hat{k}_i$, then the amplitude of $\vec{E}_i$ (and $\vec{B}_i$) must be perpendicular to it. We will now consider two special cases of transverse electromagnetic waves[19]: $\vec{E}_{0,i}$ is parallel to the incidence plane ($(\vec{E}_{0,i})_p$), and $\vec{E}_{0,i}$ is perpendicular to the incidence plane ($(\vec{E}_{0,i})_s$)

[19] The sub-indexes s and p come from the German words, *senkrecht* and *parallel*, meaning "perpendicular" and "parallel", respectively. When the literature mentions "s-polarized" waves, it indicates that the amplitude of the field lies in a plane perpendicular to the incidence plane. On the other hand, a "p-polarized" wave will refer to those where the amplitude rests parallel to the incidence plane. Other notations might include using the symbol $\parallel$ for p-polarized waves and $\perp$ for s-polarized ones.

Any vector can be decomposed into two perpendicular components that, when added, result in the original vector. Consequently, we can decompose the amplitude of $\vec{E}_i$ in any two components we want, as long as they form a vector base. By selecting a coordinate base such that one component is parallel to the propagation direction, another contained in the incidence plane, and a third one parallel to the incidence plane's normal, the following derivations are applicable regardless of the plane that contains the amplitude of the field.

Let $\vec{E}_i$ be an incident field with amplitude $\vec{E}_{0,i}$, incidence angle θ_i and phase $\varphi(\vec{r}, t)_i$, given by

$$\begin{aligned} \vec{E}_i &= (E_{x,i},\ E_{y,i},\ E_{z,i}) e^{-i\varphi(\vec{r},t)_i} = \\ &= \left(-(E_{0,i})_p \cos\theta_i,\ (E_{0,i})_s,\ (E_{0,i})_p \sin\theta_i\right) e^{-i\varphi(\vec{r},t)_i} \quad , \end{aligned} \tag{2.53}$$

where the sub-index i refers to the incident wave or medium, and the sub-indexes x, y, and z to each component of the amplitude of $\vec{E}$. We know that the electric and magnetic fields are proportional through Eq. 2.31, which, with $\mu = 1$, leads to the following magnetic field intensity:

$$\begin{aligned} \vec{H}_i &= (H_{x,i},\ H_{y,i},\ H_{z,i}) e^{-i\varphi(\vec{r},t)_i} = \\ &= \left(-(H_{0,i})_s \cos\theta_i,\ -(H_{0,i})_p,\ (H_{0,i})_s \sin\theta_i\right) \sqrt{\epsilon_i} e^{-i\varphi(\vec{r},t)_i} \quad . \end{aligned} \tag{2.54}$$

In the case where there are no surface currents, we know that the components of $\vec{E}$ and $\vec{H}$ that are tangential to the surface must be

conserved (Eqs. 2.42 and 2.43). Then, the x and y components of the field, tangent to the surface defined by the plane (x, y), must obey:

$$\begin{aligned} E_{x,i} + E_{x,r} &= E_{x,t} \quad , \\ E_{y,i} + E_{y,r} &= E_{y,t} \quad , \\ H_{x,i} + H_{x,r} &= H_{x,t} \quad , \quad \text{and} \\ H_{y,i} + H_{y,r} &= H_{y,t} \quad . \end{aligned} \tag{2.55}$$

By substituting 2.53 and 2.54 in equations 2.55 and considering the phase conservation $\varphi_i = \varphi_r = \varphi_t$, the reflection law $\theta_i = \theta_r$, and the fact that the incident and reflected wave are on the same medium ($\epsilon_i = \epsilon_r$), we obtain the following:

$$\begin{aligned} \left[(E_{0,i})_p + (E_{0,r})_p\right] \cos\theta_i &= (E_{0,t})_p \cos\theta_t \quad , \\ (E_{0,i})_s + (E_{0,r})_s &= (E_{0,t})_s \quad , \\ \left[(H_{0,i})_s + (H_{0,r})_s\right] \cos\theta_i \sqrt{\epsilon_i} &= (H_{0,t})_s \cos\theta_t \sqrt{\epsilon_t} \quad , \quad \text{and} \\ \left[(H_{0,i})_p + (H_{0,r})_p\right] \sqrt{\epsilon_i} &= (H_{0,t})_p \sqrt{\epsilon_t} \quad . \end{aligned}$$

We know by equations 2.28 and 2.30 that the $\vec{E}$ and $\vec{B}$ fields are proportional to each other through v and that $\vec{H}$ is also related to $\vec{B}$ through μ, which we are assuming to be $\mu = 1$ for the case of non-magnetic media. Taking this information into account allows us to rewrite the previous equations in terms of the parallel and perpendicular components of the $\vec{E}$, leading to the following relationships:

$$\begin{aligned} r_s &= \left(\frac{E_{0,r}}{E_{0,i}}\right)_s = \frac{n_i \cos\theta_i - n_t \cos\theta_t}{n_i \cos\theta_i + n_t \cos\theta_t} \quad , \\ r_p &= \left(\frac{E_{0,r}}{E_{0,i}}\right)_p = \frac{n_t \cos\theta_i - n_i \cos\theta_t}{n_t \cos\theta_i + n_t \cos\theta_i} \quad , \text{ and} \end{aligned} \tag{2.56}$$

$$\begin{aligned} t_s &= \left(\frac{E_{0,t}}{E_{0,i}}\right)_s = \frac{2n_i \cos\theta_i}{n_i \cos\theta_i + n_t \cos\theta_t} \quad , \\ t_p &= \left(\frac{E_{0,t}}{E_{0,i}}\right)_p = \frac{2n_i \cos\theta_i}{n_t \cos\theta_i + n_t \cos\theta_i} \quad . \end{aligned} \tag{2.57}$$

The previous equations are known as the Fresnel equations, and they denote the amplitude of the electric field that is kept by each component (parallel to the incidence plane p, or perpendicular to it s) of the reflected ($r_{s,p}$, Eqs. 2.56) and transmitted ($t_{s,p}$, Eqs. 2.57) waves. While the reflection amplitudes are constricted to the range $[-1, 1]$, the transmission amplitudes are always in the range $[0, 1]$ due to θ_i being restricted to the range of $(0, 90)$ degrees.

There are several points of interest we can analyze in the amplitudes of the transmitted and reflected waves. For example, when $n_i < n_t$, Fresnel's equations behave as depicted in Fig. 2.12. The shape of t_p and t_s is very similar, going from a maximum transmittance at low incidence angles (perpendicular to the surface) to completely disappearing at higher angles of incidence (parallel to the surface). Analogously, the reflection amplitudes r_p and r_s have similar shapes, going from a maximum to a minimum, but r_s is always negative, while r_p exists with positive values. A negative reflection amplitude indicates that the reflected field is *flipped*

with respect to the incident one, i.e., a phase change of π is introduced in $\vec{E}_r$. The point where r_p goes from positive to negative is known as Brewster's angle (θ_B). At this angle, only the r_s amplitude exists, which means that even if the incident field is unpolarized, i.e., its amplitude is randomly oriented, the reflected field's amplitude will be polarized in the plane perpendicular to the surface. This phenomenon can be used to generate polarized light from unpolarized sources.

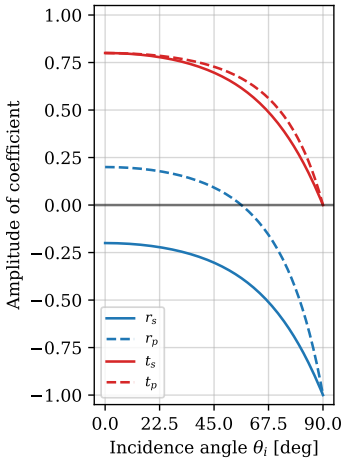

Figure 2.12: Value of the amplitude coefficients given by Fresnel's equations in terms of the angle of incidence with $n_i = 1$ and $n_t = 1.5$.

Now, let us consider the case where $n_i > n_t$ (Fig. 2.13). We see that there is no transmitted wave to the second medium, so all of the amplitude is kept in the first one. This case is denoted as total internal reflection or TIR, which again has a Brewster angle (θ'_B) where the reflected wave has only a perpendicular component. In contrast to the previous case, now there is a set of angles at which the reflectance amplitude is zero[20]. This angle is known as the critical angle (θ_c) and can be obtained directly from Snell's law (Eq. 2.52) when $\theta_t = 90°$.

All four equations are reduced to their simplest form when the incidence is normal to the surface ($\theta_i = 0$). In such cases

$$r_p(\theta_i = 0) = -r_s(\theta_i = 0) = \frac{n_t - n_i}{n_t + n_i} \text{ , and} \tag{2.58}$$

$$t_p(\theta_i = 0) = t_s(\theta_i = 0) = \frac{2n_i}{n_t + n_i} \text{ .} \tag{2.59}$$

[20] Having an incident wave and no transmitted or reflected waves would violate the energy conservation principle. In reality, there are additional factors that need to be taken into account, as we will explore in the next section.

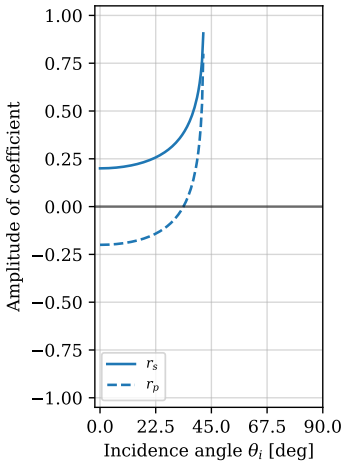

Figure 2.13: Value of the amplitude coefficients given by Fresnel's equations in terms of the angle of incidence with $n_i = 1.5$ and $n_t = 1$. Note that, for this refractive index configuration, there is no transmitted wave, and the reflected wave is present for a reduced set of incidence angles.

2.4.5 Reflectance and Transmittance

We have seen before that the power deposition per unit area is defined as the irradiance (Eq. 2.37), which was derived from the definition of Poynting's vector (Eq.2.33). By recalling what was said when deriving its equation, $\vec{S}$ represents the amount of energy that leaves the volume V through surface A and, as a consequence, I must be the irradiance on a surface perpendicular to $\vec{S}$. This definition applies in the case of normal incidence, but the irradiance will be modified according to the angle of incidence θ_i. Taking all of this into account, we can define the reflectance R as the ratio of energies deposited in an area A between the incident and reflected wave as

$$R = \frac{I_r A \cos\theta_r}{I_i A \cos\theta_i} = \frac{I_r}{I_i} \text{ ,} \tag{2.60}$$

where we have used the reflection law (Eq. 2.51) to remove the angular dependency. If we consider the definition of I (Eq. 2.37), R becomes

$$R_{p,s} = \frac{c\epsilon_r (E_{0,r})^2_{p,s}}{c\epsilon_i (E_{0,i})^2_{p,s}} = \left(\frac{E_{0,r}}{E_{0,i}}\right)^2_{p,s} = r^2_{p,s} \text{ ,} \tag{2.61}$$

which means that the amount of reflected energy can be directly obtained from Fresnel's reflected amplitudes (Eqs. 2.56). By following the same rationale for the transmittance T, defined as the ratio of energies deposited in an area A between the incident and transmitted waves, we reach

$$T_{p,s} = \frac{(I_t)_{p,s} A \cos\theta_t}{(I_i)_{p,s} A \cos\theta_i} = \frac{n_t \cos\theta_t}{n_i \cos\theta_i} \left(\frac{E_{0,t}}{E_{0,i}}\right)^2_{p,s} = \frac{n_t \cos\theta_t}{n_i \cos\theta_i} t^2_{p,s} \text{ .} \tag{2.62}$$

Note that the previous equation is not directly proportional to Fresnel's transmission amplitudes (Eq. 2.57), nor directly proportional to the ratio of irradiances I_t/I_i, but instead, we need to consider the incidence angle θ_i. The equations of the reflectance (Eqs. 2.60 and 2.61) and transmittance (Eq. 2.62) yield values between $[0, 1]$ that slightly vary between the p and s waves (Fig. 2.14). Reflectance is low for low incidence angles, which coincides with the fact that at normal incidence, most of the light is transmitted (Fig. 2.12), and the opposite occurs for higher incidence angles. In Fig. 2.14, it is also visible Brewster's angle θ_B, corresponding to the angle at which $R_p = 0$, leading to the reflected wave being constricted to the s plane. We additionally see that R and T are complementary; when one increases, the other decreases and vice versa. Although not proven here, it can be easily shown[21] that

$$\begin{aligned} R_p + T_p &= 1 \quad , \text{ and} \\ R_s + T_s &= 1 \quad . \end{aligned}$$

Finally, in the case of normal incidence ($\theta_i = 0$), the reflectance and transmittance equations are reduced to:

$$\begin{aligned} R = R_p = R_s &= \left(\frac{n_t - n_i}{n_t + n_i}\right)^2 = \frac{I_r}{I_i} \quad , \text{ and} \\ T = T_p = T_s &= \frac{4 n_t n_i}{(n_t + n_i)^2} = \frac{I_t}{I_i} \quad . \end{aligned} \tag{2.63}$$

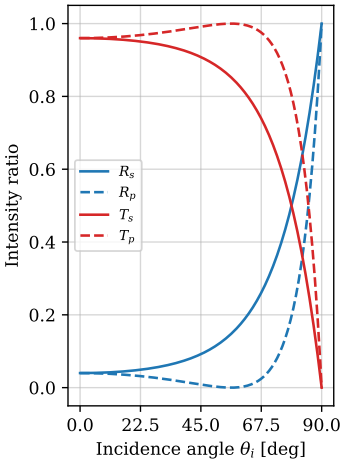

Figure 2.14: Reflectance (blue) and transmittance (red) of the s and p waves as a function of the incidence angle θ_i when $n_i = 1$ and $n_t = 1.5$.

[21] We refer to section 4.6.3 of reference [2] for the full derivation.

2.4.6 Evanescent waves and Attenuation

Let us recall Snell's law of refraction (Eq. 2.52) that relates the orientation of the incident (θ_i) and transmitted (θ_t) waves, given the refractive indexes of the media in which the waves are traveling. Specifically, the transmitted angle can be derived as

$$\sin\theta_t = \frac{n_t}{n_i} \sin\theta_t \quad .$$

Now, this equation poses an interesting case when $n_t > n_i$, given that there is a set of incidence angles that would lead to a complex-valued[22] θ_t

$$\exists \;\; n_t > n_1 \text{ such that } \sin\theta_t > 1 \implies \theta_t \in \mathbb{C} \quad ,$$

which occurs when the incidence angle θ_i is greater than the critical angle θ_c given by

$$\sin\theta_c = \frac{n_t}{n_i} \quad .$$

According to Fresnel's equations 2.56 and 2.57, when $\theta_i > \theta_c$, there would not be any reflected or transmitted wave (see Fig. 2.13). Since we know energy must be conserved, this cannot be entirely true. It is not that, over the critical angle, the electromagnetic field disappears, but, instead, what Fresnel's equations indicate is that there is no longer an energy flow *across* the boundary, i.e., that goes from the first medium to the second medium. That does not mean that there is no magnetic field in the second medium. To evaluate the field, we need to go back to the

[22] $\mathbb{C}$ indicates the set of complex numbers.

phase of $\vec{E}$ and, particularly, to the effect a complex transmitted angle has on $\vec{E}$. Let $\vec{E}$ be a complex-valued field with a phase that is a function of position and time $\varphi(\vec{r}, t)$, with angular frequency ω and position vector $\vec{k}$, so that

$$\vec{E} = \vec{E}_0 e^{-i\varphi(\vec{r},\vec{t})} \text{ , with } \varphi(\vec{r}, t) = \omega\left(\vec{k}\cdot\vec{r} - t\right) \text{ .} \tag{2.64}$$

In section 2.4.3 we have seen that the unitary propagation vector of the transmitted field, $\vec{E}_t$, is $\hat{k}_t = (\sin\theta_t, 0, -\cos\theta_t)$, which would lead to a phase for the transmitted wave given by

$$\varphi_t(\vec{r}, t) = \omega\left(\frac{x\sin\theta_t}{v_t} - \frac{z\cos\theta_t}{v_t} - t\right) \tag{2.65}$$

We can write $\sin\theta_t$ and $\cos\theta_t$ in terms of θ_i by using Snell's law (Eq. 2.52) and the trigonometric identity $\cos^2\theta = \pm\sqrt{1-\sin^2\theta} = \pm i\sqrt{\sin^2\theta - 1}$, leading to

$$\sin\theta_t = \frac{n_i\sin\theta_i}{n_t} \text{ , and}$$
$$\cos\theta_t = \pm i\sqrt{\left(\frac{n_i\sin\theta_i}{n_t}\right)^2 - 1} \text{ .}$$

Applying these expressions to the phase in Eq. 2.65 would lead to an exponent of the field in Eq. 2.64 given by

$$\begin{aligned} e^{-i\varphi} &= \exp\left[-i\omega\left(\frac{xn_i\sin\theta_i}{n_t v_t} \mp \frac{iz}{v_t}\sqrt{\left(\frac{n_i\sin\theta_i}{n_t}\right)^2 - 1} - t\right)\right] = \\ &= \exp\left[-i\omega\left(\frac{xn_i\sin\theta_i}{n_t v_t} - t\right)\right]\exp\left(\mp\frac{\omega z}{v_t}\sqrt{\left(\frac{n_i\sin\theta_i}{n_t}\right)^2 - 1}\right) = \\ &= e^{\omega}e^{-if(x,t)}e^{\pm f(z)} \text{ ,} \end{aligned} \tag{2.66}$$

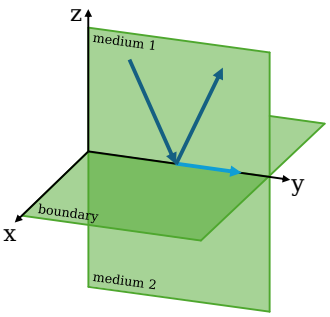

Figure 2.15: Drawing of the main propagation directions of a wave that incides in a medium 2 with a refractive index smaller than that of the medium it originates from. Part of the wave (evanescent wave) travels along the boundary without ever entering the second medium.

This exponent contains two position-dependent terms and one time-dependent term. For the position-dependent terms, there is a part of the field on the $\hat{x}$ and $\hat{z}$ directions (Fig. 2.15). The first position-dependent term ($\hat{x}$), when combined with the general expression of the field (Eq. 2.64), leads to a *wave* that travels along the surface of the boundary (parallel to $\hat{x}$) without ever entering it. The rest of the energy enters the second medium ($\hat{z}$), even if the angle is complex, as an exponential alteration of the *amplitude* $\vec{E}_{0,t}$. The term on $\hat{z}$ has two signs, but we must keep only the negative one. Otherwise, having a positive exponent would lead to an infinitely increasing amplitude, which would not have any physical meaning. We can re-write the exponent (Eq. 2.66) in terms of its two components as

$$e^{-i\varphi} = e^{-i\varphi(x,t)} + e^{-\beta z} \quad ,$$

and the transmitted field would be

$$\vec{E}_t = \vec{E}_{0,t} e^{-\beta z} e^{-i\varphi(x,t)} \quad , \tag{2.67}$$

where we have defined

$$\beta = \frac{\omega}{v_t}\sqrt{\left(\frac{n_i \sin\theta_i}{n_t}\right)^2 - 1} = \frac{2\pi n_t}{\lambda_0}\sqrt{\left(\frac{n_i \sin\theta_i}{n_t}\right)^2 - 1} \quad , \tag{2.68}$$

with λ_0 being the wavelength of the wave in vacuum. The parameter β is known as the attenuation coefficient, given that it represents the exponential decay light suffers when entering a medium with a higher refractive index than the surrounding media.

Recalling Fresnel's transmission amplitude again (Eqs. 2.57), when $n_i > n_t$, there is no transmitted amplitude through the boundary to the second medium, and the resulting transmittance (Eq. 2.62) would be zero. We have seen in this section that this definition is incomplete, given that there is no *wave* transmitted to the second medium, but a part of the *amplitude* does travel within it, up to a penetration depth defined by

$$\delta = \frac{1}{\beta} \quad . \tag{2.69}$$

We must remember that we have obtained the coefficients $t_{s,p}$ ($r_{s,p}$) from the definition of the transmittance (reflectance), T (R), and not the other way around. Most real use-case measurements are performed from air ($n_i = 1$) to a sample ($n_i > 1$), which would qualify for the $n_t > n_i$ scenario. In such real cases, given an incident irradiance I_i, a measured reflected irradiance I_r, and/or a measured transmitted irradiance I_t, we will use the more generally applied definition of reflectance and transmittance

$$R = \frac{I_r}{I_i} \quad , \text{ and} \tag{2.70}$$

$$T = \frac{I_t}{I_i} \quad , \tag{2.71}$$

unless indicated otherwise.

2.5 Light-matter interaction in dispersive, discontinuous media

This section examines how light interacts with non-uniform biological tissues with complex internal structures, such as skin or muscle. We will explore how these tissues can absorb and scatter light and how the refractive index changes when the medium is dispersive. As before, this section is a comprehensive summary of the reference textbooks [1] and [2], except when indicated otherwise.

2.5.1 Dispersion and the complex refractive index

Until now, we have only derived magnitudes from Maxwell's equations, which hold in continuous media, where ϵ and μ are constant. Nonetheless, we have also mentioned that all these magnitudes are wavelength (i.e., frequency) dependent. The term *dispersion* refers to the frequency dependence of the refractive index, and, to understand it, we must explore what happens when a medium is not continuous but instead made of molecules.

We know (see Sec. 2.2.1) that a field $\vec{E}$ applied to a material will move the charges of the material according to its electric polarization $\vec{P}$ (Eq. 2.20). We also know that $\vec{E}$ fields can be described as oscillating fields with frequency ω, where ω is given by the wavelength. If the charges in the media were massless, the alignment between $\vec{P}$ and $\vec{E}$ would be instantaneous, independently of the frequency state of $\vec{E}$. However, charges have mass and are often not free to move throughout the material but are bound to molecular clouds. In any case, masses have inertia, which is the resistance the mass poses to moving. Depending on the frequency of $\vec{E}$, the response of the charges might be faster or slower according to their inertia.

Let us consider first a single electron with charge q_e and mass m_e inside a material. Given an oscillating field with magnitude $E(t) = E_0 \cos \omega t$, the force this electron suffers is given by Eq. 2.1

$$F_E = q_e E_0 \cos \omega t$$

Considering the second Newton law, the movement equation of this electron is given by the force balance

$$m_e \frac{d^2x}{dt^2} = q_e E_0 \cos \omega t - m_e \omega_0^2 x - m_e \gamma \frac{dx}{dt} \quad , \tag{2.72}$$

where the breakdown of the different terms is as follows:

- $m_e(d^2x/dt^2)$: total force applied on the electron given by the mass times the acceleration of the charge.
- $q_e E_0 \cos \omega t$: force applied by the electric field on the charge F_e.
- $m_e \omega_0^2 x$: restoring force of a simple harmonic oscillator ($F = -\mathrm{k}_E x$), where the harmonic motion comes from the opposition to the oscillatory electric field, given by the resonance frequency ω_0.
- $m_e \gamma (dx/dt)$: damping term that represents the speed reduction of the electron due to collisions with the material's lattice, given a damping constant γ.

When the damping constant $\gamma = 0$, Eq. 2.72 accepts a solution such as

$$x = \frac{q_e}{m_e} \frac{1}{\omega_0^2 - \omega^2} E(t) \tag{2.73}$$

which easily lets us see that the relationship between ω_0 and ω will dictate the movement of the electron. Specifically, if the field's frequency is smaller than ω_0, the electron will move against[23] the field. In contrast, over the resonance frequency, the electron will align with $\vec{E}$.

[23] Remember the electron charge is negative: $q_e = -\mathrm{e} = -1.60217 \times 10^{-19} \mathrm{C}$.

The magnitude of the electric polarization P can be evaluated as a sum of the dipole moments p_d of the set of moving charges that have a displacement x due to the field $\vec{E}(t)$. If the set of charges is given by N equal charges per unit volume that move according to Eq. 2.73, the electric polarization magnitude would be

$$||\vec{P}|| = P = q_e x N \quad .$$

By making use of this equation in the relationship between $\vec{P}$ and $\vec{E}$ (Eq. 2.20), we can conclude that the electric permittivity of the medium is

$$\epsilon = \epsilon_0 + \frac{P(t)}{E(t)} = \epsilon_0 + N\frac{q_e^2}{m_e}\frac{1}{\omega_0^2 - \omega^2} \quad ,$$

and its associated refractive index (with $\mu = 1$) is

$$n(\omega) = \frac{\epsilon}{\epsilon_0} = 1 + \frac{q_e^2}{\epsilon_0 m_e}\frac{N}{\omega_0^2 - \omega^2} \quad . \tag{2.74}$$

Eq. 2.74 is known as the dispersion relationship, which describes the frequency-dependence of the refractive index. If, instead of N charges per volume unit, we consider N molecules per volume unit, each molecule would have M associated oscillators with their own natural frequency and transition probability f, leading to

$$n(\omega) = \frac{\epsilon}{\epsilon_0} = 1 + \frac{q_e^2}{\epsilon_0 m_e} N \sum_{j=1}^{M} \frac{f_j}{\omega_{0,j}^2 - \omega^2} \quad . \tag{2.75}$$

In the case where $\gamma \neq 0$, the solution of Eq. 2.72 is such that we must add the term $i\gamma_j\omega$ to the denominator of Eq. 2.75. Finally, by also considering that the charges are affected by the neighboring fields created by other proximal charges, it can be shown[24], the dispersion relationship becomes

$$\frac{n^2 - 1}{n^2 + 2} = \frac{N q_e^2}{3\epsilon_0 m_e} \sum_{j=1}^{M} \frac{f_j}{\omega_{0,j}^2 - \omega^2 + i\gamma_j\omega} \quad .$$

[24] We refer to section 3.5.1 of reference [2] and 2.2.3 of reference [1] for the full derivation.

2.5.2 Propagation effects of the complex refractive index

We have just seen that the refractive index is a complex number. As such, it will have a real (n) and a complex (κ) component, given by

$$\tilde{n} = n + i\kappa \quad .$$

If we consider a harmonic field as a solution of the wave equation, given by

$$\vec{E} = \vec{E}_0(x, y)e^{i(kz - \omega, t)} \quad ,$$

we can substitute the complex refractive index in the wavenumber $k = \omega\tilde{n}c^{-1}$, leading to

$$\vec{E} = \vec{E}_0(x, y)e^{i\omega(\frac{n}{v}z - \omega, t)}e^{-\omega\frac{\kappa}{c}z} \quad . \tag{2.76}$$

This equation is very similar to Eq. 2.67, where again there is an exponentially decaying term that travels along the propagation direction of

the wave. We have previously introduced the attenuation coefficient (Eq. 2.68) when derived from Snell's law in continuous media, with constant ϵ and μ. An alternative definition comes from Eq. 2.76 when considering the dispersion given by the value

$$\alpha = \frac{2\omega\kappa}{c} \quad . \tag{2.77}$$

Since the irradiance I of a field is proportional to the square of the field (Eq. 2.37), we can consider an incident harmonic field upon some boundary $\vec{E}_{in}$ with irradiance $I_0 \propto ||\vec{E}_{in}||^2$. After entering the media, the energy of the field will decay according to the attenuation given by α, and the resulting irradiance at a point z from the boundary will be

$$I(z) = I_0 e^{-\alpha z} \quad ,$$

where, again, the penetration depth will be given by $z = 1/\alpha$. Equation 2.5.2 is one of the key relationships used daily in the optical imaging domain, and we will derive it again from a different point of view in the following sections.

2.5.3 Scattering

Until this point, we have not considered the particle formalism of light; we have only treated it as an electromagnetic wave. However, if we briefly do, we can recall that light is made out of photons with an associated energy $\mathscr{E} = hf = hc/\lambda$, where h is Planck's constant[25], f is the photon's energy and λ its wavelength. When a photon enters a medium, it encounters its atoms and molecules and interacts with them, leading to a change of direction of $\mathscr{E}$. The term *scattering* refers to the redirection of the energy to a different orientation than the incident one [2].

[25] $h = 6.626068 \times 10^{-34} \frac{m^2 kg}{s}$

Let I_0 $[Js^{-1}m^{-2}]$ be the irradiance of an incident field[26]. Let the field have a propagation direction $\hat{s}$ with respect to the particle to interact with (scatterer). When the photons that compose the field reach the scatterer, part of the photons will be redirected, carrying with them a power P_s $[Js^{-1}]$. Then, the scattering cross-section is defined as

$$\sigma_s(\hat{s}) = \frac{P_s}{I_0} \quad [m^2] \quad . \tag{2.78}$$

[26] This section will not consider light polarization and, therefore, all derivations, figures, and equations described here apply to unpolarized light or to the average of all polarization states only.

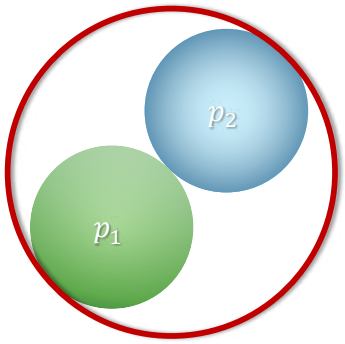

Figure 2.16: Example of the interaction of two solid particles (scatterers). In this case, the maximum (geometric) cross-section (red) occurs when the two particles are tangentially touching. If one of those particles is a photon, the cross-section depicted here would be reduced to the geometric cross-section of one scatterer.

The scattering cross-section has units of area since it represents the cross-sectional area the scatterer must have to interact with the incoming photons.

To better understand the scattering cross-section, we can consider a macroscopic example. Imagine that you have two basketballs that you want to make collide. You initially try to launch them at each other from opposite directions. However, you also want them to collide inside a standing hula hoop. To do so, the hula hoop must be big enough so that both balls can collide. If your aim is good enough, you might be able to make them collide in the exact center of the hoop, in which case the size of the hoop could be the exact size of the basketballs. Just to be safe, you also want to consider the case where they barely touch, and, for that situation, your hoop will need to be twice the size of the

basketballs. In this example, the size of the hoop represents the scattering cross-section of the elastic collision of two identical particles (basketballs) (Fig. 2.16). When the particles are not identical, you can think about the hoop stretching or shrinking to accommodate them both, and when one of the particles is a photon, the scattering cross-section reduces in this example to the geometrical size of the scatterer[27]. Generally speaking, the relationship between the scattering cross-section (σ_s) and the geometrical cross-section of the scatterer (σ_g) is denoted through its scattering efficiency (Q_s), defined as

$$\sigma_s = Q_S \sigma_g \quad . \tag{2.79}$$

[27] Note that the term *interaction* does not necessarily mean *collision*. In general, particles will have some charge, which might interact with the photons in the electromagnetic field even before reaching the scatterer. As a result, the photons can (and will) be deflected at a certain distance from the scattering center, situated in the center of the scatterer. Then, the scattering cross-section of interaction between two particles marks the area within which their paths must cross to interact, which will generally be greater than their geometrical size.

Now, in a more realistic scenario, the scattered radiation will not be a perfectly collimated beam of photons going in a particular direction but instead will have a specific angular distribution. Let $\hat{s}'$ be the direction of the scattered photons with respect to the scatterer. To calculate the angular distribution, we can consider the differential cross-section

$$\frac{d\sigma_s}{d\Omega}(\hat{s}, \hat{s}') \quad ,$$

where $d\Omega$ is the solid angle of the cone that originates on the scatterer and follows the orientation of $\hat{s}'$. If we consider a spherical particle so that

$$\sigma_s(\hat{s}) = \sigma_s \quad ,$$

then, the differential cross section will only be a function of the angle between the unitary vectors $\hat{s}$ and $\hat{s}'$,

$$\frac{d\sigma_s}{d\Omega}(\hat{s}, \hat{s}') = \frac{d\sigma_s}{d\Omega}(\hat{s} \cdot \hat{s}') = \frac{d\sigma_s}{d\Omega} \cos\theta_s \quad ,$$

where θ_s is the scattering angle between $\hat{s}$ and $\hat{s}'$. The bulk response of a material with many identical scatterers distributed according to a density ρ is defined by the scattering coefficient given by

$$\mu_s = \rho \sigma_s \quad . \tag{2.80}$$

This equation represents scattering probability. The more scatterers per volume unit (ρ) or the higher the scattering cross-section, the higher the probability of a scattering event. Therefore, we can define the length that photons can traverse before being scattered as the scattering mean free path, given by

$$l_s = \frac{1}{\mu_s} \quad . \tag{2.81}$$

We have posed the scattering cross-section (Eq. 2.78) as, essentially, an energy balance between the input irradiance and the scattered power by a particle, which then can be considered in differential cross-sections for mathematical derivations. Although the mathematical derivation of the cross-section from the electromagnetic field and Maxwell's equations is out of the scope of this thesis, there are some approximations and conclusions worth noting in terms of the size of the scatterer[28], which will be introduced in the next paragraphs.

[28] For the complete derivation, see section 13.5 of reference [1].

Rayleigh scattering When the scatterer is much smaller than the wavelength of the electromagnetic field, the angular distribution of the scattered radiation corresponds to that of a dipole. This occurs due to the charges of the scatterer being re-aligned with the slowly vibrating field surrounding it [3]. Given a scatterer of radius $a \ll \lambda$, with refractive index n_s, embedded in a medium with refractive index n_m, the differential scattering cross-section can be approximated by

$$\frac{d\sigma_s}{d\Omega} = 8\pi^4 n_m^4 \left(\frac{n_s^2 - n_m^2}{n_s^2 + 2n_m^2}\right)^2 \frac{a^6}{\lambda^4}\left(1 + \cos^2\theta_s\right) \tag{2.82}$$

which leads to the intensity of the scattered light (I_s) to be proportional to the wavelength as $I_s \propto \lambda^{-4}$ [1], with an angular distribution mainly parallel to the incident radiation (Fig. 2.17). This approximation is known as Rayleigh scattering and can be applied when $2\pi a/\lambda \ll 1$, or $a \ll \lambda$ [1, 3, 4].

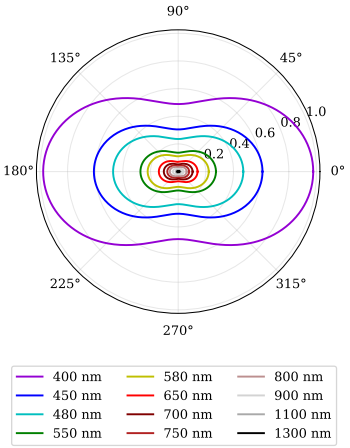

Figure 2.17: Value of the angular component of the differential scattering cross-section (Eq. 2.82), $(1 + \cos^2\theta_s)\lambda^{-4}$, with $a \ll \lambda$, for multiple wavelengths, for a fixed a. As the wavelength increases with respect to the particle, the scattered intensity is smaller. $\theta_s = 0°$ represents forward scattering, i.e., when the incident wave and the scattered radiation are parallel, and $\theta_S = 180°$ is backward scattering, i.e., when the scattered radiation is opposed to the incident field.

[29] See appendix 2A of reference [5] for the full derivation.

It can be shown [5] that the scattering efficiency in regions where the Rayleigh approximation is valid reduces to

$$Q_s = \frac{32}{27}\left(\frac{2\pi n_m}{\lambda}\right)^4 \left|\frac{n_s}{n_m} - 1\right|^2 \quad . \tag{2.83}$$

Mie scattering The general theory of light scattering by spherical particles is described by Mie scattering. Gustav Mie derived this theory in 1908 [6] when he rigorously described the diffraction of a plane monochromatic wave by a homogeneous sphere embedded in a homogeneous medium [1]. Following the expression of the electromagnetic field in this scenario leads to the general expression of the scattering efficiency for spherical particles, given by

$$Q_s = \frac{\sigma_s}{\pi a^2} = \frac{2}{k^2 a^4}\sum_{l=1}^{\infty}(2l+1)\left(|a_l|^2 + |b_l|^2\right) \quad , \tag{2.84}$$

where the parameters a_l and b_l are expressions derived from combinations of Bessel's and Hankel's functions [5]. With this definition of the scattering efficiency, it can be shown [29] that the spatial distribution of E and B is restricted to the amplitude functions $S_1(\theta)$ and $S_2(\theta)$

$$S_1(\theta) = \sum_{l=1}^{\infty}\frac{2l+1}{l(l+1)}\left[a_l\frac{P_{l,1}(\cos\theta)}{\sin\theta} + b_l\frac{d}{d\theta}P_{l,1}(\cos\theta)\right] \quad , \text{ and}$$
$$S_2(\theta) = \sum_{l=1}^{\infty}\frac{2l+1}{l(l+1)}\left[b_l\frac{P_{l,1}(\cos\theta)}{\sin\theta} + a_l\frac{d}{d\theta}P_{l,1}(\cos\theta)\right] \quad ,$$

so that the angular component of the intensity the field carries is given by

$$I_{Mie} = \frac{|S_1(\theta)|^2 + |S_2(\theta)|^2}{2} \quad , \tag{2.85}$$

through Legendre's polynomials $P_{l,m}$.

Mie theory, while powerful, involves complex mathematical expressions that can make direct interpretation of equations like Eq. 2.85 challenging. Fortunately, the significance of Mie's theory has led to the development

of numerous software libraries that facilitate its application and visualization. Using Scott Prahl's `miepython` library [7] allows us to represent the angular dependence of the intensity (Fig. 2.18). We can immediately see that the longer wavelengths produce radiation diagrams similar to that of Rayleigh's theory (Fig. 2.17), corresponding to $a \ll \lambda$, but the approximation breaks down when the wavelength is comparable to the radius of the spherical particle. In this case, the scattered intensity is greater in magnitude, but it is also distributed differently. For the shorter wavelengths, the scattering contribution points *forward*, i.e., parallel to the incident electromagnetic field.

Scattering anisotropy The relationship between the particle's radius α and the wavelength λ impacts the shape of the radiation diagram, as we have seen with Mie's expressions. The scattering anisotropy g describes this shape change and is defined as the average of the cosine of the angle, $g = \langle \cos\theta \rangle$. Nonetheless, both Q_s and g can also be defined through the amplitude functions as

$$\begin{aligned} Q_s &= \frac{1}{k^2 a^2} \int_0^\pi \left(|S_1(\theta)|^2 + |S_2(\theta)|^2 \right) \sin\theta d\theta \quad , \text{ and} \\ g = \langle \cos\theta \rangle &= \frac{1}{Q_s k^2 a^2} \int_0^\pi \left(|S_1(\theta)|^2 + |S_2(\theta)|^2 \right) \cos\theta \sin\theta d\theta \quad . \end{aligned} \tag{2.86}$$

Given that $S_1(\theta)$ and $S_2(\theta)$ are the orthogonal amplitudes of the scattered field, Eqs. 2.86 can be experimentally obtained by measuring the intensity of each component, $|S_1(\theta)|^2$ and $|S_2(\theta)|^2$, in terms of the relative orientation of the incident and scattered fields, θ.

The value of g is practical to quickly determine the scattering orientation, with $g = 0$ indicating a Rayleigh-like radiation diagram, $g = 1$ indicating forward scattering, and $g = -1$ indicating backward scattering.

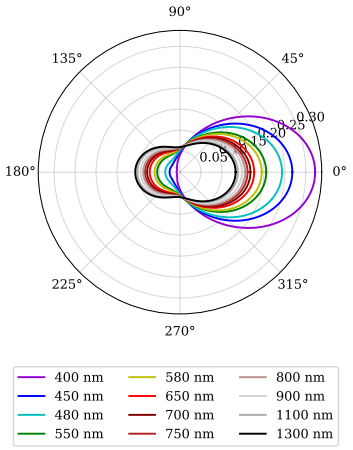

Figure 2.18: Value of the angular component of the scattered intensity (Eq. 2.85), with $a \sim \lambda$, for multiple wavelengths, for a fixed a. As the wavelength increases with respect to the particle, the scattered intensity is smaller, just like in Rayleigh's approximation. However, now there is a distinct change of shape in terms of the relationship between the radius of the particle a and the wavelength λ. $\theta_s = 0°$ represents forward scattering, i.e., when the incident wave and the scattered radiation are parallel, and $\theta_S = 180°$ is backward scattering, i.e., when the scattered radiation is opposed to the incident field.

2.5.4 Absorption

Following the derivations of the previous section, we can rethink the concept of absorption in terms of particle interactions. In this case, given an incident field with irradiance I_0 orientated parallel to $\hat{s}$ that reaches a particle to interact with (absorber), part of the power will be absorbed (P_{abs}) by the electronic, vibrational or rotational transitions of the particle, leading to an absorption cross section defined as

$$\sigma_a = \frac{P_{abs}}{I_0} \quad [m^2] \quad . \tag{2.87}$$

Again, this cross-section represents the area within two particles[30] must be so that the partial or total energy of the field is absorbed. The bulk response of a material with many identical absorbers distributed according to the numerical particle density ρ is defined by the absorption coefficient

$$\mu_a = \rho \sigma_a \quad . \tag{2.88}$$

This definition of the *absorption* coefficient in terms of particles (Eq. 2.88) complements the expression we have seen before for this parameter under

[30] Photon-absorber.

the name of *attenuation* coefficient (Eqs. 2.77). In effect, the absorption coefficient in a particle medium is defined as

$$dI = -\mu_a I dz \quad ,$$

where dz is the length differential in the direction of the light propagation. By integrating both sides of the equation, we arrive at

$$I(z) = I_0 e^{-\mu_a z} \tag{2.89}$$

which, in the context of tissue optics, receives the name of the Beer-Lambert[31] law. This expression is similar to Eq. 2.5.2, which we derived by considering the complex nature of the refractive index. Again, it indicates an exponential decay of the light's intensity as it penetrates into a medium, but this expression now relates said decay to the density and particle size of the medium. This new understanding of Eq. 2.89 opens the door for a structural-focused analysis of light's absorption inside a sample, which will be different for the different chemical components the sample may contain. The absorption coefficient can also be written in terms of the absorption mean free path l_a [cm^{-1}], the molar extinction coefficient ε_λ [$\text{cm}^2\text{mol}^{-1}$] and the molar concentration of absorbers C [cm^{-3}mol or M] as

$$\mu_a = \frac{1}{l_a} = \varepsilon_\lambda C \quad .$$

If we neglect the reflected intensity and consider only the part of the light that enters the tissue I_0, the transmitted intensity up to a point z inside the sample is given by

$$T = \frac{I(z)}{I_0}$$

The part of the light that is not transmitted (i.e., scattered) by the sample's composition will be absorbed as it travels within it. Then, we can define the absorbance (A) or optical density (OD) as [3, 12]

$$A = OD = \ln\left(\frac{I_0}{I}\right) = -\ln(T) \quad = \varepsilon_\lambda C z \quad . \tag{2.90}$$

An alternative definition of the absorbance was used in earlier spectroscopic systems, which relied on the decimal logarithms as [3, 12]

$$A = OD = \log_{10}\left(\frac{I_0}{I}\right) = -\log_{10}(T) \quad = \varepsilon C z \quad , \tag{2.91}$$

by using the *decaic* molar extinction coefficient ε, related to ε_λ through

$$\varepsilon = \varepsilon_\lambda \log_{10}(\text{e}) \quad .$$

This approximation is still being used, and some reference texts still include the decaic molar extinction coefficient instead of the natural one. Although both quantities are equivalent and differ only in one constant, it must be explicitly stated if the natural (ε_λ) or decimal (ε) logarithm is being used for absorbance calculations to avoid confusion.

All of these magnitudes are wavelength-dependent. Keeping in mind these expressions for the transmittance T and absorbance A will help us quickly determine the wavelengths of interest for chemical composition identification inside the samples.

[31] While commonly known as the Beer–Lambert Law, this principle describing the attenuation of light through a medium has a contested naming history. Although attributed to August Beer and Johann Heinrich Lambert, Pierre Bouguer's earlier work arguably establishes his contribution, leading some to advocate for the inclusion of his name, effectively renaming equation 2.89 as the Bouguer-Beer-Lambert law. In 1729, Bouguer first linked light attenuation to its distance traveled in the atmosphere [8]. Lambert formalized its mathematical formulation in 1760, which led to an exponential relationship [9]. Finally, around 100 years later, Beer further refined the understanding of light attenuation by exploring the relationship between absorption and the thickness of a colored solution for a given concentration, but did not include in his mathematical descriptions the molar concentration nor the concept of absorbance [10, 11]. It shows how complex scientific discovery can be, with contributions sometimes getting lost or overlooked.

2.5.5 Extinction

In general, light will suffer both scattering and absorption upon entering a medium. The total extinction coefficient is then given by

$$\mu_t = \mu_a + \mu_s \quad , \tag{2.92}$$

which indicates the probability that a photon is scattered or absorbed inside a medium [5]. The mean free path length

$$l = \frac{1}{\mu_t} \quad ,$$

considers both effects to describe, on average, the path a photon travels before being scattered or absorbed.

We have seen before that the intensity of the scattered radiation depends on the relationship between the particle's size and the photon's wavelength. On the other hand, not all wavelengths are equally absorbed by the samples. Therefore, some approximations can be considered when scattering is negligible to evaluate light decay in terms of only absorption and vice-versa. This document will indicate when such approximations take place.

References

[1] M. Born and E. Wolf: "Principles of Optics", Cambridge University Press, 2019. ISBN: 9781108477437.

[2] E. Hecht: "Optics", Pearson Education, Incorporated, 2017. ISBN: 9780133977226.

[3] T. Vo-Dinh: "Biomedical Photonics Handbook, Second Edition: Fundamentals, Devices, and Techniques", Taylor & Francis, 2014. ISBN: 9781420085129.

[4] J. Rayleigh: "Scientific Papers Vol. 1", University Press, 1899.

[5] L. Wang and H. Wu: "Biomedical Optics: Principles and Imaging", Wiley, 2007. ISBN: 9780471743040.

[6] G. Mie: "Beiträge zur Optik trüber Medien, speziell kolloidaler Metallösungen", *Annalen der Physik* **330**(3), 377–445 (1908). DOI: 10.1002/andp.19083300302.

[7] S. Prahl: "MiePython", https://github.com/scottprahl/miepython. Accessed: 21 March 2025. 2017.

[8] P. Bouguer: "Essai d'optique sur la gradation de la lumière", French. Claude Jombert, 1729.

[9] J. H. Lambert: "Photometria sive de mensura et gradibus luminis, colorum et umbrae", Latin. Viduae Eberhardi Klett, 1760.

[10] A. Beer: "Bestimmung der Absorption des rothen Lichts in farbigen Flüssigkeiten", German. *Annalen der Physik* **162**(5), 78–88 (1852). DOI: 10.1002/andp.18521620505.

[11] T. G. Mayerhöfer, S. Pahlow, and J. Popp: "The Bouguer-Beer-Lambert Law: Shining Light on the Obscure", *ChemPhysChem* **21**(18), 2029–2046 (2020). DOI: 10.1002/cphc.202000464.

[12] S. L. Jacques: "Optical Properties of Biological Tissues: A Review", *Physics in Medicine and Biology* **58**(11), R37–R61 (2013). DOI: 10.1088/0031-9155/58/11/R37.

Light polarization 3

The previous chapter introduced fundamental electromagnetic concepts necessary for understanding the measurement techniques employed in this thesis. However, a complete description of light propagation requires considering not only its behavior along the direction of travel but also the changes it undergoes in the plane perpendicular to it. As established, electromagnetic waves are transverse, with field amplitudes oriented perpendicular to the direction of propagation.

This chapter explores the concept of light *polarization*, which describes the behavior of the electric field (E) and magnetic induction (B) amplitudes in the plane perpendicular to the propagation direction (Fig. 3.1). Light polarization is a valuable tool for assessing the structural periodicity of tissues (e.g., collagen, muscle fibers, myelin), as the field amplitudes are modulated by the structures they encounter.

The text contained in the following sections is a summary of what can be found in multiple reference textbooks on electromagnetism and light polarization, including those by Born and Wolf [1], Hecht [2], Goldstein [3], or Gil and Ossikovsky [4], among others. As before, each reference will be indicated when necessary. Readers familiar with this content may skip to the next chapter.

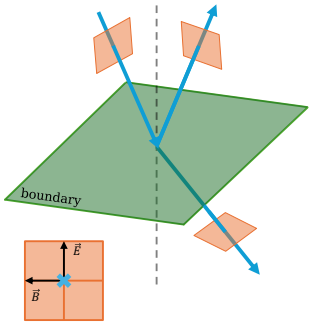

Figure 3.1: Evolution of the polarization plane (orange) for a wave (blue) that reaches a boundary between two media (green) with different refractive indices. The orientation of the electromagnetic field is depicted on the lower left, with the cross indicating that the arrows that indicate the propagation direction are looking at the reader.

3.1 Polarized light states

This section establishes the foundational concepts of light polarization, a phenomenon characterized by the preferential orientation of light wave oscillations. We will explore diverse polarization states, their mathematical representations, and the manipulation of polarized light through various optical elements.

3.1.1 The polarization ellipse

We have seen in the previous chapter that Maxwell's equations for the electromagnetic field can be combined with the material equations to arrive at the wave equation that electromagnetic fields fulfill. One particular solution of interest in the wave equation (Eq. 2.26) is the case of a harmonic plane wave, whose implications we have also explored in the previous chapter. Let $\vec{E}$ be a time-dependent electric field propagating in the $\hat{z}$ direction, $\vec{E}(z,t)$. Its amplitude will be constrained to the XY plane due to its transverse nature. Then, $\vec{E}(z,t)$ can be decomposed in two orthogonal directions parallel to $\hat{x}$ and $\hat{y}$, $\vec{E}_x(z,t)$ and $\vec{E}_y(z,t)$ respectively, so that [1, 2]

$$\vec{E}(z,t) = \vec{E}_x(z,t) + \vec{E}_y(z,t) \quad .$$

Each component can be expressed with the equation of a plane wave with the time-dependent phase[1] $\tau = \omega t - kz$ and a different initial phase

[1] Sometimes τ is referred to as the propagator, like in [3].

δ_x or δ_y. Considering these waves at $z = 0$[2] leads to

$$\begin{aligned} E_x(t) &= ||\vec{E}_x(t)|| = E_{0x}(t)\cos(\tau + \delta_x) \quad \text{, and} \\ E_y(t) &= ||\vec{E}_y(t)|| = E_{0y}(t)\cos(\tau + \delta_y) \quad , \end{aligned} \tag{3.1}$$

where $E_{0x}(t)$ and $E_{0y}(t)$ are the maximum amplitudes of the field parallel to the directions $\hat{x}$ and $\hat{y}$, respectively [3]. Although the previous equations depict time-dependent values, we will consider their instantaneous values (for a specific t) unless indicated otherwise.

To evaluate the behavior of light in the XY plane, we must remove the dependence on the propagator τ from the cosines, which can be done by making use of the cosine property $\cos(a+b) = \cos(a)\cos(b) - \sin(a)\sin(b)$. Combining this identity with Eqs. 3.1 and squaring them yields

$$\begin{aligned} \left(\frac{E_x}{E_{0x}}\sin\delta_y - \frac{E_y}{E_{0y}}\sin\delta_x\right)^2 &= \cos^2\tau\sin^2(\delta_y - \delta_x) \quad \text{, and} \\ \left(\frac{E_x}{E_{0x}}\cos\delta_y - \frac{E_y}{E_{0y}}\cos\delta_x\right)^2 &= \sin^2\tau\sin^2(\delta_y - \delta_x) \quad , \end{aligned}$$

which, by adding them together, reduces to

$$\frac{E_x^2}{E_{0x}^2} + \frac{E_y^2}{E_{0y}^2} - 2\frac{E_x}{E_{0x}}\frac{E_y}{E_{0y}}\cos(\delta_y - \delta_x) = \sin^2(\delta_y - \delta_x) \quad . \tag{3.2}$$

Equation 3.2 describes the movement of the $\vec{E}_x$ and $\vec{E}_y$ components of $\vec{E}$ in the XY plane [3]. It describes an ellipse circumscribed in a rectangle of sides $2E_{0x}$ and $2E_{0y}$. This equation is referred to as the polarization ellipse. Several magnitudes on this ellipse (Fig. 3.2) help interpret the electromagnetic field's behavior. Although we will not derive them here[3], we will introduce them here for completion.

As we will see in this section, the individual phases δ_y and δ_x are not particularly useful by themselves to describe the polarization of light. Instead, we will introduce the phase shift between both amplitudes

$$\delta = \delta_y - \delta_x \quad , \tag{3.3}$$

to help us interpret the path the electric field vector $\vec{E}$ follows on the XY plane.

The polarization ellipse has a major axis a and a minor axis b that relate to the amplitudes of the field through [5]

$$\begin{aligned} \pm ab &= E_{0x}E_{0y}\sin\delta \quad \text{, and} \\ a^2 + b^2 &= E_{0x}^2 + E_{0y}^2 \quad . \end{aligned} \tag{3.4}$$

The relationship between a and b is described by the ellipticity angle χ, given by

$$\tan\chi = \frac{\pm b}{a} \quad , \quad \chi \in \left[\frac{-\pi}{4}, \frac{\pi}{4}\right] \quad . \tag{3.5}$$

The angle of rotation Ψ of the ellipse indicates how parallel to the x axis

[2] Note that we can arbitrarily depict the calculations in this chapter at any z due to the amplitudes being restricted to the XY plane or planes parallel to it. We selected $z = 0$ to simplify the expressions.

[3] The complete derivations can be found on Sec. 1.4.2 of reference [1] and Section 4.4 of reference [3].

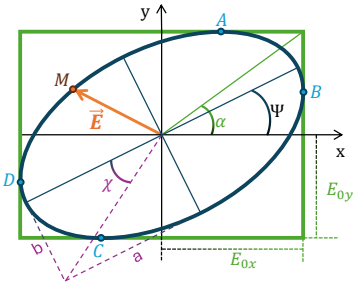

Figure 3.2: Polarization ellipse with its relevant parameters indicated: $\vec{E}$ is the instantaneous value of the electric field vector. E_{0x} and E_{0y} are the maximum amplitudes of each component of $\vec{E}$. A, B, C, and D are the tangency points between the ellipse and the rectangle. a and b are the lengths of the major and minor axes of the ellipse, respectively. α is the diagonal of the rectangle. Ψ is the inclination of the ellipse. χ is the ellipticity angle. M is the point on the ellipse that defines $\vec{E}$ with the coordinate origin. Figure adapted from [5].

it is, and it relates to the amplitudes through

$$\tan 2\Psi = \frac{2E_{0x}E_{0y}}{E_{0x}^2 E_{0y}^2}\cos\delta \quad , \quad \Psi \in [0, \pi] \quad . \tag{3.6}$$

Finally, we introduce the auxiliary angle α, which defines the diagonal of the rectangle defined by $2E_{0x}$ and $2E_{0y}$,

$$\tan\alpha = \frac{E_{0y}}{E_{0x}} \quad , \quad \alpha \in \left[0, \frac{\pi}{2}\right] \tag{3.7}$$

which relates to the other angles via [5]

$$\begin{aligned} \tan 2\Psi &= \tan 2\alpha \cos\delta \quad , \text{ and} \\ \tan 2\chi &= \sin 2\alpha \sin\delta \quad . \end{aligned} \tag{3.8}$$

Points A, B, C, and D are the tangency points of the ellipse on the rectangle that contains it. Their coordinates are given by solving equation 3.2 for E_y and evaluating where its slope with respect to E_x, dE_y/dE_x, is zero (points A and C) or infinite (points B and D), yielding

$$\begin{aligned} A &= (E_{0x}\cos\delta, E_{0y}) \quad , \\ B &= (E_{0x}, E_{0y}\cos\delta) \quad , \\ C &= (-E_{0x}\cos\delta, -E_{0y}) \quad , \text{ and} \\ D &= (-E_{0x}, -E_{0y}\cos\delta) \quad . \end{aligned} \tag{3.9}$$

3.1.2 Totally polarized states

We have derived every equation we need to evaluate the specific polarization states we will refer to throughout this thesis. We will do so by analyzing particular values of the maximum amplitudes E_{0x} and E_{0y}, and the phase shift between both components, δ, and evaluating how they perform in the ellipse equation (Eq. 3.2)[4].

[4] See chapter 4 of reference [3] for the complete derivations included in this section

Case 1: $\mathbf{E_{0x} = 0}$ or $\mathbf{E_{0y} = 0}$ When $E_{0x} = 0$, the electric field is given by

$$\vec{E}(z,t) = \vec{E_y}(z,t) = E_{0y}\cos(\tau + \delta_y)\hat{y} \quad ,$$

which means that the oscillations are restricted to the $\hat{y}$ direction. In this case, we say that light is *linearly polarized*. We might refer to $E_{0x} = 0$ as light being *vertically* polarized or, in the analogous case, when $E_{0y} = 0$, as light being *horizontally* polarized.

Case 2: $\boldsymbol{\delta = n\pi}$ with $\boldsymbol{n \in \mathbb{N}}$ In this case, $\cos\delta = (-1)^n$ and $\sin\delta = 0$, which reduces the ellipse equation to

$$\frac{E_x}{E_{0x}} - (-1)^n \frac{E_y}{E_{0y}} = 0 \quad ,$$

so that

$$E_y = (-1)^n \frac{E_{0y}}{E_{0x}} E_x \quad . \tag{3.10}$$

The previous result is the equation of a line with slope $+E_{0y}/E_{0x}$ when n is even, or with slope $-E_{0y}/E_{0x}$ when n is odd. In this case, we are still referring to linearly polarized light.

Case 3: $\delta = n\pi$ with $n \in \mathbb{N}$ and $E_{0x} = E_{0y}$ Following from Eq. 3.10, when we add the restriction of $E_{0x} = E_{0y}$, we arrive at

$$E_y = (-1)^n E_x \quad .$$

Here, light is linearly polarized at $(-1)^n 45°$. We might refer to these cases as *diagonally polarized* light. When n is even (i.e. $\delta = 0, 2\pi, 4\pi...$) we will say that light is polarized at $+45°$, whereas when n is odd ($\delta = \pi, 3\pi, 5\pi...$), we might indistinctly use the terms of light polarized at $-45°$ or at $+135°$.

Case 4: $\delta = (2n+1)\pi/2$ with $n \in \mathbb{N}$ When δ is a multiple of $\pi/2$, the polarization ellipse reduces to

$$\frac{E_x^2}{E_{0x}^2} + \frac{E_y^2}{E_{0y}^2} = 1 \quad ,$$

which is the general equation of an ellipse with its axes aligned with the XY axes ($\Psi = 0$). This case represents *elliptically polarized* light. When $E_{0x} > E_{0y}$, the major axis of the ellipse is parallel to $\hat{x}$, while when $E_{0x} < E_{0y}$, the major axis is aligned with $\hat{y}$.

Case 5: $\delta = (2n+1)\pi/2$ with $n \in \mathbb{N}$ and $E_{0x} = E_{0y} = E_0$ Following from the previous equation, when the amplitudes are equal, the remaining terms on the ellipse equation are now

$$E_x^2 + E_y^2 = E_0^2 \quad ,$$

which is the equation of a circle with radius E_0. This is the case of *circularly polarized* light.

Every other combination of δ, E_{0x} and E_{0y} In general, light coming from regular samples will not cause perfectly linear or circularly polarized light. Instead, the most common case experimentally encountered will be of elliptically polarized light at an arbitrary angle with respect to the XY axes. The only exception will come from the use of polarization optics, which are optical elements designed to produce a specific type of polarization, either by absorbing the amplitude of the field in one particular direction (linear polarizers) or by delaying the two components by an exact value of δ (retarders).[5]

[5] No optical element is perfect, so manufacturers tend to report the extinction ratio $||E_{0x}||^2/||E_{0y}||^2$ for linear polarizers. The higher the extinction ratio, the better the output linear polarization is. For optical retarders (i.e., wave plates), the value of δ is usually indicated. It is worth noting that polarization is wavelength-dependent, and not all polarizers or wave plates are valid at all wavelength ranges.

[6] See chapter 4 of reference [3] for the complete derivations included in this section

3.1.3 Handedness of Polarization

The previous sections described the instantaneous polarization state for a fixed point in time. If we want to see its evolution, we can consider the point M on the ellipse (Fig. 3.2) and what happens to its E_y component when time changes [6]. Let $\delta_x = 0$ and $\delta = \delta_y$. If we take the time

derivatives of E_y and evaluate it at $z = 0$ and $t = 0$, we arrive at

$$\frac{dE_y}{dt} = -\omega E_{0y} \sin(\delta) \ ,$$

The E_y derivative can be positive or negative in terms of δ:

Case 1: $dE_y/dt > 0$ If we are looking at the wave as if it was "coming towards us ", we would see the value of E_y increase in time, and M would move from right to left. In this case, we are describing *left* or *counter-clockwise polarized* light. This occurs for values of $\delta \in [\pi, 2\pi]$.

Case 2: $dE_y/dt < 0$ Again, when the observer is looking straight on at the wave, E_y decreases in time, and M would move from left to right. In this case, we describe *right* or *clockwise polarized* light. This occurs for values of $\delta \in [0, \pi]$.

3.2 The Jones formalism

The Jones formalism was introduced between 1941 and 1956 in eight articles published by R. Clark Jones [6–13]. Since then, it has been covered by every book[7] on light polarization. The main characteristic of this formalism is that it uses the complex notation of the field to aid in calculating the polarized state of superposed totally polarized waves. This basis makes it useful for the polarization analysis of lights in interferometers.

[7] See Sec. 8.13.2 of [2], Ch. 10 of [3], Sec. 10.4 of [4].

3.2.1 Jones vectors

As mentioned, the Jones formalism starts with the complex notation of the two components of the field

$$E_x = E_{0x} e^{i\tau} \ , \text{ and}$$
$$E_y = E_{0y} e^{i(\tau+\delta)} \ ,$$

where we have set $\delta_x = 0$, $\delta = \delta_y$, and the propagator $\tau = \omega t - kz$. The Jones formalism evaluates the superposition at a fixed point in time and space, thus setting $\tau = 0$. If we write $\vec{E}$ as a column vector with the previous expressions in mind, we arrive at [4]

$$\vec{E} = \begin{pmatrix} E_x \\ E_y \end{pmatrix} = \begin{pmatrix} E_{0x} \\ E_{0y} e^{i\delta} \end{pmatrix} \ , \tag{3.11}$$

which receives the name Jones Vector, where each component has a complex magnitude. Eq. 3.11 represents the general case for arbitrarily aligned elliptically polarized light with arbitrary handedness.

The Jones vectors are frequently presented in their normalized form, which uses the intensity of the field $I = E_0^2$. Denoting the complex conjugate as $*$, and the hermitian transpose as $\dagger$, I is calculated as[8]

[8] Note that, in this section, the field $\vec{E}$ is always represented as a column matrix according to the Jones formalism.

$$I = E_x E_x^* + E_y E_y^* = \begin{pmatrix} E_x^* & E_y^* \end{pmatrix} \begin{pmatrix} E_x \\ E_y \end{pmatrix} = \vec{E}^\dagger \cdot \vec{E} \quad = E_0^2, \tag{3.12}$$

The normalized form of the Jones vector, denoted by $\hat{E}$, is found by setting $E_0^2 = 1$ or, alternatively, $\sqrt{E_{0x}^2 + E_{0y}^2} = 1$.

One drawback of this formalism is that it can only be used to describe totally polarized light states due to it not considering the evolution of τ over time. When light is not totally polarized (i.e., natural light, incoherent superpositions, no fixed time-phase relationship), Jones' formalism is missing the time-dependent component that would explain the complete behavior of the polarization state. As such, this formalism should be used only when working with totally polarized sources.

We can go back to the pure polarization states (i.e., linear or circular) to evaluate their Jones vectors in terms of the relationship between E_{0x}, E_{0y}, and δ[9].

[9] See section 1.4 of reference [4] for the complete derivations included in this section.

Case 1: Linearly polarized light We have seen before four situations that yield linearly polarized light: $E_y = 0$ (horizontal polarization), $E_x = 0$ (vertical polarization), $\delta = n\pi$ with $n \in \mathbb{N}$ (linear polarization) and $\delta = n\pi$ with $n \in \mathbb{N}$ and $E_{0x} = E_{0y} = E_0$ (diagonal polarization). We denote the sub-indexes H for horizontal polarization, V for vertical polarization, D for ±45° diagonal polarization, and Lin for linear polarization. With this notation, the vector for horizontally polarized light is

$$\vec{E}_H = \begin{pmatrix} E_{0x} \\ 0 \end{pmatrix} \text{ or } \hat{E}_H = \begin{pmatrix} 1 \\ 0 \end{pmatrix} \ ,$$

for vertically polarized light is

$$\vec{E}_V = \begin{pmatrix} 0 \\ (-1)^n E_{0y} \end{pmatrix} \text{ or } \hat{E}_V = \begin{pmatrix} 0 \\ 1 \end{pmatrix} \ ,$$

for linear polarization is

$$\vec{E}_{Lin} = \begin{pmatrix} E_{0x} \\ (-1)^n E_{0y} \end{pmatrix} \text{ or } \hat{E}_{Lin} = \begin{pmatrix} E_{0x} \\ (-1)^n \sqrt{1 - E_{0x}^2} \end{pmatrix} \ ,$$

and for diagonal polarization is

$$\vec{E}_D = \begin{pmatrix} E_0 \\ (-1)^n E_0 \end{pmatrix} \text{ or } \hat{E}_D = \frac{1}{\sqrt{2}} \begin{pmatrix} 1 \\ (-1)^n \end{pmatrix} \ .$$

Case 2: Right-handed circularly polarized light To obtain circularly polarized light, both $E_{0x} = E_{0y} = E_0$ and $\delta = (2n+1)\pi/2$ with $n \in \mathbb{N}$ must be true. For light to be right-handed (denoted by the sub-index R), we know that δ must be comprised in the $[0, \pi]$ range or, in other words, be in the first or second quadrants. Therefore, right-handed circularly polarized light will occur for $\delta = \pi/2, 5\pi/2, 9\pi/2 \ldots = (1+4n)\pi/2$. In such cases, $e^{i\delta} = +i$, leading to the Jones vector

$$\vec{E}_R = \begin{pmatrix} E_0 \\ iE_0 \end{pmatrix} \text{ or } \hat{E}_R = \frac{1}{\sqrt{2}} \begin{pmatrix} 1 \\ i \end{pmatrix} \ .$$

Case 3: Left-handed circularly polarized light Following the rationale of the previous case, left-handed (denoted by the sub-index L) circularly polarized light must have a phase delay of $\delta = {}^{3\pi}/_{2}, {}^{8\pi}/_{2}, {}^{12\pi}/_{2}... = {}^{(3+4n)\pi}/_{2}$, with δ in the third or four quadrants. Then, $e^{i\delta} = -i$, leading to the Jones vector for left-handed circular polarized light

$$\vec{E}_L = \begin{pmatrix} E_0 \\ -iE_0 \end{pmatrix} \text{ or } \hat{E}_L = \frac{1}{\sqrt{2}} \begin{pmatrix} 1 \\ -i \end{pmatrix} \quad .$$

3.2.2 Operations with Jones vectors

As with any other vectors, Jones vectors can be added. Indeed, Jones vectors of two different polarization states, $\vec{E}_1$ and $\vec{E}_2$, can be analyzed in terms of their coherent[10] superposition at a point $\vec{r}$ when their polarization ellipses lie on the same plane XY. Then, the resulting beam will be described by the Jones vector [4]

$$\vec{E} = \vec{E}_1 + \vec{E}_2 \quad .$$

[10] Coherent superposition refers in this context to two polarization states that have a constant phase relationship that does not change over time and the same wavelength. In that case, when the two polarization states share a plane, their coherent superposition can be found in said plane.

Jones' notation is helpful to keep the phases of $\vec{E}_{1,2}$ throughout calculations and to understand how polarization changes in the presence of two or more beams.

The orthogonality of two Jones vectors can be checked by verifying the relationship

$$\vec{E}_1^{\dagger} \cdot \vec{E}_2 = 0 \quad .$$

When two Jones vectors are orthogonal, they can be used together as a basis to define or generate any other polarization state. For example, horizontal (HLP) and vertical (VLP) polarized states are orthogonal. In that case, a HLP and a VLP beam with a specific phase delay can be used to generate +45° polarized light (same phase), to generate −45° polarized light (opposed phase π), or to generate circularly polarized light (phase multiple of $\pi/2$) [4].

3.2.3 Jones matrices

The vector notation in polarization is useful to determine the state of the polarized light after the incident field $\vec{E}$ passes through a medium. Let $\vec{E}$ be the incident field and $\vec{E}'$ the field after interacting with a medium. The medium will modify each component of $\vec{E}$, E_x, and E_y by changing the amplitudes and/or the phase delay δ. The components of $\vec{E}'$, E'_x and E'_y will be combinations of E_x and E_y modified by different factors, j_{xx}, j_{xy}, j_{yx}, and j_{yy}. The notation j_{nm} contains two sub-indices, where m indicates the component of the incident field that is being modified (E_x or E_y), and n is the component of the output field that is being interrogated (E'_x or E'_y), leading to

$$\begin{aligned} E'_x &= j_{xx}E_x + j_{xy}E_y \quad \text{, and} \\ E'_y &= j_{yx}E_x + j_{yy}E_y \quad . \end{aligned}$$

This equation system can be written in matrix form

$$\begin{pmatrix} E'_x \\ E'_y \end{pmatrix} = \begin{pmatrix} j_{xx} & j_{xy} \\ j_{yx} & j_{yy} \end{pmatrix} \begin{pmatrix} E_x \\ E_y \end{pmatrix} \ ,$$

or, analogously,

$$\vec{E}' = J\vec{E} \ ,$$

where we have introduced the matrix

$$J = \begin{pmatrix} j_{xx} & j_{xy} \\ j_{yx} & j_{yy} \end{pmatrix} \ . \tag{3.13}$$

The previous equation represents the Jones matrix of the medium, which contains information about its optical characteristics. J is the transfer matrix of the medium, which reads as the changes it makes on $\vec{E}$ to produce $\vec{E}'$. Like the Jones vectors, Jones matrices are complex-valued. In principle, any 2×2 complex-valued matrix can be a Jones matrix [14].

3.3 The Stokes-Mueller formalism

Light oscillates at extremely high frequencies. In particular, for visible light, the frequencies are in the range of $\omega \sim 10^7$rad, which makes measuring the instantaneous polarization impossible with current technology. Instead, we can calculate the intensity of the polarization states by averaging the polarization behavior over time.

3.3.1 The Stokes parameters

In general, the maximum amplitudes E_{0x} and E_{0y}, the phase shift δ and the amplitudes E_x and E_y all are time dependent. Adding this information to the equation of the polarization ellipse yields [1]

$$\frac{E_x^2(t)}{E_{0x}^2(t)} + \frac{E_y^2(t)}{E_{0y}^2(t)} - 2\frac{E_x(t)}{E_{0x}(t)}\frac{E_y(t)}{E_{0x}(t)}\cos\delta = \sin^2\delta \ .$$

For monochromatic light, the maximum amplitudes and the phase shift are constant in time, but $E_x(t)$ and $E_y(t)$ are still time-dependent due to τ (Eq. 3.1). If we were to place a detector to measure each of the time-dependent magnitudes on the previous equation, the captured values would be the time-averaged magnitudes, indicated by $\langle \ldots \rangle$, over a period of time T much greater than the oscillation frequency of the field. Given the time-average of two fields $E_i(t)$ and $E_j(t)$, defined as [1]

$$\langle E_i(t)E_j(t)\rangle = \lim_{T\to\infty} \frac{1}{T}\int_0^T E_i(t)E_j(t)dt \ ,$$

the time-averaged polarization ellipse equation for monochromatic light is given by

$$\frac{\langle E_x^2(t)\rangle}{E_{0x}^2} + \frac{\langle E_y^2(t)\rangle}{E_{0y}^2} - 2\frac{\langle E_x(t)E_y(t)\rangle}{E_{0x}E_{0y}}\cos\delta = \sin^2\delta \ . \tag{3.14}$$

There are three time-averages in Eq. 3.14. We can obtain their expressions by considering the definitions of $E_x(t)$ and $E_y(t)$ (Eqs. 3.1), which leads to

$$\frac{\frac{1}{2}E_{0x}^2}{E_{0x}^2} + \frac{\frac{1}{2}E_{0y}^2}{E_{0y}^2} - 2\frac{\frac{1}{2}E_{0x}E_{0y}\cos\delta}{E_{0x}E_{0y}}\cos\delta = \sin^2\delta \quad ,$$

which, removing the denominator by multiplying by $4E_{0x}^2E_{0y}^2$ and grouping terms, reduces to [11]

$$(E_{0x}^2 + E_{0y}^2)^2 - (E_{0x}^2 - E_{0y}^2)^2 - (2E_{0x}E_{0y}\cos\delta)^2 = (2E_{0x}E_{0y}\sin\delta)^2 \quad . \tag{3.15}$$

[11] See section 5.2 of reference [3] for the full step-by-step derivation.

Each of the terms in the previous equations are the Stokes parameters, named after G. G. Stokes, who introduced them first in 1852 [15]. The Stokes parameters are usually written as a column vector $\vec{S}$[12]. Two notations can be found in the literature: $\vec{S} = (I, Q, U, V)^T$ or $\vec{S} = (S_0, S_1, S_2, S_3)$. We will use the latter. Each of the parameters refers to the following terms of Eq. 3.15:

$$\begin{aligned} S_0 &= I = E_{0x}^2 + E_{0y}^2 \quad , \\ S_1 &= Q = E_{0x}^2 - E_{0y}^2 \quad , \\ S_2 &= U = 2E_{0x}E_{0y}\cos\delta \quad , \text{ and} \\ S_3 &= V = 2E_{0x}E_{0y}\sin\delta \quad , \end{aligned} \tag{3.16}$$

[12] Although the Stokes vector shares $\vec{S}$ as a symbol with Poynting's vector, note that the latter was written in terms of the time average of the electromagnetic field. Throughout the rest of this document, we will reserve the notation $\vec{S}$ to refer to the Stokes vector.

and so they fulfill the following relationship:

$$S_0^2 = S_1^2 + S_2^2 + S_3^2 \quad . \tag{3.17}$$

Considering that real measurements depend on the time-average of the fields, it is necessary to consider the complex notation of the field

$$\begin{aligned} E_x(t) &= E_{0x}e^{i\delta_x}e^{i\omega t} = E_x e^{i\omega t} \quad , \text{ and} \\ E_y(t) &= E_{0y}e^{i\delta_y}e^{i\omega t} = E_y e^{i\omega t} \quad , \end{aligned}$$

which enables the calculation of the Stokes parameters (Eqs. 3.16) as [3]

$$\begin{aligned} S_0 &= I = E_x E_x^* + E_y E_y^* \quad , \\ S_1 &= Q = E_x E_x^* - E_y E_y^* \quad , \\ S_2 &= U = E_x E_y^* + E_y E_x^* \quad , \text{ and} \\ S_3 &= V = i(E_x E_y^* - E_y E_x^*) \quad . \end{aligned} \tag{3.18}$$

The interpretation of Stokes parameters can be easily understood by remembering the relevant magnitudes of the polarization ellipse (Fig. 3.2) and their relation to the phase delay (Eqs. 3.4-3.7):

- $S_0 \in [0, 1]$ is the maximum intensity carried by the field.
- $S_1 \in [-1, 1]$ is the relationship between the intensity of horizontally polarized light ($S_1 = 1$) and vertically polarized light ($S_1 = -1$)
- $S_2 \in [-1, 1]$ is the relationship between the intensity of light polarized at $+45°$ ($S_2 = 1$) and at $-45°$ ($S_2 = 1$)
- $S_3 \in [-1, 1]$ is the intensity of circularly polarized light counterclockwise ($S_3 = 1$) and clockwise ($S_3 = -1$).

When light is not monochromatic, Eq. 3.15 and the Stokes parameters

will be valid for very short time intervals [3]. However, Eq. 3.17 will no longer be true and, instead, the inequality

$$S_0^2 \geq S_1^2 + S_2^2 + S_3^2 \tag{3.19}$$

holds [1, 3]. The degree of polarization of a wave is then defined as

$$DOP = \frac{\sqrt{S_1^2 + S_2^2 + S_3^2}}{S_0} \leq 1 \ , \tag{3.20}$$

which can only be 1 for totally polarized (monochromatic) light.

3.3.2 The Poincaré sphere

It can be shown that the Stokes parameters can also be written in terms of magnitudes of the polarization ellipse as[13] [3]:

$$\begin{aligned} S_0 &= E_{0x}^2 + E_{0y}^2 \ , \\ S_1 &= S_0 \cos 2\chi \cos 2\Psi \ , \\ S_2 &= S_0 \cos 2\chi \sin 2\Psi \ , \text{ and} \\ S_3 &= S_0 \sin 2\chi \ . \end{aligned} \tag{3.21}$$

[13] See section 5.3.6. of reference [3]

If we normalize these equations by dividing them by S_0, they behave as a spherical coordinate system of azimuth

$$\varphi = 2\Psi \ ,$$

and polar angle

$$\vartheta = 90° - 2\chi \ .$$

Polarized light can be represented in this coordinate system. Any polarized light state with a Stokes vector $\vec{S}$ can be represented as a point in the sphere of radius S_0 given by Eq. 3.17, which receives the name of Poincaré sphere (Fig. 3.3).

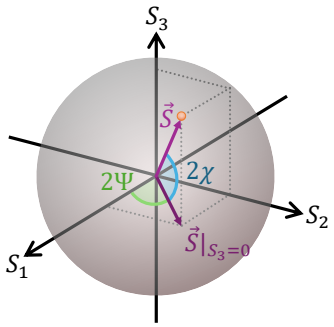

Figure 3.3: Poincaré sphere of radius S_0 represented in the coordinate system given by S_1, S_2 and S_3. The orange dot represents a polarized light state with Stokes vector $\vec{S}$. The azimuth angle is defined between the projection on the plane S_1S_2 of $\vec{S}$, $\vec{S}|_{S_3=0}$ and the S_1 axis, and the polar angle between the same projection and the vector $\vec{S}$. Figure adapted from [5].

A polarized light state will be represented as points on the surface of the sphere of radius S_0 for totally polarized light (Eq. 3.17) or inside the sphere for partially polarized light (Eq. 3.19). All linearly polarized states collapse to the S_1S_2 plane ($S_3 = 0$), while elliptically polarized ones will be out of said plane ($S_3 \neq 0$). States on the northern hemisphere of the ellipse are left-polarized ($S_3 > 0$) and, on the southern hemisphere, right-polarized ($S_3 < 0$). Circularly polarized states are found on the poles of the sphere, directly over the S_3 axis. Horizontally and vertically polarized states sit on the S_1 axis ($S_2 = 0$) and, ±45° polarized ones, on the S_2 axis ($S_1 = 0$).

3.3.3 Mueller matrices

As with Jones vectors, any Stokes vector $\vec{S}$ corresponding to one polarized light state will change after interacting with a medium, leading to a different Stokes vector $\vec{S}'$. The medium can and will act over the incident vector by changing its amplitudes and phase delay and, possibly, induce some loss of coherence that will depolarize part of the original $\vec{S}$. The

effect the medium induces over $\vec{S}$ is modeled through the system of equations given by the set of 16 real coefficients $\{M_{ij}\}_{i,j=1,\dots,16} \in \mathbb{R}$, where [3]

$$\begin{pmatrix} S_0' \\ S_1' \\ S_2' \\ S_3' \end{pmatrix} = \begin{pmatrix} M_{11} & M_{12} & M_{13} & M_{14} \\ M_{21} & M_{22} & M_{23} & M_{24} \\ M_{31} & M_{32} & M_{33} & M_{34} \\ M_{41} & M_{42} & M_{43} & M_{44} \end{pmatrix} \begin{pmatrix} S_0 \\ S_1 \\ S_2 \\ S_3 \end{pmatrix} ,$$

$$M = \begin{pmatrix} M_{11} & M_{12} & M_{13} & M_{14} \\ M_{21} & M_{22} & M_{23} & M_{24} \\ M_{31} & M_{32} & M_{33} & M_{34} \\ M_{41} & M_{42} & M_{43} & M_{44} \end{pmatrix} = M_{11} \begin{pmatrix} m_{11} & m_{12} & m_{13} & m_{14} \\ m_{21} & m_{22} & m_{23} & m_{24} \\ m_{31} & m_{32} & m_{33} & m_{34} \\ m_{41} & m_{42} & m_{43} & m_{44} \end{pmatrix} . \tag{3.22}$$

The intermediate matrix, M (Eq. 3.22), receives the name of Mueller matrix, and it is a crucial element that describes all the polarization properties of a sample, including its depolarization, retardance, or diattenuation, as we will see in the following chapters [4]. In contrast with Jones's matrices, Mueller's matrices are real and, thus, measurable. Matrix M can often be depicted by normalizing every element to M_{11}, which depicts the total measured intensity. The normalized Mueller matrix will be described with the lowercase coefficients $\{m_{ij}\}_{i,j=1,\dots,16} \in \mathbb{R}$ (Eq. 3.22). Another alternative representation lies in writing it as a block matrix [4]

$$M = M_{11} \begin{pmatrix} 1 & \vec{D}^T \\ \vec{P} & m_{3\times3} \end{pmatrix} . \tag{3.23}$$

In the previous equation, vector $\vec{P} = (m_{21}, m_{31}, m_{41})^T$ is the polarizance, which indicates the ability of the medium to polarize a completely unpolarized incident Stokes vector. Vector $\vec{D} = (m_{12}, m_{13}, m_{14})^T$ is the diattenuation, which describes the preference of the medium for absorbing one of the two perpendicular amplitudes (i.e., a linear polarizer). $m_{3\times3}$ represents the lower right 3×3 block of the Mueller matrices.

3.3.4 Physical realizability of a Mueller matrix

Not all 4×4 real-valued matrices are physically realizable Mueller matrices M, meaning that a sample's Mueller matrix must fulfill some conditions to be associated with a "real" medium. First, the sample cannot generate polarization states with a $DOP > 1$. A way to test this condition is by evaluating the next two equations, namely the forward and reverse passivity conditions (Eqs. 3.24) [16]

$$\begin{aligned} &M_{11}(1 + ||\vec{D}||) \leq 1 \text{ , and} \\ &M_{11}(1 + ||\vec{P}||) \leq 1 . \end{aligned} \tag{3.24}$$

The second condition involves constructing a related matrix, known as the covariance matrix, and examining its properties. The covariance matrix, denoted as $H(M)$, is derived from the elements of the Mueller matrix, M, using the following formula:

$$H = \frac{1}{4} \sum_{i,j=1}^{4} M_{ik} \sigma_i \otimes \sigma_j , \tag{3.25}$$

where σ_i are the Pauli matrices and $\otimes$ represents the tensor product. Any physically realizable Mueller matrix matrix has a covariance matrix where its eigenvalues are all real and non-zero [17]. The set of two conditions that a M must fulfill to be physically realizable receive the name of the *ensemble criterion* [4].

3.4 Mueller matrices of relevant optical elements

Biological samples with some polarimetric behavior often have Mueller matrices with a non-straightforward interpretation. As such, several methods will be introduced in subsequent sections to describe matrices M in terms of equivalent, simpler materials, such as diattenuators, retarders, and rotators. Therefore, it is necessary to introduce the basic polarimetric behavior of these materials through their Mueller matrices.

3.4.1 Diattenuators

[14] Throughout this thesis, we will refer to *linear diattenuators* as *diattenuators* for simplicity unless indicated otherwise. Both elliptical and circular diattenuators exist, which describe the anisotropic absorption of perpendicular elliptically and circularly polarized light states. Section 4.3 of reference [4] contains a complete description of all types of diattenuators.

A linear diattenuator [14] is an optical element that attenuates the light polarization component parallel to its absorption axis. In other words, given a set of two orthogonal axes on the diattenuator, $\hat{x}_D$ and $\hat{y}_D$, components polarized parallel to $\hat{x}_D$ will get more attenuated than those parallel to $\hat{y}_D$, or vice-versa [3]. Linear diattenuators are often referred to as linear polarizers. The critical parameter of a diattenuator is then its diattenuation, D, also called dichroism, that describes its anisotropic intensity attenuation [4]. An ideal diattenuator does not affect the phase of the field.

Let E_x and E_y be the amplitudes of an incident beam parallel to the axes $\hat{x}_D$ and $\hat{y}_D$ of the diattenuator, respectively. Let E'_x and E'_y be the amplitudes transmitted after the interaction with the diattenuator parallel to the axes $\hat{x}_D$ and $\hat{y}_D$, respectively. Let p_x and p_y be the transmittance of the diattenuator along the axes $\hat{x}_D$ and $\hat{y}_D$, respectively.

By the definition of transmittance, the amplitudes of the field before and after the diattenuator are

$$\begin{aligned} E'_x &= p_x E_x \ , \text{ and} \\ E'_y &= p_y E_y \ . \end{aligned}$$

Knowing that the Stokes vectors before ($\vec{S}$) and after ($\vec{S}'$), the diattenuator are related through its Mueller matrix (M_D), and applying the definition of the Stokes vector (Eqs. 3.18), leads to a matrix given by [3]

$$M_D = \begin{pmatrix} p_x^2 + p_y^2 & p_x^2 - p_y^2 & 0 & 0 \\ p_x^2 - p_y^2 & p_x^2 + p_y^2 & 0 & 0 \\ 0 & 0 & 2p_x p_y & 0 \\ 0 & 0 & 0 & 2p_x p_y \end{pmatrix} . \tag{3.26}$$

Parameters of a diattenuator

The diattenuator matrix (Eq. 3.26) can also be represented as a block matrix. Let $\{M_{D,ij}\}$, $i, j \in [1, 4]$ be the elements of M_D. Then, its block matrix representation is given by

$$M_D = M_{D,11} \begin{pmatrix} 1 & \vec{D}^T \\ \vec{D} & m_D \end{pmatrix} \ , \tag{3.27}$$

where we have introduced the following quantities by considering that M_D is a symmetric matrix:

- $M_{D,11} = \frac{1}{2}(p_x^2 + p_y^2)$ is the maximum transmittance of the diattenuator.
- $\vec{D}$ is the column vector given by $\vec{D}^T = \frac{1}{M_{D,11}}(M_{D,21}, M_{D,31}, M_{D,41})$, also known as the diattenuation vector.
- m_D is the lower right 3×3 block of M_D after dividing it by M_{11}, whose expression can be calculated as

$$m_D = \left(\sqrt{1 - ||\vec{D}||^2}\right) \mathbf{I}_3 + \left(1 - \sqrt{1 - ||\vec{D}||^2}\right) \hat{D}\hat{D}^T \ , \tag{3.28}$$

  where $\mathbf{I}_3$ is the 3×3 identity matrix and $\hat{D}$ is the unitary diattenuation vector, $\hat{D} = ||\vec{D}||^{-1}\vec{D}$.

Any diattenuator matrix is completely defined by M_{11} and $\vec{D}$. Any diattenuator, i.e., not only linear ones, has a diattenuation vector defined as

$$\vec{D} = \begin{pmatrix} D_1 \\ D_2 \\ D_3 \end{pmatrix} = \frac{1}{M_{D,11}} \begin{pmatrix} M_{D,21} \\ M_{D,31} \\ M_{D,41} \end{pmatrix} \ ,$$

whose definition can be used to calculate the total diattenuation D, the linear diattenuation D_L and the circular diattenuation D_C as

$$\begin{aligned} D &= ||\vec{D}|| = \sqrt{D_1^2 + D_2^2 + D_3^2} \ , \\ D_L &= \sqrt{D_1^2 + D_2^2} \ , \text{ and} \\ D_C &= ||D_3|| \ . \end{aligned} \tag{3.29}$$

Linear diattenuators will have $D_C = 0$, circular diattenuators will have $D_L = 0$ and elliptical diattenuators will be defined by $D_L \neq 0$ and $D_C \neq 0$.

Linear polarizers

The matrix of a linear diattenuator describes the behavior of commonly used optical elements. For example, an ideal linear polarizer has transmission only along one of the two axes and completely absorbs the field along the other. A horizontal linear polarizer is defined by $p_x = 1$ and

$p_y = 0$, so its Mueller matrix is

$$M_{HP} = \frac{1}{2}\begin{pmatrix} 1 & 1 & 0 & 0 \\ 1 & 1 & 0 & 0 \\ 0 & 0 & 0 & 0 \\ 0 & 0 & 0 & 0 \end{pmatrix} . \tag{3.30}$$

Analogously, a vertical linear polarizer given by $p_x = 0$ and $p_y = 1$ has a Mueller matrix defined by

$$M_{VP} = \frac{1}{2}\begin{pmatrix} 1 & -1 & 0 & 0 \\ -1 & 1 & 0 & 0 \\ 0 & 0 & 0 & 0 \\ 0 & 0 & 0 & 0 \end{pmatrix} . \tag{3.31}$$

In general, we can define $p^2 = p_x^2 + p_y^2$ to describe a linear polarizer with its transmission axis aligned at an angle γ with respect to the x axis (i.e., $\hat{x}_D = \hat{x}\cos\delta$) as [3]

$$M_{LP} = \frac{p^2}{2}\begin{pmatrix} 1 & \cos 2\gamma & 0 & 0 \\ \cos 2\gamma & 1 & 0 & 0 \\ 0 & 0 & \sin 2\gamma & 0 \\ 0 & 0 & 0 & \sin 2\gamma \end{pmatrix} \tag{3.32}$$

where its maximum transmittance is given by

$$\frac{p^2}{2} = \frac{p_x^2 + p_y^2}{2} .$$

Ideal linear polarizers will have a maximum transmittance of $1/2$. However, real linear polarizers do not have complete transmission and complete absorption along their perpendicular axis. Let us say that a real linear polarizer has a transmittance along its transmission axis of p_t^2 and p_e^2 along its extinction axis. Manufacturers often specify the extinction ratio (ER) of their linear polarizers, which is usually written as

$$ER = 1 : \frac{p_t^2}{p_e^2} . \tag{3.33}$$

The ER specifies how close to an ideal one a linear polarizer is. For example, a linear polarizer with $ER = 1 : 10000$ will have a Mueller matrix much closer to that of an ideal linear polarizer than one with $ER = 1 : 100$.

Neutral density filters

Diattenuation is the anisotropic absorption of two perpendicularly polarized beams. Still, the general matrix of a diattenuator (Eq. 3.26) can also be applied when the absorption is isotropic, i.e., when $p_x = p_y = p$. In such case, the matrix takes the shape [3]

$$M_{ND} = p^2\begin{pmatrix} 1 & 0 & 0 & 0 \\ 0 & 1 & 0 & 0 \\ 0 & 0 & 1 & 0 \\ 0 & 0 & 0 & 1 \end{pmatrix} . \tag{3.34}$$

The matrix represented in Eq. 3.34 describes mathematically a homogeneous transmittance regardless of the orientation of the optical element without affecting the polarization state otherwise. In reality, this matrix characterizes neutral density filters, which are used in optical setups to lower the intensity of a beam without changing the polarization state.

The intensity of the outgoing beam I' with respect to the incident one I is given by

$$I' = p^2 I \ ,$$

and the corresponding Stokes vectors, $\vec{S}'$ and $\vec{S}$, are related as

$$\vec{S}' = p^2 \vec{S} \ .$$

3.4.2 Retarders

A linear retarder[15] is an optical element that shifts the phase of two orthogonally polarized light states by a factor of ϕ. In other words, given a set of two orthogonal axes on the retarder, $\hat{x}_R$ and $\hat{y}_R$ components polarized parallel to $\hat{x}_R$ (fast axis) will gain an additional phase $+\phi/2$, while those parallel to $\hat{y}_R$ (slow axis) will be changed by a phase factor of $-\phi/2$ [3]. Ideal retarders do not affect the intensity of the field. Following on the derivations of Sec. 3.4.1, a linear retarder will relate the incident and outgoing field amplitudes as

$$E'_x = e^{+i\phi/2} E_x \ , \text{ and}$$
$$E'_y = e^{-i\phi/2} E_y \ ,$$

leading to a Mueller matrix M_R defined by

$$M_R = \begin{pmatrix} 1 & 0 & 0 & 0 \\ 0 & 1 & 0 & 0 \\ 0 & 0 & \cos\phi & \sin\phi \\ 0 & 0 & -\sin\phi & \cos\phi \end{pmatrix} \ . \tag{3.35}$$

[15] Throughout this book, we will refer to *linear retarders* as *retarders* for simplicity unless indicated otherwise. Other names are used in the literature, such as *phase shifters*, *wave plates*, or *phase compensators*. [3]. Both elliptical and circular retarders exist, which describe the applied phase shift of perpendicular elliptically and circularly polarized light states. Section 4.2 of reference [4] contains a complete description of all types of retarders.

Parameters of a retarder

As before, the general expression for a retarder (Eq. 3.35) can be rewritten as a block matrix

$$M_R = \begin{pmatrix} 1 & \vec{0}^T \\ \vec{0} & m_R \end{pmatrix}$$

with the aid of the following quantities:

- $\vec{0}$ is the column vector given by $\vec{0}^T = (0, 0, 0)$.
- m_R is the lower right 3×3 block of M_R.

The absolute retardance R is obtainable through specific calculations on M_R. For now, we will introduce the absolute retardance R, defined as

$$R = \cos^{-1}\left(\frac{\text{trace}(M_R)}{2} - 1\right) \in [0, \pi] \ , \tag{3.36}$$

but additional derivations related to the retardance will be discussed in the following sections.

Quarter-wave plates

A case of particular interest is when the introduced phase shift of a retarder is $\phi = \pi/2$. This type of retarder is known as a quarter-wave plate because each of the two field components is modified by $\pm\pi/4$:

$$E'_x = e^{+i\pi/4}E_x \quad \text{, and}$$
$$E'_y = e^{-i\pi/4}E_y \quad .$$

The Mueller matrix of a quarter-wave plate with its fast axis parallel to the x axis is given by

$$M_{QWP} = \begin{pmatrix} 1 & 0 & 0 & 0 \\ 0 & 1 & 0 & 0 \\ 0 & 0 & 0 & 1 \\ 0 & 0 & -1 & 0 \end{pmatrix} \quad . \tag{3.37}$$

If the incident light is linearly polarized at ±45° with respect to the fast axis of the waveplate,

$$\vec{S}_{\pm 45} = \begin{pmatrix} 1 \\ 0 \\ \pm 1 \\ 0 \end{pmatrix} ,$$

then, the output light state is given by

$$\vec{S}'_{\pm 45} = M_{QWP}\vec{S}_{\pm 45} = \begin{pmatrix} 1 \\ 0 \\ 0 \\ \mp 1 \end{pmatrix} = \vec{S}_{LR} \quad ,$$

which indicates that a quarter-wave plate with its fast axis oriented at±45° with respect to the horizontal can transform the incident linearly polarized light $\vec{S}_{\pm 45}$ into left-handed or right-handed circularly polarized light $\vec{S}_{LR}$.

3.4.3 Rotators

So far, the specific cases of diattenuators and retarders we have seen have been optical elements aligned with some particular orientations with respect to the components of the field. However, a straightforward way of transforming them into diattenuators or retarders at any specific orientation is by considering a rotation matrix R given by

$$M_{Rot}(\theta) = \begin{pmatrix} 1 & 0 & 0 & 0 \\ 0 & \cos 2\theta & \sin 2\theta & 0 \\ 0 & -\sin 2\theta & \cos 2\theta & 0 \\ 0 & 0 & 0 & 1 \end{pmatrix} \quad , \tag{3.38}$$

where the rotation angle of the optical element with respect to the x axis is given by θ. The rotation of any optical element with a matrix M is then given by [3]

$$M = M_{Rot}(-2\theta)MM_{Rot}(2\theta) \tag{3.39}$$

Rotated linear polarizer

Following on the expression of the general linear polarizer (Eq. 3.32), the matrix of a rotated, ideal ($\gamma = 0°$) linear polarizer ($M_{LP,Rot}$), with transmission p, is derived by Eq. 3.39 [3]

$$M_{LP,Rot} = M_{Rot}(-2\theta)M_{LP}M_{Rot}(2\theta) \ ,$$

so that

$$M_{LP,Rot} = \frac{p^2}{2}\begin{pmatrix} 1 & \cos 2\theta & \sin 2\theta & 0 \\ \cos 2\theta & \cos^2 2\theta & \sin 2\theta \cos 2\theta & 0 \\ \sin 2\theta & \sin 2\theta \cos 2\theta & \sin^2 2\theta & 0 \\ 0 & 0 & 0 & 0 \end{pmatrix} \ . \tag{3.40}$$

Rotated quarter-wave plates

Following the same derivations as before, the general Mueller matrix of a quarter-wave plate (Eq. 3.37) rotated by an angle θ with respect to the x axis, $M_{QWP,Rot}$, is given by

$$M_{QWP,Rot} = M_{Rot}(-2\theta)M_{QWP}M_{Rot}(2\theta) \ ,$$

so that

$$M_{QWP,Rot} = \begin{pmatrix} 1 & 0 & 0 & 0 \\ 0 & \cos^2 2\theta & \sin 2\theta \cos 2\theta & -\sin 2\theta \\ 0 & \sin 2\theta \cos 2\theta & \sin^2 2\theta & \cos 2\theta \\ 0 & \sin 2\theta & -\cos 2\theta & 0 \end{pmatrix} \ . \tag{3.41}$$

3.4.4 Depolarizers

Depolarizers are optical elements that turn polarized light into depolarized light. If an incident state is totally polarized, the components of its Stokes vector $\vec{S}$ fulfill $S_0^2 = S_1^2 + S_2^2 + S_3^2$. A total depolarizer will transform the said vector into $\vec{S}'$ where its components relate to those of $\vec{S}$ through $S_0' = S_0$, and $S_1'^2 + S_2'^2 + S_3'^2 = 0$. In other words, an ideal depolarizer has a Mueller matrix, M_Δ given by [3]

$$M_\Delta = \begin{pmatrix} 1 & 0 & 0 & 0 \\ 0 & 0 & 0 & 0 \\ 0 & 0 & 0 & 0 \\ 0 & 0 & 0 & 0 \end{pmatrix} \ . \tag{3.42}$$

[16] See reference [3] for the complete derivations

If the depolarizer is not ideal, it is possible that $S_0^2 > S_1'^2 + S_2'^2 + S_3'^2 > 0$. Experimentally, one often can encounter four different cases[16].

Case 1: The depolarizer is isotropic The depolarizer is not ideal, but it has the same effect on S_1, S_2, and S_3. Then, its Mueller matrix is given

by:

$$M_\Delta = \begin{pmatrix} 1 & 0 & 0 & 0 \\ 0 & a & 0 & 0 \\ 0 & 0 & a & 0 \\ 0 & 0 & 0 & a \end{pmatrix} , \tag{3.43}$$

where $0 < a < 1$ is the factor by which the components of $\vec{S}$ are modified.

Case 2: The depolarizer is not isotropic The depolarizer is not ideal and does not have the same effect on S_1, S_2, and S_3. Then, its Mueller matrix is given by:

$$M_\Delta = \begin{pmatrix} 1 & 0 & 0 & 0 \\ 0 & a & 0 & 0 \\ 0 & 0 & b & 0 \\ 0 & 0 & 0 & c \end{pmatrix} , \tag{3.44}$$

where $0 < a < 1$, $0 < b < 1$, and $0 < c < 1$ are the factors by which S_1, S_2 and S_3 are modified, respectively.

Case 3: The depolarizer is isotropic and reflecting The depolarizer is not ideal, but it has the same effect on S_1, S_2, and S_3, except for an additional reflection of S_2 and S_3. Then, its Mueller matrix is given by:

$$M_\Delta = \begin{pmatrix} 1 & 0 & 0 & 0 \\ 0 & a & 0 & 0 \\ 0 & 0 & -a & 0 \\ 0 & 0 & 0 & -a \end{pmatrix} , \tag{3.45}$$

where $0 < a < 1$ is the factor by which the components of $\vec{S}$ are modified.

Case 4: The depolarizer is reflecting but not isotropic The depolarizer is not ideal, does not have the same effect on S_1, S_2, and S_3, and reflects S_2 and S_3. Then, its Mueller matrix is given by:

$$M_\Delta = \begin{pmatrix} 1 & 0 & 0 & 0 \\ 0 & a & 0 & 0 \\ 0 & 0 & -b & 0 \\ 0 & 0 & 0 & -c \end{pmatrix} , \tag{3.46}$$

where $0 < a < 1$, $0 < b < 1$, and $0 < c < 1$ are the factors by which S_1, S_2 and S_3 are modified, respectively.

Parameters of a depolarizer

The key parameter of a depolarizer its the total depolarization Δ, defined by the diagonal of M_Δ as [18]

$$\Delta = 1 - \frac{\text{trace}(M_\Delta) - 1}{3} \in [0, 1] \ . \tag{3.47}$$

Additional derivations related to depolarization will be derived in the following sections.

3.5 Mueller matrix decomposition methods

Mueller matrices provide a complete description of how a material or system affects polarized light. Still, their interpretation can be difficult due to the mixed effects of retardance, diattenuation, and depolarization. Various decomposition methods have been developed to extract the fundamental optical properties of the samples, i.e., their retardance, diattenuation, and depolarization, by understanding the samples as a mixture of known elements. This section explores the most common techniques for interpreting and decomposing Mueller matrices. While some decomposition methods have unique solutions, others provide partial interpretation subject to the chosen order of matrix equivalents selected for decomposing the matrix of the sample.

Although the contents described below are extracted from Mieites *et al.* [19], the original theory was first defined by many different authors. As such, each original article or book will be mentioned when necessary.

3.5.1 Matrix invariants

Metrics like indices of polarimetric purity (IPPs) and anisotropy coefficients provide valuable quantitative measures of a medium's depolarizing and anisotropic behavior, respectively. Since these are not decompositions *per se*, these magnitudes can be considered invariants.

Indices of polarimetric purity

The indices of polarimetric purity are derived from the covariance matrix $H(M)$ defined in Eq. 3.25. Let the set of four eigenvalues of $H(M)$, $\{\lambda_i\}_{i=0,\dots,3}$, with $\hat{\lambda_1} \geq \hat{\lambda_2} \geq \hat{\lambda_3} \geq \hat{\lambda_4} \geq 0$, and $\hat{\lambda_i} = \lambda_i / \text{trace}(H)$. Then, the indices of polarimetric purity are defined as [20, 21]

$$\begin{aligned} P1 &= \hat{\lambda_1} - \hat{\lambda_2} \ , \\ P2 &= \hat{\lambda_1} + \hat{\lambda_2} - 2\hat{\lambda_3} \ , \text{ and} \\ P3 &= 4 - \hat{\lambda_2} \ , \end{aligned} \tag{3.48}$$

and the degree of polarimetric purity is

$$P_\Delta = \sqrt{\frac{1}{3}\left(2P_1^2 + \frac{2}{3}P_2^2 + \frac{1}{3}P_3^2\right)} \ . \tag{3.49}$$

The IPPs depict the degree of polarization the sample maintains so that $0 \leq P_1 \leq P_2 \leq P_3 \leq 1$, with 1 being a totally polarizing sample and 0 a totally depolarizing one.

The characteristic decomposition, which is out of the scope of this book, transforms the Mueller matrix into a sum of four matrices, one of which is pure (non-depolarizing), the second is a non-pure equiprobable

mixture of two pure matrices, the third one is a non-pure equiprobable mixture of three matrices, and the fourth one depicts an ideal depolarizer [22]. Without diving into details[17], the IPPs represent the portion of the medium that behaves as each of the matrices in the characteristic decomposition. Specifically:

[17] See Gil and Ossikovski [22], section 6.3 for a full derivation of the IPPs and their interpretation.

- $P1$ represents the portion of the medium that behaves as a pure matrix,
- $P2 - P1$ is the portion of the medium that behaves as a non-pure mixture of two pure matrices, and
- $P3 - P2$ is the portion of the medium that behaves as a non-pure mixture of three pure matrices. In other words, $P3$ represents the part of the medium that is not a perfect depolarizer.

Anisotropy

The anisotropy of the sample can also be evaluated directly from the experimental Mueller matrices through the anisotropy coefficients. Given the 3×3 sub-matrix of M, $m_{3\times3}$ (see Eq. 3.23), we can introduce vectors [23]:

$$\vec{k} = \frac{1}{\sqrt{3}}(k_1, k_2, k_3)^T, \quad \vec{r} = (r_1, r_2, r_3)^T, \quad \vec{q} = (q_1, q_2, q_3)^T \quad , \tag{3.50}$$

where

$$m_{3\times3} = \begin{pmatrix} k_1 & r_3 & r_2 \\ q_3 & k_2 & r_1 \\ q_2 & q_1 & k_3 \end{pmatrix} \quad . \tag{3.51}$$

An auxiliary quantity is then defined as

$$\Sigma = 3(1 - ||\vec{k}||^2) + 2\vec{D}^T\vec{P} - 2\vec{r}^{\,T}\vec{q} \quad .$$

By making use again of the block structure of the matrices (Eq. 3.23), the linear (α_L) and circular (α_C) anisotropy coefficients are derived from combinations of vectors $\vec{k}$, $\vec{r}$, $\vec{q}$, $\vec{P}$ and $\vec{D}$, so that

$$\begin{aligned} \alpha_L &= \sqrt{\frac{(D_1 + P_1)^2 + (r_1 - q_1)^2 + (D_2 + P_2)^2 + (r_2 - q_2)^2}{\Sigma}} \quad , \text{ and} \\ \alpha_C &= \sqrt{\frac{(D_3 + P_3)^2 + (r_3 - q_3)^2}{\Sigma}} \quad , \end{aligned} \tag{3.52}$$

and the total anisotropy of the sample is derived as

$$P_\alpha = \sqrt{\alpha_L^2 + \alpha_C^2} \leq P_\Delta \leq 1 \quad . \tag{3.53}$$

Due to their definition, the degree of anisotropy of a sample can not exceed its polarimetric purity since the anisotropy can only be calculated where there is polarized light. As a consequence, depolarizing samples (low P_Δ) will have low anisotropy, but low anisotropy does not imply low polarimetric purity [19].

3.5.2 Forward polar decomposition

As previously mentioned, decomposition methods help understand the experimental Mueller matrices by extracting fundamental optical properties like retardance, diattenuation, and depolarization. While various techniques exist, the Lu-Chipman decomposition [18], also known as the forward polar decomposition, remains widely used, particularly for biological tissues like brain tissue, due to its straightforward interpretation.

The forward polar decomposition assumes that the polarization effects of any sample can be represented by a sequential combination of depolarization (Δ) and retardance (R). It rewrites any arbitrary matrix M[18] as a product of the pure matrices M_Δ (ideal depolarizer), M_R (ideal retarder), and M_D (ideal diattenuator), according to

$$M = \begin{pmatrix} 1 & \vec{D}^T \\ \vec{P} & m \end{pmatrix} = M_{\Delta P} \cdot M_R \cdot M_D \quad . \tag{3.54}$$

[18] Typically, the matrices M are first normalized by their first element, $\hat{M} = M \cdot M[1,1]^{-1}$, before applying any decomposition method.

Matrices M_R and M_D represent pure retarders and diattenuators and have a block form according to what was described in Sec. 3.4 so that

$$M_R = \begin{pmatrix} 1 & \vec{0}^T \\ \vec{0} & m_R \end{pmatrix} \text{ , and } M_D = \begin{pmatrix} 1 & \vec{D}^T \\ \vec{D} & m_D \end{pmatrix} \quad . \tag{3.55}$$

However, the depolarizer in this decomposition form, $M_{\Delta p}$, does not keep the diagonal form of Eq. 3.42. Instead, its block form has the shape

$$M_{\Delta P} = \begin{pmatrix} 1 & \vec{0}^T \\ \vec{P}_{\Delta P} & m_{\Delta P} \end{pmatrix} \quad . \tag{3.56}$$

In other words, the forward polar decomposition does not consider a *pure* depolarizer, but instead a depolarizer with polarizance.

The typical pipeline of the forward polar decomposition involves the following steps[19], as defined in the literature [18, 22]. Starting with matrices

[19] Several steps can be simplified when matrices are singular, as explained in Sec. 8 of reference [18] and Sec. 8.2.2 of reference [22].

1. Normalize the experimental Mueller matrix M by its first element: $M \rightarrow M/M[1,1]$.
2. Identify its polarizance $\vec{P}$, its diattenuation $\vec{D}$, and its lower block m by evaluating its block form (Eq. 3.54).
3. Construct the diattenuator matrix M_D from its diattenuation $\vec{D}$ and its lower block m_D (Eq. 3.28) by evaluating its block form (Eq. 3.55).
4. Find the polarizance of the depolarizer, $\vec{P}_{\Delta P}$, as

$$\vec{P}_{\Delta P} = \frac{\vec{P} - m\vec{D}}{\sin^2 \sqrt{1 - ||\vec{D}||^2}}$$

5. Find the matrix $M_{\Delta P} M_R$ from Eq. 3.54 as $M_f \coloneqq M_{\Delta P} M_R = M M_D^{-1}$.
6. Keep the lower 3×3 block of M_f, m_f.
7. Calculate matrix $\overline{m}$ as $\overline{m} = m_f m_f^T$.

8. Find the set of eigenvalues $\{\lambda\}_{i=1,2,3}$ of $\overline{m}$, with $\lambda_1 \geq \lambda_2 \geq \lambda_3 \geq 0$.
9. Find the set of (column) eigenvectors $\{\vec{v}_i\}_{i=1,2,3}$ of $\overline{m}$, associated with each of its eigenvalues.
10. Construct matrix m_{R2} from the eigenvectors of $\overline{m}$ as $m_{R2} = (\vec{v}_1, \vec{v}_2, \vec{v}_3)$.
11. Calculate the quantity ϵ from matrix M as

$$\epsilon = \frac{\det(M)}{|\det(M)|} \quad .$$

12. Construct the lower 3×3 block of the depolarizer matrix, $m_{\Delta P}$, as

$$m_{\Delta P} = m_{R2}(\lambda_1, \lambda_2, \varepsilon\lambda_3) m_{R2}^T$$

13. Build the depolarizer matrix, $M_{\Delta P}$, from $m_{\Delta P}$ and $\vec{P}_{\Delta P}$, from its block form (Eq. 3.56).
14. Construct the lower 3×3 block of the retarder matrix, m_R, as

$$m_R = m_{\Delta P}^{-1} m_f$$

15. Build the retarder matrix, M_R, from its block form (Eq. 3.55).

Once matrix M is decomposed according to the product in Eq. 3.54 and the steps mentioned above, the magnitudes of the pure equivalents, Δ, R, and D (see Sec. 3.4), are derived as:

$$\begin{aligned} \Delta &= 1 - \frac{|\text{trace}(M_{\Delta P}) - 1|}{3} \in [0,1] \quad , \\ R &= \cos^{-1}\left(\frac{\text{trace}(M_R)}{2} - 1\right) \in [0,\pi] \quad , \text{ and} \\ D &= ||\vec{D}|| = ||(M_D(1,0), M_D(2,0), M_D(3,0))^T|| \in [0,1] \quad . \end{aligned} \tag{3.57}$$

We have seen in Sec. 3.4 that a material's response will depend on the alignment between its optical axis, given by the orientation of the polarization ellipse Ψ, and the polarization axes. To recover the orientation of the optical axis, i.e., of the polarization ellipse, Ghosh *et al.* [24] propose modeling the retarder, defined by M_R, as a combination of an arbitrarily oriented linear retarder with matrix M_{LR}, and a circular retarder M_C. Given the initial orientation of the optical axis of M_{LR} $\Psi = \theta$ (see fig. 3.2), its phase delay (ϕ), and the phase delay of the optical rotation α the retarder M_R can be further decomposed as

$$M_R = M_{LR} \cdot M_C \quad , \text{ with}$$

$$M_{LR} = \begin{pmatrix} 1 & \vec{0}^T \\ \vec{0} & m_{LR} \end{pmatrix} \quad ,$$

$$m_{LR} = \begin{pmatrix} \cos^2(2\theta) + \sin^2(2\theta)\cos(\phi) & \sin(2\theta)\cos(2\theta)(1-\cos(\delta)) & -\sin(2\theta)\sin(\delta) \\ \sin(2\theta)\cos(2\theta)(1-\cos(\phi)) & \sin^2(2\theta) + \cos^2(2\theta)\cos(\phi) & \cos(2\theta)\sin(\phi) \\ \sin(2\theta)\sin(\phi) & -\cos(2\theta)\sin(\phi) & \cos(\phi) \end{pmatrix},$$

$$\text{and } M_C = \begin{pmatrix} 1 & 0 & 0 & 0 \\ 0 & \cos(2\alpha) & \sin(2\alpha) & 0 \\ 0 & -\sin(2\alpha) & \cos(2\alpha) & 0 \\ 0 & 0 & 0 & 1 \end{pmatrix} \quad .$$

Then, the orientation of the optical axis can be recovered as:

$$\theta = \frac{1}{2}\tan^{-1}\left(\frac{M_{LR}(4,2) - M_{LR}(2,4)}{M_{LR}(3,4) - M_{LR}(4,3)}\right) . \tag{3.58}$$

3.5.3 Symmetric decomposition

The forward decomposition selects a specific order for the equivalent depolarizer, retarder, and diattenuator matrices. Since matrix multiplication is not commutative, altering this order yields different sets of equivalent matrices. Specifically, M_Δ resulting from the polar decomposition can contain non-zero off-diagonal elements, indicating the presence of polarizance or diattenuation even if it represents the matrix of a depolarizer. To address these limitations, R. Ossikovski [25] has proposed a five-layer serial model with two retarders as follows

$$M = M_{D2}M_{R2}M_{\Delta d}M_{R1}^T M_{D1} \ . \tag{3.59}$$

This model utilizes two retarders (M_{R1} and M_{R2}) and two diattenuators (M_{D1} and M_{D2}) to ensure that the depolarizer obtained with this decomposition is purely diagonal ($M_{\Delta d}$), given that the product matrices $M_{j2} = M_{D2}M_{R2}$ and $M_{j1} = M_{R1}^T M_{D1}$ represent non-depolarizing (pure) components [25].

The (non-normalized) diagonal depolarizer is represented by

$$M_{\Delta d} = \begin{pmatrix} d_0 & 0 & 0 & 0 \\ 0 & d_1 & 0 & 0 \\ 0 & 0 & d_2 & 0 \\ 0 & 0 & 0 & d_3 \end{pmatrix} , \tag{3.60}$$

and, for it to be obtained, the Mueller matrix M must be diagonalizable. Let $G = \mathrm{diag}(1,-1,-1,-1)$. Then, the applicability of the symmetric decomposition can be verified by checking if matrix N, defined as

$$N = GM^T GM \ , \tag{3.61}$$

is diagonalizable [25].

If the symmetric decomposition can be applied, the diattenuators can be found by deriving vectors $\vec{s}_{D1} = (1, \vec{D_1})^T$ and $\vec{s}_{D2} = (1, \vec{D_2})^T$. These vectors, which are related to the diattenuation vectors of M_{D1} and M_{D2}, respectively, can be found by the eigenvalue-eigenvector equations [25]

$$\begin{aligned} &(M^T GMG)\vec{s}_{D1} = (\vec{d_0})^2\vec{s}_{D1} \ , \text{ and} \\ &(MGM^T G)\vec{s}_{D2} = (\vec{d_0})^2\vec{s}_{D2} \ . \end{aligned} \tag{3.62}$$

Then, the diattenuator matrices are recovered from the components of $\vec{s}_{D1}$ and $\vec{s}_{D2}$ by constructing it according to its block expression (Eq. 3.27) and its lower 3×3 block (Eq. 3.28). At this point, verifying that the inequalities $D_{1,2} \leq 1$ hold is necessary.

The next steps involve applying singular value decomposition (SVD) to the matrix

$$M' = M_{D2}^{-1}MM_{D1}^{-1} = M_{R2}M_{\Delta d}M_{R1}^T \tag{3.63}$$

to retrieve M_{R2}, $M_{\Delta d}$ and M_{R1}, where each component of the SVD is each of the matrices.

Using the SVD has drawbacks, given that its results are invariant to some permutations and sign changes [22]. This implies that the SVD can introduce an artificial circular retardance in M_{R1} and M_{R2}. If the retarder matrices are physically realizable, ($\det M_{R1} = \det M_{R2} = +1$), one can use instead the total retardance matrix

$$M_R = M_{R1} M_{R2}^T \ , \tag{3.64}$$

since it is not affected by permutations nor sign changes in the way that M_{R1} and M_{R2} are [25, 26] [20].

[20] Additional criteria can be established here to always derive the same M_{R1} and M_{R2} by minimizing the retardance (see [22, 25, 26]), in this book we will only consider the total retardance matrix M_R for ease of interpretation.

3.5.4 Differential decomposition

While convenient, the assumption of complete uniformity along the optical path often fails to capture the real behavior of macroscopic samples. The differential decomposition [27, 28] addresses this by considering a differential Mueller matrix, $m(z)$, for each infinitesimal element of the optical path length (dz). This differential matrix relates to the overall Mueller matrix, $M(z)$, through

$$\frac{dM(z)}{dz} = m(z)M(z) \ . \tag{3.65}$$

In the simplified scenario where m is independent of z, Equation 3.65 admits a solution expressed in terms of the matrix logarithm (assuming $z = 1$), as

$$m = \ln(M) \ . \tag{3.66}$$

Even in the general case where m depends on z, a matrix logarithm, $L = \ln(M)$, can be defined and analyzed analogously to m to evaluate the polarization properties of the medium [27, 28].

Again, this decomposition uses the Minkowski metric matrix $G = \mathrm{diag}(1, -1, -1, -1)$. Then, the concept of G-transpose of an arbitrary matrix A is defined as

$$A^G = GA^TG \ , \tag{3.67}$$

and the concepts of G-symmetry and G-antisymmetry are respectively fulfilled when

$$\begin{aligned} A^G &= A \ , \text{ and} \\ A^G &= -A \ . \end{aligned} \tag{3.68}$$

The differential decomposition focuses then on the separation of the matrix logarithm L in terms of its G-symmetric (L_u) and G-antisymmetric (L_m) parts, given by

$$L = \ln(M) = L_m + L_u = \frac{1}{2}(L - GL^TG) + \frac{1}{2}(L + GL^TG) \ . \tag{3.69}$$

The L_m component encodes the spectroscopic properties of M, including linear and circular retardance and diattenuation. More precisely, L_m represents the spatial or temporal average of these properties, as shown in [29], given by

$$L_m = \begin{pmatrix} 0 & -LD_H & -LD_{45} & CD \\ -LD_H & 0 & CB & LB_{45} \\ -LD_{45} & -CB & 0 & -LB_H \\ CD & -LB_{45} & LB_H & 0 \end{pmatrix}, \tag{3.70}$$

Here, LB and LD denote linear retardance and diattenuation, CB and CD represent circular retardance and diattenuation. The subscripts 45 and H indicate the orientation of the linear properties with respect to the +45° and horizontal axes, respectively. In contrast, the L_u component contains the information to calculate the average variances ($|\Delta L_H|^2$, $|\Delta L_{45}|^2$, $|\Delta C|^2$) and covariances ($\Delta L_H \Delta L_{45}^*$, $\Delta L_H \Delta C^*$, $\Delta L_{45} \Delta C^*$) of these properties [19, 22].

The differential decomposition assumes that a Mueller matrix, M, can be constructed from an infinite series of infinitesimal matrices, m. Consequently, each differential matrix, m (or its matrix logarithm L), must possess individual physical meaning. This condition can be verified by assessing the positive semi-definiteness of the reduced coherency matrix, which is related to the G-symmetric component of m (or L) [19]. A comprehensive formulation of this verification process is provided in [30].

The differential model is particularly well-suited for analyzing thin samples in transmission configurations, where the optical path length is often the thickness of the sample. In other scenarios, precisely determining the optical path might not be possible. However, this model has also been applied to backscattering configurations, demonstrating its versatility in diverse optical setups [31].

References

[1] M. Born and E. Wolf: "Principles of Optics", Cambridge University Press, 2019. ISBN: 9781108477437.

[2] E. Hecht: "Optics", Pearson Education, Incorporated, 2017. ISBN: 9780133977226.

[3] D. H. Goldstein: "Polarized Light", CRC Press, 2017. ISBN: 9781315217789.

[4] J. Gil and R. Ossikovski: "Polarized Light and the Mueller Matrix Approach", Series in Optics and Optoelectronics. CRC Press, 2017. ISBN: 9781482251562.

[5] V. Mieites et al.: "Revealing stress-induced changes equivalence between polarization-sensitive optical coherence tomography and polarimetric camera measurements", *Optics and Lasers in Engineering* **175** (2024). DOI: 10.1016/j.optlaseng.2023.107985.

[6] R. C. Jones: "A New Calculus for the Treatment of Optical Systems I Description and Discussion of the Calculus", *Journal of the Optical Society of America* **31**(7), 488 (1941). DOI: 10.1364/JOSA.31.000488.

[7] H. Hurwitz and R. C. Jones: "A New Calculus for the Treatment of Optical Systems II Proof of Three General Equivalence Theorems", *Journal of the Optical Society of America* **31**(7), 493 (1941). DOI: 10.1364/JOSA.31.000493.

[8] R. C. Jones: "A New Calculus for the Treatment of Optical Systems III The Sohncke Theory of Optical Activity", *Journal of the Optical Society of America* **31**(7), 500 (1941). DOI: 10.1364/JOSA.31.000500.

[9] R. C. Jones: "A New Calculus for the Treatment of Optical Systems IV", *Journal of the Optical Society of America* **32**(8), 486 (1942). DOI: 10.1364/JOSA.32.000486.

[10] R. C. Jones: "A New Calculus for the Treatment of Optical Systems V A More General Formulation, and Description of Another Calculus", *Journal of the Optical Society of America* **37**(2), 107 (1947). DOI: 10.1364/JOSA.37.000107.

[11] H. F. Jones et al.: "Importance of muscle biopsy to establish pathogenicity of DMD missense and splice variants", *Neuromuscular Disorders* **29**(12), 913–919 (2019). DOI: 10.1016/j.nmd.2019.09.013.

[12] R. C. Jones: "A New Calculus for the Treatment of Optical Systems VII Properties of the N-Matrices", *Journal of the Optical Society of America* **38**(8), 671 (1948). DOI: 10.1364/JOSA.38.000671.

[13] R. C. Jones: "New Calculus for the Treatment of Optical Systems VIII Electromagnetic Theory", *Journal of the Optical Society of America* **46**(2), 126 (1956). DOI: 10.1364/JOSA.46.000126.

[14] J. C. Ramella- et al.: "Polarized Light in Biomedical Imaging and Sensing", Switzerland: Springer Nature Switzerland, 2023. ISBN: 978-3-031-04741-1.

[15] G. G. Stokes: "Mathematical and Physical Papers", Cambridge University Press, 2009. ISBN: 9781108002646.

[16] I. San José and J. J. Gil: "Characterization of passivity in Mueller matrices", *Journal of the Optical Society of America A* **37**(2), 199 (2020). DOI: 10.1364/JOSAA.37.000199.

[17] J. J. Gil: "Characteristic properties of Mueller matrices", *Journal of the Optical Society of America* **17**(2), 328–334 (2000). DOI: 10.1364/JOSAA.17.000328.

[18] S.-Y. Lu and R. A. Chipman: "Interpretation of Mueller matrices based on polar decomposition", *Journal of the Optical Society of America A* **13**(5), 1106–1113 (1996). DOI: 10.1364/JOSAA.13.001106.

[19] V. Mieites Alonso et al.: "PoLambRimetry: a multispectral polarimetric atlas of lamb brain", *Journal of Biomedical Optics* **29**(09) (2024). DOI: 10.1117/1.JBO.29.9.096002.

[20] I. San José and J. J. Gil: "Invariant indices of polarimetric purity: Generalized indices of purity for n×n covariance matrices", *Optics Communications* **284**(1), 38–47 (2011). DOI: 10.1016/j.optcom.2010.08.077.

[21] J. J. Gil: "Structure of polarimetric purity of a Mueller matrix and sources of depolarization", *Optics Communications* **368**, 165–173 (2016). DOI: 10.1016/j.optcom.2016.01.092.

[22] J. J. Gil and R. Ossikovski: "Polarized Light and the Mueller Matrix Approach", Series in Optics and Optoelectronics. CRC Press, 2022 215–228. ISBN: 9781000568660.

[23] O. Arteaga, E. Garcia-Caurel, and R. Ossikovski: "Anisotropy coefficients of a Mueller matrix", *Journal of the Optical Society of America A* **28**(4), 548–553 (2011). DOI: 10.1364/JOSAA.28.000548.

[24] N. Ghosh, M. F. G. Wood, and I. A. Vitkin: "Mueller matrix decomposition for extraction of individual polarization parameters from complex turbid media exhibiting multiple scattering, optical activity, and linear birefringence", *Journal of Biomedical Optics* **13**(4), 044036 (2008). DOI: 10.1117/1.2960934.

[25] R. Ossikovski: "Analysis of depolarizing Mueller matrices through a symmetric decomposition", *Journal of the Optical Society of America A* **26**(5), 1109–1118 (2009). DOI: 10.1364/JOSAA.26.001109.

[26] J. Vizet and R. Ossikovski: "Symmetric decomposition of experimental depolarizing Mueller matrices in the degenerate case", *Applied Optics* **57**(5), 1159–1167 (2018). DOI: 10.1364/AO.57.001159.

[27] N. Ortega-Quijano and J. L. Arce-Diego: "Mueller matrix differential decomposition", *Optics Letters* **36**(10), 1942–1944 (2011). DOI: 10.1364/OL.36.001942.

[28] R. Ossikovski: "Differential matrix formalism for depolarizing anisotropic media", *Optics Letters* **36**(12), 2330–2332 (2011). DOI: 10.1364/OL.36.002330.

[29] R. Ossikovski and O. Arteaga: "Statistical meaning of the differential Mueller matrix of depolarizing homogeneous media", *Optics Letters* **39**(15), 4470–4473 (2014). DOI: 10.1364/OL.39.004470.

[30] R. Ossikovski and V. Devlaminck: "General criterion for the physical realizability of the differential Mueller matrix", *Optics Letters* **39**(5), 1216–1219 (2014). DOI: 10.1364/OL.39.001216.

[31] N. Ortega-Quijano and J. L. Arce-Diego: "Mueller matrix differential decomposition for direction reversal: application to samples measured in reflection and backscattering", *Optics Express* **19**(15), 14348–14353 (2011). DOI: 10.1364/OE.19.014348.

Part III

Materials and methods

Optical imaging technologies | 4

This chapter explores the optical imaging technologies that are central to this thesis. As mentioned in the introduction, these non-invasive techniques offer unique advantages for studying muscular dystrophies, providing detailed chemical and structural information without requiring extensive sample preparation. We will examine the principles and applications of each method, highlighting their specific strengths and how they can contribute to a comprehensive understanding of the biological samples.

Specifically, Chapter 4 will focus on the following optical methods: Optical Coherence Tomography (OCT), Spatial Frequency Domain Imaging (SFDI), Hyperspectral Imaging (HSI), Polarization-Sensitive OCT (PS-OCT), and Mueller Matrix Imaging. Each technique will be described in detail, outlining its theoretical background, implementation, and data analysis procedures. By combining the information gathered from these imaging modalities, we aim to achieve a multifaceted perspective on any sample in general and specifically on muscular dystrophy samples.

4.1 Optical Coherence Tomography (OCT)

Optical Coherence Tomography OCT is an interferometry-based imaging technique that uses low-coherence light to capture micrometer-resolution images of biological tissues. First introduced in the 1990s by James G. Fujimoto's group at MIT [1], OCT is often called *optical ultrasound*. Just as ultrasound utilizes sound waves to generate images based on their echoes, OCT employs light waves, specifically from a laser source, to reconstruct the internal structure of a sample by measuring the delay of backscattered light. This approach allows for non-invasive, cross-sectional visualization of tissue micro-structures without any sample preparation required.

OCT offers a valuable compromise between the high resolution of optical microscopy and the deep penetration of ultrasound. While ultrasound can image deep into tissues but lacks the resolution to see fine details, optical microscopy provides excellent detail but can only penetrate a short distance. OCT finds a balance, capturing micrometer-scale resolution while achieving millimeter-level penetration [2]. This capability makes OCT ideal for visualizing tissue structures at depths where both fine detail and penetration depth are essential.

4.1.1 Fundamentals

OCT uses low-coherence interferometry to construct three-dimensional images of the internal structure of the samples. As such, we will revise both concepts, interference and coherence, here to contextualize this technique. This section contains a summary of the most relevant steps for OCT specifically, as described in *Principles of Optics* [3].

Interference of two monochromatic waves

Let us consider two monochromatic waves that overlap at a point in space, $\vec{E}_i$ with $\{i\}_{1,2}$. Each wave travels with a propagation $\vec{k}_i\vec{r}$ and a frequency ω. We will also consider an initial phase shift between the waves, so each has an additional phase ϕ_i. Both waves are then defined as

$$\begin{aligned}\vec{E}_1(\vec{r},t) = \vec{E}_1 = \mathcal{R}\left[\vec{E_{01}}(t)e^{-i(\vec{k}_1\cdot\vec{r}-\omega t+\phi_1)}\right] \ , \text{ and} \\ \vec{E}_2(\vec{r},t) = \vec{E}_1 = \mathcal{R}\left[\vec{E_{02}}(t)e^{-i(\vec{k}_2\cdot\vec{r}-\omega t+\phi_2)}\right] \ ,\end{aligned} \tag{4.1}$$

where $\mathcal{R}[\cdot]$ describes the real part of the field, given by $\mathcal{R}[\vec{a}] = \frac{1}{2}[\vec{a}+\vec{a}^*]$, with $*$ denoting the complex conjugate [3]. We will also consider in this section the three-dimensional nature of the amplitudes given by

$$\vec{E_{0i}}(t) = (E_{0i,x}(t), E_{0i,y}(t), E_{0i,z}(t)) \ .$$

The total field at the point in space where the two fields overlap is given by

$$\vec{E}(\vec{r},t) = \vec{E}_1(\vec{r},t) + \vec{E}_2(\vec{r},t) \ .$$

According to what was introduced in chapter 2 (Eq. 2.37), the irradiance carried by the superposition of these fields at this point in space will be proportional to their added time average [3], as [3]

$$I \propto \langle\vec{E}^2\rangle = \langle\vec{E}_1^2 + \vec{E}_2^2 + 2\vec{E}_1\vec{E}_2\rangle = \langle\vec{E}_1\rangle + \langle\vec{E}_2\rangle + \langle\vec{E}_1\vec{E}_2\rangle \ .$$

If we drop the proportionality and focus only on the squared fields, the intensity at the point in space where two fields overlap is given by

$$\begin{aligned}I = I_1 + I_2 + J_{12} \ , \text{ with} \\ I_1 = \langle\vec{E}_1^2\rangle = \langle\vec{E}_1\cdot\vec{E}_1^*\rangle \ , \\ I_2 = \langle\vec{E}_2^2\rangle = \langle\vec{E}_2\cdot\vec{E}_2^*\rangle \ , \text{ and} \\ J_{12} = 2\langle\vec{E}_1\cdot\vec{E}_2\rangle \ .\end{aligned} \tag{4.2}$$

Let us evaluate the term J_{12}, denoted *interference term* [3], to see how different configurations of $\vec{E}_{1,2}$ affect the total intensity I. According to the fields in Eqs. 4.1, and given their relative phase difference ϵ, it can be shown[1] the interference term is[2]

$$J_{12} = 2\langle\vec{E}_1\cdot\vec{E}_2\rangle = \frac{1}{2}(E_{01,x}E_{02,x} + E_{01,y}E_{02,y} + E_{01,z}E_{02,z})\cos\epsilon \ . \tag{4.3}$$

For simplicity, let us now consider the case of two linearly polarized waves along the x direction so that $E_{01,y} = E_{02,y} = E_{01,z} = E_{02,z} = 0$, that are propagating along the z-direction. In this case, the total intensity is

[1] We refer to Section 7.2 of reference [3] for the full derivation.

[2] Note that, according to Eq. 4.3, if two co-propagating waves (i.e., $E_{01,z} = E_{02,z} = 0$) are perpendicularly polarized (i.e., $E_{01,y} = E_{02,x} = 0$), their interference term is zero and the total intensity is their added individual intensities. This is also the case for unpolarized light, where $I = I_1 + I_2$ and $J_{1,2} = 0$ [3].

$$
\begin{aligned}
I_1 &= \frac{1}{2}E_{01,x}^2 \quad , \\
I_2 &= \frac{1}{2}E_{02,x}^2 \quad , \\
J_{12} &= E_{01,x}E_{02,x}\cos\epsilon \quad \text{and} \\
I &= I_1 + I_2 + 2\sqrt{I_1 I_2}\cos\epsilon \quad .
\end{aligned}
\tag{4.4}
$$

The maxima and minima of this function correspond to those of $\cos\epsilon$ (Fig. 4.1). We can introduce the difference in the optical path length between both waves, ΔL, so the phase delay ϵ is

$$
\epsilon = \frac{2\pi}{\lambda_0}\Delta L \quad , \tag{4.5}
$$

where λ_0 is the central wavelength of the fields. In case they are monochromatic, $\lambda_0 = \lambda$.

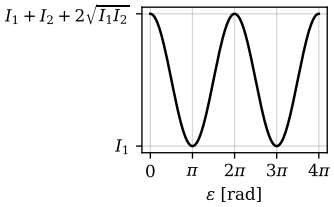

Figure 4.1: Total intensity for two parallel, linearly polarized waves along the x axis, with $I_2 = 4I_1$, in terms of their relative phase delay, ϵ.

As a result, the interference pattern created in J_{12} is directly related to the difference in the optical path that each wave travels. Any relative optical path difference change will manifest as a different interference pattern. This phenomenon is crucial to understanding how an OCT system functions.

The Michelson interferometer

At the core of every OCT, the system is an interferometer, which is usually configured according to a Michelson interferometer [4] (Fig. 4.2).

This configuration is formed by two possible optical paths. One contains the source (S), a mirror (M_1), and the plane that contains point P and is parallel to M_1 (i.e., interference plane). The other arm contains S, another mirror (M_2), and ends in the interference plane as well. Both paths are connected via a beam splitter (BS) and a compensation plate (C). When a field (1) exits the source and reaches the beam splitter, it divides into two fields (2 and 3). Ideally, both fields will carry the same intensity. Then, field 2 goes through the first optical path, reaches mirror $M1$, bounces back to the beam splitter, traverses it again, and exits on its other side after having passed through the beam splitter three times. Field 3 continues forward through the beam splitter, then through plaque C, bounces on mirror M_2, passes through plaque C, reaches the back of the beam splitter, and reflects down. Since 3 passes only through the beam splitter once, the compensation plate has the same thickness and refractive index, so the delay the beam splitter introduces does not affect the interference pattern.

If the distance between mirror M_2 and the beam splitter and between mirror M_1 and the beam splitter is not the same, there will be a difference in the optical path length that causes an interference pattern between 2 and 3 when the lens makes them converge at the same point P. If we consider the image of M_2 using the back of the beam splitter (M_2') as

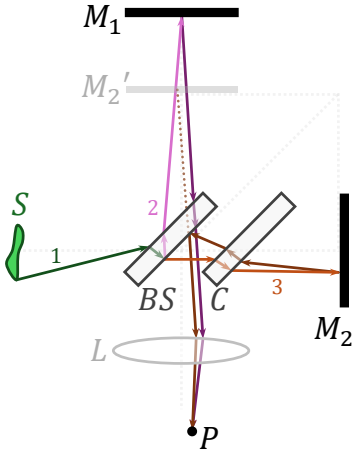

Figure 4.2: Schematics of a Michelson interferometer as depicted in [3]. A light source (S) produces light rays (1) that reach a beam splitter (BS). Part of the intensity (2) bounces in a mirror (M_1) in one of the arms of the interferometer. The other part (3) continues forward, passes through a compensation plate (C) with the same thickness and refractive index of BS, and reaches another mirror M_2. Both beams recombine at the back of BS and travel parallel until they reach a collimation lens L, which focalizes the interference pattern in the plane that contains P and is parallel to M_1. M_2' represents the image of M_2 when mirrored around the back of BS.

a reference, we see that the optical path length difference will be the distance between M_1 and M_2'. Then, the phase delay will be

$$\epsilon = \frac{2\pi}{\lambda_0}(\overline{M_1, M_2'}) \ ,$$

where $(\overline{A, B})$ indicates the Euclidean distance between A and B. The consequent interference pattern will have a frequency given by ΔL. Therefore, by capturing the interference pattern, we can reconstruct the intensity that originates at a distance of ΔL.

[3] These systems are known as *Time-Domain* OCT systems (TD-OCT), but are rarely used nowadays due to their low speeds caused by having moving parts.

Early OCT systems[3] were based on this same principle. One of the mirrors was replaced by the sample itself in the *sample arm* of the interferometer, while the other was attached to a moving stage in the *reference arm*. The interference plane was fixed on the detector, so the only possible measure of interference was when both arms had the same length. If, for example, one moved the reference mirror so that its optical path matched the surface of the sample, what the OCT capture would be the profilometry of the sample, but by lengthening the reference arm, one could capture the interference pattern coming from *inside* the sample.

Coherence

In reality, there is no perfectly monochromatic light, meaning that interference is not always visible in experiments dedicated to observing the characteristic interference fringe patterns. If the path length of the interferometer is increased enough, the fringes eventually disappear. Born and Wolf provide an intuitive example in section 7.5.8 of their book [3] in terms of *wave trains*. A monochromatic source is not one continuous field but is made up of randomly and continuously produced finite wave trains instead of infinite ones. By the time one wave train enters the interferometer, if the phase delay it induces is greater than its (finite) length, by the time beam 3 reaches point P (see Fig. 4.2), beam 2 is still in the other arm. As a consequence, no interference is observed at P.

The formal definition of this phenomenon is also described in the same section [3] but has been included below for completeness. This definition focuses on evaluating what occurs at point P. Once a wave train reaches P, the measured intensity will change for some period of time T. We will introduce this time-dependent field change, or disturbance, as $F(t)$. By doing so, we can analyze $F(t)$ in terms of its Fourier integral,

$$F(t) = \int_{-\infty}^{\infty} f(\nu) e^{-2\pi i \nu t} d\nu \ ,$$

or, in terms of its Fourier transform $f(\nu)$,

$$f(\nu) = \int_{-\infty}^{\infty} F(t) e^{2\pi i \nu t} dt \ .$$

By observing over some time, a total of N wave trains will have reached the detector, each of them at a time t_n, so the total detected field will be

$$V = \sum_{n=1}^{N} F(t - t_n) \ .$$

The intensity recorded over a period of $2T$ is calculated as the integral of the total field. However, real measurement periods will be much longer than the average duration of each wave train, so integrating over $2T$ is equivalent to doing an infinite integral. As a result, the total intensity is given by [3]

$$I = \frac{1}{2T}\int_{-\infty}^{\infty} |V|^2 dt = \frac{N}{T}\int_{-\infty}^{\infty} |f(\nu)|^2 d\nu \quad . \tag{4.6}$$

To arrive at the interference intensity pattern, we will next consider a disturbance given by train waves of duration Δt, which corresponds to a unique frequency ν_0, so that [3]

$$F(t) = f_0 e^{-2\pi i \nu_0 t} \quad , \text{ if } \quad |t| \leq \frac{\Delta t}{2}$$

and its Fourier transform, which represents the intensity captured at point P (Eq. 4.6), is [3]

$$f(\nu) = f_0 \Delta t \left[\frac{\sin\left(\pi\Delta t(\nu - \nu_0)\right)}{(\pi\Delta t(\nu - \nu_0))}\right] \tag{4.7}$$

The elements between brackets in Eq. 4.7 represent a sinc function, and the associated intensity pattern will have a sinc squared function as a principal element (Eq. 4.6). This function has a maximum value at ν_0 (Fig. 4.7) and then quickly fades out as the frequency moves away from it.

The measured intensity, i.e., the integral of the squared sinc, will essentially correspond to those frequencies around the central ν_0 so that the Fourier spectrum is contained within the frequency range given by [3]

$$\Delta\nu = \nu - \nu_0 \sim \frac{1}{\Delta t} \quad .$$

The frequency range $\Delta\nu$ and the average train wave duration Δt satisfy the inequality $\Delta t \Delta\nu \geq (4\pi)^{-1}$, we can also relate them through the following expression [3]

$$\Delta l = c\Delta t \sim \frac{c}{\Delta\nu}\frac{\lambda_0^2}{\Delta\lambda} \quad . \tag{4.8}$$

In Eq. 4.8, we have included the central wavelength of the source λ_0, which corresponds to the average wavelength of all wave trains the source emits, and also its bandwidth $\Delta\lambda$ as a measurement of the wavelength-spread of the source.

Eq. 4.8 represents the crucial physical magnitudes that OCT systems are based on, namely the *coherence time* Δt and *coherence length* Δl. These magnitudes represent the maximum duration or length, respectively, that the wave trains the source emits. If the delay introduced by the interferometer, ΔL, is greater than the coherence length of the light, Δl, the first part of the wave train will exit the interferometer at least Δt before the other; in other words, they will not coincide in the same place at the same time, so there will be no interference detected.

Additionally, the detected interference pattern will be restricted to a specific region of the Fourier spectrum, meaning its interference will not be infinite, as suggested by Eq. 4.4. Therefore, the coherence length is

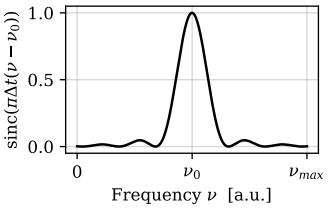

Figure 4.3: Function $\mathrm{sinc}(\pi\Delta t(\nu - \nu_0))$ for $\nu_0 = (\Delta t)^{-1}$.

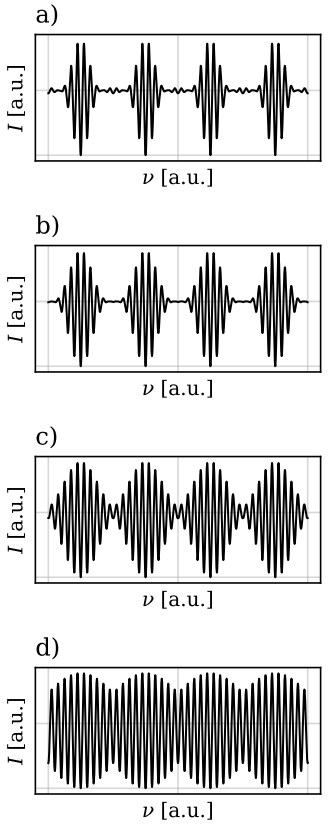

Figure 4.4: (a) Four different intensity patterns corresponding with interference caused by scattering at four points inside the sample. The coherence properties of the waves give the shape of the envelope of each pattern. As the points get closer (b-d), their frequency range gets wider, and the points are no longer independently identifiable.

directly related to the minimum distance (i.e., the resolution) an OCT system will be able to measure. For the OCT to distinguish two points of the sample, A and B, separated by Δz, their distance must be at least Δl. Otherwise, the interference created by reflecting or scattering off A and the one created by reflecting off B will overlap in the detector. This effect is illustrated in Fig. 4.4. In Fig. 4.4 (a), four interference patterns as produced by four different points of the sample (A, B, C, and D) are captured at various regions of the Fourier frequency spectrum, i.e., they reach the detector at different times. Even though the four intensity patterns are different, their envelope is the same since it is regulated by the width of the sinc function related to the coherence properties of the source. If points A, B, C, and D are closer to each other (Fig. 4.4, b-d), there is a minimum distance between points required so that the individual patterns are still discernible. Otherwise, their respective frequency ranges will be larger, so the signals would mix, and the points will no longer be distinguishable in the OCT images.

4.1.2 OCT notation

Before moving on to the description of the OCT we used in this thesis, it is worth briefly introducing the notation used in OCT imaging.

OCT devices generally perform single-point measurements on a sample. Variations in the sample's internal structure along the measurement's direction will yield different reflectance and backscattering responses, creating a specific intensity pattern dictated by the sample's structure. Changes in material (i.e., in refractive index) through the sample will often translate into high recorded intensities corresponding to the boundary between materials, according to the Fresnel coefficients (see Chapter 2).

A single-point measurement will correspond to a one-dimensional intensity curve (I) versus depth values after transforming the frequencies into time and later into depth (z). Such one-dimensional measurements receive the name of *A-scan* ($I(z)$) or axial scan [5]. At the end of the interferometer, a motorized component usually enables the redirection of the source light. This component allows for the combination of adjacent A-scans, providing a two-dimensional image of x- or y-displacement and depth, where the color is provided by the intensity I. This two-dimensional images are named *B-scans* ($I(x, z)$ or $I(y, z)$). Finally, the concatenation of B-scans generates three-dimensional cubes, named *C-scans*, where the data has three spatial dimensions and the values correspond to those of the intensity ($I(x, y, z)$).

Other types of scans include *T-scans*, which are obtained by fixing a depth value, z = constant, to produce $I(x, y)$ data, and *M-scans*, which are obtained by concatenating A-scans obtained over time (t), as if recording a video of A-scans, to produce $I(z, t)$ data.

Although it is not a type of scan since it involves data processing, the maximum intensity projection, or MIP, is often used to compress the z axis in data visualizations. Let $I(x, y, z)$ be the C-scan. Then, the MIP is calculated as the maximum along the $z-$ direction of the data, according to

$$\mathrm{MIP}(x, y) = \max|_z I(x, y, z) \quad . \tag{4.9}$$

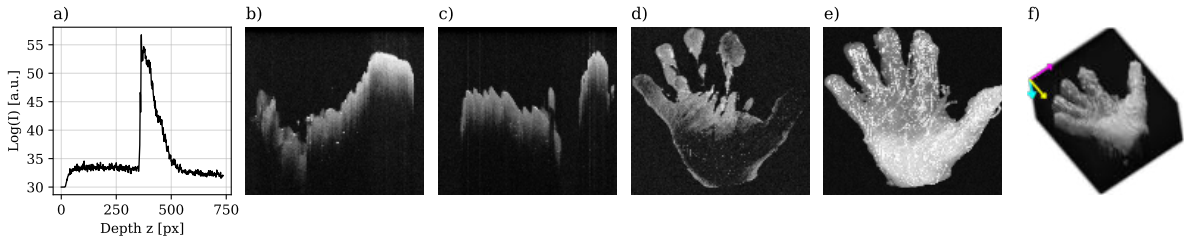

Figure 4.5: Representation of an OCT measurement of a 3D-printed hand. (a) A-scan in the center of the sample. (b) B-scan obtained by fixing y as a constant in the center of the hand. (c) B-scan obtained by fixing x as a constant in the center of the hand, perpendicularly to (b). (d) T-scan obtained by fixing z as a constant in the center of the hand, perpendicularly to (b) and (c). (e) MIP calculated according to Eq. 4.9. (f) C-scan. The yellow arrow is the x axis, the magenta is the y axis, and the cyan is the z axis. The C-scan occupied a volume of $(10 \times 10 \times 3)$ mm^3.

Fig. 4.5 shows the different visualizations mentioned in this section[4]. Note that since the coordinate origin is at the top left corner of the C-scan (Fig. 4.5,f), the A-scans are defined from the top to the bottom of the data cube. As such, the flat region at the beginning of the A-scan corresponds to the air on the top of the sample. When the source reaches the sample's surface, the first refractive index change appears, and a prominent intensity peak is recorded due to Fresnel's reflectance. After this first surface, the light decays exponentially (or linearly when represented logarithmically), indicating a uniform sample interior.

[4] The M-scan is not shown as this is a stationary sample, so $I \neq I(t)$.

4.1.3 Instrumentation

The OCT system used in this thesis is the commercial device TEL221PS (Thorlabs) [6]. This base unit uses a Superluminescent Diode (SLED) with a central wavelength of $\lambda_0 = 1300$nm and a bandwidth of $\Delta\lambda = 135$nm. The resolution along the z direction (Δz) is calculated by considering the minimum width of the Gaussian beam the source outputs. As such, Eq. 4.8 becomes

$$\Delta z = \frac{\Delta l}{n} = \frac{1}{n}\frac{2\ln(2)}{\pi}\frac{\lambda_0^2}{\Delta\lambda} \quad , \tag{4.10}$$

where n is the refractive index of the sample and ln the natural logarithm. In the air ($n = 1$), the optical depth resolution is $\Delta z = 5.5\mu m$, while in water ($n = 1.33$) becomes $\Delta z = 4.2\mu m$.

The maximum penetration depth of this device is

$$d_z = \frac{3.6 \text{ mm}}{n} \quad , \tag{4.11}$$

where, again, the refractive index will influence the maximum penetration. In the air, $d_z = 3.6$ mm, while in water, it becomes $d_z = 2.6$ mm.

The system's speed can be modified to capture between 5.5 kHz and 76 kHz, meaning even at the lowest speeds, this device can capture over 5000 A-scans per second. The high speed comes from the system's configuration. Its capture mode is not based on time-domain OCT, but instead on Spectral-domain OCT (SD-OCT). In this configuration, the detector is a spectrometer, and the A-scan is reconstructed from the Fourier transform of the spectrum, as indicated in previous sections [6].

The source is then coupled to a volume-optics Michelson interferometer (OCTP-1300PS/M, Thorlabs) [7], designed for wavelengths of 1300 or 1325 nm. Our OCT device has three interchangeable lenses that can be attached to the interferometer (OCT-LK2, OCT-LK3, OCT-LK4, Thorlabs) [8–10], but for this book we used the OCT-LK3 lens since it provided a good trade-off between the optical lateral resolution ($\Delta x_o, \Delta y_o$)

$$\Delta x_o, \Delta y_o = 13\ \mu m \quad ,$$

the lateral field of view ($\text{FOV}_{x,y}$)

$$\text{FOV}_{x,y} = 10 \times 10\ \text{mm}^2 \quad , \tag{4.12}$$

and the effective focal length (EFL)

$$\text{EFL} = 36\ \text{mm}. \tag{4.13}$$

Notice that we mentioned the *optical lateral resolution* instead of the *lateral resolution*. The reason is that this OCT system can be configured to digitally increase the number of pixels along the x and y spatial dimensions by moving the galvanometer motor that controls the source's position. Specifically, the *digital lateral resolution* ($\Delta x_d, \Delta y_d$) is given in terms of the maximum lateral field of view in each direction and the pixel number along x or y ($p_{x,y}$), so that

$$\Delta x_d, \Delta y_d = \frac{FOV_{x,y}}{p_{x,y}} = \frac{10\ \text{mm}}{p_{x,y}} \quad .$$

The greater the number of pixels, the higher the digital resolution. However, when $p_{x,y}$ is such that the digital resolution is higher than the optical resolution, $\Delta x_d, \Delta y_d < \Delta x_o, \Delta y_o$, the system will not be obtaining new information, but instead, it will be oversampling the same point while increasing the file size. For this reason, we will keep the system's configuration so that $\Delta x_d, \Delta y_d = \Delta x_o, \Delta y_o = \Delta_x, \Delta y$ or, in other words,

$$\delta x, y = 13\frac{\mu m}{p_{x,y}} \quad . \tag{4.14}$$

Oversampling can be helpful to increase the light captured at each point and improve the signal-to-noise ratio (SNR). However, the complete $10 \times 10 \times 3.6/n$ mm^3 data cubes our system produces, at the optical resolution of $\Delta x, y = 13\ \mu_m/p_{x,y}$ and $\Delta_z = 5\ \mu_m/p_z$, occupy between 2 Gb and 10 Gb each, in terms of the imaging mode selected. The size of the datasets is also something to consider when configuring an OCT measurement.

4.1.4 Optical properties

The principal optical property obtained with conventional OCT imaging is the attenuation or extinction coefficient μ_t, representing the combined effect of the absorption μ_a and scattering μ_s of the sample. As we have

introduced in Eq. 2.92 on Chapter 2,

$$\mu_t = \mu_a + \mu_s \quad .$$

The detected photocurrent on an OCT system, $i^2(x, y, z)$, contains the intensity changes due to the effects of the system, $S(x, y, z)$, and the sample's behavior, $I(x, y, z)$

$$i^2(x, y, z) \propto S(x, y, z) \cdot I(x, y, z) \quad . \tag{4.15}$$

We know that the sample will behave according to the Beer-Lambert law (Eq. 2.89)

$$I(x, y, z) = I_0(x, y)e^{-2\mu_t z} \quad . \tag{4.16}$$

In the context of OCT imaging, $I_0(x, y)$ is the intensity at the sample's surface, i.e., the intensity given by the sample's profilometry. A factor of 2 is introduced in the exponential to account for the double pass the light has in the interferometer. Going first towards the sample and then returning to the detector, the light will be attenuated twice as much as if it had just gone through the sample once.

Following the previous paragraphs, this section will explore multiple ways of obtaining the attenuation coefficient.

Following the Beer-Lambert law

The fastest way to obtain the attenuation of the sample is by taking each A-scan and fitting it to Eq. 4.16 so that

$$i^2(x, y, z) = a(x, y) \cdot I_0(x, y) \cdot e^{-2\mu_t z} \quad .$$

The term $a(x, y)$ is introduced to remove the proportionality from Eq. 4.15. It compensates for any factor that might reduce the intensity and is not due to the sample's attenuation, like specular reflections on its surface.

However, OCT intensity values are high, in the order of 10^9, which might harm optimization methods based on reducing the error through gradient descent. Instead, logarithms are often taken in Eq. 4.16, so that

$$\ln[i^2(x, y, z)] = \ln[I(x, y, z)] = A(x, y) + \ln[I_0(x, y)] - 2\mu_t z \quad . \tag{4.17}$$

The Beer-Lambert law, as described above, has two main limitations in OCT imaging:

1. It is described for homogeneous media.
2. It does not consider the intensity variations along depth caused by the system ($S(z)$).
3. It holds only for the single-scattering region ($\mu_t z \leq 3$) [11].

By following this approach for non-homogeneous media (i.e., samples with layers, holes, heterogeneous composition...), the attenuation coefficient μ_t will not be precisely calculated, and the higher the heterogeneity, the higher the fitting error will be.

Two common ways of characterizing the error are using the mean squared error (MSE) or the root mean squared error[5] (RMSE), defined as follows. Let $\{y_i\}_{i=0,\dots,N}$ be a set of real data points and $\{\hat{y}_i\}_{i=0,\dots,N}$ their theoretical values as derived from a model. Then, the mean squared error (MSE) of the model is

$$\text{MSE} = \sum_{i=0}^{N} (y_i - \hat{y}_i)^2 \quad , \tag{4.18}$$

and its root mean squared error is

$$\text{RMSE} = \sqrt{\text{MSE}} \quad . \tag{4.19}$$

[5] The RMSE is used to compare the model's results with the experimental data since they share the same units.

Although high MSE or RMSE values indicate a poor fitting result, in the case of OCT, they can be used as a measurement of the heterogeneity of the sample. In other words, these magnitudes can determine how uniform the tissue is on the inside, even if its attenuation is not accurately derived.

Adding the point spread function

There are several approaches to consider the effects of the system, $S(z)$, on the Beer-Lambert model. The first one is to consider the change point spread function (PSF) of the system so that the detected photocurrent is

$$i^2(x, y, z) = \text{PSF}(z) \cdot I(x, y, z) \quad .$$

The PSF of the system is a measurement of the maximum diameter of the beam along the z direction or, in other words, of how concentrated the light is. The lower the PSF, the higher the intensity counts measured are. The PSF of a Gaussian beam of the lens is defined as [12]

$$\text{PSF}(z) \coloneqq h(z) = \frac{1}{\left(\frac{z}{z_r}\right)^2 + 1} \quad , \tag{4.20}$$

where z_r is the Rayleigh distance of the beam, defined as

$$z_r = \alpha \frac{2\pi n r_0^2}{\lambda} \quad , \tag{4.21}$$

with $\alpha = 1$ for specular reflections, $\alpha = 2$ for diffuse reflections, and r_0 being the diameter of the spot at the focal distance of the lens.

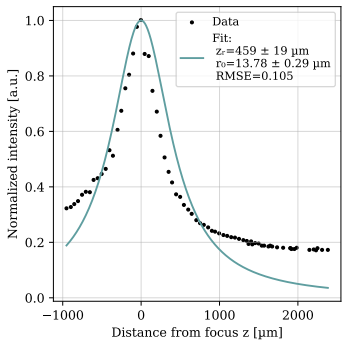

Figure 4.6: PSF of the OCT-LK3 lens. The z_R was obtained by fitting the experimental data to Eq. 4.20, r_0 by calculating it from z_r according to Eq. 4.21, and the RMSE by using its definition (Eq. 4.19).

As indicated by E. Real in his work [13], the PSF can be measured by setting an inclined mirror under the OCT lens with the measurement point being at the focal distance. Then, by adjusting the interferometer length to displace the focal distance, the intensity reflected off the mirror will go down. This procedure was followed to obtain the PSF of the OCT-LK3 lens (Fig. 4.6). $z_r = 456 \pm 19\ \mu m$ was obtained by fitting the experimental data to Eq. 4.20, $r_0 = 13.78 \pm 0.29$ by applying z_R in 4.21, and the root mean squared error (RMSE) by using Eq. 4.19.

Finally, the detected photocurrent considering the PSF is

$$i^2(x,y,z) = \frac{a(x,y)\cdot I_0(z,y)\cdot e^{-2\mu_t z}}{\left(\frac{z}{z_r}\right)^2 + 1} \quad . \tag{4.22}$$

Using a reference material

Although the PSF function is symmetric (Eq. 4.20), the experimental data is not (Fig. 4.6). As the distance from the focus increases, the system receives less intensity. This effect is known as the intensity Roll-Off, which is linked to the digitization errors of the Fourier transform. [13].

One way to consider all of the effects of the source ($S(x,y,z)$) is by introducing a reference sample in the measurement pipeline. This method, described by L. Scolaro *et al.* in their 2012 article [11], is described below for completion.

We have already introduced that the detected photocurrent of any measurement ($i^2(x,y,z)$) is given by the effects of the system ($S(x,y,z)$) and those of the sample ($I(x,y,z)$), so that

$$i^2(x,y,z) \propto S(x,y,z)\cdot I(x,y,z) \quad .$$

Similarly, for a reference sample with magnitudes indicated by the subscript ref, its detected photocurrent will be

$$i^2_{ref}(x,y,z) \propto S(x,y,z)\cdot I_{ref}(x,y,z) \quad .$$

Since the properties of the system are the same for both measurements, it is possible to remove their influence by using the relationship between both samples as

$$\left(\frac{i^2(x,y,z)}{i^2_{ref}(x,y,z)}\right) \propto \left(\frac{I_0(x,y)}{I_{0,ref}(x,y)}\right) e^{-2z(\mu_t-\mu_{t,ref})} \quad ,$$

or, applying logarithms to both sides of the equation,

$$\ln\left[\frac{i^2(x,y,z)}{i^2_{ref}(x,y,z)}\right] = A(x,y) + \ln\left[\frac{I_0(x,y)}{I_{0,ref}(x,y)}\right] - 2z(\mu_t-\mu_{t,ref}) \quad . \tag{4.23}$$

In this thesis, we used the Polybead Microspheres (07307-15) [14]. According to Mie's theory, its reference attenuation coefficient is

$$\mu_{t,ref} = 8.1134\ \text{mm}^{-1} \quad . \tag{4.24}$$

Considering the heterogeneity of the sample

Having prior knowledge of all the inhomogeneities a sample has inside it is a complex task, so there will always be some error in using the conventional Beer-Lambert as a base to obtain the attenuation coefficient. Vermeer *et al.* proposed a depth-resolved method to find the attenuation coefficient throughout the depth of the sample instead of transforming

the whole A-scan into a single attenuation value [15]. By doing so, global inhomogeneities are assumed to be locally homogeneous, so the differences between the sample layers are considered. Their model, which is also derived from Beer-Lambert, is defined as

$$\mu_t(x,y,z) = \frac{1}{2\Delta z} log\left(1 + \frac{I(x,y,z)}{\sum_{i=z+1}^{p_z} I(x,y,i)}\right) \approx \frac{I(x,y,z)}{2\Delta z \sum_{i=z+1}^{p_z} I(x,y,i)} \quad , \tag{4.25}$$

where Δz is the axial resolution and p_z the number of pixels in the z direction.

Although this method is useful to determine local attenuation, the attenuation estimate worsens as the depth increases. This occurs due to the denominator of Eq. 4.25. As i grows, the fewer pixels considered in the denominator lead to an artificial increment of μ_t, and the noise in these last pixels is greater due to the reduced SNR given by the roll-off. To compensate for these factors, Li *et al.* [16] propose a correction of expression 4.25 that considers the noisier last pixels of the data cube. The modified expression is

$$\mu_t(x,y,z) = \frac{I(x,y,z)}{2\Delta z \sum_{i=z+1}^{p_z} I(x,y,i)} \left(1 - \exp\left[-2\Delta z \sum_{i=z+1}^{p_z} \mu_t(x,y,i)\right]\right) \quad . \tag{4.26}$$

Equation 4.26 contains the attenuation coefficient in the exponent as well, but not for the same z value; in other words, the attenuation coefficient at a depth z depends on the coefficients below it. The equation is then solved through backwards recursion. The authors propose starting by taking the last $100\mu m$ of the A-scan first, located after considering the noise-floor level of the OCT data and the surface of the sample, and fit them with the conventional Beer-Lambert model (Eq. 4.17) to use that as the basal attenuation value to obtain $\mu_t(x,y,z)$, starting at $i = p_z$ and ending at $i = 1$.

4.2 Polarization-Sensitive Optical Coherence Tomography (PS-OCT)

Polarization-sensitive optical coherence tomography (PS-OCT) is an extension of OCT that provides it with the additional capability of measuring the polarization state of light backscattered from biological tissues. By producing the interference with polarized light, the PS-OCT system can be used to obtain the phase retardance that the sample induces.

4.2.1 Fundamentals

The Michelson interferometer of the OCT system used in this thesis contains one quarter-wave plate in each of its arms. This allows the user to select a specific polarization state to illuminate the sample. Given that there might not be prior knowledge of the orientation of the optical axes for some samples, the system is configured to illuminate with circularly polarized light with a Stokes vector $\vec{S}_s$ to illuminate all directions evenly.

Then, upon interaction with the sample, the vector is transformed to $\vec{S}$, which, in general, will depict elliptically polarized light. Given the Mueller matrix of the sample, $\vec{M}$, then the system is configured so that

$$\vec{S} = M \cdot \vec{S}_s = \begin{pmatrix} m_{11} & m_{12} & m_{13} & m_{14} \\ m_{21} & m_{22} & m_{23} & m_{24} \\ m_{31} & m_{32} & m_{33} & m_{34} \\ m_{41} & m_{42} & m_{43} & m_{44} \end{pmatrix} \vec{S}_0 \quad .$$

Although other authors have devised Mueller-OCT imaging systems [17–19], the commercial system used in this thesis does not have this functionality since it would require adapting the wave plates to illuminate the sample with enough states $\vec{S}_s$ to solve the 16 parameters in M. Instead, the TEL221PS measures the Stokes parameters of the light backscattered by the sample.

4.2.2 Optical properties

According to the manufacturer's manuals, the TEL221PS can construct the complex reflectances r_0 and r_1 from the Fourier transform of the interference patterns detected in two detectors. The detectors are configured to measure perpendicularly polarized light states. Then, the system reconstructs the Stokes vectors as

$$\begin{aligned} S_0 &= I = r_1 \cdot r_1^* + r_0 \cdot r_0^* \quad , \\ S_1 &= Q = r_1 \cdot r_1^* - r_0 \cdot r_0^* \quad , \\ S_2 &= U = 2\mathcal{R}(r_1 \cdot r_0^*) \quad , \text{ and} \\ S_3 &= V = -2\mathcal{I}(r_1 \cdot r_0^*) \quad . \end{aligned} \tag{4.27}$$

Comparison with Eqs. 3.18 indicates that what the system is measuring is the complex amplitudes of the field in the x and y axes, so that $r_1 \coloneqq E_x$ and $r_0 \coloneqq E_y$.

Since r_0 and r_1 are three-dimensional in PS-OCT, so will be each Stokes parameter. Evaluating their stability along the penetration depth z can serve to explore the changes in anisotropy a sample might have. For example, a layered structure with even layers can have uniform three-dimensional Stokes vectors, while uneven layers would lead to sections with distinct Stokes parameters. Aside from $\vec{S}$ itself, other relevant optical properties can be obtained from Eqs. 4.27, which will be derived in the following sections.

Orientation of the optical axis

Remembering the definition of the Stokes parameters in terms of the polarization ellipse (Eqs. 3.16), S_1 and S_2 can be used to obtain the orientation of the ellipse, i.e., of the optical axis Ψ, as

$$\Psi = \frac{1}{2} \tan^{-1}\left(\frac{S_2}{S_1}\right) \in \left[\frac{-\pi}{2}, \frac{\pi}{2}\right] \quad . \tag{4.28}$$

Many programming languages include the function `atan2(numerator, denominator)` to correctly determine the arctangent by considering the signs of its arguments.

Auxiliary angle α

Remembering the definition of the auxiliary angle from the polarization ellipse (Eq. 3.7), it represents the diagonal of the rectangle described by E_{0x} and E_{0y}. Given the data structure our system captures, the angle can be calculated from the complex reflectances as

$$\alpha = \tan^{-1}\left(\frac{r_0}{r_1}\right) \in \left[0, \frac{\pi}{2}\right] \quad . \tag{4.29}$$

This magnitude represents the proportion of the intensity measured by each detector, i.e., in each polarization state [20].

Degree of polarization uniformity (DOPU)

We have seen before that the Stokes parameters can be used to calculate the degree of polarization of a polarized light state (see Eq. 3.20). However, since OCT is an interferometric technique, only the totally polarized light ($S_0^2 = S_1^2 + S_2^2 + S_3^2$) will create an interference pattern. Since the system illuminates with totally polarized light, the depolarized light fraction will have an interference term that averages to zero

$$J_{12} = 0 \text{ for unpolarized light.}$$

Remembering that the depth information comes from the *phase* of the interference pattern and not from its intensity, the gathered three-dimensional data by the OCT system will represent the fraction of totally polarized light.

This implies that the degree of polarization (DOP) is DOP = 1 for all measurements. The degree of polarization uniformity (DOPU) is often used as an alternative depolarization measurement [19]. It is calculated by finding the local, three-dimensional average of the Stokes parameters,

$$\text{DOPU} = \sqrt{\langle S_1\rangle_k^2 + \langle S_2\rangle_k^2 + \langle S_3\rangle_k^2} \in [0, 1] \quad , \tag{4.30}$$

where $\langle\cdot\rangle_k$ represents the spatial average in a neighborhood defined by a kernel k and the Stokes parameters can be taken as is or normalized with respect to S_0. Then, in regions with high DOPU, the sample can be considered non-depolarizing due to the stability of Stokes vectors. Analogously, in regions with low DOPU, the sample can be considered depolarizing due to the random orientation of the Stokes parameters.

Birefringence

Anisotropic samples tend to have two different refractive indexes, n_1 and n_2, where one affects the light propagating along the anisotropic axis, and the other affects the light propagating perpendicularly to it. The

difference between these two refractive indexes is known as birefringence (Δn)

$$\Delta n = n_1 - n_2 \quad . \tag{4.31}$$

So far, we have only introduced the optical properties of the *polarized light* that can be obtained from PS-OCT measurements. However, the birefringence is a property of the *sample* that can also be obtained with PS-OCT devices, and that is a good indicator of sample anisotropy, given that isotropic samples are non-birefringent ($\Delta n = 0$).

Chin *et al.* introduced a method to calculate the birefringence of samples using PS-OCT imaging. The method, wholly described in their article [21], is included below for completion.

Let $\hat{S}(z) = (S_1/S_0, S_2/S_0, S_3/S_0)^T$ be the depth-dependent[6] Stokes vector measured for a sample. Let $\hat{S}_{ref}$ be the Stokes vectors on the surface of the sample located at $z = 0$ so that $\hat{S}_{ref} = \hat{S}(z = 0)$. The angle between these vectors, $\phi_r(z)$, is given by their dot product as

$$\cos(\phi_r(z)) = \hat{S_{ref}} \cdot \hat{S}(z) \coloneqq C_{in}(z) \quad .$$

This product that will change along depth can be interpreted as an amplitude modulation, $A(z)$, and a phase change in z, $\phi_c(z)$, so that

$$\hat{S_{ref}} \cdot \hat{S}(z) \coloneqq C_{in}(z) = A(z)\cos(\phi_c(z)) \quad .$$

To remove the amplitude modulation and consider only the phase, the quadrature component of $C_{in}(z)$, defined as $C_{quad}(z)$, can be calculated through its Hilbert transform as

$$C_{quad}(z) = \mathrm{H}[C_i n(z)] = A(z)\sin(\phi_c(z)) \quad ,$$

where $\mathrm{H}[\cdot]$ indicates the Hilbert transform. Then, the demodulated phase is the angle between $C_{in}(z)$ and $C_{quad}(z)$, given by

$$\phi_c(z) = \angle|C_{in}(z) + iC_{quad}(z)| \quad .$$

Phase $\phi_c(z)$ will be wrapped, meaning it will oscillate between 0 and 2π. The method requires having the total accumulated phase up to depth z, so instead, the discrete, unwrapped phase $\phi_u(z)$ is calculated as

$$\phi_u(z) = \sum_i = 1^z \phi_c(i) - \phi_c(i-1) \quad . \tag{4.32}$$

The result of Eq. 4.32 will be monotonically increasing by definition. If the sample is uniform, the slope of $\phi_u(z)$, δu, can be calculated to finally derive the birefringence of the sample as

$$\delta n = \frac{n \delta u \lambda_0}{2\pi} \tag{4.33}$$

where n is the bulk refractive index of the sample, δu the slope of $\phi_u(z)$, and λ_0 the central wavelength.

As we will see in the following chapters, this method is advantageous for distinguishing completely isotropic samples from samples with some degree of anisotropy.

[6] Although the Stokes vectors measured with OCT are three-dimensional, this method considers only their depth-behavior. As such, only the parameter (z) is kept on the functions described in this section.

4.3 Hyperspectral imaging (HSI)

Hyperspectral imaging (HSI) originated as a combination of optical spectroscopy and remote sensing. Optical spectroscopy provides the foundation for detecting the unique spectral fingerprints of each material. By analyzing light reflected from or transmitted through a sample in terms of its wavelength response, spectroscopy reveals detailed information about its composition and properties [22]. Conventional optical spectrometers analyze the light that emerges from a single point at a time. Although helpful, in heterogeneous samples such as biological ones, point-wise measurements can be lengthy and sometimes impracticable. One research area where point-wise spectroscopy was not possible was earth observation. As a result, researchers in the field of remote sensing in the early 80s [23, 24] started to use and devise systems that could obtain spectral data in each pixel of an image, which, at the time, were referred to as imaging spectrometers. Nowadays, these imaging spectrometers receive the name of multispectral (MSI, between 4 and 20 wavelengths) or hyperspectral (more than 20 wavelengths) imaging systems.

HSI and MSI devices have been proven useful in the field of biological imaging, too, due to their easily interpretable results and the lack of sample preparation required [25, 26]. Although there are many possible configurations for an HSI device [7], as was mentioned in Chapter 1, here we will focus on the description of the used HSI systems.

[7] We refer to the comprehensive overview of HSI and MSI configurations as described in the Ph.D. thesis by A. Pardo Franco [27], J. A. Guitérrez-Gutiérrez [28], and P. B. García-Allende [29].

4.3.1 Fundamentals

HSI systems capture the light emitted by a source after passing through the sample. The spectral content of the light changes as some wavelengths get absorbed by the sample's different chemical components. Since, typically, HSI devices are illuminated from the same side the light is collected, these devices often work in the reflection configuration. Due to a mixture of reflection and backscattering, the light enters the sample, travels within it for a bit, and returns to the sensor. This phenomenon, known as diffuse reflectance, will be discussed in the following sections.

Diffuse reflectance

When light encounters a medium, part of it will be reflected, according to Fresnel's equations, without ever entering it. This type of reflection, which only contains information about the initial field, is known as *specular* or *mirror-like* reflections, in analogy to what a mirror does to a field. For HSI systems to capture the spectral information of the sample, the light has to enter it. Once it does, it will be scattered and redirected within the sample, but also backward. While the light scatters, some of it will travel along the first few centimeters and, at some point, exit the sample from the top to be captured by the sensor. Since light is emitted to the sample and captured from the same side, this is still considered reflection but receives the name of *diffuse reflectance*. The term *diffuse* refers to the randomization of the optical path within the sample due to scattering.

The fraction of light that will be recovered by the camera (R_d) will be the one that is not absorbed by the sample. Then, the absorption coefficient in terms of the wavelength $\mu_a(\lambda)$ is going to dictate how much light is absorbed in a path length differential δL, according to [30]

$$\mu_a(\lambda) = -\frac{1}{R_d(\lambda)} \frac{\delta R_d(\lambda)}{\delta L(\lambda)} \ ,$$

which can be rewritten as

$$R_d(\lambda) = e^{-\mu_a(\lambda) L(\lambda)} \in [0, 1] \ . \tag{4.34}$$

The different chemical components that absorb the light are known as *chromophores*. Given a concentration of chromophore (in mol·L^{-1} or M), and a molar extinction coefficient $\varepsilon(\lambda)$ in (cm^{-1}·M^{-1}), the total absorption coefficient can also be described in terms of a combination of N chromophores as [30]

$$\mu_a(\lambda) = \ln(10) \sum_{i=1}^{N} C_i \varepsilon_i(\lambda) \ .$$

4.3.2 Instrumentation

Spectroscopic imaging systems can be considered color cameras that capture many more color channels instead of the red-green-blue (RGB) conventional ones. A traditional color camera achieves color by adding RGB wavelength filters on top of each pixel on the sensor according to a Bayer pattern. The HSI cameras used in this work, which have been thoroughly described elsewhere [27, 28, 31], are comprised of three fundamental elements: a lens, a camera, and a spectrograph. Although the lens and the camera are key elements to define the spatial resolution and field-of-view of the system, the core of the HSI device is the spectrograph which decomposes the light captured by the lens after passing through a slit into the corresponding spectra. Each point on the slit will create a spectrum that is recorded in one column of the camera's sensor. Then, a rotating mirror module is situated in front of the lens to perform line-scanning of the sample and capture all its spectral information.

Two systems were used throughout this thesis: one in the visible-near infrared (VISNIR) and another in the short-wave infrared (SWIR) wavelength range. The VISNIR captures the spectrum between 400 and 1000 nm, while the SWIR is restricted from 1000 to 1700 nm. Due to the size of the samples, a macro lens was used in both systems. The spatial resolution for the devices, which have the same lens, is approximately 100 μm/px with the zoom settings selected. The spectral resolution was 3 and 5 nm for the VISNIR and SWIR devices, respectively.

Experimental derivation of the reflectance

Ideally, the samples would be illuminated with a collimated source of perfect white light. Then, the captured spectra will differ from the unity only at those wavelengths being absorbed by the sample. However, experimentally available light sources do not have a flat spectrum, which

means that it is necessary to remove the combined effect of the spectrum of the source and the spectral response of the system, $I_0(\lambda)$, from the one of the sample, $I_s(\lambda)$, so that the diffuse reflectance can be derived as

$$R_d(\lambda) = \frac{I_s(\lambda)}{I_0(\lambda)} \quad .$$

To find $I_0(\lambda)$, a reference sample is used (Spectralon). This sample has known optical properties [32] and an almost perfect, spectrally flat reflectance. Therefore, Spectralon measurements are equivalent to I_0 measurements.

Additionally, if the samples are not in a perfectly dark environment, spurious illumination can enter the sensor and affect the measurements. To remove it, a dark measurement ($I_d(\lambda)$) with the source off can be done to correct the reflectance as

$$R_d(\lambda) = \frac{I_s(\lambda) - I_d(\lambda)}{I_0(\lambda) - I_d(\lambda)} \quad . \tag{4.35}$$

If the detector has some baseline noise, I_{bg}, it can also be removed from the samples as

$$R_d(\lambda) = \frac{I_s(\lambda) - I_{bg}}{I_0(\lambda) - I_{bg}} \quad . \tag{4.36}$$

The baseline noise is implicitly removed in Eq. 4.35 through $I_d(\lambda)$ since it is present in all intensity measurements.

Finally, although discouraged, measuring the light source and the sample at different exposure times is possible to speed up the measurement process. If τ_s is the exposure time of the sample and τ_0 is the exposure time of the light source, the reflectance can be corrected by multiplying it by the factor of τ_s/τ_0. Acquiring images at multiple exposure times and correcting the measured reflectance is one of the most straightforward methods to perform high dynamic range imaging, allowing for well-exposed highlights and shadows [33]. Although, in theory, this factor can account for the difference in R_d, there are sources of detector noise that originate due to an increased photon count, which will be less noticeable in the measurements of the light source due to their shorter exposure time. This could lead to quantification errors that affect the areas of low SNR in the samples.

4.3.3 Optical properties

We have seen that HSI systems can be used to determine the absorption coefficient from the reflectance (Eq. 4.34). If the attenuation coefficients of the individual components of the sample, $\mu_{a,i}$, are known, then the coefficient can be rewritten in terms of the volume fraction of each component X_i,

$$\mu_a(\lambda) = \sum_{i_1}^{N} X_i \mu_{a,i}(\lambda) \quad . \tag{4.37}$$

Then, this can be combined with the expression of the reflectance as

$$R_d(\lambda) = e^{-L(\lambda)\sum_{i_1}^{N} X_i \mu_{a,i}(\lambda)}, \tag{4.38}$$

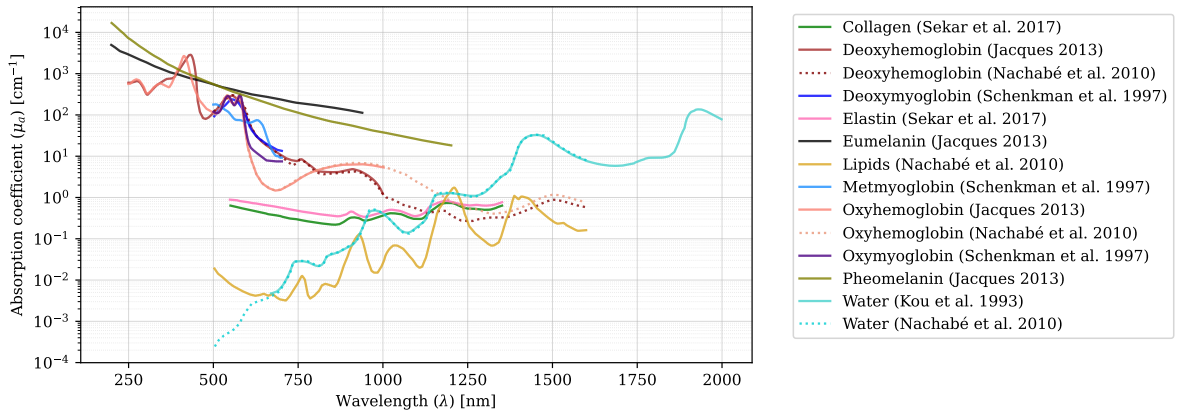

Figure 4.7: Reference attenuation coefficients (μ_a [cm^{-1}]) in terms of the wavelength (λ [nm]) of the most common biological chromophores. The data of Schenkman *et al.* [34], originally depicted in optical density, has been transformed to attenuation by matching the optical path so that the hemoglobin peaks coincide with those of Jacques [30]. Data adapted from [30, 34–38].

which, by taking logarithms, can be rewritten as

$$\mathrm{OD}(\lambda) = -\ln(R_d(\lambda)) = L(\lambda) \sum_{i_1}^{N} X_i \mu_{a,i}(\lambda) \quad . \tag{4.39}$$

Experimental measurements calculated according to Eq. 4.35 or 4.36 can then be fitted to Eq. 4.39 to obtain the volume fraction of each chemical component in the sample. Most times, having the pure spectra of all the chromophores of a sample is not possible due to the complexity of the sample or the lack of spectral libraries, which can be considered in the previous equations by adding wavelength-dependent bias terms. Additionally, the value $-\ln(R_d(\lambda))$ has been renamed to OD, which stands for *optical density*, a parameter often reported in the literature instead of the reflectance.

Reference spectra

This thesis focuses on the analysis of biological samples and, specifically, of muscle tissue. Bulk muscle, as we have discussed before, is comprised of fiber bundles that include collagen and elastin, which get substituted by water (edema) or fat in dystrophic samples. The oxygen reserve of muscles is myoglobin, a molecule very similar to hemoglobin, that stays in the muscle cells themselves. Myoglobin takes the form of oxymyoglobin when carrying oxygen, while deoxymyoglobin is the form it takes once it deposits the oxygen. Muscles also include metmyoglobin, which cannot bind oxygen due to its molecules being already oxidized. All these components, along with the basic biological chromophores, have a distinct spectral fingerprint (Fig. 4.7).

The spectral differences in the absorption coefficients of the chromophores will allow us to find their presence in the samples by considering their spectral shape when fitting them to the optical density (Eq. 4.39).

Influence of scattering

So far, we have only discussed absorption when we know that samples will also scatter light. In the near-infrared or short-wave infrared, the scattering can be dismissed since we have seen before that scattering happens when the wavelength is comparable or in the range of the scatterer size (see Sec. 2.5.3).

In the visible range, however, scattering will have a fingerprint, which should decay as the wavelength increases and its presence is less noticeable. Returning to Fig. 4.7, we see that both eumelanin and pheomelanin, which are two known highly scattering substances [30], follow this pattern.

One of the earliest methods developed to deal with absorption and scattering at the same time was proposed by Kubelka and Munk in 1931 to explore the spectral properties of pigments [39]. This method treats the sample as a semi-infinite medium and makes the assumption explicit by renaming the reflectance as R_∞. Then, the reflectance can be related to the scattering and absorption coefficients as

$$\frac{(1-R_\infty)^2}{2R_\infty} = \frac{\mu_a}{\mu_s'} \quad , \tag{4.40}$$

where the absorption coefficient can be expressed in terms of the component mixture model (Eq. 4.37). This expression uses the reduced scattering coefficient (μ_s') instead of the conventional scattering coefficient (μ_s). Both are related through the anisotropy coefficient g, which indicates that the reduced version of the coefficient accounts for the anisotropic behavior of the scattering pattern according to

$$\mu_s' = \mu_s(1-g) \quad . \tag{4.41}$$

The equation proposed by Kubelka and Munk is in terms of the quotient of the attenuation and scattering coefficients. Similarly, Jacques [40] derived a semi-empirical equation based on Monte Carlo simulations, given by

$$R_d = \exp\left[\frac{-7}{3\left(1+\frac{\mu_s'}{\mu_a}\right)}\right] \quad , \tag{4.42}$$

which also contains a similar term to represent the scattering and absorption contributions.

Krishnaswamy *et al.* introduced the scattered amplitude $A \in [0,1]$ and the scattering power $b \in [0,+\infty)$ to define the detected reflectance when no absorption is present and the only light decay is due to scattering [41]. Then, the diffuse reflectance can be fitted to an exponential law as

$$R_d(\lambda) = A \cdot \lambda^{-b} \quad . \tag{4.43}$$

If the main chromophore is blood, the authors also provide the combination of the scattering influence with the absorption due to the hemoglobin products, as

$$R_d(\lambda) = A \cdot \lambda^{-b} \exp\left[-L \cdot c\left(d \cdot \mu_{HbO2} + (1-d)\mu_{Hb}\right)\right] \quad , \tag{4.44}$$

where L is the optical path length, c is a parameter related to the total blood concentration, d is the fraction of oxyhemoglobin (HbO_2) and $(1-d)$ the fraction of hemoglobin.

Jacques [30] proposes approximating the scattering coefficient by using two empirically derived equations. The simplest one is

$$\mu_s' = a\left(\frac{\lambda}{500(nm)}\right)^{-b} \quad , \tag{4.45}$$

which is similar to the proposal of Krishnaswamy *et al.* with an additional normalization so that the quotient $\lambda/500$ is dimensionless. Although the resulting A and b would not be exactly the same between the two models, both represent the same information, with A containing the units and b the scattering power.

In the same article, Jacques [30] proposes a second model, given by

$$\mu_s' = A\left(f_{Ray}\left(\frac{\lambda}{500}\right)^{-4} + (1-f_{Ray})\left(\frac{\lambda}{500}\right)^{-b}\right) \quad . \tag{4.46}$$

This model considers the different scattering distribution due to Mie and Rayleigh scattering, being f_{Ray} the fraction of light that follows Rayleigh scattering.

The scattering correction can, and should, be applied to regions of the spectrum with high scattering (i.e., visible range) so that the final reflectance is approximated as a combination with the Beer-Lambert reflectance

$$R_d(\lambda) = \mu_s'(\lambda)e^{-L(\lambda)\mu_a(\lambda)} \quad , \tag{4.47}$$

or, in terms of the optical density, as

$$OD(\lambda) = -\ln(R_d(\lambda)) = R_d(\lambda) = -\ln(\mu_s') - L(\lambda)\mu_a(\lambda) \quad . \tag{4.48}$$

4.4 Spatial Frequency Domain Imaging (SFDI)

We have just seen that HSI is an imaging method that will be affected by scattering and absorption simultaneously. OCT is not affected by absorption as much since it measures backscattered light, and the wavelengths in the infrared are typically chosen so that the main tissue chromophores will not absorb them. Nonetheless, neither imaging modality can decouple the effects of scattering and absorption.

Spatial Frequency Domain Imaging (SFDI) was born as the frequency counterpart to diffuse optical spectroscopy to decouple the influence of the scattering and absorption effects of the samples [42]. The method works by illuminating the sample with structured light, specifically by projecting fringe patterns onto the sample. The different frequencies encode information about the reflectance at different depths of the sample, and the higher the frequency, the lower the penetration of the frequency-modulated component of the light source is [43] (Fig. 4.8).

4.4.1 Fundamentals

SFDI is based on probing the Modulation Transfer Function (MTF), i.e., in obtaining the frequency response of the sample. The diffuse reflectance measured will change when the sample is illuminated with fringe patterns of different frequencies. Then, the resulting MTF can be related to the absorption and scattering coefficients of the sample [44].

Diffusion approximation

The diffusion equation dictates how light propagates inside a sample. As such, the diffuse reflectance $R_d(\lambda, f)$ captured at different spatial frequencies κ is derived from the diffusion equation. Although a complete derivation of the diffusion equation is out of the scope of this book[8], here we will summarize the fundamental steps to understand SFDI. The following theory described in this section was obtained from Cuccia *et al.* [43].

[8] We refer to the work of Cuccia *et al.* [43, 44], and of Gioux *et al.* [45]

To begin, it is necessary to introduce some magnitudes that will help to simplify the equations, such as the transport coefficient

$$\mu_{tr} = \mu_a + \mu_s' \quad , \tag{4.49}$$

and the effective coefficient

$$\mu_{eff} = \sqrt{3\mu_a\mu_{tr}} \quad . \tag{4.50}$$

The transport coefficient represents the total light loss as the equivalent to the extinction coefficient μ_t, but considering the reduced scattering coefficient. Finally, the effective coefficient indicates the local absorption and redirection of light in a medium.

The albedo a' must be introduced as well, defined as

$$a' = \frac{\mu_s'}{\mu_{tr}} \quad , \tag{4.51}$$

which represents the fraction of light that is scattered out of the total.

Figure 4.8: Simulation of the maximum penetration depth of the modulated component of light in terms of the spatial frequency. On the left, a high spatial frequency enters up to a depth d_0, while the lower frequency on the right reaches a depth d_1, which is almost twice as deep as d_0. Notice that, below d_1, the sample is the same color, suggesting that the non-modulated component of the light source reaches the same depth inside the sample. Image adapted from [27].

Given a total illumination $q_0(z)$ modulated by two cosines, one in the x direction with frequency $f_x = k_x(2\pi)^{-1}$ and another in the y direction with frequency $f_y = k_y(2\pi)^{-1}$, the modulation is defined as

$$q(x, y, z) = q_0(z)\cos(k_x x + \alpha)\cos(k_y y + \beta) \quad . \tag{4.52}$$

The penetration depth of the modulated light in Eq. 4.52 is given by

$$\delta_{eff}(k_x, k_y)' = \frac{1}{\mu'_{eff}(k_x, k_y)} = \frac{1}{\sqrt{\mu_{eff}^2 + k_x^2 + k_y^2}} \quad , \tag{4.53}$$

where the mark $'$ has been included to indicate the frequency dependence of δ'_{eff} and μ'_{eff}[9].

[9] Note that μ_{eff} and $\delta_{eff} = \mu_{eff}^{-1}$ are exclusively sample-dependent. However, as some light gets absorbed or scattered, the conditions at a specific depth z are different than at the surface of the sample, yielding a modification of μ_{eff} and δ_{eff} due to the modulation.

It can be shown [43] that given a proportionality constant

$$A = \frac{1 - R_{eff}}{2(1 + R_{eff})} \quad , \tag{4.54}$$

with an empirically derived effective reflectance of

$$R_{eff} \approx 0.0636n + 0.668 + \frac{0.710}{n} - \frac{1.440}{n^2} \quad ,$$

the frequency-dependent diffuse reflectance, as calculated from the diffusion approximation, is derived as

$$R_d(\lambda, k_x, k_y) = \frac{3Aa'}{\left(\frac{\mu'_{eff}}{\mu_{tr}} + 1\right)\left(\frac{\mu'_{eff}}{\mu_{tr}} + 3A\right)} \quad . \tag{4.55}$$

The reflectance in Eq. 4.55 changes in terms of the modulation frequency, so, for a set of optical properties, the frequency-dependent R_d represents the diffuse MTF of the sample, which changes as the frequency increases.

This version of the diffuse reflectance is essentially modified by the quotient $\mu'_{eff}\mu_{tr}^{-1}$. As indicated in [43], this magnitude reduces to

$$\frac{\mu'_{eff}}{\mu_{tr}} = \begin{cases} \sqrt{3(1 - a')} & \text{if } k_x = k_y = 0 \\ \frac{k_x + k_y}{\mu_{tr}} & \text{if } k_x, k_y \gg \mu_{eff} \end{cases} \quad .$$

The first case indicates that reflectance will only be modified by the albedo when there is no frequency modulation or when the frequencies are very slowly varying. On the other hand, for the high-frequency range, R_d becomes proportional to μ_{eff}. In this regime, the penetration δ'_{eff} is very low (Eq. 4.53), so most light will not have the time to be absorbed and the reflectance will be originated by the scattering of the sample.

Working outside of the diffusion approximation

The diffusion approximation holds when $\mu'_s \gg \mu_a$ [43]. Outside of this range, alternative methods must be applied to obtain the theoretical diffuse reflectance. One typically used alternative is based on Monte

Carlo simulations. One can obtain the theoretical diffuse reflectance by simulating the random walk of the photons inside a sample governed by an absorption and a scattering coefficient. However, the number of photons necessary on each pixel to simulate a spatially-modulated light source would be very high.

Instead, a point source can be used. Simulating a point source would yield the point spread function (PSF), which is the Fourier transform of the MTF. Let ρ be the distance traveled by the photons, and $R_d(\rho)$ be the Fourier transform of $R_d(k)$, with k being an arbitrary spatial frequency. Let $J_0(kr)$ be the zero-order Bessel function of the first kind. Then, the relationship between $R_d(\rho)$ and $R_d(k)$ is given by

$$R_d(k) = 2\pi \int \rho \cdot J_0(k\rho) \cdot R_d(\rho) d\rho \quad ,$$

or, by binning the distance ρ into N finite intervals Δ_ρ,

$$R_d(k) = 2\pi \sum_{i=1}^{N} \rho_i \cdot J_0(k\rho_i) \cdot R_d(\rho_i) \Delta\rho_i \quad . \tag{4.56}$$

4.4.2 Instrumentation

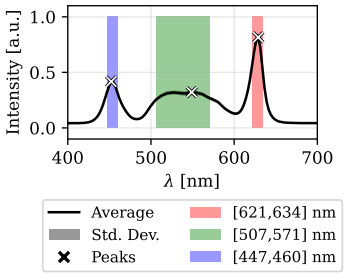

Figure 4.9: Measurement of the projector's illumination spectrum. The three peaks correspond to the central wavelength of each pixel. The dark solid line is the average spectrum, and the dark shaded area is its standard deviation. The color-shaded areas correspond with the spectral regions of interest of high SNR, namely $\lambda_r \in [621, 634]$ nm, $\lambda_g \in [507, 571]$ nm, and $\lambda_b \in [477, 460]$ nm for the red, green, and blue channels.

The SFDI equipment used in this thesis shares the detection path with the HSI-VISNIR system, so the spatial and spectral resolution is the same between both devices.

An angled projector is attached to the device as a light source that can be modulated [27, 28, 46]. However, as most RGB projectors, the areas of the spectrum that are not completely covered by the projector's LEDs have extremely low SNR or no signal at all. The results of SFDI presented in this book are restricted to the areas of higher SNR, by finding the peaks of the projector and selecting the spectral regions that have, at least, 80% of the intensity of the corresponding peak. The resulting ranges are $\lambda_r \in [621, 634]$ nm, $\lambda_g \in [507, 571]$ nm, and $\lambda_b \in [477, 460]$ nm for the red, green, and blue channels, respectively.

Experimental derivation of the modulation transfer function

Similarly to what occurs in HSI, there are several steps involved in one measurement of diffuse reflectance. Our system follows the protocol introduced by Cuccia *et al.* [43], which is included in the following paragraphs for completion.

We configured our system so that the source illumination S is given by a frequency (f_x) modulation on the x direction over a maximum intensity of S_0, according to

$$S(f_x, \alpha_i) = \frac{S_0}{2}[1 + M_0 \cos(2\pi f_x x + \alpha_i)] \quad ,$$

where the phase α_i is also variable.

When the system is configured to measure the diffuse reflectance of a sample, the intensity is modeled as a combination of a constant (I_{DC}) and

an alternating signal (I_{AC}), so that the total captured intensity is given by [43]

$$I = I_{AC} + I_{DC} \quad . \tag{4.57}$$

In the case of $f_x = 0$, the intensity captured by the sensor will be identical to what would be measured with a direct current (DC) light source. When f_x is non-zero, the captured intensity will be modulated by an amplitude envelope M_{AC} and a phase given by the cosine so that [43]

$$I(x, f_x, \alpha_i) = M_{AC}(x, f_x)\cos(2\pi f_x x + \alpha_i) \quad .$$

The aim is to find M_{AC} and M_{DC}, which define the MTF of the sample. It is then necessary to capture measurements that can identify I_{AC} and I_{DC} individually.

The reason to leave α_i as a variable phase is due to the necessity of calculating M_{AC} and M_{DC}, which also helps illuminate the whole sample equally. By changing the phase, the cosine is displaced by a known magnitude, and the parts of the sample that fell in the dark stripes of the pattern for phase α_0 will be illuminated for phase α_1. By setting the phases as $\{\alpha_i\}_{i=1,2,3} = \{0, 2\pi/3, 4\pi/3\}$ rad, the $M_{AC}(x, f_x)$ is calculated as

$$\begin{aligned} M_{AC}(x, f_x) = \frac{\sqrt{2}}{3}\Big[& (I(x, f_x, \alpha_1) - I(x, f_x, \alpha_2))^2 + \\ & (I(x, f_x, \alpha_2) - I(x, f_x, \alpha_3))^2 + \\ & (I(x, f_x, \alpha_3) - I(x, f_x, \alpha_1))^2\Big]^{1/2} \end{aligned} \quad , \tag{4.58}$$

and its DC counterpart as

$$M_{DC}(x) = \frac{1}{3}\Big[I(x, f_x = 0, \alpha_1) + I(x, f_x = 0, \alpha_2) + I(x, f_x = 0, \alpha_3)\Big] \quad . \tag{4.59}$$

In SFDI measurements, as in the other imaging methods, the MTF of the system must be considered since the M_{AC} of the sample will be influenced by it as

$$M_{AC}(x, f_x) = S_0 \cdot MTF_{system}(x, f_x) \cdot R_d(x, f_x) \quad .$$

If we measure a reference phantom of known optical properties, its diffuse reflectance can be predicted from the previously mentioned models, so that its measurement will be

$$M_{AC,ref}(x, f_x) = S_0 \cdot MTF_{system}(x, f_x) \cdot R_{d,ref,pred}(x, f_x) \quad .$$

As before, the experimental diffuse reflectance of the sample, R_d, can be derived by considering the ratio between the two measurements so that

$$R_d(x, f_x) = \frac{M_{AC}(x, f_x)}{M_{AC,ref}(x, f_x)} R_{d,ref,pred}(x, f_x) \quad . \tag{4.60}$$

In this thesis, we used a Spectralon disk of known optical properties and thickness 2.66 ± 0.02 mm [46], which has known absorption and scattering coefficients [32] (Fig. 4.10). Its properties have been taken to derive its $R_{d,ref,pred}(x, f_x)$ by using white Monte Carlo modeling [47, 48]. The result is saved in a lookup table (LUT) to speed up the retrieval of the final R_d [46].

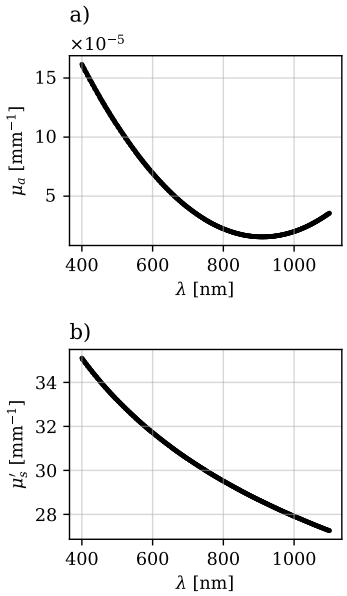

Figure 4.10: Optical properties of Spectralon as derived by Majaron and Žel [32] in terms of the wavelength. (a) Absorption coefficient. (b) Reduced scattering coefficient. The absorption coefficient of Spectralon is 10^5 times less intense than its scattering properties.

Influence of the background

The M_{AC} and M_{DC} are obtained from the intensity measurements of the sample under structured light illumination, $I(x, f_x, \alpha)$. For illumination, we use a white-light projector with RGB LEDs. Usually, this type of projector has a minimum intensity even when the projection is all black. This value, present in all measurements, is also a DC component superimposed on the measurements. As such, this spurious intensity (I_{bg}) can be removed from the calculations by subtracting it from the intensity of the sample ($I_S(x, f_x)$), as in HSI measurements, as

$$I(x, f_x) = I_s(x, f_x) - I_{bg} \quad ,$$

and from the intensity of the reference, as

$$I_{ref}(x, f_x) = I_0(x, f_x) - I_{bg} \quad .$$

Influence of the profilometry of the sample

SFDI obtains the optical properties from spatial modulations of a known frequency. However, even if the known frequency is constant, the closer the measurements are to the source, the higher the frequency will be. Samples often have uneven surfaces that alter the initial modulation in terms of their height. Then, the M_{AC} will modified in function of the height (h) [45].

To obtain the modulation change with height, the Spectralon was set at $k = 9$ known heights (h_k), from 0 to 0.8 cm in 0.1 cm increments[10]. Then, the M_{AC} of the Spectralon was obtained at the different heights, $M_{AC,ref,k}$, as a function of $h_{k,ref}$, so that [45]

$$M_{AC,ref,k} = f(h_{k,ref}) \quad . \tag{4.61}$$

This procedure served as a calibration for *how* the pattern is modified at different heights when captured on Spectralon. Once this behavior is known, the next step involves obtaining the profilometry of the sample and combining it with $M_{AC,ref,k}$. By doing so, we will be *simulating* how the Spectralon pattern would change if it had the exact profile of the sample.

To obtain the profile of the sample, we applied phase-shifting profilometry (PSP), which derives the surface by considering the change in frequency of one of the (f_x, α_i) pairs when the sample deforms it [49]. Then, given the height profile of the sample h_s, and the PSP-derived profilometry function $f(h_s)$, the corrected M_{AC} of the reference that contains the height of the sample, $M_{AC,ref,corrected}$, is derived by interpolating the function $f(h_S)$ to the points of $f(h_{k,ref})$. For that, the measurements

[10] It is worth noting that the surfaces of the samples explored in this thesis did not have more than a couple of millimeters of variation. If the sample had varied more, it would have been necessary to increment the maximum height of the Spectralon calibration.

performed to obtain $f(h_{k,ref})$ must at least contain the $h_{min} = 0$ and $h_{max} = h_{max,sample}$ to avoid extrapolating.

Finally, the diffuse reflectance of the sample with all the corrections is obtained as

$$R_d(x, f_x) = \frac{M_{AC}(x, f_x)}{M_{AC,ref,corrected}(x, f_x)} R_{d,ref,pred}(x, f_s) \tag{4.62}$$

4.4.3 Optical properties

The first way to obtain the optical properties in SFDI is by applying the diffusion approximation (Eq. 4.55) to the experimental reflectance, to obtain the attenuation μ_a and reduced scattering coefficient μ_s', following a similar pipeline to HSI imaging.

If the diffusion approximation does not hold, one can perform simulations. By doing Monte Carlo simulation for a set of attenuation coefficients, $\{\mu_a\}_{i=1,...,N}$ and a set of reduced scattering coefficients $\{\mu_s'\}_{i=1,...,M}$, one can obtain the corresponding reflectances $R_d(\rho)$ that can be transformed to $R_d(k)$. Then, by comparison of the experimental $R_d(k)$ with the values obtained from the simulations, one can infer the attenuation and scattering of the sample.

To extract the volume fractions of the individual chromophores, one can then fit the attenuation to Eq. 4.37.

Regardless of the method of choice, SFDI is the only technique of the ones explored in this book that is able to identify the contributions of absorption and scattering individually.

At this point, it is worth remembering that all magnitudes obtained SFDI are wavelength-dependent as well, and can be fully quantified since the system used here is embedded in the HSI device.

4.5 Mueller Matrix Imaging (MMI)

Mueller Matrix Imaging (MMI) is a powerful optical technique that provides a characterization of the polarization properties of a sample. MMI measures the response of a sample by capturing its Mueller matrix M, which describes how the sample alters the polarization state of light through effects like birefringence, diattenuation, and depolarization. MMI is complementary to techniques like PS-OCT, which focuses on measuring the polarization state of the backscattered light.

To understand MMI, the following sections focus on the fundamental principles behind the technique, understanding the instrumentation involved in acquiring Mueller matrices, extracting meaningful optical properties from these matrices, and ensuring accurate measurements through proper calibration procedures.

4.5.1 Fundamentals

As introduced before, MMI is used to obtain the wavelength-dependent Mueller matrix of the sample, $M(\lambda)$. This is achieved by illuminating the sample with a collection of at least four controlled polarized light states $\vec{S}_{in}$ and measuring the resulting Stokes vectors after interaction with the sample, $\vec{S}_{out}$, according with Eq. 3.22.

An MMI system contains two essential parts: the polarization state generator (PSG) and the polarization state analyzer (PSA). The polarization state generator corresponds to every optical element that is situated *before* the sample (i.e., polarizers, waveplates, light sources...), and the polarization state analyzer corresponds to all components situated *after* the sample (in our case, the slider-mounted waveplate and polarized-sensor camera).

The collection of four polarized light states can be written in a matrix, denoted the Polarization State Generator matrix,

$$M_G = \left(\vec{S}_{in,1} \quad \vec{S}_{in,2} \quad \vec{S}_{in,3} \quad \vec{S}_{in,4}\right) = \\ = \begin{pmatrix} S_{in,0,1} & S_{in,0,2} & S_{in,0,3} & S_{in,0,4} \\ S_{in,1,1} & S_{in,1,2} & S_{in,1,3} & S_{in,1,4} \\ S_{in,2,1} & S_{in,2,2} & S_{in,2,3} & S_{in,2,4} \\ S_{in,3,1} & S_{in,3,2} & S_{in,3,3} & S_{in,3,4} \end{pmatrix} . \tag{4.63}$$

In the most straightforward configurations, the PSG matrix contains only $n = 4$ states. However, an arbitrary number of illumination states can be used, making matrix M_G have a $4 \times n$ shape.

The corresponding measured states are recorded and modified by the rest of the optical path according to the matrix of the Polarization State Analyzer given by

$$M_A = \begin{pmatrix} \vec{S}_{out,1} \\ \vec{S}_{out,2} \\ \vec{S}_{out,3} \\ \vec{S}_{out,4} \end{pmatrix} = \begin{pmatrix} S_{out,0,1} & S_{out,1,1} & S_{out,2,1} & S_{out,3,1} \\ S_{out,0,2} & S_{out,1,2} & S_{out,2,2} & S_{out,3,2} \\ S_{out,0,3} & S_{out,1,3} & S_{out,2,3} & S_{out,3,3} \\ S_{out,0,4} & S_{out,1,4} & S_{out,2,4} & S_{out,3,4} \end{pmatrix} . \tag{4.64}$$

As before, the simplest PSA matrix has $m = 4$ states and a shape of $m \times 4$, but $m > 4$ is possible if more states are detected.

Given a real Mueller matrix of a sample $M(\lambda)$ and the corresponding measured matrix $\hat{M}(\lambda)$, the relationship between them is given by

$$\hat{M}(\lambda) = M_A(\lambda) M(\lambda) M_G(\lambda) \ , \tag{4.65}$$

which is the MMI equation that describes how the polarization properties of the system affect the measurements.

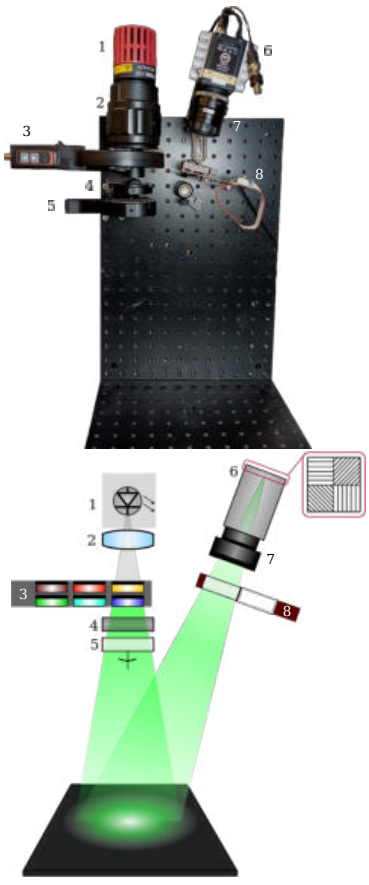

Figure 4.11: Photograph and schematics of MMI v1.0. (1) LED light source, (2) LED collimator, (3) filter wheel, (4) linear polarizer, (5) rotating mount with $\lambda/4$ retarding film, (6) polarization camera, (7) lens, and (8) sliding filter mount with $\lambda/4$ retarding film. The oblique detection angle is approximately 7 degrees. Figure reproduced from [50].

4.5.2 Instrumentation

The multispectral MMI systems employed in this thesis, designed and constructed as part of this doctoral work, were configured for reflection-based measurements as inspired by common MMI architectures [51, 52].

A detailed description of the first version of the system can be found in Mieites *et al.* [50], and it is reproduced here for completeness.

MMI v1.0

In the first version of the system (Fig. 4.11), a white light LED served as the illumination source, with its spectral output restricted to the 450-680 nm range by using a rotating filter wheel equipped with six color filters (Tab. 4.1).

The polarization state generation was built from a linear polarizer and an achromatic quarter-wave plate within a motorized rotation mount (PRM1/MZ8, Thorlabs). A polarimetric camera (PolarCam snapshot micropolarizer camera, 4D Technology) paired with a wide-field lens (NMV50M1, Navitar) was used for the polarization state analyzer. This camera features an integrated array of micropolarizers oriented at four different angles, allowing for the simultaneous capture of all linear polarization components. To allow for the measurement of phase information, an additional achromatic quarter-wave retarding film was incorporated into a sliding filter mount (ELL6K, Thorlabs), which was inserted at specific points in the measurement procedure. The spectral response of the PSA is represented in Fig. 4.12.

The system contained a platform that allowed the sample to be raised to perform measurements at a maximum working distance of 46 cm and a minimum of 36 cm. The corresponding FoV ranged between 8×7 cm^2 and 6×5 cm^2, with a minimum lateral resolution of $\approx 120\ \mu m/px$ and a maximum of $\approx 90\ \mu m/px$, respectively[11].

Name	λ_0 nm	$\Delta\lambda$ [nm]
Blue	450	40
Cyan	500	40
Green	550	40
Yellow	590	10
Red	650	40
Far red	680	10

Table 4.1: Central wavelength (λ_0) and full-width half-maximum ($\Delta\lambda$) of the filters included in the wheel of MMI v1.0.

[11] The measurements realized with MMI v1.0 presented in this document were performed at 46 cm with $\approx 120\ \mu m/px$ lateral resolution.

MMI v2.0

The second version of the system was built to provide incremental upgrades over v1.0. The first change was the substitution of the filter wheel and white LED source by a multi-LED light source (Niji, Bluebox Optics). This change provided better coverage of the whole spectrum, now between 390 and 780 nm, higher illumination power since the output is not getting filtered, and better robustness due to eliminating one moving part. The camera in v2.0 was changed to a different polarimetric camera (PolarSens, Sony) due to availability. The corresponding spectral characteristics of MMI v2.0 are represented in Fig. 4.13, and the spectral information of the individual LEDs of the source in Tab. 4.2.

Since the new LED source adapts to a 5 mm liquid light guide, a diffuser was introduced at the end of the light guide and before the first polarizer to randomize the polarization introduced by the positioning of the fiber.

Additionally, the fixed horizontal linear polarizer incorporated in v1.0 was substituted by a polarizer on another rotating mount, allowing for an extra degree of freedom on the polarization state generator.

Finally, all linear polarizers were substituted by the WP25M-VIS (Thorlabs, rated between 420-700 nm, extinction ratio > 1:800) for their better extinction ratio and broader spectral coverage, and all the waveplates were substituted by the achromatic $\lambda/4$ waveplate AQWP10M-580 (Thorlabs,

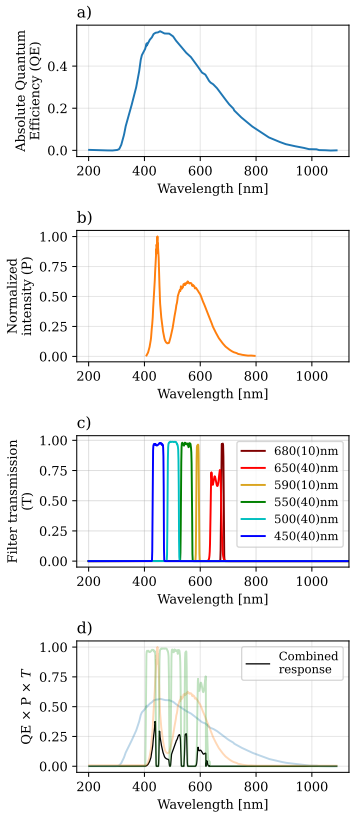

Figure 4.12: Spectral response of the PSG of MMI v2.0. (a) Quantum efficiency of the PolarCam camera. (b) Spectral emission of the LED source. (c) Bandpass transmission of the filters. (d) Combined PSG response. The data represented in this figure was obtained from the manuals of the manufacturers of the camera (4D Technology), the light source (Thorlabs), and the filters (Thorlabs).

Name	λ_0 nm	$\Delta\lambda$ [nm]
UV	393	15
Royal Blue	446	23
Blue	471	21
Cyan	501	30
Green	546	71
Red	636	20
Far red	731	40

Table 4.2: Central wavelength (λ_0) and full-width half-maximum ($\Delta\lambda$) of the LEDs included in the source of MMI v2.0.

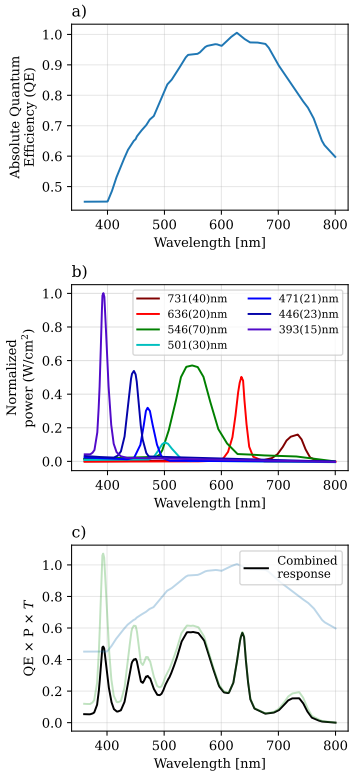

Figure 4.13: Spectral response of the PSG of MMI v1.0. (a) Spectral sensitivity of the PolarSens camera. (b) Spectral emission of the LED source. (c) Combined PSG response. The data represented in this figure was obtained from the manuals of the manufacturers of the camera (Sony) and the light source (Bluebox Optics).

rated between 350-850 nm, average reflectance <1.0%) to unify all the retarding elements of the system.

4.5.3 Calibration

In the context of MMI, calibration involves deriving the mathematical expressions of the matrices of the PSA, M_A, and of the PSG, M_G, so that the actual Mueller matrix of the sample, M, can be derived from an experimental measurement, $\hat{M}$ (see Eq. 4.65). To calibrate the devices mentioned before, we applied the Eigenvalue Calibration Method (ECM), described by Compain *et al.* [53]. This method is based on doing sequential measurements of known polarizing samples (i.e., polarizers and waveplates) to compare their experimental matrices $\hat{M}$ with their theoretical ones, M. Since the MMI v1.0 and v2.0 are wavelength-tunable, a separate calibration was performed for each central wavelength of each system. The method is valid for transmission and reflection systems. The article provides a complete derivation of the solution and choice of calibration samples, but the essential steps for completion are included below.

Solution of the system

In their article, Compain *et al.* use uppercase letters to refer to theoretical matrices and lowercase letters to refer to their experimental equivalent [53]. Then, the ECM can be described as follows.

Let m_A and m_G be the experimental matrices of the PSA and PSG, respectively. Let $\mathbb{H}_M$ be a mapping from the set of 4×4 real matrices $\mathbb{M}_4(\mathbb{R})$ ito itself. Let M be a theoretical Mueller matrix from a calibration sample corresponding to a real matrix measurement m. Let X be an arbitrary theoretical matrix in the set of $\mathbb{M}_4(\mathbb{R})$. Then, the mapping $\mathbb{H}_M$ acting over X is defined as [53]

$$\begin{aligned}\mathbb{H}_M : \mathbb{M}_4(\mathbb{R}) &\longrightarrow \mathbb{M}_4(\mathbb{R}) \\ X &\longrightarrow MX - X(m_A m_G)^{-1}(m_A m m_G) \quad .\end{aligned} \tag{4.66}$$

Then, for a well-defined set of calibration matrices M, M_G is found as the solution to the set of equations given by

$$MX - X(m_A m_G)^{-1}(m_A m m_G) = 0 \quad . \tag{4.67}$$

To solve Eq. 4.67, it is useful to find a basis of $\mathbb{M}_4(\mathbb{R})$ to transform Eq. 4.67 into a vector equation. Let $\{g_i\}_{i=1,\dots,16} \in \mathbb{M}_4(\mathbb{R})$ be a basis of 16 real-valued 4×4 matrices. On this basis, a matrix X is transformed into a 16-element vector $\vec{X} = (x_1, \dots, x_{16})$ by

$$X = \sum_{i=1}^{16} x_i g_i \quad ,$$

and the mapping $\mathbb{H}_M$ is represented by a 16×16 matrix, H_M, so that solving Eq. 4.67 is equivalent to solving equation

$$H_M \vec{X} = 0 \quad . \tag{4.68}$$

For a set of calibration samples with matrices $\{M_i\}_{i=1,...,C}$, there will be a different mapping $\mathbb{H}_{M,i}$ for each M_i. Consequently, there will be a different vectorized mapping $H_{M,i}$ for each M_i. Then, Eq. 4.68 can be solved by solving

$$K\vec{X} = 0 \quad , \tag{4.69}$$

$$K = \begin{pmatrix} H_{M,1} & \dots & H_{M,C} \end{pmatrix} \begin{pmatrix} H_{M,1} \\ \dots \\ H_{M,C} \end{pmatrix} = H_{M,1}^T H_{M,1} + \dots + H_{M,C}^T H_{M,C} \quad . \tag{4.70}$$

The solution to the calibration problem lies in the form of K in Eq. 4.70. Due to the original definition of the mapping $\mathbb{H}_M$, the solution of Eq. 4.69 is the vectorized form of the generator matrix, $\vec{m_G}$, which can be found as the eigenvector corresponding to the smallest eigenvalue of K [53].

Calibration samples

The mapping $\mathbb{H}_M$ (Eq. 4.66) has two distinct elements. The first one, MX, is the product of a *theoretical* matrix of a calibration sample, M, by an arbitrary theoretical matrix, X. The second element, $X(m_A m_G)^{-1}(m_A m m_G)$, considers two additional products. The product $(m_A m_G)$ contains the multiplication of the experimental matrices of the generator and the analyzer. If we compare it with Eq. 4.65, we see that this product corresponds with one capture of the system without any sample in it, i.e., with one measurement of air.

$$\hat{M}_{AIR} = m_A I m_G = m_A m_G \quad ,$$

where we have substituted the theoretical matrices for the analyzer and the generator, M_A and M_G, for their experimentally derived counterparts. The second product of interest is $(m_A m m_G)$, which corresponds to the experimental measurement of the calibration sample of the theoretical matrix M.

We can define the set of matrices $\{C_i\}_{i=1,...,C}$ as

$$C_i = M_{AIR}^{-1}(m_A m_i m_G) \quad , \tag{4.71}$$

so that the mapping $\mathbb{H}_M$ for each calibration sample i is rewritten as

$$\begin{aligned} \mathbb{H}_{M,i} : \mathbb{M}_4(\mathbb{R}) &\longrightarrow \mathbb{M}_4(\mathbb{R}) \\ X &\longrightarrow M_i X - X C_i \quad . \end{aligned}$$

Although defining C_i is not a requirement to solve the eigenvalue calibration method, it will be helpful to determine its step-by-step implementation.

The ECM can be performed with as few as two calibration samples if we consider a measurement of air as one of the two. Solving it with more samples is also possible, which increases the precision of the derived calibration [53]. Here, we used four calibration samples:

1. Air: Corresponding theoretical matrix $M_{AIR} = I$.
2. Horizontal linear polarizer: Corresponding theoretical matrix M_{HLP} (Eq. 3.32), with a maximum transmittance p_{HLP}, and a diattenuation γ_{HLP} with respect to the x axis of the system.

3. Vertical linear polarizer: Corresponding theoretical matrix M_{VLP} (Eq. 3.32), with a maximum transmittance p_{VLP}, and a diattenuation γ_{VLP} with respect to the x axis of the system.
4. Quarter wave plate aligned at 30° with respect to the x axis: Corresponding theoretical matrix M_{QWP} (obtained from the product of a diattenuator Eq. 3.32 and a retarder 3.35), with a maximum transmittance p_{QWP}, retardance ϕ_{QWP}, diattenuation γ_{QWP}.

Even as calibration samples, the chosen ones are not *ideal* samples, so their transmittance, diattenuation, and retardance must be taken into account for the construction of their theoretical matrices. Nonetheless, all those values can be obtained from their experimental measurements, particularly from the eigenvalues of their C_i matrix equivalent. Let $\{\eta_i\}_{i=1,\dots,4}$ be the (real or complex) eigenvalues of C_i, that are sorted in an ascending manner ($\eta_1 < \eta_2 < \eta_3 < \eta_4$), first by their magnitude and then by their complex part, so that all real eigenvalues are first. Then, the properties of the non-ideal calibration samples can be obtained as follows [53].

Case 1: the calibration sample is a horizontal linear polarizer Here, the four eigenvalues are real. The diattenuation angle γ, which indicates the orientation of the polarizer with respect to the horizontal axis, is calculated as

$$\gamma_{HLP} = \frac{\pi}{2} - \arctan\left(\frac{\eta_4}{\eta_1}\right) \quad ,$$

and the transmittance as

$$p_{HLP} = \frac{2\eta_4}{1 + \cos(2\gamma_{HLP})} \quad .$$

Case 2: the calibration sample is a vertical linear polarizer Here, the four eigenvalues are real as well. The diattenuation angle γ, is calculated as

$$\gamma_{VLP} = \arctan\left(\frac{\eta_4}{\eta_1}\right) \quad ,$$

and the transmittance as

$$p_{VLP} = \frac{2\eta_4}{1 + \cos(2\gamma_{VLP})} \quad .$$

Notice that there is a rotation in γ between the horizontal and vertical polarizers.

Case 3: the calibration sample is a rotated quarter wave plate Here, the corresponding C matrix, C_{QWP}, contains two real and two complex eigenvalues. Its theoretical matrix, M_{QWP}, is constructed as if the sample was not rotated since its rotation is introduced later. If the two complex eigenvalues are $\eta_2 < \eta_3$[12], then the retardance is obtained as the angle between them

$$\phi = \angle(\eta_3, \eta_2) \quad . \tag{4.72}$$

[12] At this point, it is convenient to check that the corresponding retardance angle is positive. Otherwise, the eigenvalues are most likely flipped.

The diattenuation the waveplate might have is calculated from the two real eigenvalues, $\eta_1 < \eta_4$, as

$$\gamma_{QWP} = \arctan\left(\sqrt{\frac{\eta_4}{\eta_1}}\right) \quad ,$$

and its transmittance as

$$p_{QWP} = \frac{2\lambda 1}{1 + \cos(2\gamma_{QWP})} \quad .$$

ECM implementation

To experimentally implement the ECM, the following steps were followed:

1. Measurement of the calibration samples with theoretical matrices $M_{AIR} = m_A m_G$, M_{HLP}, M_{VLP}, M_{QWP} and experimental matrices $m_{AIR} = M_{AIR}$, m_{HLP}, m_{VLP}, m_{QWP}.
2. Calculation of the inverse of the air measurement, M_{AIR}^{-1}.
3. Construction of the C_i matrices (Eq. 4.71) for each calibration sample.
4. Construction of the theoretical matrix for the polarizers and the waveplates (M_{HLP}, M_{VLP}, M_{QWP}) by considering their transmittance, diattenuation, and retardance as indicated in the previous section.
5. Rotation of the M_{QWP} by using a rotation matrix at angle θ, $M_{Rot}(\theta)$ (Eq. 3.38).
6. Construction of the vectorized mapping $H_{M,i}$, for each calibration matrix i, using the Kroenecker product ($\otimes$), the 4×4 identity matrix, and the conjugate transpose ($\dagger$), as

$$H_{M,i} = I \otimes M_i - C_i^{\dagger} \otimes I \quad .$$

7. Construction of matrix K (Eq. 4.70) with the three mappings. Note that, at this point, $K \equiv K(\theta)$.
8. Find m_G by calculating all eigenvalues and eigenvectors of K for all possible values of θ. The actual m_G will be the eigenvector corresponding to the smallest eigenvalue of K, which will appear when the angle θ coincides with the real orientation of the quarter wave plate, which in this book was set to 30°.
9. Find m_A by using the air measurement, $m_A = M_{AIR} m_G^{-1}$.

4.5.4 Calibration error estimation

In the previous sections, we have indistinctly used the real matrices of the generator and the analyzer, m_G and m_A, and their theoretical matrices, M_G and M_A. If the matrices were exactly the same, and there were no experimental uncertainties, the smallest eigenvalue of K (Eq. 4.70), which we use to solve for m_G, will be zero. Since experimental uncertainties exist, the ECM provides an easy way to estimate the calibration error by looking at how far from zero the smallest eigenvalue of K is [53]. If λ_{16}

is the smallest eigenvalue, and λ_{15} the second smallest eigenvalue of K, then the calibration error can be estimated as

$$\epsilon_{ECM} = \frac{\lambda_{16}}{\lambda_{15}} \ll 1 \quad . \tag{4.73}$$

4.5.5 Effect of a non-square PSA

By having a polarimetric camera with four distinct linear polarizers on its sensor and a two-position slider (one position containing a quarter wave plate and the other position being left empty), the total number of states in the PSA matrix is eight, leading to an 8×4 matrix. By selecting only four states for the polarization state generator so that its matrix M_G is 4×4, all the previous derivations are independent of the dimensions of M_A and the Moore-Penrose pseudo-inverse can be used on the air measurements to obtain matrices C_i[13].

The ECM can be extended to work with non-square PSA and PSG matrices, as proposed by Rosales *et al.* [55]. Although worth mentioning, this method, along with other calibration methods, will not be discussed here as they were not used in this work.

4.5.6 System conditioning

Characterizing the theoretical PSG and PSA matrices is helpful in understanding the performance of the constructed MMI system. Specifically, the states of the PSG and the PSA must be chosen so that the matrices are as far from singular matrices as possible since singular matrices are non-invertible. The condition number of a matrix indicates how sensitive it is to perturbations. For example, some measurement conditions with an MMI system can yield noisier measurements, which might give similar, but slightly different, PSA and PSG matrices than with varying conditions of measurement. The theoretical matrices of the PSA and, especially, of the PSG must be such that their condition number is low so that their experimental measurements are less affected by noise. This number, obtained as the quotient between the largest and smallest singular values of a matrix, is a measurement of how evenly spaced the vectors in the matrix are; the more independent from each other, the smaller the condition number.

For the PSG matrix, M_G, its ideal condition number (CN) that minimizes the influence of noise [56] is $\sqrt{3}$. In the case of MMI v1.0, a condition number so low was not achievable due to the PSG having only one degree of freedom: the orientation angle (θ) of the rotating wave plate. In that case the optimal PSG, chosen with the lowest CN possible, is [57]

$$M_G = \begin{pmatrix} M_{HLP}M_{QWP}(\theta = -45°) \\ M_{HLP}M_{QWP}(\theta = 0°) \\ M_{HLP}M_{QWP}(\theta = 30°) \\ M_{HLP}M_{QWP}(\theta = 60°) \end{pmatrix}^T = \begin{pmatrix} 1.00 & 1.00 & 1.00 & 1.00 \\ 0.00 & 1.00 & 0.25 & 0.25 \\ 0.00 & 0.00 & 0.43 & 0.43 \\ -1.00 & 0.00 & 0.87 & 0.87 \end{pmatrix} ,$$

yielding a conditioning number of $CN = 3.63$. The Stokes vectors generated by MMI v1.0 according to the previous PSG matrix are represented in Fig. 4.14.

[13] This derivation was recently demonstrated by Montes-Gonzalez et al. in a study that, at the time of writing this thesis, has been accepted for publication and is awaiting public availability [54].

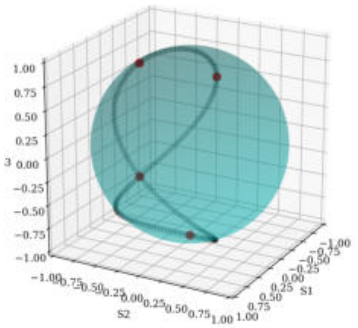

Figure 4.14: Possible polarization states (grey) and generated polarization states (red) by MMI v1.0. $CN = 3.63$.

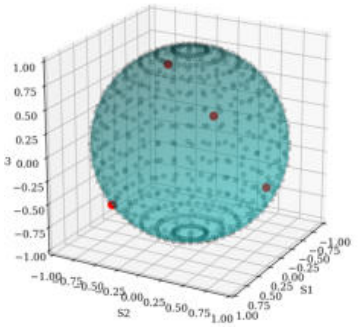

Figure 4.15: Possible polarization states (grey) and generated polarization states (red) by MMI v2.0. $CN = \sqrt{3} \approx 1.73$.

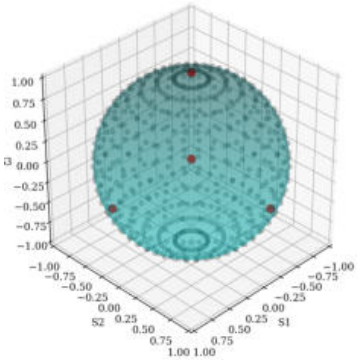

Figure 4.16: Front view of the states generated in MMI v2.0.

The MMI v2.0 has an additional degree of freedom: the orientation angle θ' of the linear polarizer. This system is a complete polarimeter, meaning it can generate any polarization state. Its optimal matrix is given by [56]

$$M_G = \begin{pmatrix} M_{HLP}(\theta = -85.13°)M_{QWP}(\theta = -67.5°) \\ M_{HLP}(\theta = -4.87°)M_{QWP}(\theta = -22.5°) \\ M_{HLP}(\theta = 4.87°)M_{QWP}(\theta = 22.5°) \\ M_{HLP}(\theta = 85.13°)M_{QWP}(\theta = 67.5°) \end{pmatrix}^T =$$

$$\begin{pmatrix} 1 & 1 & 1 & 1 \\ 1/\sqrt{3} & -1/\sqrt{3} & -1/\sqrt{3} & 1/\sqrt{3} \\ 1/\sqrt{3} & 1/\sqrt{3} & -1/\sqrt{3} & -1/\sqrt{3} \\ 1/\sqrt{3} & -1/\sqrt{3} & 1/\sqrt{3} & -1/\sqrt{3} \end{pmatrix},$$

which provides the ideal condition number of $CN = \sqrt{3} \approx 1.73$. The states generated by the system, represented in Figs. 4.15, 4.16, and 4.17 form a regular tetrahedron on Poincaré's sphere, which is the volume that can be constructed with four states that maximize its intersection with the sphere.

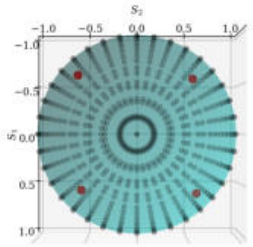

Figure 4.17: Top-down view of the states generated in MMI v2.0.

4.5.7 Optical properties

The multispectral MMI systems derived for this thesis are able to obtain the wavelength-dependent Mueller matrix of the samples, $M(\lambda)$. Once the system is calibrated for each wavelength and the matrices are derived, any decomposition method (see Sec. 3.5) can be applied to link the properties of the matrices with the polarimetric properties of the samples, i.e., to their diattenuation, retardance, or depolarization. The decomposition method applied will be specified for each sample throughout this document.

References

[1] D. Huang et al.: "Optical Coherence Tomography", *Science* **254**(5035), 1178–1181 (1991). DOI: 10.1126/science.1957169.

[2] J. G. Fujimoto et al.: "Optical Coherence Tomography: An Emerging Technology for Biomedical Imaging and Optical Biopsy", *Neoplasia* **2**(1-2), 9–25 (2000). DOI: 10.1038/sj.neo.7900071.

[3] M. Born and E. Wolf: "Principles of Optics", Cambridge University Press, 2019. ISBN: 9781108477437.

[4] A. A. Michelson: "The relative motion of the Earth and of the luminiferous ether", *American Journal of Science* **s3-22**(128), 120–129 (1881). DOI: 10.2475/ajs.s3-22.128.120.

[5] W. Drexler and J. G. Fujimoto: "Optical Coherence Tomography:Technology and Applications", Berlin: Springer, 2008. ISBN: 978-3-540-77549-2.

[6] Thorlabs: "Thorlabs - TEL221PS Telesto PS-Oct Base Unit, 1300 nm, 5.5 µm resolution, 5.5 to 76 khz", Online. 2020. URL: https://www.thorlabs.com/thorproduct.cfm?partnumber=TEL221PS.

[7] Thorlabs: "OCTP-1300PS/M - User-Customizable Scanner for 1300 nm & 1325 nm PS-OCT Systems, Metric ", Online. 2018. URL: https://www.thorlabs.com/thorproduct.cfm?partnumber=OCTP-1300PS/M.

[8] Thorlabs: "OCT-LK2 - OCT Scan Lens Kit, 18 mm EFL, 1250 to 1380 nm ", Online. 2016. URL: https://www.thorlabs.com/thorproduct.cfm?partnumber=OCT-LK2.

[9] Thorlabs: "OCT-LK3 - OCT Scan Lens Kit, 36 mm EFL, 1250 to 1380 nm ", Online. 2016. URL: https://www.thorlabs.com/thorproduct.cfm?partnumber=OCT-LK3.

[10] Thorlabs: "OCT-LK4 - OCT Scan Lens Kit, 54 mm EFL, 1250 to 1380 nm ", Online. 2016. URL: https://www.thorlabs.com/thorproduct.cfm?partnumber=OCT-LK4.

[11] L. Scolaro et al.: "Parametric Imaging of the Local Attenuation Coefficient in Human Axillary Lymph Nodes Assessed Using Optical Coherence Tomography", *Biomedical Optics Express* **3**(2), 366 (2012). DOI: 10.1364/BOE.3.000366.

[12] D. J. Faber et al.: "Light absorption of (oxy-)hemoglobin assessed by spectroscopic optical coherence tomography", *Optics Letters* **28**(16), 1436–1438 (2003). DOI: 10.1364/OL.28.001436.

[13] E. Real Peña: "Fotónica y técnicas de interpretación aplicadas al diagnóstico de patologías cardiovasculares y dermatológicas", PhD thesis. Santander: Universidad de Cantabria, 2017. http://hdl.handle.net/10902/11362.

[14] Polysciences Inc.: "Polybead microspheres description", URL: https://www.polysciences.com/india/awfile/index/attach/file/TDS_788.pdf/.

[15] K. A. Vermeer et al.: "Depth-resolved model-based reconstruction of attenuation coefficients in optical coherence tomography", *Biomedical Optics Express* **5**(1), 322 (2014). DOI: 10.1364/boe.5.000322.

[16] K. Li et al.: "Robust, accurate depth-resolved attenuation characterization in optical coherence tomography", *Biomedical Optics Express* **11**(2), 672 (2020). DOI: 10.1364/BOE.382493.

[17] S. Jiao et al.: "Optical-fiber-based Mueller optical coherence tomography", *Optics Letters* **28**(14), 1206–1208 (2003). DOI: 10.1364/OL.28.001206.

[18] S. Jiao et al.: "Contrast mechanisms in polarization-sensitive Mueller-matrix optical coherence tomography and application in burn imaging", *Applied Optics* **42**(25), 5191–5197 (2003). DOI: 10.1364/AO.42.005191.

[19] K. Li et al.: "Quantitative characterization of zebrafish development based on multiple classifications using Mueller matrix OCT", *Biomedical Optics Express* **14**(6), 2889–2904 (2023). DOI: 10.1364/BOE.488614.

[20] J. F. de Boer and T. E. Milner: "Review of polarization sensitive optical coherence tomography and Stokes vector determination", *Journal of Biomedical Optics* **7**(3), 359–371 (2002). DOI: 10.1117/1.1483879.

[21] L. Chin et al.: "En face parametric imaging of tissue birefringence using polarization-sensitive optical coherence tomography ", *Journal of Biomedical Optics* **18**(6), 066005 (2013). DOI: 10.1117/1.jbo.18.6.066005.

[22] M. Hollas: "Modern spectroscopy", Fourth. Chichester: John Wiley and Sons, 2004. ISBN: 0470844167.

[23] A. F. H. Goetz and L. C. Rowan: "Geologic Remote Sensing", *Science* **211**(4484), 781–791 (1981). DOI: 10.1126/science.211.4484.781.

[24] A. F. H. Goetz et al.: "Imaging Spectrometry for Earth Remote Sensing", *Science* **228**(4704), 1147–1153 (1985). DOI: 10.1126/science.228.4704.1147.

[25] H. Akbari et al.: "Hyperspectral imaging and quantitative analysis for prostate cancer detection", *Journal of Biomedical Optics* **17**(7), 0760051 (2012). DOI: 10.1117/1.JBO.17.7.076005.

[26] G. Lu and B. Fei: "Medical hyperspectral imaging: a review", *Journal of Biomedical Optics* **19**(1), 010901 (2014). DOI: 10.1117/1.JBO.19.1.010901.

[27] A. Pardo Franco: "Light, machines, and cancer: imaging systems and processing techniques for wide-field diagnostics in scattering media", PhD thesis. Santander: Universidad de Cantabria, 2022. https://hdl.handle.net/10902/26190.

[28] J. A. Gutiérrez Gutiérrez: "Contribuciones a la traslación de instrumentación fotónica al ámbito clínico", Español. PhD thesis. Santander: Universidad de Cantabria, 2024. https://hdl.handle.net/10902/31878.

[29] P. B. García Allende: "Contribuciones al desarrollo de nuevas técnicas de interpretación y sistemas basados en espectroscopía de imagen", PhD thesis. Universidad de Cantabria, 2010.

[30] S. L. Jacques: "Optical Properties of Biological Tissues: A Review", *Physics in Medicine and Biology* **58**(11), R37–R61 (2013). DOI: 10.1088/0031-9155/58/11/R37.

[31] J. A. Gutiérrez-Gutiérrez et al.: "Custom Scanning Hyperspectral Imaging System for Biomedical Applications: Modeling, Benchmarking, and Specifications", *Sensors* **19**(7), 1692 (2019). DOI: 10.3390/s19071692.

[32] B. Majaron and T. Žel: "Optical properties of Spectralon assessed by replication of literature data in Monte Carlo simulations", in: *Tissue Optics and Photonics II*. Ed. by V. V. Tuchin, W. C. P. M. Blondel, and Z. Zalevsky. **12147**. International Society for Optics and Photonics. SPIE, 2022 1214704. DOI: 10.1117/12.2620704.

[33] S. Battiato, A. Castorina, and M. Mancuso: "High dynamic range imaging for digital still camera: an overview", *Journal of Electronic Imaging* **12**(3), 459–469 (2003). DOI: 10.1117/1.1580829.

[34] K. A. Schenkman et al.: "Myoglobin oxygen dissociation by multiwavelength spectroscopy", *Journal of Applied Physiology*, 86–92 (1997). DOI: 10.1152/jappl.1997.82.1.86.

[35] S. K. V. Sekar et al.: "Diffuse optical characterization of collagen absorption from 500 to 1700 nm", *Journal of Biomedical Optics* **22**(1), 015006 (2017). DOI: 10.1117/1.jbo.22.1.015006.

[36] S. Konugolu Venkata Sekar et al.: "Broadband diffuse optical characterization of elastin for biomedical applications", *Biophysical Chemistry* **229**, 130–134 (2017). DOI: 10.1016/j.bpc.2017.07.004.

[37] R. Nachabé et al.: "Estimation of biological chromophores using diffuse optical spectroscopy: benefit of extending the UV-VIS wavelength range to include 1000 to 1600 nm", *Biomedical Optics Express* **1**(6), 1432–1442 (2010). DOI: 10.1364/BOE.1.001432.

[38] L. Kou, D. Labrie, and P. Chylek: "Refractive indices of water and ice in the 065- to 25-μm spectral range", *Applied Optics* **32**(19), 3531 (1993). DOI: 10.1364/AO.32.003531.

[39] P. Kubelka and F. Munk: "Ein Beitrag Zur Optik Der Farbanstriche.", *Zeitschrift für Technische Physik* **15**(12), 593–601 (1931).

[40] S. L. Jacques: "Tissue Optics", tech. rep. 2020.

[41] V. Krishnaswamy et al.: "Quantitative imaging of scattering changes associated with epithelial proliferation, necrosis, and fibrosis in tumors using microsampling reflectance spectroscopy", *Journal of Biomedical Optics* **14**(1), 014004 (2009). DOI: 10.1117/1.3065540.

[42] N. Dögnitz and G. Wagnières: "Determination of Tissue Optical Properties by Steady-State Spatial Frequency-Domain Reflectometry", *Lasers in Medical Science* **13**(1), 55–65 (1998). DOI: 10.1007/BF00592960.

[43] D. J. Cuccia et al.: "Quantitation and mapping of tissue optical properties using modulated imaging", *Journal of Biomedical Optics* **14**(2), 024012 (2009). DOI: 10.1117/1.3088140.

[44] D. J. Cuccia et al.: "Modulated Imaging: Quantitative Analysis and Tomography of Turbid Media in the Spatial-Frequency Domain", *Optics Letters* **30**(11), 1354 (2005). DOI: 10.1364/OL.30.001354.

[45] S. Gioux et al.: "Three-dimensional surface profile intensity correction for spatially modulated imaging", *Journal of Biomedical Optics* **14**(3), 034045 (2009). DOI: 10.1117/1.3156840.

[46] V. Mieites et al.: "Wide-field optical properties estimation of whole limbs in muscle dystrophy murine models via SFDI: a case study", in: *Translational Biophotonics: Diagnostics and Therapeutics III*. Ed. by Z. Huang and L. D. Lilge. **12627**. International Society for Optics and Photonics. SPIE, 2023 1262731. DOI: 10.1117/12.2670573.

[47] E. Alerstam, S. Andersson-Engels, and T. Svensson: "White Monte Carlo for time-resolved photon migration", *Journal of Biomedical Optics* **13**(4), 041304 (2008). DOI: 10.1117/1.2950319.

[48] E. Alerstam, T. Svensson, and S. Andersson-Engels: "Parallel computing with graphics processing units for high-speed Monte Carlo simulation of photon migration", *Journal of Biomedical Optics* **13**(6), 060504 (2008). DOI: 10.1117/1.3041496.

[49] J. A. Gutiérrez-Gutiérrez et al.: "Comparison between optical coherence tomography and phase shifting profilometry for surface estimation", in: *Translational Biophotonics: Diagnostics and Therapeutics III*. Ed. by Z. Huang and L. D. Lilge. **12627**. International Society for Optics and Photonics. SPIE, 2023 126271P. DOI: 10.1117/12.2670564.

[50] V. Mieites Alonso et al.: "PoLambRimetry: a multispectral polarimetric atlas of lamb brain", *Journal of Biomedical Optics* **29**(09) (2024). DOI: 10.1117/1.JBO.29.9.096002.

[51] J. Rehbinder et al.: "Diagnosis of uterine cervix cancer using Mueller polarimetry: a comparison with histopathology", in: *Novel Biophotonics Techniques and Applications III*. OSA, 2015 95400W. ISBN: 9781628417050. DOI: 10.1364/ECBO.2015.95400W.

[52] J. Rehbinder et al.: "Ex vivo Mueller polarimetric imaging of the uterine cervix: a first statistical evaluation", *Journal of Biomedical Optics* **21**(7), 71113 (2016). DOI: 10.1117/1.JBO.21.7.071113.

[53] E. Compain, S. Poirier, and B. Drevillon: "General and self-consistent method for the calibration of polarization modulators, polarimeters, and Mueller-matrix ellipsometers", *Applied Optics* **38**(16), 3490–3502 (1999). DOI: 10.1364/AO.38.003490.

[54] I. Montes-Gonzalez et al.: "Generalized eigenvalue calibration method for Mueller imaging polarimeters based on micropolarized sensors with optimal set of calibration samples.", Accepted. 2024.

[55] S. A. Rosales, E. G. Caurel, and R. Ossikovski: "Extended eigenvalue calibration method for overdetermined Mueller matrix polarimeters", *Optics Letters* **49**(5), 1165–1168 (2024). DOI: 10.1364/OL.513929.

[56] J. S. Tyo: "Noise equalization in Stokes parameter images obtained by use of variable-retardance polarimeters", *Optics Letters* **25**(16), 1198–1200 (2000). DOI: 10.1364/OL.25.001198.

[57] A. Ambirajan and D. C. Look Jr.: "Optimum angles for a polarimeter: part I", *Optical Engineering*, 1651–1655 (1995). DOI: 10.1117/12.202093.

Analysis of optical imaging measurements

5

This chapter aims to summarize all of the analysis techniques applied to the measurements taken in this thesis. Some methods, like those based on image or signal processing, are universally applicable to all systems, as the data can be treated arbitrarily. Others are based on understanding the optical properties probed by each system and getting the most out of them. Most of the latter were already described in the previous chapter as mathematical models representing the optical properties of interest in each case. Still, any additional data treatment is described in the following sections.

5.1 Signal detection in OCT

The optical models in OCT imaging often describe the behavior of light once it enters the sample. Nonetheless, OCT captures a three-dimensional data cube that contains the sample within it. Consequently, it is necessary to locate the surface of the sample in the data cube so that the models are evaluated only in regions where the sample is.

As light travels from the top to the bottom of the cube, it gets absorbed and scattered by the sample. Regardless of the maximum theoretical penetration of OCT systems, if the sample extinguishes all of the light, the system is not going to be able to measure anything beyond the maximum optical path. Areas beyond this point will not have enough SNR to be measured.

This section describes the methods used to detect the sample's surface and those used to limit the calculations to high SNR areas only.

5.1.1 Air thresholding and Low SNR detection

The first step of sample segmentation involves removing the influence of air. Given that the samples treated in this book were fairly absorbent, the bottom of the OCT data cube was always empty, aside from the speckle noise characteristic of OCT imaging. The air shares the same properties, but it is not always visible in the same areas since some samples might have uneven surfaces that leave air in some regions of the OCT cube but not in others. The simplest way to remove air from the data cube is by thresholding.

Let $I(x, y, z)$ be the intensity in one OCT data cube. Let z be the dimensions representing height in the data cube, with $z \in [0, Z_{max}]$. Let $I_b(x, y, z_{max} - 50 : z_{max})$ be the slice of $I(x, y, z)$ that represents the background noise, evaluated at the z slice given by bottom 50 z values in the data cube, after all light is absorbed by the sample[1]. Then, the intensity of the sample $I_s(x, y, z)$ can be separated from that of air $I_{air}(x, y, z)$ by setting to zero all those intensity values below the threshold given by

$$\text{Th} = \text{mean}(I_b(x, y, z_{max} - 50 : z_{max})) \quad . \tag{5.1}$$

[1] The number 50 is arbitrary. Our system captures 1024 z values, and the sample is always positioned as close as possible to $z = 0$. Given that biological samples have significant absorption at 1300 nm, the wavelength used by the OCT system, the bottom 50 pixels are always empty, meaning no sample data is going to be influencing the air and low-SNR areas segmentation.

5.1.2 Surface detection

Given an intensity $I(x, y, z)$, the associated surface intensity, $I_s(x, y)$, is two-dimensional. Since light comes from air into the sample, the most significant refractive index change occurs at the surface of the sample, yielding a high-intensity peak (see the representation of an A-scan in Fig. 4.5). Then, the most straightforward way of identifying the surface is by searching for the position (argument) of the maxima along the z direction[2],

$$I_s(x, y) = \text{argmax}_z(I(x, y, z)) \quad . \tag{5.2}$$

[2] Note that this way of finding the surface is finding the position of the MIP (Eq. 4.9).

Biological samples often come fresh or fixed in liquid solutions to avoid their degradation. This liquid can act as a refractive index matching liquid in OCT measurements, meaning the intensity peak is no longer as sharp as for dry, solid samples. Then, applying Eq. 5.2 for surface detection may yield imprecise results. However, there are methods to mitigate this imprecision.

Here, we opted for a multi-step process to find the surface:

1. Find a first estimate of the surface as Eq. 5.2.
2. Soften the intensity with a three-dimensional Gaussian filter with $\sigma = 2$ to remove abrupt changes in intensity caused by specular reflections or noise.
3. Threshold the Air, as indicated in the previous sub-section, in the softened version of the intensity.
4. Duplicate the intensity between the threshold limit and the surface. If the first surface is well detected, the values on top of it, even if duplicated, should be orders of magnitude below the OCT first peak. If that is not the case, then the surface is updated by re-detecting the maximum intensity in this range.
5. Finally, the surface is softened with a two-dimensional morphological disk of radius 2 to minimize the effect of specular reflections.

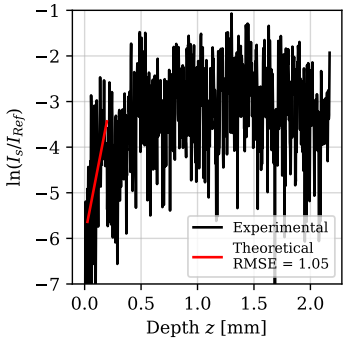

Figure 5.1: Example of fit of the calibrated OCT data before denoising.

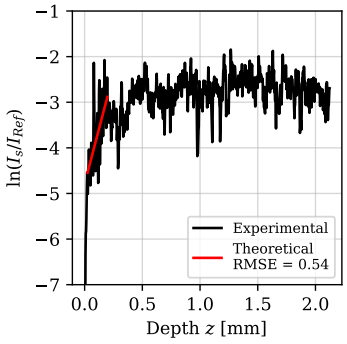

Figure 5.2: Example of fit of the calibrated OCT data after denoising with a Gaussian filter with $\sigma = 1$.

5.2 OCT denoising

Any method of noise removal can be applied to OCT data in any combination of dimensions. In this work, the data is fitted to models along the z (depth) dimension, so the aim is to minimize the noise along this direction without compromising the detail in the data.

The fitting attenuation data calibrated with a reference phantom is especially sensitive to noise (Eq. 4.23). Since the intensity of the data can be much less than that of the phantom, the calibrated data often has values much smaller than one. When transforming it to logarithmic data, the signal and the noise get enhanced equally (Fig. 5.1) and, as a result, the data passed to the least squares-based fitting algorithms can yield high MSE (or RMSE).

To avoid potential artifacts from filtering along the depth axis, which could be problematic in samples with multiple layers, all OCT 3D data was laterally smoothed. This was achieved using a 2D Gaussian filter applied to each B-scan (a cross-sectional image at a constant depth). The filter employed a 3D kernel with $\sigma_{3D} = (\sigma = 1, \sigma = 1, 0)$, effectively

smoothing only in the lateral dimensions (x and y). The rationale was to assume signal continuity between neighboring A-scans to reduce noise while preserving the relative intensity of each pixel within its local context. With this approach, the RMSE is approximately reduced in half (Fig. 5.2).

5.3 Spectral data compression for visualization

Spectral data derived from HSI systems is, as OCT data, three-dimensional. However, instead of having three spatial dimensions like the latter, HSI has one spectral and two spatial dimensions. To visualize the data in two-dimensional images, it is necessary to compress the spectral dimension in a way that preserves the spectral contents of the sample. As in OCT, the mean or max (spectral) intensity can be used for compression, as well as fitting the data to relevant optical properties. However, there is a method exclusive to visualize HSI-VISNIR data, which is to transform it into a color image of the sample.

5.3.1 Color reconstruction in HSI

HSI captures and processes information across the electromagnetic spectrum, going beyond the three color channels of conventional RGB cameras. While traditional RGB cameras combine three color channels in specific ways to produce color, HSI utilizes color matching functions (CMFs) to achieve this. CMFs describe the sensitivity of the human eye to different wavelengths of light, which indicates how a human would receive the spectral data to translate it into XYZ tristimulus values, defined by the International Commission of Illumination (CIE), which can then be translated into various color spaces like RGB for display [1, 2].

The XYZ tristimulus values are calculated from the CMFs, $\overline{x}$, $\overline{y}$, and $\overline{z}$, which approximate the response of an observer for the red, green, and blue wavelengths. Then, given some light, reflected or emitted, defined by a spectrum $\phi(\lambda)$, the tristimulus values are calculated as [3, 4]

$$\begin{aligned} X &= K \sum_{i=1}^{n} \phi(\lambda_i)\overline{x}(\lambda_i)\Delta\lambda \quad , \\ Y &= K \sum_{i=1}^{n} \phi(\lambda_i)\overline{y}(\lambda_i)\Delta\lambda \quad , \text{ and} \\ Z &= K \sum_{i=1}^{n} \phi(\lambda_i)\overline{z}(\lambda_i)\Delta\lambda \quad , \end{aligned} \tag{5.3}$$

where $\Delta\lambda$ represents the spectral resolution. The constant K, when the light comes from a reflectance spectrum, is defined in terms of the green CMF ($\overline{y}(\lambda)$) due to it being the better representation of the stimulus-response of the human eye [4]. In such case, given a source with a spectrum defined by $S(\lambda)$, the constant is obtained as

$$K = \frac{100}{\sum_{i=1}^{N} S(\lambda_i)\overline{y}(\lambda_i)\Delta\lambda} \quad .$$

Once the XYZ values are obtained, any color space transformation can be applied through the corresponding transfer matrix. In this case, we used the RGB color space for representation, which relates to the XYZ color space through [4].

$$\begin{pmatrix} R \\ G \\ B \end{pmatrix} = \begin{pmatrix} 3.24 & 1.54 & 0.50 \\ 0.97 & 1.88 & 0.04 \\ 0.06 & 0.20 & 1.05 \end{pmatrix} \begin{pmatrix} X \\ Y \\ Z \end{pmatrix} \quad .$$

5.3.2 Color encoding for visualization

Visualizing multiple optical properties in a single image can be achieved by mapping each property to a dimension of a color space, such as Hue, Saturation, and Value, the components of the HSV color space. This approach is particularly useful when the optical properties are co-registered, either through simultaneous measurement or manual alignment. HSV offers an advantage over RGB by separating color (Hue) from intensity (Value), allowing for independent control of how each optical property is represented [5].

Hue, typically represented as a cyclic value (0-360 degrees or 0-1), can lead to visual confusion due to the cyclical nature of red hues. To address this, we restrict the Hue values to a range of 0.2 to 1.0, effectively creating a "rainbow" colormap that spans from green to red. This truncated range avoids the red-orange-yellow portion of the spectrum, preventing potential misinterpretations while retaining red values at the higher end for the representation of a specific feature. Critically, this modified HSV to RGB conversion remains valid, ensuring compatibility with standard visualization tools [6].

To create a combined HSV image, each of the three desired optical properties is assigned to one of the HSV components (H, S, or V). Since HSV values range from 0 to 1, all measurement data must be normalized to this range. For datasets with multiple samples, we scale each sample's data individually to a range between 0 and 1 using the dataset's overall minimum and maximum values. This global scaling ensures consistency across all samples and allows for a single, unified legend.

However, simply scaling data to 0-1 does not guarantee optimal HSV visualization. Outliers in one sample can compress the dynamic range of other samples, making color distinctions difficult. To compensate, we employ a non-linear rescaling based on the dataset's cumulative distribution function. This global equalization expands compressed ranges while respecting the overall data distribution, improving color differentiation, and enabling the use of a single HSV legend for all samples. This method complements the general principle that the human eye is more sensitive to luminance variations than color changes for discerning textural information, influencing our parameter assignments [7].

In this work, we assigned birefringence, a clinically relevant property for distinguishing between control and pathological samples, to Hue (H). Control samples are visualized in green, while pathological samples appear in red. Other parameters, such as the sample's profilometry and its attenuation, which exhibit strong spatial variations, are mapped

to Saturation (S) and Value (V) [6]. This allows us to represent these properties as variations in color intensity or brightness, respectively, leveraging the eye's sensitivity to luminance for textural analysis.

5.4 Monte Carlo simulations for optical properties derivations

In the previous chapter, it was briefly mentioned that Monte Carlo simulations can be used to derive the optical properties of the sample. A look-up table can be created by simulating multiple combinations of attenuation and scattering, which will yield various reflectance values. Then, given a measured reflectance, the corresponding optical properties are found through the look-up table. The main advantage of using simulations instead of models to derive the optical properties of biological tissue is that most reflectance models do not consider the influence of multiple scattering, which occurs at the deeper regions of the sample. The only assumption simulations make is about the internal structure of the sample, which, in most cases, can be considered homogeneous. This section will briefly explain the steps of the Monte Carlo Multi-Layer simulation method applied in this work. The Monte Carlo theory for the simulation of the optical properties of samples is thoroughly described in the references [8–10], but is included in the following section for completeness.

5.4.1 Monte Carlo Multi-Layer

CUDAMCML [11], which is a GPU-accelerated version of the Monte Carlo model for Multi-Layered tissues (MCML) [8], was used in this work to simulate the optical properties of the samples. Although this method considers the option to include multiple sample layers, given a known thickness and refractive index, it is also possible to consider only one semi-infinite layer. In this case, we chose the latter since the muscle samples are not expected to have multiple layers. This Monte Carlo method, as introduced by Wang *et al.* [8], is a multiple-step process that involves launching a photon and simulating its optical path in terms of a given absorption and scattering. The optical path of a single photon will resemble a random walk, so it is necessary to simulate a high number of photons to estimate the optical path of the average photon correctly. The simulation space is divided into bins to save the absorbed photons (Fig. 5.3).

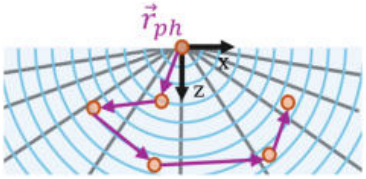

Figure 5.3: Example of the initial positioning of the photon (red circles) in the simulation. The position of the photon is given by the vector $\vec{r}_{ph}$, whose coordinates are updated as the simulation continues. The space is divided into radial (blue circles) and angular (grey lines) bins so that the final location of the absorbed photons inside the sample is known.

Photon launch

In the Monte Carlo method, an initial amount of photons is launched with a certain spatial distribution. The number of photons launched represents the incident intensity. Then, the photons will be scattered and absorbed according to the optical properties set for the simulation. This gives different amounts of transmitted, absorbed, and reflected photons, which can be detected at the end of the simulation to calculate the transmittance, absorbance, and reflectance.

Photon position and orientation

The instantaneous position and orientation of the photon packet are defined as follows Let $\vec{r}_{ph} = (x_{ph}, y_{ph}, z_{ph})$ be the coordinates of one photon, and the boundary between air and sample be set at $z = 0$. Then, the directional cosines[3] are given by $c_x = \vec{r}_{ph} \cdot \hat{x}$, $c_y = \vec{r}_{ph} \cdot \hat{y}$, and $c_z = \vec{r}_{ph} \cdot \hat{z}$, defined between the photon's position $\vec{r}_{ph}$ and the unitary vectors of the coordinate system set on the air-sample interface ($\hat{x}$, $\hat{y}$ and $\hat{z}$).

[3] Named directional cosines because they indicate where does the photon position vector "point" to.

Absorption

If a photon *packet* was sent, the absorption given by μ_a would cause a number of the photons in the packet to be absorbed. Instead, since the simulations are done with a photon at a time, absorption is considered as an absorbed *weight* of each photon. To implement it, each photon is assigned an initial weight W. By dividing the simulation space into bins, some of the weight of the photon, given by $\Delta W = W \cdot \mu_a / \mu_t$, is deposited into the destination bin. After the absorption event, the weight of the photon is updated as $W \rightarrow W - \Delta W$.

[4] Note that the actual involvement of the scattering coefficient in the simulation is included in the weight depletion caused by the absorption as indicated in the previous section.

Scattering

Scattering, while given by μ_s[4], is simulated as a random reorientation of the direction cosines based on the anisotropy coefficient, g. Specifically, given a random variable ξ, and a deflection angle $\theta \in [0, \pi)$ that symbolizes the reorientation of the photon packet, the magnitude $\cos\theta$ is updated as

$$\cos\theta = \begin{cases} \frac{1}{2g}\left(1 + g^2 - \left[\frac{1-g^2}{1-g+2g\xi}\right]^2\right) \text{ if } g \neq 0 \\ 2\xi - 1 \text{ otherwise} \end{cases} .$$

The angle that defines the azimuth, $\Psi \in [0, 2\pi]$, is also randomly estimated as

$$\Psi = 2\pi\xi \ .$$

Finally, the direction cosines are updated as [8]

$$\begin{aligned} c_x &\rightarrow \frac{\sin\theta}{\sqrt{1-c_z^2}}(c_x c_z \cos\Psi - c_y \sin\Psi) + c_x \cos\theta \ , \\ c_y &\rightarrow \frac{\sin\theta}{\sqrt{1-c_z^2}}(c_y c_z \cos\Psi - c_x \sin\Psi) + c_y \cos\theta \ , \text{ and} \\ c_z &\rightarrow -\sin\theta\cos\Psi\sqrt{1-c_z^2} + c_z \cos\theta \ . \end{aligned}$$

To avoid numerical errors, when the angle of the new direction of the photon packet is near the surface's normal[5], then the direction cosines

[5] $|c_z| > 0.99999$ [8]

can be approximated as

$$
\begin{aligned}
c_x &\rightarrow \sin\theta\cos\Phi \ , \\
c_y &\rightarrow \sin\theta\sin\Phi \ , \text{ and} \\
c_z &\rightarrow \text{SIGN}(c_z)\cos\theta \ .
\end{aligned}
$$

Photon death

The simulation is halted when the photons are considered *dead*. There are two cases when the photon is terminated: (1) if the photon exits the medium through the surface situated at $z = 0$, and (2) if its weight is too small after being moved to a new position. In the second case, the weight of the photon (W) is evaluated with respect to a threshold (i.e., $W_{th} = 0.0001$ from an initial weight of $W = 1$). The threshold represents the probability of the photon surviving when having a small weight. If its weight is below the threshold, a random variable ξ is sampled and, if its value is smaller than W_{th}, then the photon continues with $1/W_{th}$ the weight ($W \rightarrow W/W_{th}$). Otherwise, the photon is terminated. This way of terminating the photons, known as the *roulette*, means that there is a high chance that their simulation will not continue if their weight is small, but if they do continue, their weight must be increased to conserve the total weight introduced in the simulation.

Monte Carlo pipeline

Then, the steps followed to simulate the optical properties, according to Wang *et al.* [8], are, for each photon, the following:

1. Launch a single photon *inside* the medium at $\vec{r}_{ph} = (0, 0, 0)$ with directional cosines $c_x = 0$, $c_y = 0$ and $c_z = -1$.
2. Sample a random variable ξ to get the step size s the photon is going to move to next, in terms of the extinction coefficient[6], as $s = -\ln(\eta)\mu_t^{-1}$.
3. Calculate the distance to the air-sample boundary d_b[7].
    a) If the photon crosses the surface, i.e., if the step size is larger than the distance to the air-sample boundary ($d_b\mu_t^{-1} \leq s$), then the photon is saved in the bin over the sample's surface as a diffusely reflected photon, and its simulation terminates.
    b) If the photon does not cross the surface, it is moved to the next position, given by s/μ_t. Then, the path is updated as $s \rightarrow 0$, and the absorption and scattering are calculated as described above at a new position.
4. Find if the photon is dead to determine if it crossed the boundary.
5. If the photon is not dead, evaluate its weight with respect to the threshold.
    a) If the photon does not survive the roulette, its weight is set to zero in the corresponding final bin and added to the absorbed energy.
    b) If the photon survives the roulette, the process goes back to step 2 and repeats until the photon is terminated.
6. Repeat steps 1 to 5 until all the photons are simulated.

[6] This expression is derived from the sampling of the probability distribution for a photon's free path. See reference [10] for details

[7] If multiple layers are being considered (which here is not the case), the distance to the layer-layer boundary should be calculated as well, and the Reflection and Transmission properties must be calculated according to Fresnel's equations. Then, part of the simulation continues in the same layer as an internally reflected weight, while some continues as a transmitted weight in the new layer.

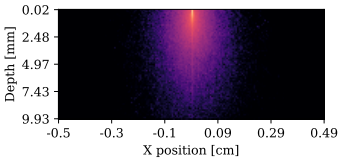

Figure 5.4: Random walk of 10^5 photons simulated for a semi-infinite sample with $\mu_a = 1cm^{-1}$, $\mu_s = 100cm^{-1}$, $g = 0.9$ and $n = 1.4$. Notice the *forward shaped* photon distribution due to the high anisotropy coefficient.

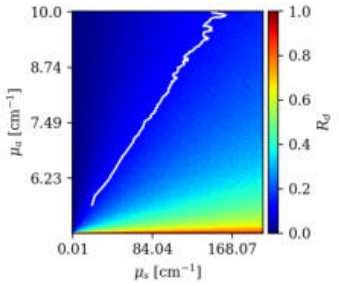

Figure 5.5: Diffuse reflectance (R_d) LUT created by simulating 200×150 pairs of $\mu_a \times \mu_s$ with $g = 0.9$ and $n = 1.4$. The white line represents all of the (μ_a, μ_s) pairs that yield a reflectance of $R_d = 0.13$

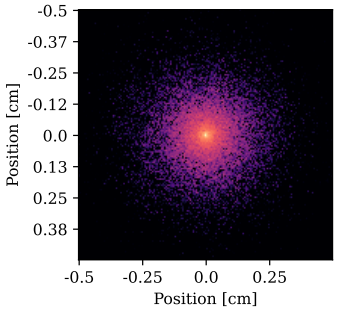

Figure 5.6: Reflectance as a top-down view of the total exited photons out of the 10^5 photons simulated for a semi-infinite sample with $\mu_a = 10cm^{-1}$, $\mu_s = 100cm^{-1}$, $g = 0.9$ and $n = 1.4$.

[8] This value is commonly used in the literature for many biological tissues.

[9] Assuming a point source.

5.4.2 MCML-derived reflectance

A wide range of optical properties must be simulated to use the LUT for every biological sample. As a first approach, we chose attenuation values of $\mu_a \in [0.001, 10]$, with a step of 0.05, and scattering values of $\mu_s \in [0.01, 500]$, with a step of 50. This created a 200×150 LUT which, due to the high number of simulations, was limited to 1000 photons per simulation.

The simulation space was considered to be one single semi-infinite layer that was binned in the x, y, and z spatial dimensions to save the results. The refractive index needs to be considered as well to find Fresnel's reflectance and transmittance contributions at the boundaries. Jacques provided a comprehensive list of refractive indexes, attenuation, and scattering properties of biological samples based on the compilation of multiple scientific articles [12]. Most biological samples have a refractive index (n) between 1.33 and 1.51, which increases with the diminution of water content. In this case, the refractive index was set at[8] $n = 1.4$ as in other works focused on mice muscles [13]. Similarly, a value of $g = 0.9$ was used due to it being often selected for muscles [13].

For each pair (μ_a, μ_s), the total number of photons[9] will have an internal spatial distribution similar to what is shown in Fig. 5.4, with more or less penetration depth in terms of absorption and scattering properties. Notice that even if the penetration depth of the photons is in the range of millimeters, the actual optical path length they follow is much longer, sometimes even exiting the sample after traveling through all of it before exiting through the top surface. This highlights the limitation that the analytical models often have since the estimation of the optical path length is hindered by the erratic photon movement, which is also wavelength-dependent.

The reflectance is obtained by calculating the ratio of the photons that exit the surface (i.e., those that are not absorbed) to the total simulated photons. The reflectance for the whole 200×150 LUT is shown in Fig. 5.5. The relationship between R_d, μ_a, and μ_s is non-linear and ill-conditioned, in the sense that there is more than one (μ_a, μ_s) pair that yields a similar reflectance value. For example, the white line in Fig. 5.5 represents all the pairs that cause a reflectance of 0.13, considering a maximum deviation of 0.0001. Although the LUT has some noise due to the small number of photons per simulation and, like any analytical model, has limitations, it is still helpful to determine the behavior of the reflectance in terms of scattering and attenuation. In general, the higher the attenuation, the lower the reflectance due to the sample absorbing more photons. Similarly, the higher the scattering, the higher the reflectance due to most photons exiting the sample without penetrating deep into the sample. In the regions of high albedo ($\mu_s' >> \mu_a$), the reflectance varies slowly with scattering changes but falls rapidly if the attenuation increases, while in the regions of low albedo ($\mu_s' << \mu_a$), absorption dominates the diffuse reflectance and little to no energy is reflected.

5.4.3 Reflectance at different spatial frequencies

The previous chapter introduced that the simulation of a point source can be transformed into the frequency response of a sample through a transform that involves the Bessel functions (see Eq. 4.56). To do so, it is necessary to obtain from the simulations the spatial distribution of the diffuse reflectance in terms of the xy distance to the point source (Fig. 5.6), given by $\rho = \sqrt{x^2 + y^2}$, so that $R_d := R_d(\rho)$. Then, the reflectance in terms of the spatial frequency is found using Eq. 4.56. The results from the simulations for the Spectralon[10] in terms of the spatial frequency and wavelength is shown in Fig. 5.7. In this case, and in general, the lower the spatial frequency, the higher the captured reflectance. For this material, each wavelength has only one distinct pair (μ_a, μ_s) (see Fig. 4.10), yielding one distinct value of R_d for each wavelength k.

When comparing the (wavelength-averaged) diffuse reflectance derived from the simulations and the diffusion approximation (Eq. 4.55), we see that given the properties of the Spectralon, the diffusion approximation mostly coincides with the simulations (Fig. 5.8). Only for very low spatial frequencies does the approximation slightly overestimate the reflectance.

As before, for each spatial frequency, the diffuse reflectance is undetermined due to there being multiple combinations of μ_a and μ_s that yield the same value. However, the real optical properties of the samples can be found by measuring more than one spatial frequency since the $\mu_a - \mu_s$ surfaces at the different frequencies are not parallel (Fig. 5.9), solving the indeterminacy.

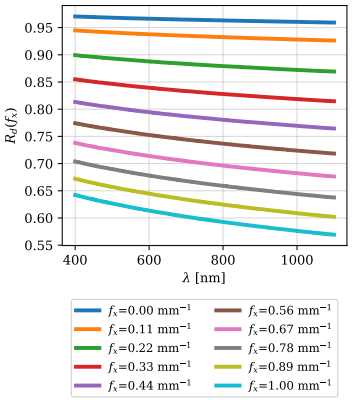

Figure 5.7: Monte Carlo modeling of the optical properties of Spectralon at ten spatial frequencies in terms of the wavelength. [14].

[10] Reference material used to calibrate HSI and SFDI measurements, introduced in the previous chapter.

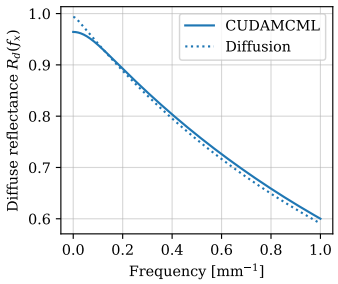

Figure 5.8: Comparison with the results of the Monte Carlo simulations with the diffusion approximation (Eq. 4.55).

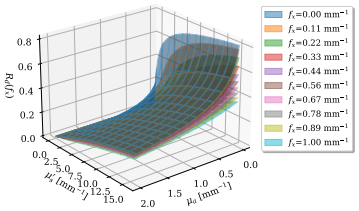

Figure 5.9: Frequency-transformed LUT used for the samples.

5.5 Machine learning

Machine learning is a powerful tool for understanding complex information, especially when dealing with high-dimensional datasets. It can be applied to classify data according to their clinical category based on their optical properties or to reduce their dimensionality and make datasets easier to handle. Machine learning encompasses many different types of algorithms ranging from something very simple, like linear regression, to something as complex as deep neural networks. This section will provide a brief overview of the machine learning methods used in this work and highlight their key concepts and use cases.

5.5.1 Supervised and unsupervised machine learning

In machine learning, tasks are categorized as either supervised or unsupervised, depending on the availability of labeled data. Supervised methods use a set of labeled data points to train algorithms to predict some property of new, unlabeled data. This approach requires prior knowledge of the training data and enough labeled examples for the algorithm to learn the relationships between features and classes [15]. On the other hand, unsupervised methods aim to discover inherent groupings within data without prior knowledge of class labels. These algorithms analyze the relationships between data points based on their

characteristics, forming clusters of points that share similar features. The choice between supervised and unsupervised classification depends on the specific application, the availability of labeled data, and the overall goal of the analysis.

5.5.2 Dimension reduction methods

Although we have already discussed some ways of compressing spectral data to two dimensions for visualization, other dimension reduction techniques can be generally applied to any dataset characterized by a specific set of features. These methods, which are usually unsupervised, search for particular metrics that can represent the behavior of the data in the original space to project the points onto a dimension-reduced space. Thus, they remove unnecessary information like noise while keeping the main relationships between features.

Principal component analysis

Principal Component Analysis (PCA) is a linear transformation technique used to reduce the dimensionality of complex datasets. It identifies the most important patterns and relationships within the data and represents them using a new set of independent variables called principal components.

PCA analyzes the variance of the data. The first principal component is derived so that the projection of the data onto it represents the most variance in the dataset. Subsequent components are orthogonal to the previous ones and capture decreasing amounts of variance. The original data points are then projected onto these new components, resulting in a lower-dimensional representation [16].

Dimensionality reduction with PCA involves selecting a subset of principal components that adequately represent the data. This selection is typically based on the cumulative variance explained by the components. For example, one might choose the number of components that capture 95% or 99% of the total variance. However, it is also possible to decide the number of components in terms of a desired output size, for example, for 2D representation purposes [16].

t-Distributed stochastic neighbor embedding

t-Distributed Stochastic Neighbor Embedding (t-SNE) is a technique often used for visualizing high-dimensional data by mapping similar objects to nearby points in a lower-dimensional space while focusing on preserving local structures.

The algorithm begins by converting Euclidean distances between high-dimensional points ($\{x_n\} \in \mathbb{R}^N$) into conditional probabilities that represent their similarity [17]. These probabilities reflect the likelihood of $x_i \in \{x_n\}$ choosing $x_j \in \{x_n\}$ as a neighbor. Corresponding points $y_i, y_j \in \{y_m\}$, with $\{y_m\} \in \mathbb{R}^M$ ($M < N$) are then created in the lower-dimensional space, and their distances are defined by similar conditional probabilities to those in the original space.

t-SNE optimizes the low-dimensional mapping by minimizing the difference between the probability distributions in the high and low-dimensional spaces, meaning it would search for a dimension-reduced space that optimizes the similarity between the probabilities before and after reduction [17]. This process reveals clusters and patterns based on data similarity. Perplexity is a key parameter of t-SNE that is related to the number of considered neighbors, which influences the results and needs careful consideration.

Isometric Feature Mapping

Isometric Feature Mapping (Isomap) is a non-linear dimensionality reduction technique that aims to preserve the global structure of data by focusing on geodesic distances, which represent the shortest paths between two points along a curved surface (manifold). The idea is similar to that of t-SNE, which consists of preserving the distance between points. Still, instead of basing the algorithm on conditional probabilities, it is based on searching for the underlying graph structure that globally connects all data points [18].

The algorithm starts by constructing a neighborhood graph, where the number of neighbors can be determined using K-Nearest Neighbors[11] or prior knowledge. This graph approximates the underlying manifold of the data, i.e., its spatial distribution. Next, Isomap estimates geodesic distances between all pairs of points using shortest-path algorithms and, finally, it applies scaling to this distance matrix to embed the data into a lower-dimensional space while preserving the geodesic distances [18].

[11] See the section 5.5.3 for more details on the K-Nearest Neighbors method.

The key advantages of Isomap are its ability to capture the global structure of the data and its global optimization approach. However, it can be sensitive to "shortcuts" between clusters and computationally expensive for high-dimensional data.

5.5.3 Classification

Data is often acquired with the aim of classifying it, whether it is done through supervised or unsupervised methods. The following sections discuss some of the possible classification techniques that have been applied in this book.

K-Nearest Neighbors classification

K-Nearest Neighbors (KNN) is a supervised classification method that divides the data into different classes by evaluating the class of its neighbors. The process starts by finding the distance between one data point and all points in the dataset. Given the class of a pre-defined number of neighbors (K_N), KNN assigns a class to the data point based on the most numerous class among its nearest neighbors [19].

This method depends heavily on the selection of K_N. If K_N is low, the algorithm memorizes the training dataset[12] and is not able to generalize when test data[13] are used, leading to very accurate results when training, but poor when testing. When the number of neighbors is too high, KNN

[12] A dataset used to train the algorithms based on its features, which means obtaining the parameters that define said algorithms. In optical imaging, this dataset may be comprised of attenuation, scattering or absorption values of some samples.

[13] Here we refer to test data as the validation dataset, which is different from the training dataset in that the algorithms have never seen any feature of the test dataset when obtaining their defining parameters. Splitting the data into train and test requires not having any overlapping information. For example, if many spectra from different specimens are used, it is strictly necessary to verify that the spectra in the train and test dataset come from different specimens so that the algorithms do not learn based on the specific specimen but on the spectral features.

can stabilize if the classes are well defined or even start failing for the training dataset if there is too much overlap between classes. Furthermore, the higher the number of neighbors, the slower the algorithm is since it needs to check more neighbors for each data point. The optimal number of neighbors can be optimized based on the accuracy of the algorithm on the test dataset to ensure it generalizes as best as it can, although this recursive process makes training the algorithm a time-consuming process due to it needing to evaluate every possibility [20].

K-means clustering

K-means clustering is an unsupervised method that creates classes (i.e., clusters) by grouping the data according to the similarity of its features. It starts by initializing the centroids of the clusters in random positions and dividing the data into the pre-defined number of clusters K_C according to the distance between the points and the nearest centroid. Then, the centroids are recalculated as the mean of the data points assigned to the cluster, and the dataset is divided again according to the new centroids. This process is repeated until the position of the clusters does not change [21].

K-means is also heavily conditioned by the number of clusters K_C, but often, this number will be something of interest, like the number of clinical categories in a dataset (i.e., healthy vs. diseased). Nonetheless, since the method searches for similarities between features and does not use any prior knowledge of the data, it might separate the points in clusters that are not clinically relevant[14], so the clearer the distinction between clusters according to one feature, the better K-means clustering will perform.

[14] Examples of this behavior are depicted in Ch. 8.

Multi-layer perceptron

A Multi-Layer Perceptron (MLP) is the simplest of the neural network architectures. It often consists of a series of fully connected hidden layers that move the data introduced through the input layer up to the output layer (feed-forward). The data that reaches a layer is multiplied by a weight and added to a bias. The weights and biases of each neuron, which generate linear combinations of the inputs, are randomly initialized and optimized by minimizing a loss function, which, when used for classification, is often the error between the expected and real labels of the data [22]. Activation functions are used between layers to add non-linearities to the possible data combinations after applying the corresponding weights and biases. Here, we used Rectified linear units (ReLU) as the activation function, which returns the maximum between the neuron's output and 0 [23–25].

The larger the network, the more complex the problem it approximates can be. However, larger networks are also prone to overfitting, as they have more capacity to memorize training data but can not extrapolate the results to validation data. In this document, we will specify the configuration of each network when evaluating the results to see how it influences them.

Autoencoders

Unlike the previous methods, which directly evaluate the data fed into them, autoencoders are neural networks designed to learn compressed representations of data. They consist of an encoder that scales down the original features to a small-dimensional set of latent features and a decoder that reconstructs the original input from this latent set [26]. This configuration forces the autoencoder to learn the most important features of the data and combine them so that the most information is kept. Autoencoders are used for various tasks, including dimensionality reduction, denoising data, and anomaly detection, by learning the underlying structure and patterns within the data [27, 28]. Here, our use of autoencoders focused on classifying the data but also allowed us to create a dimension-reduced version of the acquired datasets.

Supervised Autoencoders A Supervised Autoencoder (SAE) is a type of autoencoder that combines unsupervised learning (reconstruction) with supervised learning (classification) [29]. There are four main parts to a Supervised Autoencoder:

- Encoder: The encoder compresses the input data (x) into a lower-dimensional latent representation (z). This is achieved by sequentially reducing the number of neurons in each layer of the encoder. The first layer has an input with the number of neurons given by the number of features of x, while the last layer has z outputs.
- Decoder: The decoder reconstructs the input data ($\hat{x}$) from the latent representation (z). Inversely to the encoder, the decoder is created by incrementing the number of neurons in each layer. Its first layer has z inputs, and its last layer has as many neurons as x has features. Although there are no restrictions between the structure of the encoder and the decoder, the decoder is typically the same network as the encoder but inverted.
- Bottleneck: The bottleneck is the layer between the encoder and the decoder where the latent representation (compression) occurs. It is given by the number of neurons z, and the smaller this number, the larger the compression applied to the data.
- Classifier: A separate branch is used to classify the data using the latent representation (z) as an input to predict the class labels ($\hat{y}$).

The SAE is trained by minimizing two loss functions at the same time: a reconstruction loss that measures the difference between the inputs and the reconstructed data (x and $\hat{x}$), and a classification loss that measures the difference between the actual and predicted labels (y and $\hat{y}$). The loss function for classification was cross-entropy, which is often used for multi-class classification problems since it measures the difference between two probability distributions [30]. The larger the cross-entropy, the worse the classification is. For the reconstruction, we minimized the mean squared error between x and $\hat{x}$ [30].

By minimizing both loss functions at the same time, the SAE is forced to generate a latent space that can reconstruct the data well and that clusters the labeled data points while minimizing the overlap between clusters.

Conventional parameters, like the choice of activation function or loss functions, the size of the dataset, or the training epochs, will influence the

reconstruction and classification results. Still, the critical parameter in a SAE is the size of the bottleneck since it limits the space the autoencoder can generate to provide its best performance. In this book, we tested bottleneck sizes of 2, 3, and 4 neurons. The proposed SAE was also trained with dropout, a technique that randomly deactivates a fraction of neurons in a layer during each training iteration. Dropout prevents the network from relying too heavily on any single neuron and forces it to learn more generalizable features to reduce overfitting.

5.6 Validation and explainability

Validation is a critical step of any machine learning method since it can tell how well an algorithm performs in a given dataset, but also how well it will behave upon encountering new data. Some methods are very straightforward to evaluate, while the interpretation of others might be more cumbersome. Currently, validating the methods, while still necessary, is being complemented with explainable AI (XAI) metrics that do not only tell *how* an algorithm performs, but also *why* it behaves as it does. This section provides information on some validation and explainability methods used in this work.

5.6.1 Accuracy

It is generally accepted that accuracy is a good marker of how a classifier performs due to it being an easily interpretable metric that can be applied universally to any classifier. Let x be a data point that has a class y assigned to it. Based on its training, an algorithm will provide a prediction for the class of x, defined as $\hat{y}$. Given N data points, accuracy increases by $1/N$ when the prediction is correct ($\hat{y} = y$) and by 0 when the prediction is not correct ($\hat{y} \neq y$). In the end, accuracy can be understood as the percentage of data points correctly classified by the algorithm.

Supervised algorithms are directly or indirectly trained to maximize the accuracy they provide, but accuracy should also always be evaluated based on new data to interpret how well an algorithm generalizes its classification performance.

5.6.2 Cross-validation

Although accuracy is a good general metric for interpreting a classifier's performance, it depends on how the data is split between the train and test datasets. If, for example, the test dataset contains many outliers, the test accuracy will be low, but this does not mean that the classifier cannot generalize well. Cross-validation aims to reduce these types of ambiguities by testing the algorithm with multiple test datasets.

The main idea of cross-validation is to divide the available data into multiple subsets, often referred to as *folds*. The algorithm is trained on some of these folds and then tested on the remaining fold. This process is repeated, with each fold taking a turn as the test set. The results from all the test folds are then averaged to give a more robust estimate of the

model's performance than a single train-test split would provide. This helps assess how well the model generalizes to new data.

There are many types of cross-validation. Some examples are *k-fold cross-validation*, which divides the data into a pre-defined number of folds; *leave-one-out cross-validation*, which uses a single data point to test the model at each fold; or *leave-one-group-out cross-validation*, which can test the data of one group (i.e., one patient) each time. Here, we use the latter to avoid the algorithms from focusing on the features of one specific sample instead of the common features between all samples with the same clinical category.

5.6.3 XAI: Feature importance

Assessing feature importance goes a step beyond the previously mentioned methods. Instead of evaluating the overall performance of the algorithm, feature performance metrics analyze which features of a dataset are the most useful for a classifier to distinguish between the desired categories. In other words, evaluating feature performance gives information about what is important and what is not for a specific task.

Currently, evaluating feature importance falls under the umbrella of explainability or explainable AI. This broad term encompasses any analysis that assists in interpreting data, models, or features [31]. Here, we focus on the latter, given that one of the objectives of this thesis is to identify which optical property, or which combination of them, best distinguishes between healthy and dystrophic muscle.

To evaluate feature importance, we opted for the *random permutations* method because it is universally applicable given that it is based on the accuracy metric [32]. Conceptually, the random permutations method is simple and can be illustrated through an example. Let us say that we have some data points of healthy and diseased samples characterized by two features: height and density. Then, we train a classifier to distinguish between healthy and diseased based on the two features, and we obtain a good result (i.e., 90% accuracy for the test dataset). To find out what is influencing our classifier more between the two features, we apply the random permutations method by randomly shuffling the height data and leaving the density as is. If height is important for the classification, the shuffled data must decrease the accuracy, given that we are removing the relationship between clinical category and height. We repeat the random shuffling a number of times and calculate, on average, how much the accuracy decreases when shuffling the height. Then, the process is repeated with the density. If, for a given feature, the average accuracy decreases, then the feature is important for classification and should be kept; if it remains the same, the feature does not add any information for classification and can be removed; finally, if the average accuracy increases after randomly permuting the data, it means that the feature adds noise that hinders classification and must be removed.

In this work, the decrease in average accuracy through random permutations will be used to evaluate the feature importance of those features used in each classification task.

References

[1] P. W. Trezona: "Derivation of the 1964 CIE 10° XYZ colour-matching functions and their applicability in photometry", *Color Research & Application* **26**(1), 67–75 (2001). DOI: 10.1002/1520-6378(200102)26:1<67::AID-COL7>3.0.CO;2-4.

[2] A. Stockman and L. T. Sharpe: "The spectral sensitivities of the middle- and long-wavelength-sensitive cones derived from measurements in observers of known genotype", *Vision Research* **40**(13), 1711–1737 (2000). DOI: 10.1016/S0042-6989(00)00021-3.

[3] E. J. Giorgianni and T. E. Madden: "chapter 14 - Color Encoding in the Photo CD System", in: *Color for Science, Art and Technology*. Ed. by K. Nassau. AZimuth. North-Holland, 1998 389–422. ISBN: 9780444898463. DOI: 10.1016/S1387-6783(98)80017-2.

[4] A. Pardo Franco: "Light, machines, and cancer: imaging systems and processing techniques for wide-field diagnostics in scattering media", PhD thesis. Santander: Universidad de Cantabria, 2022. https://hdl.handle.net/10902/26190.

[5] C. Ware: "Information Visualization: Perception for Design", Information Visualization: Perception for Design. Elsevier Science, 2013. ISBN: 9780123814647.

[6] V. Mieites et al.: "Single-Image Multi-Parametric Representation of Optical Properties through Encodings to the HSV Color Space", *Applied Sciences* **14**(1) (2023). DOI: 10.3390/app14010155.

[7] C. Ware, M. Stone, and D. A. Szafir: "Rainbow Colormaps Are Not All Bad", *IEEE Computer Graphics and Applications* **43**(3), 88–93 (2023). DOI: 10.1109/MCG.2023.3246111.

[8] L. Wang, S. L. Jacquesa, and L. Zhengb: "MCML-Monte Carlo modeling of light transport in multi-layered tissues", *Computer Methods and Programs in Biomedicine* **47**, 131–146 (1995). DOI: 10.1016/0169-2607(95)01640-F.

[9] L. Wang and H. Wu: "Biomedical Optics: Principles and Imaging", Wiley, 2007. ISBN: 9780471743040.

[10] L. Wang and S. L. Jacques: "Monte Carlo Modeling of Light Transport in Multi-layered Tissues in Standard C", tech. rep. 1992.

[11] E. Alerstam, T. Svensson, and S. Andersson-Engels: "Parallel computing with graphics processing units for high-speed Monte Carlo simulation of photon migration", *Journal of Biomedical Optics* **13**(6), 060504 (2008). DOI: 10.1117/1.3041496.

[12] S. L. Jacques: "Optical Properties of Biological Tissues: A Review", *Physics in Medicine and Biology* **58**(11), R37–R61 (2013). DOI: 10.1088/0031-9155/58/11/R37.

[13] B. R. Klyen et al.: "Optical coherence tomography can assess skeletal muscle tissue from mouse models of muscular dystrophy by parametric imaging of the attenuation coefficient", *Biomedical Optics Express* **5**(4), 1217 (2014). DOI: 10.1364/boe.5.001217.

[14] B. Majaron and T. Žel: "Optical properties of Spectralon assessed by replication of literature data in Monte Carlo simulations", in: *Tissue Optics and Photonics II*. Ed. by V. V. Tuchin, W. C. P. M. Blondel, and Z. Zalevsky. **12147**. International Society for Optics and Photonics. SPIE, 2022 1214704. DOI: 10.1117/12.2620704.

[15] M. Berry, A. Mohamed, and B. Yap: "Supervised and Unsupervised Learning for Data Science", Unsupervised and Semi-Supervised Learning. Springer International Publishing, 2019. ISBN: 9783030224752.

[16] M. Greenacre et al.: "Principal component analysis", *Nature Reviews Methods Primers* **2**(1), 100 (2022). DOI: 10.1038/s43586-022-00184-w.

[17] J. Soni, N. Prabakar, and H. Upadhyay: "Visualizing High-Dimensional Data Using t-Distributed Stochastic Neighbor Embedding Algorithm", in: *Principles of Data Science*. Ed. by H. R. Arabnia et al. Cham: Springer International Publishing, 2020 189–206. ISBN: 978-3-030-43981-1. DOI: 10.1007/978-3-030-43981-1_9.

[18] J. B. Tenenbaum, V. de Silva, and J. C. Langford: "A Global Geometric Framework for Nonlinear Dimensionality Reduction", *Science* **290**(5500), 2319–2323 (2000). DOI: 10.1126/science.290.5500.2319.

[19] T. Cover and P. Hart: "Nearest neighbor pattern classification", *IEEE Transactions on Information Theory* **13**(1), 21–27 (1967). DOI: 10.1109/TIT.1967.1053964.

[20] V. Mieites Alonso et al.: "PoLambRimetry: a multispectral polarimetric atlas of lamb brain", *Journal of Biomedical Optics* **29**(09) (2024). DOI: 10.1117/1.JBO.29.9.096002.

[21] J. MacQueen: "Some methods for classification and analysis of multivariate observations", in: *Proceedings of the fifth Berkeley symposium on mathematical statistics and probability*. Ed. by L. Lecam and J. Neyman. **1**. University of California Press, 1967 281–297.

[22] M.-C. Popescu et al.: "Multilayer perceptron and neural networks", *WSEAS Transactions on Circuits and Systems* **8**(7), 579–588 (2009). Ed. by V. Mladenov.

[23] E. Grigsby, K. Lindsey, and D. Rolnick: "Hidden Symmetries of ReLU Networks", in: *Proceedings of the 40th International Conference on Machine Learning*. Ed. by A. Krause et al. **202**. Proceedings of Machine Learning Research. PMLR, 2023 11734–11760.

[24] A. K. Dubey and V. Jain: "Comparative Study of Convolution Neural Network's Relu and Leaky-Relu Activation Functions", in: *Applications of Computing, Automation and Wireless Systems in Electrical Engineering*. Ed. by S. Mishra, Y. R. Sood, and A. Tomar. Singapore: Springer Singapore, 2019 873–880.

[25] S. R. Dubey, S. K. Singh, and B. B. Chaudhuri: "Activation functions in deep learning: A comprehensive survey and benchmark", *Neurocomputing* **503**, 92–108 (2022). DOI: 10.1016/j.neucom.2022.06.111.

[26] G. E. Hinton and R. R. Salakhutdinov: "Reducing the dimensionality of data with neural networks", *Science* **313**, 504–507 (2006). DOI: 10.1126/science.1127647.

[27] W. Lopez Pinaya et al.: "Autoencoders", in: *Machine Learning*. Netherlands: Elsevier, 2019 193–208. ISBN: 9780128157398. DOI: 10.1016/B978-0-12-815739-8.00011-0.

[28] E. R. Ardelean et al.: "A study of autoencoders as a feature extraction technique for spike sorting", *PLoS ONE* **18** (2023). DOI: 10.1371/journal.pone.0282810.

[29] L. Le, A. Patterson, and M. White: "Supervised autoencoders: Improving generalization performance with unsupervised regularizers", in: *Advances in Neural Information Processing Systems*. Ed. by S. Bengio et al. **31**. Curran Associates, Inc., 2018.

[30] I. Goodfellow, Y. Bengio, and A. Courville: "Deep Learning", http://www.deeplearningbook.org. MIT Press, 2016. ISBN: 9780262035613.

[31] R. Dwivedi et al.: "Explainable AI (XAI): Core Ideas, Techniques, and Solutions", *ACM Comput. Surv.* **55**(9) (2023). DOI: 10.1145/3561048.

[32] A. Jain and D. Zongker: "Feature selection: evaluation, application, and small sample performance", *IEEE Transactions on Pattern Analysis and Machine Intelligence* **19**(2), 153–158 (1997). DOI: 10.1109/34.574797.

Part IV

Results and discussion

OCT and PS-OCT measurements of dystrophic mice muscles

6

6.1 Samples description

Most of the measurement and analysis of the samples, especially at the early stages of this work, focused on OCT and PS-OCT measurements. As such, the sample dataset analyzed with these techniques is the most complete out of all the imaging modalities. The datasets are described in this section, but all imaging modalities will refer to these datasets when indicated.

All samples analyzed in this work are from α-sarcoglican deficit model mice. Sarcoglycans, which connect the cell membrane to the cytoskeleton, help maintain internal muscle stability. Alterations in the sarcoglycans can lead to Limb-girdle muscular dystrophy (LGMD) or Myofibrillar myopathies (MFM) (see Ch. 1).

Two muscle datasets and one whole legs dataset are used in this book, all originating from and validated by Hospital de la Santa Creu I Sant Pau and by the John Walton Muscular Dystrophy Research Centre. The samples are identified as control samples, coming from wild-type (WT) mice, while the dystrophic ones have the knock-out (KO) identification. Samples are identified with a number related to the mouse from which they came. If two samples share the same number, it means they come from the same animal. The letter that accompanies the muscles, when present[1], indicates the muscle that the sample is (C: quadriceps, TR: triceps, B: biceps, D: diaphragm, or GC: gastrocnemius). Any other letter indicates that more than one quadriceps was measured for the same mouse.

[1] If no letter is written next to the sample ID number, it means that the sample is a quadriceps.

The first dataset is composed of 17 samples (Fig. 6.1), of which 4 are muscle samples of WT and 13 KO mice, executed at different ages. The ages of the controls was not considered in this dataset. Most samples were quadriceps, with the exception of those of the one-month-old (KO-1mo) mouse. The complete description is in table 6.1. This dataset receives the name of *Muscle Dataset 1* or *MD1*.

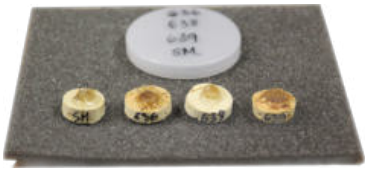

Figure 6.1: Control samples of MD1 after defrosting.

The second dataset contains 26 samples of only quadriceps, with a total of 13 WT and 13 KO samples. The samples in this dataset have varying ages, coming from mice executed at 3, 7, 8, 9, 11 or 12 months old. The complete description is in table 6.2. This dataset receives the name of *Muscle Dataset 2* or *MD2*.

Additional whole-leg samples were received and measured (Fig. 6.2), but due to their different nature, they are considered and analyzed as their own dataset. The *Leg Dataset* (LD), comprised of one of the whole legs of mice 814, 895, and 896, see Tab. 6.2) where measured after retracting the skin to expose the muscle and other tissues like fat and leg fasciae.

Figure 6.2: Leg of sample 742 of LD before defrosting. The left leg's quadriceps is included in MD2.

The samples were received frozen in dry ice and fixed to a cork base of 2.2 cm in diameter, and their size ranged between 3 mm to up to 1 cm (Fig. 6.1). The samples were kept at -50 ° until they were measured.

Table 6.1: Samples description for the dataset MD1. The number is an indicator of the animal, meaning that the same number in the sample ID indicates that the sample comes from the same mouse. In KO-1mo, all samples were from the same mouse, and the letters indicate the sample type, i.e., the muscle group they come from. In KO-3mo, two quadriceps were received from the same mouse, identified with different letters. In parentheses, *F* indicates Female, *M* indicates Male, and the suffixes *mo* and *yo* are month-old and year-old, respectively.

	Controls (WT)	Dystrophic, 1 month old (KO-1mo)	Dystrophic, 3 month old (KO-3mo)	Dystrophic, 6 month old (KO-6mo)
Samples	4	5	5	3
Sample type	Quadriceps	Quadriceps (C), Triceps (TR), Biceps (B), Diaphragm (D), Gastrocnemius (GC)	Quadriceps	Quadriceps
Sample ID	SM, 636, 638, 639	731-TR, 731-B, 731-C, 731-D, 731-GC	774-A, 774-B, 878, 883, 885, 886	809, 810, 811

For defrosting, first, they were changed to a -18 ° freezer for one hour, followed by storing them in the refrigerator at +3 °. Then, they were

Table 6.2: Samples description for the dataset MD2. The whole leg samples in LD (814, 895, 896) come from the mice with the same number in dataset MD2.

	Controls (WT)	Dystrophic (KO)
Samples	13	13
Sample type	Quadriceps	Quadriceps
Sample ID	520 (F, 1yo), 536 (M, 10mo), 540 (M, 11mo), 548 (M, 11mo), 595 (M, 8mo), 805(M, 3mo), 808 (M, 3mo), 814 (M, 11mo), 861 (M, 3mo), 862 (M, 3mo), 863 (M, 3mo), 895 (M, 1yo), 896 (M, 1yo)	531 (M, 10mo), 534 (F, 10mo), 545(M, 10mo) 564 (M, 9mo), 565 (M, 9mo), 578 (F, 8mo), 581 (F, 8mo), 621 (M, 7mo), 628 (F, 7mo), 741 (M, 1yo), 742 (M, 1yo), 867 (F, 3mo), 870 (F, 3mo)

taken out of the fridge to rest one additional hour at ambient temperature before measurement. For the samples in dataset MD1, all samples were measured on the same day, meaning that some stayed refrigerated for longer than others. In contrast, samples in the remaining datasets were measured on different days to minimize the variance in the storage conditions between samples.

6.2 Overview of the measurements

It is helpful to explore the raw OCT data to aid in the interpretation of the following sections. Here, one healthy sample of the first dataset, MD1, was used to represent the general behavior of any healthy sample.

In general, the average A-scan (Fig. 6.3, a) has a sharp peak right on the surface of the sample due to a combination of Fresnel reflection at the surface and the existence of specular reflections that saturate the detector. The latter appear on regions of the sample that are perpendicular to the beam, where the reflection is maximized, and often in low-scattering areas, like water deposits. After the peak, the exponential decay follows the Beer-Lambert law (Eq. 4.16)[2]. As the light goes past the single-scattering region, the Beer-Lambert law approximation is no longer valid, and light is scattered and absorbed faster.

[2] Note that the vertical axis on Fig. 6.3 (a) is in logarithmic scale, so that the Beer-Lambert law is transformed as line $\log(I_0) - 2\mu_z z \log e$.

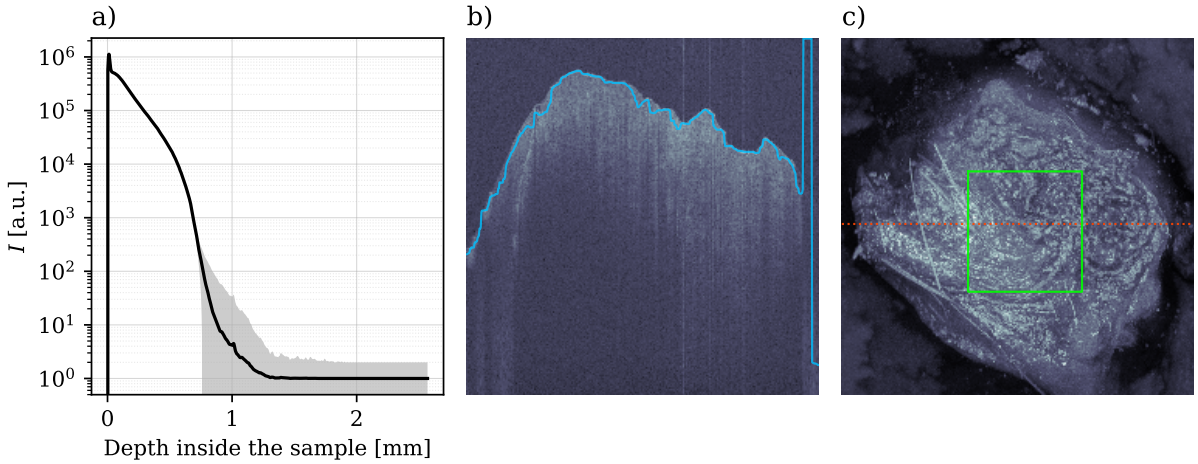

Figure 6.3: Detail on the data for the control sample 636 of MD1. (a) Average A-scan (solid line) and standard deviation (shaded area) of the sample. (b) Central B-scan of the sample with its surface detected in blue. (c) MIP with the B-scan of (b) marked in red and the area chosen for the average and standard deviation in (a) marked in green.

The intensity decay inside the sample is not homogeneous (Fig. 6.3, b). There are denser areas that extinguish the light closer to the surface than others. Consequently, deeper regions in the sample have fewer A-scans with intensity higher than the noise floor, so the standard deviation increases with the penetration depth (Fig. 6.3, a).

The MIP is the OCT equivalent to a regular grayscale camera image - it shows the sample as viewed from above. This representation is helpful in determining different regions in the sample. Surface features, like the hairs visible in Fig. 6.3, (c), hinder the proposed surface detection algorithm enough to cause a mismatch between the real and the calculated surface of a sample of a few pixels. However, this mismatch never goes beyond the single scattering region, leaving enough pixels to fit the A-scans to the models. Additionally, artifacts are visible in the detected surface where there is no sample or where its intensity is very low (Fig. 6.3, b). Still, those areas are not considered for calculations after selecting the region of interest of each sample since they are barely visible in the MIP.

Some samples had higher first reflection intensity peaks than others (Fig 6.4). Since the attenuation coefficient μ_z is derived from the intensity of the A-scans as the slope of the logarithmic version of the Beer-Lambert law, only data inside the sample, i.e., beyond the peak, must be considered. Experimentally, the first reflection peak was within the first 5 px (≈ 13 μm) of the A-scan, so the fit to the single-scattering region was done from the first 10 px (≈ 25 μm) and up to 250 px (≈ 250 μm), where the single scattering dominates [1].

Additionally, some samples have higher variances in their A-scans that start earlier in the sample, particularly those with initially lower intensities. Without considering the initial peaks, each sample has different slopes, meaning that each sample will provide a different attenuation value. The healthy samples (WT in Fig. 6.4, b) had similar average slopes, while more inter-sample variation is observed in the dystrophic ones (KO in Fig. 6.4, b). The following regions provide further details on this topic.

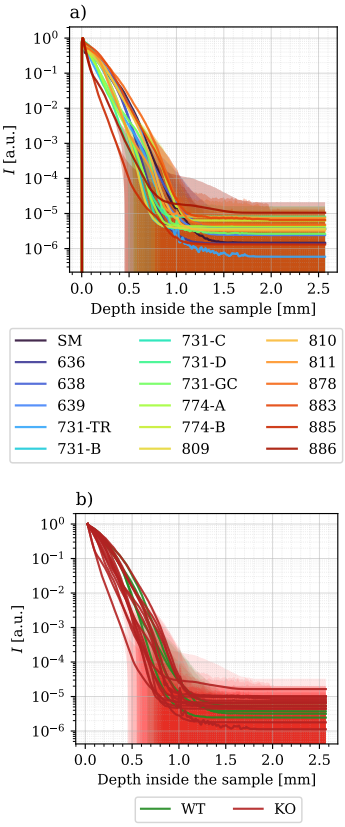

Figure 6.4: Average A-scan and standard deviation of the samples in dataset MD1, colored by sample (a) and by sample state (b). The data has been normalized to the intensity peak.

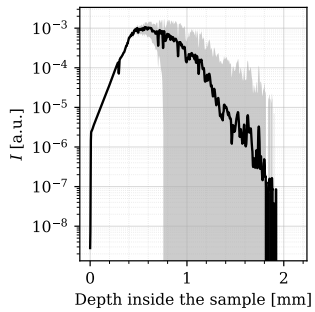

Figure 6.5: Average A-scan and standard deviation of the control sample 636 in dataset MD1 calibrated with the reference phantom. The non-calibrated intensity is shown in Fig. 4.4, (a).

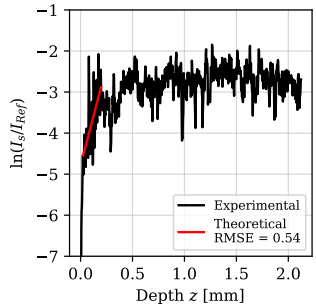

Figure 6.6: Example of one A-scan in the control sample 636 (black) with the result predicted by the model (Eq. 4.23). The fit region is selected to be located inside the single-scattering region.

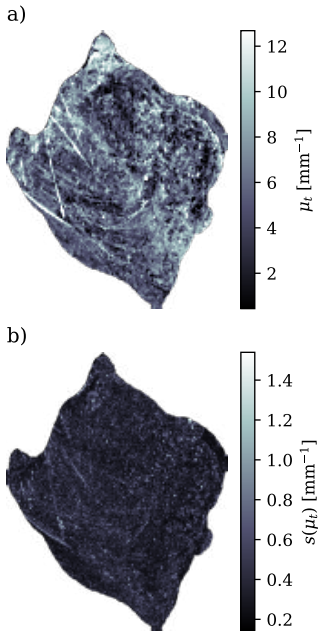

Figure 6.7: Attenuation μ_t (a) and its uncertainty (b) for sample 636 predicted by the model (Eq. 4.23).

6.3 Introduction of the calibration phantom

To find the attenuation, the intensity of the samples was calibrated against a phantom with known properties, as explained in Chapter 4. The initial light decay model for the logarithmic intensity of a sample, $\ln(I_s)$, with attenuation coefficient μ_t is given by the Beer-Lambert law (Eq. 4.17)

$$\ln(I_s) \propto -2\mu_t Z \quad .$$

The calibration of the intensity involves dividing the sample's intensity, I_s, by the intensity of a reference phantom, I_{ref}, with reference attenuation coefficient $\mu_{t,ref}$ so that the Beer-Lambert law is modified as

$$\ln\left(\frac{I_s}{I_{ref}}\right) \propto -2z(\mu_t - \mu_{t,ref}) \quad .$$

This second equation can now have positive values in regions where the attenuation of the phantom is higher than that of the sample (Fig. 6.5). The resulting calibrated logarithmic data showcases a much more linear behavior than its non-calibrated counterpart (Fig. 4.4), meaning that a significant part of the apparent initial deviations from the Beer-Lambert model come from the loss of sensitivity of the system along the z axis, instead of from the sample. The introduction of the calibration phantom mitigates these deviations.

6.4 Attenuation

Following the previous section, the samples were calibrated with the measurements from a controlled phantom to obtain the attenuation μ_z, the proportionality parameter A, and the MSE via least squares fitting. The uncertainty of the parameters was obtained from the covariance matrix as well.

Fig. 6.6 shows the fit result on one of the control samples. The fit region was chosen inside the single scattering region given, approximately by $z \leq 250\mu m$ [1]. After calibrating the sample, the single scattering region manifests itself as a linear portion of the calibrated A-scan. Once the system starts detecting less signal, either because it is getting extinguished by the sample or because it is too deep in the sample, the linear region disappears just outside the single scattering area. Having a positive slope on the calibrated data is an indicator of the attenuation coefficient of the sample being smaller than that of the reference phantom.

The resulting attenuation is, in general, not homogeneous across the sample, even if its uncertainty is (Fig. 6.7). Areas with high attenuation in this image correspond to the areas with less light penetration in the B-scan shown in Fig. 6.3. This showcases the existence of variations in attenuation and scattering inside the sample, i.e., of structural and chemical changes that can be taking place. Kylen *et al.* [2] explored the attenuation coefficient in healthy mice muscle samples and revealed that, even in this ideal case, the attenuation coefficient as obtained with OCT imaging is subject to spatial variations, given the orientation change in the myofibers of the muscle. Regardless of the orientation of the sample

in the system, the myofibers are not arranged in "layers" and, therefore, there is no orientation to set the muscle in that has the myofibers running perfectly perpendicular to the OCT beam. The attenuation of all samples in datasets MD1 and MD2 is represented in figures 6.8 and 6.9.

Kylen *et al.* [2] also analyzed dystrophic mice samples in their work from a different mouse model, the *mdx* mouse model, which introduces a mutation in the DMD gene. The OCT attenuation results after choosing known areas in their samples with and without necrotic lesions revealed that non-necrotic regions (i.e., intact myofibers) had an average of μ_t = 3.7 ± 1.1 mm^{-1}. In contrast, necrotic areas showed attenuation of μ_t = 10 ± 0.07 mm^{-1}. The threshold that separates the attenuation of necrotic and non-necrotic fibers is 7.5 mm^{-1} [2].

The majority of the data points of the control samples in dataset MD1 have attenuation values below the necrotic fiber threshold (Fig. 6.10, a). However, most of the KO samples are below the threshold as well, with the exception of those from the 1-month-old KO mouse (731). Interestingly, these younger dystrophic samples have data above the threshold while being different muscles, which indicates a whole-body distribution of the muscular disruption. Similar results are obtained for the dataset MD2 (Fig. 6.11), but better separation is achieved between the overall distribution for wild-type and knock-out samples (Fig. 6.11, c). The fact that all samples in dataset MD2 are the same type of sample (quadriceps) and that the classes are balanced[3] might contribute to the better separability than for MD1. Training an SVM to obtain the threshold between classes yielded a necrotic threshold of $\mu_t = 5.22 mm^{-1}$, with significant overlap between classes (60% accuracy[4]).

The difference in attenuation with respect to the threshold provided by Kylen *et al.* could be due to the samples in the α-sarcoglycan deficient mice exhibiting a lower degree of necrosis than expected or compared to Duchenne's model samples. This suggests that the disease progression or the severity of muscle damage in this particular model might be less pronounced. Additionally, the threshold the authors provide is based on small regions of interest taken in healthy and necrotic muscle areas of treadmill-exercised DMD model mice and validated by evaluating the attenuation over and below the threshold for different samples using H&E as a gold standard. Here, the regions depicted are much bigger in size, with the samples ranging from 3 to 8 mm laterally, so a significant part of the variance may come from different levels of deterioration within the same muscle. There could be areas in the samples with various compositions and structures, i.e., fatty infiltrations or edema, that contribute to the overall spread of attenuation values in each sample.

Now, let us focus on some specific samples that showcase variation at different stages of the disease. For example, let us take the WT sample *SM*, the KO-3mo *774-A* and the KO-6mo *810*.

The healthy sample (*SM*), shown in the first row of Fig. 6.12, had an interesting region in the center with lower attenuation (Fig. 6.12, b) that its surroundings. Upon evaluation of the reference RGB image, the OCT system takes to help position the samples, it was seen that this control sample had a fatty protuberance right where the attenuation was detected as lower by the model that uses the reference phantom (Eq. 4.23, a).

[3] Dataset MD2 has the same number of samples in each class and the data points have been randomly sampled from each muscle so that all have the same number of values.

[4] Note that this classifier was not trained to be used as a classifier, i.e., no measures have been taken to avoid data leakage between samples and no cross-validation has been considered. This classification aimed to provide a separation threshold between the wild-type and knock-out categories as there is significant overlap between distributions to compare it directly with the bibliography.

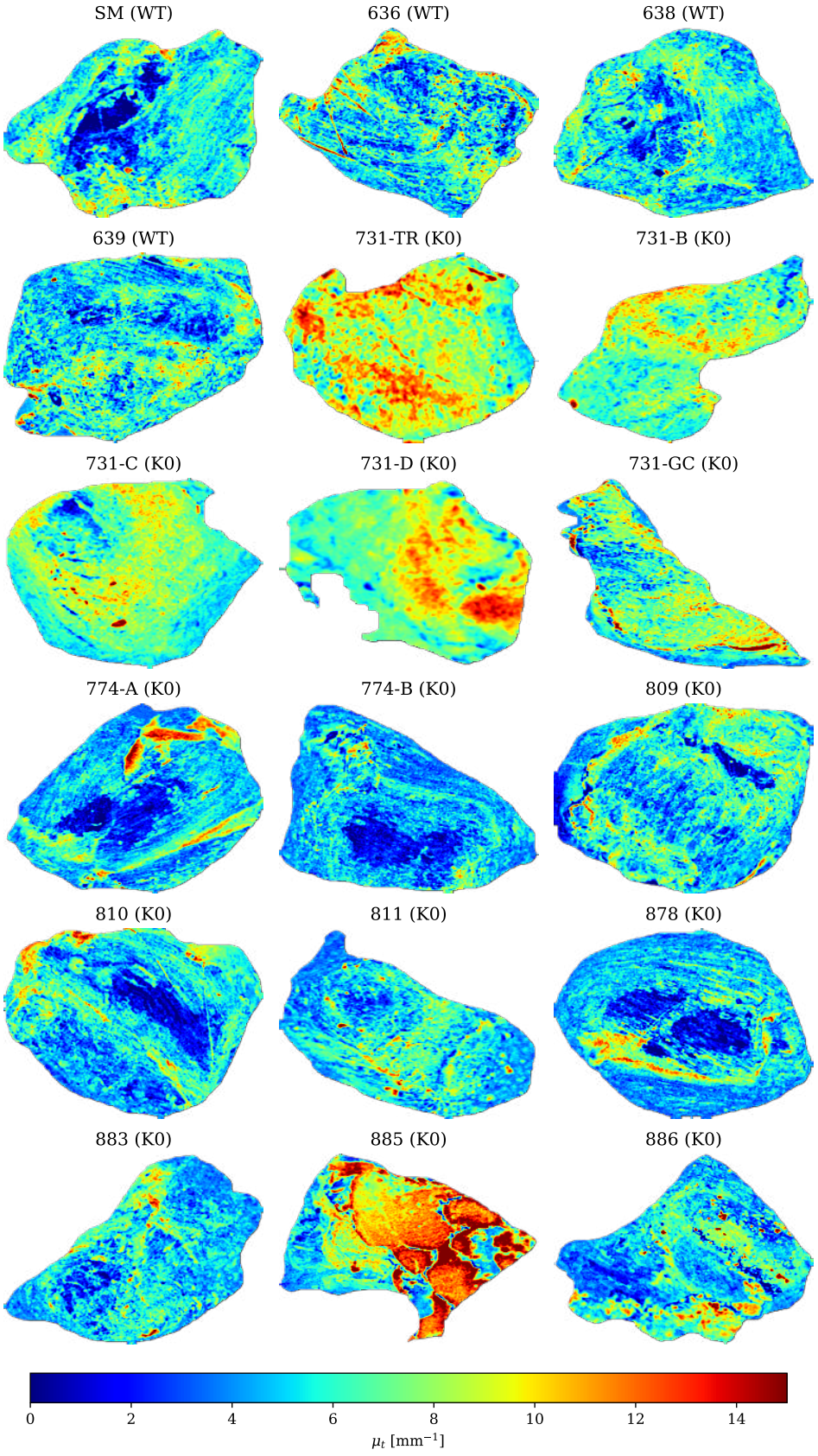

Figure 6.8: Attenuation of all samples in dataset MD1. The first four are the control (WT) samples (SM, 636, 638, 639), and the rest are dystrophic (KO) samples. Best viewed in pdf.

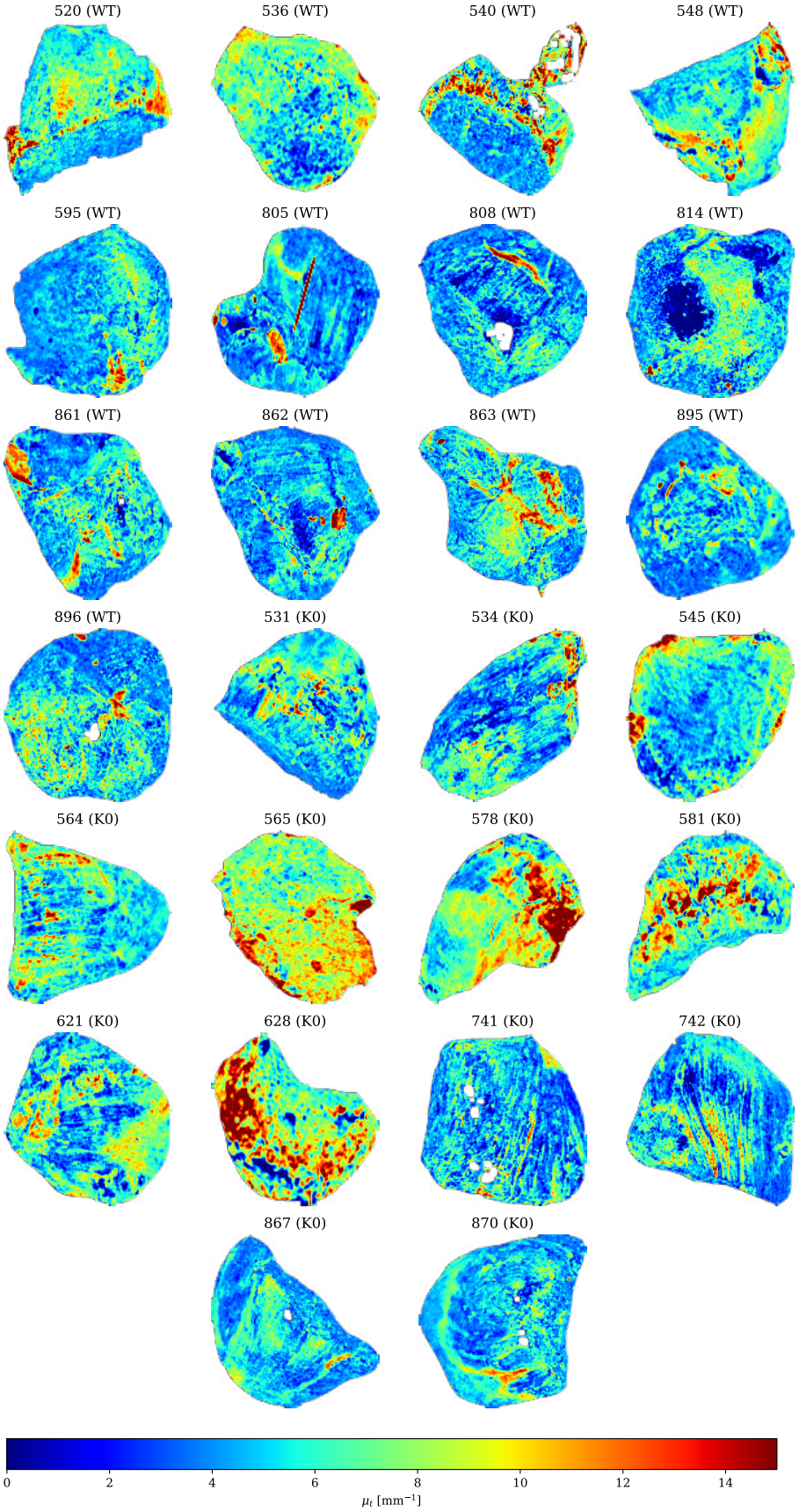

Figure 6.9: Attenuation of all samples in dataset MD2. The first 13 samples are control (WT) samples, while the rest are dystrophic (KO) ones. Best viewed in pdf.

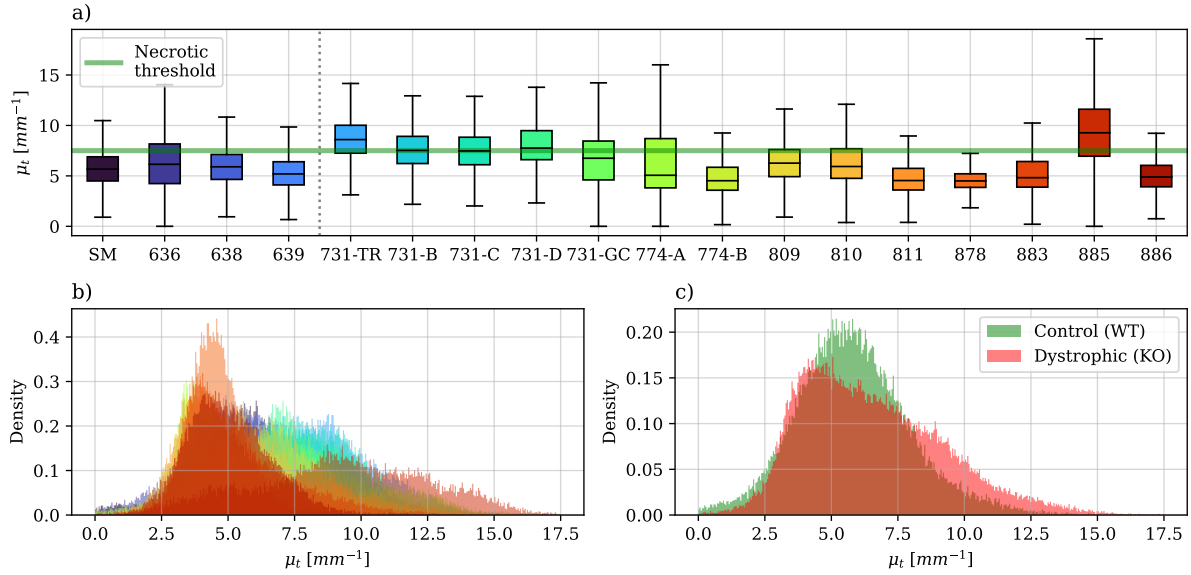

Figure 6.10: Attenuation boxplots (a) and distributions (b and c) of the samples in MD1. The data is colored by sample (a and b) or by sample state (c). The dotted vertical line separates wild-type samples (left) from knock-out ones (right). The depicted necrotic threshold has been obtained from Kylen *et al.* [2] to compare it with our results ($\mu_t = 7.5mm^{-1}$).

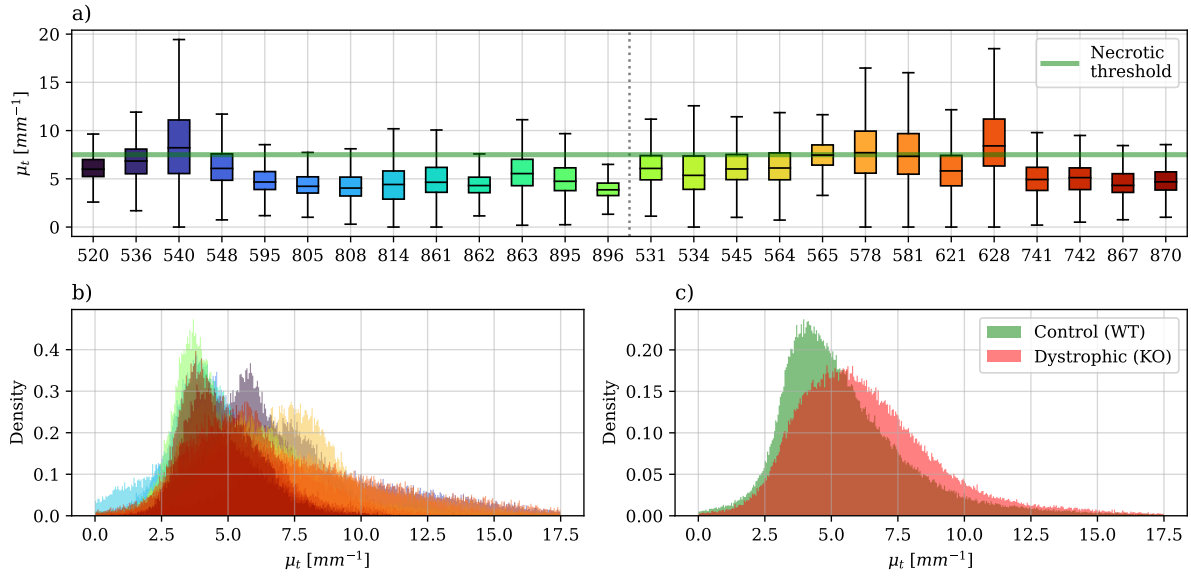

Figure 6.11: Attenuation boxplots (a) and distributions (b and c) of the samples in MD1. The data is colored by sample (a and b) or by sample state (c). The dotted vertical line separates wild-type samples (left) from knock-out ones (right). The depicted necrotic threshold has been obtained from Kylen *et al.* [2] to compare it with our results ($\mu_t = 7.5mm^{-1}$).

The KO samples, shown in the next two rows of the same figure (Fig. 6.12), also have areas with contrasting attenuation values.

To better understand the tissue changes, column (c) in Fig. 6.12 shows the (log-scaled) B-scan that passes through the different attenuation areas in the sample. Light extinction in the fatty region of the WT sample (first row in Fig. 6.12) seems higher than in the surrounding muscle, meaning that it appears that light reaches more profound points in the latter. This penetration change appears to be confirmed by the localized attenuation (Eq. 4.26) shown in the fourth column of Fig. 6.12, where regions with

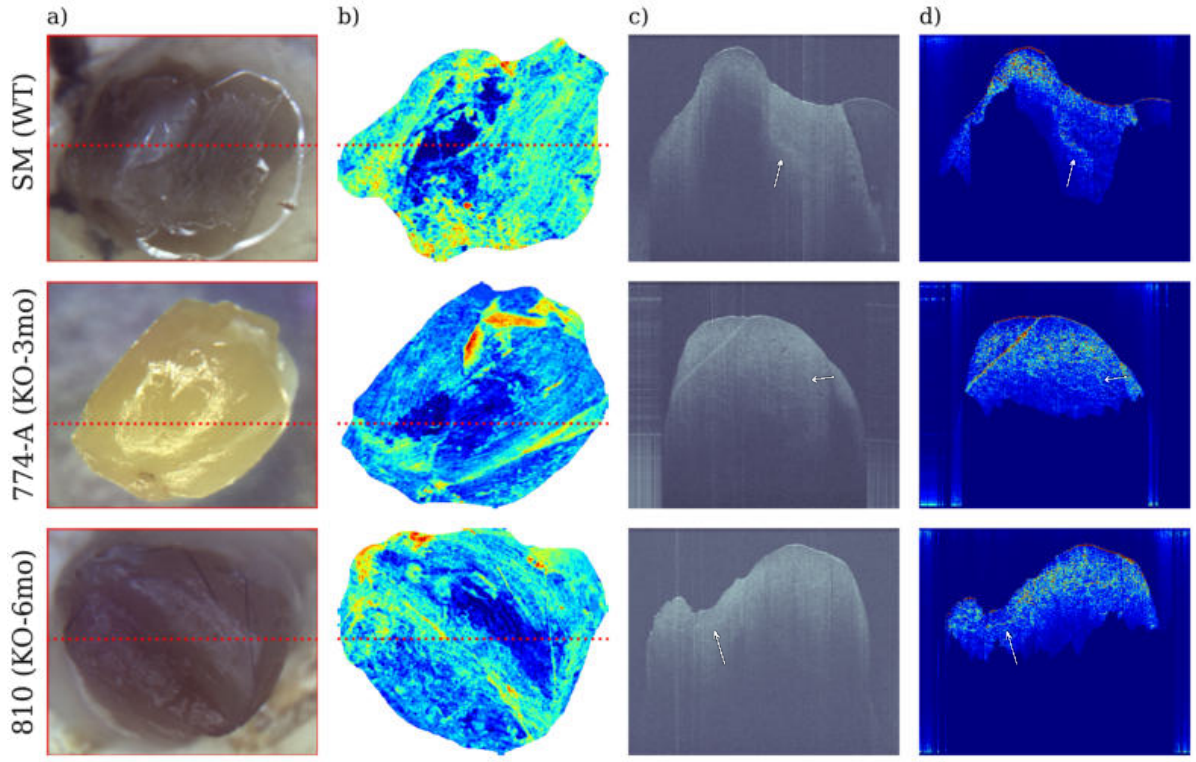

Figure 6.12: Reference RGB image (a), attenuation derived from the phantom-calibrated data (b), B-scans (c), and localized attenuation derived from the raw data (d). The first row is the WT sample *SM*, followed by the KO-3mo *774-A* in the second row, and the KO-6mo *810* in the last row. The B-scans in (c) and (d) are marked by a red, dotted horizontal line in the RGB image. The localized attenuation maximum (d) was three orders of magnitude smaller ($\approx 10^{-}3\ \mathrm{mm}^{-1}$) than the cumulative effect seen in the second column (b). The arrows point to sub-structures highlighted by (d) on the corresponding regions in (c).

shallower light penetration show higher localized attenuation than others. Even though the localized attenuation was as low as $10^{-4}\ \mathrm{mm}^{-1}$ due to the small penetration depths considered in each step of the calculations, it helped enhance structures that are barely visible in the corresponding B-scan, like the very subtle intensity changes indicated by the white arrows in 6.12.

Other easily located changes in the intensity are also highlighted by the localized attenuation. In sample 774-A, the darker area visible in the en-face attenuation image shows a line underneath it in the B-scan. This line, which marks where two muscular regions with different fiber orientations overlap, has a localized attenuation as high as the surface of the sample itself, meaning that this interface is affecting the light extinction as much as a refractive index change from air into the sample.

Evaluating the samples by using multiple models helps interpret their structure. The darker areas that are marked as less attenuating by the phantom-calibrated model are distinguished as more attenuating by the localized attenuation model. The main differentiating factor is the penetration depth considered by each model. While the former (Eq. 4.23) considers all the information within the single-scattering region, which translates to approximately 80 px from the surface of the sample, the localized model (Eq. 4.26) does not have this limitation. This is especially notable in the areas where the highest intensity is not right at the surface of the sample but slightly beneath it, which indicates that

the phantom-calibrated model might not be reaching the deeper areas of the higher signal. Additionally, the phantom-calibrated model requires surface detection, which is prone to artifacts due to specular reflections, uneven surfaces, and liquid deposits in biological samples. In contrast, the localized model starts at the limit of detection given by the noise floor and is calculated up to the top of the OCT 3D cube, meaning that surface detection is not required.

Although the localized model poses several advantages over the phantom-calibrated one, we have seen in previous chapters that (1) scattering at IR wavelengths[5] is negligible with respect to the attenuation, and that (2) the absorption of fat is one order of magnitude less than that of water, collagen, and elastin, the main components of muscle (see Fig. 4.7). These two facts suggest that the attenuation of the phantom-calibrated model might be more accurate in terms of the value of the actual optical properties of the samples than the localized model.

Regardless of the magnitude of the attenuation, both models are able to detect the change in the backscattering properties due to the sample's internal heterogeneity. Even if the data introduced to obtain the attenuation maps is different (one is calibrated with the phantom and the other is not), using both models together is the best way to gain a deeper understanding of the samples. The phantom-calibrated model points at the areas with different compositions and/or structures with the sample as seen from above, which then can be taken as a slice in the form of a B-scan and *tinted* with the localized attenuation model to search for internal features as one would in histopathology slides, providing a greatly contrasted image without needing to perform any invasive procedure on the sample.

Finally, there was one sample that stood out of all of them due to its complex attenuation pattern, which was the KO-3mo sample *885* from dataset MD1 (Fig. 6.13). This sample had a dermal-like layer fused to its surface that had significantly higher attenuation, as provided by both models. Not only did the models agree on the muscle and this extra layer, but the localized model behaved almost like a layer detection algorithm, with the higher attenuation areas matching the thickness of this additional tissue.

[5] As mentioned in earlier chapters, the OCT system used for these experiments works at 1300 nm.

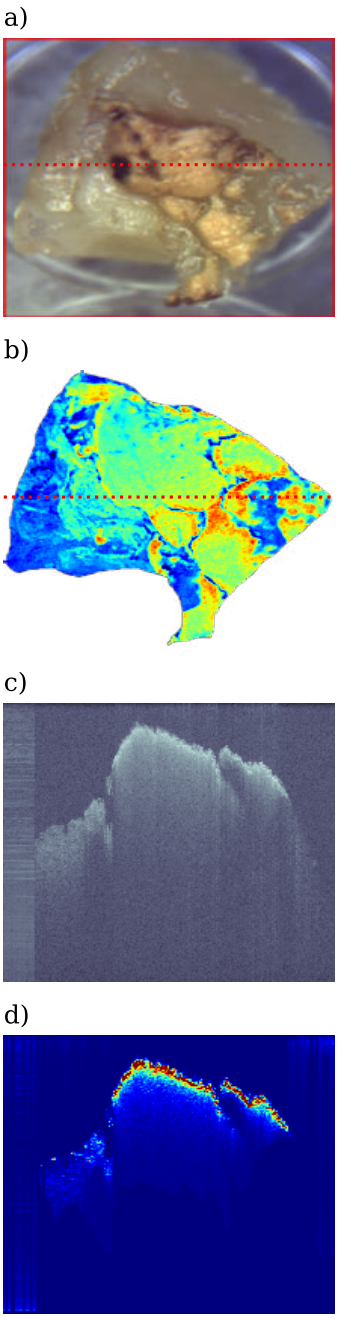

Figure 6.13: Reference RGB image (a), phantom-calibrated attenuation (b), B-scan (c) and localized attenuation (d) of the KO-3mo sample *885*. The B-scan shown in (c) and (d) is marked as a red, dashed horizontal line in (a) and (b).

6.5 Stokes parameters

After evaluating the amplitude decay of light through the attenuation coefficient, it is useful to explore what occurs with the phase through the Stokes parameters. As a brief reminder, the Stokes parameters represent the description of the light state polarization. Figure 6.14 shows the four stokes parameters for the same control sample that was used to depict the data captured by the OCT system (Fig. 6.3).

The first parameter, S_0 (or I), corresponds to the intensity images depicted in the previous section. The next two Stokes parameters, S_1 and S_2, represent the ratio of horizontally to vertically polarized light and +45° to +135° polarized light, respectively. Finally, the last parameter S_3 represents the amount of left and right polarized light.

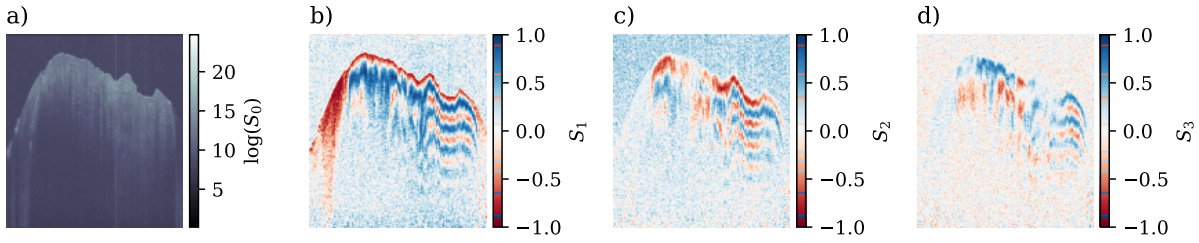

Figure 6.14: Stokes parameters of the B-scan shown in Fig. 6.3 of the WT sample 636 (MD1).(a) $S_0 = I$, (b) $S_1 = Q$, (c) $S_2 = U$, and (d) $S_3 = V$.

Every parameter other than the intensity shows a structure of periodical variations in some regions of the samples. This kind of periodicity is visible in anisotropic tissue like chordae tendinae [3], which indicates the consistency in the orientation of the internal muscle fibers.

From these magnitudes, it is at this point understood that the internal spatial variation of the Stokes parameters will yield different birefringence values corresponding to varying levels of tissue anisotropy (i.e., tissue organization) both between samples and inside each sample.

6.6 Birefringence

As introduced in the previous chapter, the phase obtained from the Stokes vector can be used to derive the birefringence of the sample. Similarly to the attenuation, the birefringence is obtained as *en face* maps by fitting the data up to a specific depth in the sample. The method to derive the birefringence [4] involves several steps, including finding the cumulative phase between the Stokes vector at the surface of the sample and the vector at some depth z (Fig. 6.15, a). This phase (ϕ_c) grows periodically from $-\pi$ to π and then has a discontinuity in the form of a jump to the next $-\pi$ to π period. By unwrapping the phase to obtain ϕ_u (Fig. 6.14, b), the phase is transformed into a monotonically growing slope. Notice that even beyond the single-scattering limit, which approximates 80 pixels deep in the sample, the phase is detectable up to the point where there is no signal. To perform the linear fitting required to obtain the birefringence, only the first two periods are considered to avoid the deeper, noisier phase due to the loss of SNR. In the regions where the tissue anisotropy is high, less than one period is often detectable, so in those cases, the signal is considered up to the noise floor. The resulting birefringence of all samples in datasets MD1 and MD2 is represented in figures 6.16 and 6.17, respectively. Both images help visualize the aforementioned spatial variation in the birefringence.

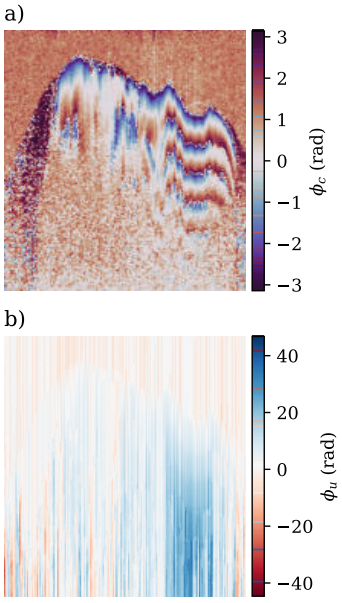

Figure 6.15: Cumulative phase ϕ_c and unwrapped phase ϕ_u as obtained from the method proposed in [4] for the WT sample in Fig. 6.14.

Yang *et al.* [5] explored the birefringence of dystrophic samples in the same model that Kylen *et al.* used for the attenuation (mdx model). In the work by Yang *et al.*, following a similar protocol to that of Kylen *et al.*, the PS-OCT-derived birefringence in selected areas in their samples with and without necrotic lesions revealed a birefringence threshold of $\Delta n = 5 \cdot 10^{-3}$ that separate necrotic and non-necrotic fibers, with healthy samples showcasing values over the threshold, and necrotic regions underneath it [6].

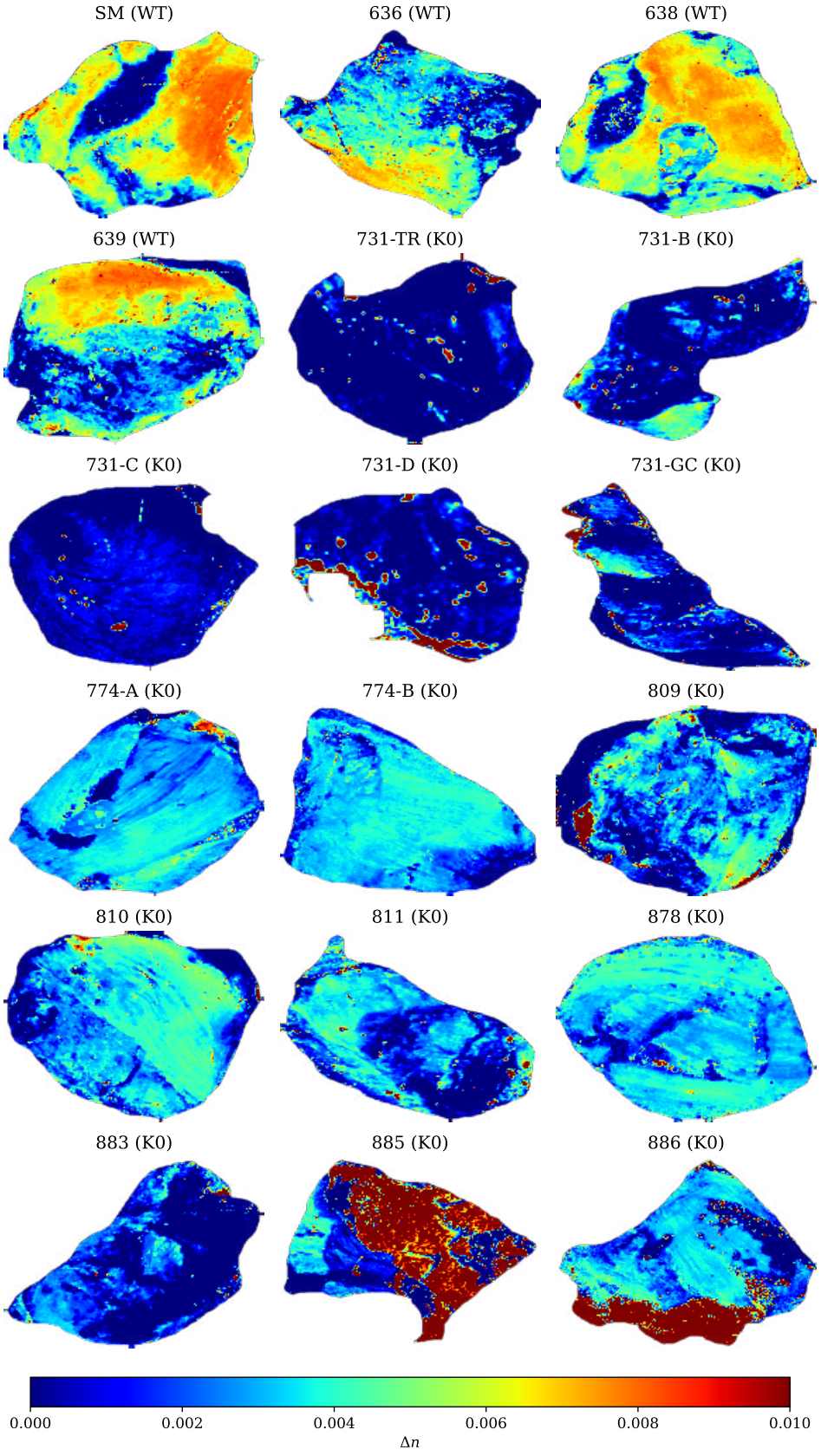

Figure 6.16: Birefringence of all samples in dataset MD1. The first four are the control (WT) samples (SM, 636, 638, 639), and the rest are dystrophic (KO) samples. Best viewed in pdf.

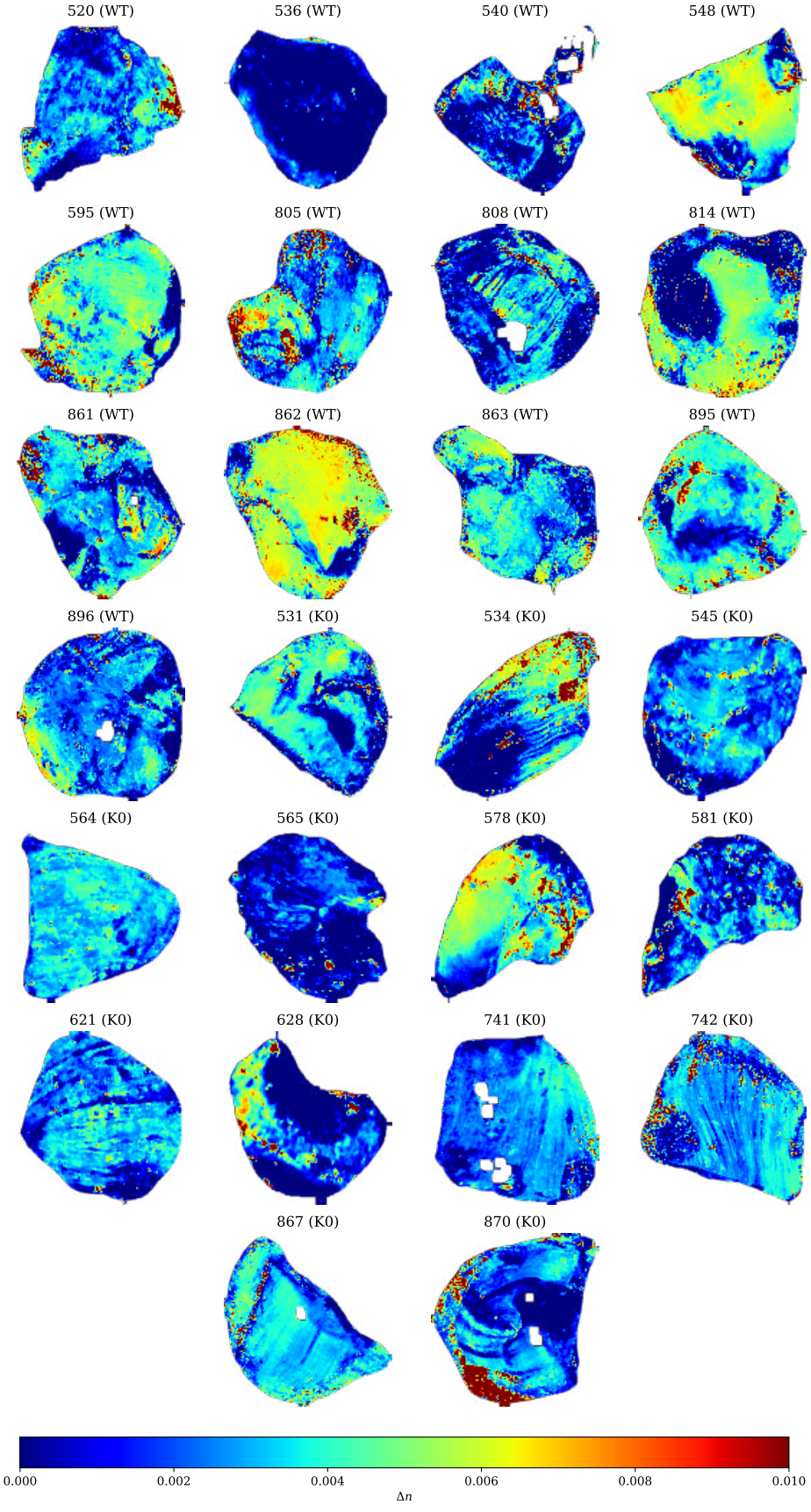

Figure 6.17: Birefringence of all samples in dataset MD2. The first 13 samples are control (WT) samples, while the rest are dystrophic (KO) ones. Best viewed in pdf.

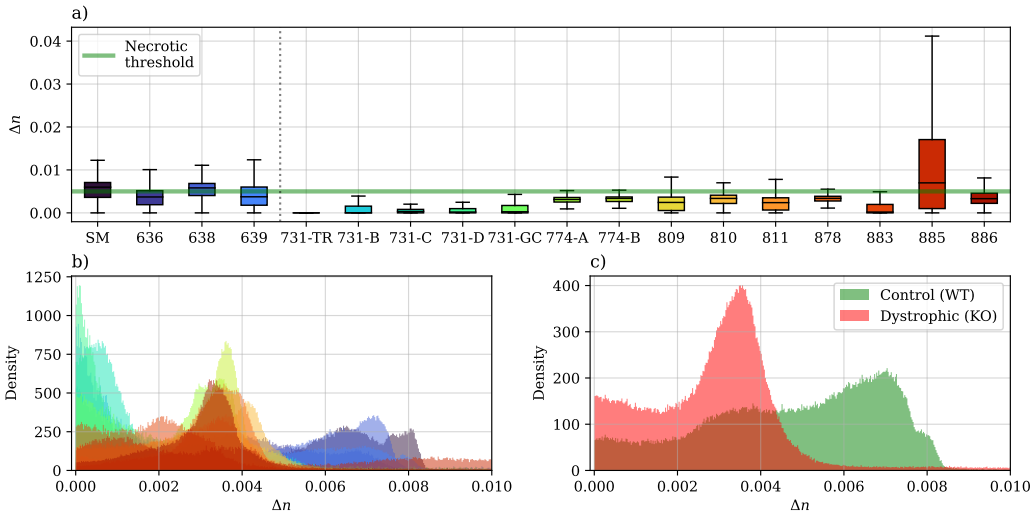

Figure 6.18: Birefringence boxplots (a) and distributions (b and c) of birefringence of the samples in MD1. The data is colored by sample (a and b) or by sample state (c). The dotted vertical line separates wild-type samples (left) from knock-out ones (right). The depicted necrotic threshold has been obtained from Yang *et al.* [5] ($\Delta n = 5 \times 10^{-3}$) to compare it with our results.

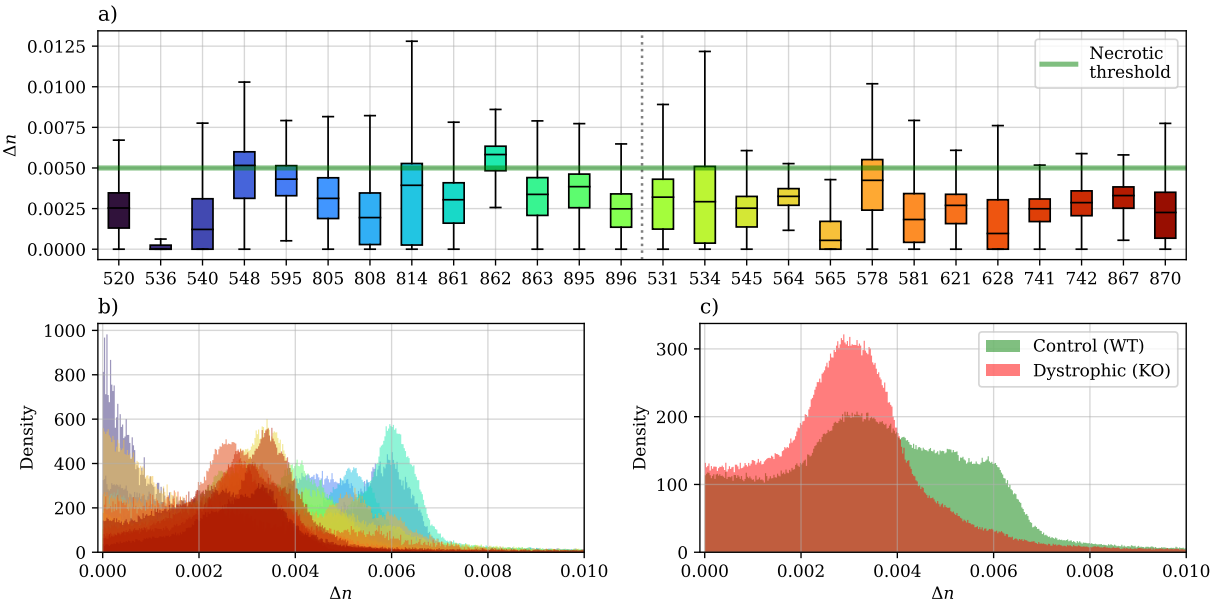

Figure 6.19: Birefringence boxplots (a) and distributions (b and c) of birefringence of the samples in MD1. The data is colored by sample (a and b) or by sample state (c). The dotted vertical line separates wild-type samples (left) from knock-out ones (right). The depicted necrotic threshold has been obtained from Yang *et al.* [5] ($\Delta n = 5 \times 10^{-3}$) to compare it with our results.

As occurred for the attenuation, there is a high variation of birefringence values between and inside each muscle. In the dataset MD1, all dystrophic samples had birefringence values under the necrotic threshold, which indicates a lower level of tissue anisotropy than for the healthy samples (Fig. 6.18), even for those samples where the attenuation was over its corresponding threshold. Similarly, for dataset MD2, the only samples that surpassed the necrotic threshold were wild-type samples. However, in the latter, and control samples had more values beneath the threshold than MD1, which could be caused by the higher variability that comes with having more samples or by using the the same type of sample (quadriceps only in MD2).

Even so, these results suggest that birefringence can be a better marker

of dystrophy than attenuation. The latter is affected by chemical changes that can start occurring at a small enough scale to not be detectable with OCT due to its resolution. However, these chemical changes will break the perfect alignment in the microstructure of the fibrous muscle cells. Even if the micro-structural changes are not individually visible by this technology, a broken anisotropy will change the polarization properties of light, which is detected through the change in birefringence.

The only KO sample in MD1 that had values over the threshold, and even over the values of healthy samples, was sample 885, which, as we have already seen, has a layer of epidermal-like tissue on its surface, which skews the distribution towards higher values, while the muscle itself is below the dystrophic threshold (Fig. 6.16). Additionally, the samples that had the highest attenuation in MD1 (KO-1mo) also have the lowest birefringence, which is a good indication that those samples, even being the youngest of both datasets, are the ones with the highest presence of diseased tissue. A possible explanation could be that the youngest KO mouse has their muscle fibers break due to the disease, but also due to their natural growing process that stabilizes as the mouse reaches a more mature age. For DM2, only six samples reach the necrotic threshold with their interquartile ranges (534, 548, 578, 595, 814, 862) (Fig. 6.19). Their corresponding *en face* birefringence maps also showcase the high variability across the muscles (Fig. 6.17). In dataset MD2, the only sample that significantly reached the dystrophic threshold was sample 578 and, in this case (Fig. 6.17), it is muscle tissue that provides the high value, suggesting that even in dystrophic specimens, some variability may arise between samples.

Birefringence maps are also valuable for showing muscle fiber directionality. A great example is shown in Fig. 6.16 for sample 774-A. We have seen in Fig. 6.12 a B-scan of this sample that shows how two different layers of fibers overlap, running non-parallel from the top to the bottom of the muscle. A different B-scan of the same sample is shown in Fig. 6.20. Although the *en face* attenuation map also shows some degree of fiber directionality, it is much more highlighted through the birefringence. Furthermore, the localized attenuation and the birefringence both mark the same central area as more necrotic than the rest of the sample, while the *en face* map of attenuation does not, due to the limited penetration depth considered to obtain it. In this case, the intensity is homogeneous in the whole area considered for the phantom-calibrated model, but the localized attenuation is modified due to considering the whole depth of the sample. The birefringence is altered similarly since the phase delay (or lack thereof) returning from the more profound points in the sample will destroy the linear cumulative phase seen in the rest of the muscle, indicating loss of sample structure.

6.7 Conclusions

This chapter explored the application of optical coherence tomography (OCT) to characterize muscle tissue samples from a mouse model of α-sarcoglycan deficiency, a condition mimicking certain aspects of muscular dystrophy. Two datasets, MD1 and MD2, were analyzed, comprising a

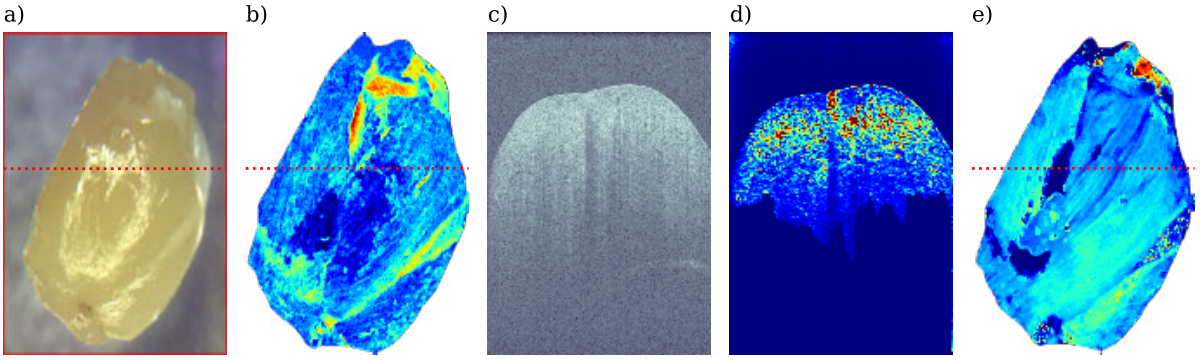

Figure 6.20: Reference RGB image (a), phantom-calibrated attenuation (b), B-scan (c), localized attenuation (d) of the KO-3mo sample *774-A*, and birefringence (e). The B-scan shown in (c) and (d) is marked as a red, dashed horizontal line in (a), (b) and (e).

range of control and knockout samples. Initial analysis focused on OCT-derived intensity, which showed a non-homogeneous light decay inside the samples, indicating structural variations both within and between samples. A phantom-calibrated light-decay model was employed to generate two-dimensional maps of attenuation (μ_t), focusing on the single scattering region (25-250 μm). The attenuation maps revealed variations in tissue density within individual samples, with strong overlap between clinical categories for dataset MD1. Although some improvement was observed in dataset MD2, neither demonstrated a clear separation between control and dystrophic samples based on bulk attenuation values. Comparison with literature-derived necrotic thresholds in a Duchenne's muscular dystrophy model suggests that either the α-sarcoglycan deficient samples exhibit less necrosis or that analyzing bulk samples, as we have done here, masks the subtle differences detectable in RoI-focused experiments.

The 2D attenuation maps highlighted internal structures, which were evaluated through cross-sectional B-scans and the subsequent application of a localized attenuation model. The two attenuation models showed some discrepancies: the phantom-calibrated model indicated lower attenuation in denser regions, while the localized model showed the opposite trend. This difference stems from the distinct calculation methods, with the phantom-calibrated model averaging attenuation over a larger depth range within the single-scattering regime, while the localized model provides pixel-wise values. Despite this, the combined information obtained through use of both models provided additional insights. The 2D phantom-calibrated maps identified regions of interest, which were then further analyzed with the localized model, which enhanced the sub-surface structural variations.

Beyond intensity-based OCT, we also investigated the potential of polarized-sensitive OCT. 2D birefringence maps were generated from the phase delay data derived from the Stokes parameters. These maps, while exhibiting significant inter- and intra-sample variability, seemed a better alternative for distinguishing between healthy and dystrophic samples. In dataset MD1, a clear separation was observed between the two clinical categories, with healthy samples exhibiting birefringence over the necrotic threshold reported in the literature, while dystrophic samples were consistently below. Dataset MD2 showed more overlap, which could originate from the number of samples per clinical state.

While dataset MD2 had an equal number of samples for each category, this was not the case for MD1, with the control category being under-represented. The superior performance of birefringence in differentiating dystrophic samples suggests that it is more sensitive to the changes associated with the disease than attenuation. While chemical changes might not be sufficient to alter attenuation significantly, the disruption of fiber integrity in dystrophic samples appears to affect the phase delay, leading to a decreased value of birefringence.

In summary, while attenuation measurements showed limited ability to distinguish between healthy and dystrophic muscle samples, birefringence proved to be a more sensitive marker of disease-related changes, likely reflecting the disruption of muscle fiber structure. Further studies with a wider age range of animals are needed to establish the temporal dynamics of these changes fully and to determine if there is a specific developmental stage where attenuation may be a more useful biomarker for this particular model of muscular dystrophy. However, as we will demonstrate in subsequent chapters, the textural information contained within the attenuation maps can be used to enhance the diagnostic potential of OCT.

References

[1] L. Scolaro et al.: "Parametric Imaging of the Local Attenuation Coefficient in Human Axillary Lymph Nodes Assessed Using Optical Coherence Tomography", *Biomedical Optics Express* **3**(2), 366 (2012). DOI: 10.1364/BOE.3.000366.

[2] B. R. Klyen et al.: "Optical coherence tomography can assess skeletal muscle tissue from mouse models of muscular dystrophy by parametric imaging of the attenuation coefficient", *Biomedical Optics Express* **5**(4), 1217 (2014). DOI: 10.1364/boe.5.001217.

[3] E. Real et al.: "Collagen birefringence assessment in heart chordae tendineae through PS-OCT", in: *Optical Coherence Tomography and Coherence Domain Optical Methods in Biomedicine XXI*. Ed. by J. G. Fujimoto, J. A. Izatt, and V. V. Tuchin. **10053**. International Society for Optics and Photonics. SPIE, 2017 1005334. DOI: 10.1117/12.2254303.

[4] L. Chin et al.: "En face parametric imaging of tissue birefringence using polarization-sensitive optical coherence tomography ", *Journal of Biomedical Optics* **18**(6), 066005 (2013). DOI: 10.1117/1.jbo.18.6.066005.

[5] X. Yang et al.: "Quantitative Assessment of Muscle Damage in the Mdx Mouse Model of Duchenne Muscular Dystrophy Using Polarization-Sensitive Optical Coherence Tomography", *Journal of Applied Physiology* **115**(9), 1393–1401 (2013). DOI: 10.1152/japplphysiol.00265.2013.

[6] Y. Dong et al.: "Quantitatively characterizing the microstructural features of breast ductal carcinoma tissues in different progression stages by Mueller matrix microscope", *Biomedical Optics Express* **8**(8), 3643 (2017). DOI: 10.1364/boe.8.003643.

HSI and SFDI measurements of dystrophic mice muscles

7

In the previous chapter, we explored the mice muscles dataset from the structural point of view. Even if the attenuation is linked to the chemical composition, the working fundamentals of OCT imply that the signal received comes mainly from the backscattering properties of the sample. This chapter will focus first on the results provided by hyperspectral imaging, which primarily informs about the chemical composition of samples, and spatial frequency domain imaging, which is the only methodology explored in this book that is able to decouple the contribution of absorption and scattering.

Due to the incremental development of the application of these imaging methodologies to the mice samples, only the second dataset (MD2) is analyzed in this chapter.

7.1 HSI reflectance of mice samples

As before, the first step after measuring the samples is to evaluate their average behavior. The reflectance measured with HSI systems has two spatial dimensions and one spectral dimension. As with OCT, a helpful way to visualize the samples is by averaging the data in the spectral dimension (Fig. 7.1, a and b). The range below 430 nm and over 900 nm in the VISNIR range was not considered due to the loss of signal caused by the detector's sensitivity. The noise increment below 950 nm and over 1650 nm in the SWIR range is also caused by the sensor's limitations.

The VISNIR and SWIR devices are equipped with lenses that provide similar spatial resolution across the two wavelength ranges. However, given that the total absorption of the chromophores in the VISNIR is slightly higher and that the scattering is orders of magnitude smaller in the SWIR, the penetration depth at these wavelengths is much longer than in the visible. The random walk of the photons inside the sample causes a natural *blurring* of SWIR wavelengths, which is exaggerated even more when averaging large spectral ranges, as in Fig. 7.1 (b). Although for most samples, this does not pose an issue, with samples as small as the mice muscles, which were less than 1 cm in their longest dimension, the blurring is much more noticeable in the SWIR range than in the VISNIR range.

The HSI-VISNIR system acts as a color camera with more than 200 color channels. As such, the average spectrum shown in Fig. 7.1 (c) represents a thorough description of the color of the sample. The higher reflectance in the range between 600 and 800, as well as the low reflectance below that, suggests that this sample had a dark red color. However, not only the color can be determined from the VISNIR range, but also its origin as well. The average spectrum has two almost overlapping valleys at 550 and 580 nm, which coincide with the absorption peaks of oxyhemoglobin (see Fig. 4.7). This suggests that this element is the main one that gives

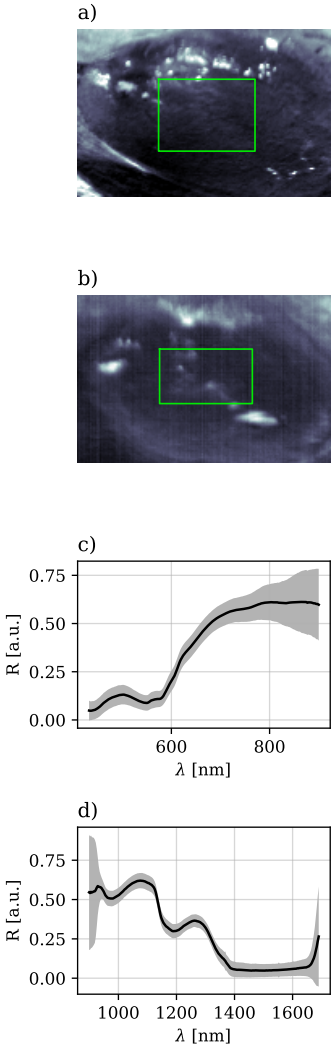

Figure 7.1: Wavelength-averaged reflectance (a, b) and spatially averaged reflectance (c, d) for the HSI VISNIR (a, c) and SWIR (b, d) systems. The data shown in this figure corresponds to sample 862 from dataset MD2.

the samples their color, possibly combined with deoxyhemoglobin or with the multiple forms of myoglobin.

The HSI-SWIR range measurements are influenced by many chromophores that are principal components of muscle tissue, such as collagen, elastin, fat, and, especially, water. Water, which is completely transparent in the visible range, is almost opaque in the infrared. Since biological samples are mostly made out of water, the biological fingerprint becomes nearly a marker of the water content in the sample. Only below 1250 nm and below 1000 nm does fat surpass the absorption of water, and elastin and collagen dominate only between 1000 and 1100 nm. The rest of the SWIR spectrum is marked by the absorption of water, making hydrated samples lose almost all diffuse reflectance over 1400 nm (Fig. 7.1, d).

The patterns observed for this sample are consistent for all samples (Fig. 7.2, a and b). Depending on their chemical composition, their chromophores affect the reflectance, providing higher or smaller values for some samples. Still, the double hemoglobin peak is always present, as well as the valleys caused by the water absorption peaks. Nonetheless, an additional peak-valley combination at 930-975 nm is also influencing the results in the NIR range. These two wavelengths correspond with the peak and valley of lipids absorption at the same wavelengths, combined with a growing absorption of water in the same range.

When considering the whole dataset into the control and dystrophic classes (Fig. 7.2, c and d), we see that the spectral variation across the different samples translates into a severe overlap between the two categories. On average, the dystrophic dataset has a "flatter" response, with higher reflectance values below 680 nm than the controls and lower after that wavelength. The average control spectrum is slightly below the dystrophic one in the SWIR range, but overall, both spectra are highly similar in this range. In the following sections, we will see how this overlap manifests itself in the results.

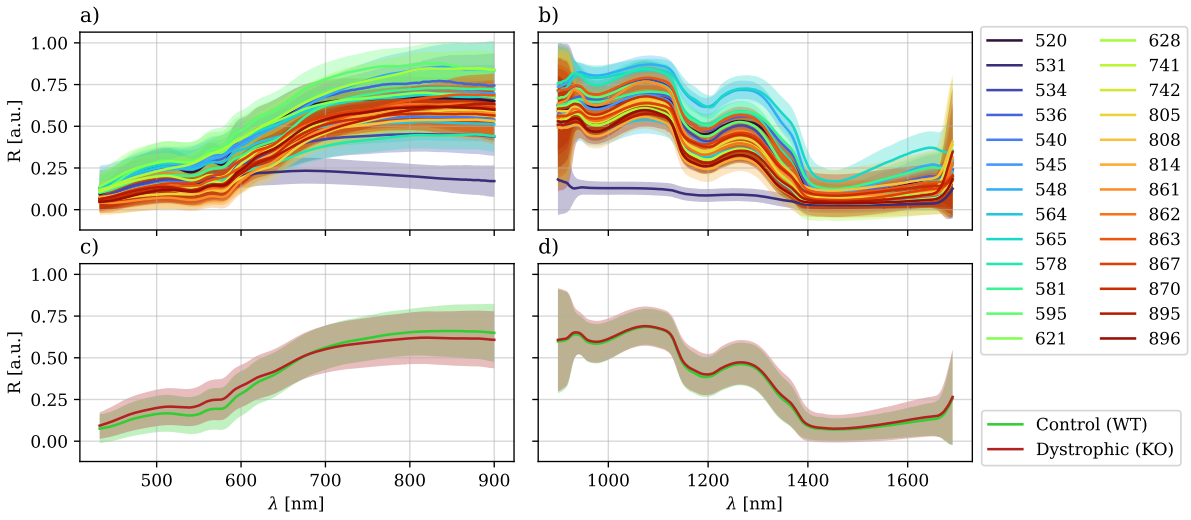

Figure 7.2: VISNIR (a) and SWIR (b) diffuse reflectance average (solid line) and standard deviation (shaded area) for all samples in dataset MD2. The average control and dystrophic spectra are shown for the two spectral ranges in (c) and (d). The top legend applies to (a) and (b), and the bottom one to (c) and (d). Sample 531 has not been considered in the average spectrum.

Only one sample in the whole dataset behaved differently from the rest: sample 531. This sample overlapped with the others below 600 nm and over 1400 nm, where the absorption of hemoglobin and water, respectively, is higher. The next section will provide additional information about the origin of this sample's discrepancy.

7.2 Color reconstruction

The HSI-VISNIR data can be used to reconstruct a color image from the hyperspectral data cube. The main advantage this color reconstruction poses with respect to a conventional color photograph of the sample is the exact coregister between the color image and the hyperspectral data. The reconstruction is shown in Fig. 7.3.

Color reconstructions help better understand the high resolution of the HSI system. Details such as muscle fibers (sample 520), damaged areas (sample 808), and fatty deposits (sample 814) are clearly identifiable thanks to this representation. The muscles ranged in color from dark brown to clear pink, with some highly translucent areas. These variations, as well as the multiple sample sizes and thicknesses, will affect the diffuse reflectance. All samples were provided fixed to a cork base with a clear fixing agent, with the only exception being sample 531, which was embedded in a dark fixing agent.

The translucent nature of the samples causes light to go all the way through them when the wavelength does not coincide with strong absorption peaks. This means that the photons will interact with the cork beneath the samples before returning to the sensor. The only sample where that does not happen is, precisely, sample 531. The dark fixating agent completely absorbs all photons that make it through the sample, and the received ones are those that did not make it through, i.e., photons that contain information *only* of the sample, without being affected by the cork at all. The spectral discrepancies this sample showcased with the rest of them suggest that the fixing agent influences the reflectance the most between 650 and 1350 nm. On the other hand, the range between 650 and 1350 nm for sample 531 is also artificially attenuated by the same agent, and its real diffuse reflectance could be over the actual measured value. In any case, the real diffuse reflectance of the samples between 650 and 1350 nm is most likely between the values of sample 531 and the values of the rest of the samples.

Fixing the samples for transport is a common practice to keep them from getting damaged in transport and to coregister contiguous samples taken from the same specimen. However, for samples as small and thin as the mice muscles, where the VISNIR-SWIR photons can travel through them, measuring the diffuse reflectance needs consideration of what is set underneath the samples so as not to influence the measurements. Ideally, the substrate should be something that (1) does not absorb and (2) does not scatter so that the diffuse reflectance of the sample is left unchanged. A substrate that better fulfills these conditions is a mirror. Although measuring on mirrors is challenging due to the specular reflectance they cause in areas where the sample does not cover them, closing the aperture of the lenses helps diminish the spurious rays so that only the light that travels perpendicularly to the surface of the mirror is captured.

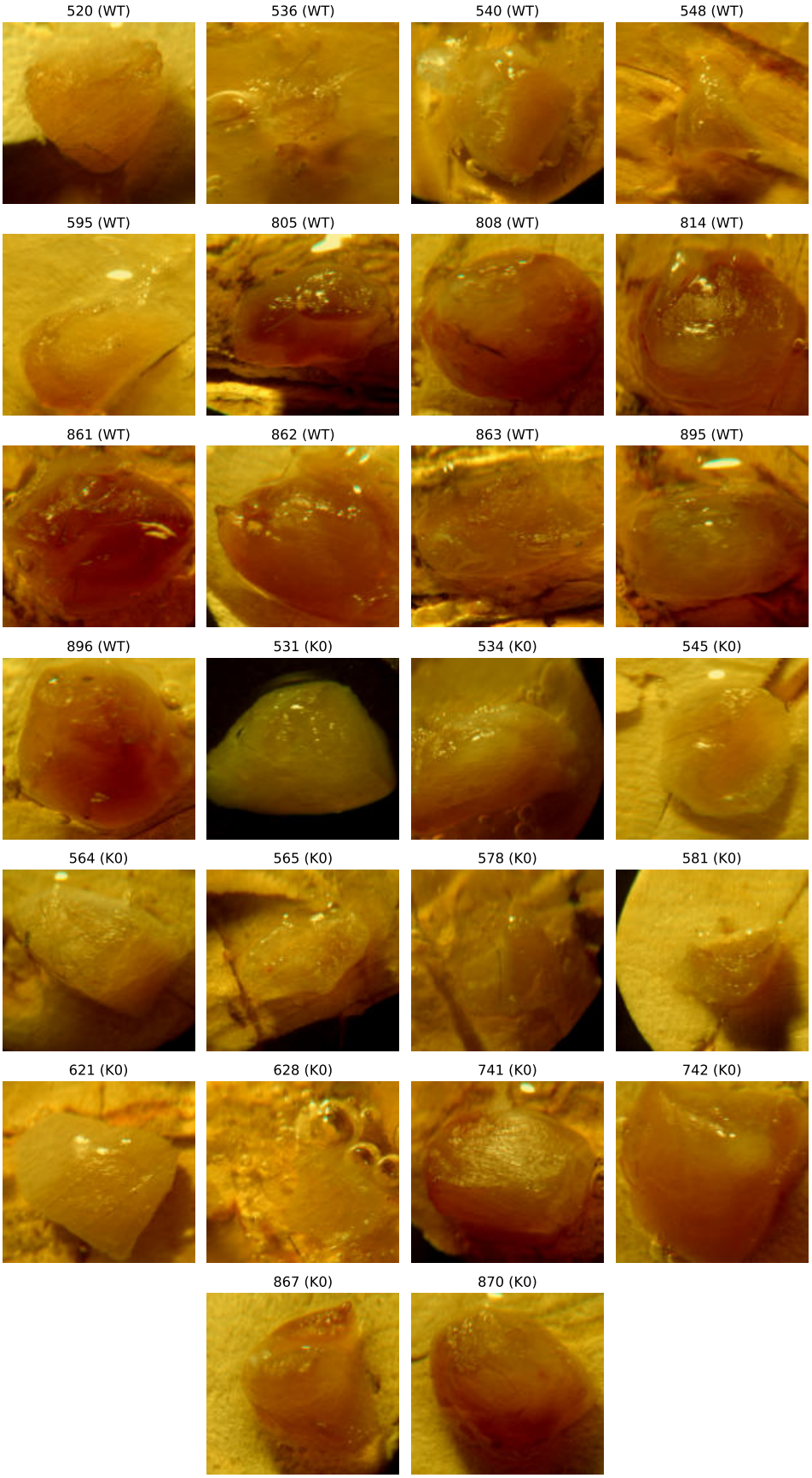

Figure 7.3: Color reconstruction from HSI-VISNIR data for all samples in dataset MD2.

7.3 Scattering and absorption in HSI

Before, we introduced the albedo of a material, which is defined as how much light it scatters out of what it extinguishes. In a medium with absorption (μ_a) and reduced scattering (μ_s'), it is defined as

$$a = \frac{\mu_s'}{\mu_s' + \mu_a} \quad .$$

Some of the reflectance models that were introduced in previous chapters estimate the reflectance in terms of the quotient[1] $N = \mu_a/\mu_s'$, which relates to the albedo through

$$N = \frac{1-a}{a} \quad \text{or} \quad a = \frac{1}{1+N}.$$

[1] This quotient coincides with the local slope of the iso-reflectance curve shown in Fig. 5.5.

When the sample does not have scattering, then $a = 0$ and $N \to \infty$; when the sample does not absorb, $a = 1$ and $N = 0$; when the absorption and scattering are comparable, $a = 0.5$ and $N = 1$.

The models proposed by Kubelka and Munk [1] (Eq. 4.40) and Jacques [2] (Eq. 4.42) were used to calculate the fraction μ_a/μ_s' to compare it with the results obtained from Monte Carlo simulations. The general behavior is shown in Fig. 7.4.

All three methods show similar general trends in the ratio between absorption and scattering as a function of wavelength, with peaks and valleys occurring at roughly the same wavelengths. This suggests some degree of agreement between the methods in capturing the fundamental optical properties of the sample. The Monte Carlo simulations are close to the empirical model provided by Jacques (Eq. 4.42), while the model by Kubelka and Munk gives values of at least one order of magnitude higher than Jacques' and two orders of magnitude higher than the simulations. The only regions where the Kubelka-Munk model approaches the simulations are below 480 nm and over 1350 nm. We have seen before that the latter corresponds to the high-absorption spectral region given by the water content of the samples. On the lower end of the wavelength spectrum, the absorption is mainly caused by the hemoglobin, combined with a high scattering signal due to the melanin content below 480 nm. The presence of highly absorbent chromophores reduces the SNR, and

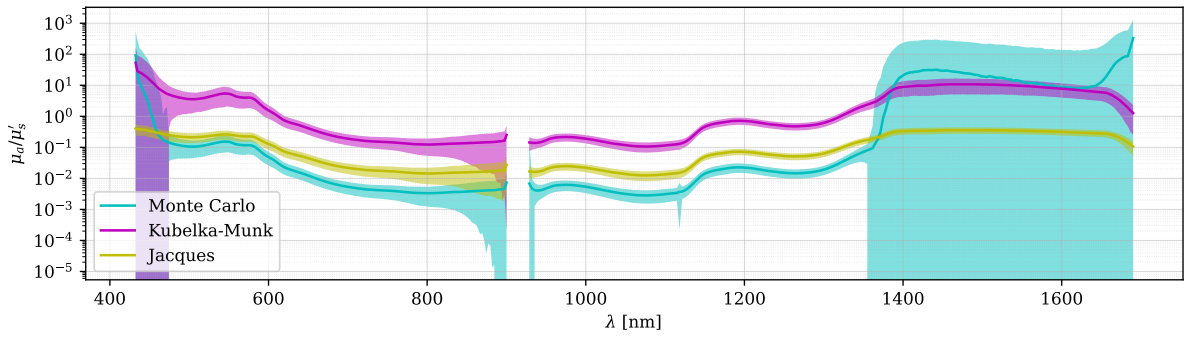

Figure 7.4: Comparison of the models proposed by Kubelka-Munk (Eq. 4.40) and Jacques (Eq. 4.42) with the derivation from Monte Carlo simulations for sample 862 (MD2).

the sensitivity of the cameras decays from 1600 to 1700 nm and from 500 to 400 nm. The low signal detected in this range may contribute to the discrepancies between models and the high standard deviation of the simulations. However, the increased absorption of the samples avoids the transmission of photons through them, which ensures that even if the signal is low, it is not contaminated by the sample's base and that the overlap in standard deviation between models is a feature of the sample's modeling.

It is also worth noting that the hemoglobin peaks are similarly highlighted[2] with the Kubelka-Munk model and with the simulation results, but the slope between 1400 and 1600 nm caused by the high water absorption peak is only visible in the simulation results.

[2] With respect to the spectrum baseline

Each model has its advantages and limitations. For example, the Monte Carlo method is generally considered the most accurate since it implicitly accounts for more complex light scattering behavior within the material, but it can be computationally expensive. To create a 200×150 ($\mu_a \times \mu'_s$) simulation map of the diffuse reflectance, only 1000 photons were considered per simulation. Still, building the reflectance took over 48h[3]. The Kubelka-Munk method was developed to model semi-infinite, homogeneous pigments. While the Monte Carlo method used in this thesis also considers a semi-infinite sample, the Kubelka-Munk method does not account for the existence of multiple scattering. Finally, the model proposed by Jacques is an empirical equation that is often used for biological materials, which was derived from Monte Carlo simulations. However, it is still an approximation that is not intended to provide an accurate description of the sample's properties but to estimate its behavior.

[3] With an Intel Core i7 (10th Gen) and 64Gb of ram.

Regardless of the model selected to evaluate the samples, the discrepancies between models and the regions where they overlap point to spectral information to consider when fitting to the chromophores' fingerprints.

7.3.1 Albedo

The albedo was calculated from the attenuation and scattering coefficients derived through the Monte Carlo simulations. Since the albedo is wavelength-dependent, the results were evaluated between 500 and 600 nm (hemoglobin/myoglobin features) and between 1200 and 1350 nm (water and fat peaks and valleys). The resulting calculations are shown in Fig. 7.5.

Let us consider that the HSI systems receive only the fraction of light that is not absorbed. Then, albedo can be interpreted as a measure of the "total reflectivity" of the sample. In the VISNIR range, high albedo would translate to brighter colors, while in the SWIR indicates high heat re-emission.

All samples had high albedo in the two selected spectral ranges, higher than 0.9 in most cases. In the SWIR range, the albedo was higher than in the VISNIR, corresponding to the much lower absorption of fat and water compared to the absorption of the hemoglobin (Fig. 7.5, a and b). As a consequence, the "reflectivity" of the samples can be much higher in the SWIR range. However, the higher spatial resolution of the HSI-VISNIR

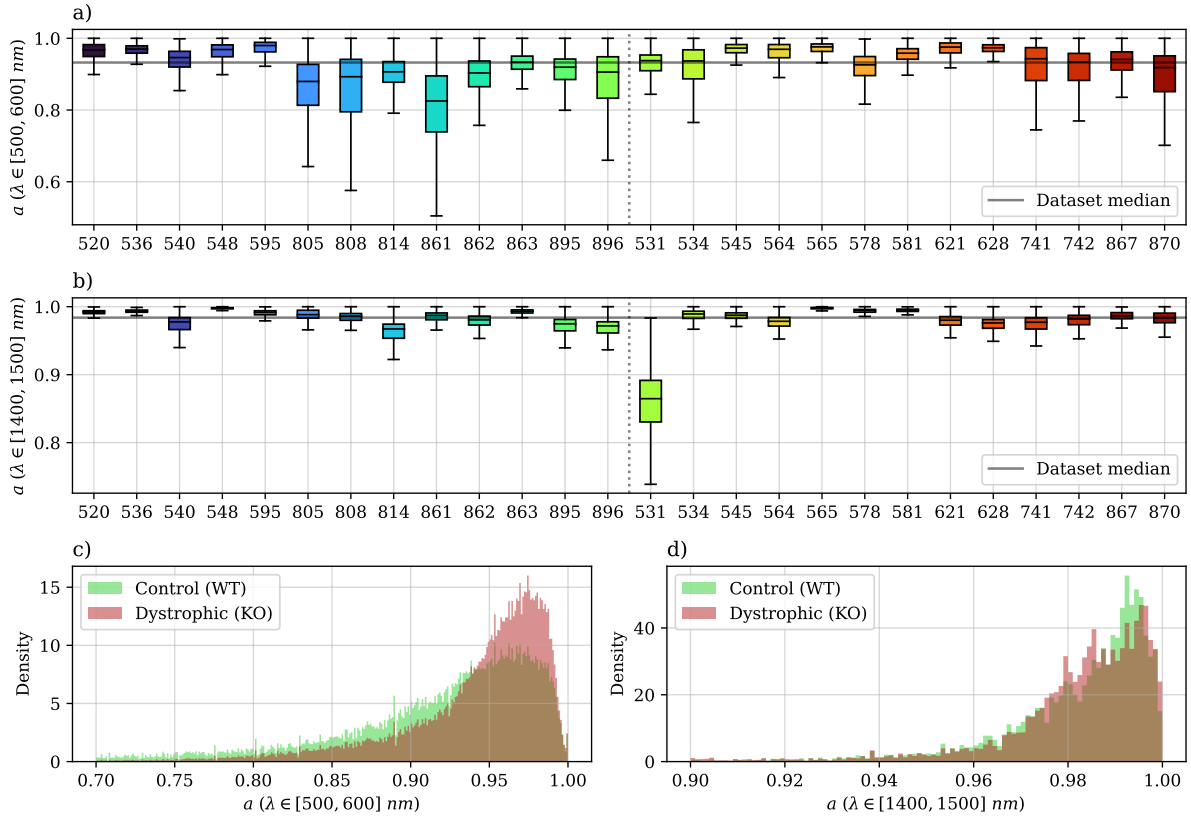

Figure 7.5: Albedo comparison for the muscle samples in dataset MD2: (a) results between 500 and 600 nm, (b) results between 1400 and 1500 nm, (c) density histograms corresponding to the boxplots in (a), (d) density histograms corresponding to the boxplots in (b). The colors in (c) and (d) correspond to the samples in the boxplots grouped according to their clinical category. The dotted vertical line in the boxplots separates the control (WT) samples on the left from the dystrophic ones (KO) on the right.

system provides a higher number of pixels in this spectral range, leading to smoother, better-defined albedo distributions[4] (Fig. 7.5, c and d).

While some samples (520, 536, 565, 867...) had similar high/low albedo behavior[5] others had high SWIR and low VISNIR albedo (564, 621, 628, 863...). The former behavior suggests an overall higher reflectivity, while the latter suggests a distinctly spectral response in both ranges due to a different chemical composition. The only additional pattern observed in the albedo distributions is the slightly lower albedo around the hemoglobin peaks for some control samples. This suggests that control samples showcase a marginally higher absorption than the dystrophic ones, which could be an indicator of higher hemoglobin content in the wild-type muscles.

Note that, depending on the model selected to calculate the albedo (Fig. 7.4), the results shown in this section will drastically vary.

[4] Both histograms in Fig. 7.5 (c) and (d) have the same number of bins (100) between 0.9 and 1.

[5] With respect to the median albedo.

7.4 Chromophores

The previous comparison of spectral models showcased that the albedo shape is conserved across models, even if the absolute value changes. The ranges below 650 nm and over 1350 nm have high absorption-to-scattering ratios, meaning that the optical path length is shorter at these

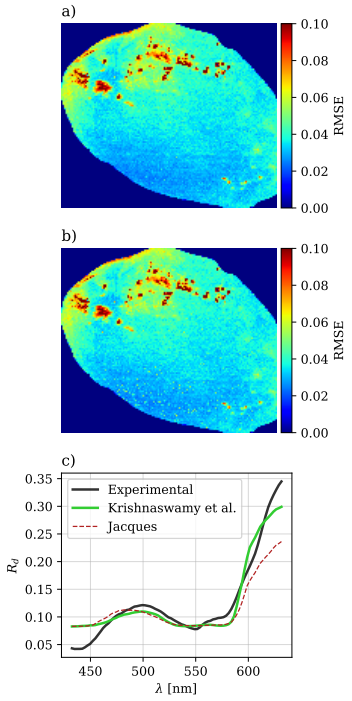

Figure 7.6: RMSE comparison between the average diffuse reflectance when using the hemoglobin and deoxyhemoglobin absorption coefficients as a reference. The data is shown for sample 862 of dataset MD2. (a) RMSE when fitting to the model of Krishnaswamy *et al.* [3]. (b) RMSE when fitting to the model proposed by Jacques [2]. (c) Average R_d spectral reconstruction by both models. In (a) and (b), the median albedo of each spectral range is indicated as a horizontal gray line.

wavelengths and that the light interacts only with the samples themselves. Thus, this spectral range is optimal for chromophore estimation.

7.4.1 Model selection

First, we considered the comparison of the principal chromophore estimation models, as explained in Chapter 4, below 650 nm. Although we have seen in the previous section that absorption dominates in this spectral range, scattering is non-negligible and thus must be considered in the calculations.

The parameters provided by fitting the reflectance data to the models proposed by Krishnaswamy *et al.* [3] and Jacques [2] vary slightly in the number of parameters. For the former, the model considered was Eq. 4.44 with an additional bias constant j, given by

$$\begin{aligned} \mu_s' &\approx A\lambda^{-b}, \quad \text{and} \\ \mu_a &\approx d \cdot \mu_{HbO2} + (1-d)\mu_{Hb}, \quad \text{so that} \\ R_d &\approx j + \mu_s' e^{-Lc\mu_a} \quad . \end{aligned} \tag{7.1}$$

where the optical path length L was obtained from the Monte Carlo simulations. The model proposed by Jacques was similarly adapted by the same additional bias constant j, but using the scattering definition that considers the Rayleigh scattering fraction (Eq. 4.46). The added constant j represents a constant reflectance intensity shift, i.e., the effect of non-diffuse phenomena like specular reflections.

The comparison between models is shown in Fig. 7.6 for one representative sample. The Rayleigh scattering fraction tends to zero ($f_{Ray} < 10^{-3}$), which coincides with both models providing similar RMSE values. While the RMSE only exceeded 0.1 in areas with specular reflections, areas with lower SNR (lower left on the sample) provided less noisy results with Eq. 7.1. For all samples, the average spectrum reconstruction with the respective average model parameters was highly similar as well, especially in the area corresponding to the hemoglobin principal features. The main spectral differences between models are near the ends of the wavelength range used for fitting, where the simpler model outperforms the one with the more complex scattering description. All of the above indicates that the Mie scattering fraction is so much higher than Rayleigh's in this wavelength range that considering the complete scattering approximation is not necessary[6]. Therefore, moving forward, only the scattering approximation provided by Krishnaswamy *et al.* will be discussed in this work.

The spectral range considered for the VISNIR data is mainly influenced by the hemoglobin or myoglobin peaks. Oxygenated (HbO_2) and deoxygenated (Hb) hemoglobin have nearly identical spectra to those of oxygenated (MbO_2) and deoxygenated (Mb) myoglobin. However, when opting for myoglobin estimation in *ex vivo* samples, it is interesting to consider the influence of metmyoglobin (MMb) as well since it represents the part of myoglobin that is completely oxidized and can no longer transport and release oxygen. A third chromophore was added to Eq. 7.1 so that the attenuation could be represented through the three myoglobins

[6] The same behavior was observed for all muscle samples.

as

$$\mu_a \approx \frac{d_1}{d_1+d_2+d_3}\mu_{Mb} + \frac{d_2}{d_1+d_2+d_3}\mu_{MbO2} + \frac{d_3}{d_1+d_2+d_3}\mu_{MMb} \quad , \quad (7.2)$$

where each of the d_i represents the fraction of one myoglobin type.

Again (Fig. 7.7), the RMSE and the average spectrum reconstruction with the addition of the third chromophore mostly coincide with those of the two previous models, most likely due to the spectral similarity between hemoglobin and myoglobin, with the only exception being low SNR areas and specular reflections. Consequently, the fraction of metmyoglobin collapses to zero due to the constraint imposed on the d_i: they must add up to one.

When fitting data to a multi-parametric equation, it is also relevant to evaluate the uncertainty of the resulting parameters. In probability, the uncertainty of a variable can be understood as the spread of the distribution that represents it. In the context of fitting some data to a model by minimizing a cost function, the uncertainty of a parameter represents the range of possible values that the parameter can take to provide the same result through the model. Then, the uncertainty of the parameters can be derived through the diagonal of their covariance matrix, which results from the fitting error minimization process [4].

Interestingly, in the three-myoglobins model, which provides reasonable RMSE values and a fairly good spectral reconstruction, the uncertainty of all fractions (d_i) is exceptionally high (Fig. 7.8). This suggests that there is an almost infinite combination of parameters d_i that can reconstruct extremely well the spectral data of the samples discussed here. The source of the high uncertainty lies in the volume fractions for the three myoglobins not being independent. Since the three fractions multiply the three myoglobin absorption spectra, the minimization algorithm can optimize two of them while collapsing the third with some arbitrary value. That, combined with the reference myoglobins being similar between them (with the exception of the oxymyoglobin peaks), suggests that the choice of which two volume fractions are being optimized can be almost arbitrary. Therefore, we will use the two-hemoglobin model (Eq. 7.1) to compare the results between samples since (1) hemoglobin and myoglobin have very similar spectra, and the former is available in the literature in a wider spectral range, and (2) adding a third chromophore to the attenuation while keeping the restriction that the fraction of each component can not be higher than the unity results in an under-defined minimization algorithm.

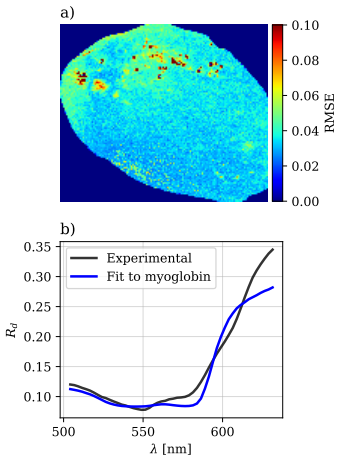

Figure 7.7: RMSE comparison between the average diffuse reflectance when using the myoglobin, the deoxymyoglobin, and the metmyoglobin absorption coefficients as a reference. The data is again shown for sample 862 of dataset MD2. (a) RMSE when fitting to the model of Krishnaswamy *et al.* [3] with the absorption modified as in Eq. 7.2. (b) Average R_d spectral reconstruction by the model.

7.4.2 Hemoglobin

All samples were fit to the simplest hemoglobin model described in Eq. 7.1 to obtain two key parameters: the oxyhemoglobin to deoxyhemoglobin content (d), and the scattering power (b). The results are shown in Fig. 7.9[7].

The scattering power (Fig. 7.9, b) was, in most cases, zero or very close to zero, meaning that the diffuse reflectance of the samples is well approximated by the absorption in the VISNIR range. Within the expression for absorption (Fig. 7.9), the samples are well described by the absorption

[7] For almost all samples, the oxyhemoglobin content was almost always 1, while the scattering power was mainly 0. This made the corresponding boxplots collapse to zero, so the average and standard deviation are represented instead in Fig. 7.9.

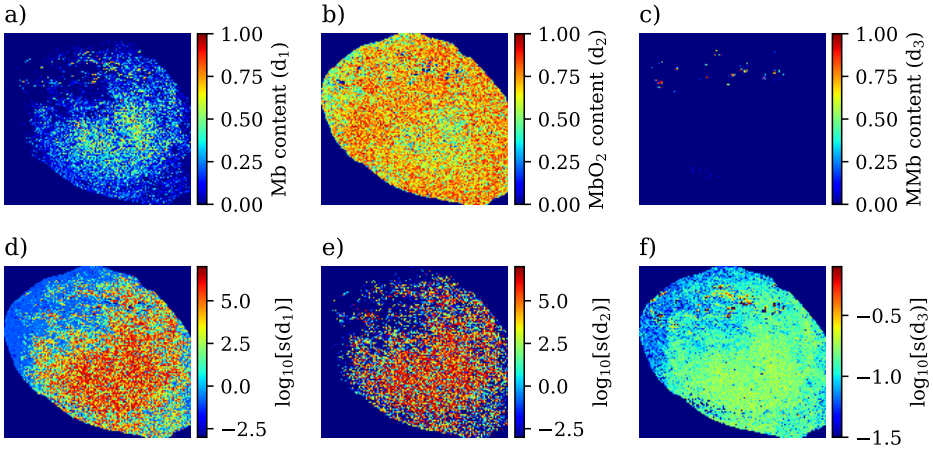

Figure 7.8: Deoxyoglobin (Mb, a), oxymyoglobin (MbO_2, b) and metmyoglobin (MMb, c) estimated with the three myoglobin absorption model represented in Eq. 7.2. The under-defined triple absorption model yields extremely high uncertainties (>10^6), which, for visualization purposes, have been represented logarithmically in the bottom row (d-f).

of the oxyhemoglobin, consistent with the double oxyhemoglobin peak that is always visible in the diffuse reflectance of all samples (Fig. 7.2).

Some samples, aside from sample 531, do not follow these trends. For example, samples 814 and 862 have a noticeably lower average hemoglobin content than the rest. Together with samples 741 and 808, these are the only samples with below-average oxyhemoglobin content, primarily due to their more significant variability. All four samples were bigger than the average, suggesting that the bigger the sample, the easier it is to find areas with hemoglobin content that have not yet been exposed to oxygen.

At this point, we should recall something we have already seen, which is that there is an infinite combination of scattering and absorption coefficients that yield the same diffuse reflectance and that no model based on a single R_d surface in the (μ_a, μ_s, R_d) space (see Fig. 5.5) can totally determine the complex chemical response of biological samples.

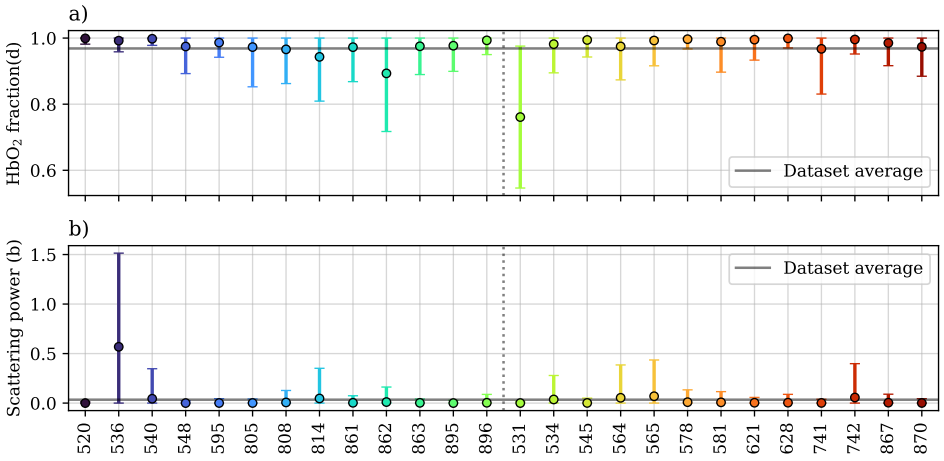

Figure 7.9: Average (solid points) and standard deviation (error bars) of the oxyhemoglobin fraction (a) and scattering power (b) for the samples in dataset MD2. The dotted vertical line separates the control samples (left) from the dystrophic ones (right).

It is worth mentioning that this does not undermine the usefulness of the reflectance models. Many samples, especially those where only absorption or scattering dominates, can be chemically interpreted through hyperspectral images. Having only μ_a or μ_s collapses the R_d surface to a single line, which essentially eliminates the indetermination discussed above.

These mice samples, nonetheless, have both non-negligible absorption and scattering when considering the whole spectral range, even if scattering can be discarded for specific wavelengths. Hence, the albedo, or simply the ratio between absorption and scattering, are the best optical properties to consider when analyzing data provided by HSI for a general application case.

7.4.3 Muscle volume fraction in the SWIR range

Several chromophores could be considered relevant in the SWIR range. For example, the content of fat in the muscle's volume is often used as a marker for muscular dystrophy. In MRI, this is quantified by evaluating the ratio of water to fat content since fat is hydrophobic and water is only present in muscle tissue. However, in optical imaging and, especially at the longer wavelengths, water is an extremely good absorber. Then, the best areas to quantify water content would be those that have less signal, making chromophore quantification a complicated task. Additionally, collagen, elastin, and hemoglobin, which are principal components of muscle tissue, also have a non-negligible absorption in the SWIR range, so those chromophores should be considered too. Since the volume fractions are not independent of each other, as we have just seen, quantification by using the absorption mixture model will yield results that are biased by the relationship between the volume fractions.

Instead, an experiment based on tissue phantoms was used to determine the fat-to-muscle content [5]. Five mixtures of chicken breast and pork lard were prepared by combining them in different amounts. All five phantoms were kept in identical containers [8] so that the volume of the phantom would not affect the results. The volume fraction of fat and muscle of each phantom is detailed in Tab. 7.1, and the resulting SWIR spectra in Fig. 7.10.

[8] 1 cm tall circular Petri dishes with 6 cm diameter.

The key spectral differences between the phantoms lie at 970, 1000, 1250, and 1500 nm. All those wavelengths coincide either with fat or water peaks or valleys (see Fig. 4.7). Water has a higher absorption coefficient than fat, so those phantoms that are dominated by muscle content have less reflectance than those whose main component is fat.

Given that the relationship between some of the peaks changes with the fat and muscle content, a ratio can be established between peaks to act as a calibration curve that can infer the muscle volume fraction of a sample. Particularly, the peaks considered for the ratio (K) [9] were those at 1211 and 1327 nm, so that

[9] Other peaks were analyzed, as shown in [5] that yield similar results.

$$K = \frac{R_d(\lambda = 1211nm)}{R_d(\lambda = 1327nm)} \quad . \tag{7.3}$$

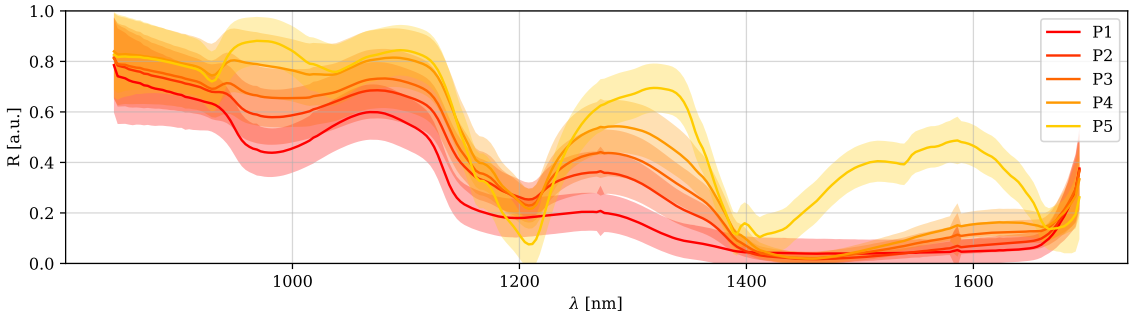

Figure 7.10: Average (solid line) and standard deviation (shaded areas) SWIR spectra of the muscle-fat phantoms detailed in Tab. 7.1. Image adapted from [5].

	Chicken breast (%)	Pork lard (%)
P1	100	0
P2	71.01	28.99
P3	46.16	53.84
P4	22.14	77.86
P5	0	100

Table 7.1: Muscle (chicken breast) and fat (pork lard) content in each phantom. The volume fractions were calculated from the measured mass by using a density for the muscle of $\rho_m = 1.06$ g/mL and for the fat of $\rho_f = 0.92$ g/mL. The densities were obtained from [6]. Data obtained from [5].

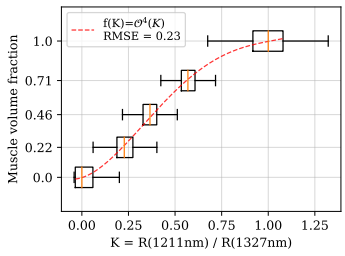

Figure 7.11: Boxplots and fourth-order polynomial of the peak ratio K calculated to derive the muscle volume fraction from SWIR measurements.

The reflectance ratio K was then re-scaled so that the medians of the boxplots coincided with the 0-1 range by using the minimum value of $K = 0.067$ and the maximum of $K = 1.7$.

Finally, the muscle volume fraction can be obtained as a function of the peak ratio, $f(K)$, by fitting K to a polynomial. Since the relationship between K and the muscle volume fraction was nonlinear and contained an inflection point, we chose a fourth-order polynomial. The value of K for the phantoms and the resulting polynomial fit are shown in Fig. 7.11.

All the data inside the interquartile range of the boxplots was used to derive the coefficients of the polynomial. The final parameters were

$$
\begin{aligned}
a &= (-230.0 \pm 8.4) \cdot 10^{-5} \ , \\
b &= (428.2 \pm 1.4) \cdot 10^{-3} \ , \\
c &= (3710.0 \pm 7.2) \cdot 10^{-3} \ , \\
d &= (-496.8 \pm 1.2) \cdot 10^{-2} \ , \text{ and} \\
e &= (1829.7 \pm 6.0) \cdot 10^{-3} \ , \text{ with}
\end{aligned}
$$

$$
f(K) = a + bK + cK^2 + dK^3 + eK^4 \ .
$$

The polynomial was then used to infer the muscle volume fraction in the mice samples. The average reflectance of the samples is shown in Fig. 7.12, and the corresponding muscle fraction results are shown in Fig. 7.13. Several things are noticeable in the images of the peak ratios. First of all, there is some variability in the average value of K between samples, with most having values over 0.9, indicating high muscle content. The exceptions are samples 536, 548, 565, and 581, which appear to have an extremely low muscle fraction. The cause lies in the small size of these samples. Instead of a whole muscle, samples 536, 548, 565, and 581 were thin muscle slices that caused light to bleed into the cork base, which increased the diffuse reflectance. Sample 520 is between the whole muscle size and the small muscle slices, which causes its muscle fraction to be between both ranges as well.

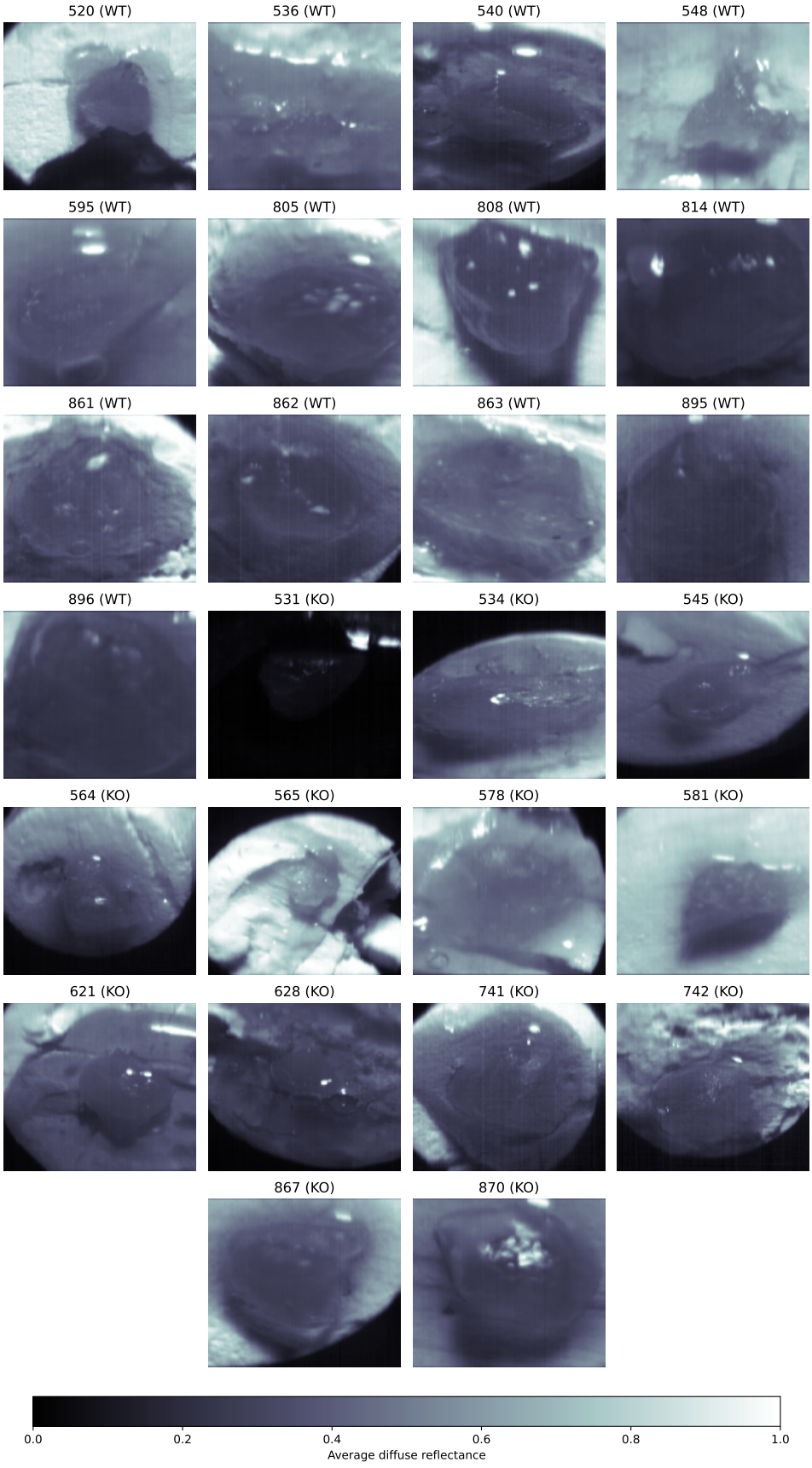

Figure 7.12: Average diffuse reflectance in the SWIR range for samples in dataset DM2.

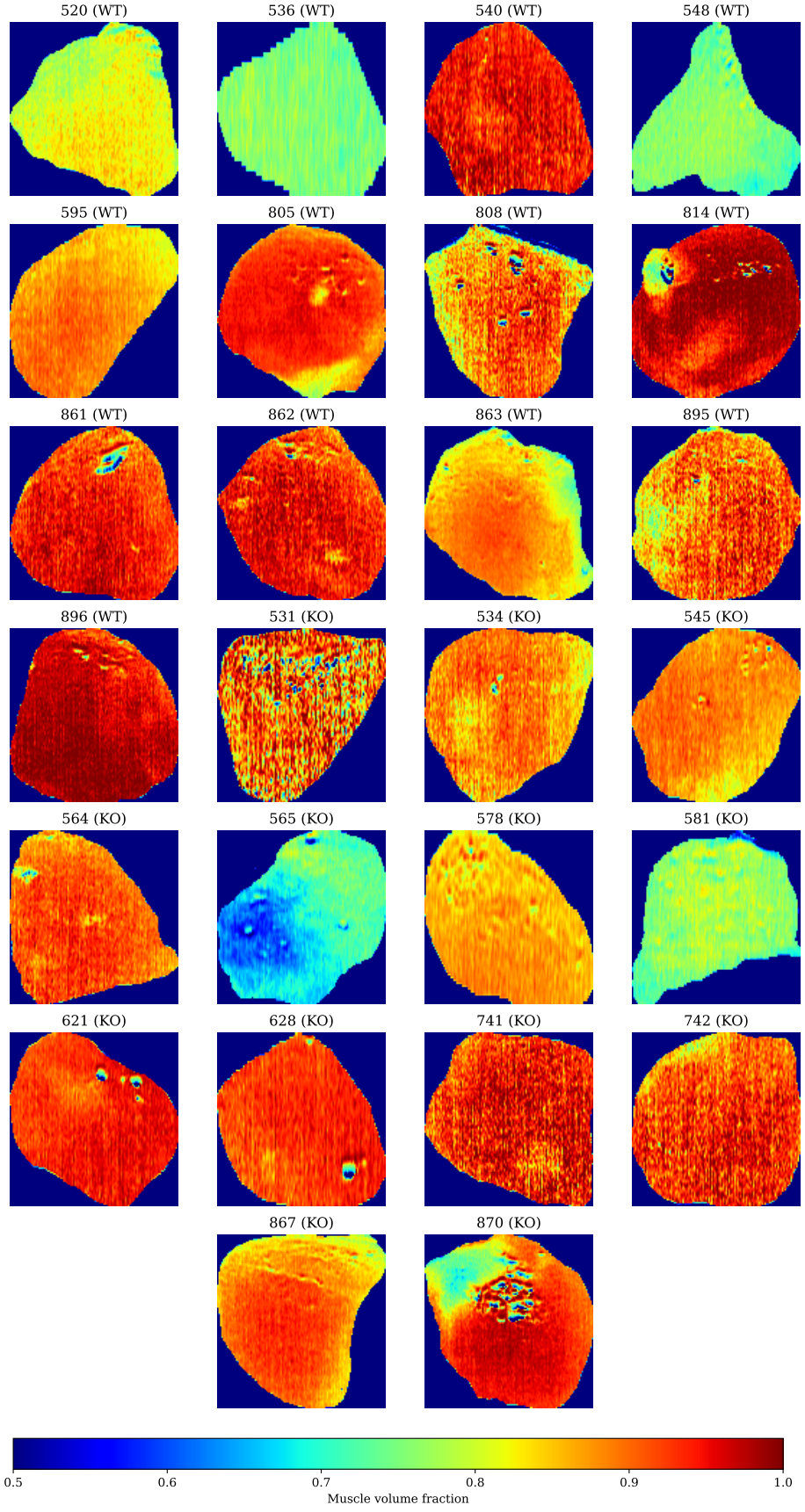

Figure 7.13: Muscle volume fraction obtained from the fourth-order fit polynomial to the peak ratio K

There are areas with low muscle volume fractions that coincide with specular reflections. We have seen before (Fig. 7.10) that the higher the water content, the lower the reflected intensity, so the specular reflections appearing as "high fat" is just an indication of their high reflectance. Interestingly, the lower reflectance end does not cause artifacts the same way specular reflections do. Sample 531 had a poor signal due to the dark fixing agent absorbing most of the light. Still, the polynomial fit is able to distinguish the muscle from the specular reflections, even if the map is noisier than for the rest of the samples

While most samples had homogeneous maps, some others showcased particularly interesting results. Samples 870 and, specifically, 814 show localized low muscle content areas that are too big to be specular reflections. In the RGB image (see Fig. 7.3), sample 870 shows a yellower, more translucent area where the low-muscle region is highlighted. On the other hand, sample 814 was mostly uniform, with the exception of some fat inclusions that correspond to the low-muscle maps. Both samples were big ($\approx 6-7$ mm) when compared with the samples in the dataset. Given that the phantoms were even thicker (≈ 1 cm), using the polynomial model might be more suitable for bigger samples, where light is not interacting with the surrounding media.

While additional phantoms with more complex compositions or future modifications to the phantom-derived polynomial model might provide better results, the current model shows promise in noninvasive muscle quantification of dystrophic samples. It allows for subsequent analysis of the same samples without interfering with the results provided by other imaging methods.

7.5 SFDI reflectance of mice samples

In the previous sections, we have seen that HSI can determine the albedo, i.e., the "reflectivity" of a sample, but not the independent contributions from absorption and scattering. SFDI can decouple absorption and scattering by measuring the diffuse reflectance coming from at least two different spatial frequencies. Then, by comparison with the Monte Carlo-derived LUT (see Fig. 5.9), we obtain the value of μ_a and μ_s'.

The control sample 814 from dataset MD2 was chosen to exemplify the type of data captured with SFDI due to the muscle/fat content that was made evident in the previous section. All samples in dataset MD2 were measured at ten spatial frequencies. We have seen in chapter 4 through the diffusion approximation that the higher the spatial frequency, the shallower the penetration of the modulated component of the light source is, which corresponds to a reflectance decay (Fig. 7.14). The expected reflectance decay at higher frequencies is observed both in the sample and the reference Spectralon (Fig. 7.15).

At this point, it is helpful to explore this idea further to better understand the fundamentals of SFDI through a real sample. We know, because we have seen it experimentally and through simulations, that higher frequencies penetrate less inside the samples. This can be understood by revisiting the diffusion approximation. We have represented the diffuse reflectance according to the diffusion approximation for multiple ranges

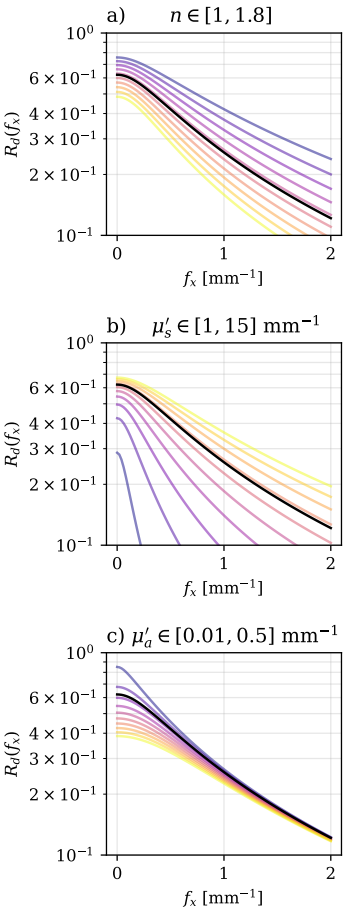

Figure 7.14: Variations of the diffuse reflectance caused by refractive index (a), reduced scattering (b) or absorption (c) changes, represented through diffusion approximation (Eq. 4.55). Lighter colors indicate higher values of the variable, darker colors lower values, and the black curve was calculated with $n = 1.38$, $\mu_s' = 10\ mm^{-1}$, and $\mu_a = 0.1\ mm^{-1}$, which are typical values found in biological tissues. Figure adapted from [7].

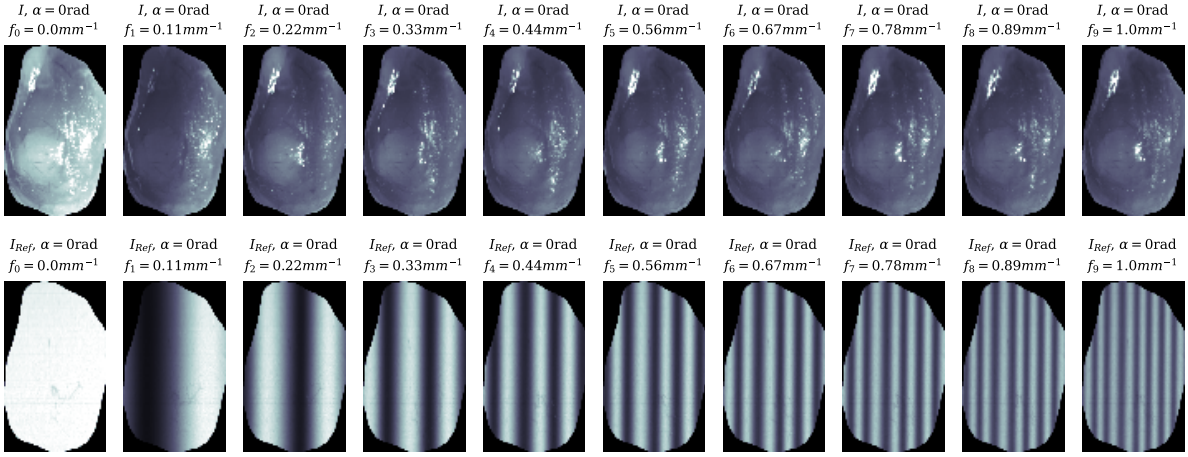

Figure 7.15: From left to right: sample intensity (I, top row) and projected illumination (I_{Ref}, bottom row) for sample 814 of dataset MD2 with the increased spatial frequency. The images correspond to the wavelength-averaged intensity measured for the first spatial phase ($\alpha = 0$ rad).

of values (Fig. 7.14). An increment of refractive index (a) causes the diffuse reflectance to drop, as the larger mismatch with air will yield stronger Fresnel reflections that leave less light to enter the tissue and diffusely reflect. The scattering coefficient alters the rate of diffuse reflectance decay with the frequency, meaning that higher scattering materials allow for the modulated component of light to be detectable at higher spatial frequencies. This is expected since samples with high scattering increase the chances of the photons being immediately scattered away at the surface or near the surface of the sample and captured by the sensor. Additionally, the higher the spatial frequency, the stronger the diffuse reflectance is affected by variations in the scattering coefficient. The absorption coefficient behaves almost in the opposite way, barely affecting higher frequencies but strongly altering lower frequencies. Samples with a higher absorption coefficient will have less diffuse reflectance as more photons get absorbed, but the effect is less noticeable at high frequencies. Cuccia *et al.* [8] put this as homogeneous turbid samples behaving like "low-pass filters", meaning that biological samples favor the penetration of the frequency-modulated component of the illumination at lower frequencies, yielding higher reflectance values.

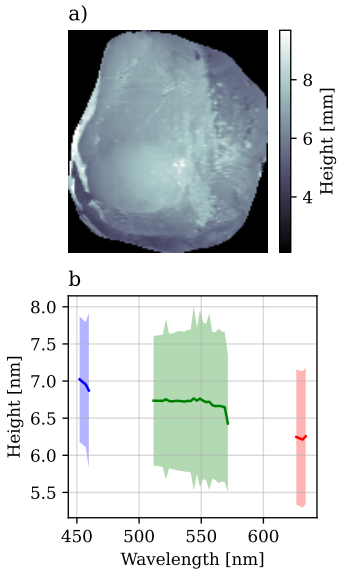

Figure 7.16: Profilometry obtained by applying phase-shift profilometry [9] with $f = 0.15mm^{-1}$. Notice how the higher wavelengths, where penetration is higher, cause a blurring of the spatial frequencies that is interpreted as a marginally smaller height.

The mice samples have a fast drop of diffuse reflectance on the first few frequencies, which indicates that their behavior is most likely dominated by low scattering, but variations in absorption are also non-negligible at these frequencies. The different tissues within each sample have different frequency responses. Notice how, for example, the projected shadows are more noticeable in the muscle tissue than over the fatty deposit on the center of the sample (see 0.44 mm^{-1} in Fig. 7.15), and tissue contrast is better at lower frequencies.

Figure 7.16 showcases the profilometry results obtained using phase-shift profilometry with the projected frequency of 0.15 mm^{-1}. Notably, the results exhibit a consistent trend: a slight decrease in the captured height as the wavelength increases. This decrease is attributed to the increased penetration depth at longer wavelengths. As light penetrates deeper into the sample, it undergoes more scattering events, leading to a blurring of the spatial frequencies. This blurring effect is interpreted as a marginally

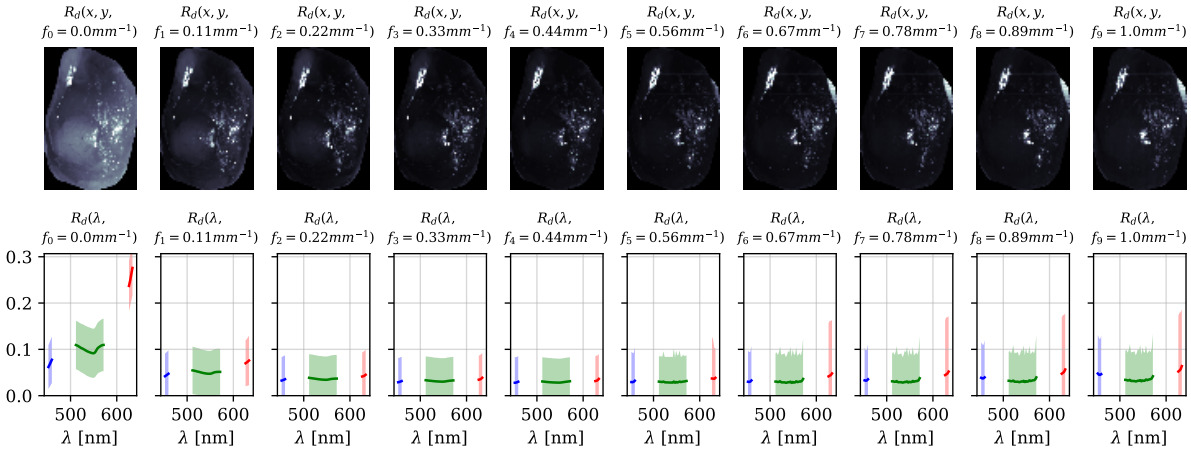

Figure 7.17: From left to right: (wavelength) averaged ($R_d(x, y)$, top row) and (spatially) averaged sample diffuse reflectance ($R_d(\lambda)$, bottom row) for sample 814 of dataset MD2 with the increased spatial frequency. The missing parts of the spectra in the bottom row are due to the non-considered regions of low SNR given by the valleys in the projector's emission spectrum.

smaller height in the profilometry measurements.

It is important to note that the variability observed in the measured height across different wavelengths is primarily due to the non-flat nature of the samples themselves. Biological samples have inherent surface variations, especially at this small scale, that contribute to the spread of the measured values. Nonetheless, the measured heights closely align with the actual heights of the samples.

Figure 7.17 shows the spatially resolved ($R_d(x, y)$, top row) and spectrally averaged ($R_d(\lambda)$, bottom row) diffuse reflectance sample 814 across various spatial frequencies and wavelengths.

The diffuse reflectance is almost immediately lost, even at low spatial frequencies, something that is particularly noticeable at the longer wavelengths. This loss is consistent with the principle that the modulated component of higher spatial frequencies penetrates less deeply, leading to a weaker diffuse reflectance signal. The further noise increment at higher frequencies due to the lower SNR causes artifacts at all wavelengths.

The reflectance increases with wavelength, corresponding to the reddish color of the sample, but this distinct wavelength response is quickly lost as the frequency increases, which reflects the wavelength-dependent absorption and scattering properties of the tissue. Furthermore, one of the hemoglobin absorption peaks falls within the high signal-to-noise area of the green LED, while the other lies outside this range. In the next section, we will see how this translates into the absorption and scattering properties of the samples in dataset MD2.

7.6 Optical properties in SFDI and HSI

SFDI was used to obtain the absorption and scattering for all samples, following the methodology explained in Ch. 4. The maps of μ_a and μ_s' can be identified by using data captured at multiple spatial frequencies. The results for sample 814 are shown in Fig. 7.18.

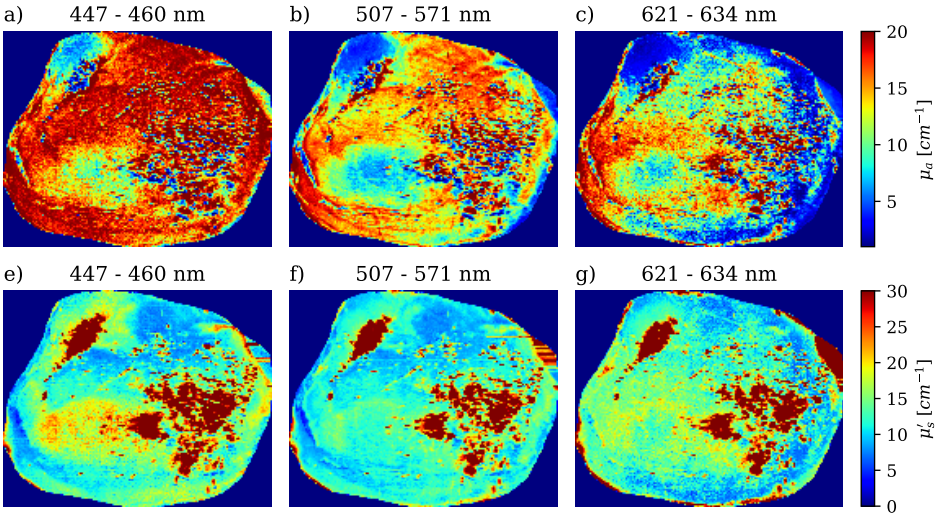

Figure 7.18: Attenuation (a, b, c) and reduced scattering coefficient (d, e, f) for the control sample 814 of dataset MD2. The data was wavelength-averaged in the blue (a, d), green (b, e), and red (c, f) wavelength ranges, corresponding to the high SNR peaks of the LED projector. The top color bar is shared between the attenuation images, while the bottom one is shared between the scattering images.

Several things stand out immediately in the μ_a and μ_s' images. For example, the absorption decays as the wavelength increases, which is expected given that the samples are reddish, meaning that they absorb more blue than red light. However, the fatty regions in sample 814 are less absorbing than the surrounding muscle, consistent with their overall whiter and more translucent color. Furthermore, the two main lipidic lobes (top left and bottom left of the sample) do not behave equally; the top one appears to be consistently less absorbent than the bottom one, suggesting a higher fat content at the top of the sample. The orientation of the sample may also affect how the attenuation in the lipidic areas is detected. For example, the upper lobe is situated sideways with respect to the camera, while the bottom one is viewed from the top. Given the sideways orientation of the upper lobe, there is no muscle underneath it. At the same time, that is not the case on the bottom lobe, which could be incrementing its attenuation, especially at shorter wavelengths, due to the light interaction with multiple tissue types.

Although the sample's scattering response is very similar across all wavelengths, it does not exactly follow a descending trend. Specifically, it appears to be slightly lower in the green color range. This could occur because the hemoglobin peaks present in the sample are the main agents in light extinction at this wavelength, the reduced SNR at these wavelengths may be influencing the results. The fatty lobes are also viewed in the scattering images as higher scattering areas. Interestingly, the bottom lobe appears to have a slightly higher scattering signal than the top one. The photons that enter the sample in this area will also encounter the boundary between fat and muscle so that their Fresnel normal reflectance at this boundary will also contribute to the scattering signal, possibly causing the scattering increment at this position.

The specular reflections on the sample (see Fig. 7.17) cause high-scattering artifacts, visible in the bottom row of the figure, that translate to areas with low absorption on the top row. Additionally, artifacts due to shadows at some wavelengths appear as horizontal lines. These are caused by

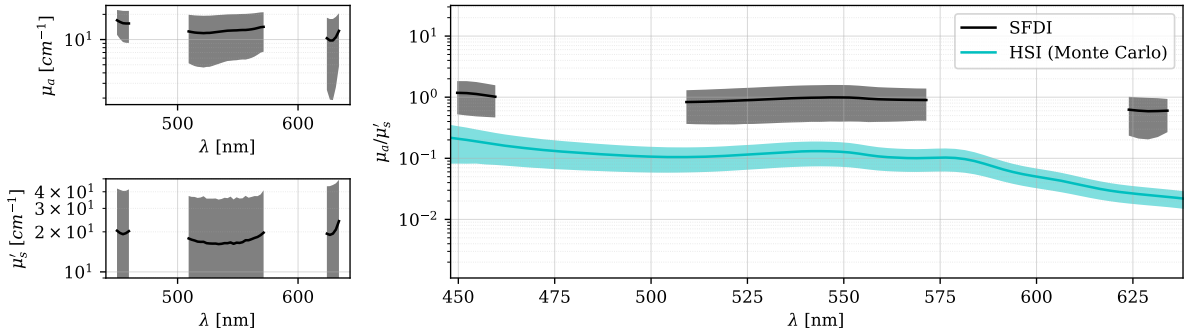

Figure 7.19: Spatially averaged attenuation (a) and reduced scattering coefficient (b) and comparison of the quotient μ_a/μ_s' between the SFDI- and HSI- derived data for sample 814 of dataset MD2. The results of HSI have been calculated using the Monte Carlo method.

the cumulative nature of the phase shift profilometry method stretching the shadows from left to right. Since these artifacts are of a few lines in width, they can be removed by any simple spatial filtering method.

At this point, we can compare the value of $N = \mu_a/\mu_s'$ with the results obtained with conventional hyperspectral imaging. The results for the same sample are shown in Fig. 7.19. Even though the first hemoglobin peak is subtly detectable in SFDI measurements, the absorption/scattering ratio is much flatter and almost one order of magnitude higher when measured with SFDI than with HSI. The placement of the reference Spectralon on the measurements can be the cause of this discrepancy. For HSI, the Spectralon is placed leveled with the *top* of the sample to avoid finding areas with reflectance higher than one due to the sample being "closer" to the light source than the Spectralon. However, for SFDI, the Spectralon is placed leveled with the **base** of the sample, as it is then modified according to the profilometry of the sample. This leads to different reference measurements between systems, which yields different reflectance signals and, in turn, different optical properties.

Another possible cause for this difference is the time it takes to measure the samples. On average, one whole muscle measurement took 2.9 minutes in the HSI-VISNIR system that also contains the projector to perform SFDI. Each SFDI frequency requires three measurements, one for each phase, totaling 8.75 minutes per frequency. Given that we measured ten frequencies, the total duration of the SFDI measurements was approximately one and a half hours.

The projector does not emit heat, so no chemical changes are expected to occur in the samples during this time. However, their air exposure causes water to evaporate, leading to the samples shrinking in size, which would modify their scattering signal. Since the measurements are taken by increasing the frequency each time, the lower frequencies would be unaffected by the drying, and this change would not be detectable at higher frequencies due to their low penetration in the sample and overall low signal (Fig. 7.17). The samples are re-hydrated in a saline solution between measurement techniques but not during the measurements so as to not influence the results. Even with this re-hydration, the samples reach the HSI measurements with much less water content than at the beginning, leading to higher scattering than in SFDI and the overall reduction in μ_a/μ_s' detectable in Fig. 7.19.

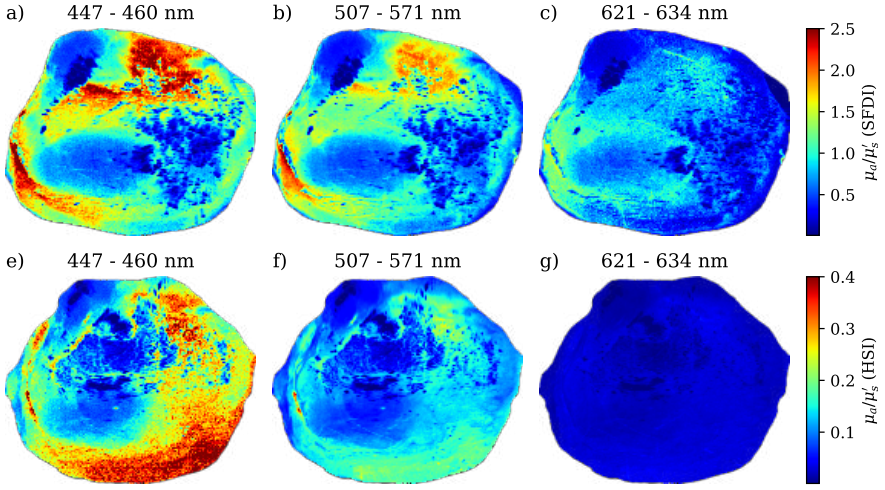

Figure 7.20: Ratio μ_a/μ_s' for SFDI (a, b, c) and HSI (d, e, f) data for the control sample 814 of dataset MD2. The data was wavelength-averaged in the blue (a, d), green (b, e), and red (c, f) wavelength ranges, corresponding to the high SNR peaks of the LED projector. The top color bar is shared between the SFDI images, while the bottom one is shared between the HSI images.

[10] For example, the mice muscles could be measured using a frequency up to 0.22 mm^{-1}, which would reduce the measurement time by 75%.

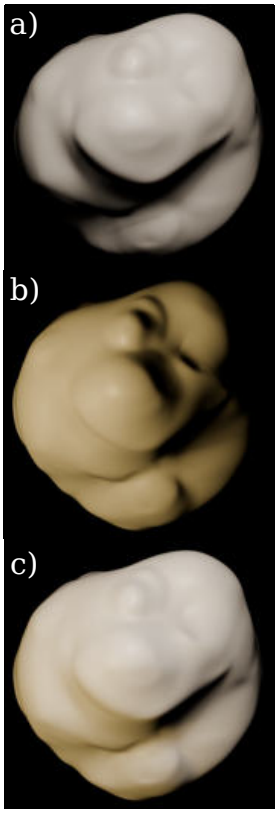

Figure 7.21: Simulated change in the detected sample shape due to a different orientation of the light source. (a): White light illuminating the sample from the top, (b) yellow light illuminating the sample from the left, (c) combined effect of both light sources. Note how areas that are visible in (a) disappear due to the shadows in (b) and vice-versa.

This effect is critical when measuring biological samples *ex vivo*, which is why current SFDI systems are opting for measuring a low number of frequencies or for performing single-snapshot optical properties measurements [10–13]. Regardless, both alternatives require prior knowledge of the frequency response of the samples to know what is the maximum frequency and what is an adequate number of them to measure so that the samples can be properly characterized. Therefore, two conclusions can be extracted from this experiment: (1) the mice muscle samples dry quickly, and long measurement durations should be avoided[10], and (2) the subsequent HSI measurements can be affected by an artificially reduced water amount.

The drying of the samples is not the only cause influencing the comparison. We can see in Fig. 7.20 that the shape of the samples is different as viewed by both imaging methods. If this were only due to the samples shrinking as they lose water we would have seen, essentially, the same shape in SFDI images (Fig. 7.20, a-c) than in HSI ones (Fig. 7.20, e-g), but smaller in the latter. Although some landmarks do appear to be closer together in HSI, like the lipidic regions, some areas seem to have different overall shapes, like those at the bottom and the left of the samples.

The sample and the camera remain static between measurements, so the only source for the apparent slightly different shape is the light source. While the projector is in line with the camera, the halogen lamp used for HSI measurements is situated on the same plane as the projector but rotated 90º with respect to it. This difference in the light source positioning causes shading in different regions of the sample, leading to a different image of the sample in the detector for each measurement method. This effect is illustrated in Fig. 7.21, where a simulated shape is captured by the same camera when illuminated with a white light from the top and a yellow light from the left. When illuminated from the left, the rightmost areas of the sample are not visible due to the shadows cast by its higher regions. The opposite is also true when illuminated from the top, with areas on the bottom of the image being completely in the dark. This occurs in HSI and SFDI, too, leading to changes in SNR even

though the sample and camera remain in the same place. Aside from that, the position of the specular reflections changes too, leading to the darker patch in the center of Fig 7.20 e-g, which impedes the measurement of the ratio between absorption and scattering between both lipidic regions. Aside from that, both systems seem to be in good agreement with the relationship between fat and muscle, with fat being consistently lower in the absorption/scattering ratio images.

7.6.1 Scattering and absorption

As shown in the previous section, the key advantage of SFDI as an imaging technique lies in its ability to decouple absorption from scattering. Therefore, we can compare the optical response of the samples (Figs. 7.22 and 7.23 for absorption and scattering, respectively).

Initially, no clear separation is seen in the absorption properties of the samples when comparing healthy and dystrophic samples, as both categories have samples with low and high absorption at all wavelength ranges (Fig. 7.22). This corresponds with the peak-valley-peak nature of the histograms viewed in the green (Fig. 7.22, e) and red (Fig. 7.22, f) color ranges that originates from the dispersion in absorption values. As the wavelength moves towards smaller values the absorption increases, as expected from samples that had red hues. However, the effect in this color range is not properly quantified by our Monte Carlo simulations, as there are some control samples (814 and 861, Fig. 7.22, a) and some dystrophic ones (621, 628, 741, 742, 867, 870, Fig. 7.22, a) that saturate for the blue wavelengths to the maximum possible value. This limitation comes from the range chosen to simulate the optical properties, which was limited to 20 cm^{-1} as this is known to be over the hemoglobin absorption at this spectral range (Fig. 4.7), which is the strongest absorbing chromophore in biological tissues [2]. Still, this was not enough to encompass the complexity of the mouse samples, and the Monte Carlo LUT must be completed with more simulations to quantify the absorption in the blue range properly. Even with that limitation, we see that the relative tendency between the samples is maintained at the different spectral ranges, so we can infer that samples that had high absorption in red and green will behave similarly in blue, suggesting an overall increase in chromophore density in those samples. The overall median absorption value varies between 12 mm^{-1} and 17 mm^{-1} between spectral ranges, which is also consistent with the variation observed for each individual sample.

For the scattering (Fig. 7.23), most samples are close to the median of the dataset at the three spectral ranges, suggesting that the tissue organization is fairly similar for all samples, at least at the scale given by the spatial resolution of the SFDI system. Some control samples have larger scattering, which sways the distributions towards higher values than the dystrophic ones. Still, most data collapses to values of approximately 12-15 cm^{-1}, depending on the spectral range, which coincides with the values provided in the literature for muscle [14] and, specifically, mouse muscle [15].

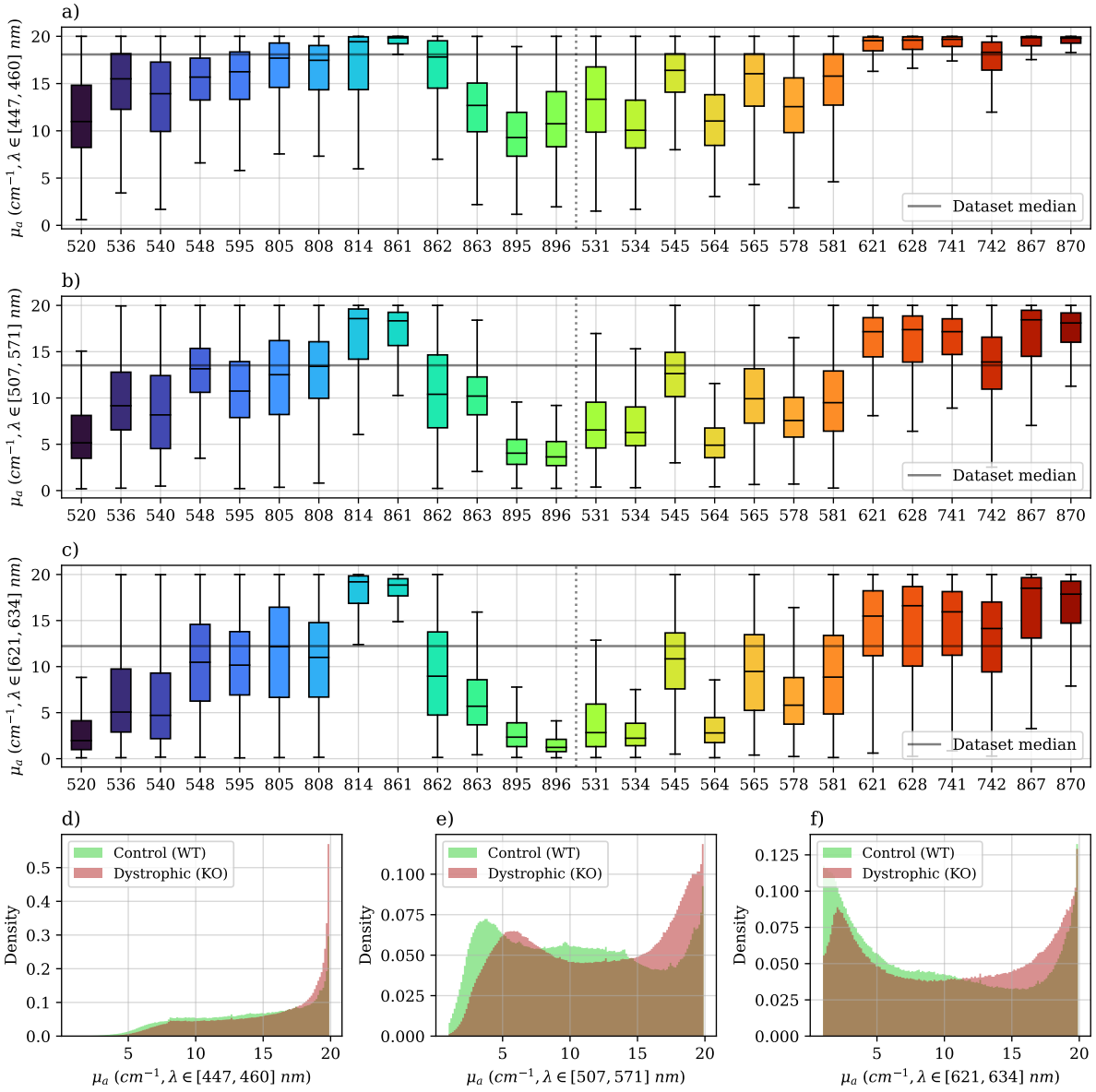

Figure 7.22: Absorption coefficient comparison for the muscle samples in dataset MD2 for the high-SNR areas of the projector in the blue (a, d), green (b, e) and red (c, f) color ranges. The colors in d-f correspond to the samples in the boxplots grouped according to their clinical category. The dotted vertical line in the boxplots separates the control (WT) samples on the left from the dystrophic ones (KO) on the right.

7.6.2 Albedo

As with HSI-derived data, we can calculate the albedo with SFDI measurements to compare its response between different samples. The corresponding data is shown in Fig. 7.24.

Even if the individual absorption and scattering distributions overlap significantly, the subtleties of each coefficient appear to compensate for the other to provide better separation between clinical categories in the albedo distributions, which have a much larger dynamic range than their HSI counterparts. When considering the whole boxplots, all samples keep their relative behavior throughout the spectrum, meaning that high albedo samples will be high in the entire spectral range, while low albedo

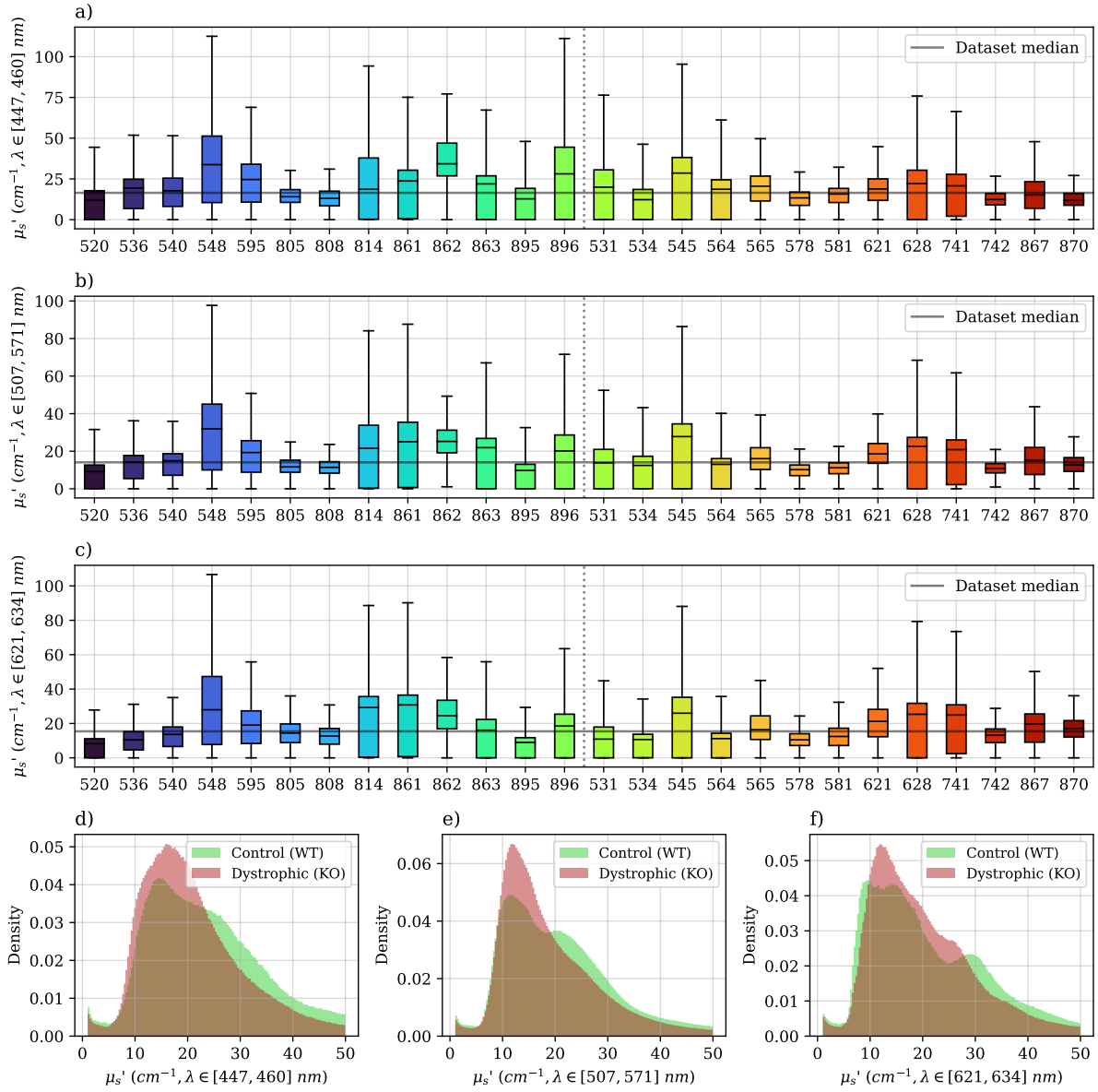

Figure 7.23: Scattering coefficient comparison for the muscle samples in dataset MD2 for the high-SNR areas of the projector in the blue (a, d), green (b, e) and red (c, f) color ranges. The colors in d-f correspond to the samples in the boxplots grouped according to their clinical category. The vertical line in the boxplots separates the control (WT) samples on the left from the dystrophic ones (KO) on the right.

samples will stay low, with only slight changes to their distribution spread.

Although there is high inter-sample variability, healthy samples have, overall, lower albedo than dystrophic ones, suggesting darker samples at the three wavelength ranges. We have seen before that fat content is a disease marker, given that muscular dystrophies tend to cause fatty substitution of muscular tissue. We have also seen that fat is lighter (i.e., less absorbing) and whiter (more scattering) than muscle, which means that fatty tissue has a higher albedo than muscle tissue (threshold in $a = 0.5$, $a = 0.55$ and $a = 0.6$ for the blue, green, and red wavelength ranges, respectively). Therefore, the high-albedo results obtained in most dystrophic samples may be caused by fatty infiltrations that are too small

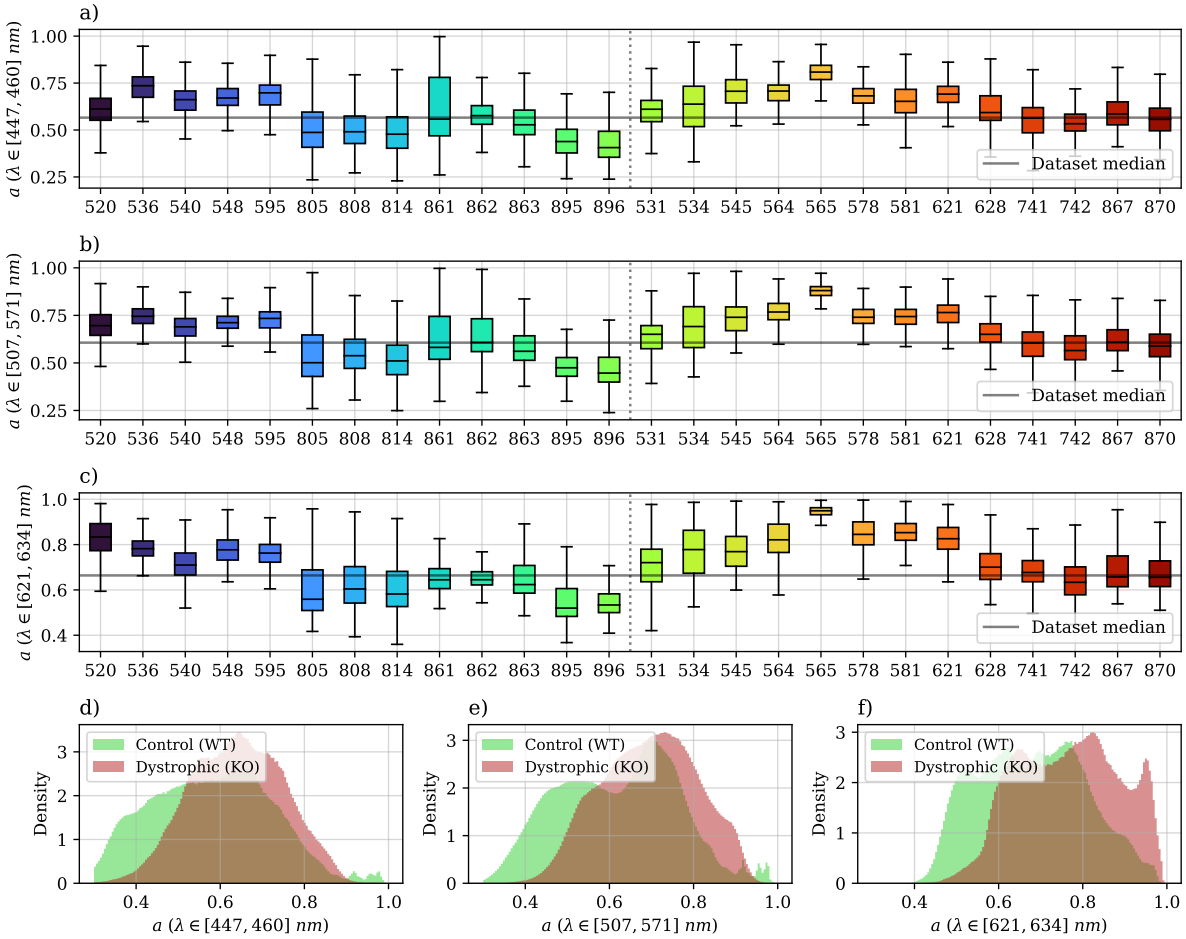

Figure 7.24: Albedo comparison for the muscle samples in dataset MD2 for the high-SNR areas of the projector in the blue (a, d), green (b, e) and red (c, f) color ranges. The colors in d-f correspond to the samples in the boxplots grouped according to their clinical category. The vertical line in the boxplots separates the control (WT) samples on the left from the dystrophic ones (KO) on the right.

to be individually resolved by the SFDI system but big enough to cause changes in the perceived albedo. Further research is needed to validate this hypothesis by quantifying the fat content in histology images.

7.7 Conclusions

This chapter analyzed the application of hyperspectral imaging (HSI) and spatial frequency domain imaging (SFDI) to characterize muscle tissue samples from dataset MD2, focusing on the chemical changes associated with α-sarcoglycan deficiency. Initial analysis of average reflectance spectra in the visible-near infrared (VISNIR) and short-wave infrared (SWIR) ranges revealed distinct spectral characteristics. VISNIR spectra exhibited higher reflectance above 600 nm, consistent with the reddish color of the samples, and characteristic hemoglobin/myoglobin absorption valleys around 550 and 580 nm. SWIR spectra, while influenced by chromophores like collagen, elastin, and fat, were primarily dominated by water absorption. The measurement of the thin muscle samples proved to be challenging in the low-absorption ranges of both VISNIR and SWIR, which allowed light to penetrate to the underlying

substrate, distorting spectral measurements in certain regions. These affected regions were excluded from further analysis.

Three different models – Monte Carlo simulations, an empirical approximation, and the theoretical Kubelka-Munk method – were compared for their ability to estimate the ratio of absorption to scattering. While each model relies on distinct assumptions, all three exhibited similar spectral trends in high SNR regions, differing primarily in baseline offset. This consistency suggests that each model can effectively capture the spatial distribution of chromophores. The Monte Carlo-based approach, being the most general approach due to its inherent consideration of multiple scattering, was chosen for subsequent albedo calculations. Comparison of albedo between sample categories revealed similar, high albedo values in both spectral ranges, with no clear distinction between control and knockout samples. However, slightly lower albedo in the hemoglobin-dominated spectral range in some control samples hinted at potentially higher hemoglobin content. Chromophore estimation using a two-hemoglobin model revealed that most samples exhibited near 100% oxyhemoglobin content, with deviations observed only in the four largest samples. This observation suggests that a larger sample volume facilitates the detection of areas with hemoglobin not fully exposed to oxygen. Given the limitations of separating absorption and scattering in these samples, albedo or average reflectance were deemed more suitable metrics for further analysis.

In the SWIR range, a phantom-based experiment was conducted to estimate fat content, a key marker of muscular dystrophy. A model based on the reflectance ratio between two relevant fat-water peaks, similar to those applied in MRI for dystrophy diagnosis, successfully identified areas with low muscle content in samples exhibiting fatty inclusions, demonstrating the potential of this approach for detecting fatty replacement in dystrophic muscle tissue. However, further refinement and testing with phantoms of varying thicknesses are necessary to address challenges posed by thinner samples where light penetration extends beyond the sample boundaries. Our current work focuses on refining this metric by using silicone phantoms of known optical properties and thicknesses placed on different substrates to evaluate and decouple their spectral influence from that of the phantoms [16].

SFDI reflectance measurements were also performed, focusing on the red-green-blue color peaks to avoid low SNR regions in the LED projector output. The rapid decay of reflectance with increasing spatial frequency (beyond 0.22 mm^{-1}) suggests low scattering in the samples. This information could be used to optimize measurement protocols and minimize sample drying during long SFDI sessions. SFDI also highlighted the fatty regions previously identified through HSI-SWIR as less absorbing and more scattering than surrounding tissue, which is consistent with the expected optical behavior of fat. A comparison of absorption/scattering ratios derived from HSI and SFDI revealed a significant discrepancy, with HSI-derived ratios being an order of magnitude lower than their SFDI counterparts. This difference is likely attributable to the different placement of the reference Spectralon during measurements. Additionally, variations in illumination paths between the two systems, combined with potential sample drying between HSI and SFDI acquisitions, pose challenges for direct comparison.

Decoupling absorption and scattering parameters across the dataset revealed overlapping distributions between sample categories. In the red range, half of the dystrophic samples exhibited absorption above the dataset median, while control samples mostly remained below, suggesting higher red light absorption in dystrophic samples. In the blue range, where hemoglobin dominates, and beyond 600 nm, where fat and water content increase, the observed trends suggest potential fat accumulation in dystrophic samples. Scattering was more homogeneous, with dystrophic samples tending towards slightly lower values. However, both categories exhibited inter-sample variability, consistent with variations in sample shape and preparation. Analysis of albedo, however, revealed a separation between groups better than what was observed with HSI alone. Dystrophic samples exhibited consistently higher albedo, indicative of greater overall reflectivity and further supporting the hypothesis of increased fat content.

References

[1] P. Kubelka and F. Munk: "Ein Beitrag Zur Optik Der Farbanstriche.", *Zeitschrift für Technische Physik* **15**(12), 593–601 (1931).

[2] S. L. Jacques: "Optical Properties of Biological Tissues: A Review", *Physics in Medicine and Biology* **58**(11), R37–R61 (2013). DOI: 10.1088/0031-9155/58/11/R37.

[3] V. Krishnaswamy et al.: "Quantitative imaging of scattering changes associated with epithelial proliferation, necrosis, and fibrosis in tumors using microsampling reflectance spectroscopy", *Journal of Biomedical Optics* **14**(1), 014004 (2009). DOI: 10.1117/1.3065540.

[4] P. Bevington and D. K. Robinson: "Data Reduction and Error Analysis for the Physical Sciences", McGraw-Hill Education, 2003. ISBN: 9780072472271.

[5] J. A. Gutiérrez-Gutiérrez et al.: "Rotating Mirror Short-Wave Infrared Hyperspectral Imaging System: Characterization and Applications.", Available at SSRN. 2024. DOI: 10.2139/ssrn.4961885.

[6] W. C. Etchison: "Letter to the editor response", United States, 2011. DOI: 10.1177/1941738111422691.

[7] A. Pardo Franco: "Light, machines, and cancer: imaging systems and processing techniques for wide-field diagnostics in scattering media", PhD thesis. Santander: Universidad de Cantabria, 2022. https://hdl.handle.net/10902/26190.

[8] D. J. Cuccia et al.: "Quantitation and mapping of tissue optical properties using modulated imaging", *Journal of Biomedical Optics* **14**(2), 024012 (2009). DOI: 10.1117/1.3088140.

[9] J. A. Gutiérrez-Gutiérrez et al.: "Comparison between optical coherence tomography and phase shifting profilometry for surface estimation", in: *Translational Biophotonics: Diagnostics and Therapeutics III*. Ed. by Z. Huang and L. D. Lilge. **12627**. International Society for Optics and Photonics. SPIE, 2023 126271P. DOI: 10.1117/12.2670564.

[10] S. Ségaud et al.: "Trident: A dual oxygenation and fluorescence imaging platform for real-time and quantitative surgical guidance", *Frontiers in Photonics* **3** (2022). DOI: 10.3389/fphot.2022.1032776.

[11] L. Cinelli et al.: "Single snapshot imaging of optical properties (SSOP) for perfusion assessment during gastric conduit creation for esophagectomy: An experimental study on pigs", *Cancers* **13**(23) (2021). DOI: 10.3390/cancers13236079.

[12] E. Aguénounon et al.: "Real-time, wide-field and high-quality single snapshot imaging of optical properties with profile correction using deep learning", *Biomedical Optics Express* **11**(10), 5701 (2020). DOI: 10.1364/boe.397681.

[13] M. Schmidt et al.: "Real-time, wide-field, and quantitative oxygenation imaging using spatiotemporal modulation of light", *Journal of Biomedical Optics* **24**(07), 1 (2019). DOI: 10.1117/1.jbo.24.7.071610.

[14] S. L. Jacques: "Tissue Optics", tech. rep. 2020.

[15] G. Hall et al.: "Goniometric measurements of thick tissue using Monte Carlo simulations to obtain the single scattering anisotropy coefficient", *Biomedical Optics Express* **3**(11), 2707–2719 (2012). DOI: 10.1364/BOE.3.002707.

[16] J. A. Gutiérrez-Gutiérrez, V. Mieites, and O. M. Conde: "Influence of Substrate Selection for Thin ex-vivo Specimens on Hyperspectral Imaging Measurements of Silicone Phantoms", in: *Translational biophotonics: diagnostics and therapeutics (ECBO 2025)*. Under review. SPIE-Intl Soc Optical Eng, 2025.

Multispectral Mueller-matrix imaging of dystrophic mice muscles

8

The remaining standalone imaging technique explored in this work is multispectral Mueller Matrix Imaging (MMI). The main advantage of this technology is its ability to decouple the polarization properties of the light from those of the sample, providing a direct characterization of the different tissue types. Since the MMI system is configured in reflectance mode for the measurement of thick biological samples, the used wavelength will affect how the polarization properties manifest themselves, given the changes in optical path caused by different absorption and scattering properties. Therefore, the addition of the multispectral light source will aid in inferring the chemical/structural causes of polarization changes.

This imaging method was implemented at the final stages of this thesis when all muscle samples had already been measured and moved into long-term storage. Thus, the three remaining whole control legs were used for this exploratory work (dataset LD). Additionally, the MMI system v2.0 (see Ch. 4) had not had all the upgrades implemented at the time due to production delays in some of the required components, so the states of the Polarization State Generator (PSG) are those of the v1.0, but the light source used was that of the v2.0, which provides better spectral coverage and adds one additional wavelength with respect to v1.0.

The next sections will follow the same development of Mieites *et al.* [1] applied this time to the mouse legs, starting with an overview of the measurements, followed by the direct properties that can be obtained from the Mueller matrices and, finally, by the results derived from the matrix decomposition methods and machine learning techniques.

8.1 Sample preparation and dataset description

The samples were defrosted according to the protocol indicated for the mice quadriceps (Ch. 6). Then, the skin was removed for the three legs (Fig. 8.1), and, finally, the samples were re-hydrated with saline solution to minimize water evaporation between measurements.

It is worth noting that the apparent aspect of the three skin-off legs was strikingly different, even if the three samples corresponded with male, wild-type 11 and 12-month-old mice. Specifically, there were regions with exposed fat and muscle visible in the three samples. Still, all of them contained a white, anisotropic structure that was different between them and that is not observed in skin-off specimens when the samples are freshly excised [2, 3]. The muscle samples did not contain the same kind of structure since they were fixed to the cork completely covered by the clear fixing agent[1] that cleared off the muscle samples after defrosting. We believe that those white structures are actually parts of the muscle groups that did not freeze properly on the legs, which were not protected by the fixing agent in the same way the muscle samples were. As a consequence,

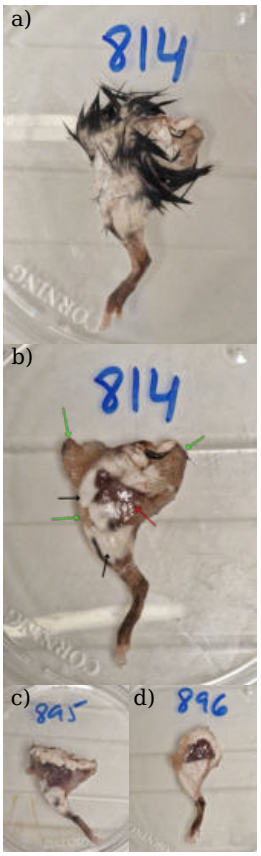

Figure 8.1: Leg 814 before (a) and after (b) skin removal. Legs 895 (c) and 896 (d) after skin removal. The red arrow in (b) points to exposed healthy muscle, the green one points to fatty deposits, and the black ones point to freeze-damaged muscle.

[1] Note that "clear fixing agent" refers in this chapter to the glue that was used to fix the muscle biopsies to the cork for transportation. The samples themselves were received frozen, without any fixation.

the water crystals in those regions ended up breaking the micro-structure of the muscles, increasing the scattering to the point where the samples appeared completely white. This hypothesis is compatible with the defects observed in incorrectly frozen muscle samples: when muscles are properly frozen, their structure, as observed in histological sections, is homogeneous, while frozen-damaged muscle breaks apart at multiple levels of muscular organization [4]. It would also explain why the regions were different between the three samples, as the parts of the legs that were not affected by this phenomenon were those that were covered by hair, which is known to be a thermal insulator.

The anatomical landmarks of a mouse leg guided the identification of different regions of interest in the dissection images. These included regions of healthy muscle, damaged muscle, and fat, all labeled based on their macroscopic appearances (Fig. 8.2).

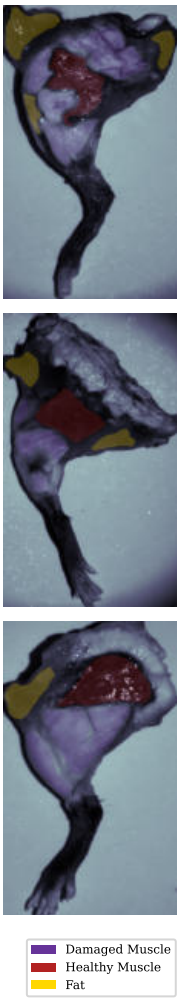

Figure 8.2: Top to bottom: Intensity (M_{11}) images captured by the MMI system of legs 814, 895, and 896 from dataset LD. The labeled areas included healthy muscle, freeze-damaged muscle, and fat.

8.2 Mueller matrices

The analysis of the acquired Mueller matrices showed that they were predominantly diagonal across all samples and wavelengths (Fig. 8.3), with both the normalized components m_{ij}, where $i, j \in [1, 4]$, and the first non-normalized element M_{11} forming a diagonal matrix. This polarimetric behavior suggests that the mouse leg tissues primarily depolarize light. However, faint non-zero elements are also shown outside of the diagonal, particularly in the polarizance vector[2].

An analysis of the physical realizability of the Mueller matrices was conducted to validate the measurements (see Sec. 3.3.4). A tolerance of $tol = 10^{-5}$ [1] was employed in evaluating these conditions to account for numerical inaccuracies and noise in the measurements.

By evaluating the ensemble criterion, we obtained either physically realizable or non-realizable areas in each sample at each wavelength (Fig. 8.4). These non-realizable regions were associated with areas exhibiting specular reflections. In our previous work [1], we have seen that the edges of the sample, where water can accumulate, regions with very low SNR or reflections caused by elements surrounding the sample can also introduce areas of no physical realizability.

8.2.1 Indices of polarimetric purity and anisotropy coefficients

To further investigate the polarimetric properties of the mouse leg tissues, the indices of polarimetric purity (IPPs) (Eq. 3.48) and the degree of polarimetric purity (Eq. 3.49) were derived for each sample. As depicted in Figure 8.5, the polarimetric purity generally decreased with increasing wavelength, although a slight increase was observed at 546 nm, similar to our previous findings [1]. This wavelength-dependent decrease in polarimetric purity can be attributed to the increased scattering and longer optical paths associated with longer wavelengths, which leads to an increment in depolarization. The polarimetric purity shown satisfies the inequality $1 > P3 > P2 > P1 > 0$, and some regions of the samples have high $P3$ values, suggesting that the samples are non-pure but that

[2] see the block expression of the Mueller matrices in Eq. 3.23.

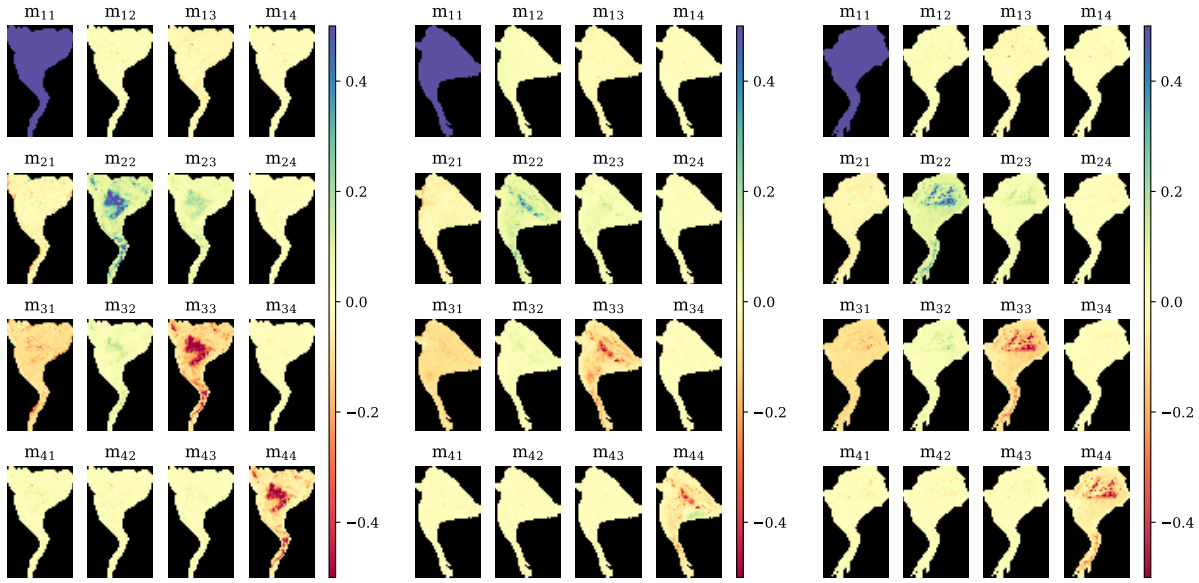

Figure 8.3: Mueller matrix of the whole-leg samples 814 (left), 895 (center), and 896 (right) of dataset LD. The non-normalized first element of the matrix, M_{11}, is represented in Fig. 8.2 with the regions of interest on top, while the rest of the coefficients, m_{ij} $(i, j \in [1, 4])$ shown in this image are normalized to M_{11}. The colormaps have been adjusted to the range (-0.5, 0.5) for visualization purposes.

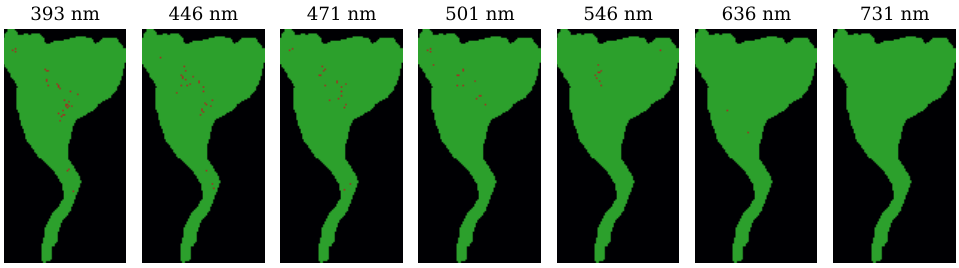

Figure 8.4: Ensemble criterion applied to sample 814 from dataset LD at the seven available wavelengths. Areas where the ensemble criterion is fulfilled are represented in green, while red represents where the matrices are not physically realizable.

some of their areas are further away from being a perfect depolarizer, as indicated by the off-diagonal elements of the matrices. Furthermore, the analysis revealed variations in polarimetric purity across different tissue types. For instance, the areas labeled as fatty tissue and damaged muscle (Fig. 8.2) exhibited lower polarimetric purity compared to healthy muscle tissue, consistent with their higher scattering [5] and consequent depolarization.

Regarding the anisotropy, the overall observed total anisotropy was low for the three samples (P_α<0.15) in the three tissue types (Fig. 8.6). Nonetheless, some interesting patterns have been observed. For example, the linear and circular anisotropy values are in similar ranges[3]. While the whole surface of the legs appears to have similar levels of linear anisotropy, only healthy muscle tissue has circular anisotropy. Although anisotropy values are low and further histological verification is needed, this result is particularly interesting when comparing freeze-damaged and healthy muscle since it suggests that the damage induced by the faster freezing of some muscle areas is enough to break some micro-structural chirality but not the larger linear anisotropy of the muscle fiber bundles. Finally, unlike what was observed in brain [1], the anisotropy coefficients appear stable throughout the whole wavelength range, with

[3] When not considering the specular reflections

the exception of the linear anisotropy at 501 nm, which causes an overall decrease in the total anisotropy at the same wavelength, suggesting the presence of chromophores that are not present in brain tissue.

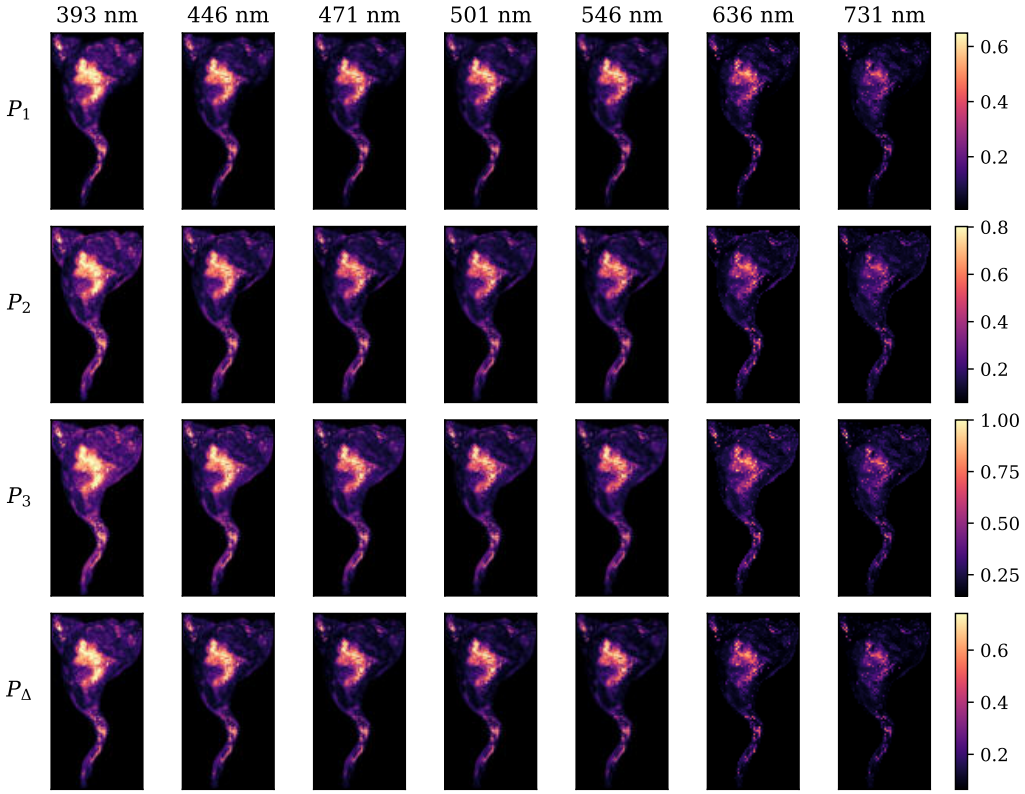

Figure 8.5: Indices P_1, P_2, P_3 and degree of polarimetric purity P_Δ represented at all seven wavelengths for sample 814 of dataset LD. The colormaps have been adjusted to exclude all values below the 1st and over the 99th percentiles of each magnitude.

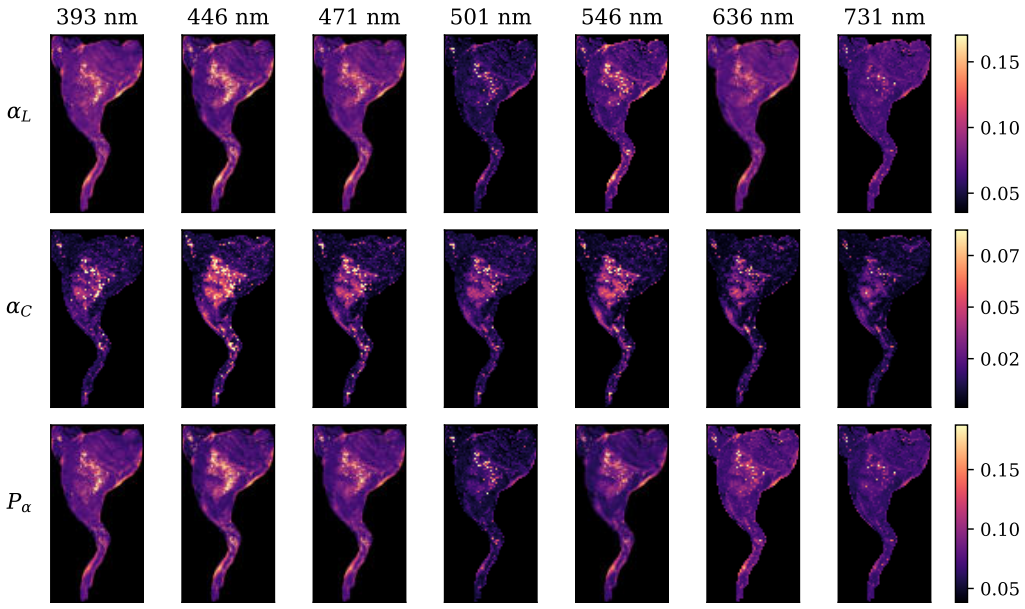

Figure 8.6: Linear (α_L) and circular anisotropy (α_C), and total anisotropy (P_α) represented at all seven wavelengths for sample 814 of dataset LD. The colormaps have been adjusted to exclude all values below the 1st and over the 99th percentiles of each magnitude.

8.3 Matrix decomposition methods

8.3.1 Forward polar decomposition

Since the measurements were performed in a reflectance configuration, a common approach is to multiply the matrices by the diagonal matrix $diag(1, 1, -1, -1)$[4] so that the same reference frame is used for the light beams illuminating and exiting the sample [6, 7]. This transformation is applied due to the Lu-Chipman decomposition assuming that the sign of the eigenvalues calculated during the derivation of $M_{\Delta P}$ and M_R (see Sec. 3.5) is the same for the three eigenvalues, which is not always the case and leads to depolarization and retardance matrices that do not correspond with the sample [6, 8]. By applying this transformation on the Mueller matrix of the sample, the polar decomposition can be used by only modifying the derivation of $m_{\Delta P}$ and m_R, only if the determinant of $m_{\Delta P}$ is negative, to calculate them using the SVD, as in the symmetric decomposition [6, 9].

[4] Matrix of an ideal mirror reflection.

After applying forward polar decomposition, the total depolarization (Δ), retardance (R), and diattenuation (D) were computed for the three mouse legs. Figure 8.7 illustrates representative images of these polarimetric parameters for a lateral view of one leg. To enhance visualization, the color scales have been adjusted to encompass 99% of the data, clipping extreme values. This results in the following ranges: $\Delta \in$[0.3,0.98], $R \in$[0, 2.5], and $D \in [7 \times 10^{-6}, 0.01]$. Diattenuation values are presented on a logarithmic scale to enhance contrast.

Depolarization effectively differentiates healthy muscle from damaged muscle or fat, consistent with the whiter appearance of the last two, which indicates higher scattering. Furthermore, depolarization generally increases with wavelength, likely due to the increased optical path length

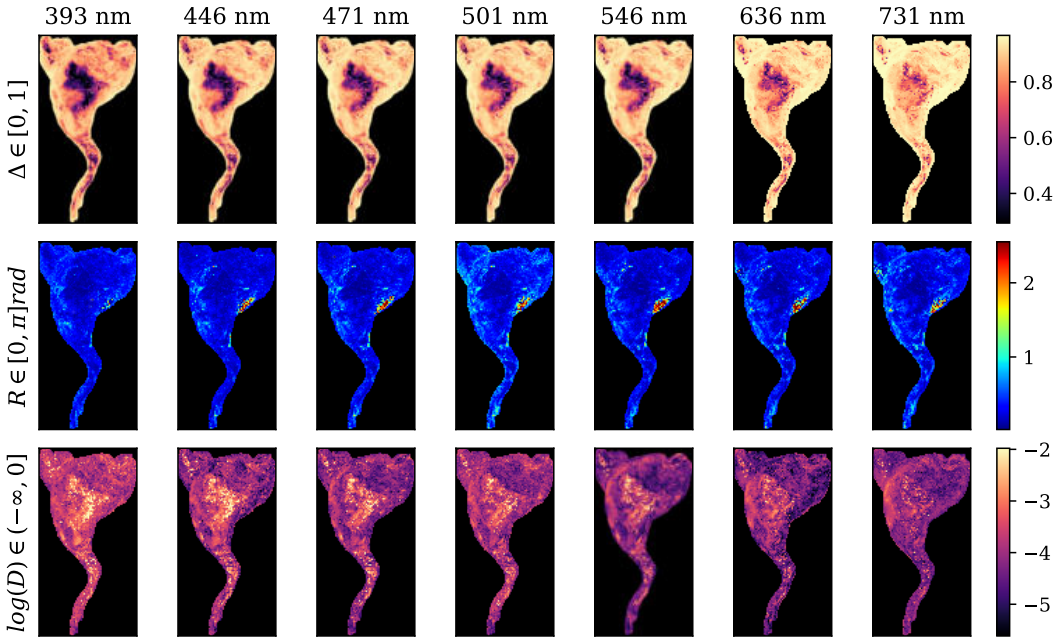

Figure 8.7: Depolarization (Δ), retardance (R), and diattenuation (D) of the skin-off leg 814 from dataset LD, from 393 nm to 731 nm.

at greater penetration depths, which further randomizes polarization, but muscle is still highlighted as the least depolarizing element of the sample. At the central wavelengths (446 - 546 nm), depolarization appears mostly unchanged. It is only below that range that more detail is appreciable due to the shorter penetration depth, while the longer wavelengths blur the differences between tissue.

Retardance remains relatively consistent across wavelengths, with a very slight increase observed at 501 nm near the damaged muscle areas. This stability is expected due to the anisotropic nature of skeletal muscle. However, the measured retardance values are low, suggesting two possibilities: (1) the microstructure of the sample has degraded, suppressing detectable retardance, or (2) the small internal structures within the mouse muscle result in photons traversing multiple muscle groups with varying orientations, effectively averaging the overall retardance to near-zero.

Diattenuation exhibits an interesting behavior. Like retardance, diattenuation is initially low but decreases with wavelength instead of remaining constant. Most of the incident light is depolarized by the sample, especially in damaged muscle or fat and at long wavelengths. Given that the initial diattenuation is low, the longer path length could be influencing the loss of diattenuation in a way that is more apparent than in the retardance images. Notably, diattenuation highlights healthy muscle areas, suggesting that there is a diattenuating component to the arrangement of the muscle fibers. Diattenuation also highlights textures more than depolarization or retardance, suggesting that the diattenuation data might represent the uppermost layers of the tissue, where the light has not been completely depolarized yet.

This behavior is consistent across all samples: depolarization primarily differentiates healthy muscle from other tissues and increases with wavelength; retardance remains stable; and diattenuation, while low, is able to pick up on complex tissue anatomy. Shorter wavelengths generally offer better image detail due to shallower light penetration and lesser blurring.

The consistency observed between the three samples allowed for the grouping of their results according to the identified labels (Fig. 8.8). As indicated before, the diattenuation decreases consistently for all sample types with the incrementing wavelength and shows low values overall while being slightly higher for healthy muscle samples. Something similar occurs for the retardance, which showcases low values for the three tissue types. Interestingly, the retardance between healthy (a) and damaged (b) muscle was very similar and lower than that of fatty tissues (c). Although fat has no structural elements that should indicate the presence of retardance in the tissue, the small size of the mouse legs implies that light that enters or exits the sample through the lipidic areas is going to interact with muscle tissue and tendons as well, so the received retardance signal on the fat is most likely due to the underlying muscle tissue, tendons or fasciae. This would also explain why the retardance average is so separated from its median on fatty regions, meaning that there is more variance in the distribution than for muscle tissue. The principal magnitude that separates healthy muscle tissue from the rest is, as indicated before, depolarization, with values ranging from 0.0 to 0.1, while damaged muscle remains over 0.65 and fat over 0.7. This suggests

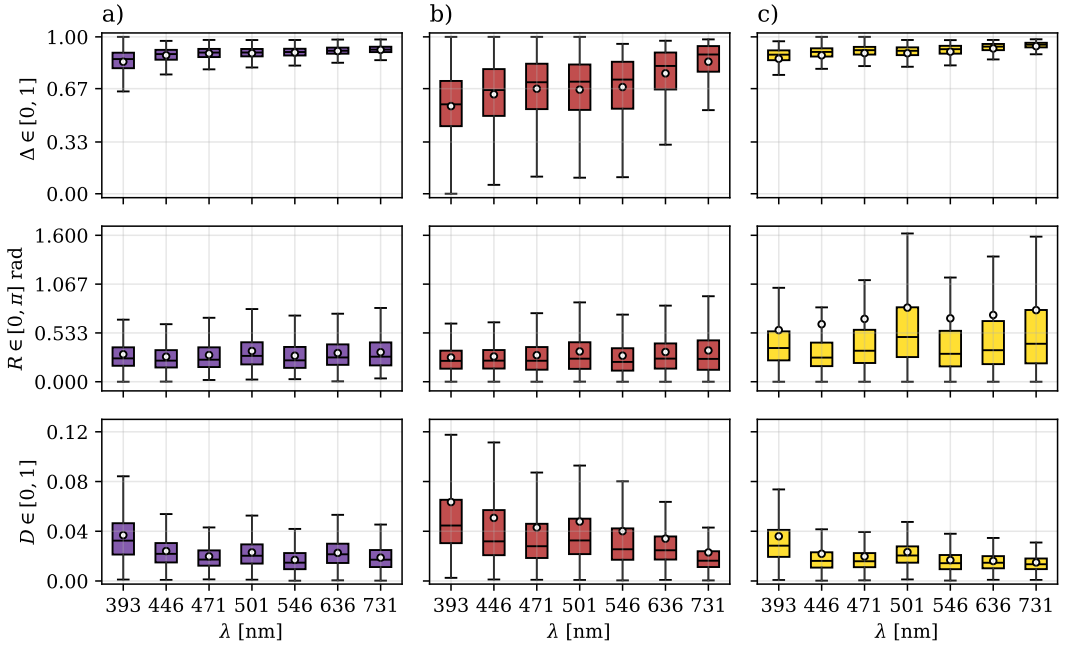

Figure 8.8: Overall depolarization (Δ), retardance (R) and diattenuation (D) of damaged muscle (column a), healthy muscle (column b), and fat (column c) for the three samples of dataset LD. The data was sampled so that the three labels and the three samples contributed to the boxplots with the same number of data points. The white dots represent the overall average, more affected by the non-plotted outliers than the rest of the boxplot.

that the best marker of healthy muscle is low depolarization values, which, combined with higher diattenuation, indicates a high level of tissue structure that is able to maintain the polarimetric properties of the incident light.

8.3.2 Differential decomposition

A significant drawback of serial decomposition methods, such as the forward and reverse polar decompositions, is their inherent order dependence. The sequential arrangement of the depolarizer, retarder, and diattenuator matrices influences the resulting individual matrix elements. Different orders produce different sets of equivalent matrices, leading to ambiguities in the extracted polarization parameters. This is addressed by the symmetric decomposition method, but it still reduces the sample to a sequence of five optical elements.

The differential decomposition aims to overcome these limitations by interpreting the sample as an infinite number of infinitesimal optical elements. The method involves calculating the matrix logarithm (see Sec. 3.5), which, similarly as before, is often obtained by previously multiplying the Mueller matrix of the sample by the mirror reflection matrix since the matrix logarithm of a Mueller matrix captured with a reflectance system does not often exist [10].

Once the matrix logarithm L was obtained, the linear retardance R_L and diattenuation D_L were derived as[5]

$$R_L = \frac{1}{\sqrt{2}}\sqrt{(L_{4,3} - L_{3,4})^2 + (L_{2,4} - L_{4,2})^2} \quad \text{, and} \tag{8.1}$$

[5] The circular counterparts of R_L and D_L were negligible and thus not considered in the analysis.

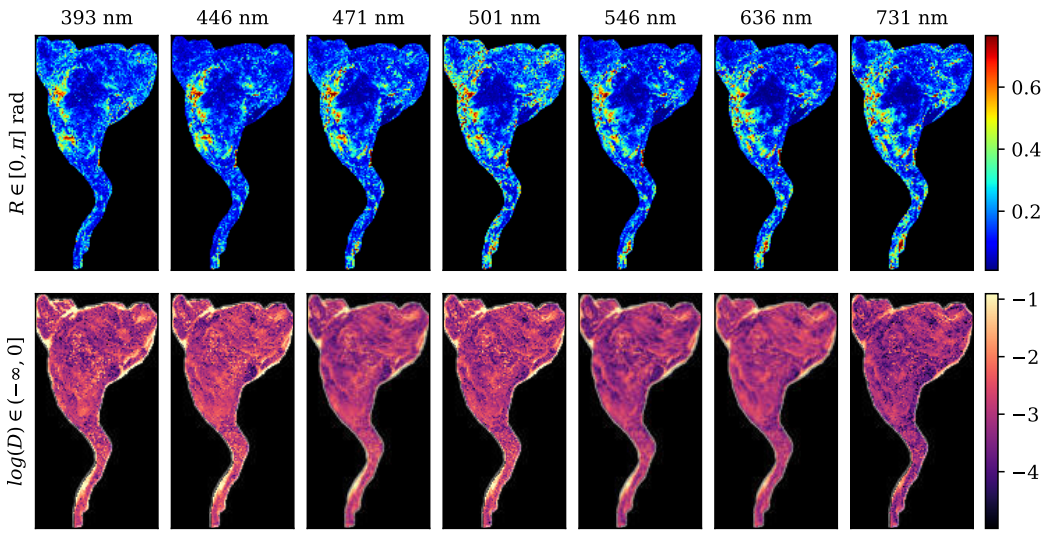

Figure 8.9: Linear retardance (R_L) and diattenuation (D_L), as obtained from the differential decomposition, represented at all seven wavelengths for sample 814 of dataset LD. The colormaps have been adjusted to exclude all values below the 1st and over the 99th percentiles of each magnitude.

$$D_L = \frac{1}{\sqrt{2}}\sqrt{(-L_{1,2} - L_{2,1})^2 + (-L_{1,3} - L_{3,1})^2} \quad . \tag{8.2}$$

The resulting maps of retardance and diattenuation are shown in Fig. 8.9.

As occurred with the forward polar decomposition, the diattenuation obtained through the differential decomposition highlights textural details of the sample, but its value is overall low and non-discriminative between tissues. On the retardance maps, however, some interesting changes are visible in the non-healthy muscle areas. Specifically, the retardance seems to be higher in regions where the frozen-damaged muscle is more visible. The difference between the results provided with the polar decomposition and the differential decomposition lies in the fundamentals of each decomposition method: if the sample is described as a discrete (polar decomposition) set of matrices, the matrices in the set are going to be different from a sample that is defined as a continuum set of matrices (differential decomposition).

Pardo *et al.* [10] also analyzed the wide-field properties of skeletal muscle with the differential decomposition, using a multispectral system that measures at 420, 455, 460, and 780 nm. In their work, using a pork fillet as a sample, the depolarization increased with the wavelength for all tissue types, similar to what is observed for the mice samples through the degree of polarimetric purity (Fig. 8.5). The diattenuation values the authors report also coincide with what we observe for the mice samples (Fig. 8.9): values below 0.1, which are slightly higher in healthy skeletal muscle regions, especially at low wavelengths. Finally, the work by Pardo *et al.* describes the retardance of the sample being higher in connective tissue and muscle, followed by skin, and finally fat having the lowest retardance signal. We could then infer that the mice samples showing higher retardance in this region is not necessarily due to the damaged muscle but to the connective tissue present below it since the high retardance is observed in the muscle areas closer to the knee for

the three samples, where most leg tendons coincide. The authors also report retardance values below 0.6, and they show an increase with the wavelength, as we have also seen before in brain tissue, possibly due to the longer penetration of the photons accumulating more retardance on their way out of the sample [1, 10].

It is worth noting that the retardance increase with wavelength observed in these samples is very subtle for both decomposition methods. In contrast, for lamb brain, we observed a more significant increase [1], with a relative increase similar to what Pardo *et al.* report on their work for porcine skeletal muscle [10]. However, Bonaventura *et al.* [11] and Carlson *et al.* [12] report a decrease of the retardance with the increasing wavelength when analyzing fixed ferret brains. Although fixation does affect the polarization properties of the samples, as Gros *et al.* demonstrated [13], and that all these samples and systems are different, it is also possible that the size of the anatomical structures analyzed is affecting the results. The lamb and porcine experiments have a fairly big size (≈2-6 cm thickness) when compared with the ferret and mice ones (< 1 cm thickness), so photons of the same wavelength are much more likely to stay in the same anatomical structure in the former than in the latter. As a consequence, measurements of ferret or mice samples are much more likely to cause polarization averaging as the photons travel from one anatomical structure (i.e., muscle, bone, fat) to the next one, effectively increasing the depolarization and reducing the retardance and the diattenuation.

8.4 Importance of the Mueller matrix elements

Mueller Matrix Imaging is a measurement technology that obtains a significant number of parameters, especially when combined with multispectral capabilities. Each parameter informs about a different polarization property of the sample. Still, unlike the other techniques we have seen in this thesis, those properties have a complex interpretation which may vary depending on the decomposition method selected. It is then necessary when analyzing Mueller data to compare multiple decomposition methods and validate the system and the measurements with the use of reference samples.

All of the above raises the question of "is it necessary to capture and derive all the polarimetric properties of the sample, or can we instead use a subset of those properties?". The answer to that question will depend on the problem at hand. If the experiments aim to characterize the polarimetric properties of the sample, then the more data captured and the more decomposition methods utilized, the better. However, if the experiments aim to detect one type of tissue, then we can focus our efforts on optimizing the methodology to detect that type of tissue properly. If optimized, Mueller polarimetry can be stripped of its complexity and used instead to find only those matrix elements that help solve each problem.

In this section, we will explore some classification methods to understand the important matrix elements that distinguish the healthy muscle areas from the rest of the samples in the mouse legs. The dataset used for the classification was balanced by random sampling so that the same

number of data points were taken for each label (Fig. 8.2) and each sample. A total of 22125 pixels were taken for each label and sample. The features introduced to the dataset were all the normalized Mueller matrix elements but the first one ($M_{1,1}$) at the seven wavelengths.

8.4.1 K-nearest neighbors supervised classification

Following our previous work [1], we started by classifying the data using K-Nearest Neighbors classification (KNN). The key parameter is the number of neighbors to use, which, in this case, was optimized by choosing the number of neighbors that maximized the accuracy for the test dataset after leave-one-sample-out cross-validation. The final number of neighbors was $K_N = 5$, similar to the value of $K_N = 8$ we obtained for a different dataset with different features when considering all wavelengths [1]. Then, the data was classified through KNN and validated using leave-one-group-out cross-validation. This method ensures that all of the data points of one of the samples (groups) are selected as the test dataset while the others remain in the training dataset, and no crossing of the data occurs between training and testing. The average confusion matrices for the train and test datasets are shown in Fig. 8.10.

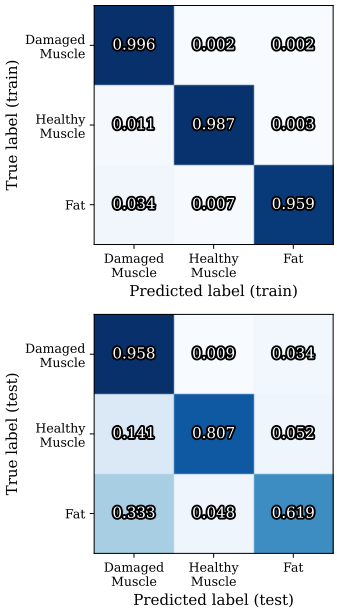

Figure 8.10: Average confusion matrices for the train and test datasets after performing leave-one-group-out cross-validation with a KNN classifier with $K = 5$ neighbors.

Overall, a 98.9% accuracy was obtained for the training dataset while, for the test dataset, the KNN classifier achieved a 79.8% accuracy. However, the per-class accuracy is variable depending on the class. When training, the damaged muscle was the easiest class for the model to accurately determine with a 99.6% accuracy, followed closely by the healthy muscle with 98.7%. On the other hand, while the accuracy of the damaged muscle detection dropped only to 95.8% on the test dataset, the healthy muscle detection dropped up to 80.7%, which is more than a 15% decrease. This suggests that while the frozen-damaged muscle has fairly uniform polarimetric properties across samples, the healthy muscle has a polarimetric signature that is more difficult to identify correctly. This is consistent with the damaged muscle being governed by scattering, which suggests that depolarization is enough to detect it adequately. At the same time, other components might need to be checked when classifying the data in order to segment healthy muscle. Interestingly, the most complex category for the model to properly identify was fat, with an accuracy of 95.9% in the training dataset and only 61.9% in the test dataset. Furthermore, the classifier often classified fat in the test data as damaged muscle, which also suggests that depolarization is the main tissue identifier the classifier is looking for since damaged muscle and fat had similar depolarization properties. Anatomically, fat often presents itself on top of muscle tissue, so the accuracy decrease in the test dataset might arise from polarization data containing information about the fat but also about the underlying muscle, which might be too subtle for the KNN classifier to identify fat properly.

To verify these arguments, we then derived the importance of each feature in the Mueller matrix as viewed by the KNN classifier. As mentioned before, this method focuses on one estimator that summarizes the performance of the classifier (i.e., accuracy) and evaluates the importance of each feature in the dataset through changes in the performance metric. By randomizing the entries in one feature at a time, if the feature is important for the classifier, the performance metric must drop after the

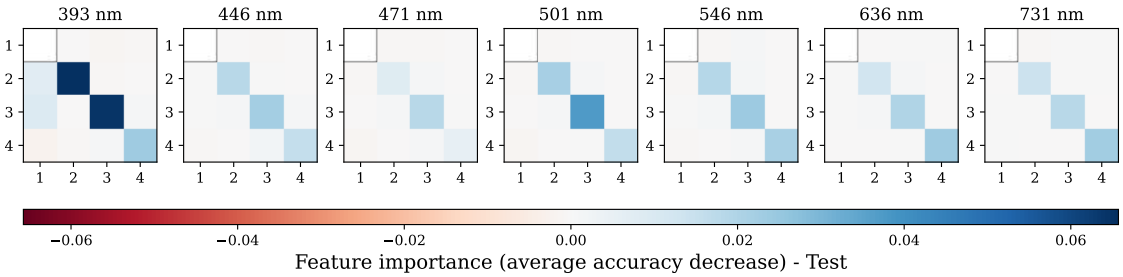

Figure 8.11: Feature importance evaluated as the average accuracy decreases through random permutations with a KNN classifier ($K_N = 5$ neighbors). The features in the dataset were each of the Mueller matrix elements at the seven wavelengths, with the only exception being the first element (M_{11}), which was not included in the dataset due to the matrices being normalized. The average feature importance through random permutations was evaluated after considering the three folds obtained by performing leave-one-group-out cross-validation.

feature is randomized. Analogously, if the feature is not important or if it is too noisy, the performance metric must stay unchanged or even improve after randomizing the feature. The results are shown in Fig. 8.11.

As expected, the most important features for classification are indeed the diagonals of the matrices, which, since the matrices obtained are mostly diagonal, indicates that depolarization is the main discriminant feature between these tissue types, as observed in our previous work [1]. This also explains why the diagonal elements of the matrix at 393 nm are the most important, given that shorter wavelengths penetrate less into the tissue, avoiding mixing polarimetric signals from different tissues, which makes this depolarization more useful than at longer wavelengths. However not all elements in the diagonal are equally important for classification. In particular, the last element of the diagonal is less important than the rest, which indicates that all tissue types affect circularly polarized light in a way that is less discriminant than the effect they have on linearly polarized light. Finally, the second most important wavelength for classification is 501 nm, which corresponds with the slight increment in retardance we observed through the Lu-Chipman decomposition (Fig. 8.8). It has been seen before [10, 14] that the absorption of hemoglobin (or myoglobin in this case) might affect the polarization properties by decreasing the depolarization, i.e., the light that is absorbed by the chromophores is not captured as depolarized light. However, in this experiment, we observe a plateau in depolarization at 501 nm, which corresponds with a valley in oxy- and deoxyhemoglobin (or myoglobin), but also a peak in metmyoglobin (Fig. 4.7), suggesting that the presence of metmyoglobin might aid in correct muscle classification.

Building and validating a multispectral Mueller imaging system can be an arduous task, and we have just seen that not all features are needed to provide fairly good classification results. In scenarios where system complexity should be reduced to the minimum possible, such as surgical vision or real-time imaging, achieving full Mueller polarimetry might not be an option. Instead, a system can be built to obtain a subset of the Mueller elements for a specific task based on the features that are most important for said task. Here, we simulated such a system by repeating the KNN classification using only the elements $M(2,2)$ and $M(3,3)$ of the multispectral Mueller matrices, reducing the number of features from 105 to 14. The resulting confusion matrices are shown in Fig. 8.12.

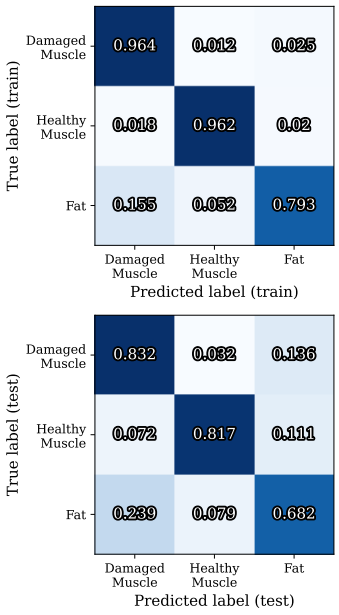

Figure 8.12: Average confusion matrices for the train and test datasets after performing leave-one-group-out cross-validation with a KNN classifier with $K = 23$ neighbors. The data considered for classification were the elements $M(2,2)$ and $M(3,3)$

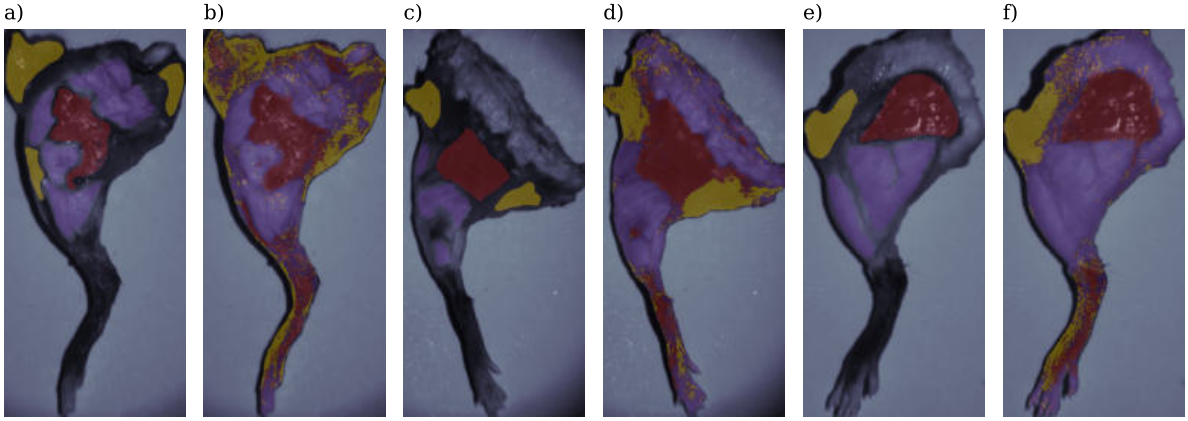

Figure 8.13: Classification of healthy muscle (red), frozen-damaged muscle (purple) and fat (yellow) with a KNN classifier ($K_N = 5$ neighbors). The reference labeled data (a, c, e) is shown next to the output of the model (b, d, f).

Although we optimized the number of neighbors again ($K_N = 23$) to use only the linear elements of the diagonal of the matrices, the average accuracy decreased by 2% when going from 105 to 14 features. This accuracy loss is due to the feature-reduced classifier worsening its prediction for the frozen-damaged muscle (-12.6% accuracy). However, this decrease is compensated on average by the slightly better performance at detecting fat (+6.3% accuracy) and healthy muscle (+1% accuracy). If the task for this classifier were to detect healthy areas of muscle, this suggests that reducing the number of features does not alter but improves the classification performance by removing data related to the other classes. In other words, the polarimetric signal of the muscle lies in the linear elements of the diagonal, which enables the development of partial 3×3 multispectral polarimeters for this task, which are systems that only require linear polarizers, can be calibrated following the same methods detailed in this work and provide faster acquisition and interpretation of the results [15].

Finally, the output of the classifier trained with all features is shown in Fig. 8.13. At this point, it is worth noting that not all labeled pixels were used for classification since the dataset was balanced to include the same number of pixels per sample and per class. Still, the classifier does a good job at detecting the healthy and damaged muscle areas, even in regions around the knee where there is a greater mixture between tissue types. The noisier areas correspond to fatty tissue, as expected, given the decrease in accuracy observed in the test dataset for this category.

8.4.2 K-means unsupervised clustering

To evaluate the results of this classifier, we compared it with the output of an unsupervised clustering method: K-means. This method assesses the similarity of the data points provided by arranging them into K_C different clusters. The results are shown in Fig. 8.14. We evaluated using two to four different clusters, given that only three labels have been identified. Although the data introduced in the clustering method is labeled, K-means does not access it. Instead, it assigns a cluster to each data point by searching for the K_C centroids that maximize cluster

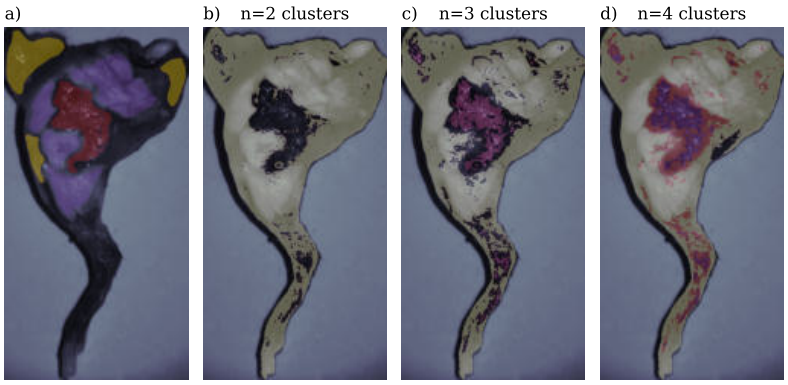

Figure 8.14: Clustering of the data points in sample 814 from dataset Mice leg dataset (see Tab. 6.2) (LD) obtained with K-means with 2-4 clusters. The class assignment (color) to each cluster is randomized, but each color still represents a separate cluster.

separation. Therefore, the classes assigned to each cluster are random, which is the reason why the class number changes for each class when more clusters are added to the method.

When using two clusters, K-means is still able to separate the area we labeled as healthy muscle from the rest of the image, suggesting that, even when unsupervised, there are enough polarimetric differences between the muscle and everything else to determine its margins. When incrementing the number of clusters, K-means is not able to separate the other two types of labeled tissue. Instead, it assigns more clusters to the boundary between the healthy muscle and the surrounding tissues. Although this potentially highlights where one tissue transitions into the next, the unsupervised K-means method was less reliable and more swayed by the specular reflections than the supervised K-neighbors classifier.

8.5 Classification through feature extraction with a supervised autoencoder

Both classifier types described in the previous section are based on finding distinctive features among the ones introduced with the aim of maximizing the separation between classes, regardless of whether the method is supervised or unsupervised. We have also seen that not all features are equally important, so compressing the data before classifying may improve the results.

To test this, we used a supervised autoencoder (SAE, see Ch. 5), which is a type of neural network that is optimized with two objectives: (1) to provide data compression possible while reconstructing the data as good as possible while (2) considering the classes of the data points to generate the compression algorithm. This way, the data represented in the compressed space is clustered in terms of the class each point belongs to while maximizing the separation between classes and ensuring data reconstruction. The bottleneck of the autoencoder represents the smallest layer in the network and is the layer that provides the compressed representation of the data.

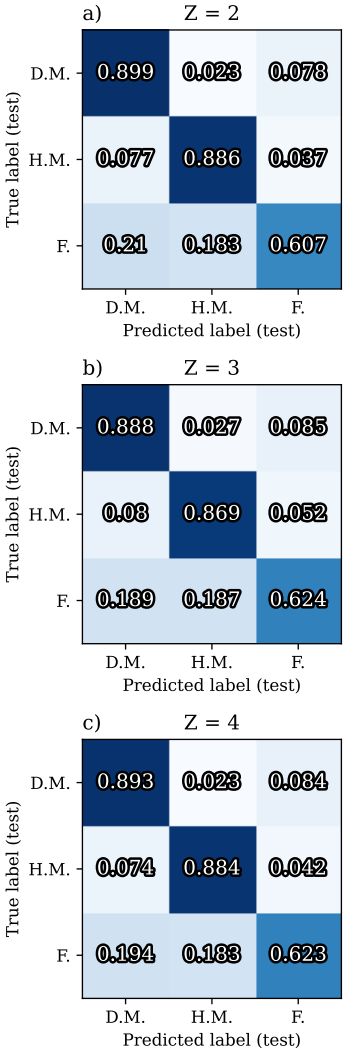

Figure 8.15: Average confusion matrices for the test dataset after performing leave-one-group-out cross-validation with a SAE, using $Z = 2$ (a), $Z = 3$ (b) and $Z = 4$ (c) bottleneck neurons. D.M.: Damaged muscle; H.M.: Healthy muscle; F.: Fat.

8.5.1 Classification

We implemented three different networks characterized by a different number of bottleneck neurons: $Z = 2, 3$ and 4. The number of epochs used for training was 400, with a batch size of 32. No overfitting was observed within the 400 epochs, and the test dataset accuracy was stable for all folds from 200 epochs onward. As before, the dataset comprised the elements of the wavelength-dependent Mueller matrices as features (excluding M_{11}), and leave-one-group-out cross-validation was used to evaluate the results. The confusion matrices for the test dataset are shown in Fig. 8.15 and the corresponding pixel-wise classification in Fig. 8.16.

The SAE provided a cross-validated accuracy of 79.7%, 79.4%, and 80.0% with $Z = 2$, $Z = 3$, and $Z = 4$ neurons in the bottleneck, respectively. The size of the bottleneck, within the ones explored, does not seem to impact the results strongly, with the most significant improvement being a 2% increase in fat detection between 2 and 3 neurons.

When evaluating the global results of the SAE, it does not provide improved nor worsened results when compared with the KNN classifier. However, the per-class accuracy does show differences between both classifiers. Specifically, the SAE shows between a 5% and 6% decline in accuracy when classifying the damaged muscle but, at the same time, shows between an 8-9% increase in accuracy when identifying the healthy muscle. The pixels identified as fat have approximately the same accuracy for both classifiers, but the SAE does not always confuse fat with damaged muscle. Instead, it provides almost the same probability for choosing a pixel as damaged or healthy muscle when fat is not properly identified.

These results show how, even when two methods provide similar global results, one may be better than others at specific tasks. In this case, since the objective is to separate the areas of healthy muscle from the rest, using a SAE can be a better approach than using a KNN classifier.

The output of the SAE and KNN classifier is very similar (Figs. 8.13 and 8.16), but the former's are significantly less noisy, especially in the fatty regions. While both classifiers coincide in the bigger areas, the SAE is able to pick up subtle regions, like the fatty area situated on top of the

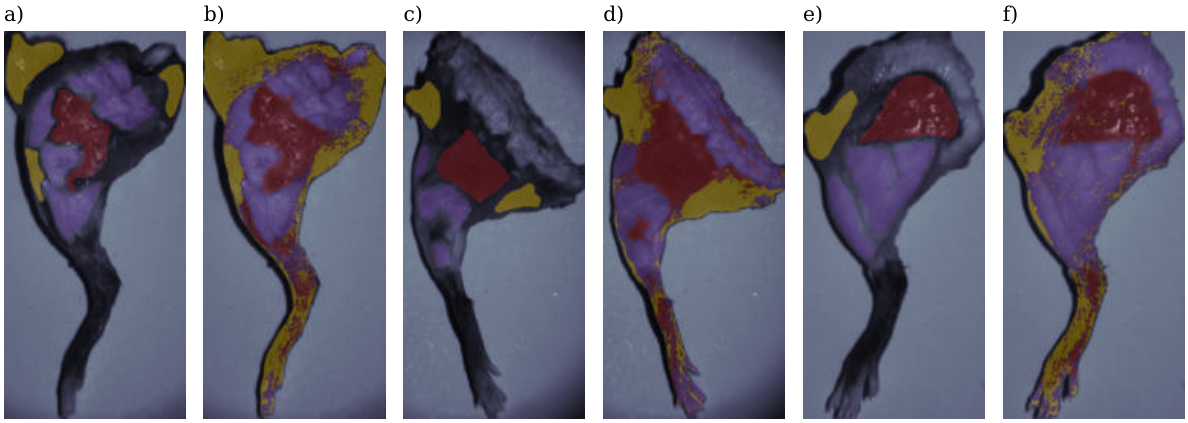

Figure 8.16: Classification of healthy muscle (red), frozen-damaged muscle (purple) and fat (yellow) with a SAE classifier ($Z = 2$ neurons in bottleneck). The reference labeled data (a, c, e) is shown next to the output of the model (b, d, f).

knee labeled in Fig. 8.16 (a), which is completely overlooked by the KNN algorithm, as well as the non-labeled muscle region below it, which is also better defined with the autoencoder. Other examples like these are visible in the center of Fig. 8.16 (d) and below the main muscle area in Fig. 8.16 (f), where small regions of unlabeled data are identified as muscle tissue, suggesting that this method is able to infer the dominant component in a specific area.

8.5.2 Data compression

A notable characteristic of autoencoders is the implicit data compression that occurs in the bottleneck. In this case, the data, which has 105 input features[6], is compressed to two when the bottleneck has only two neurons. This means that the multispectral Mueller matrix data, which initially required 105 images to visualize it, can now be represented with only two images that contain all the polarimetric and colorimetric data.

[6] (16-1)×7 Mueller matrix elements, considering the 7 wavelengths and removing the intensity (M_{11}) from each matrix.

To do so, the input features are passed through the encoder and reach the bottleneck, where they get projected onto a two-dimensional latent space[7] through a transformation that has been optimized to separate data from the different classes. For this dataset (Fig. 8.17), the transformation kept all the data points for the damaged muscle very close to the coordinate origin and later on focused on separating the two other classes as well as possible. The region where the three classes overlap leads to the off-diagonal elements of the confusion matrices represented in Fig. 8.15, where the more overlap between classes, the worse the accuracy will be.

[7] The latent space has as many dimensions as the bottleneck has neurons.

When represented as figures data, the bottleneck can be viewed in as many images as it has neurons (Fig. 8.19). This kind of representation effectively rearranges the information on the polarimetric properties of the sample to provide two images where tissue differentiation is maximum. While the second neuron (Z_1) highlights only the muscle, the first neuron (Z_0) provides a representation comparable to the output of the classifier (Fig. 8.16, b), aiding in tissue identification even before classifying the data.

The compression provided by the SAE is not lossless. In fact, this method also focuses on constructing the compressing encoder by keeping the most important data for classification. The autoencoder first compresses the data (x) to generate the latent space transformation (z). The data on

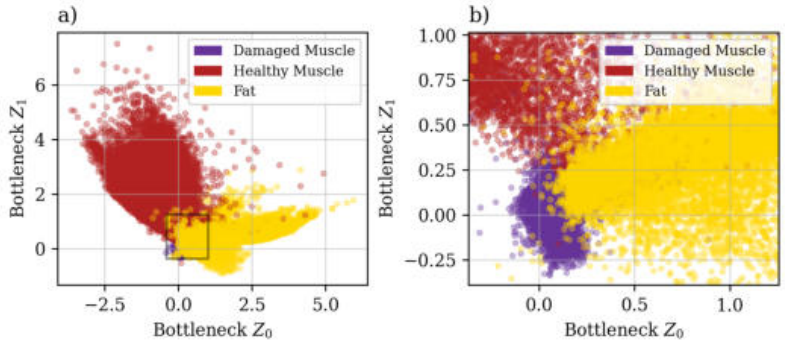

Figure 8.17: Representation of the labeled data points in the dimensionality-reduced space created in the 2-neuron bottleneck (a) and zoom in the central section (b). The wavelength-dependent Mueller matrix data (105 elements total) is compressed into only two dimensions that properly separate the three classes.

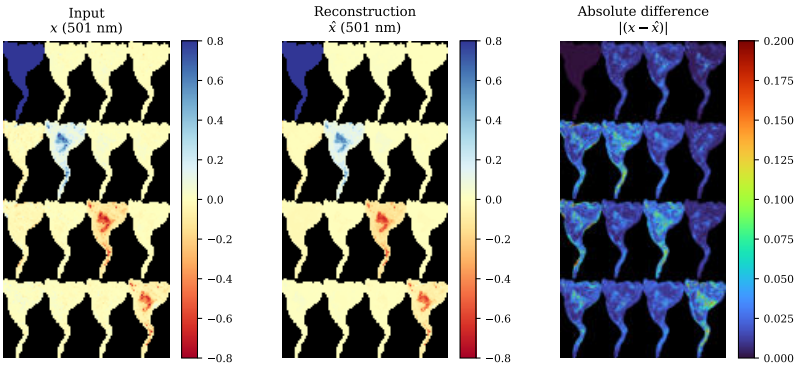

Figure 8.18: Comparison of the input data (x) at 501 nm with the SAE-reconstructed data ($\hat{x}$) using the compressed features contained in the two-dimensional bottleneck (z). Their absolute difference $|x - \hat{x}|$ is depicted to the right.

the latent space is used to classify each pixel into a different class ($\hat{y}$) by minimizing the classification error through comparison with the real labeling (y). At the same time, the second branch of the autoencoder decodes the data in the latent space (z) so that the decoded data ($\hat{x}$) resembles the input data (x) as much as possible. In the same way we used the accuracy to evaluate how well the SAE classifies the data, we can indirectly quantify which feature is the most important for classification by evaluating the reconstruction error between the decoded data ($\hat{x}$) and the input (x). One example is shown in Fig. 8.18.

Overall, the absolute difference between the original data and the reconstruction was approximately 0.1 for all features, which is 5% of the whole data range considered in Mueller imaging ($M(i,j) \in [-1,1]$), a value on the range of calibration accuracy [1]. The decoder is also able to reconstruct the spatial distributions of the polarimetric properties since it provides a mostly depolarizing (diagonal) Mueller matrix where the muscle tissue is less depolarizing than fat or damaged muscle, as we have seen before. This suggests that the compression generated by the encoder, even when reducing a large number of features (105), is enough to keep the basic polarimetric properties of the tissue.

Although the absolute difference between x and $\hat{x}$ is slightly larger on the diagonal, it is worth noting that the off-diagonal elements have values between 0 and 0.05. Even if these numbers seem low at first, the off-diagonal elements of these Mueller matrices, in particular, are very close to zero (< 0.01 in most cases). This means that, relative to the value of the inputs, the autoencoder does a much better job at reconstructing the data in the diagonal of the matrix than out of it. Given that this high absolute difference in the off-diagonal elements still allowed for

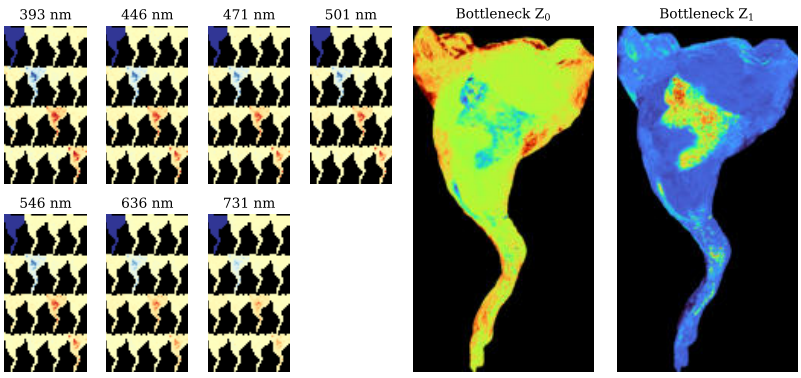

Figure 8.19: On the left, a representation is shown containing the seven multispectral Mueller matrices of sample 814. On the right, the two images represent each neuron of a two-dimensional bottleneck.

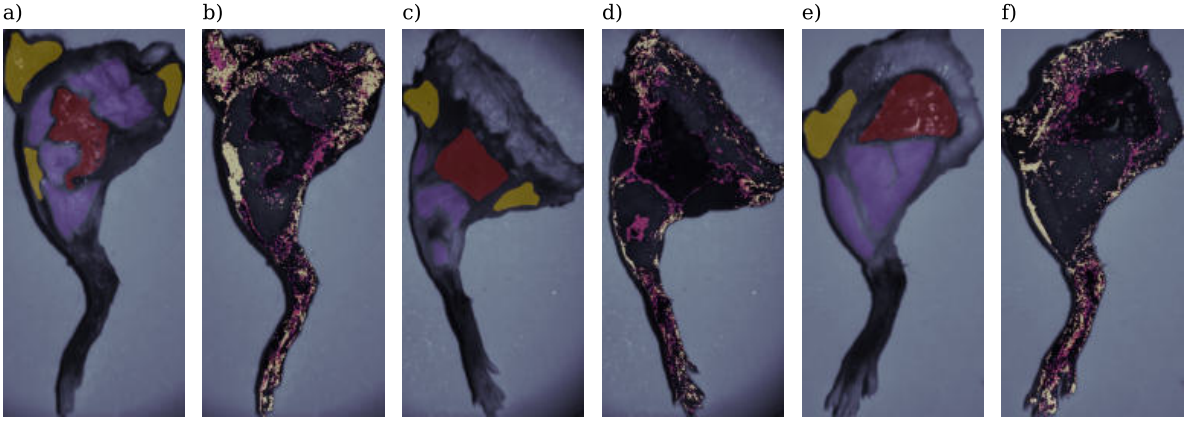

Figure 8.20: Classification comparison between KNN ($K_N = 5$ neighbors) and SAE ($z = 2$ neurons). The reference labeled data (a, c, e) is shown next to the absolute classification difference between the two models (b, d, f). Areas where the models coincide are shown in black. Areas where fat is being confused with damaged muscle are shown in light yellow. Areas where healthy muscle is being confused with fat or damaged muscle are shown in purple. The samples are 814 (a,b), 895 (c,d), and 896 (e,f).

a good classification, we can conclude that the off-diagonal elements are not the main ones contributing to the classification results. Instead, coinciding with the KNN classifier, the diagonals are the main sources of information for tissue identification in this dataset when using a supervised autoencoder.

8.5.3 Tissue margins

The two supervised methods we trained - the KNN classifier and the supervised autoencoder - both provided similar classification maps on the tissue. However, there were discrepancies between the outputs provided by both methods. If we assume that any classifier is going to perform worse where there is a mixture of tissues, then we can find the frontiers between tissue types, i.e., the margins, by focusing on the areas where the classifiers do not coincide.

The absolute classification difference provided by both classifiers was calculated. The results are shown in Fig 8.20. As we have seen in the previous section, the SAE is able to correctly identify some areas that the KNN classifier is not, like the fat close to the knee in Fig. 8.20 (a). This leads to the difference between classifiers highlighting this area as a potential mixture of damaged muscle and fat, something that occurs too in the same area of sample 896 (Fig. 8.20, f). Although both supervised classifiers mostly coincide in the healthy muscle classification, the extension of said areas is not exactly the same. As such, the difference between them outlines the margins of healthy muscle areas with regions of potential healthy muscle-fat and healthy muscle-damaged muscle mixtures.

8.6 Conclusions

This chapter explored the application of multispectral Mueller Matrix Imaging (MMI) to characterize mouse leg tissue samples (dataset LD).

Sample preparation involved defrosting, skin removal, and rehydration. Striking visual differences were observed between the three legs despite being from age-matched wild-type mice. White, anisotropic structures, likely indicative of freeze-damaged muscle due to improper freezing, were present in varying degrees. We identified several regions of interest for the subsequent analysis, including healthy muscle, freeze-damaged muscle, and fat.

The analysis of the acquired Mueller matrices revealed predominantly diagonal structures across all samples and wavelengths, suggesting dominant depolarization. Faint off-diagonal elements were also observed, particularly in the polarizance vector. Specular reflections and other measurement artifacts were detected as regions with non-physical realizability, while the rest of the areas in the samples were physically realizable.

Next, we calculated the indices of polarimetric purity and the degree of polarimetric purity. Polarimetric purity generally decreased with increasing wavelength, likely due to the longer path length of the photons inside the samples. Fatty tissue and damaged muscle exhibited lower polarimetric purity compared to healthy muscle. The total anisotropy was low across all samples and tissue types, with faint variations in linear and circular anisotropy.

To obtain the polarimetric properties of the tissue, we started by applying the forward polar decomposition to derive depolarization (Δ), retardance (R), and diattenuation (D). Depolarization effectively distinguished healthy muscle from damaged muscle and fat, and increased with wavelength. Retardance remained relatively stable, while diattenuation, although low, highlighted healthy muscle areas. Shorter wavelengths provided better image detail, consistent with the reduced penetration length inside the tissue. The boxplots of these parameters across tissue types confirmed the trends, with low depolarization being the primary marker of healthy muscle.

The differential decomposition was also applied to calculate linear retardance (R_L) and diattenuation (D_L). Again, the diattenuation highlighted textural details but was not strongly discriminative, but retardance appeared higher in damaged muscle areas, potentially due to underlying connective tissue. A comparison with literature values for skeletal muscle revealed similarities in diattenuation and depolarization trends, while differences in retardance trends could originate from variations in sample volume and tissue structure.

MMI obtains a large amount of data, so tissue classification was performed to evaluate the importance of the importance of individual Mueller matrix elements for the detection of healthy muscle to assess if a reduced Mueller dataset can be used for the same task. K-nearest neighbors (KNN) supervised classification achieved 79.8% accuracy in leave-one-group-out cross-validation. Feature importance analysis revealed that diagonal elements, particularly at shorter wavelengths, were the most relevant for this task, indicating depolarization as the primary discriminant. A simplified classifier using only the multispectral M_{22} and M_{33} achieved comparable accuracy, suggesting the feasibility of partial Mueller polarimetry for the specific task of detecting healthy muscle in a complex tissue environment, which would minimize the cost and

measurement duration for clinical applications. K-means unsupervised clustering was also performed, but it was less reliable for the same task than the supervised KNN classifier, suggesting the need for supervised methods for this task.

Finally, a supervised autoencoder (SAE) was employed for feature extraction and classification. The SAE achieved similar accuracy to KNN but with improved per-class performance, particularly for healthy muscles. The inherent data compression within the SAE bottleneck allowed for the representation of the multispectral Mueller matrix data with only two images, aiding in tissue identification through the two-dimensional images. An analysis of the reconstruction error highlighted the importance of diagonal matrix elements for classification, which was consistent with previous findings. The comparison of the output of the SAE and KNN classifiers highlighted areas of potential tissue mixture, particularly around the manually identified RoIs of healthy muscle, indicating that MMI can also be used for margin detection tasks.

References

[1] V. Mieites Alonso et al.: "PoLambRimetry: a multispectral polarimetric atlas of lamb brain", *Journal of Biomedical Optics* **29**(09) (2024). DOI: 10.1117/1.JBO.29.9.096002.

[2] P. K. J. Amend Sarah R. Valkenburg Kenneth C.: "Murine Hind Limb Long Bone Dissection and Bone Marrow Isolation", *Journal of Visualized Experiments* (110), e53936 (2016). DOI: doi:10.3791/53936.

[3] P. Bi et al.: "Stage-specific effects of Notch activation during skeletal myogenesis", *eLife* **5**, e17355 (2016). Ed. by A. C. Ferguson-Smith. DOI: 10.7554/eLife.17355.

[4] A. Kumar et al.: "Do's and don'ts in the preparation of muscle cryosections for histological analysis.", *Journal of Visualized Experiments* (99), e52793 (2015). DOI: 10.3791/52793.

[5] S. L. Jacques: "Optical Properties of Biological Tissues: A Review", *Physics in Medicine and Biology* **58**(11), R37–R61 (2013). DOI: 10.1088/0031-9155/58/11/R37.

[6] J. Qi et al.: "Extended polar decomposition method of Mueller matrices for turbid media in reflection geometry", *Optics Letters* **42**(20), 4048 (2017). DOI: 10.1364/ol.42.004048.

[7] R. Ossikovski: "Analysis of depolarizing Mueller matrices through a symmetric decomposition", *Journal of the Optical Society of America A* **26**(5), 1109–1118 (2009). DOI: 10.1364/JOSAA.26.001109.

[8] D. M. Hayes: "Error propagation in decomposition of Mueller matrices", in: *Proceedings Volume 3121, Polarization: Measurement, Analysis, and Remote Sensing*. 1997. DOI: 10.1117/12.278963.

[9] R. Ossikovski, M. Anastasiadou, and A. De Martino: "Product decompositions of depolarizing Mueller matrices with negative determinants", *Optics Communications* **281**(9), 2406–2410 (2008). DOI: 10.1016/j.optcom.2007.12.076.

[10] I. Pardo et al.: "Wide-field Mueller matrix polarimetry for spectral characterization of basic biological tissues: Muscle, fat, connective tissue, and skin", *Journal of Biophotonics* **17**(1) (2024). DOI: 10.1002/jbio.202300252.

[11] J. Bonaventura et al.: "Evaluating backscattering polarized light imaging microstructural mapping capabilities through neural tissue and analogous phantom imaging", *Journal of Biomedical Optics* **29**(5), 52914 (2023). DOI: 10.1117/1.JBO.29.5.052914.

[12] R. Carlson et al.: "Backscattering Mueller matrix polarimetry estimates microscale anisotropy and orientation in complex brain tissue structure", *Journal of Medical Imaging* **12**(01) (2024). DOI: 10.1117/1.JMI.12.1.016001.

[13] R. Gros et al.: "Effects of formalin fixation on polarimetric properties of brain tissue: fresh or fixed?", *Neurophotonics* **10**(02) (2023). DOI: 10.1117/1.nph.10.2.025009.

[14] V. Mieites et al.: "Wide-field optical properties estimation of whole limbs in muscle dystrophy murine models via SFDI: a case study", in: *Translational Biophotonics: Diagnostics and Therapeutics III*. Ed. by Z. Huang and L. D. Lilge. **12627**. International Society for Optics and Photonics. SPIE, 2023 1262731. DOI: 10.1117/12.2670573.

[15] J. Qi, D. S. Elson, and D. Stoyanov: "Eigenvalue calibration method for 3 × 3 Mueller polarimeters", *Optics Letters* **44**(9), 2362 (2019). DOI: 10.1364/ol.44.002362.

Combination of optical imaging data from different modalities

9

The previous chapters focused on obtaining the optical properties derived from each imaging method to provide an in-depth discussion of how each property can be used for muscular dystrophy evaluation on its own. Each imaging method was chosen based on the information about the sample they provided (i.e., structural/chemical) so that their outputs could be evaluated together to allow for a deeper understanding of the pathology.

This chapter will show the results obtained by combining the optical properties derived from the previous ones through two different approaches: statistical and visualization-based. While the statistical approach can be taken in any dataset, integrating data for visualization purposes poses various challenges that will be discussed in the following sections.

9.1 Visualization of co-registered images

This section presents the results of the multi-modal visualization approach to co-registered optical property maps derived from murine muscle samples following our previous work [1]. Here, the results presented are those of dataset MD1 and MD2, where both attenuation (μ_t) and birefringence (Δn) were acquired using OCT and PS-OCT, respectively. As we have seen in Ch. 6, these optical properties provide complementary information about tissue structure and composition, with μ_t reflecting light scattering and potential changes in cell size and morphology, while Δn is sensitive to tissue anisotropy and the presence of ordered structures. Given the importance of both structural and compositional information in understanding muscular dystrophy progression, we employed a color-based visualization approach to integrate and simultaneously display these co-registered parameters. The transformation is based on assigning an optical property to each component of the HSV color space to transform three independent maps into a single image.

9.1.1 Assignment of optical properties

The main objective of the proposed color transformation is to create one image that conveys as much information about a sample as possible, but also that aids in the identification of healthy or diseased areas. Between attenuation and birefringence, we have seen that birefringence provides better separability between the two tissue classes than attenuation, while the latter shows better-defined morphological structures. This suggests that the better disease biomarker is Δn, which we will assign to the color (hue, H) in the HSV representation. High birefringence values are assigned to greener colors, while low birefringence ones are assigned to redder colors, corresponding with the healthy/diseased categories, respectively.

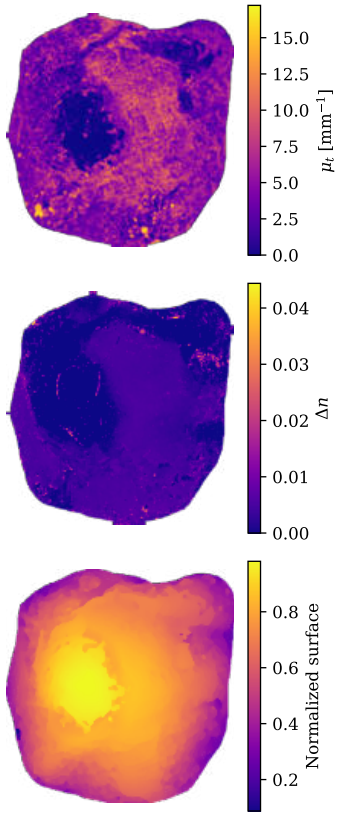

Figure 9.1: Optical properties used for the multi-parametric HSV representation, exemplified in sample 814 of dataset MD2. From top to bottom: attenuation (μ_t), birefringence (Δn) and normalized profilometry of the sample.

Attenuation is assigned to the value (V), where dark and bright colors indicate low and high attenuation, respectively. Since the value of μ_t does not vary significantly between samples, this will essentially provide the texture of the images, which, as we have mentioned before, is better visualized in intensity variations [2].

In order for the three components to be independent, as they would in a conventional color image represented in the HSV space, the parameter chosen to represent saturation (S) can not be related to the attenuation or the birefringence of the sample. Therefore, we choose the normalized profilometry of the sample. This way, high points in the sample will appear as highly saturated colors, while lower ones will show as grayish ones. If the sample does not have abrupt height changes, the whole surface will have similarly saturated colors. The three maps that will be combined in a single HSV image are exemplified in Fig. 9.1 [1].

9.1.2 Effects of histogram equalization

Although the birefringence values of the samples are contained in a small region of all possible values, most samples have areas with specular reflections or other impurities whose birefringence is much higher than in the sample. This causes the dynamic range of the birefringence to be compressed in the lower-valued side, which translates into a small color variation when assigned to hue.

We used *histogram equalization* to enhance the contrast in birefringence values so that they are not linearly translated into hue values. Instead, the assignment is done according to the Δn cumulative distribution function so that the small dynamic range is stretched throughout more hue (H) values, and the higher parts of the birefringence distribution are compressed to a small color variation. To maintain color consistency across the dataset, the $\Delta n \rightarrow H$ assignment is done according to the distribution of the whole dataset and, later on, applied to each sample individually (Fig. 9.2). This implies that the individual histograms of the samples are not equalized, but their contrast is still stretched to fill the whole range (Fig. 9.2, d).

Notice that, even after equalizing the dataset's Δn, the histogram does not fill the 0-1 range (Fig. 9.2, b). This range was chosen due to the hue being a cyclic magnitude, meaning low and high hue values are represented by the same color, which is something to avoid when the assigned optical property (i.e., birefringence) is not cyclic and low and high values must be represented by different colors.

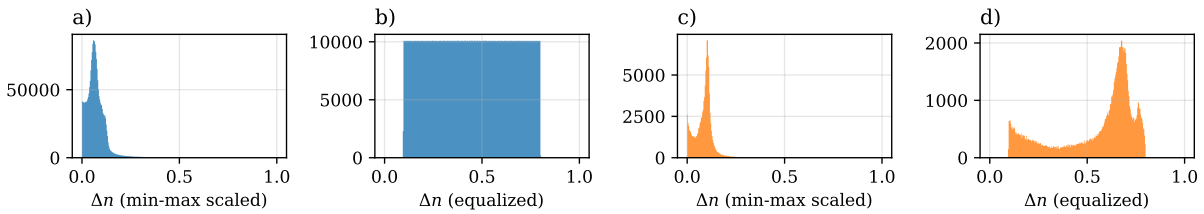

Figure 9.2: Effect on the min-max scaled birefringence histograms before and after equalization for (a, b) the whole dataset and (c, d) sample 814, represented in 9.1.

9.1.3 HSV representation of multi-parametric data

The color transformation for sample 814 of dataset MD2 is represented in Fig. 9.3. The hue before and after equalization is shown in images 9.3 (a) and (b), which correspond to the histograms represented in Fig. 9.2, (c) and (d). The contrast enhancement between low and high birefringence areas is immediately visible, but high Δn values appear as *darker* H values after equalization. The equalized hue was inverted before combining it with the saturation and value so that high birefringence, which is the marker of healthy samples, is represented in green, which is the color represented by low H values in the HSV color space. Thus, the color legend for all samples is unique and is represented in Fig. 9.3 (e). Notice that the horizontal axis of the legend is not linearly spaced, i.e. the higher the birefringence the less color separation between birefringence values, so that values over 0.005 are represented by cyan/green colors, and values below 0.005 are depicted in blue/magenta/red. That way, more than half of the possible colors correspond with different degrees of disease ($\Delta n < 0.005$), and healthy tissue is always represented in greener colors.

The effect on the sample before and after equalization is also immediate. Without equalization, the color representation of the image collapses to a pinkish-red hue, while, after equalizing, values with high birefringence are represented in green. Combining the μ_t with Δn allows us to see the texture associated with this high birefringence, which disappears in the low birefringence areas of fatty tissue, corroborating that birefringence is higher in regions of well-organized, anisotropic tissue.

This behavior is also observed across all samples of both datasets. In dataset MD1 (Fig. 9.4), the four control samples are the ones with larger healthy areas depicted as highly-textured green regions but also contain some impurities corresponding with fatty inclusions or less anisotropic tissue areas. On the other hand, the most damaged samples in the dataset (mouse 731) are viewed as bright red, randomly organized tissue, indicating its clinical state. Interestingly, the mouse's 731 diaphragm (sample 731-D) had the highest normalized height variation, which causes the out-of-focus areas to be less saturated than the well-focused tissue, which also makes them less distracting to the end user, allowing us to focus our attention in the regions that are properly measured. The remaining samples have a mixture of very damaged and slightly damaged tissue, represented as colorful images with no green areas.

Dataset MD2 (Fig. 9.5) showed two distinct birefringence distributions for healthy and diseased samples that overlapped slightly more than those of dataset MD1. This greater overlap translates into a less evident color distinction between control and dystrophic samples. Although the majority of green, highly-birefringent tissue is shown in wild-type samples, some knock-out ones, like sample 578, have a non-negligible high-birefringence component, suggesting that some mice resist better the effects of the disease. As before, some samples had fat inclusions that are viewed as reddish, non-isotropic areas. The most evident one is sample 814, which we have already discussed, but also the knock-out sample 742, which contained a small translucent bump on its lower left area, which is immediately detectable as an almost-circular color change

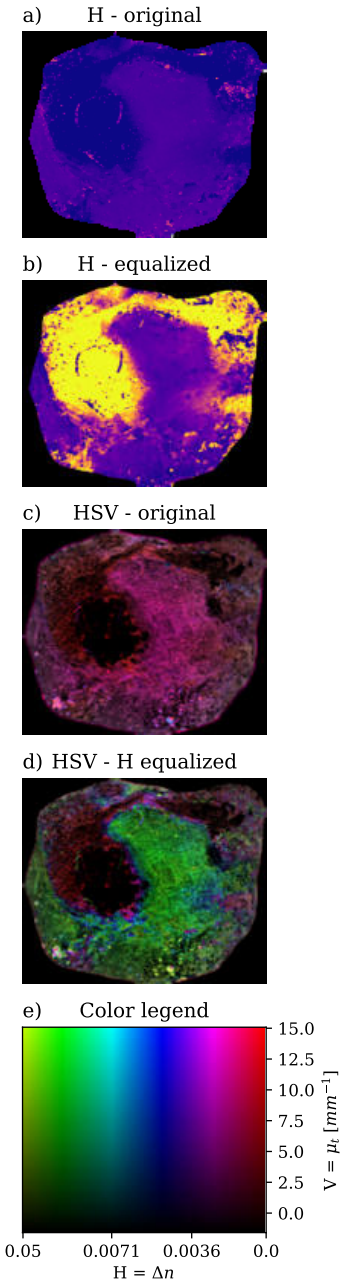

Figure 9.3: Resulting HSV image representation of attenuation, birefringence and profilometry for sample 814 of dataset MD2: (a) min-max normalized birefringence (hue), (b) histogram-equalized hue, (c) color reconstruction without equalization and (d) color reconstruction with histogram-equalized hue. The color legend is shown in (e) for maximum saturation.

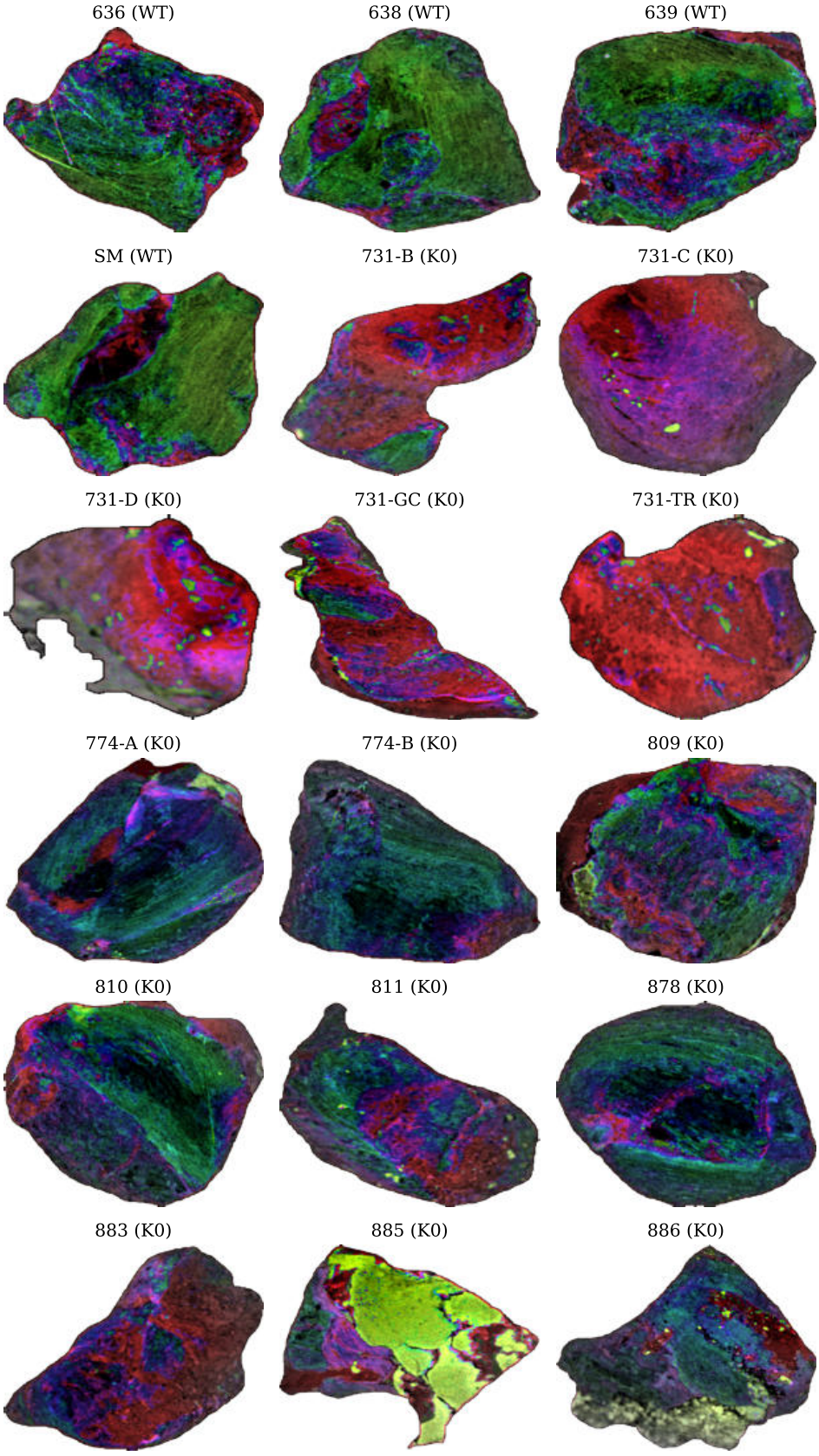

Figure 9.4: Color transformation of all samples in dataset MD1 according to their birefringence (hue), profilometry (saturation) and attenuation (value). The first four are the control (WT) samples (SM, 636, 638, 639), and the rest are dystrophic (KO) samples. Best viewed in pdf.

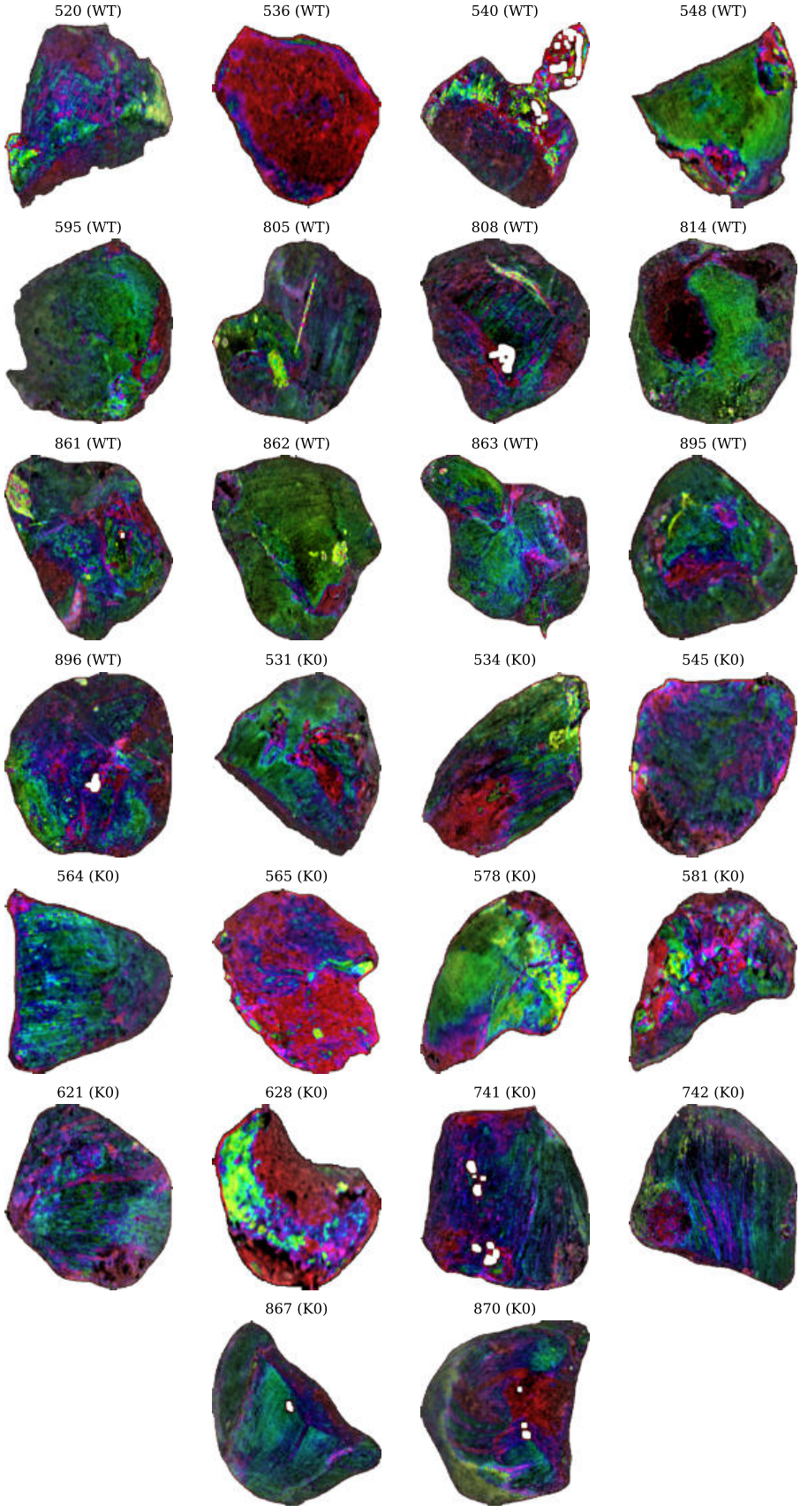

Figure 9.5: Color transformation of all samples in dataset MD2 according to their birefringence (hue), profilometry (saturation) and attenuation (value). The first 13 samples are control (WT) samples, while the rest are dystrophic (KO) ones. Best viewed in pdf.

in the HSV representation which, upon further inspection, also shows a textural change with respect to the surrounding tissue.

Some samples, like the 536 (WT), 540 (WT), 545 (KO), 565 (KO), and 628 (KO) were fixed to the cork based with their cross-section facing the system, either perfectly perpendicular or at a slight angle, which explains why those samples, even the control one, have such low birefringence values. Additionally, the multi-parametric representation shows a lumpy texture in those samples, corresponding with the cross-section of the fiber bundles in the muscles, which is not visible in other samples where the tissue was placed on its side, resulting in fibrous, directional textures in the images.

An adequate sample placement is crucial when evaluating *ex-vivo* tissue. Birefringence is caused by the phase delay the waves gain when traveling through anisotropic tissues. When the cross-section of the muscle fibers is placed perpendicular to the system, the fibers run parallel to the propagation direction of the wave, so the phase of the wave remains unchanged due to both axes of the field experiencing identical tissue structures. Therefore, samples must be placed on their side when the aim is to measure the birefringence of the tissue.

This orientation issue is generally irrelevant for *in-vivo* measurements because muscles and tendons are naturally anchored at their ends. This anatomical constraint means that when measuring birefringence *in-vivo*, the only option is almost always measuring it laterally (across the fibers) [3]. Therefore, the "correct" orientation for birefringence measurement is automatically taken care of by the natural structure of this type of tissue.

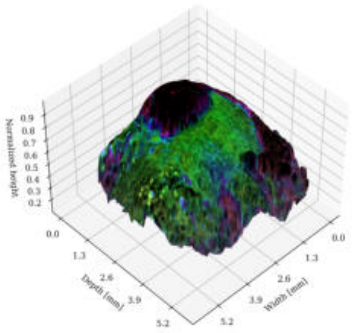

Figure 9.6: Three-dimensional representation of sample 814 colored according to its HSV transformation. Best viewed in PDF.

Finally, the profilometry of the sample did not significantly affect the images aside from in very irregular samples, corresponding with our previous findings [1]. However, the normalized height maps extracted from the OCT images can also be used to create three-dimensional representations of the samples, as depicted in Fig. 9.6. This additional representation provides an even deeper understanding of the sample since not only the disease marker (color) and sample anisotropy (texture) is depicted, but it also allows for the identification of sample impurities and their relative size compared to the rest of the sample.

The HSV encoding of multiple independent parameters presented in this section and our previous work [1] is extremely useful to create color images that can be interpreted from various points of view, but its use is restricted to a single scenario: the represented properties must be perfectly aligned. In OCT-derived measurements, this is an easy task, given that all the represented properties are automatically taken in the same area and derived from different Stokes vectors. However, when the data is taken from multiple systems, additional efforts must be taken to ensure image co-registration. The HSV encoding was also applied to human aortic samples, which, since they are too big for the OCT system, are imaged using a bi-dimensional grid that frames the region being imaged in each OCT sample [1]. Then, the sample with the grid still firmly placed on top of it is taken to the HSI device to measure its hyperspectral image. Finally, the images from both systems are aligned using the grid, and the resolution is matched through interpolation. This method was not available at the time of the muscle dataset measurements. Thus, the

HSV method was only applied to OCT data, but further iterations of this experiment could include a smaller grid to be used with these ex-vivo small samples and combine data from multiple systems together.

9.2 Statistical analysis of the dataset

Throughout this book, we have seen how several optical properties obtained with multiple imaging systems can be used to describe the behavior of healthy and dystrophic mice samples. Each system has its strengths and challenges and evaluates the data from one point of view, but as we have discussed in the previous section, to compare the images pixel-wise directly requires the 2-dimensional optical property maps to be co-registered. Since that is not the case, we sampled the same number of data points from each muscle to evaluate their behavior statistically. This section aims to distinguish between healthy and dystrophic samples by ranking the optical properties according to how well they classify the samples, but also to see if their combination can improve the results provided by only the best magnitude.

9.2.1 Dataset description

The complete optical properties dataset of samples in MD2 is depicted in Fig. 9.7. Each row represents a different optical property, namely:

- (a) Attenuation coefficient (μ_t) at λ =1300 nm, in mm^{-1} (OCT).
- (a) Birefringence (Δn) at λ =1300 nm (OCT).
- (b) Average reflectance ($\overline{R}_V$), within the spectral range defined by λ <600 nm (HSI-VISNIR).
- (c) Average reflectance ($\overline{R}_S$), within the spectral range defined by λ >1300 nm (HSI-SWIR).
- (d) Absorption coefficient (μ_a(red)), within the spectral range defined by 621< λ <634 nm, in cm^{-1} (SFDI).
- (e) Absorption coefficient (μ_a(green)), within the spectral range defined by 507< λ <571 nm, in cm^{-1} (SFDI).
- (f) Absorption coefficient (μ_a(blue)), within the spectral range defined by 447< λ <460 nm, in cm^{-1} (SFDI).
- (g) Reduced scattering coefficient (μ'_s(red)), within the spectral range defined by 621< λ <634 nm, in cm^{-1} (SFDI).
- (h) Reduced scattering coefficient (μ'_s(green)), within the spectral range defined by 507< λ <571 nm, in cm^{-1} (SFDI).
- (i) Reduced scattering coefficient (μ'_s(blue)), within the spectral range defined by 447< λ <460 nm, in cm^{-1} (SFDI).

The first two columns represent the data introduced through figures in the previous chapters, where we show the different distributions according to the clinical category (first column) or for each specific sample (second column). The next two columns divide the same distributions according to the sex of the mouse (third column) and their age (fourth column). The key difference between the first and the last two columns is that, for the former, the dataset contains the same number of data points for control and dystrophic samples but also for each mouse. However, the data on the sex and age of the mice is not balanced throughout the samples.

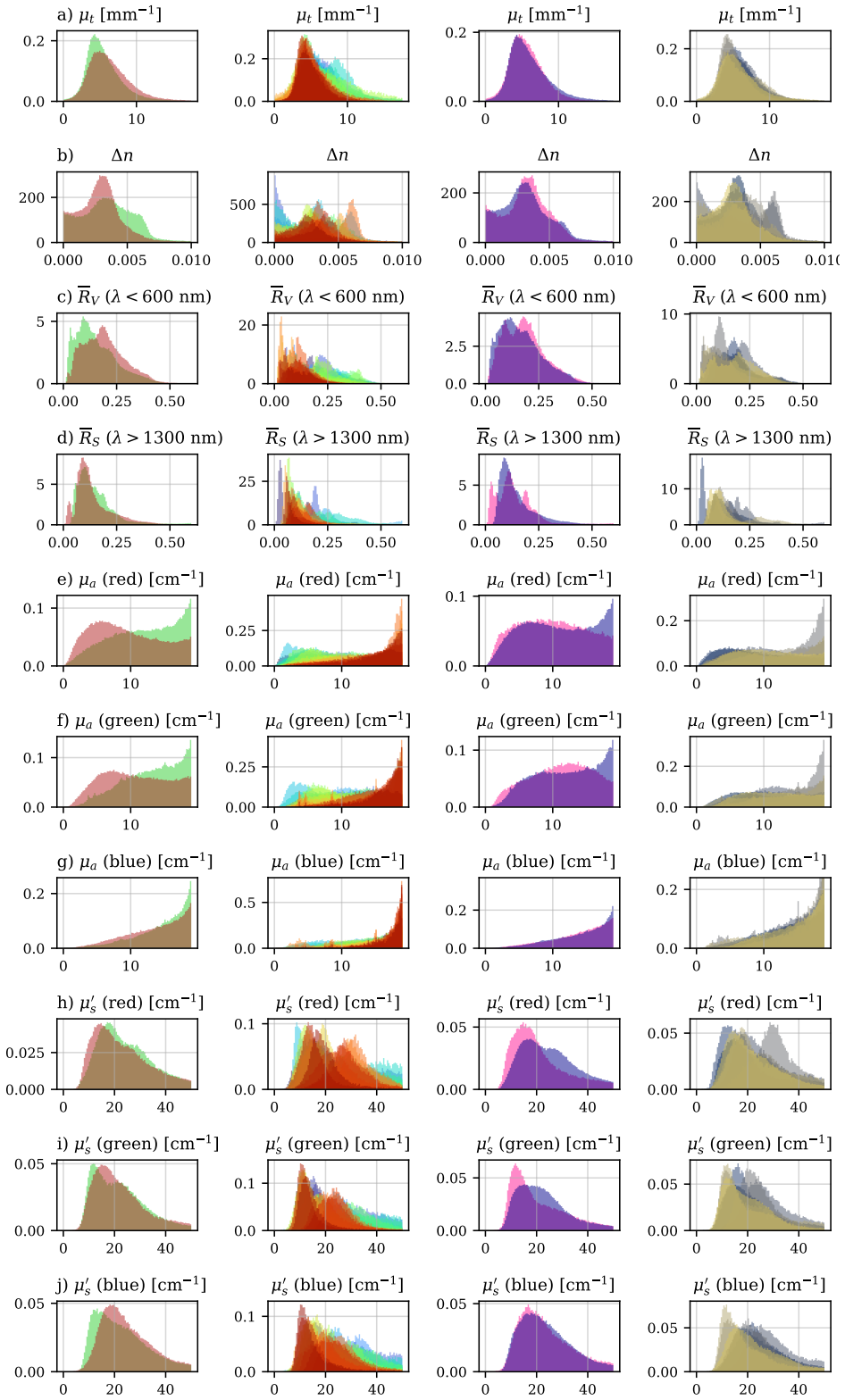

Figure 9.7: Complete optical properties of dataset MD2. Each optical property (rows) has been sampled so that the dataset contains the same number of points for each one, as well as for each sample. The data is depicted, from left to right, (column 1) according to the clinical category of the samples (red: WT, green: WT), (column 2) for each sample, (column 3) according to the sex of the mouse (male: blue, female: pink), and (column 4) according to the age of the mouse (bluer: younger, yellower: older).

This means, for example, that most data corresponded with male mice instead of females and that some ages were more common than others in the dataset. Balancing the dataset according to these last two categories was not possible, as it would have required removing too much data for the resulting distributions to represent the behavior of the whole dataset properly.

Still, it is interesting to evaluate the distributions according to these two extra categories. For example, we see that the distributions represented according to the sex of the mouse are completely overlapping. Even if some magnitudes, like the average reflectance in the SWIR range (row d) or the absorption and scattering coefficients (rows e, f, h and i) are not perfectly equal[1], the dynamic range of the distributions is always the same suggesting that, once the disease is active, the muscular decay is similar in male and female specimens. Similar results are obtained when separating the data according to the age of the mice but with a wider spread between age ranges. As each mouse grows, the stage of the disease appears to be different but not necessarily predictable. As some age brackets contain very few samples, it is challenging to establish the stage of the disease according to these optical properties, as the age-sorted distributions might not be able to represent the inter-sample variations present due to the small number of muscles of each age in the dataset.

[1] Which could originate from the different number of data points in each distribution.

By looking at Fig. 9.7 we see that some magnitudes separate the data between wild-type and knock-out samples better than others. Although most distributions are non-gaussian due to the influence of each sample, we calculated the average and standard deviation of each optical property[2] clinical category. As each feature (x) is within its own range of values, we standardized them by removing their average (μ) and dividing them by their standard deviation (σ), so that their standardized version (x_s) is defined as

$$x_s = \frac{x - \mu}{\sigma} \quad .$$

This centers the distributions around zero and establishes their standard deviation to one so that comparatives can be made about the information provided by each feature. After standardization, we represented each feature, sorted by decreasing value for the control samples (Fig. 9.8, a).

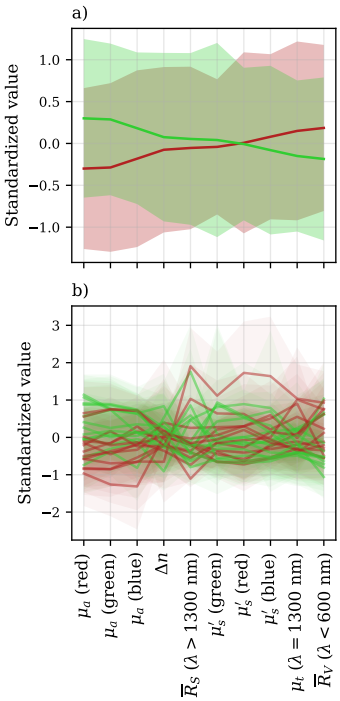

Figure 9.8: (a) Average and (b) individual behavior of the optical properties, sorted by decreasing standardized magnitude for the control samples (green). The opposite average tendency is observed for the dystrophic samples (red), although inter-sample variations cause significant overlap between the distributions.

We see that, on average, the healthy samples have higher absorption and birefringence, comparable reflectance over 1300 nm and scattering in the visible range, and lower attenuation coefficient at 1300 nm and reflectance below 600 nm than dystrophic samples. Considering what we have seen throughout the previous chapters, this combination of optical properties suggests that, on average, healthy samples have higher dominating chromophore concentrations in the visible range, which, in the case of biological tissue, coincides with higher hemoglobin or myoglobin content. The structural trends hinted by the scattering coefficient in the visible range and the attenuation coefficient at 1300 nm showcase that, at the longest wavelengths, scattering is higher for the dystrophic samples. Generally speaking, larger particles cause more scattering, which could be an indicator of the dystrophic samples having more fat than muscle [4], again supported by the higher birefringence in healthy samples. However, there is several overlaps between both distributions, especially when considering the results of all samples 9.8, b), which poses several

[2] From now on, we will refer to the optical properties as *Features* (of the dataset), unless explicitly specified otherwise.

challenges for the separability.

9.2.2 Dataset statistics and separability

The next step involved calculating the average and standard deviation of all optical properties for both categories, as well as the Fisher ratio. The Fisher ratio is a measure of linear separability between two classes. If only two classes are considered, with averages μ_1 and μ_2, and standard deviations σ_1 and σ_2, Fisher's Discriminant Ratio (FDR) is defined as

$$FDR = \frac{(\mu_1 - \mu_2)^2}{\sigma_1^2 + \sigma_2^2} \quad ,$$

which is essentially the distance between the two distributions weighted by their mutual overlap [5]. For example, two overlapping Gaussian distributions ($\sigma_1 = \sigma_2 = \sigma$, $\mu_1 = \mu_2$) would have an $FDR = 0$, while two equal Gaussian distributions with their peaks separated at least one standard deviation ($\sigma_1 = \sigma_2 = \sigma$, $\mu_1 - \mu_2 = \sigma$) would have an $FDR = 1/2$.

We also performed the two-sided Kolmogorov–Smirnov test (KS test), which tests the null hypothesis that two distributions are identical based on the distance between their cumulative distribution functions. In the same example as before, the KS test for two overlapping Gaussian distributions is close to zero, while two non-overlapping distributions would yield a value closer to one. This method poses the advantage of being applicable to any empirical distribution. It is better suited for distributions with more than one peak like the ones observed for the dataset MD2 caused by the inter-sample variations [6].

The results of the previous statistical metrics are shown in table 9.1. Although the KS test could not reject the null hypothesis, the value of its statistic is still useful to compare the separability given by the different magnitudes. Interestingly, the feature with the best linear separability, according to the FDR, was the absorption coefficient in the red color range, followed by the same magnitude in the green color range. Both features have almost twice as much separability as the next one, which is the average reflectance below 600 nm, again closely related to the previous two. Interestingly, Fisher's ratio and the Kolmogorov-Smirnov test sort the first four features with more separability in the same order,

Table 9.1: Average (μ), standard deviation (σ), Fisher's discriminant ratio (FDR) and Kolmogorov-Smirnov statistic (KS test), for the control (WT) and dystrophic (KO) samples, according to their optical features. The table is sorted by descending KS test.

	$\mu_1(WT)$	$\mu_2(KO)$	$\sigma_1(WT)$	$\sigma_2(KO)$	FDR	KS test
μ_a (red)	0.300	-0.300	0.947	0.961	0.198	0.256
μ_a (green)	0.287	-0.287	0.906	1.007	0.180	0.239
$\overline{R}_V$ ($\lambda < 600$ nm)	-0.185	0.185	0.974	0.992	0.071	0.202
μ_a (blue)	0.182	-0.182	0.906	1.055	0.068	0.165
Δn	0.075	-0.075	1.006	0.988	0.011	0.157
μ_t ($\lambda = 1300$ nm)	-0.150	0.150	0.902	1.068	0.046	0.137
$\underline{\mu}'_s$ (blue)	-0.080	0.080	1.007	0.986	0.013	0.126
$\overline{R}_S$ ($\lambda > 1300$ nm)	0.054	-0.054	1.025	0.971	0.006	0.088
μ'_s (red)	-0.007	0.007	0.911	1.081	0.000	0.073
μ'_s (green)	0.041	-0.041	1.160	0.807	0.003	0.039

but the KS test highlights the birefringence as the fifth one, which is consistent with what we have observed in previous chapters, while the FDR indicates that the OCT-derived attenuation is the next feature with best separability. This shows the main limitation of the FDR: as it only compares the average of the distributions and their standard deviations, using it for non-symmetrical functions can sway its predictions. Still, both metrics coincide in that the worse separability is given by the average reflectance over 1300 nm, and the scattering coefficient in the red and green (FDR) or green and red (KS test) ranges. Since most SFDI systems do not have hyperspectral capabilities, these results indicate that using a SFDI device operating in the blue wavelength range may provide the best absorption/scattering results to differentiate between healthy and dystrophic mice samples.

9.2.3 Dimension reduction

The separability of the distributions is swayed by the actual properties of the samples and by the outliers. Dimension reduction can aid in removing unnecessary information while keeping the defining features of the classes intact. Here, we tested PCA, t-SNE and Isomap as three dimension reduction alternatives with the aim of evaluating the separability again, but in a two-dimensional space instead of the original ten-dimensional space.

	FDR	KS test
Isomap (1)	0.2916	0.2991
PCA (1)	0.2144	0.2746
t-SNE (1)	0.1014	0.2393
t-SNE (2)	0.1278	0.2185
PCA (2)	0.086	0.2109
Isomap (2)	0.0175	0.1616

Table 9.2: Distribution separability for each dimension (1,2) of the data projected onto the reduced two-dimensional spaces created by PCA, t-SNE and Isomap, corresponding to the data in Fig. 9.9 and 9.10. The data is sorted by descending value of the KS test.

Although the 2D maps given by each method are visually different (Fig. 9.9), the behavior observed is similar regardless of the method applied. These methods aim to separate the data according to different metrics blindly, and the three of them have regions in their respective spaces where only healthy or dystrophic data points are found. This suggests that there is some separability among the statistical overlap, even if it is minimal.

Again, when representing the data color-coded according to their sex, we see a more significant overlap, as well as when identifying the data according to their age, suggesting that these two factors are not biasing the optical properties derived in this thesis.

We have indicated throughout all the results chapters that there is some variation between samples. The three tested blind dimension reduction methods pick up on these variations and separate the different samples in the 2D projections. This is evident in the case of t-SNE, as its neighbors-based approach tends to create clusters with each sample first and then organize the clusters according to their clinical category. Similar results are also obtained with PCA and Isomap but with more overlap between samples as well.

If we separate the data according to each dimension, like for the 10-feature dataset, we can assess the overlap between distributions again, but in the reduced spaces created by the three mappings. Although the dimension reduction methods are able to transform the distributions into smoother functions by effectively "sorting" the data coming from different samples, there is still significant overlap between the control and dystrophic categories (Fig. 9.10). This becomes evident when evaluating Fisher's discriminant ratio and the statistic of the Kolmogorov-Smirnov test, as the values are within the same ranges as for the complete dataset.

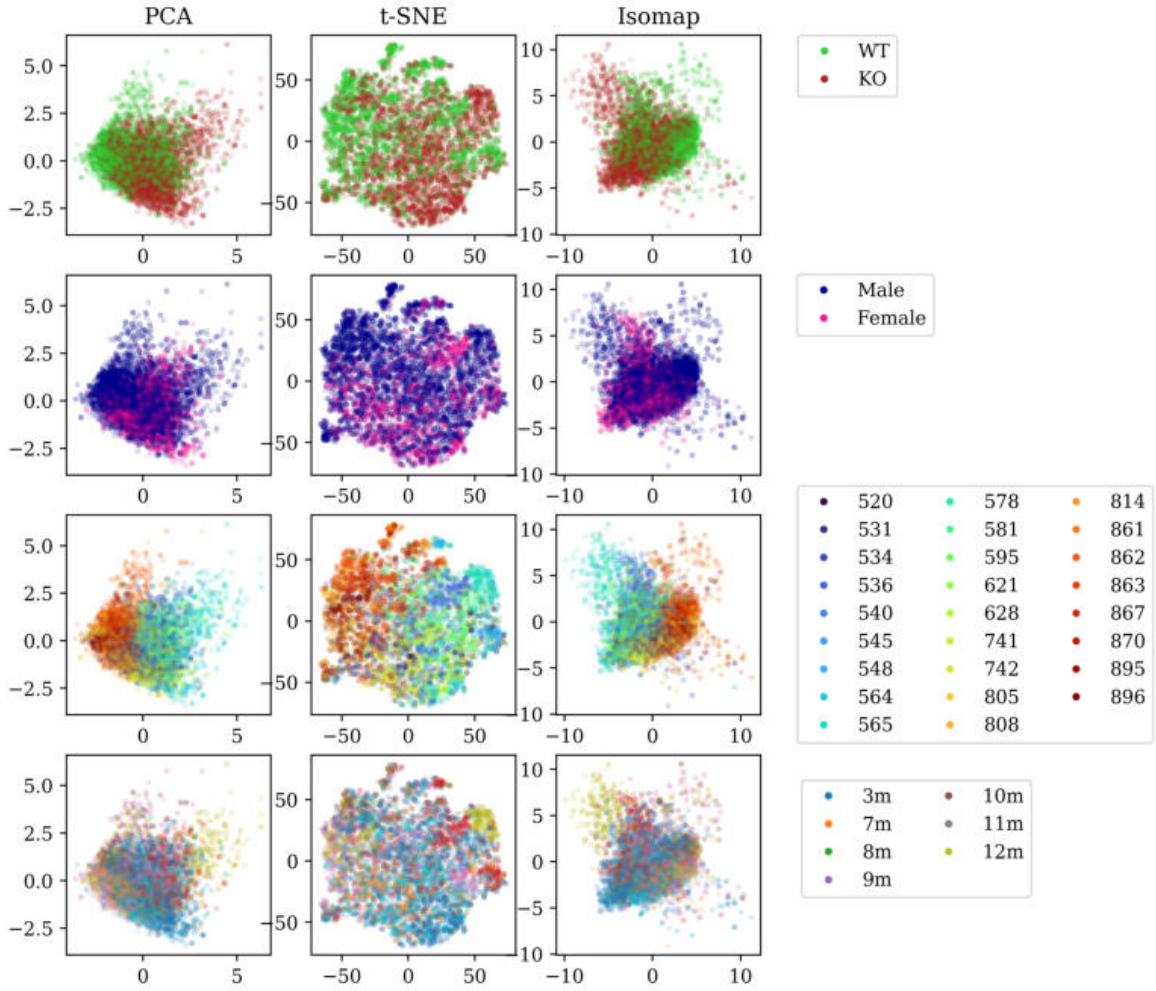

Figure 9.9: Dimension-reduced optical properties dataset for the samples in MD2 with PCA (first column), t-SNE (second column) and Isomap (third column), labeled by sample type (first row), sample sex (second row), sample ID (third row) and sample age (fourth row).

The first dimension of Isomap and PCA do provide better separability than the best acquired by a single feature of the complete dataset, with a 10% improvement achieved with an 80% reduction of the dataset. This improvement suggests that there is some noise that both Isomap and PCA are able to remove and that there exists a mapping that combines the

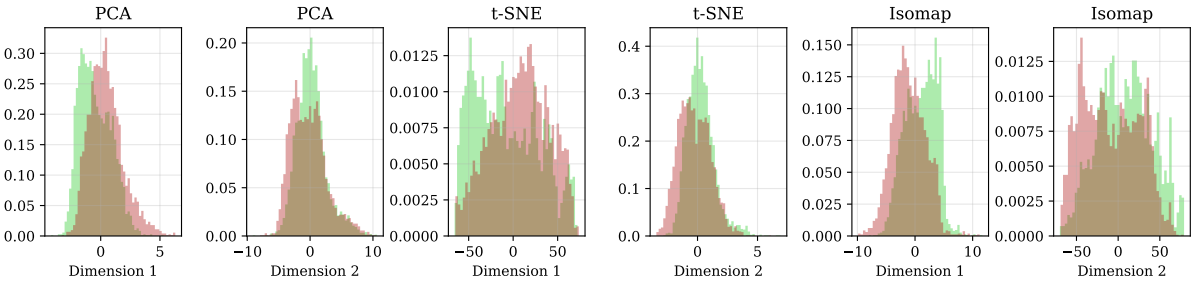

Figure 9.10: Dimension-reduced optical properties dataset for the samples in MD2 with PCA, t-SNE and Isomap labeled by sample type (WT: green, KO: red). Each image corresponds to a different dimension of the data represented in Fig. 9.9.

data in a way that can improve separability. Nonetheless, the dimension-reduced spaces lack interpretability, so in this case, we will still consider the 10-feature dataset, as the improvement with dimension reduction is not enough to justify the high compression performed by these methods in a dataset with few features like the one used here. However, these metrics must be considered when working with higher-dimensional data, as a 10% improvement in those cases can be significant with enough features.

9.2.4 Classification

The previous sections have shown that (1) optical properties alone can provide some separability when analyzing healthy and dystrophic mice samples and that (2) there exists a space on which the properties can be projected that improves separability. This raises the question of how a classifier performs on this data.

To answer it, we trained a fully connected feed-forward neural network (Multi-Layer Perceptron, MLP). The tested network architectures included one or two hidden layers, with the number of neurons varying between 10, 50, 100, and 200 per layer.

Two samples were kept for testing the performance, one of each category (WT and KO), and the remaining 24 were used for training. The performance was tested through the average accuracy after cross-validation by changing the samples used for testing each fold, with a total of 13 folds. At this point, we must recall that we will consider the entirety of the samples instead of specific regions of interest, and that they are not spatially homogeneous, which will pose challenges when classifying the data.

10-feature dataset classification

The first network (50 neurons, one hidden layer) trained over the ten features depicted in Fig. 9.7 provided 80.0% average accuracy for the test dataset after 13-fold cross-validation. However, the parameters the network learns are not enough to generalize to the test data, which, on average, had an accuracy of 50.2%. Considering we are training two classes only, an accuracy of 50% implies that the network is not learning features that can characterize the data according to their clinical category but instead is overfitting to the training data. Modifying the number of neurons or layers did not seem to improve the results of the test dataset.

On each fold, there were two samples to test: one control (WT) and one dystrophic (KO). Therefore, upon evaluation of the average results, we focused on the output of each sample to search for the origin of this low accuracy. In Fig. 9.11 we see that the accuracy of the test samples is heavily fold-dependent, meaning that some samples had good results with over 90% accuracy; for others, the network was not able to decide (50% accuracy), and for some, the prediction was completely wrong (10% accuracy).

We have seen before that, on average, there are features able to differentiate between the two clinical categories (Fig. 9.8), so even if the inter-sample

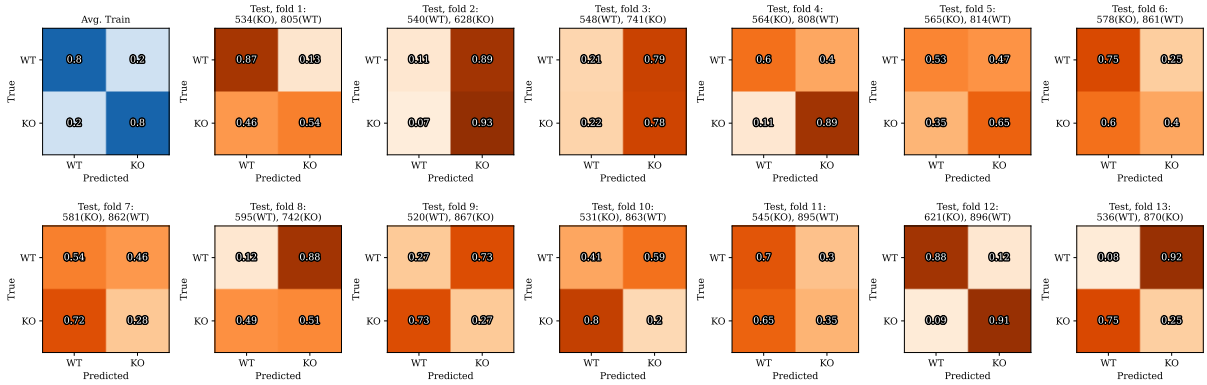

Figure 9.11: Confusion matrices derived from classifying the data with an MLP by using all the optical properties. The first element corresponds to the average confusion matrices for the train data after considering all folds. The remaining matrices correspond to the test data per fold.

variation is high, the networks should be able to pick up on those tendencies when evaluating individual samples. One reason why that might not be happening here is the random sampling. As we need to balance the classes to avoid biasing the MLP towards one class or one sample, we decided to randomly sample values for each feature and sample until the same number of pixels are considered. However, by doing random sampling on one feature, i.e., on the attenuation data, there is no guarantee that the randomly sampled points on other features, like the HSI reflectance, are the same. This requires co-registration of images from different devices, which can be achieved by adding fiducial markings for proper sample orientation and measurement analysis across systems. Given that the samples are non-homogeneous, we might be sampling points from fatty areas in one feature and from muscle areas in a different feature, leading to tendencies that do not match even for the same sample.

Classification by optical imaging method

To test whether random sampling mixes areas of the same sample between different features, we focused on repeating the classification process by creating individual datasets for each imaging system. That way, even if we take a random sample for each muscle to balance the dataset according to the number of pixels of each muscle, we will keep the sampled pixels co-registered between the different features, as the two-dimensional optical property maps taken with one system have the same resolution and spatial distribution.

The new datasets have the following features:

- OCT/PS-OCT: attenuation (μ_t) and birefringence (Δn).
- HSI-VISNIR: average reflectance below 600 nm (R_V), and reflectance values at 536, 563, and 576 nm, corresponding to the peaks of hemoglobin/oxyhemoglobin.
- HSI-SWIR: average reflectance over 1300 nm (R_S) and reflectance values at 927, 970, 1121, and 1327 nm, corresponding to the peaks of water and lipids.
- SFDI (RGB): average absorption (μ_a) and reduced scattering coefficient (μ_s') at the red, green, and blue color ranges.

To further evaluate their behavior, aside from the average cross-validated accuracy, we also considered their sensitivity[3], specificity, false positive rate, and false negative rate of each network. The results are depicted in Tab. 9.3, and Figs. 9.12, 9.13, 9.14, and 9.15.

The models were trained with the same network architecture (200 neurons, one hidden layer, 20% dropout, but still yielded different and interesting results[4]. For example, while the 10-feature dataset trained MLP provided the best train results, it did not generalize as its accuracy corresponded to random guessing (50%). This was not the case, for example, for the networks trained with only OCT or SFDI data, which achieved around 60% accuracy. The SFDI-trained MLP provided a 60.3% sensitivity, but the OCT-trained one had slightly more specificity. Still, the specificity improvement of the OCT-MLP with respect to the SFDI-MLP was only 0.2%, which suggests that the data gathered by SFDI might be better rounded out to identify both WT and KO samples. OCT provides better estimates for KO data but tends to create more false negatives, meaning that healthy samples might be identified as dystrophic.

[3] Sensitivity (Sens): out of all pixels in the control (WT) category, how many are correctly identified as control. Specificity (Spec): out of all pixels in the dystrophic (KO) category, how many are correctly identified as dystrophic. False negative rate (FNR): out of all pixels in the control category, how are many are incorrectly identified as dystrophic (1-Spec). False positive rate (FPR): out of all pixels in the dystrophic category, how many are incorrectly identified as control (1-Sens).

[4] The network's architecture was validated by using it to successfully classify MNIST [7] with 100% accuracy in the test data and 98.2% accuracy in the test data, with over 97% accuracy in all ten classes. The MLP trained for 50 epochs used for HSI-SWIR still provided over 98% accuracy in the test data for the MNIST dataset.

Table 9.3: Classification results for the different optical properties datasets, for the samples in MD2, separated by train and test data. Acc: Accuracy. Sens: Sensitivity, true positive rate. Spec: Specificity, true negative rate. FNR: False negative rate. FPR: false positive rate. Green marks the best result for each column, and red marks the worst. Full dataset indicates the MLP trained with the 10 features with random sampling. The remaining datasets are separated by imaging system. *The HSI-SWIR network had to be trained only 50 epochs due to it being prone to overfitting.

	Ac. train	Sens (train)	Spec (train)	FNR(train)	FPR (train)
Full dataset	80.0%	79.9%	80.0%	20.1%	20.0%
OCT/PS-OCT	61.9%	56.2%	67.7%	43.8%	32.3%
HSI-VNIR	67.0%	64.3%	69.7%	35.7%	30.3%
HSI-SWIR*	56.1%	61.1%	51.1%	38.9%	48.9%
SFDI (RGB)	77.0%	73.5%	80.5%	26.5%	19.5%

	Acc test	Sens (test)	Spec (test)	FNR (test)	FPR (test)
Full dataset	50.2%	46.7%	53.7%	53.3%	46.3%
OCT/PS-OCT	58.0%	52.3%	63.6%	47.7%	36.4%
HSI-VNIR	55.6%	52.9%	58.3%	47.1%	41.7%
HSI-SWIR*	39.1%	49.2%	29.1%	50.8%	70.9%
SFDI (RGB)	61.9%	60.3%	63.4%	39.7%	36.6%

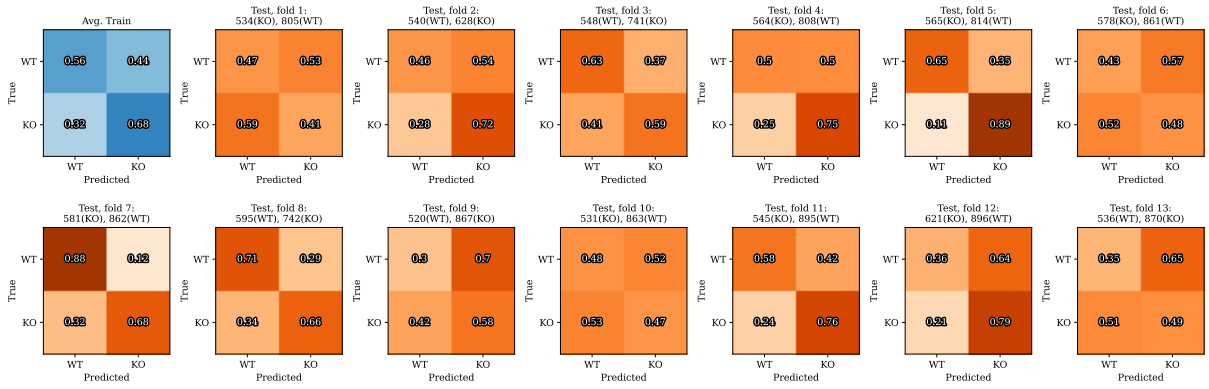

Figure 9.12: Confusion matrices derived from classifying the data with an MLP by using only the OCT/PS-OCT dataset.

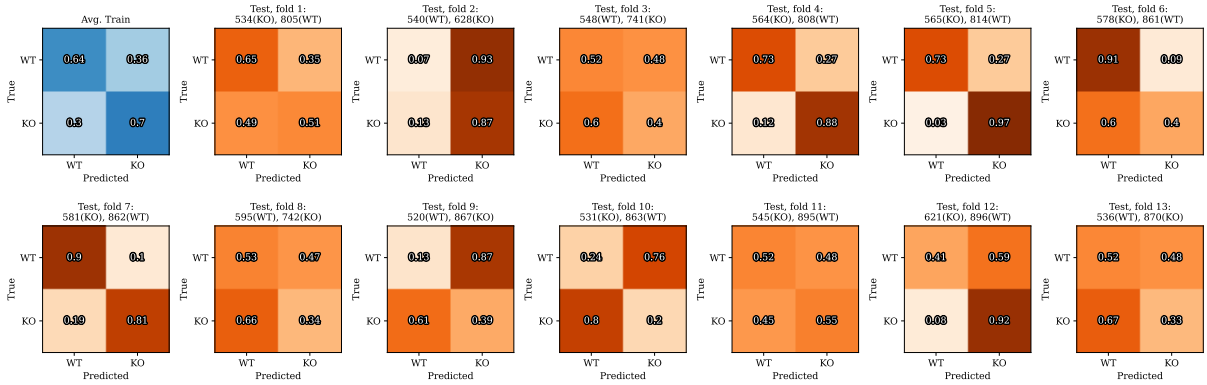

Figure 9.13: Confusion matrices derived from classifying the data with an MLP by using only the HSI-VNIR dataset.

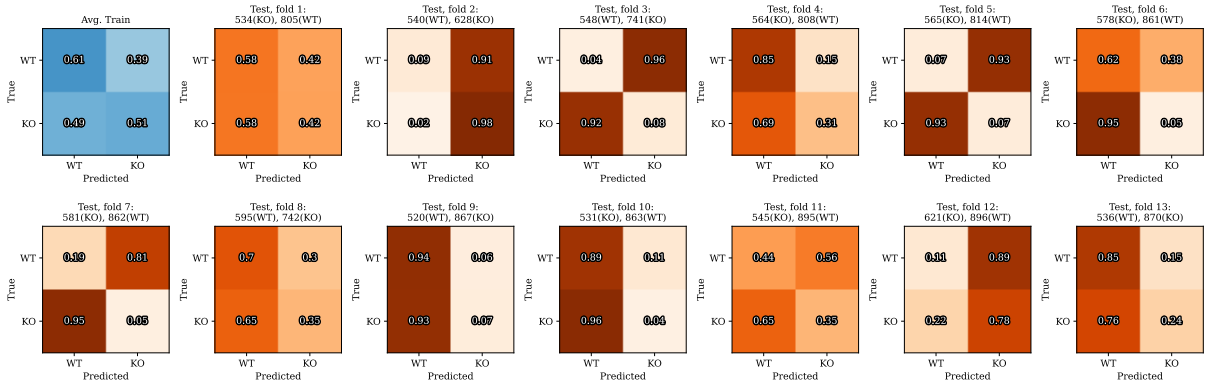

Figure 9.14: Confusion matrices derived from classifying the data with an MLP by using only the HSI-SWIR dataset.

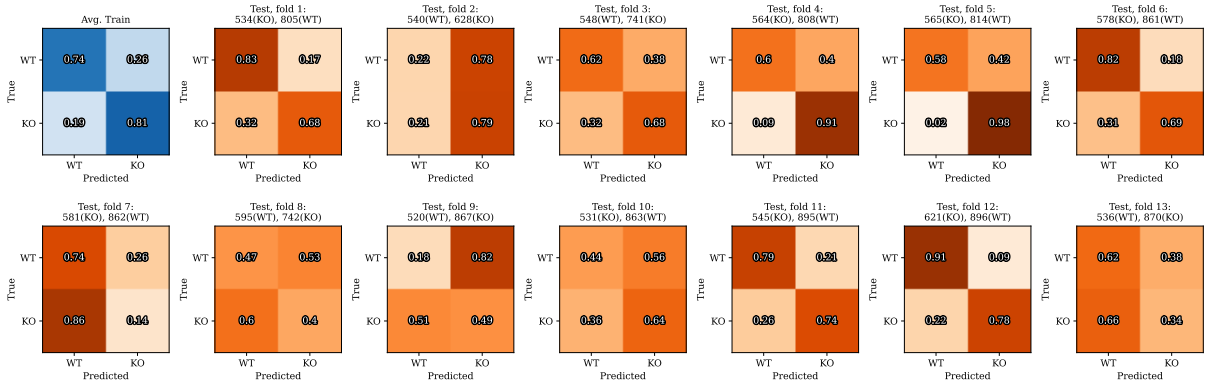

Figure 9.15: Confusion matrices derived from classifying the data with an MLP by using only the SFDI (RGB) dataset.

If any of these optical techniques were to be used to provide a first estimate of the clinical state of the samples before, for example, doing more invasive analyses, higher false negatives would mean sending more samples to be tested but will not pose any other issue. On the other hand, relying only on these techniques to diagnose them would cause more than 30% of the samples to be incorrectly identified as healthy.

We must consider the possible sources of the high accuracy variation observed between folds. The confusion matrices of all methods still showed significant variations for each MLP trained on single-optical-

system data, suggesting that the improvements gained by removing the random sampling between features are not enough to remove the inter-sample variations completely. Additionally, the best possible networks are going to perform as well as the statistical data distributions allow them to, meaning that if there is a high overlap between the control and dystrophic categories in a set of features, the accuracy will represent the amount of data that does not overlap. We see this effect in Tab. 9.3 when comparing the train and test results. In SFDI data, there was less overlap than that of OCT data, which implies that the MLP learns to separate better the training dataset for the former than for the latter, leading to higher train accuracy and a larger gap between train and test accuracy. Although this could be a sign of overfitting, training the SFDI-MLP with a smaller number of neurons caused the accuracy of both sets to drop, suggesting that the networks are not overfitting but, instead, learning the maximum separability they can. Similarly, incrementing the number of neurons in the OCT-MLP did not improve the accuracy on the training or testing datasets significantly, consistent with the overlap of OCT/PS-OCT distributions for the control and dystrophic samples.

Consistent with our findings in previous chapters, the approximately 40%-50% accuracy shown in the test data for the HSI networks suggests that the data considered in these cases does not have enough separability between the control and dystrophic groups to identify each whole sample successfully. Further research is needed to decouple the influence of the samples' substrate from the HSI measurements so that only the spectral data related to the disease is captured in these cases.

9.3 Conclusions

This chapter explored the combination of optical imaging data from different modalities, specifically focusing on OCT, PS-OCT, HSI, and SFDI, to enhance the understanding of muscular dystrophy progression. Two main approaches were investigated: visualization-based and statistical analysis.

The visualization approach involved using a color-mapping technique to create two-dimensional disease maps based on multiple optical parameters. Specifically, optical properties like attenuation, birefringence, and profilometry are assigned to different components of the HSV color space. The results from murine muscle samples demonstrated the effectiveness of this technique in highlighting key differences between healthy and dystrophic tissues, particularly in visualizing variations in birefringence and tissue organization. The inclusion of profilometry data further complemented the visualization by providing a three-dimensional variation of the two-dimensional maps.

To quantify the separability between healthy and dystrophic samples, a statistical analysis was performed on a dataset combining various optical properties, including attenuation, birefringence, reflectance, absorption, and scattering. Statistical metrics, including Fisher's discriminant ratio and the Kolmogorov-Smirnov test, were employed to assess the discriminatory power of each optical property. While individual properties showed some degree of separability, the combination of multiple properties through dimensionality reduction techniques like PCA, t-SNE, and

Isomap led to a slightly improved discrimination between healthy and dystrophic samples. Still, the overlap between distributions is significant, likely due to inter-sample variations. This suggests a need for larger sample sizes to achieve higher statistical significance.

A classification analysis using an MLP assessed the separability of healthy and dystrophic muscle samples based on their optical properties. The initial approach consisted of training on a 10-feature dataset, combining all optical modalities, which yielded poor generalization, likely due to random sampling inconsistencies across modalities. The subsequent classification experiments used modality-specific datasets to ensure feature co-registration. While the 10-feature training achieved the highest training accuracy, it generalized poorly, achieving random-guessing accuracy on the test set. Conversely, modality-specific training, particularly with SFDI and OCT/PS-OCT, improved test accuracy, though with varying sensitivity and specificity. These results suggest that while multi-modal data is promising, current random sampling introduces hindering inconsistencies. On the other hand, differences between train and test accuracy, especially for SFDI, suggest the network learns the maximum possible separability limited by the inherent distribution overlap between sample groups.

Nevertheless, combining data from different modalities allows for a noninvasive and comprehensive analysis and discussion of chemical and structural tissue properties. This could be valuable in guiding the selection of samples for further, more invasive, traditional analysis techniques.

References

[1] V. Mieites et al.: "Single-Image Multi-Parametric Representation of Optical Properties through Encodings to the HSV Color Space", *Applied Sciences* **14**(1) (2023). DOI: 10.3390/app14010155.

[2] C. Ware, M. Stone, and D. A. Szafir: "Rainbow Colormaps Are Not All Bad", *IEEE Computer Graphics and Applications* **43**(3), 88–93 (2023). DOI: 10.1109/MCG.2023.3246111.

[3] G. Tortora and B. Derrickson: "Principles of Anatomy and Physiology", John Wiley & Sons, 2008. ISBN: 9780470084717.

[4] S. L. Jacques: "Tissue Optics", tech. rep. 2020.

[5] S. Theodoridis: "Chapter 7 - Classification: a Tour of the Classics", in: *Machine Learning (Second Edition)*. Ed. by S. Theodoridis. Second Edition. Academic Press, 2020 301–350. ISBN: 978-0-12-818803-3. DOI: 10.1016/B978-0-12-818803-3.00016-7.

[6] M. Hollander, D. Wolfe, and E. Chicken: "Nonparametric Statistical Methods", Wiley Series in Probability and Statistics. Wiley, 2013. ISBN: 9781118553299.

[7] Y. LeCun et al.: "Handwritten Digit Recognition with a Back-Propagation Network", in: *Advances in Neural Information Processing Systems 2 (NIPS)*. Ed. by D. Touretzky. Morgan-Kaufmann, 1989.

Part V

Additional contributions

Additional contributions in other fields of research

10

Part IV of this thesis detailed the analysis of dystrophic mice muscles using optical imaging technologies. However, the application of these techniques extends far beyond this specific dataset. A key advantage of optical imaging is its non-invasive nature, a crucial factor when working with scarce or delicate samples. Just as with the rare muscle tissues studied in Part IV, preserving the integrity of art and archaeological artifacts is imperative. Similarly, in clinical settings, non-invasive techniques are essential for both patient safety and maintaining efficient workflows.

Optical imaging offers the potential to revolutionize various medical procedures and laboratory analyses. In surgery, this could involve providing surgeons with enhanced real-time visualization of tissues, aiding in the identification of anatomical structures. Beyond the operating room, optical imaging can automate time-consuming laboratory tasks, such as cell counting on microscopy slides or analyzing tissue samples for disease markers, increasing both efficiency and accuracy in diagnostics.

This chapter explores how the optical imaging methods we developed in Part IV were adapted and refined through their application in diverse fields, including heritage conservation, bioengineering, ophthalmology, and brain anatomy. The results presented here highlight the versatility and broad potential of these techniques, particularly in their ability to improve both efficiency and accuracy across a range of applications.

10.1 Ophthalmology

Uveitis is the manifestation of inflammatory diseases through the appearance of cells, or cell aggregates, suspended in the anterior chamber of the eye [1]. It is a sight-threatening condition that can lead to vision loss if left untreated. In clinical practice, one of the standard parameters used to quantify the degree of uveitis is based on using a 1 mm × 1 mm slit lamp to manually illuminate the eye and count the number of hyperreflective particles observed in the beam. Due to the nature of the method, inter-observer variability exists due to the subjectivity of the evaluators. To facilitate quantification and reduce such variability, the Standardization of Uveitis Nomenclature (SUN) [2] method proposes grading into six levels based on the number of particles (Tab. 10.1). However, the number of cells increases with the disease grade, allowing for more variability in the cell count as the disease worsens.

Grade	Cells in Field
0	<1
0.5	1-5
1+	6-15
2+	16-25
3+	26-50
4+	>50

Table 10.1: Uveitis grading according to the SUN guidelines [2].

Current efforts in cell quantification methods in uveitis patients utilize OCT system scans for cell detection and extraction of other metrics. OCT is ideal for the analysis of the eye, given that the lenses in the eye do not absorb the infrared light used in OCT the same way other biological tissues do, allowing for deeper scanning. The OCT-uveitis studies are based on comparing the number of particles detected on specific B-scans using image analysis software[1]. The use of image analysis software has the advantage of being able to implement the desired cell

[1] Most commonly, ImageJ, an image processing and analysis program in Java.

counting techniques straightforwardly. Still, oftentimes, it also has the disadvantage of having to adjust the analysis to the characteristics of each specific OCT image. The most commonly used validation methods rely on comparing the results provided by automated cell-counting techniques with the SUN grade [2, 3], or directly with the manual cell count performed on the OCT B-scans [4, 5].

In this work, we proposed an automatic counting method that does not require user input, and that is able to generalize enough to extract the number of particles, regardless of the characteristics of the OCT image [6]. The proposed method detects cellular aggregates in the anterior chamber of the eye based on the statistics of the intensity values detected in regions with and without cellular aggregates, thus saving analysis time, avoiding user assistance, and eliminating subjectivity.

10.1.1 System specifications

This study utilized Optical Coherence Tomography (OCT) scans of the anterior chamber of the eye to perform automatic, unsupervised counting of hyperreflective particles.

The specific device used was a Spectralis OCT (Heidelberg Engineering Co., Heidelberg, Germany). This device is known for its high resolution and image quality, which are crucial for accurate particle identification. The Spectralis OCT operates at a wavelength of 870 nm and offers a lateral resolution of 21.68 μm/pixel and an axial resolution of 3.87 μm/pixel. These specifications ensure that the OCT images have sufficient detail to resolve small particles or cell aggregates within the anterior chamber.

10.1.2 Data collection

The method described here was applied to 27 eyes from 16 patients, of which 16 eyes presented with hyperreflective particles and 11 served as controls. The inclusion of a control group is essential to establish a baseline and validate the accuracy of the automated counting method. The measurements were acquired by trained ophthalmologists in their clinical practice within the Ophthalmology Department of the Hospital Marqués de Valdecilla (HUMV), with the authorization of the Clinical Research Ethics Committee of Cantabria[2].

[2] Code 2019.010

10.1.3 Image segmentation and automated particle count

An automated method was developed and employed to perform the cell count. This method involves scanning the entire aqueous humor area of the OCT scan to identify and label distinct groups of connected pixels, which, in this case, represent cellular aggregates.

However, before applying the cell count method, it is crucial to segment and binarize the image effectively. Segmentation is used to identify the cornea and divide the image into three regions: air, cornea, and aqueous humor. On the other hand, binarization converts the grayscale OCT image into a black-and-white image to isolate the particles of interest from the

interferometric background noise, making them easier to identify and quantify.

A multi-step process was used for cornea segmentation. All OCT images suffer from roll-off, so even in ideal B-scans, the regions of the cornea that are closer to the OCT's lens will have a higher intensity than those further away from it (Fig. 10.1, a). Since all the methods applied in this work were intensity-based, it is necessary to unify the brightness and contrast in the cornea to segment it properly. Histogram equalization was used for this task. This method enhances the contrast in an image by finding the Cumulative Distribution Function (CDF) of the histogram and modifying it so that the resulting CDF is a uniform, monotonously growing function (Fig. 10.1, b). Then, the image is well described by two intensity distributions: the one that represents the cornea and the one that represents the noise. This allows for the use of Otsu thresholding [7], which is an automatic method based on finding the optimal value that separates the two intensity distributions by evaluating all possible threshold options and choosing the one that maximizes the variance between the datasets at each side of the threshold [7]. Finally, the threshold is applied to binarize the image, and simple morphological edge detection is used by subtracting the binary image from its dilated version (Fig. 10.1, c). The image is then separated into three areas according to the number of pixels in each one, where the biggest one is the anterior chamber of the eye, followed by the cornea and, finally, by the air (Fig. 10.1, d).

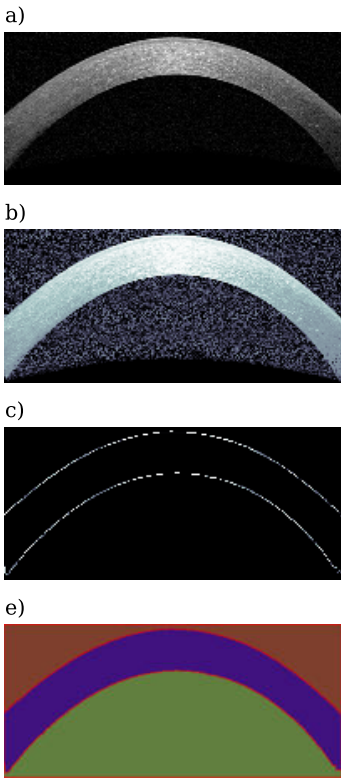

Figure 10.1: Step-by-step cornea segmentation: (a) raw B-scan, (b) histogram-equalized B-scan, (c) edge detection by morphological operations and (d) segmented air (brown), cornea (purple) and anterior chamber (green)

A second binarization process is applied to the data in the anterior chamber to segment the cell aggregates and distinguish them from the background speckle noise inherent in OCT images. Speckle in OCT images follows a specific distribution. In regions with only speckle, the average intensity value and the standard deviation have certain maximum values. However, in the presence of cellular aggregates, these values change. Cellular aggregates exhibit a much higher average intensity than speckle noise, and their presence also causes an increase in the local standard deviation within their neighborhood.

To implement the cell-detection binarization method, the average intensity values and standard deviations are calculated within 3×3 pixel neighborhoods throughout the previously segmented air and aqueous humor regions. This neighborhood size is chosen to minimize any alteration to the size of the detected cellular aggregates after binarization.

The maximum value reached by the mean-standard deviation pair in regions with only speckle (air) defines the threshold value used for binarization. Any pixel in the aqueous humor region with an intensity value exceeding this threshold is attributed solely to cellular aggregates.

10.1.4 Main findings

The automatic particle counting method was compared to the median of the manual counting performed by 17 observers on OCT images (Fig. 10.2). A good correlation was found between the two methods (R^2=0.88, N=26 B-scans evaluated by 17 observers, Fig. 10.3), with greater inter-observer variability observed in images with a higher number of particles. This variability highlights the inherent challenges in manual cell counting, as factors like image quality, speckle pattern, and even

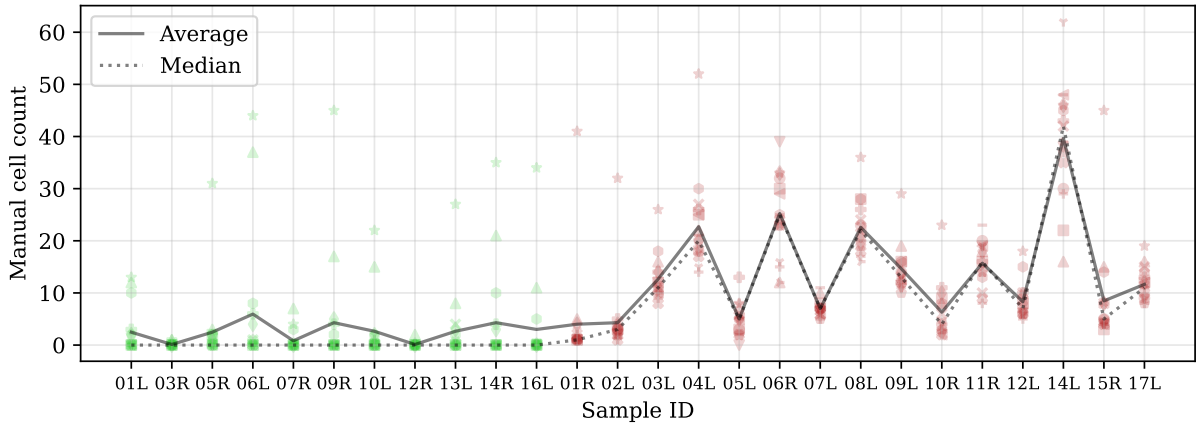

Figure 10.2: Particles detected by manual counting them in the B-scan images by 17 observers. Each marker represents one observer. The control samples are depicted in green, while the pathological ones are shown in red. Note how the average is swayed by the extremes of the distribution while the median, especially on the control samples, remains closer to where more data points are.

the viewing conditions can influence observer perception and lead to discrepancies in the reported cell counts.

It is important to highlight that, in this study, a relatively large number of observers (17) were employed for manual cell counting, which included OCT experts and non-trained observers, which is often not the case in similar studies that establish the same gold standard. For instance, the study by Baghdasaryan *et al.* [5] establishes the gold standard relying on a single uveitis expert for manual quantification. This reliance on a single observer potentially introduces bias and limits the generalization of their findings when evaluated by a regular ophthalmologist, who may not be as proficient in identifying subtle signs of uveitis, potentially leading to delayed or inaccurate diagnoses.

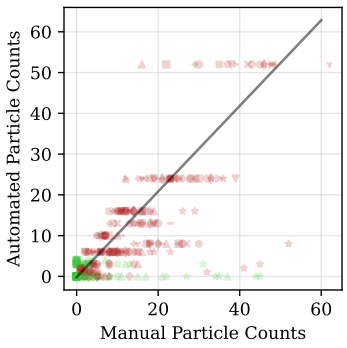

Figure 10.3: Comparison between the manual count performed by 17 observers and the resulting automated count obtained by applying the proposed method. The linear model, corresponding with $y = -0.18 + 1.05x$ provided an R^2 value of 0.88, indicating a good performance by the proposed model. The same control and pathological data points represented in Fig. 10.2 are shown in this figure in green and red, respectively, and the markers represent each of the observers.

A key advantage of our proposed method is that the parameters are not modified for individual B-scans; they are applied universally to all analyzed OCT images. This standardized approach avoids user bias and subjectivity, ensuring consistency in particle quantification across all samples.

Additionally, the algorithm demonstrated that it can accurately detect the presence of cell aggregates by grouping the data into two: control and disease. The classification showcased high precision (0.93), negative predictive value (0.72), accuracy (0.85), specificity (0.88), and sensitivity (0.82) in differentiating between healthy and pathological eyes, suggesting its potential as a valuable tool for initial uveitis screening and minimizing the early false negative cases.

Finally, it is worth noting that the automated analysis of the entire anterior chamber volume, rather than just a single B-scan, could provide a more comprehensive assessment of cellular infiltration. Future research should explore the use of C-scans and 3D analysis to enhance further the accuracy and clinical utility of automated uveitis assessment.

10.2 Archaeology

This second study focused on analyzing a prehistoric quartz blade (scraper), employing OCT as a primary, non-invasive imaging technique. The ability of OCT to reveal subsurface structures without compromising the artifact's delicate integrity made it an ideal starting point for a multi-methodological approach to analysis. Unlike other techniques commonly used on cultural heritage pieces, such as UV-luminiscence, laser-induced breakdown spectroscopy, X-ray diffraction, Raman spectroscopy, or hyperspectral imaging, OCT could precisely locate features within the artifact's depth without causing damage nor needing to extract sample. This allowed OCT data to guide subsequent analyses, potentially enhancing the effectiveness of these techniques.

This research builds upon previous successes in applying OCT to the analysis of paintings and ceramics, extending its use to the examination of prehistoric stone tools. The translucent nature of the quartz blade made it particularly well-suited for OCT imaging, as the light could penetrate the material and highlight subsurface features and differentiate those from the superficial deposits. This allowed for the identification of elements like fibers and spots based on their unique scattering signals, which contrasted with the surrounding quartz attenuation.

10.2.1 Sample description

Here, we examined a prehistoric quartz scraper containing residue that, potentially, could come from a handle. The piece was found in a cave, at a level dated to be 70000 years old, which would indicate that the population that created it was Neanderthal. If the residue was from a handle, it would indicate a high level of development of this Neanderthal tribe. The residue consisted of fibers of unknown origin (animal or vegetable) and dark spots presumed to be iron oxide. To determine the nature of the fibers, their attenuation coefficient and intensity decay profiles were compared with those of known plant (*urtica dioica stalk*) and animal (*bison bonasus tendon*) samples. These samples were selected for their historical relevance to the location and period to which the quartz knife is thought to belong.

10.2.2 OCT system

The analysis employed the same OCT system used in the rest of this document (TEL221PS from Thorlabs) to generate high-resolution 3D images of the knife and its residue. As mentioned earlier, this system, equipped with a 1300 nm laser source, provided a depth resolution of 5.5 μ_m in air and a lateral resolution of 13 μm. While the system has polarization-sensitive capabilities, these were not utilized in this study due to the lack of significant polarimetric behavior observed in the materials. Therefore, the analysis focused on intensity-based data only.

10.2.3 Preprocessing

The objective of this work was to obtain the morphological and optical properties of the two residue types found on the quartz scrapers: the dark spots and the fibers. For that, the preprocessing of the acquired data involved two main blocks: profilometry of the sample's surface and labeling of the two residue types.

As for the mice muscles, the first step in the profilometry is air removal and surface detection, which was performed according to the steps described in Ch. 5. Then, denoising was performed by using Block-Matching and 3D Filtering (BM3D) [8]. BM3D is an image-denoising algorithm that exploits the similarity between patches within an image to reduce noise while preserving detail. It groups similar 2D image patches into 3D stacks, applies a collaborative filter in the transform domain, and then aggregates the denoised patches back into the image. In the context of a 3D OCT cube, BM3D denoising operates by selecting a 2D patch from a single B-scan and identifying similar patches within neighboring B-scans. These patches are grouped into a 3D stack, transformed into a domain where noise and signal are more easily separated[3], and then filtered to reduce noise. The denoised 3D stack is then projected back to the original 2D patch, and this process is repeated for all patches across all B-scans in the OCT cube. This approach leverages the inherent redundancy within the OCT data to effectively reduce noise while preserving critical structural details.

[3] In this case, by using wavelet transforms.

Finally, to enhance the visualization of surface features and aid in the morphological measurements, topographic hill shading was applied to the OCT data. This technique involves calculating the derivatives of the surface in two directions (x and y), and simulating the effect of illuminating the surface with light from different angles [9]. This creates a visual representation of the surface topography with enhanced contrast and depth perception, making subtle variations in surface texture and structure more apparent.

The analysis involved labeling two distinct types of residue observed on the prehistoric quartz knife. The first type, characterized by thin, fiber-like structures, was labeled manually due to the limited number and intricate nature of these features. In contrast, the second type of residue, consisting of larger, more distinct spots, was labeled using an automated process.

The automated labeling process for the spot-like residue involved a multi-faceted approach. First, a 3D features cube was built by stacking images, where the first layer is the surface of the sample, and the second layer is the topographic hill-shaded version of it. The remaining twenty layers are twenty slices of the $\mu_z(z)$ cube calculated with Vermeer's model (Eq. 4.25), from its surface to 100 pixels below it. Aside from the surface structures and the attenuation cube, a selection of textural features are calculated with the Hessian matrix output for each of the layers in the attenuation cube. Let $g(\sigma)$ be a Gaussian kernel with standard deviation σ. Let $I_i(x, y)$ be the intensity value for the pixel (x, y) of a layer i. The textural features for each layer i are calculated as a Hessian matrix $H_i(x, y, \sigma)$ given by [10]:

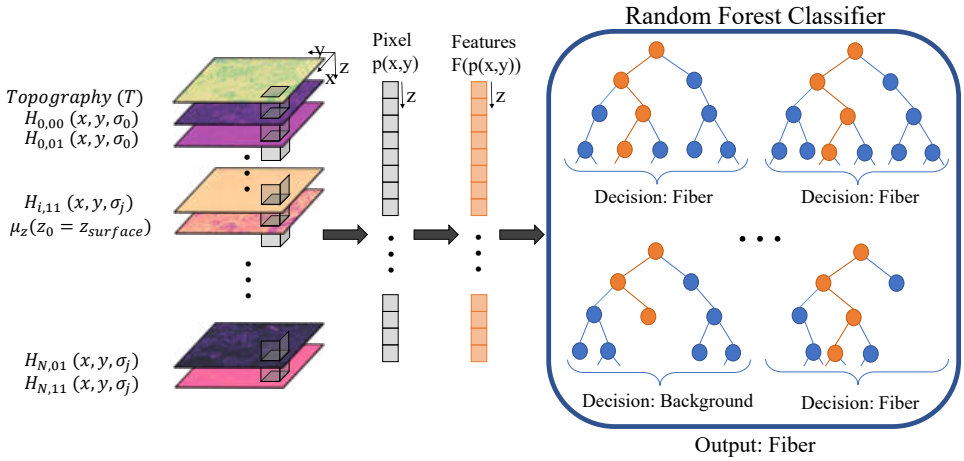

Figure 10.4: Classification via random forest classifier. First, the features cube to analyze is built based on the surface, the hill-shaded surface, the attenuation, and the Hessian features of the attenuation. Then, for each pixel, a group of features is obtained and passed to the random forest classifier. While the structure of the features in each tree is set by training with the labeled data, the features that are missing are dropped at random to avoid biases. The final decision for each pixel is made with the overall vote of the forest.

$$H_i(x,y,\sigma) = \begin{bmatrix} H_{00i} & H_{01i} \\ H_{10i} & H_{11i} \end{bmatrix} = \begin{bmatrix} L_{xx}(x,y,\sigma)_i & L_{xy}(x,y,\sigma)_i \\ L_{yx}(x,y,\sigma)_i & L_{yy}(x,y\sigma)_i \end{bmatrix} \tag{10.1}$$

where $L_{mn}(x,y,\sigma)_i$ is the second derivative across a direction mn of a gaussian blurred version of $I_i(x,y)$, given by:

$$L_{mn}(x,y,\sigma)_i = \frac{\partial^2}{\partial m \partial n} g(\sigma) \circledast I_i(x,y) \tag{10.2}$$

The completed feature cube was then passed to an automated labeling process that employed a Random Forest classifier [11] to label the spot-like residue. This machine learning technique constructs multiple decision trees, each trained on a random subset of the features extracted from the OCT data cube (Fig. 10.4). Some trees utilized all available features, while others had randomly missing features or truncated areas, introducing diversity into the model. Each tree independently classified a pixel based on its available features, and the final label was determined through a majority vote among all trees in the forest.

10.2.4 Main findings

The manual and automated labeling processes resulted in the datasets shown Fig. 10.5. An analysis of the length and width of the identified residues revealed significant variability in both fibers and spots. While the fibers showed significant variability in length, their width remained relatively consistent with few exceptions. Conversely, the spots exhibited greater variability in width but less so in length. These observations suggest that the spots may have originated from a paste-like substance that fragmented into thicker but irregular pieces, while the fibers were mostly intact, having been cut only lengthwise. This difference in size

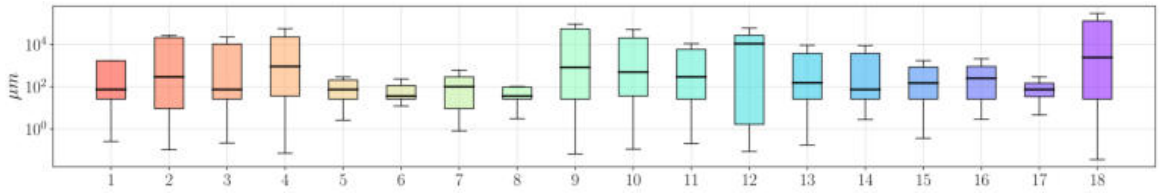

Figure 10.6: Boxplots of the curvature of the fibers. The numbering and color coincide with what is shown in Fig. 10.5.

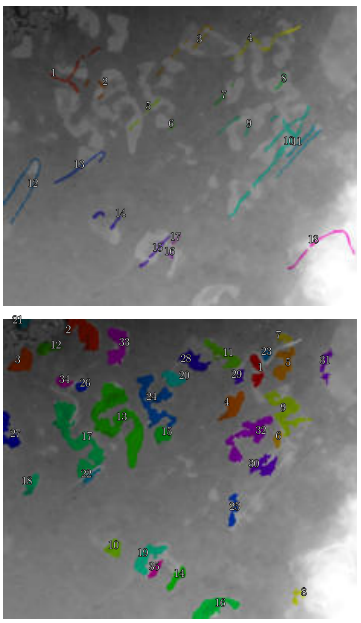

Figure 10.5: Obtained labels for the fibers (top) through manual labeling and for the spots (bottom) via automated random-forest labeling. Each label has a color and a number associated to it that is used throughout the graphs in this results section.

distribution could indicate distinct formation or deposition processes for the two residue types.

Further investigation into the properties of the fibers involved analyzing their curvature radius as an indicator of their flexibility (Fig. 10.6). This analysis revealed an average curvature radius of around 1 mm, suggesting that the fibers were mostly unbent. However, some fibers exhibited small curvature radii without any signs of breakage, indicating a high degree of flexibility, which could aid in identifying their origin.

Optical properties

For the comparison of optical properties, three distinct regions were chosen: inside the skeleton of a fiber, inside a spot far from the fiber, and inside the quartz scraper far from the fiber (Fig. 10.7). The attenuation coefficient of the three materials was then derived according to the Beer-Lambert law (Eq. 4.16), which resulted in three distinct curves. In the case of having only quartz (Fig. 10.7, i), the simplest behavior is shown: there is an intensity peak at the surface of the quartz, followed by an exponential decay according with Beer-Lambert. Inside the spot (Fig. 10.7, h), the same behavior is present but twice, once for each interface: air-spot and spot-quartz. For the fiber (Fig. 10.7, g), the intensity peak is 2.5-3 times less intense when comparing it with the other materials.

Fitting the data to the Beer-Lambert law (Fig. 10.7, g, h, i), provides the attenuation coefficient of each material in units of px^{-1}. To convert those units to physical magnitudes, we assumed that our quartz crystal has a refractive index similar to that of SiO_2 [12, 13], $n_{quartz} = 1.4469$.

With that information, the obtained attenuation coefficient of light for the quartz is:

$$\mu_z = (0.577 \pm 0.048)px^{-1} = (0.167 \pm 0.014)\mu m^{-1}$$

For the spots, we assumed that our material was mainly comprised of iron oxide (II or III), which has a refractive index of $n_{spots} = 2.2385$ [14]. Therefore, its attenuation coefficient is:

$$\mu_z = (0.776 \pm 0.036)px^{-1} = (0.224 \pm 0.010)\mu m^{-1}$$

We did not repeat this calculation for the fiber since we were not able to identify its refractive index, so the px^{-1} attenuation coefficient obtained is:

$$\mu_z = (0.168 \pm 0.011)px^{-1} \tag{10.3}$$

The exponential decay of the historically relevant vegetable (*urtica dioica stalk*) and animal (*bison bonasus tendon*) samples is shown in Fig. 10.8.

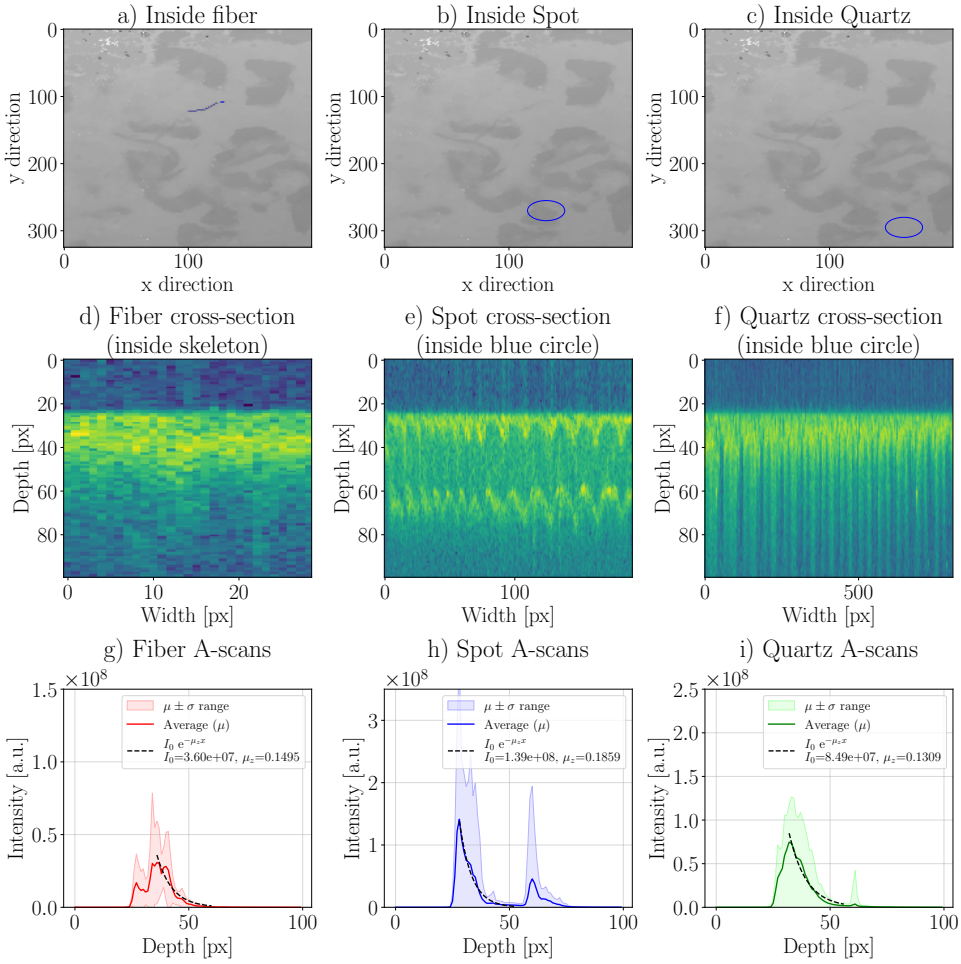

Figure 10.7: Comparison between the intensity decay in three regions: (a, d, g) inside a slice of the skeleton of the fiber, (b, e, h) inside a spot in a region far from the fiber, and (c, f, i) outside the fibers and spots. The B-scans (d, e, f) are generated by concatenating the information in the regions shown in the first row. The surface is leveled prior to showing the A-scans and averaging them (g, h, i). The mosaic-like patterns are caused by concatenating the B-scans inside the blue circles to show them as unified, wider B-scans before surface leveling. The solid colored line on figures (g), (h), and (i) represents the average (μ) A-scan for each sample type, the shaded area represents one standard deviation (σ) from the average, and the black dotted line is the result of fitting the average A-scan to an exponential decay.

The animal sample has a less regular depth profile than the vegetable one (Fig. 10.8), and it is more similar to the profile of the analyzed fiber. The obtained attenuation coefficient for the animal sample reflects that behavior. It sits within the experimental uncertainty of the value of the analyzed fiber, unlike the coefficient obtained for the vegetable sample.

$$\mu_{z,vegetable} = (0.1864 \pm 0.0096) px^{-1}$$
$$\mu_{z,animal} = (0.163 \pm 0.015) px^{-1}$$
$$\mu_{z,fiber} = (0.168 \pm 0.011) px^{-1}$$

To evaluate the repeatability of this first result, we derived the attenuation coefficient for all fibers and compared those values with the vegetable and animal measurements (Fig. 10.9).[4] Contrary to the behavior of fiber number 1, the overall average of the fibers

$$\mu_{z,average} = (0.2245 \pm 0.0034) px^{-1}$$

[4] Fibers 5 and 8 were not analyzed and are not represented in Fig. 10.9 since they were completely on top of the metallic spots, leaving 16 fibers for the analysis.

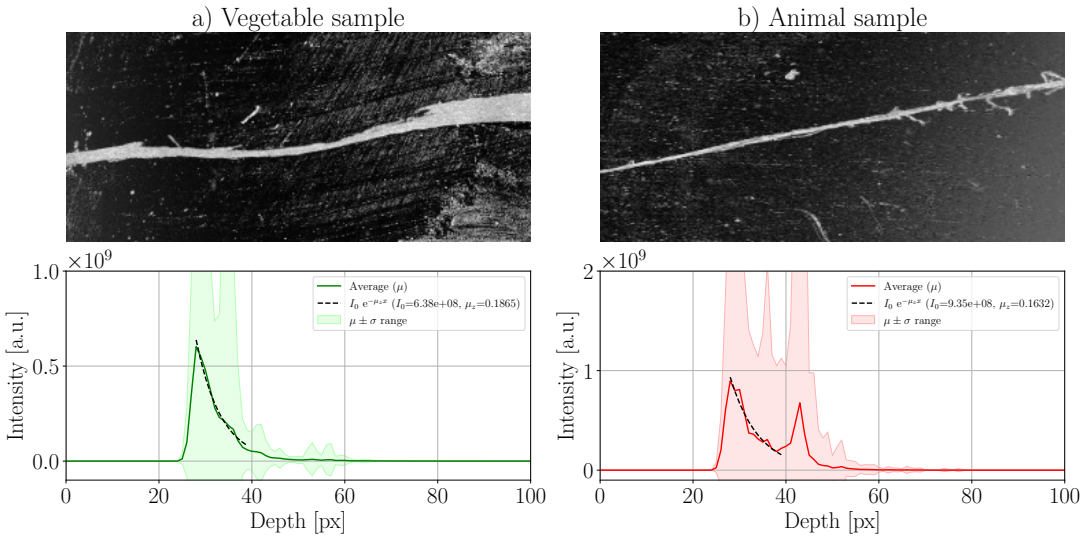

Figure 10.8: Comparison between the exponential decay in a vegetable sample (a) and an animal sample (b).

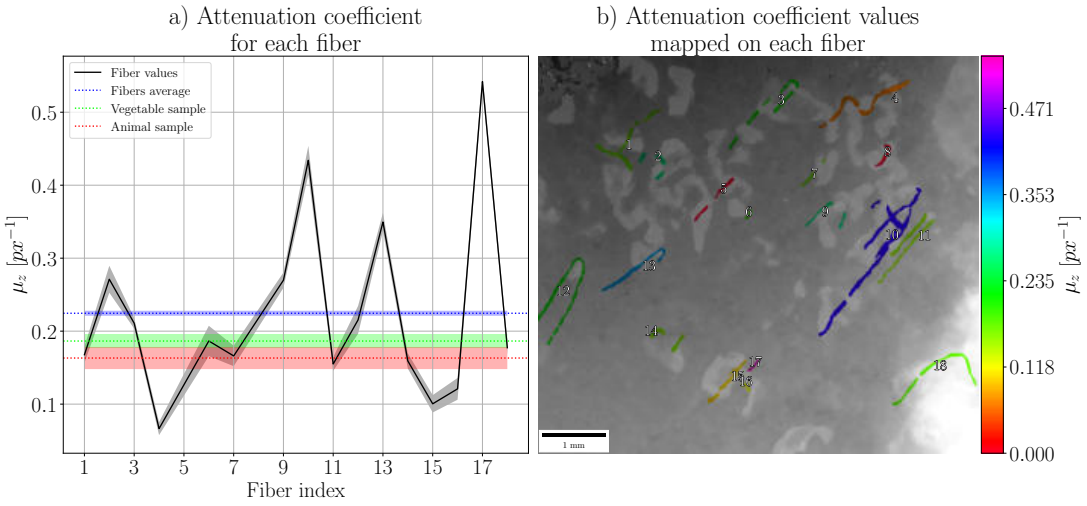

Figure 10.9: Attenuation coefficient of all fibers compared to those of the vegetable and animal samples. The solid lines to the left (a) indicate the average attenuation coefficient of each fiber (black), of the vegetable sample (green), and of the animal sample (red). The blue line represents the overall average of all fibers. The shaded colors indicate the uncertainty of the represented attenuation coefficients. The average values of each fiber are indicated as a color scale over the average OCT intensity image (b).

is closer to the vegetable value than to the animal one and greater than both of them, with 8 fibers closer to the vegetable sample and 8 to the animal sample. To ensure that the highest values are not biasing the average, we also calculated the median of the attenuation coefficient of the fibers, yielding a value of

$$\mu_{z,median} = (0.182 \pm 0.011) px^{-1}$$

which, again, points to the vegetable sample as a possible origin for the fibers.

10.3 Neuroscience

Polarization imaging, particularly Mueller Matrix Imaging (MMI), has emerged as a valuable tool in medical imaging due to its ability to discern structural changes in tissues by analyzing their anisotropy [15]. MMI captures all inherent polarization properties of a sample, enabling comprehensive characterization of tissue properties [16]. In brain imaging, MMI has shown promise in various applications, including the study of white matter tract orientation [17–20], Alzheimer's disease progression [21], and tumor detection [22].

However, the field of brain tissue polarimetry exhibits significant heterogeneity in experimental approaches, sample types, imaging systems, and analysis methods. This variation poses challenges in comparing findings across studies and determining optimal imaging parameters. This work [23] aimed to address this gap by providing a detailed analysis of the polarimetric properties of healthy whole brain specimens and their sub-structures using multispectral MMI, building upon preliminary findings [24]. The goal is to establish a comprehensive dataset that can serve as a reference for future research and clinical applications in brain imaging.

10.3.1 Ex-vivo brain samples

This study utilized twenty regions from six fresh lamb brains, sectioning thirteen samples for visualization of specific areas like the brain stem and diencephalon, while seven remained intact (Fig. 10.10). Four macro-regions were identified: the brain hemisphere, basal ganglia/diencephalon, brain stem, and cerebellum. Specific white matter (WM) and grey matter (GM) regions were labeled based on macroscopic appearance and anatomical landmarks, referencing existing literature [25, 26].

10.3.2 Optical system and measurement procedure

The system employed was the multispectral MMI, v1.0, described in Ch. 4. As a brief reminder, the reflection configuration MMI system [23] features a collimated white LED light source filtered between 450-680 nm using a rotating filter wheel. The Polarization State Generator (PSG) consists of a linear polarizer and a $\lambda/4$ retarder in a motorized mount. A polarimetric camera with a wide-field lens served as the detector. The Polarization State Analyzer (PSA) comprised the camera and a sliding filter mount with another $\lambda/4$ retarder in one of its positions.

Measurements were taken at six wavelengths (450, 500, 550, 590, 650, and 680 nm), with exposure times adjusted for each measurement. Each measurement involved capturing 32 images to derive the Mueller matrix. A total of 3840 images were captured, yielding 120 Mueller matrices. Mueller matrices were calibrated using the Eigenvalue Calibration Method (ECM) [27] to determine PSA and PSG matrices, with an average calibration error of 6.3%.

10.3.3 Mueller matrix data analysis

Following the same pipeline presented in Ch. 8, the normalized Mueller matrix elements, m_{ij}, were analyzed, along with the first element, M_{11}. The ensemble criterion [28] was used to assess the physical realizability of the matrices [29, 30]. The Indices of Polarimetric Purity and the degree of polarimetric purity were also calculated [31, 32]. Finally, the linear and circular anisotropy coefficients, and the overall degree of anisotropy were also determined.

Three decomposition methods were applied to evaluate the polarization properties of the samples:

- Forward Polar Decomposition (Lu-Chipman): used to separate depolarization (Δ), retardance (R), and diattenuation (D), as well as the orientation of the optical axis (θ).
- Symmetric Decomposition: used to derive depolarization (Δ), retardance (R), and diattenuation (D_1, D_2), without the matrix arrangement requirements of the polar decomposition.
- Differential Decomposition: used to analyze the matrix logarithm L to obtain linear and circular retardance and diattenuation and their variances and covariances.

The same classification method that was presented for the mice samples (Ch. 8) was previously applied to the acquired brain dataset. K-Nearest Neighbors classification was used to distinguish between GM and WM, with 6-fold cross-validation. To evaluate the influence of the Mueller properties in the results, feature importance was assessed via random

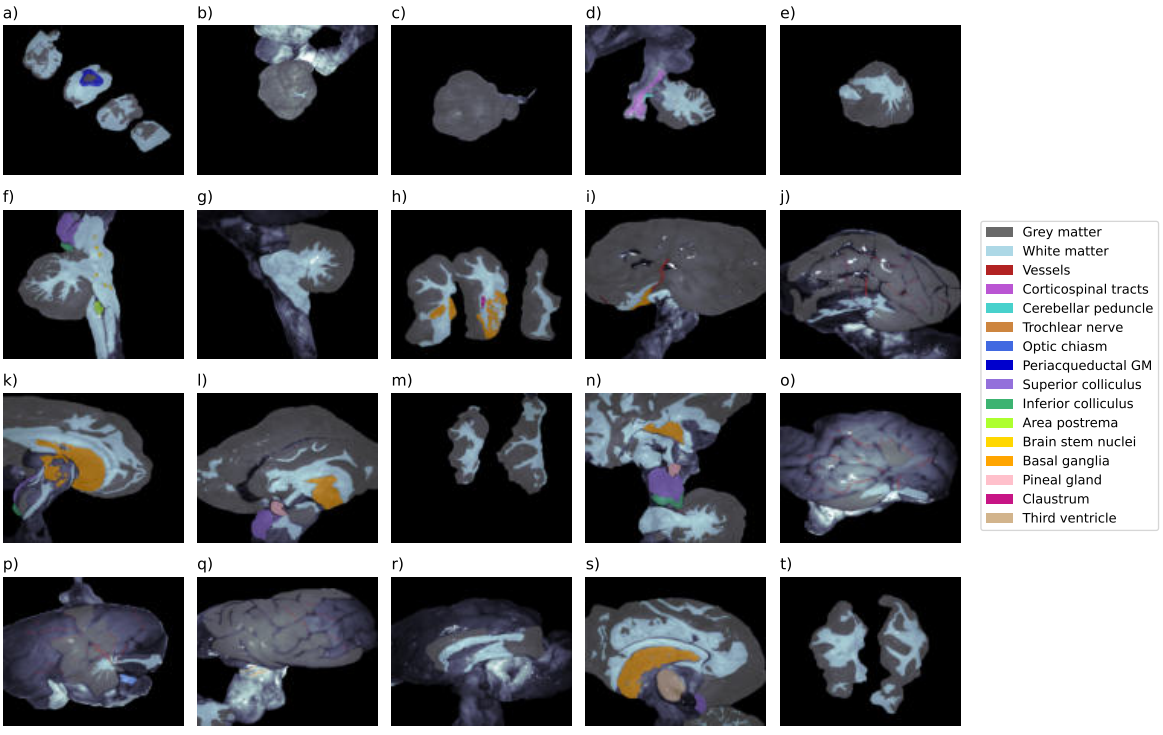

Figure 10.10: Labels identified on the 20 measurements taken of lamb brain in multiple regions: brain stem (a), lateral (b, c) and medial (e-g) views of cerebella, frontal basal ganglia sections (h), lateral (i, j), medial (k, l) and sectional (m) views of left hemispheres, pineal region (n) and lateral (o-q), medial (r, s) and sectional (t) views of right hemispheres. Figure and caption reproduced from [23].

permutations [11] and Sequential Forward (SFFS) and Backward (SBFS) Floating Selection [33–38].

10.3.4 Main findings

The measured Mueller matrices, M, were predominantly diagonal for all samples and wavelengths, indicating a strong depolarizing effect of brain tissue, similarly to what was observed for the mice samples. This observation was consistent across all wavelengths, with finer details observed at shorter wavelengths due to reduced optical path lengths and associated blurring.

Analysis of the physical realizability of the Mueller matrices using the ensemble criterion revealed that certain regions, such as areas with specular reflections, water accumulation, and lower signal, failed to meet the criteria. These non-realizable regions were excluded from further analysis to avoid artifacts.

Matrix decomposition methods

The Indices of Polarimetric Purity showed a general trend of decreasing polarimetric purity with increasing wavelength, which is consistent with the expected increase in depolarization due to longer optical paths at longer wavelengths. White matter exhibited lower purity than grey matter, suggesting more depolarization in the former, that would be tied to the higher scattering that gives it its whiter appearance.

The anisotropy coefficients revealed that linear anisotropy dominated over circular anisotropy, suggesting the presence of linear retardance or

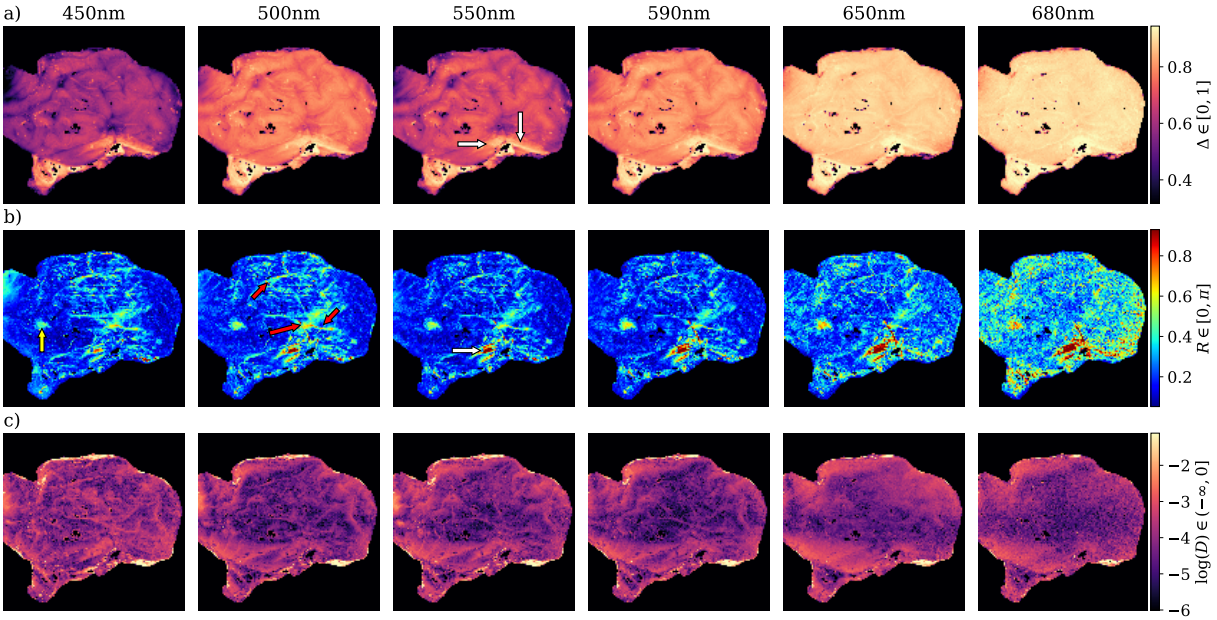

Figure 10.11: Depolarization (a), retardance (b), and diattenuation (c) of a lateral view of one left hemisphere, from 450 nm to 680 nm. The white arrows indicate white matter presence, the red ones point to some vessels, and the yellow one to sub-cortical structures. D has been represented logarithmically. The data has been clipped to $\Delta \in [0.31, 0.94]$, $R \in [0.052, 0.93]$, $D \in [2.5 \times 10^{-3}, 0.33]$ for visualization purposes. Figure and caption reproduced from [23].

diattenuation. However, the overall degree of anisotropy was low in all images and brain structures.

The forward polar decomposition showed that depolarization increased with wavelength and was higher in WM than in GM (Fig. 10.11). Retardance also increased slightly with wavelength and was useful for visualizing blood vessels. Diattenuation was generally low, with more detail observed at shorter wavelengths, but did not seem relevant for grey/white matter distinction.

The symmetric decomposition yielded similar results for depolarization and retardance, with the latter showing greater resistance to noise at longer wavelengths compared to the forward polar decomposition. Diattenuation values remained negligible in this representation as well.

Finally, the differential decomposition did not reveal clear patterns of diattenuation or retardance, highlighting the complex polarimetric behavior of brain tissue dominated by depolarization. However, a slight decrease in depolarization at 550 nm was observed, consistent with findings from other decomposition methods.

Grey and white matter identification

The analysis of grey matter and white matter focused on evaluating the ability of depolarization, retardance, and diattenuation to differentiate between these tissue types. A balanced dataset was created by randomly sampling GM pixels to match the number of WM pixels.

Depolarization showed the most distinct behavior, increasing with wavelength for both grey and white matter, with the latter exhibiting consistently higher values (Fig. 10.12). The greatest separation between both tissue types was observed at 450 nm. Retardance also increased with wavelength for both tissue types, again with high retardance areas pointing to white matter structures. Diattenuation remained negligible across all wavelengths, showing a significant overlap between grey and white matter.

Statistical analysis using the Mann-Whitney U test confirmed that all three polarization properties had distinct distributions for grey and white matter across the analyzed wavelengths. K-Nearest Neighbors classification models were trained to distinguish between both sample types, using both single-wavelength and multiple-wavelength features.

Models using shorter wavelengths (<590 nm) achieved higher accuracy in classifying the samples. Feature importance analysis revealed that depolarization was the primary discriminating factor, particularly at shorter wavelengths, as occurred with the mice muscles.

The models that incorporated multiple wavelengths outperformed single-wavelength models, achieving 97% accuracy. This suggests that multispectral information enhances the ability to distinguish between grey and white matter, potentially by capturing subtle variations in depolarization across different wavelengths. Sequential floating selection methods were used to identify optimal features for classification, confirming the importance of depolarization at shorter wavelengths. Classifying with only the three most significant multi-wavelength features provided a 95% accuracy, which, even if it is smaller than using the whole multispectral

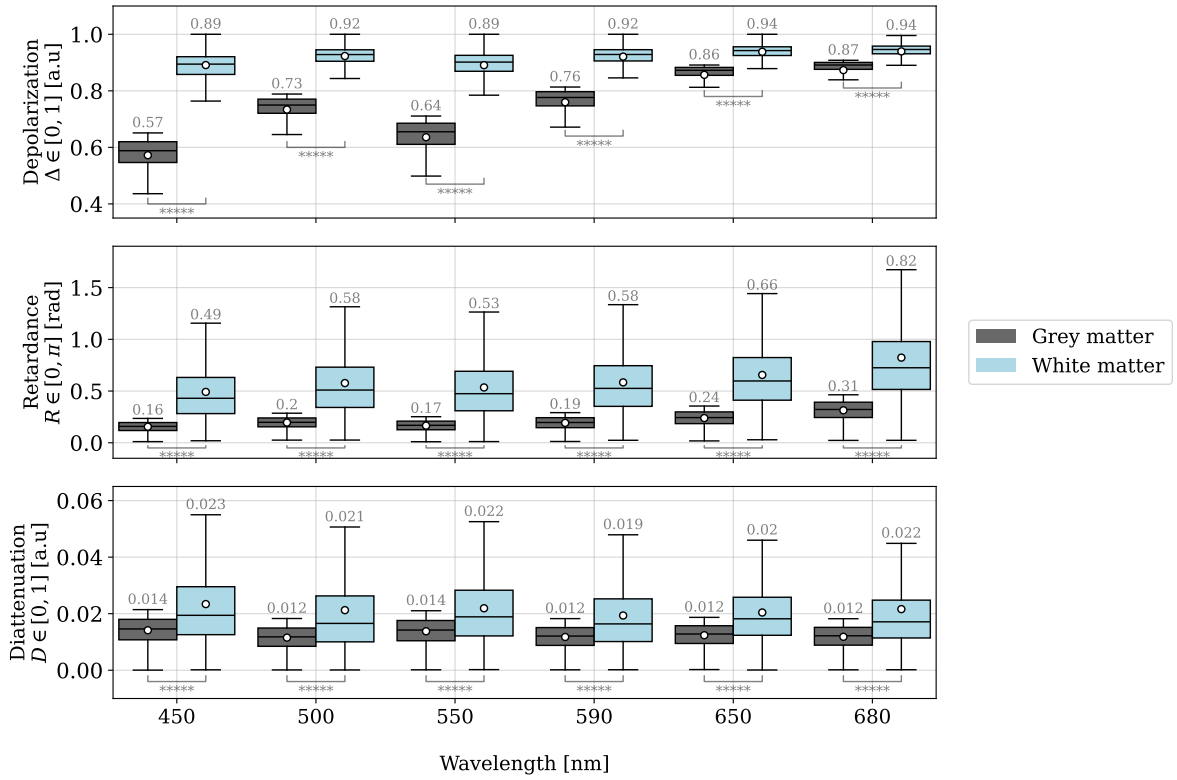

Figure 10.12: Depolarization Δ, retardance R, and diattenuation D for Grey (GM) and White (WM) matter, sorted by wavelength. The two-sided Mann-Whitney U test indicated p-values of $p < 10^{-5}$ (*****) for all pairs GM-WM. The average of each distribution is indicated both as a white scatter point and as the number on top of each boxplot.

matrices, is high enough to justify focusing only on those features for future experiments. The success of the multi-wavelength models with respect to the single-wavelength ones underscores the value of multi-spectral MMI in providing richer data for tissue classification compared to single-wavelength approaches.

10.3.5 Analysis by brain region

The results were further analyzed by grouping the data according to specific brain regions:

Brain hemispheres In the brain hemispheres, both depolarization and retardance increased with increasing wavelength for all tissue types. Blood vessels exhibited polarization properties overlapping with both grey matter and white matter. Other structures, such as the basal ganglia and optic chiasm, showed values between those of grey matter and white matter. Diattenuation remained low for all hemispheric tissues.

Cerebellum Analysis of the cerebellum revealed similar trends for depolarization, retardance, and diattenuation as observed in the hemispheres. The cerebellar peduncle, a white matter structure, exhibited higher depolarization values than the surrounding white matter.

Brain stem The brain stem region showed a complex combination of grey matter and white matter, with some structures exhibiting polarization properties closer to grey matter and others closer to white matter. Notably, the brain stem grey matter and white matter had wider interquartile ranges for depolarization and retardance compared to other brain stem structures.

Overall, these findings highlight the variation in polarization properties across different brain regions and tissue types. The observed trends for depolarization and retardance are consistent with the general behavior of these parameters with respect to wavelength and tissue composition. The low diattenuation values across all regions suggest that it may not be a primary discriminator of tissue types in this context.

10.3.6 Discussion

This study focused on analyzing the polarization properties of healthy brain tissue using multispectral Mueller Matrix Imaging in fresh, whole animal specimens. The choice of fresh samples aimed to provide a realistic representation of tissue properties closer to an in vivo scenario, while the use of whole specimens allowed for a comprehensive analysis of various brain regions and their sub-structures [23].

The multispectral analysis revealed that depolarization was the primary differentiating factor between grey matter and white matter, with white matter exhibiting higher depolarization values across all wavelengths [23]. This finding is consistent with previous studies [17, 18, 39] and is attributed to the denser composition and lower absorption of white matter. The experiment performed here also showed a decrease in depolarization at 550 nm, likely due to hemoglobin absorption, suggesting multispectral Mueller Matrix Imaging as a sensitive tool to assess cerebral blood volume and oxygenation [23].

The importance of depolarization in tissue classification was further emphasized by the superior performance of multi-wavelength KNN models, which achieved higher accuracy than single-wavelength models. This highlights the value of multispectral information in capturing subtle variations in polarization properties across different wavelengths [23].

Comparison with previous studies using fixed brain tissue [40] revealed differences in retardance values, emphasizing the potential impact of tissue fixation and animal model variability on polarization properties. Furthermore, the wavelength used also influences the visualization of different brain structures, given that shorter wavelengths are ideal for resolving finer details, while longer wavelengths enhance the visualization of deeper structures [23].

Retardance can also be explored as a marker of tissue anisotropy, particularly in differentiating between different types of white matter tracts. However, measurements at longer wavelengths can be inaccurate due to depolarization and calibration errors, making them difficult to acquire [23].

10.4 Bioengineering

Cardiac fibrosis, a pathological condition characterized by excessive extracellular matrix protein deposition, is a significant contributor to heart disease progression and adverse outcomes. While initially a protective mechanism after myocardial damage, persistent fibrosis leads to increased stiffness and impaired cardiac function. Current therapies for cardiac fibrosis are limited, hampered by the lack of suitable human cardiac models. Animal models, while valuable, do not fully recapitulate human disease [41]. Engineered heart models, such as Engineered Connective Tissue (ECT) models, offer a promising alternative. ECT models, composed of cardiac fibroblasts embedded in collagen hydrogels, mimic the 3D architecture of the fibrotic environment. This study utilized Engineered Connective Tissue models to investigate the effects of an anti-fibrotic drug, CTPR390, on the mechanical, biochemical, and structural characteristics of fibroblasts and of the extracellular matrix [41].

A key aspect of understanding the efficacy of anti-fibrotic therapies lies in the detailed analysis of the engineered connective tissue's structure, including collagen fiber alignment and organization. Therefore, this study aimed to employ Polarization-Sensitive Optical Coherence Tomography (PS-OCT) to visualize and quantify changes in collagen structure and fibroblast behavior within the ECT model following treatment with CTPR390.

10.4.1 Engineered connective tissue samples

Engineered connective tissue models were generated using adult human left ventricular cardiac fibroblasts. Following established protocols, a collagen type I solution was mixed with DMEM, neutralized, and combined with human cardiac fibroblasts [41]. The resulting cell-collagen mixture was cast in 48-well plates with flexible poles and allowed to condense. The ECTs were cultured for 13 days. Fibrosis was induced using TGFβ1, and the anti-fibrotic treatment consisted of CTPR390 [41].

10.4.2 Polarization-Sensitive OCT analysis

PS-OCT was used to image the ECT samples using the device described in previous chapters. With it, we measured the parallel and perpendicular components of the electric field, which were used to calculate Stokes parameters. The angle of polarization was also derived from these parameters (Fig. 10.13). Following the methods described in Ch. 4, we derived the attenuation coefficient (μ_z) with the phantom-calibrated method. Then, Kernel Density Estimation (KDE) [42] was employed to analyze the two-dimensional distributions of the samples in the U-μ_z plane, and to calculate the overlap between the distributions of the control, TGBβ and CTPR ECTs. The overlap was estimated by deriving the intersection-over-union of the 60% of the data in each distribution. We also analyzed the evolution of the xy-averaged Stokes parameter U along depth (0-100 μm) to characterize tissue organization and fiber alignment inside the samples [41].

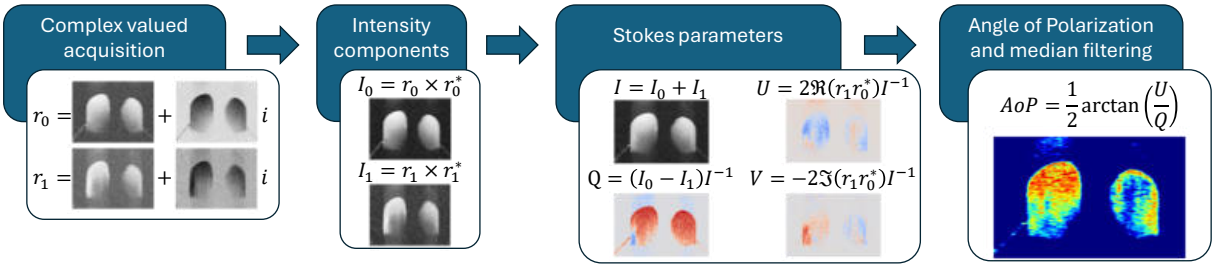

Figure 10.13: Schematic illustration of the Angle of Polarization (AoP) calculation with the analysis pipeline to obtain the angle of polarization using the PS-OCT system. From left to right, the first block indicates the captured values as complex magnitudes. The second block shows the procedure to calculate the parallel (I_0) and perpendicular (I_1) intensities of the electric field. The third block shows the calculation of the Stokes parameters (I, Q, U, V). The fourth block indicates the calculation of the Angle of Polarization using Stokes' second and third components (U, Q). The final data are median filtered with a disk of diameter 3 as a kernel to remove speckle noise. Figure and caption adapted from [41].

10.4.3 Main findings

PS-OCT was applied to three experimental groups: Control, TGFβ1 (fibrosis induction), and CTPR390 (anti-fibrotic treatment), with one sample on each category. PS-OCT imaging proved to be a useful non-invasive method to generate three-dimensional images of the ECTs. The subsequent analysis focused on characterizing tissue compactness (through the attenuation coefficient) and the degree of fiber alignment (through the Stokes parameters) within the ECTs [41]. The main results related to PS-OCT are depicted in Fig. 10.14.

Initially, no difference was seen between the three ECT models in the three-dimensional maps (Fig. 10.14, a). However, these allow for a better understanding of the structural features of the sample than with the information given only by the *en face* maps. Similarly, the two-dimensional attenuation maps were not able to detect differences between the samples, suggesting a similar arrangement of cell sizes inside the three samples [41].

As the attenuation maps were derived by considering the first 100 μm of the sample, we derived the Stokes parameters up to the same depth for consistency. Then, we contrasted the information given by the Stokes parameters with that of the attenuation coefficient and found that comparing the parameter U with μ_t (Fig. 10.14, b) showed three different distinct patterns when comparing the control sample with the fibrotic and treated one. Specifically, the corresponding dispersion maps generated showed a higher degree of similarity in compactness between the Control and CTPR390-treated ECTs (64.5% overlap) compared to both Control/TGFβ1 (56.9%) and CTPR390/TGFβ1 (40.7%) comparisons. This suggests that CTPR390 treatment can cause the ECT to return to a fiber density closer to that observed in the healthy control samples [41].

Further analysis of the Angle of Polarization at a depth of 100 μm hinted at differences in fiber orientation between the three samples. The TGFβ1-treated ECT exhibits a predominance of highly structured fibers aligned at angles below 60°. In other words, the TGFβ1-treated ECT tends to align itself with the contraction axis of the ECT, potentially over-stiffening the sample. In contrast, the CTPR390 treatment reverted this effect, with the angle of polarization distribution in this ECT resembling that of the Control, specifically showing a reduction in the number of fibers oriented

at angles above 120° [41]. Polarized light imaging measurements also corroborated these findings [41].

Finally, since the Stokes parameters are also three-dimensional, we evaluated the rate of change of the xy-averaged Stokes parameter U along the depth (0-100 μm). A linear relationship between U and z was observed for the three samples, with a different evolution rate (slope) for the three ECTs. On average, the rate of change of U was faster through the layers for the TGFβ1, suggesting that the more random distribution of cellular orientation viewed in the angle of polarization in the Control and CTPR390-treated ECTs leads to smaller variations in the Stokes parameters, on average [41].

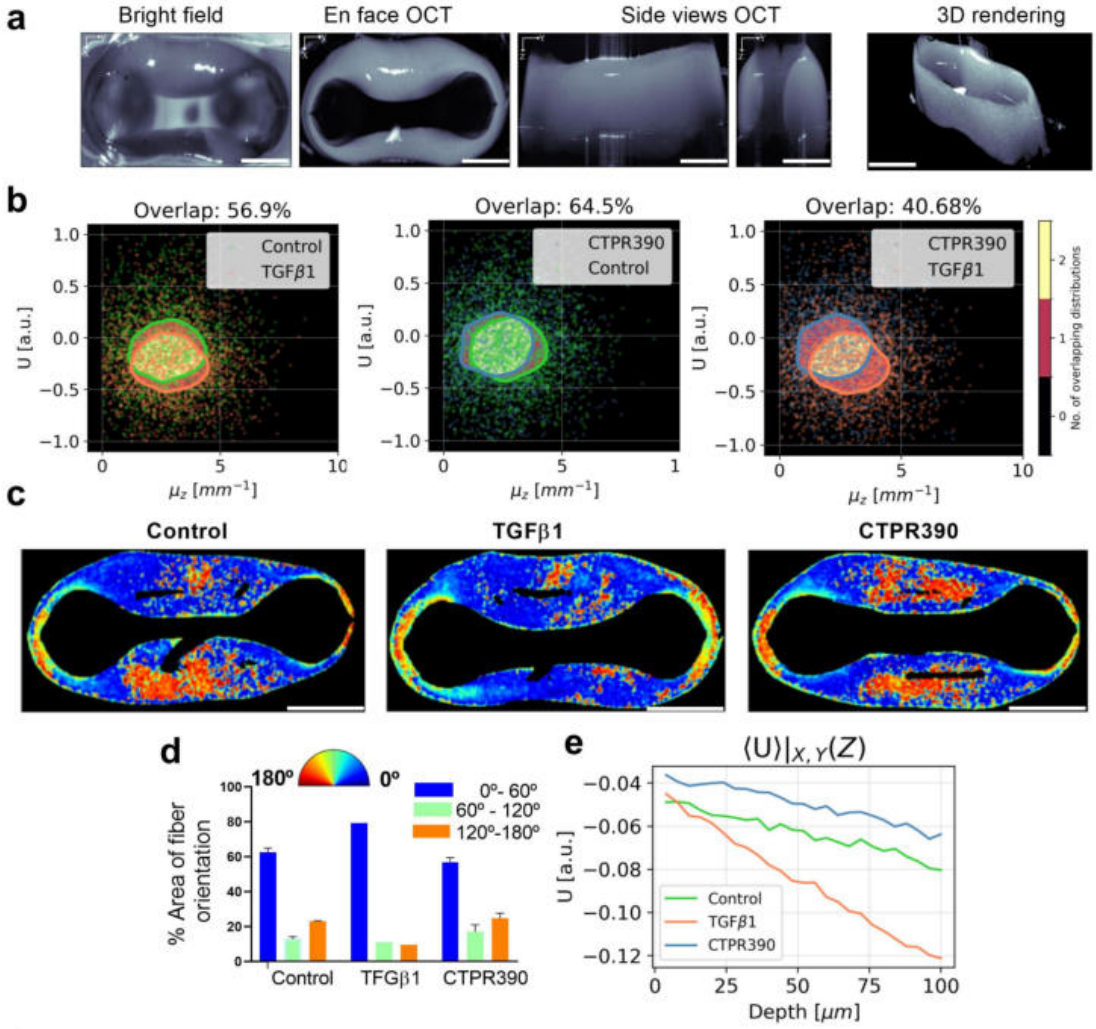

Figure 10.14: (a) Representative images (bright field image, en face view, side views, and 3D rendering) of an ECT using PS-OCT. The white scale bar indicates 1.3 mm. (b) Three panels showing the correlative behavior observed within one standard deviation the Stokes U and the attenuation coefficient distributions, assuming a refractive index of n=1.38, typical of biological samples, evaluated up to the first 100 micrometers. (c) Representative ECT images of the angle of polarization (AoP) orientation aligned with the fibers within the ECT using the same color-coding as in panel (d). (d) Bar graph illustrating the quantification of areas with the same percentage of AoP aligned. AoP color code: blue (0° - 60°), green (60° - 120°), and orange (120° - 180°). (e) Evolution along depth (z) of the xy-averaged Stokes U parameter (a.u.) among the Control, TGFβ1, and CTPR390 groups within the initial 100 μm from the surface of the ECT. The behavior can be approximated by lines with the following equations: Control Y = (-554.8e-04 ± 8.0e-04) + (-129.8e-05 ± 5.7e-05) X; TGFβ1 Y = (-525.7e-04 ± 8.1e-04) + (-362.1e-05 ± 5.8e-05) X; CTPR390 Y = (-431.9e-04 ± 8.0e-04) + (-138.3e-05 ± 5.7e-05) X. Figure and caption adapted from [41].

10.5 Conclusions

This chapter provided an overview of how the optical imaging techniques discussed in this book, were successfully applied across diverse fields, including ophthalmology, archaeology, neuroscience, and bioengineering. Each application demonstrated the versatility and potential of these non-invasive methods in addressing research questions and improving practices in various domains.

In ophthalmology, an automated cell-counting method using OCT was developed to enhance the quantification of uveitis, offering a more objective and efficient approach compared to manual counting, with the aim of improving diagnostic accuracy and standardizing uveitis assessment. The archaeological study showcased the use of OCT in analyzing a prehistoric quartz scraper, highlighting subsurface features and residues without damaging the artifact. This non-invasive approach allowed for the identification and characterization of different residue types. The neuroscience section explored the application of multispectral MMI in brain imaging, providing a detailed analysis of the polarimetric properties of healthy brain tissue. This research aimed to contribute to a better understanding of brain structure and function, with potential implications for the diagnosis and monitoring of neurological conditions. Finally, the bioengineering application demonstrated the use of PSOCT in analyzing Engineered Connective Tissue models for cardiac fibrosis research. This technique allowed for the visualization and quantification of changes in collagen structure and fibroblast behavior following anti-fibrotic treatment, offering a valuable tool for evaluating the efficacy of new therapies.

Overall, the noninvasive and nondestructive nature of optical imaging, along with its high resolution and ability to provide both structural and functional information made these technologies powerful tools for research and clinical applications. Future developments in optical imaging promise to further expand its capabilities and impact across various disciplines.

References

[1] S. Muñoz-Fernández and E. Martín-Mola: "Uveitis", *Best Practice and Research Clinical Rheumatology* **20**(3), 487–505 (2006). Spondyloarthropathies. DOI: 10.1016/j.berh.2006.03.008.

[2] D. A. Jabs et al.: "Standardization of Uveitis Nomenclature for Reporting Clinical Data. Results of the First International Workshop", *American Journal of Ophthalmology* **140**(3), 509–516 (2005). DOI: 10.1016/j.ajo.2005.03.057.

[3] V. Llorenc et al.: "Swept source optical coherence tomography objective composite activity score for uveitis", *Acta Ophthalmologica* **99**(7), 756–764 (2021). DOI: 10.1111/aos.14739.

[4] A. Invernizzi et al.: "Objective Quantification of Anterior Chamber Inflammation: Measuring Cells and Flare by Anterior Segment Optical Coherence Tomography", *Ophthalmology* **124**(11), 1670–1677 (2017). DOI: 10.1016/j.ophtha.2017.05.013.

[5] E. Baghdasaryan et al.: "Analysis of ocular inflammation in anterior chamber involving uveitis using swept source anterior segment OCT", *International Ophthalmology* **39**(8), 1793–1801 (2019). DOI: 10.1007/s10792-018-1005-0.

[6] V. Mieites et al.: "Conteo automatizado de agregados celulares en procesos de uveitis mediante tomografia de coherencia óptica.", in: *XIII Reunion Nacional de Óptica*. SEDOPTICA, 2021 47.

[7] N. Otsu: "A Threshold Selection Method from Gray-Level Histograms", *IEEE Transactions on Systems, Man, and Cybernetics* **9**(1), 62–66 (1979). DOI: 10.1109/TSMC.1979.4310076.

[8] M. Lebrun: "An Analysis and Implementation of the BM3D Image Denoising Method", *Image Processing On Line* **2**, 175–213 (2012). DOI: 10.5201/ipol.2012.l-bm3d.

[9] P. J. Kennelly: "Terrain maps displaying hill-shading with curvature", *Geomorphology* **102**(3), 567–577 (2008). DOI: 10.1016/j.geomorph.2008.05.046.

[10] R. Lakemond, C. Fookes, and S. Sridharan: "Affine Adaptation of Local Image Features Using the Hessian Matrix", in: *2009 Sixth IEEE International Conference on Advanced Video and Signal Based Surveillance*. 2009 496–501. DOI: 10.1109/AVSS.2009.8.

[11] L. Breiman: "Random Forests", *Machine Learning* **45**(1), 5–32 (2001). DOI: 10.1023/A:1010933404324.

[12] I. H. Malitson: "Interspecimen Comparison of the Refractive Index of Fused Silica", *The Journal of the Optical Society of America* **55**(10), 1205–1209 (1965). DOI: 10.1364/JOSA.55.001205.

[13] C. Z. Tan: "Determination of refractive index of silica glass for infrared wavelengths by IR spectroscopy", *Journal of Non-Crystalline Solids* **223**(1), 158–163 (1998). DOI: 10.1016/S0022-3093(97)00438-9.

[14] M. R. Querry: "Optical constants", Accesed 24 March 2025. 1985. URL: https://apps.dtic.mil/sti/citations/ADA158623.

[15] N. Ghosh: "Tissue polarimetry: concepts, challenges, applications, and outlook", *Journal of Biomedical Optics* **16**(11), 110801 (2011). DOI: 10.1117/1.3652896.

[16] J. Qi, C. He, and D. S. Elson: "Real time complete Stokes polarimetric imager based on a linear polarizer array camera for tissue polarimetric imaging", *Biomedical Optics Express* **8**(11), 4933 (2017). DOI: 10.1364/boe.8.004933.

[17] P. Schucht et al.: "Visualization of White Matter Fiber Tracts of Brain Tissue Sections with Wide-Field Imaging Mueller Polarimetry", *IEEE Transactions on Medical Imaging* **39**(12), 4376–4382 (2020). DOI: 10.1109/TMI.2020.3018439.

[18] O. Rodríguez-Núñez et al.: "Polarimetric visualization of healthy brain fiber tracts under adverse conditions: ex vivo studies", *Biomedical Optics Express* **12**(10), 6674 (2021). DOI: 10.1364/boe.439754.

[19] L. Felger et al.: "Robustness of the wide-field imaging Mueller polarimetry for brain tissue differentiation and white matter fiber tract identification in a surgery-like environment: an ex vivo study", *Biomedical Optics Express* **14**(5), 2400 (2023). DOI: 10.1364/boe.486438.

[20] D. Ivanov et al.: "Impact of corpus callosum fiber tract crossing on polarimetric images of human brain histological sections: ex vivo studies in transmission configuration", *Journal of Biomedical Optics* **28**(10) (2023). DOI: 10.1117/1.jbo.28.10.102908.

[21] M. Borovkova et al.: "Evaluating β-amyloidosis progression in Alzheimer's disease with Mueller polarimetry", *Biomedical Optics Express* **11**(8), 4509 (2020). DOI: 10.1364/boe.396294.

[22] B. Liu et al.: "Mueller polarimetric imaging for characterizing the collagen microstructures of breast cancer tissues in different genotypes", *Optics Communications* **433**, 60–67 (2019). DOI: 10.1016/j.optcom.2018.09.037.

[23] V. Mieites Alonso et al.: "PoLambRimetry: a multispectral polarimetric atlas of lamb brain", *Journal of Biomedical Optics* **29**(09) (2024). DOI: 10.1117/1.JBO.29.9.096002.

[24] V. Mieites et al.: "Multispectral Mueller matrix imaging: a potential tool to visualize white matter tracts", in: *Tissue Optics and Photonics III*. SPIE-Intl Soc Optical Eng, 2024 25. DOI: 10.1117/12.3017499.

[25] B. Nitzsche et al.: "A stereotaxic, population-averaged T1w ovine brain atlas including cerebral morphology and tissue volumes", *Frontiers in neuroanatomy* **9**, 69 (2015). DOI: 10.3389/fnana.2015.00069.

[26] J. A. Johnson et al.: "The sheep brain atlas", Accesed 24 March 2025. URL: https://brains.anatomy.msu.edu/brains/sheep/index.html.

[27] E. Compain, S. Poirier, and B. Drevillon: "General and self-consistent method for the calibration of polarization modulators, polarimeters, and Mueller-matrix ellipsometers", *Applied Optics* **38**(16), 3490–3502 (1999). DOI: 10.1364/AO.38.003490.

[28] J. Gil and R. Ossikovski: "Polarized Light and the Mueller Matrix Approach", Series in Optics and Optoelectronics. CRC Press, 2017. ISBN: 9781482251562.

[29] J. J. Gil: "Characteristic properties of Mueller matrices", *Journal of the Optical Society of America* **17**(2), 328–334 (2000). DOI: 10.1364/JOSAA.17.000328.

[30] I. San José and J. J. Gil: "Characterization of passivity in Mueller matrices", *Journal of the Optical Society of America A* **37**(2), 199 (2020). DOI: 10.1364/JOSAA.37.000199.

[31] I. San José and J. J. Gil: "Invariant indices of polarimetric purity: Generalized indices of purity for n×n covariance matrices", *Optics Communications* **284**(1), 38–47 (2011). DOI: 10.1016/j.optcom.2010.08.077.

[32] J. J. Gil: "Structure of polarimetric purity of a Mueller matrix and sources of depolarization", *Optics Communications* **368**, 165–173 (2016). DOI: 10.1016/j.optcom.2016.01.092.

[33] P. Pudil, J. Novovičová, and J. Kittler: "Floating search methods in feature selection", *Pattern Recognition Letters* **15**(11), 1119–1125 (1994). DOI: 10.1016/0167-8655(94)90127-9.

[34] A. Jain and D. Zongker: "Feature selection: evaluation, application, and small sample performance", *IEEE Transactions on Pattern Analysis and Machine Intelligence* **19**(2), 153–158 (1997). DOI: 10.1109/34.574797.

[35] Y. Peng, Z. Wu, and J. Jiang: "A novel feature selection approach for biomedical data classification", *Journal of Biomedical Informatics* **43**(1), 15–23 (2010). DOI: 10.1016/j.jbi.2009.07.008.

[36] P. B. Garcia-Allende et al.: "Automated identification of tumor microscopic morphology based on macroscopically measured scatter signatures", *Journal of Biomedical Optics* **14**(3), 034034 (2009). DOI: 10.1117/1.3155512.

[37] P. B. García-Allende et al.: "Spectral processing technique based on feature selection and artificial neural networks for arc-welding quality monitoring", *NDT & E International* **42**(1), 56–63 (2009). DOI: 10.1016/j.ndteint.2008.07.004.

[38] A. M. Laughney et al.: "System analysis of spatial frequency domain imaging for quantitative mapping of surgically resected breast tissues", *Journal of Biomedical Optics* **18**(3), 036012 (2013). DOI: 10.1117/1.jbo.18.3.036012.

[39] R. Gros et al.: "Effects of formalin fixation on polarimetric properties of brain tissue: fresh or fixed?", *Neurophotonics* **10**(02) (2023). DOI: 10.1117/1.nph.10.2.025009.

[40] J. Bonaventura et al.: "Backscattering Mueller Matrix polarimetry on whole brain specimens shows promise for minimally invasive mapping of microstructural orientation features", *Frontiers in Photonics* **3**, 01–11 (2022). DOI: 10.3389/fphot.2022.1034739.

[41] D. Maestro et al.: "Cardiac fibrosis inhibitor CTPR390 prevents structural and morphological changes in collagen and fibroblasts of engineered human connective tissue", Preprint. 2025. DOI: 10.1101/2025.01.15.633162.

[42] Y.-C. C. and: "A tutorial on kernel density estimation and recent advances", *Biostatistics & Epidemiology* **1**(1), 161–187 (2017). DOI: 10.1080/24709360.2017.1396742.

Part VI

Final remarks

Final remarks

This doctoral thesis aimed to answer one specific question: can optical imaging methodologies aid in the diagnosis of muscular dystrophies? The concept of "aid in diagnosis" is broad, and in the context of this thesis, it ranges from enhancing visualization of samples to optical imaging providing optical biomarkers of disease. The main drawback that all these technologies have in common is their reduced penetration depth inside tissues, which makes them difficult to implement in vivo for the follow-up of patients, thus limiting the existing research of optical methods in dystrophy diagnosis. However, medicine goes beyond bedside practices. Whether it is through different situations where the tissue of a patient might be exposed (i.e., surgery) or through animal models that are being developed to test the effectiveness of various drugs, optical technologies can aid in this field by providing additional or alternative information that, in many cases, can be obtained in real-time without interfering with the gold-standard analysis often performed on dystrophic tissues. In such cases, optical imaging can be introduced in the laboratory pipelines to provide an estimate of which samples should be analyzed first, to indicate which are more uniform, or to guide region-of-interest sampling for methodologies that are not able to analyze bulk tissue in the way that optical imaging is able to.

Answering this research question was not straightforward, and involved evaluating the samples from different points of view with as many technologies as possible in a first-of-its-kind comprehensive analysis of the optical properties of dystrophic mice samples. Specifically, we focused on the use of optical coherence tomography (OCT) and polarization-sensitive OCT (PS-OCT) to evaluate the structural changes of the samples at the micrometric scale. We accompanied those results with hyperspectral imaging (HSI) and spatial frequency domain imaging (SFDI) to infer the chemical and structural changes that might be taking place in the samples. Finally, we used multispectral Mueller imaging (MMI) to deduce if the polarimetric properties of the samples can be used to detect areas of non-damaged muscle tissue. To conclude, we also evaluated whether the combination of optical properties can provide a better disease estimate than the individual information provided by each system separately.

The following sections include the main findings provided by each imaging system, as well as the future research lines associated with each of them.

Intensity and polarization-sensitive OCT OCT and PS-OCT analysis revealed that birefringence, a measure of tissue anisotropy derived from the phase delay experienced by light as it travels through the muscle fibers, is a more sensitive marker of muscular dystrophy-related changes than attenuation, which primarily reflects light scattering. This difference in sensitivity likely stems from the disruption of muscle fiber structure characteristic of muscular dystrophy. While this disruption significantly affects the organization and anisotropy of the tissue, leading to alterations in birefringence, it may not substantially alter the overall

light scattering properties, as measured by attenuation. This finding establishes birefringence derived from PS-OCT as a promising optical property for assessing muscle health and disease progression in a non-invasive and label-free manner.

Future work should focus on longitudinal studies to track birefringence changes over time in muscular dystrophy samples, correlating these changes with disease progression and sample metadata (i.e., age, sex...). Comparative studies across different types and stages of muscular dystrophy are needed to determine the specificity and sensitivity of birefringence as a diagnostic marker. The comparison of the observed birefringence alterations with histological analysis is crucial to assess the validity of this marker, considering not only a small region of the samples but the whole sample, if possible. Finally, validation in larger cohorts and potentially in human samples or in vivo studies will be crucial to confirm the clinical utility of PS-OCT-derived birefringence.

Hyperspectral and spatial frequency domain imaging HSI analysis revealed distinct spectral characteristics in the visible-near infrared (VISNIR) and short-wave infrared (SWIR) ranges, with VISNIR spectra highlighting hemoglobin/myoglobin absorption and SWIR spectra dominated by water and fat absorption. While challenges were encountered in measuring thin muscle samples due to light penetration to the underlying substrate, the analysis of the data allowed for the estimation of chromophore content and the identification of potential fatty inclusions in dystrophic muscle tissue. The use of albedo, or average reflectance, was deemed a suitable metric for further analysis in this context, as it was able to identify control samples as containing more hemoglobin than the dystrophic ones, consistent with the higher fat content on the latter. SFDI measurements further corroborated the findings of HSI, particularly in highlighting fatty regions as less absorbing and more scattering than surrounding tissue. Analysis of absorption and scattering properties revealed trends suggestive of fat accumulation in dystrophic samples. Notably, SFDI-derived albedo measurements showed a clearer separation between healthy and dystrophic samples than HSI alone, with dystrophic samples exhibiting higher albedo, indicative of greater overall reflectivity and further supporting the hypothesis of increased fat content.

Future research should refine HSI measurement techniques to analyze thin muscle samples better and avoid substrate interference. Validating the initial findings by studying a larger group of healthy and dystrophic muscle samples is essential. To confirm the accuracy of HSI and SFDI, as with OCT-derived data, their results need to be compared with traditional histological analysis. In this case, the direct application of these techniques is not as straightforward as for OCT, as more validation is needed before moving on to human samples or in vivo experiments.

Multispectral Mueller matrix imaging MMI analysis of mouse leg tissue samples showed that depolarization, a measure of the scattering-induced loss of polarization information, is a key parameter for distinguishing healthy muscle from frozen-damaged muscle and fat. The analysis of polarimetric purity indices supported this finding, as did the application of polar decomposition techniques and the results of

supervised classification using K-Nearest Neighbors. Notably, a simplified classifier using only the second and third multispectral elements of the diagonals of the matrices achieved comparable accuracy to the full Mueller matrix analysis, suggesting the potential for partial Mueller polarimetry in muscle tissue characterization. Additionally, applying a supervised autoencoder to detect healthy tissue further confirmed the importance of depolarization for tissue classification and enabled efficient feature extraction and data compression, facilitating the identification of healthy muscle regions within a complex tissue environment.

The next steps using MMI should explore the role of depolarization in identifying different tissue types, particularly healthy and dystrophic muscle, and fat. Further investigation into polarimetric purity indices and polar decomposition techniques will help solidify the findings discussed in this thesis. Given the comparable accuracy of a simplified classifier using only specific elements of the Mueller matrix, exploring the potential of partial Mueller polarimetry for muscle tissue characterization is crucial for performing fast in vivo measurements of the samples and simplifying the system's configuration.

Multimodal data analysis Combining data from different optical imaging modalities, including OCT, PS-OCT, HSI, and SFDI, offered a richer, more comprehensive analysis of muscle tissue. A visualization approach using a color-mapping technique effectively highlighted key differences between healthy and dystrophic tissues, particularly in visualizing variations in birefringence and tissue organization. Statistical analysis demonstrated that while individual optical properties showed some separability, combining them through dimensionality reduction techniques led to slightly improved discrimination. Classification using a fully connected feed-forward neural network, however, revealed limitations in leveraging the combined dataset due to high inter-sample variability. This suggests that the random sampling approach used to combine optical features from different systems may have inadvertently introduced noise by matching disparate regions within the same sample through the various optical properties. Still, treating each imaging modality as an independent source of information with its own set of optical features yielded equal or superior performance compared to combining all features into a single dataset. This suggests that a more targeted approach, where each modality contributes its unique strengths to the analysis, may be more effective for classifying dystrophic samples. This finding opens exciting possibilities for developing specialized devices tailored to specific optical modalities, potentially leading to more accurate and targeted diagnostic tools. Furthermore, while the combined dataset may not be ideal for classification in its current form, it has enabled a comprehensive discussion of the data, considering both the chemical and structural aspects of the samples, which could inform future research directions and analytical approaches.

The next actions required for an improved multimodal analysis involve developing a co-register system so that the same samples can be measured with multiple devices while keeping the labeling consistent between measurements. This way, there will be no need for random sampling, which would allow for a real combination of all optical systems and a better interpretation of the results from a physicochemical standpoint.

Additional contributions The versatility of the optical imaging techniques employed in this research is underscored by their successful application across diverse fields, including ophthalmology, archaeology, neuroscience, and bioengineering. These techniques have enabled advancements such as automated cell counting in uveitis, non-destructive analysis of archaeological artifacts, detailed brain tissue characterization, and the evaluation of anti-fibrotic treatments in engineered cardiac tissue. The non-invasive and high-resolution nature of these optical methods, coupled with their ability to provide both structural and functional information, highlights their broad potential across various disciplines.

This book has demonstrated the significant potential of optical imaging techniques in advancing our understanding and assessment of muscular dystrophy. Improvements need to be considered to fully optimize these technologies for the task of identifying muscular dystrophies, mainly through an increase in the number of samples used to derive the optical parameters of each category and avoid the effect of inter-sample variations. Still, the ability to probe both structural and chemical properties of muscle tissue non-invasively offers valuable insights into disease progression and treatment response and can be used quantitatively to complement conventional diagnostic and analytic methods that can not be used as regularly due to their invasive nature.

While this research has focused primarily on ex vivo analysis, future efforts should explore the translation of these techniques to in vivo applications, potentially through the development of minimally invasive probes or endoscopic imaging systems, or continuing with in vivo animal models where light penetration is not as big of an issue. In their current state, all the optical methods presented in this thesis can and have already been used in surgical environments with minimal adaptations, but their use in the clinics remains a challenge. Specifically, out of the four technologies explored, OCT is the most straightforward one to be adapted to in vivo applications by using needle probes to reach the muscle without the need for biopsies.

Additionally, expanding the investigation to a wider range of muscular dystrophy models and incorporating longitudinal studies will be crucial for establishing the clinical utility of these optical biomarkers. Once validated, the datasets and the algorithms created during this thesis will be stored in open-access repositories. Ultimately, the continued development and refinement of optical imaging technologies hold great promise for improving the diagnosis and monitoring of muscular dystrophies, paving the way for better patient outcomes.

Resumen Global en Castellano

Resumen global en castellano

En este capítulo se incluye una visión general de los temas y contribuciones discutidos a lo largo de esta tesis. La distribución de este capítulo es similar al seguido en el documento principal, comenzando por una breve introducción cuyo enfoque reside en establecer la motivación de este trabajo y los objetivos principales de esta tesis. A continuación, se incluye una breve explicación de las técnicas de imagen aplicadas durante este trabajo, así como los resultados principales obtenidos del uso de cada técnica de forma individual, pero también de su combinación. Finalmente, se incluye una sección con trabajos adicionales realizados en función de métodos derivados del objetivo principal de la tesis, seguido de una breve explicación futuras líneas de trabajo.

Introducción y motivación del trabajo

Las distrofias musculares (MD) son un grupo de enfermedades genéticas hereditarias que causan debilidad y degeneración muscular progresivas, impactando significativamente las capacidades físicas y la calidad de vida [1]. Estas enfermedades, aunque raras (con una prevalencia, por ejemplo, de 6 en 100.000 hombres para la más común [1]), afectan a individuos, a menudo con un inicio temprano (5-30 años), y frecuentemente involucran complicaciones cardíacas [2]. Más allá de los desafíos físicos, las distrofias musculares conllevan cargas emocionales, sociales y económicas, incluyendo la pérdida de independencia, el aislamiento social y un coste médico elevado. El diagnóstico temprano es fundamental para maximizar los beneficios de los tratamientos disponibles pero los métodos de diagnóstico actuales, como las biopsias musculares, son invasivos y tienen limitaciones. Esto hace necesaria la creación de herramientas de diagnóstico no invasivas y accesibles.

Esta tesis doctoral explora el potencial de las tecnologías de imagen óptica para abordar esta necesidad. Centrándose en un conjunto de datos único de tejido muscular esquelético *ex vivo* de ratones (tanto sanos como con distrofia), esta tesis evalúa cuatro técnicas de imagen óptica específicas: Tomografía de Coherencia Óptica en Intensidad (OCT) y Sensible a la Polarización (PS-OCT), Imagen Hiperespectral (HSI) en los rangos espectrales del visible/infrarrojo cercano (VISNIR) e infrarrojo de onda corta (SWIR), Imagen en el Dominio de las Frecuencias Espaciales (SFDI) e Imagen de Mueller Multiespectral (MMI). Cada técnica ofrece información única sobre la estructura, composición y función del tejido muscular. El objetivo principal de esta tesis es evaluar la viabilidad y eficacia de estas técnicas, individualmente y en su combinación, para caracterizar la patología muscular en la distrofia muscular.

Al estudiar y combinar estas técnicas, se pretende desarrollar un enfoque integral para evaluar la salud muscular, visualizar los cambios estructurales y de composición, y extraer parámetros ópticos como posibles biomarcadores de la enfermedad. Además, se presenta una metodología para integrar los datos de diferentes técnicas, creando visualizaciones

combinadas y realizando análisis estadísticos para evaluar las correlaciones entre los parámetros. Finalmente, se evalúan técnicas de aprendizaje automático para mejorar las capacidades de diagnóstico.

Técnicas de imagen óptica y métodos de análisis

Tomografía de coherencia óptica (OCT)

OCT es una técnica de imagen basada en fenómenos de baja coherencia para reconstruir la estructura interna de una muestra. Esta técnica está basada en los principios de interferometría, donde la combinación de dos ondas de luz puede amplificar o disminuir la señal combinada en base a su diferencia de fase. El elemento central de un sistema OCT es, típicamente, un interferómetro de Michelson (Fig. 11.15), el cual divide un haz de luz en dos caminos donde uno se dirige hacia la muestra y el otro a un brazo de referencia de longitud fija. A través de analizar el patrón de interferencia de los dos haces cuando se recombinan se puede obtener una medida de la estructura interna de las muestras.

La propiedad óptica principal obtenida con OCT es el coeficiente de atenuación (μ_t), el cual representa el efecto combinado de la absorción de la luz (μ_a) y *scattering*[5] (μ_s) de una muestra. Las diferencias en coeficiente de atenuación permiten identificar variaciones en la estructura interna de las muestras, las cuales pueden ser indicadores de distrofia. En esta tesis se han considerado varios métodos para calcular el coeficiente de atenuación, incluyendo:

1. La ley de Beer-Lambert [4-6]: Modela la atenuación de la luz al atravesar un medio turbio como una función decayente exponencial en términos de la distancia recorrida en el medio (profundidad de penetración), z.
2. La función de dispersión de punto (PSF): Considera el efecto de la óptica incluida en el equipo OCT en los cambios de intensidad medidos.
3. Método del material de referencia (*phantom*): Utiliza una muestra de referencia conocida para calibrar las medidas a través de una versión modificada de la ley de Beer-Lambert. ([7])
4. Atenuación localizada: Calcula la atenuación en cada punto de la muestra a través de considerar incrementos locales.

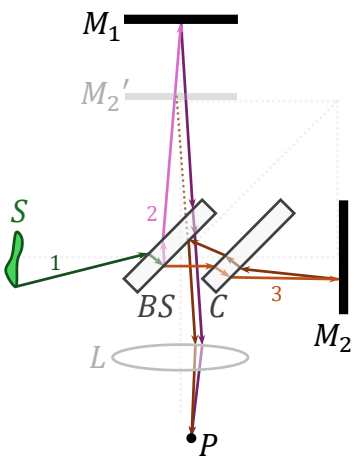

Figura 11.15: Esquema de un interferómetro de Michelson adaptado de [3]. Una fuente de luz (S) produce rayos (1) que llegan a un divisor de haz (BS). Parte de la intensidad (2) se dirige hacia un espejo de referencia (M_1). La otra parte atraviesa una placa de compensación C, que cuenta con el mismo grosor e índice de refracción que el divisor de haz, antes de alcanzar un segundo espejo M_2.Ambos haces se recombinan en la sección trasera del divisor y viajan de forma paralela hasta alcanzar una lente de colimación (L), la cual focaliza el patrón de interferencia en el plano que contiene P y que es paralelo a M_1. M_2' representa la imagen de M_2 duplicada en torno la cara trasera del divisor de haz.

[5] El término *scattering* describe el redireccionamiento de la luz cuando ésta interacciona con las partículas de un medio. En este capítulo se utiliza el término en inglés para evitar confusión con otros términos similares.

OCT sensible a la polarización (PS-OCT)

La modalidad alternativa de OCT sensible a la polarización (PS-OCT) utiliza una versión modificada del interferómetro de Michelson al cual se le introducen láminas retardadoras en cada brazo para seleccionar el estado de polarización con el que se ilumina la muestra. Eso permite no solo capturar la intensidad de scattering recibida, si no también la fase de la onda medida.

El sistema PS-OCT reconstruye la reflectancia compleja a partir de los patrones de interferencia detectados. Esas reflectancias se utilizan para calcular los parámetros del vector de Stokes, los cuales proporcionan información acerca del estado de polarización de la luz.

A partir de los vectores de Stokes se pueden obtener ciertos parámetros de polarización relevantes, como la orientación del eje óptico o la uniformidad del grado de polarización. Sin embargo, el más importante y utilizado en esta tesis es la birrefringencia de la muestra. La birrefringencia mide la diferencia entre los índices de refracción de una muestra anisotrópica a lo largo de sus dos ejes. El método descrito por Chin *et al.* [8] permite calcular la birrefringencia en base al cambio de fase del vector de Stokes con la profundidad de penetración de la luz en la muestra.Una birrefringencia alta indica un alto grado de anisotropía entre los dos índices de refracción, mientras que una muestra isótropa no presenta birrefringencia. De esta manera se pretende separar los músculos sanos, altamente anisotrópicos, de los músculos dañados por distrofia.

Imagen hiperespectral (HSI)

Los sistemas de imagen hiperespectral (HSI) capturan la luz emitida por una fuente después de atravesar un medio y reflejarse en él de forma difusa. El contenido espectral de la fuente de luz cambia en base a las propiedades de la muestra.

La reflectancia difusa se produce cuando la luz entra la muestra, sufre scattering en su interior y sale de la muestra para ser capturada por el sensor. La cantidad de luz recogida está relacionada con la absorción de cada componente de la muestra. Una forma de interpretar el funcionamiento de un sistema HSI es considerarlo como una cámara de color avanzada que, en lugar de tres canales de color, cuenta con cientos de ellos. Fundamentalmente, consisten en una lente y una cámara acoplados a un espectrógrafo, el cual descompone la luz capturada en sus componentes espectrales.

En la práctica, la reflectancia medida necesita ser corregida debido a factores como el espectro no uniforme de la fuente de luz, la introducción de fuentes de luz no controladas en el sistema (reflexiones) o el ruido del detector. Esto involucra utilizar una muestra de referencia (Spectralon) y realizar medidas de corrección de ruido.

HSI se puede utilizar para estimar las fracciones de volumen de diferentes componentes químicos a través de modelos físicos que consideran la absorción y scattering de las muestras bajo ciertas suposiciones. La mayoría de modelos se basan en obtener la absorción como la suma de absorciones de componentes individuales. Estos componentes, denominados cromóforos, se obtienen a partir de medidas puras de los mismos. Algunos cromóforos típicos de tejidos biológicos son la hemoglobina, mioglobina, lípidos, elastina, colágeno o agua, entre otros (Fig. 11.16). Utilizando HSI se pretende relacionar el contenido de dichos componentes con marcadores clínicos de distrofia como la cantidad de grasa o músculo en las muestras.

En este libro se comparan varios modelos que consideran los efectos del scattering de formas diferentes:

1. Modelo de Kubelka-Munk [9]: Estima el scattering asumiendo que la muestra se puede tratar como un medio semi-infinito. Originalmente, este modelo se definió para estimar la absorción y scattering

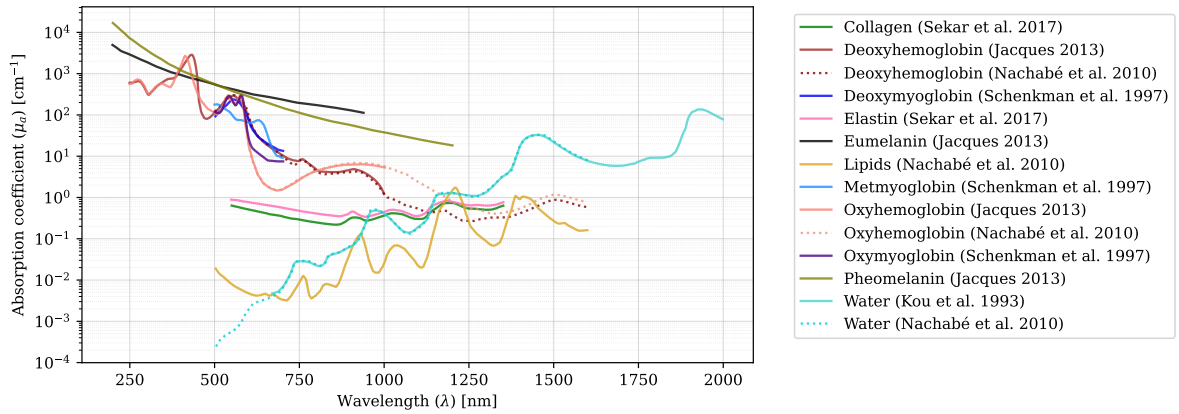

Figura 11.16: Coeficientes de atenuación (μ_a [cm^{-1}]) de los cromóforos de referencia más comunes en función de la longitud de onda (λ [nm]). Los datos de Schenkman *et al.* [12], originalmente definidos en función de la densidad óptica, han sido transformados a atenuación por medio de la comparación del camino óptico para hacer que los picos coincidan con los defindos por Jacques [13]. Datos adaptados de [12-17].

de pigmentos en polvo, las cuales cuentan con un alto coeficiente de scattering.

2. Aproximación empírica de Jacques [10]: Considera el efecto de absorción y scattering a través de una aproximación empírica del comportamiento observado en simulaciones de Monte Carlo.
3. Simulaciones de Monte Carlo: Se deriva la relación entre absorción y scattering a partir de una tabla obtenida de múltiples simulaciones de Monte Carlo.
4. Modelo de Krishnaswamy *et al.* [11]: Estima la influencia del scattering como una relación decreciente exponencial con la longitud de onda.
5. Modelo de Jacques [10]: Similar al anterior, pero separa las contribuciones de scattering de Mie y Rayleigh.

Imagen en el dominio de las frecuencias espaciales (SFDI)

La imagen en el dominio de las frecuencias espaciales (SFDI) es una técnica óptica que, al contrario que HSI o OCT, puede desacoplar los efectos de absorción y scattering de una muestra. Esto se consigue a través de controlar el patrón de iluminación aplicado a las medidas, específicamente a través de la proyección de patrones periódicos (en este caso, bandas) de diferentes frecuencias.

De esta manera, SFDI se basa en analizar la función de transferencia de modulación (MTF), la cual describe cómo un medio afecta a la modulación de una fuente de luz en función de su frecuencia espacial (Fig. 11.17). La reflectancia difusa medida a las distintas frecuencias se relaciona con la absorción y el scattering, de forma independiente, a través de modelos físicos o aproximaciones.

La ecuación de difusión se utiliza para modelar la propagación de la luz en el interior de la muestra desacoplando las contribuciones de absorción y scattering. Sin embargo, este modelo solamente es aplicable bajo ciertas condiciones. Específicamente, la ecuación de difusión se utiliza cuando el scattering es mucho mayor que la absorción ($\mu_s' \gg \mu_a$). Fuera de ese rango deben usarse métodos alternativos como la obtención de las

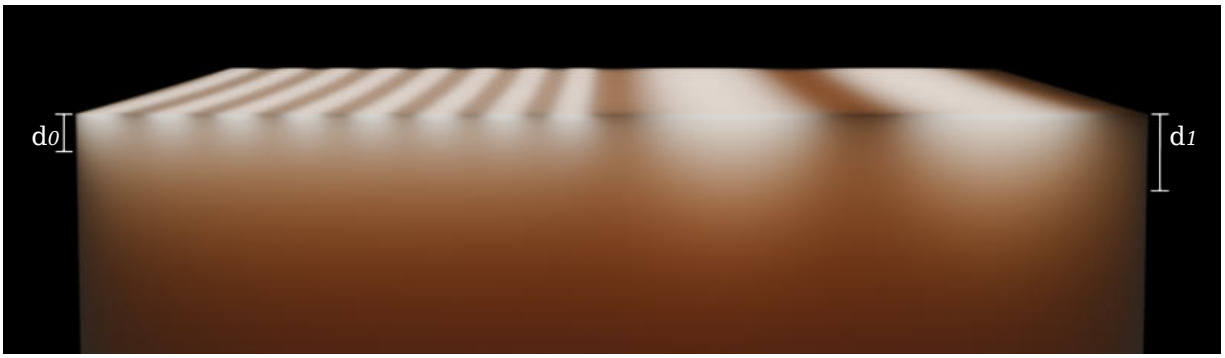

Figura 11.17: Simulación de la penetración de profundidad máxima de la porción modulada de una fuente de luz en función de la frecuencia espacial. A la izquierda, una frecuencia espacial alta penetra hasta una profundidad d_0, mientras que la frecuencia inferior mostrada a la derecha alcanza una profundidad d_1, mucho mayor que d_0. Imagen adaptada de [18].

propiedades ópticas a través de simulaciones de Monte Carlo [19]. En este caso se ha optado por la segunda opción dado que es la primera vez que se analizan las muestras consideradas en esta tesis con SFDI. De esta manera, los resultados obtenidos serán independientes de si se cumple la aproximación de difusión o no.

La obtención experimental de la MTF se obtiene al capturar múltiples imágenes de reflectancia difusa utilizando varias frecuencias y fases espaciales. Al igual que en HSI, en SFDI es necesario compensar los efectos de la fuente de la iluminación y del fondo de ruido para desacoplarlos de aquellos procedentes de la muestra. Particularmente, la forma no regular de la muestra deforma los patrones espaciales proyectados. Para compensar este efecto se realiza una medida de perfilometría de la muestra que permite eliminar la influencia de la deformación y obtener de forma precisa las propiedades de absorción y scattering de la muestra. En este caso, el equipo SFDI utilizado comparte dispositivo con el equipo HSI, lo que permite evaluar la dependencia de las propiedades ópticas con la longitud de onda utilizada.

Imagen de Mueller multiespectral (MMI)

La imagen de matriz de Mueller (MMI) es una técnica óptica utilizada para caracterizar las propiedades de polarización de una muestra por medio de cómo ésta altera el estado de polarización de la luz incidente. Con MMI se puede obtener información sobre efectos como la birrefringencia, la diatenuación o la despolarización de la muestra.

Los equipos MMI consisten en dos componentes principales:

- Generador de estados de polarización (PSG): Genera un conjunto de estados de luz polarizada controlados para iluminar la muestra. Está compuesto por la fuente de iluminación y la óptica de polarización necesaria.
- Analizador de estados de polarización (PSA): Mide la polarización del estado de la luz después de interaccionar con la muestra. Contiene óptica de polarización adicional y el detector.

La matriz de Mueller, que describe las propiedades de polarización de la muestra, se obtiene tras analizar cómo la muestra transforma los estados de polarización generados en los detectados. Dado que el PSA y el PSG

cuentan con sus propias matrices conocidas, la matriz de la muestra se desacopla de las del sistema por medio de cálculos matriciales.

En esta tesis se han desarrollado dos versiones de un sistema de imagen de Mueller. La primera versión (MMI v1.0) utiliza una fuente de iluminación LED con una rueda de filtros para seleccionar distintas longitudes de onda. El PSG contiene un polarizador fijo y una lámina retardadora orientable para generar los estados de polarización. El PSA está formado por una cámara polarimétrica y una lámina retardadora que se introduce o no en el camino óptico en las distintas medidas. La segunda versión (MMI v2.0) consiste en una mejora del anterior a través de modificaciones del PSG. La fuente de LED blanca y la rueda de filtros se sustituyen por una fuente de múltiples LED sintonizable. Además, el polarizador ha sido introducido en una montura orientable para mayor flexibilidad a la hora de generar los estados de polarización.

La calibración de los sistemas MMI es crucial para obtener medidas precias. En esta tesis se utiliza el método de calibración de los valores propios (ECM) para determinar las matrices del PSA y PSG, las cuales son utilizadas a continuación para extraer la matriz de Mueller de la muestra a partir de los datos medidos [20]. Este proceso involucra la medida de muestras conocidas (aire, polarizadores, láminas retardadoras) y la comparación de las medidas experimentales con los valores teóricos de cada una de ellas. Otro factor a considerar en el diseño de estos equipos es el número de condicionamiento de las matrices del PSG y PSA. Este número se utiliza como un indicador de la sensibilidad de dichas matrices al ruido, y su origen reside en el espacio que ocupan los estados generados y medidos dentro de la esfera de Poincaré. La esfera de Poincaré es una representación tridimensional de los estados de polarización posibles y, con cuatro estados, el número de condicionamiento ideal es $\sqrt{3}$, el cual se corresponde con el tetraedro regular que maximiza el espacio que ocupa en la esfera.

Una vez obtenida la matriz de Mueller se aplicaron varios métodos de descomposición matricial para extraer propiedades ópticas específicas de la muestras, como la despolarización, la diatenuación y el retardo. Al igual que con PS-OCT, estas métricas se relacionan con el nivel de organización estructural de los tejidos, pero también con sus propiedades de scattering, lo que puede ayudar a identificar zonas de fibras musculares sanas o dañadas tanto a través de organizaciones irregulares o cambios de tamaños de centros de scattering.

Resultados principales

Comportamiento óptico de las muestras con OCT y PS-OCT

El capítulo 6 explora la aplicación de OCT para la caracterización de muestras de tejido muscular obtenidas de un modelo animal en ratón con deficiencia de α-sarcoglicano. Esta deficiencia se relaciona con ciertas modalidades de distrofia muscular como la distrofia muscular de cadera (LGMD) o las miopatías miofribilares (MFM). Se analizaron dos conjuntos de datos[6], MD1 y MD2, los cuales contenían un rango de muestras de

[6] En adelante, *datasets*

control (WT) y distróficas (KO). Los primeros análisis se centraron en la intensidad derivada de medidas OCT, la cual demostró un decaimiento no homogéneo en el interior de las muestras, indicador de variaciones estructurales en cada muestra pero también entre ellas.

El método del material de referencia se utilizó para generar mapas bidimensionales de atenuación (μ_t), centrándonos en el análisis en la región de scattering simple, que se aproxima a las 250 μm más superficiales de los tejidos biológicos (Fig. 11.18, b). Los mapas de atenuación mostraron alteraciones en la densidad de los tejidos para cada muestra con un fuerte solapamiento de las distribuciones estadísticas de atenuación entre muestras sanas y distróficas para el dataset MD1. A pesar de que se ha obtenido una mejor separación en el dataset MD2, ningún dataset ha proporcionado una separación clara entre categorías clínicas por medio del análisis de atenuación de muestras volumétricas. Una comparación con los valores obtenidos por otros grupos para el umbral de atenuación entre tejido sano y necrótico en un modelo animal de distrofia muscular de Duchenne sugiere que (1) o los modelos con déficit de α-sarcoglicano muestran menos necrosis que los de Duchenne, (2) o que el análisis de todo el volumen de las muestras, en lugar de regiones específicas, introducen una variabilidad que difumina el umbral de atenuación entre los dos tipos de tejido.

Los mapas bidimensionales de atenuación señalaron zonas de variación interna, las cuales fueron posteriormente evaluadas a través de la visualización de secciones transversales (Fig. 11.18, c) y de la aplicación del modelo de atenuación localizada (Fig. 11.18, d). Los dos modelos mostraron discrepancias: Mientras que el método del material de referencia mostraba atenuación más baja en zonas densas, el modelo localizado mostraba la tendencia opuesta. Esta diferencia surge de la forma de calcular la atenuación específica de cada método: mientras que el método del material de referencia promedia la respuesta de los tejidos en un rango de profundidad mayor, el modelo localizado muestra valores pixel a pixel. A pesar de ello, la información combinada obtenida por medios modelos proporcionó una comprensión mayor que utilizando solamente uno. Específicamente el método del material de referencia identificó zonas de interés con la muestra "vista desde arriba" que facilitó la selección de cortes transversales específicos que evaluar en cada muestra, ayudando

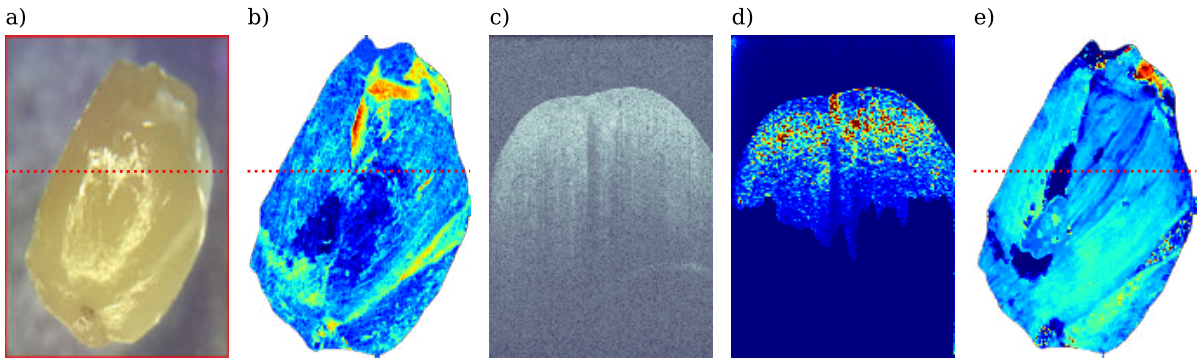

Figura 11.18: (a) Imagen en color de referencia, (b) mapa bidimensional de atenuación obtenido con el método del material de referencia (b), (c) corte transversal de la muestra en la línea indicada en (a) y (b), (d) atenuación localizada en el corte transversal enseñado en (c) y (e) mapa bidimensional de birrefringencia. La muestra mostrada en la imagen se corresponde con una muestra distrófica de tres meses de edad.

además a la identificación de estructuras sub-superficiales.

Además de las medidas de intensidad, en el mismo capítulo también se exploró el potencial de PS-OCT para documentar las propiedades de los tejidos sanos y distróficos. Para ello, se generaron mapas bidimensionales de birrefringencia a partir del retardo de fase obtenido de los parámetros de Stokes (Fig. 11.18, e). Estos mapas, aunque también exhiben una variación inter- e intra-muestral significativa, proporcionaron una separabilidad entre controles y muestras distróficas mayor que la proporcionada por la atenuación. En concreto, en el dataset MD1 se observó una clara separación entre las dos categorías clínicas, donde las muestras sanas proporcionaron consistentemente unos valores de birrefringencia mayores que el umbral considerado en la bibliografía entre tejido sano y necrótico, y donde las muestras distróficas se encontraron consistentemente debajo de ese umbral. El segundo dataset (MD2) también mostraba una separación mayor de birrefringencia que su análogo de atenuación, pero ligeramente inferior que para el dataset MD1. La variación obtenida entre datasets puede tener su origen en la cantidad de muestras. Mientras que el dataset MD1 contaba solamente con cuatro muestras sanas, el dataset MD2 contenía el mismo número de muestras sanas que distróficas (13 por categoría), lo cual indica que, aunque con menor separabilidad, este dataset es más representativo de la variación que se observaría en un caso real. En cualquier caso, la mejora de los resultados utilizando birrefringencia que utilizando atenuación indica que la variante PS-OCT es más sensible a los cambios asociados con la enfermedad. A pesar de que las muestras distróficas sufren cambios químicos, éstos pueden no ser lo suficientemente fuertes como para manifestarse en cambios de atenuación pero si para alterar la estructura muscular lo suficiente como para ser detectados a través de una caída de birrefringencia.

En resumen, el análisis con OCT y PS-OCT demostró que estas técnicas pueden ser sensibles a cambios estructurales para distinguir muestras sanas de distróficas. Estudios adicionales con un rango de edades mayores en los modelos animales podrían ayudar a determinar las dinámicas temporales de los cambios en atenuación y birrefringencia con la evolución de la enfermedad, pero también para determinar si existe una ventana temporal óptima donde la necrosis se manifieste lo suficiente para poder utilizar la atenuación como marcador clínico de distrofia en modelos de déficit α-sarcoglicano.

Análisis de absorción y scattering con HSI y SFDI

El capítulo 7 analizó la aplicación de HSI y SFDI para la caracterización de las muestras del dataset MD2 con el objetivo de obtener información acerca de los cambios químicos que ocurren en el modelo de deficiencia de α-sarcoglicano. Los análisis iniciales de los espectros de referencia en el rango visible/infrarrojo cercano (VISNIR) e infrarrojo de onda corta (SWIR) mostraron características espectrales específicas para estas muestras. Los espectros VISNIR cuentan con una reflectancia mayor por encima de los 600 nm, consistente con el color rojizo de las muestras, además de que también contienen los picos y valles característicos de la absorción de la hemoglobina o mioglobina entre 500 y 580 nm. Los espectros SWIR, a pesar de estar influenciados por cromóforos como

elastina y grasa, estaban principalmente dominados por la absorción del agua. Las muestras, al proceder de modelos de ratón, son finas, lo cual supone un desafío a la hora de medirlas con HSI. En concreto, las regiones espectrales que no cuentan con absorción significativa permiten el viaje de los fotones hasta atravesar toda la muestra, lo cual hace que la base sobre la que se deposita las muestras altera la respuesta espectral en dichos rangos. En concreto, para la determinación de los siguientes análisis, se consideraron solamente los espectros, aproximadamente, por debajo de los 600 nm y por encima de los 1300 nm, donde la absorción de las muestras evita la influencia de la base.

En este análisis se probaron tres modelos que evalúan de forma diferente la relación entre absorción y scattering: el modelo de Kubelka-Munk, la aproximación empírica de Jacques y el cociente derivado de las simulaciones de Monte Carlo. Aunque cada modelo se basa en diferentes suposiciones, los tres mostraron tendencias similares en las regiones de alta relación señal-ruido (SNR). A pesar de que cada uno proporcionó una diferente relación absorción/scattering en cuanto a su valor absoluto, la consistencia espectral indica que los tres métodos son capaces de detectar variaciones espaciales de cromóforos cualitativas en cada muestra. El método de Monte Carlo está considerado generalmente como la aproximación más utilizable, ya que considera implícitamente los eventos de scattering múltiple, los cuales no son generalmente explicados por los modelos más tradicionales. Por ello, el cociente entre absorción y scattering y el cálculo del albedo se derivó a partir de las simulaciones.

La comparación del albedo entre las categorías clínicas mostró unos resultados similarmente altos en ambos rangos espectrales, sin una distinción clara entre las muestras sanas y las distróficas. Sin embargo, si que se observó un albedo ligeramente inferior en algunas muestras de control en el rango dominado por la hemoglobina, lo cual sugiere una mayor concentración de este compuesto químico en las muestras sanas. La estimación de la oxihemoglobina y desoxihemoglobina, utilizando el método de suma de absorción de cromóforos, enseñó que casi el 100 % del contenido total estimado de hemoglobina se corresponde con su forma oxigenada, con desviaciones de este comportamiento solamente para las muestras de mayor tamaño. Esta observación sugiere que un volumen de muestra mayor facilita la detección de áreas de hemoglobina que no han sido expuestas al oxígeno. Dadas las limitaciones existentes para separar las contribuciones de la absorción y el scattering de las muestras con la técnica HSI, se consideró para los siguientes análisis que los mejores marcadores de las propiedades ópticas de las muestras son o el cociente entre absorción y scattering, o el albedo, o directamente los espectros de reflectancia o sus estimadores estadísticos.

En el rango SWIR se utilizó un experimento basado en mezclas de materiales conocidas (*phantoms*). Específicamente, se hicieron varios phantoms con diferentes cantidades de grasa y músculo, ya que en las distrofias musculares el músculo se transforma en grasa con el tiempo. Un modelo basado en la relación de reflectancias a dos longitudes de onda relacionadas con el contenido de grasa y agua sirvió para estimar zonas de grasa localizada en algunas de las muestras, demostrando el potencial de este método para seguir la evolución de la transformación del músculo en grasa en enfermedades musculares. Sin embargo, la mayoría de las muestras de ratón cuentan con un muy pequeño volumen

muestral, con lo que es necesario refinar el método de los phantoms de mezclas conocidos por medio de evaluar diferentes volúmenes de phantoms. Esto ayudará a estimar cuál es el grosor muestral necesario para obtener una determinación de grasa precisa en el rango espectral SWIR, donde los fotones recorren una mayor longitud en el interior de las muestras.

A continuación se realizaron medidas de reflectancia difusa a varias frecuencias espaciales con la técnica SFDI, donde los resultados se centraron en los rangos de color rojo-verde-azul cercanos a los picos de iluminación máxima del proyector utilizado. El decaimiento rápido de la reflectancia con el aumento de la frecuencia espacial (hasta 0.22 mm^{-1}) sugiere un bajo scattering de las muestras. Esta información puede utilizarse para optimizar los protocolos de medida y minimizar el secado de las muestras durante sesiones de medida SFDI. Además, SFDI también señalaba a las regiones grasas previamente identificadas a partir de HSI-SWIR como regiones de menos absorción y mayor scattering que el tejido circundante. Una comparación de los cocientes absorción/scattering con los obtenidos con HSI (Fig. 11.19) reveló una discrepancia significativa, donde los derivados de HSI eran casi un orden de magnitud inferiores a los obtenidos de SFDI. El posible origen de esta diferencia surge de la colocación del material de referencia (Spectralon) utilizado para calibrar los sistemas en función de su respuesta espacial durante las medidas; mientras que en HSI se coloca alineado con la parte superior de la muestra para evitar el cálculo de reflectancias mayores de la unidad, en SFDI se sitúa alineado con la base y se utiliza la perfilometría para adaptar la medida de referencia al volumen de la muestra. Además, la variación existente en el camino óptico entre las medidas HSI y SFDI, combinado con el secado de las muestras entre ambas medidas dan lugar a que las comparaciones entre ellas, aunque factibles, no sean directas.

Desacoplar la absorción del scattering con SFDI mostró distribuciones diferentes, pero solapadas, entre las categorías clínicas para los tres rangos de color. En el rango del rojo, la mitad de las muestras distróficas exhibió una absorción por encima de la media del dataset, mientras que las muestras de control permanecieron, en general, por debajo. En el rango azul, donde la hemoglobina domina la absorción, y por encima de los 600 nm, donde la presencia espectral del agua y de la grasa comienza a no ser despreciable, las tendencias observadas sugiere

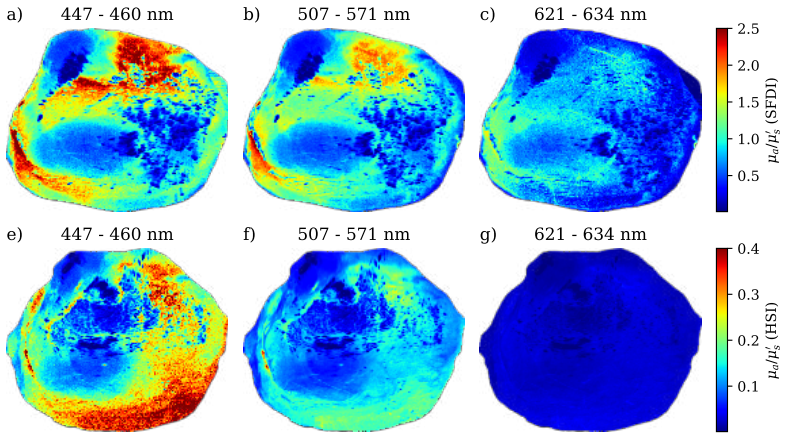

Figura 11.19: Cociente μ_a/μ_s' obtenido con SFDI (a, b, c) y HSI (d, e, f) para la muestra de control 814 del dataset MD2. Las imagenes mostradas se corresponden con promedios en longitud de onda en el rango espectral del azul (a, d), verde (b, e) y rojo (c, f), correspondiente con los picos de alta SNR del proyector LED. La barra de color superior cuantifica las imágenes SFDI, mientras que la inferior cuantifica las imágenes HSI.

una potencial acumulación de grasa en las muestras distróficas. La respuesta de scattering obtenida es más homogénea, donde las muestras distróficas tienden hacia valores ligeramente más bajos. Sin embargo, ambas categorías demostraron variabilidad inter-muestra, consistentes con las diferentes formas y preparación muestral a la hora de fijar los músculos a su sustrato. Finalmente, el análisis del albedo mostró una separación entre las dos clases clínicas mejores que la obtenida directamente de HSI. Las muestras distróficas dieron lugar a un albedo consistentemente más alto, un indicador de reflectividad generalmente más alta que apoya la hipótesis de un mayor contenido de grasa en estas muestras, consistente con los cambios que las muestras sufren en estas enfermedades.

Respuesta polarimétrica de los tejidos obtenida con MMI

El capítulo 8 exploró la aplicación de la imagen de matriz de Mueller multiespectral (MMI) para caracterizar el tejido muscular en patas completas de ratón (dataset LD). La preparación de las muestras involucró la descongelación, la retirada de la piel y la rehidratación. Inmediatamente tras la retirada de la piel se observaron diferencias visuales entre las tres patas, a pesar de ser todas pertenecientes a ratones sanos de once o doce meses de edad. En concreto, una serie de estructuras anisotrópicas blancas cubrían diferentes regiones de las patas, cuyo origen puede ser un daño de las muestras inducido por el proceso de congelación. Utilizamos estas propiedades para identificar regiones de interés específicas, entre las que se eligieron zonas dañadas por la congelación, zonas de músculo sano y zonas con mayor cantidad de grasa.

Las matrices de Mueller adquiridas son predominantemente diagonales a lo largo de todos los tipos de tejidos y longitudes de onda, lo que sugiere una muestra principalmente despolarizante. También se observó la existencia de elementos no diagonales débiles, particularmente en el vector de polarizancia. Las reflexiones especulares y otros artefactos de medida se detectaron en zonas consideradas no físicamente realizables por los criterios de realizabilidad, con lo cual se excluyeron de los siguientes análisis. Por otra parte, el resto de las regiones de interés son físicamente realizables a todas las longitudes de onda.

A continuación se calcularon los índices de pureza polarimétrica y el grado de pureza polarimétrica. La pureza obtenida es decreciente con el aumento de la longitud de onda, consistente con el mayor camino recorrido por los fotones en el interior de la muestra, el cual da lugar a una mayor despolarización por el aumento de eventos de scattering. El tejido graso y el dañado por congelación muestran menor pureza polarimétrica que el músculo sano. La anisotropía total observada es baja en todas las regiones y a todas las longitudes de onda, con leves variaciones en anisotropía lineal y circular.

Para obtener las propiedades polarimétricas del tejido comenzamos por la aplicación de la descomposición polar para derivar la despolarización (Δ), el retardo (R) y la diatenuación (D). La despolarización obtenida es capaz de distinguir el músculo sano del músculo dañado y de la grasa, y se observó una tendencia creciente con la longitud de onda. El retardo se mantuvo relativamente estable mientras que la diatenuación,

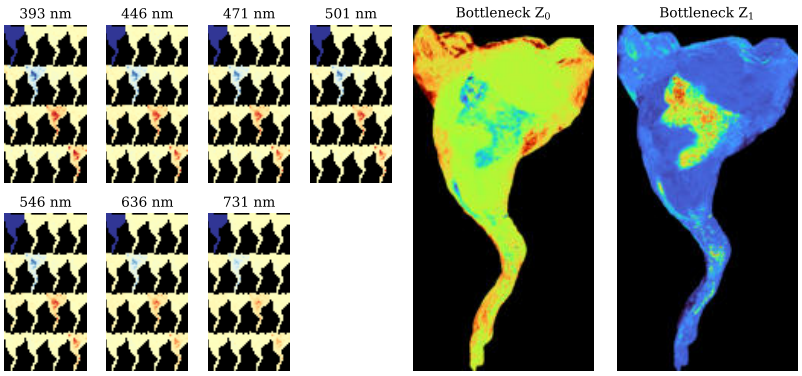

Figura 11.20: A la izquierda, representación de las siete matrices de Mueller multiespectrales de la muestra 814. A la derecha, las dos imágenes representan la interpretación de esas matrices dada por las dos neuronas del cuello de botella de un autoencoder.

aunque débil, señalaba a zonas de músculo sano. Las longitudes de onda más cortas proporcionan mejor detalle en las imágenes, lo cual es esperado debido a la menor longitud óptica de penetración en el tejido. Los diagramas de cajas de estos parámetros para los distintos tipos de tejido confirman las tendencias observadas en las imágenes, donde una inferior despolarización actúa como el marcador principal de músculo sano.

La descomposición diferencial también se aplicó al cálculo del retardo (R_L) y diatenuación lineales (D_L). De nuevo, la diatenuación señala diferencias texturales en las muestras pero no es lo suficientemente discriminatoria para identificar tipos de tejidos diferentes. En esta representación, el retardo calculado es mayor en zonas de músculo dañado, potencialmente debido al existente tejido conectivo presente por debajo de las zonas dañadas. Una comparación con los valores obtenidos en la literatura para músculo esquelético reveló resultados similares en las tendencias de diatenuación y despolarización, pero también diferentes en retardo, lo cual puede deberse a variaciones de volumen de muestra y estructuras de tejido obtenidas en los distintos experimentos.

MMI obtiene una cantidad de datos (propiedades ópticas) significativa en comparación con otras técnicas. Por ello se decidió realizar la clasificación de los distintos tipos de tejidos no para distinguir el tejido sano del dañado por congelación o de la grasa, si no para identificar los elementos individuales de las matrices de Mueller que definen el músculo sano y evaluar la posibilidad de utilizar un dataset de Mueller reducido para la misma tarea. Para comenzar se realizó una clasificación por medio del método de los K-vecinos más próximos (KNN), la cual proporcionó una precisión promedio de 79.8 % tras considerar validación cruzada. El análisis de importancia de características indicó que los elementos diagonales de las matrices, particularmente a las longitudes de onda más cortas, son las más relevantes para detectar el músculo sano. Un clasificador simplificado que utiliza solamente los elementos multiespectrales M_{11} y M_{22} proporcionó una precisión comparable, sugiriendo la posibilidad de utilizar polarimetría parcial de Mueller para la tarea específica de la detección de musculo sano en un entorno complejo de tejidos. El método no-supervisado de agrupamiento de los K-promedios también señalaba al tejido sano pero con menor exactitud y repetitividad que el método supervisado KNN, lo cual indica la necesidad de métodos supervisados para esta tarea.

Finalmente, un codificador automático (*autoencoder*) supervisado (SAE) se

utilizó para la extracción de las características principales y la clasificación de tejidos simultánea. El SAE consiguió una precisión similar a KNN, pero con un rendimiento mayor para cada clase de forma individual, especialmente para músculos sanos. La compresión de datos inherente que ocurre dentro del cuello de botella del SAE permitió representar la información principal de las matrices de Mueller multiespectrales con solamente dos imágenes (Fig. 11.20), señalando inmediatamente las zonas de músculo sano. Un análisis del error de reconstrucción apuntó a los elementos de la diagonal de las matrices como aquellos más importantes para una correcta clasificación, de forma similar a lo obtenido con los otros métodos. De la misma manera, una comparación de los resultados de la clasificación entre SAE y KNN destacó áreas de discrepancias, potencialmente dominadas por una mezcla de tejidos, indicando que MMI también se puede explotar para tareas de detección de márgenes.

Combinación de propiedades ópticas

El capítulo 9 se centró en utilizar las propiedades ópticas derivadas de las diferentes modalidades de imagen, específicamente en el uso de OCT, PS-OCT, HSI y SFDI, para mejorar la comprensión de la evolución de las distrofias musculares. Estas propiedades se evaluaron desde dos aproximaciones diferentes: una basada en visualización y otra basada en el análisis estadístico.

El análisis por visualización involucra utilizar una técnica de asignación de color para crear mapas bidimensionales de enfermedad basados en tres propiedades ópticas simultáneamente. Específicamente, la atenuación, birrefringencia y perfilometría de las muestras se asignaron a diferentes componentes del espacio de color matiz-saturación-valor (HSV). Los resultados obtenidos de las muestras de ratón demostraron la efectividad de esta técnica para destacar diferencias clave entre muestras sanas y distróficas, particularmente al visualizar variaciones de estructuración a través de la birrefringencia (Fig. 11.21). La inclusión de la perfilometría ayudó a completar la visualización y sirvió para crear mapas tridimensionales de variación de propiedades ópticas.

Para cuantificar la separabilidad entre las distribuciones de las propiedades ópticas obtenidas entre las muestras sanas y las distróficas con las múltiples técnicas de imagen, se creó un dataset combinado con todas ellas, incluyendo atenuación, birrefringencia, reflectancia, absorción y scattering. Se utilizaron métricas estadísticas, como la relación discriminante de Fisher y el test de Kolmogorov-Smirnov, para evaluar el poder discriminante de cada propiedad. Aunque individualmente las propiedades mostraron cierto grado de separabilidad, su combinación (Fig. 11.22), obtenida por métodos de reducción de dimensionalidad como PCA, t-SNE y Isomap, dio lugar a una ligera mejoría en la separabilidad. Sin embargo, el solapamiento entre las distribuciones es significativo, posiblemente debido a la variación observada de éstas propiedades entre muestras y en cada una de ellas.

Un análisis realizado por medio de una red neuronal (MLP) permitió evaluar la separabilidad a partir de las propiedades ópticas. En primera instancia, se utilizó el dataset generado con las diez propiedades ópticas resultante de combinar todos los métodos de imagen. Los experimentos

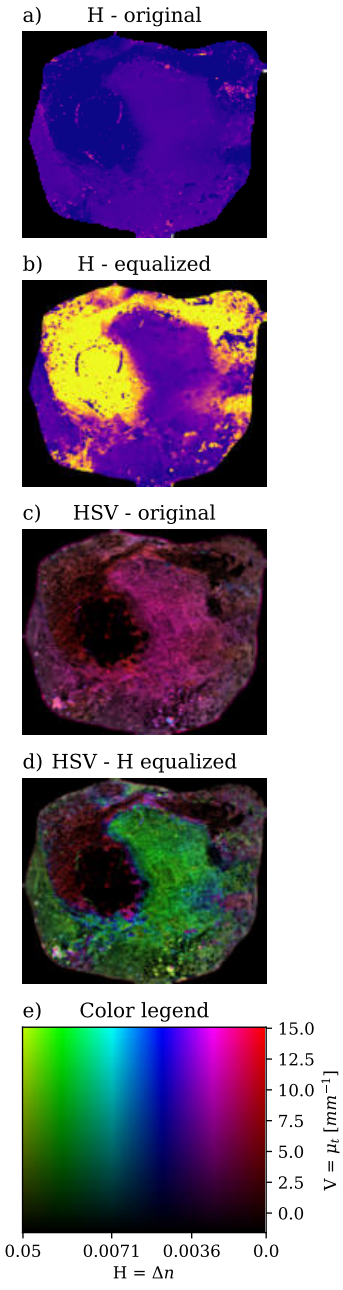

Figura 11.21: Representación resultante en el espacio de color HSV de la atenuación, birrefringencia y perfilometría para la muestra 814 del dataset MD2: (a) birrefringencia normalizada (matiz, H), (b) matiz ecualizado, (c) reconstrucción de color en el espacio HSV sin ecualización y (d) con ecualización. La leyenda de color se muestra en (e) para la máxima saturación.

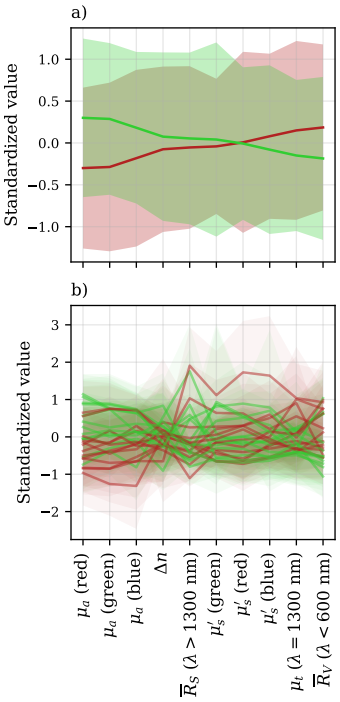

Figura 11.22: Comportamiento(a) promedio e (b) individual de las propiedades ópticas, ordenadas decrecientemente en función del valor promedio para las muestras de control (verde). Se observa la tendencia opuesta para lass muestras distróficas (rojo), aunque la variación intermuestral da lugar a un elevado solapamiento entre ambas categorías.

de clasificación realizados con este dataset no eran capaces de generalizar, posiblemente debido a que la falta de consistencia entre campo de visión y resolución de cada tecnología obligó a realizar un muestreo aleatorio de cada propiedad en las medidas, lo cual mezcla las inhomogeneidades de cada propiedad óptica. Los siguientes experimentos se centraron en la clasificación independiente de cada sistema de medida para asegurar el corregistro entre las distintas propiedades. Al contrario que el dataset global, las clasificaciones realizadas para cada modalidad proporcionaron una mejoría en el dataset de test, especialmente con las propiedades derivadas de SFDI y OCT/PS-OCT, con variaciones en sensibilidad y especificidad. Estos resultados sugieren que aunque la combinación mutlimodal es prometedora, los métodos actuales de muestreo generan inconsistencias que dificultan la clasificación. Por el contrario, el aumento de precisión obtenido al evaluar las técnicas de forma independiente sugieren que, aunque el solapamiento es elevado, existe una ligera separabilidad que los clasificadores son capaces de aprender.

Finalmente, aunque la combinación de datos de diferentes modalidades en su estado actual no es la óptima para realizar clasificación de medidas, su comportamiento conjunto apoya la discusión de las muestras desde un punto de vista químico y estructural de forma no invasiva y no destructiva, lo cual puede aprovecharse para hacer un primer filtrado de las muestras antes de realizar experimentos cuantitativos.

Resultados adicionales en otros campos de aplicación

El capítulo 10 proporciona una visión general de cómo las técnicas de imagen discutidas en este libro fueron aplicadas a otros campos de investigación, incluyendo la oftalmología, la arqueología, la neurociencia y la bioingeniería. Cada aplicación demuestra la versatilidad y potencial de estos métodos no invasivos para apoyar o responder a diversas preguntas de investigación o a mejorar protocolos en varios dominios.

En oftalmología se diseñó un método de segmentación conteo celular automático utilizando OCT para mejorar la cuantificación de la uveítis, ofreciendo una métrica objetiva y un protocolo eficiente comparado con el conteo manual, con el fin de mejorar la precisión diagnóstica y de estandarizar la evaluación de esta enfermedad. El estudio arqueológico se centró en el uso de OCT para la evaluación de un raspador de cuarzo prehistórico, donde se detectaron estructuras sub-superficiales y se evaluaron los residuos depositados en la pieza sin dañarla. La sección de neurociencia explora la aplicación de MMI en imágenes de cerebro, proporcionando un análisis detallado de las propiedades polarimétricas del tejido cerebral sano. Este experimento tiene como objetivo contribuir a una comprensión mejor de las estructuras y funciones del cerebro, con potenciales implicaciones para el diagnóstico y el monitorizado de ciertas condiciones neurológicas. Finalmente, se demostró el uso de PS-OCT en el ámbito de la bioingeniería para el análisis de modelos de tejido conectivo para el estudio de la fibrosis cardiovascular. Estas técnicas permitieron la visualización y cuantificación de cambios en las estructuras fibrosas antes y después del tratamiento, para ayudar en la evaluación de la eficacia de nuevas terapias.

En general, naturaleza la no-invasiva y no-destructiva de la imagen óptica, en conjunto con su alta resolución y capacidad de proporcional información estructural y funcional, convierte estas tecnologías en fuertes herramientas para la investigación en general y en aplicaciones clínicas.

Conclusiones globales y líneas de trabajo futuras

El objetivo principal de esta tesis doctoral consistió en responder a una pregunta específica: ¿pueden las técnicas de imagen óptica ayudar en el diagnóstico de las distrofias musculares? El concepto de "ayudar en el diagnóstico" es amplio y, en el contexto de este libro, comprende desde una mejora en la visualización de las muestras hasta el uso de las propiedades ópticas como marcadores de enfermedad. El inconveniente principal que todas estas técnicas tienen en común es su reducida capacidad de penetrar en los tejidos, lo cual dificulta su implementación *in vivo* para el seguimiento de pacientes, lo cual limita los recursos invertidos por la comunidad científica en la exploración de los métodos ópticos para las distrofias musculares. Sin embargo, la medicina va más allá de las clínicas. Ya sea a través de diferentes situaciones en las que el tejido de un paciente podría estar expuesto (por ejemplo, cirugía) o a través de modelos animales que se están desarrollando para probar la eficacia de diversos fármacos, las tecnologías ópticas pueden ayudar en este campo proporcionando información adicional o alternativa que, en muchos casos, se puede obtener en tiempo real sin interferir con el análisis de referencia que a menudo se realiza en tejidos distróficos. En esos casos, la imagen óptica puede introducirse en las prácticas de laboratorio habituales para proporcionar una estimación de qué muestras deben analizarse primero, para indicar cuáles son más uniformes o para guiar el muestreo de regiones de interés de específicas para metodologías que no pueden evaluar todo el tejido disponible.

Responder a esta pregunta de investigación no fue sencillo e implicó evaluar las muestras desde diferentes puntos de vista con tantas tecnologías como fuera posible en un análisis exhaustivo, pionero en su tipo, de las propiedades ópticas de muestras de ratones distróficos. Específicamente, nos centramos en el uso de la tomografía de coherencia óptica (OCT) y la OCT sensible a la polarización (PS-OCT) para evaluar los cambios estructurales de las muestras a escala micrométrica. Acompañamos esos resultados con imágenes hiperespectrales (HSI) e imágenes de dominio de frecuencia espacial (SFDI) para inferir los cambios químicos que podrían estar ocurriendo en las muestras. Finalmente, utilizamos imágenes de Mueller multiespectrales (MMI) para deducir si las propiedades polarimétricas de las muestras pueden utilizarse para detectar áreas de tejido muscular no dañado. Para concluir, también evaluamos si la combinación de propiedades ópticas es una mejor estimación de la enfermedad que la información individual proporcionada por cada sistema.

Este libro ha demostrado el potencial significativo de las técnicas de imagen óptica para avanzar en nuestra comprensión y evaluación de la distrofia muscular. Se deben considerar mejoras para optimizar completamente estas tecnologías para la tarea de identificar distrofias musculares, principalmente a través de un incremento de muestras para derivar los parámetros ópticos de cada categoría y evitar el efecto de las variaciones

inter-muestrales. Aun así, la capacidad de sondear tanto las propiedades estructurales como químicas del tejido muscular de forma no invasiva ofrece información valiosa sobre la progresión de la enfermedad y la respuesta al tratamiento, y puede utilizarse cuantitativamente para complementar los métodos diagnósticos y analíticos convencionales que no se pueden utilizar con tanta regularidad debido a su naturaleza invasiva.

Aunque esta investigación se ha centrado principalmente en el análisis ex vivo, los esfuerzos futuros deberían explorar la traducción de estas técnicas a aplicaciones in vivo, potencialmente a través del desarrollo de sondas mínimamente invasivas o sistemas de imágenes endoscópicas, o continuando con modelos animales in vivo donde la penetración de la luz no es un problema tan significativo. Además, expandir la investigación a una gama más amplia de modelos de distrofia muscular e incorporar estudios longitudinales será crucial para establecer la utilidad clínica de estos biomarcadores ópticos. En última instancia, el desarrollo y perfeccionamiento continuo de las tecnologías de imagen óptica son muy prometedores para mejorar el diagnóstico y el seguimiento de las distrofias musculares, allanando el camino para mejores resultados para los pacientes.

Referencias

[1] D. Verhaert et al.: "Cardiac Involvement in Patients With Muscular Dystrophies", *Circulation: Cardiovascular Imaging* **4**(1), 67-76 (2011). DOI: 10.1161/CIRCIMAGING.110.960740.

[2] E. Blaszczyk, J. Gröschel y J. Schulz-Menger: "Role of CMR Imaging in Diagnostics and Evaluation of Cardiac Involvement in Muscle Dystrophies", *Current Heart Failure Reports* **18**(4), 211-224 (2021). DOI: 10.1007/s11897-021-00521-2.

[3] M. Born y E. Wolf: "Principles of Optics", Cambridge University Press, 2019. ISBN: 9781108477437.

[4] A. Beer: "Bestimmung der Absorption des rothen Lichts in farbigen Flüssigkeiten", German. *Annalen der Physik* **162**(5), 78-88 (1852). DOI: 10.1002/andp.18521620505.

[5] J. H. Lambert: "Photometria sive de mensura et gradibus luminis, colorum et umbrae", Latin. Viduae Eberhardi Klett, 1760.

[6] L. Wang y H. Wu: "Biomedical Optics: Principles and Imaging", Wiley, 2007. ISBN: 9780471743040.

[7] L. Scolaro et al.: "Parametric Imaging of the Local Attenuation Coefficient in Human Axillary Lymph Nodes Assessed Using Optical Coherence Tomography", *Biomedical Optics Express* **3**(2), 366 (2012). DOI: 10.1364/BOE.3.000366.

[8] L. Chin et al.: "En face parametric imaging of tissue birefringence using polarization-sensitive optical coherence tomography ", *Journal of Biomedical Optics* **18**(6), 066005 (2013). DOI: 10.1117/1.jbo.18.6.066005.

[9] P. Kubelka y F. Munk: "Ein Beitrag Zur Optik Der Farbanstriche.", *Zeitschrift für Technische Physik* **15**(12), 593-601 (1931).

[10] S. L. Jacques: "Tissue Optics", inf. téc. 2020.

[11] V. Krishnaswamy et al.: "Quantitative imaging of scattering changes associated with epithelial proliferation, necrosis, and fibrosis in tumors using microsampling reflectance spectroscopy", *Journal of Biomedical Optics* **14**(1), 014004 (2009). DOI: 10.1117/1.3065540.

[12] K. A. Schenkman et al.: "Myoglobin oxygen dissociation by multiwavelength spectroscopy", *Journal of Applied Physiology*, 86-92 (1997). DOI: 10.1152/jappl.1997.82.1.86.

[13] S. L. Jacques: "Optical Properties of Biological Tissues: A Review", *Physics in Medicine and Biology* **58**(11), R37-R61 (2013). DOI: 10.1088/0031-9155/58/11/R37.

[14] S. K. V. Sekar et al.: "Diffuse optical characterization of collagen absorption from 500 to 1700 nm", *Journal of Biomedical Optics* **22**(1), 015006 (2017). DOI: 10.1117/1.jbo.22.1.015006.

[15] S. Konugolu Venkata Sekar et al.: "Broadband diffuse optical characterization of elastin for biomedical applications", *Biophysical Chemistry* **229**, 130-134 (2017). DOI: 10.1016/j.bpc.2017.07.004.

[16] R. Nachabé et al.: "Estimation of biological chromophores using diffuse optical spectroscopy: benefit of extending the UV-VIS wavelength range to include 1000 to 1600 nm", *Biomedical Optics Express* **1**(6), 1432-1442 (2010). DOI: 10.1364/BOE.1.001432.

[17] L. Kou, D. Labrie y P. Chylek: "Refractive indices of water and ice in the 065- to 25-μm spectral range", *Applied Optics* **32**(19), 3531 (1993). DOI: 10.1364/AO.32.003531.

[18] A. Pardo Franco: "Light, machines, and cancer: imaging systems and processing techniques for wide-field diagnostics in scattering media", Tesis doct. Santander: Universidad de Cantabria, 2022. https://hdl.handle.net/10902/26190.

[19] D. J. Cuccia et al.: "Quantitation and mapping of tissue optical properties using modulated imaging", *Journal of Biomedical Optics* **14**(2), 024012 (2009). DOI: 10.1117/1.3088140.

[20] E. Compain, S. Poirier y B. Drevillon: "General and self-consistent method for the calibration of polarization modulators, polarimeters, and Mueller-matrix ellipsometers", *Applied Optics* **38**(16), 3490-3502 (1999). DOI: 10.1364/AO.38.003490.

Resumo Global en Galego

Resumo global en galego

Neste capítulo inclúese una visión xeral dos temas e das contribucións discutidos ao longo desta tese. A distribución do capítulo e similar á seguida no documento principal, comezando por unha breve introdución cuxo enfoque reside en establecer a motivación deste traballo e os obxectivos principais desta tese. A continuación inclúese unha breve explicación das técnicas de imaxe aplicadas durante este traballo, seguido dunha visión xeral dos métodos de análises utilizados. As seguintes seccións discuten os resultados principais obtidos do uso de cada técnica de xeito individual, pero tamén da súa combinación. Finalmente, inclúese unha sección con traballos adicionais realizados en función de métodos derivados do obxectivo principal da tese, seguido dunhas conclusións globais e futuras liñas de traballo.

Introdución e motivación do traballo

As distrofias musculares (MD) son un grupo de enfermidades xenéticas hereditarias que causan debilidade e dexeneración muscular progresivas, impactando de xeito significativo as capacidades físicas e a calidade de vida [1]. Estas enfermidades, aínda que raras (cunha prevalencia, por exemplo, de 6 en 100.000 homes para a máis común [1]), afectan a individuos, a miúdo cun inicio temperán (5-30 anos), e frecuentemente involucran complicacións cardíacas [2]. Máis alá dos desafíos físicos, as distrofias musculares supoñen cargas emocionais, sociais e económicas, incluíndo a perda de independencia, o illamento social e un custo médico elevado. O diagnóstico temperán é fundamental para maximizar os beneficios dos tratamentos dispoñibles pero os métodos de diagnóstico actuais, como as biopsias musculares, son invasivos e teñen limitacións. Isto fai necesaria a creación de ferramentas de diagnóstico non invasivas e accesibles.

Esta tese doutoral explora o potencial das tecnoloxías de imaxe óptica para abordar esta necesidade. Centrándose nun conxunto de datos único de tecido muscular esquelético *ex vivo* de ratos (tanto sans como con distrofia), esta tese avalía catro técnicas de imaxe óptica específicas: Tomografía de Coherencia Óptica en Intensidade (OCT) e Sensible á Polarización (PS-OCT), Imaxe Hiperespectral (HSI) nos rangos espectrais do visible/infravermello próximo (VISNIR) e infravermello de onda curta (SWIR), Imaxe no Dominio das Frecuencias Espaciais (SFDI) e Imaxe de Mueller Multiespectral (MMI). Cada técnica ofrece información única sobre a estrutura, composición e función do tecido muscular. O obxectivo principal desta tese é avaliar a viabilidade e eficacia destas técnicas, individualmente e na súa combinación, para caracterizar a patoloxía muscular na distrofia muscular.

Ao estudar e combinar estas técnicas, preténdese desenvolver un enfoque integral para avaliar a saúde muscular, visualizar os cambios estruturais e de composición, e extraer parámetros ópticos como posibles biomarcadores da enfermidade. Ademais, preséntase unha metodoloxía para

integrar os datos de diferentes técnicas, creando visualizacións combinadas e realizando análises estatísticas para avaliar as correlacións entre os parámetros. Finalmente, avalíanse técnicas de aprendizaxe automática para mellorar as capacidades de diagnóstico.

Técnicas de imaxe óptica e métodos de análise

Tomografía de coherencia óptica (OCT)

OCT é unha técnica de imaxe baseada en fenómenos de baixa coherencia para reconstruír a estrutura interna dunha mostra. Esta técnica está baseada nos principios de interferometría, onde a combinación de dúas ondas de luz pode amplificar ou diminuír o sinal combinado en base á súa diferenza de fase. O elemento central dun sistema OCT é, tipicamente, un interferómetro de Michelson (Fig. 12.23), o cal divide un feixe de luz en dous camiños onde un se dirixe cara á mostra e o outro a un brazo de referencia de lonxitude fixa. A través de analizar o patrón de interferencia dos dous feixes cando se volven a combinar pódese obter unha medida da estrutura interna das mostras.

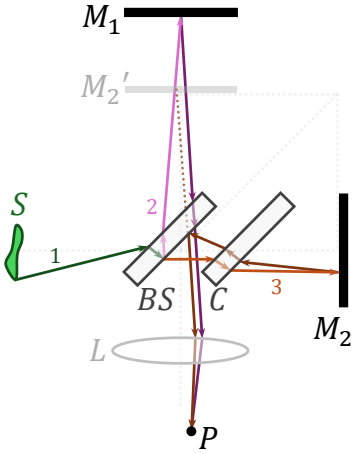

Figura 12.23: Esquema dun interferómetro de Michelson adaptado de [3]. Unha fonte de luz (S) produce raios (1) que chegan a un divisor de feixe (BS). Parte da intensidade (2) diríxese cara a un espello de referencia (M_1). A outra parte atravesa unha placa de compensación C, que conta co mesmo grosor e índice de refracción que o divisor de feixe, antes de alcanzar un segundo espello M_2. Ambos feixes se vólvense a combinar na sección traseira do divisor e viaxan de forma paralela ata alcanzar unha lente de colimación (L), a cal focaliza o patrón de interferencia no plano que contén P e que é paralelo a M_1. M_2' representa a imaxe de M_2 duplicada en torno á cara traseira do divisor de feixe.

A propiedade óptica principal obtida con OCT é o coeficiente de atenuación (μ_t), o cal representa o efecto combinado da absorción da luz (μ_a) e *scattering*[7] (μ_s) dunha mostra. As diferenzas en coeficiente de atenuación permiten identificar variacións na estrutura interna das mostras, as cales poden ser indicadores de distrofia. Nesta tese consideráronse varios métodos para calcular o coeficiente de atenuación, incluíndo:

1. A lei de Beer-Lambert [4–6]: Modela a atenuación da luz ao atravesar un medio turbio como unha función decadente exponencial en termos da distancia percorrida no medio (profundidade de penetración), z.
2. A función de dispersión de punto (PSF): Considera o efecto da óptica incluída no equipo OCT nos cambios de intensidade medidos.
3. Método do material de referencia (*phantom*): Utiliza unha mostra de referencia coñecida para calibrar as medidas a través dunha versión modificada da lei de Beer-Lambert. ([7])
4. Atenuación localizada: Calcula a atenuación en cada punto da mostra a través de considerar incrementos locais.

OCT sensible á polarización (PS-OCT)

A modalidade alternativa de OCT sensible á polarización (PS-OCT) utiliza unha versión modificada do interferómetro de Michelson ao cal se lle introducen láminas retardadoras en cada brazo para seleccionar o estado de polarización co que se ilumina a mostra. Iso permite non só capturar a intensidade de scattering recibida, senón tamén a fase da onda medida.

O sistema PS-OCT reconstrúe a reflectancia complexa a partir dos patróns de interferencia detectados. Esas reflectancias utilízanse para calcular os parámetros do vector de Stokes, os cales proporcionan información acerca do estado de polarización da luz.

[7] O termo *scattering* describe a redirección da luz cando esta interactúa coas partículas dun medio. Neste capítulo utilízase o termo en inglés para evitar confusión con outros termos similares.

A partir dos vectores de Stokes pódense obter certos parámetros de polarización relevantes, como a orientación do eixe óptico ou a uniformidade do grao de polarización. Non obstante, o máis importante e utilizado nesta tese é a birrefrinxencia da mostra. A birrefrinxencia mide a diferenza entre os índices de refracción dunha mostra anisótropa ao longo dos seus dous eixes. O método descrito por Chin *et al.* [8] permite calcular a birrefrinxencia en base ao cambio de fase do vector de Stokes coa profundidade de penetración da luz na mostra. Unha birrefrinxencia alta indica un alto grao de anisotropía entre os dous índices de refracción, mentres que unha mostra isótropa non presenta birrefrinxencia. Desta maneira preténdese separar os músculos sans, altamente anisótropos, dos músculos danados por distrofia.

Imaxe hiperespectral (HSI)

Os sistemas de imaxe hiperespectral (HSI) capturan a luz emitida por unha fonte despois de atravesar un medio e reflectirse nel de forma difusa. O contido espectral da fonte de luz cambia en base ás propiedades da mostra.

A reflectancia difusa prodúcese cando a luz entra na mostra, sofre scattering no seu interior e sae da mostra para ser capturada polo sensor. A cantidade de luz recollida está relacionada coa absorción de cada compoñente da mostra. Unha forma de interpretar o funcionamento dun sistema HSI é consideralo como unha cámara de cor avanzada que, en lugar de tres canais de cor, conta con centos deles. Fundamentalmente, consisten nunha lente e unha cámara acopladas a un espectrógrafo, o cal descompón a luz capturada nos seus compoñentes espectrais.

Na práctica, a reflectancia medida necesita ser corrixida debido a factores como o espectro non uniforme da fonte de luz, a introdución de fontes de luz non controladas no sistema (reflexións) ou o ruído do detector. Isto involucra utilizar unha mostra de referencia (Spectralon) e realizar medidas de corrección de ruído.

HSI pódese utilizar para estimar as fraccións de volume de diferentes compoñentes químicos a través de modelos físicos que consideran a absorción e scattering das mostras baixo certas suposicións. A maioría de modelos baséanse en obter a absorción como a suma de absorcións de compoñentes individuais. Estes compoñentes, denominados cromóforos, obtéñense a partir de medidas puras dos mesmos. Algúns cromóforos típicos de tecidos biolóxicos son a hemoglobina, mioglobina, lípidos, elastina, coláxeno ou auga, entre outros (Fig. 12.24). Utilizando HSI preténdese relacionar o contido de ditos compoñentes con marcadores clínicos de distrofia como a cantidade de graxa ou músculo nas mostras.

Neste libro compáranse varios modelos que consideran os efectos do scattering de formas diferentes:

1. Modelo de Kubelka-Munk [9]: Estima o scattering asumindo que a mostra pódese tratar como un medio semi-infinito. Orixinalmente, este modelo definiuse para estimar a absorción e scattering de pigmentos en po, os cales contan cun alto coeficiente de scattering.

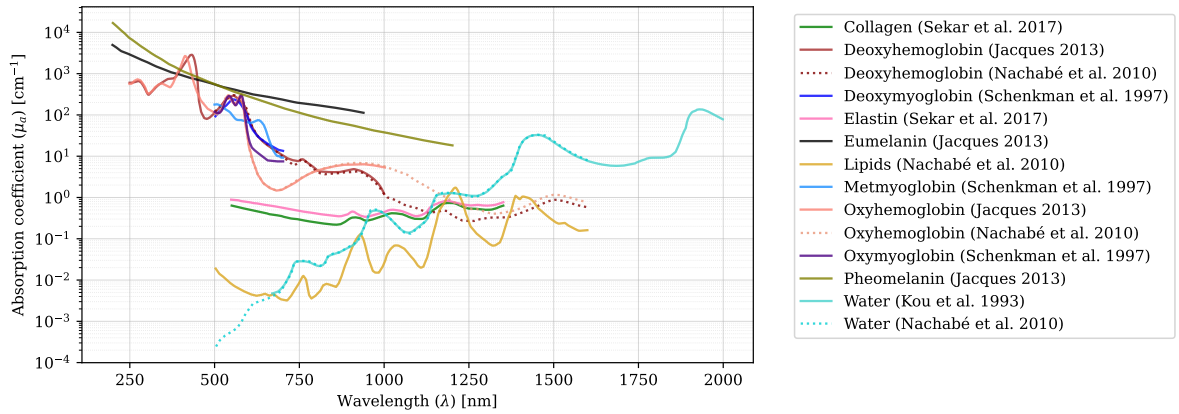

Figura 12.24: Coeficientes de atenuación (μ_a [cm^{-1}]) dos cromóforos de referencia máis comúns en función da lonxitude de onda (λ [nm]). Os datos de Schenkman *et al.* [12], orixinalmente definidos en función da densidade óptica, foron transformados a atenuación por medio da comparación do camiño óptico para facer que os picos coincidan cos definidos por Jacques [13]. Datos adaptados de [12–17].

2. Aproximación empírica de Jacques [10]: Considera o efecto de absorción e scattering a través dunha aproximación empírica do comportamento observado en simulacións de Monte Carlo.
3. Simulacións de Monte Carlo: Derívase a relación entre absorción e scattering a partir dunha táboa obtida de múltiples simulacións de Monte Carlo.
4. Modelo de Krishnaswamy *et al.* [11]: Estima a influencia do scattering como unha relación decrecente exponencial coa lonxitude de onda.
5. Modelo de Jacques [10]: Similar ao anterior, pero separa as contribucións de scattering de Mie e Rayleigh.

Imaxe de Mueller multiespectral (MMI)

A imaxe de matriz de Mueller (MMI) é unha técnica óptica utilizada para caracterizar as propiedades de polarización dunha mostra por medio de como esta altera o estado de polarización da luz incidente. Con MMI pódese obter información sobre efectos como a birrefrinxencia, a diatenuación ou a despolarización da mostra.

Os equipos MMI consisten en dous compoñentes principais:

- Xerador de estados de polarización (PSG): Xera un conxunto de estados de luz polarizada controlados para iluminar a mostra. Está composto pola fonte de iluminación e a óptica de polarización necesaria.
- Analizador de estados de polarización (PSA): Mide a polarización do estado da luz despois de interactuar coa mostra. Contén óptica de polarización adicional e o detector.

A matriz de Mueller, que describe as propiedades de polarización da mostra, obtense tras analizar como a mostra transforma os estados de polarización xerados nos detectados. Dado que o PSA e o PSG contan coas súas propias matrices coñecidas, a matriz da mostra sepárase das do sistema por medio de cálculos matriciais.

Nesta tese desenvolvéronse dúas versións dun sistema de imaxe de Mueller. A primeira versión (MMI v1.0) utiliza unha fonte de iluminación LED cunha roda de filtros para seleccionar distintas lonxitudes de onda. O PSG contén un polarizador fixo e unha lámina retardadora orientable para xerar os estados de polarización. O PSA está formado por unha cámara polarimétrica e unha lámina retardadora que se introduce ou non no camiño óptico nas distintas medidas. A segunda versión (MMI v2.0) consiste nunha mellora do anterior a través de modificacións do PSG. A fonte de LED branca e a roda de filtros substitúense por unha fonte de múltiples LED sintonizable. Ademais, o polarizador foi introducido nunha montura orientable para maior flexibilidade á hora de xerar os estados de polarización.

A calibración dos sistemas MMI é crucial para obter medidas precisas. Nesta tese utilízase o método de calibración dos valores propios (ECM) para determinar as matrices do PSA e PSG, as cales son utilizadas a continuación para extraer a matriz de Mueller da mostra a partir dos datos medidos [18]. Este proceso involucra a medida de mostras coñecidas (aire, polarizadores, láminas retardadoras) e a comparación das medidas experimentais cos valores teóricos de cada unha delas. Outro factor a considerar no deseño destes equipos é o número de condicionamento das matrices do PSG e PSA. Este número utilízase como un indicador da sensibilidade de ditas matrices ao ruído, e a súa orixe reside no espazo que ocupan os estados xerados e medidos dentro da esfera de Poincaré. A esfera de Poincaré é unha representación tridimensional dos estados de polarización posibles e, con catro estados, o número de condicionamento ideal é $\sqrt{3}$, o cal se corresponde co tetraedro regular que maximiza o espazo que ocupa na esfera.

Unha vez obtida a matriz de Mueller aplicáronse varios métodos de descomposición matricial para extraer propiedades ópticas específicas das mostras, como a despolarización, a diatenuación e o retardo. Ao igual que con PS-OCT, estas métricas relaciónanse co nivel de organización estrutural dos tecidos, pero tamén coas súas propiedades de scattering, o que pode axudar a identificar zonas de fibras musculares sans ou danadas tanto a través de organizacións irregulares ou cambios de tamaños de centros de scattering.

Resultados principais

Comportamento óptico das mostras con OCT e PS-OCT

O capítulo 6 explora a aplicación de OCT para a caracterización de mostras de tecido muscular obtidas dun modelo animal en rato con deficiencia de α-sarcoglicano. Esta deficiencia relaciónase con certas modalidades de distrofia muscular como a distrofia muscular de cadeira (LGMD) ou as miopatías miofribilares (MFM). Analizáronse dous conxuntos de datos[8], MD1 e MD2, os cales contiñan un rango de mostras de control (WT) e distróficas (Knock-out (referring to dystrophic mice) (KO)). As primeiras análises centráronse na intensidade derivada de medidas OCT, a cal demostrou un decaemento non homoxéneo no interior das mostras, indicador de variacións estruturais en cada mostra pero tamén entre elas.

[8] En adiante, *datasets*

O método do material de referencia utilizouse para xerar mapas bidimensionais de atenuación (μ_t), centrándonos na análise na rexión de scattering simple, que se aproxima ás 250 μm máis superficiais dos tecidos biolóxicos (Fig. 12.25, b). Os mapas de atenuación mostraron alteracións na densidade dos tecidos para cada mostra cun forte solapamento das distribucións estatísticas de atenuación entre mostras sas e distróficas para o dataset MD1. A pesar de que se obtivo unha mellor separación no dataset MD2, ningún dataset proporcionou unha separación clara entre categorías clínicas por medio da análise de atenuación de mostras volumétricas. Unha comparación cos valores obtidos por outros grupos para o limiar de atenuación entre tecido san e necrótico nun modelo animal de distrofia muscular de Duchenne suxire que (1) ou os modelos con déficit de α-sarcoglicano mostran menos necrose que os de Duchenne, (2) ou que a análise de todo o volume das mostras, en lugar de rexións específicas, introducen unha variabilidade que esvae o limiar de atenuación entre os dous tipos de tecido.

Os mapas bidimensionais de atenuación sinalaron zonas de variación interna, as cales foron posteriormente avaliadas a través da visualización de seccións transversais (Fig. 12.25, c) e da aplicación do modelo de atenuación localizada (Fig. 12.25, d). Os dous modelos mostraron discrepancias: Mentres que o método do material de referencia mostraba atenuación máis baixa en zonas densas, o modelo localizado mostraba a tendencia oposta. Esta diferenza xorde da forma de calcular a atenuación específica de cada método: mentres que o método do material de referencia acha a resposta media dos tecidos nun rango de profundidade maior, o modelo localizado mostra valores píxel a píxel. A pesar diso, a información combinada obtida por medios modelos proporcionou unha comprensión maior que utilizando soamente un. Especificamente o método do material de referencia identificou zonas de interese coa mostra "vista desde arriba" que facilitou a selección de cortes transversais específicos que avaliar en cada mostra, axudando ademais á identificación de estruturas sub-superficiais.

Ademais das medidas de intensidade, no mesmo capítulo tamén se explorou o potencial de PS-OCT para documentar as propiedades dos tecidos sans e distróficos. Para iso, xeráronse mapas bidimensionais de birrefrinxencia a partir do retardo de fase obtido dos parámetros de Stokes (Fig. 12.25, e). Estes mapas, aínda que tamén exhiben unha variación

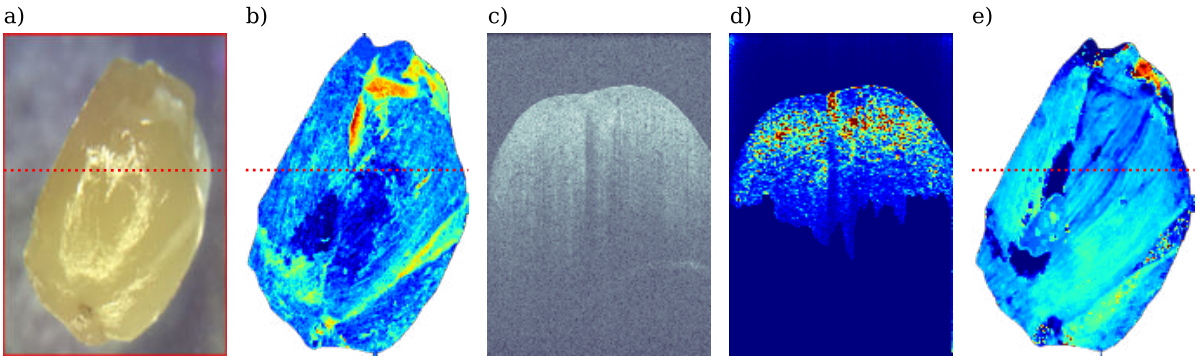

Figura 12.25: (a) Imaxe en cor de referencia, (b) mapa bidimensional de atenuación obtido co método do material de referencia (b), (c) corte transversal da mostra na liña indicada en (a) e (b), (d) atenuación localizada no corte transversal ensinado en (c) e (e) mapa bidimensional de birrefrinxencia. A mostra mostrada na imaxe correspóndese cunha mostra distrófica de tres meses de idade.

inter- e intra-mostra significativa, proporcionaron unha separación entre controis e mostras distróficas maior que a proporcionada pola atenuación. En concreto, no dataset MD1 observouse unha clara separación entre as dúas categorías clínicas, onde as mostras sas proporcionaron consistentemente uns valores de birrefrinxencia maiores que o limiar considerado na bibliografía entre tecido san e necrótico, e onde as mostras distróficas se atoparon consistentemente debaixo dese limiar. O segundo dataset (MD2) tamén mostraba unha separación maior de birrefrinxencia que o seu análogo de atenuación, pero lixeiramente inferior que para o dataset MD1. A variación obtida entre datasets pode ter a súa orixe na cantidade de mostras. Mentres que o dataset MD1 contaba soamente con catro mostras sas, o dataset MD2 contiña o mesmo número de mostras sas que distróficas (13 por categoría), o cal indica que, aínda que con menor separación, este dataset é máis representativo da variación que se observaría nun caso real. En calquera caso, a mellora dos resultados utilizando birrefrinxencia que utilizando atenuación indica que a variante PS-OCT é máis sensible aos cambios asociados coa enfermidade. A pesar de que as mostras distróficas sofren cambios químicos, estes poden non ser o suficientemente fortes como para manifestarse en cambios de atenuación pero si para alterar a estrutura muscular o suficiente como para ser detectados a través dunha caída de birrefrinxencia.

En resumo, a análise con OCT e PS-OCT demostrou que estas técnicas poden ser sensibles a cambios estruturais para distinguir mostras sas de distróficas. Estudos adicionais cun rango de idades maiores nos modelos animais poderían axudar a determinar as dinámicas temporais dos cambios en atenuación e birrefrinxencia coa evolución da enfermidade, pero tamén para determinar se existe unha xanela temporal óptima onde a necrose se manifeste o suficiente para poder utilizar a atenuación como marcador clínico de distrofia en modelos de déficit α-sarcoglicano.

Análise de absorción e scattering con HSI e SFDI

O capítulo 7 analizou a aplicación de HSI e SFDI para a caracterización das mostras do dataset MD2 co obxectivo de obter información acerca dos cambios químicos que ocorren no modelo de deficiencia de α-sarcoglicano. As análises iniciais dos espectros de referencia no rango visible/infravermello próximo (VISNIR) e infravermello de onda curta (SWIR) mostraron características espectrais específicas para estas mostras. Os espectros VISNIR contan cunha reflectancia maior por riba dos 600 nm, consistente coa cor avermellada das mostras, ademais de que tamén conteñen os picos e vales característicos da absorción da hemoglobina ou mioglobina entre 500 e 580 nm. Os espectros SWIR, a pesar de estar influenciados por cromóforos como elastina e graxa, estaban principalmente dominados pola absorción da auga. As mostras, ao proceder de modelos de rato, son finas, o cal supón un desafío á hora de medila con HSI. En concreto, as rexións espectrais que non contan con absorción significativa permiten a viaxe dos fotóns ata atravesar toda a mostra, o cal fai que a base sobre a que se depositan as mostras altere a resposta espectral en ditos rangos. En concreto, para a determinación das seguintes análises, consideráronse soamente os espectros, aproximadamente, por debaixo dos 600 nm e por riba dos 1300 nm, onde a absorción das mostras evita a influencia da base.

Neste análise probáronse tres modelos que avalían de forma diferente a relación entre absorción e scattering: o modelo de Kubelka-Munk, a aproximación empírica de Jacques e o cociente derivado das simulacións de Monte Carlo. Aínda que cada modelo baséase en diferentes suposicións, os tres mostraron tendencias similares nas rexións de alta relación sinal-ruído (SNR). A pesar de que cada un proporcionou unha diferente relación absorción/scattering en canto ao seu valor absoluto, a consistencia espectral indica que os tres métodos son capaces de detectar variacións espaciais de cromóforos cualitativas en cada mostra. O método de Monte Carlo está considerado xeralmente como a aproximación máis utilizable, xa que considera implicitamente os eventos de scattering múltiple, os cales non son xeralmente explicados polos modelos máis tradicionais. Por iso, o cociente entre absorción e scattering e o cálculo do albedo derivouse a partir das simulacións.

A comparación do albedo entre as categorías clínicas mostrou uns resultados igualmente altos en ambos rangos espectrais, sen unha distinción clara entre as mostras sas e as distróficas. Non obstante, si que se observou un albedo lixeiramente inferior nalgunhas mostras de control no rango dominado pola hemoglobina, o cal suxire unha maior concentración deste composto químico nas mostras sas. A estimación da oxihemoglobina e desoxihemoglobina, utilizando o método de suma de absorción de cromóforos, ensinou que case o 100 % do contido total estimado de hemoglobina correspóndese coa súa forma osixenada, con desviacións deste comportamento soamente para as mostras de maior tamaño. Esta observación suxire que un volume de mostra maior facilita a detección de áreas de hemoglobina que non foron expostas ao osíxeno. Dadas as limitacións existentes para separar as contribucións da absorción e o scattering das mostras coa técnica HSI, considerouse para as seguintes análises que os mellores marcadores das propiedades ópticas das mostras son ou o cociente entre absorción e scattering, ou o albedo, ou directamente os espectros de reflectancia ou os seus valores de referencia estatísticos.

No rango SWIR utilizouse un experimento baseado en mesturas de materiais coñecidas (*phantoms*). Especificamente, fixéronse varios phantoms con diferentes cantidades de graxa e músculo, xa que nas distrofias musculares o músculo transfórmase en graxa co tempo. Un modelo baseado na relación de reflectancias a dúas lonxitudes de onda relacionadas co contido de graxa e auga serviu para estimar zonas de graxa localizada nalgunhas das mostras, demostrando o potencial deste método para seguir a evolución da transformación do músculo en graxa en enfermidades musculares. Non obstante, a maioría das mostras de rato contan cun moi pequeno volume de mostra, co que é necesario refinar o método dos phantoms de mesturas coñecidas por medio de avaliar diferentes volumes de phantoms. Isto axudará a estimar cal é o grosor de mostra necesario para obter unha determinación de graxa precisa no rango espectral SWIR, onde os fotóns percorren unha maior lonxitude no interior das mostras.

A continuación realizáronse medidas de reflectancia difusa a varias frecuencias espaciais coa técnica SFDI, onde os resultados se centraron nos rangos de cor vermello-verde-azul próximos aos picos de iluminación máxima do proxector utilizado. O decaemento rápido da reflectancia co aumento da frecuencia espacial (ata 0.22 mm^{-1}) suxire un baixo

scattering das mostras. Esta información pódese utilizar para optimizar os protocolos de medida e minimizar o secado das mostras durante sesións de medida SFDI. Ademais, SFDI tamén sinalaba ás rexións graxas previamente identificadas a partir de HSI-SWIR como rexións de menos absorción e maior scattering que o tecido circundante. Unha comparación dos cocientes absorción/scattering cos obtidos con HSI (Fig. 12.26) revelou unha discrepancia significativa, onde os derivados de HSI eran case un orde de magnitude inferiores aos obtidos de SFDI. A posible orixe desta diferenza xorde da colocación do material de referencia (Spectralon) utilizado para calibrar os sistemas en función da súa resposta espacial durante as medidas; mentres que en HSI colócase aliñado coa parte superior da mostra para evitar o cálculo de reflectancias maiores da unidade, en SFDI sitúase aliñado coa base e utilízase a perfilometría para adaptar a medida de referencia ao volume da mostra. Ademais, a variación existente no camiño óptico entre as medidas HSI e SFDI, combinado co secado das mostras entre ambas medidas dan lugar a que as comparacións entre elas, aínda que factibles, non sexan directas.

A separación da absorción do scattering con SFDI mostrou distribucións diferentes, pero solapadas, entre as categorías clínicas para os tres rangos de cor. No rango do vermello, a metade das mostras distróficas exhibiu unha absorción por riba da media do dataset, mentres que as mostras de control permaneceron, en xeral, por debaixo. No rango azul, onde a hemoglobina domina a absorción, e por riba dos 600 nm, onde a presenza espectral da auga e da graxa comeza a non ser desprezable, as tendencias observadas suxiren unha potencial acumulación de graxa nas mostras distróficas. A resposta de scattering obtida é máis homoxénea, onde as mostras distróficas tenden cara a valores lixeiramente máis baixos. Non obstante, ambas categorías demostraron variabilidade inter-mostra, consistentes coas diferentes formas e preparación das mostras á hora de fixar os músculos ao seu substrato. Finalmente, a análise do albedo mostrou unha separación entre as dúas clases clínicas mellores que a obtida directamente de HSI. As mostras distróficas deron lugar a un albedo consistentemente máis alto, un indicador de reflectividade xeralmente máis alta que apoia a hipótese dun maior contido de graxa nestas mostras, consistente cos cambios que as mostras sofren nestas enfermidades.

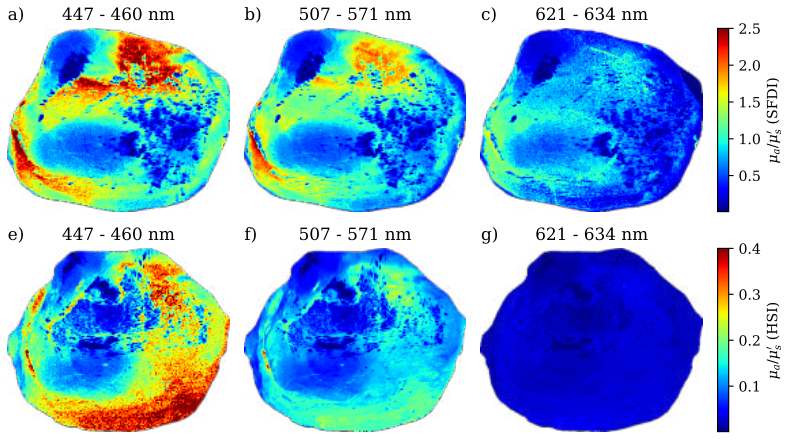

Figura 12.26: Cociente μ_a/μ_s' obtido con SFDI (a, b, c) e HSI (d, e, f) para a mostra de control 814 do dataset MD2. As imaxes mostradas correspóndense con medias en lonxitude de onda no rango espectral do azul (a, d), verde (b, e) e vermello (c, f), correspondente cos picos de alta SNR do proxector LED. A barra de cor superior cuantifica as imaxes SFDI, mentres que a inferior cuantifica as imaxes HSI.

Resposta polarimétrica dos tecidos obtida con MMI

O capítulo 8 explorou a aplicación da imaxe de matriz de Mueller multiespectral (MMI) para caracterizar o tecido muscular en patas completas de rato (dataset LD). A preparación das mostras involucrou a desconxelación, a retirada da pel e a rehidratación. Inmediatamente tras a retirada da pel observáronse diferenzas visuais entre as tres patas, a pesar de seren todas pertencentes a ratos sans de once ou doce meses de idade. En concreto, unha serie de estruturas anisotrópicas brancas cubrían diferentes rexións das patas, cuxa orixe pode ser un dano das mostras inducido polo proceso de conxelación. Utilizamos estas propiedades para identificar rexións de interese específicas, entre as que se elixiron zonas danadas pola conxelación, zonas de músculo san e zonas con maior cantidade de graxa.

As matrices de Mueller adquiridas son principalmente diagonais ao longo de todos os tipos de tecidos e lonxitudes de onda, o que suxire unha mostra principalmente despolarizante. Tamén se observou a existencia de elementos non diagonais débiles, particularmente no vector de polarizancia. As reflexións especulares e outros artefactos de medida detectáronse en zonas consideradas non fisicamente realizables polos criterios de realizabilidade, co cal se excluíron das seguintes análises. Por outra banda, o resto das rexións de interese son fisicamente realizables a todas as lonxitudes de onda.

A continuación calculáronse os índices de pureza polarimétrica e o grao de pureza polarimétrica. A pureza obtida é decrecente co aumento da lonxitude de onda, consistente co maior camiño percorrido polos fotóns no interior da mostra, o cal dá lugar a unha maior despolarización polo aumento de eventos de scattering. O tecido graxo e o danado por conxelación mostran menor pureza polarimétrica que o músculo san. A anisotropía total observada é baixa en todas as rexións e a todas as lonxitudes de onda, con leves variacións en anisotropía lineal e circular.

Para obter as propiedades polarimétricas do tecido comezamos pola aplicación da descomposición polar para derivar a despolarización (Δ), o retardo (R) e a diatenuación (D). A despolarización obtida é capaz de distinguir o músculo san do músculo danado e da graxa, e observouse unha tendencia crecente coa lonxitude de onda. O retardo mantívose relativamente estable mentres que a diatenuación, aínda que débil, sinalaba a zonas de músculo san. As lonxitudes de onda máis curtas proporcionan mellor detalle nas imaxes, o cal é esperado debido á menor lonxitude óptica de penetración no tecido. Os diagramas de caixas destes parámetros para os distintos tipos de tecido confirman as tendencias observadas nas imaxes, onde unha inferior despolarización actúa como o marcador principal de músculo san.

A descomposición diferencial tamén se aplicou ao cálculo do retardo (R_L) e diatenuación lineais (D_L). De novo, a diatenuación sinala diferenzas de textura nas mostras pero non é o suficientemente discriminatoria para identificar tipos de tecidos diferentes. Nesta representación, o retardo calculado é maior en zonas de músculo danado, potencialmente debido ao existente tecido conectivo presente por debaixo das zonas danadas. Unha comparación cos valores obtidos na literatura para músculo esquelético revelou resultados similares nas tendencias de diatenuación e despolarización, pero tamén diferentes en retardo, o cal pode deberse

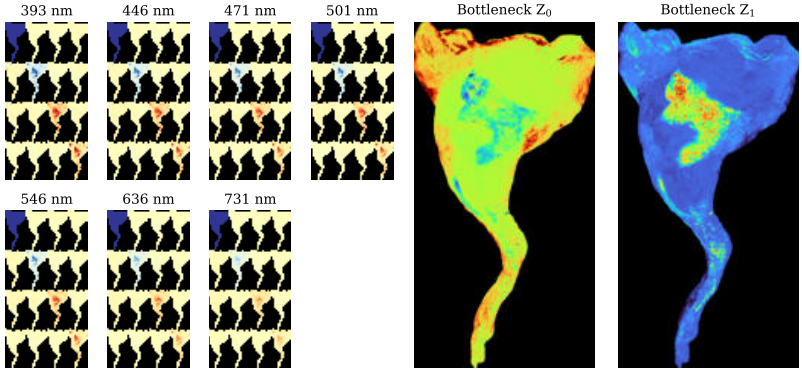

Figura 12.27: Á esquerda, representación das sete matrices de Mueller multiespectrais da mostra 814. Á dereita, as dúas imaxes representan a interpretación desas matrices dada polas dúas neuronas do pescozo de botella dun autoencoder.

a variacións de volume de mostra e estruturas de tecido obtidas nos distintos experimentos.

MMI obtén unha cantidade de datos (propiedades ópticas) significativa en comparación con outras técnicas. Por iso decidiuse realizar a clasificación dos distintos tipos de tecidos non para distinguir o tecido san do danado por conxelación ou da graxa, senón para identificar os elementos individuais das matrices de Mueller que definen o músculo san e avaliar a posibilidade de utilizar un dataset de Mueller reducido para a mesma tarefa. Para comezar realizouse unha clasificación por medio do método dos K-veciños máis próximos (KNN), a cal proporcionou unha precisión media de 79.8 % tras considerar validación cruzada. A análise de importancia de características indicou que os elementos diagonais das matrices, particularmente ás lonxitudes de onda máis curtas, son as máis relevantes para detectar o músculo san. Un clasificador simplificado que utiliza soamente os elementos multiespectrais M_{11} e M_{22} proporcionou unha precisión comparable, suxerindo a posibilidade de utilizar polarimetría parcial de Mueller para a tarefa específica da detección de músculo san nun contorno complexo de tecidos. O método non-supervisado de agrupamento das K-medias tamén sinalaba ao tecido san pero con menor exactitude e repetitividade que o método supervisado KNN, o cal indica a necesidade de métodos supervisados para esta tarefa.

Finalmente, un codificador automático (*autoencoder*) supervisado (SAE) utilizouse para a extracción das características principais e a clasificación de tecidos simultánea. O SAE conseguiu unha precisión similar a KNN, pero cun rendemento maior para cada clase de forma individual, especialmente para músculos sans. A compresión de datos inherente que ocorre dentro do pescozo de botella do SAE permitiu representar a información principal das matrices de Mueller multiespectrais con soamente dúas imaxes (Fig. 12.27), sinalando inmediatamente as zonas de músculo san. Unha análise do erro de reconstrución apuntou aos elementos da diagonal das matrices como aqueles máis importantes para unha correcta clasificación, de forma similar ao obtido cos outros métodos. Da mesma maneira, unha comparación dos resultados da clasificación entre SAE e KNN destacou áreas de discrepancias, potencialmente dominadas por unha mestura de tecidos, indicando que MMI tamén se pode explotar para tarefas de detección de marxes.

Combinación de propiedades ópticas

O capítulo 9 centrouse en utilizar as propiedades ópticas derivadas das diferentes modalidades de imaxe, específicamente no uso de OCT, PS-OCT, HSI e SFDI, para mellorar a comprensión da evolución das distrofias musculares. Estas propiedades avaliáronse desde dúas aproximacións diferentes: unha baseada en visualización e outra baseada na análise estatística.

A análise por visualización involucra utilizar unha técnica de asignación de cor para crear mapas bidimensionais de enfermidade baseados en tres propiedades ópticas simultaneamente. Especificamente, a atenuación, birrefrinxencia e perfilometría das mostras asignáronse a diferentes compoñentes do espazo de cor matiz-saturación-valor (HSV). Os resultados obtidos das mostras de rato demostraron a efectividade desta técnica para destacar diferenzas clave entre mostras sas e distróficas, particularmente ao visualizar variacións de estruturación a través da birrefrinxencia (Fig. 12.28). A inclusión da perfilometría axudou a completar a visualización e serviu para crear mapas tridimensionais de variación de propiedades ópticas.

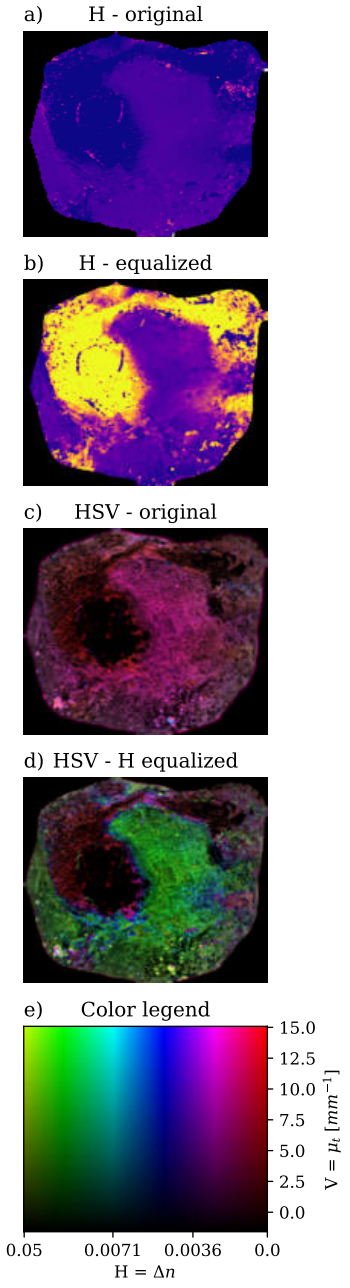

Figura 12.28: Representación resultante no espazo de cor HSV da atenuación, birrefrinxencia e perfilometría para a mostra 814 do dataset MD2: (a) birrefrinxencia normalizada (matiz, H), (b) matiz ecualizado, (c) reconstrución de cor no espazo HSV sen ecualización e (d) con ecualización. A lenda de cor móstrase en (e) para a máxima saturación.

Para cuantificar a separabilidade entre as distribucións das propiedades ópticas obtidas entre as mostras sas e as distróficas coas múltiples técnicas de imaxe, creouse un dataset combinado con todas elas, incluíndo atenuación, birrefrinxencia, reflectancia, absorción e scattering. Utilizáronse métricas estatísticas, como a relación discriminante de Fisher e o test de Kolmogorov-Smirnov, para avaliar o poder discriminante de cada propiedade. Aínda que individualmente as propiedades mostraron certo grao de separabilidade, a súa combinación (Fig. 11.22), obtida por métodos de redución de dimensionalidade como PCA, t-SNE e Isomap, deu lugar a unha lixeira melloría na separabilidade. Non obstante, o solapamento entre as distribucións é significativo, posiblemente debido á variación observada destas propiedades entre mostras e en cada unha delas.

Unha análise realizada por medio dunha rede neuronal (MLP) permitiu avaliar a separabilidade a partir das propiedades ópticas. En primeira instancia, utilizouse o dataset xerado coas dez propiedades ópticas resultante de combinar todos os métodos de imaxe. Os experimentos de clasificación realizados con este dataset non eran capaces de xeneralizar, posiblemente debido a que a falta de consistencia entre campo de visión e resolución de cada tecnoloxía obrigou a realizar un muestreo aleatorio de cada propiedade nas medidas, o cal mestura as inhomoxeneidades de cada propiedade óptica. Os seguintes experimentos centráronse na clasificación independente de cada sistema de medida para asegurar o correxistro entre as distintas propiedades. Ao contrario que o dataset global, as clasificacións realizadas para cada modalidade proporcionaron unha melloría no dataset de test, especialmente coas propiedades derivadas de SFDI e OCT/PS-OCT, con variacións en sensibilidade e especificidade. Estes resultados suxiren que aínda que a combinación mutlimodal é prometedora, os métodos actuais de muestreo xeran inconsistencias que dificultan a clasificación. Pola contra, o aumento de precisión obtido ao avaliar as técnicas de forma independente suxiren que, aínda que o solapamento é elevado, existe unha lixeira separabilidade que os clasificadores son capaces de aprender.

Finalmente, aínda que a combinación de datos de diferentes modalidades no seu estado actual non é a óptima para realizar clasificación de medidas, o seu comportamento conxunto apoia a discusión das mostras desde un punto de vista químico e estrutural de forma non invasiva e non destrutiva, o cal pode aproveitarse para facer un primeiro filtrado das mostras antes de realizar experimentos cuantitativos.

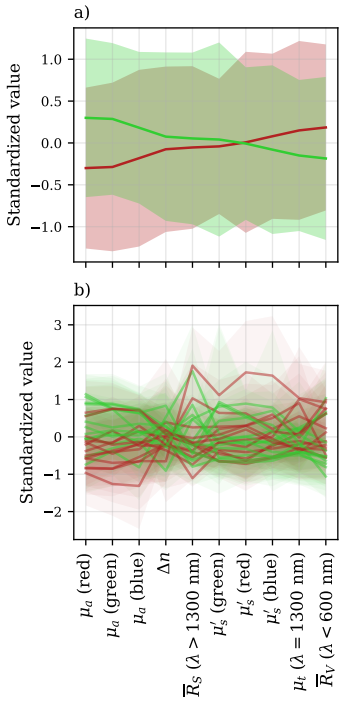

Figura 12.29: Comportamento (a) medio e (b) individual das propiedades ópticas, ordenadas decrecentemente en función do valor promedio para as mostras de control (verde). Obsérvase a tendencia oposta para as mostras distróficas (vermello), aínda que a variación intermuestral dá lugar a un elevado solapamento entre ambas categorías.

Resultados adicionais noutros campos de aplicación

O capítulo 10 proporciona unha visión xeral de como as técnicas de imaxe discutidas neste libro foron aplicadas a outros campos de investigación, incluíndo a oftalmoloxía, a arqueoloxía, a neurociencia e a bioenxeñaría. Cada aplicación demostra a versatilidade e potencial destes métodos non invasivos para apoiar ou responder a diversas preguntas de investigación ou a mellorar protocolos en varios dominios.

En oftalmoloxía deseñouse un método de segmentación de reconto celular automático utilizando OCT para mellorar a cuantificación da uveíte, ofrecendo unha métrica obxectiva e un protocolo eficiente comparado co reconto manual, co fin de mellorar a precisión diagnóstica e de estandarizar a avaliación desta enfermidade. O estudo arqueolóxico centrouse no uso de OCT para a avaliación dun raspador de cuarzo prehistórico, onde se detectaron estruturas sub-superficiais e se avaliaron os residuos depositados na peza sen danala. A sección de neurociencia explora a aplicación de MMI en imaxes de cerebro, proporcionando unha análise detallada das propiedades polarimétricas do tecido cerebral san. Este experimento ten como obxectivo contribuír a unha comprensión mellor das estruturas e funcións do cerebro, con potenciais implicacións para o diagnóstico e o monitorizado de certas condicións neurolóxicas. Finalmente, demostrouse o uso de PS-OCT no ámbito da bioenxeñaría para a análise de modelos de tecido conectivo para o estudo da fibrose cardiovascular. Estas técnicas permitiron a visualización e cuantificación de cambios nas estruturas fibrosas antes e despois do tratamento, para axudar na avaliación da eficacia de novas terapias.

En xeral, a natureza non invasiva e non destrutiva da imaxe óptica, en conxunto coa súa alta resolución e capacidade de proporcional información estrutural e funcional, converte estas tecnoloxías en fortes ferramentas para a investigación en xeral e en aplicacións clínicas.

Conclusións globais e liñas de traballo futuras

O obxectivo principal desta tese doutoral consistiu en responder a unha pregunta específica: poden as técnicas de imaxe óptica axudar no diagnóstico das distrofias musculares? O concepto de "axudar no diagnóstico" é amplo e, no contexto deste libro, comprende desde unha mellora na visualización das mostras ata o uso das propiedades ópticas como marcadores de enfermidade. O inconveniente principal que todas estas técnicas teñen en común é a súa reducida capacidade de penetrar nos tecidos, o cal dificulta a súa implementación *in vivo* para o seguimento de pacientes, o cal limita os recursos investidos pola comunidade científica na exploración dos métodos ópticos para as distrofias musculares. Non

obstante, a medicina vai máis alá das clínicas. Xa sexa a través de diferentes situacións nas que o tecido dun paciente podería estar exposto (por exemplo, cirurxía) ou a través de modelos animais que se están desenvolvendo para probar a eficacia de diversos fármacos, as tecnoloxías ópticas poden axudar neste campo proporcionando información adicional ou alternativa que, en moitos casos, se pode obter en tempo real sen interferir coa análise de referencia que a miúdo se realiza en tecidos distróficos. Neses casos, a imaxe óptica pode introducirse nas prácticas de laboratorio habituais para proporcionar unha estimación de que mostras deben analizarse primeiro, para indicar cales son máis uniformes ou para guiar a mostraxe de rexións de interese de específicas para metodoloxías que non poden avaliar todo o tecido dispoñible.

Responder a esta pregunta de investigación non foi sinxelo e implicou avaliar as mostras desde diferentes puntos de vista con tantas tecnoloxías como fose posible nunha análise exhaustiva, pioneira no seu tipo, das propiedades ópticas de mostras de ratos distróficos. Especificamente, centrámonos no uso da tomografía de coherencia óptica (OCT) e a OCT sensible á polarización (PS-OCT) para avaliar os cambios estruturais das mostras a escala micrométrica. Acompañamos eses resultados con imaxes hiperespectrales (HSI) e imaxes de dominio de frecuencia espacial (SFDI) para inferir os cambios químicos que poderían estar ocorrendo nas mostras. Finalmente, utilizamos imaxes de Mueller multiespectrais (MMI) para deducir se as propiedades polarimétricas das mostras poden utilizarse para detectar áreas de tecido muscular non danado. Para concluír, tamén avaliamos se a combinación de propiedades ópticas é unha mellor estimación da enfermidade que a información individual proporcionada por cada sistema.

Este libro demostrou o potencial significativo das técnicas de imaxe óptica para avanzar na nosa comprensión e avaliación da distrofia muscular. Débense considerar melloras para optimizar completamente estas tecnoloxías para a tarefa de identificar distrofias musculares, principalmente a través dun incremento de mostras para derivar os parámetros ópticos de cada categoría e evitar o efecto das variacións inter-mostras. Aínda así, a capacidade de sondar tanto as propiedades estruturais como químicas do tecido muscular de forma non invasiva ofrece información valiosa sobre a progresión da enfermidade e a resposta ao tratamento, e pode utilizarse cuantitativamente para complementar os métodos diagnósticos e analíticos convencionais que non se poden utilizar con tanta regularidade debido á súa natureza invasiva.

Aínda que esta investigación se centrou principalmente na análise ex vivo, os esforzos futuros deberían explorar a tradución destas técnicas a aplicacións in vivo, potencialmente a través do desenvolvemento de sondas minimamente invasivas ou sistemas de imaxes endoscópicas, ou continuando con modelos animais in vivo onde a penetración da luz non é un problema tan significativo. Ademais, expandir a investigación a unha gama máis ampla de modelos de distrofia muscular e incorporar estudos lonxitudinais será crucial para establecer a utilidade clínica destes biomarcadores ópticos. En última instancia, o desenvolvemento e perfeccionamento continuo das tecnoloxías de imaxe óptica son moi prometedores para mellorar o diagnóstico e o seguimento das distrofias musculares, allanando o camiño para mellores resultados para os pacientes.

Referencias

[1] D. Verhaert et al.: "Cardiac Involvement in Patients With Muscular Dystrophies", *Circulation: Cardiovascular Imaging* **4**(1), 67–76 (2011). DOI: 10.1161/CIRCIMAGING.110.960740.

[2] E. Blaszczyk, J. Gröschel e J. Schulz-Menger: "Role of CMR Imaging in Diagnostics and Evaluation of Cardiac Involvement in Muscle Dystrophies", *Current Heart Failure Reports* **18**(4), 211–224 (2021). DOI: 10.1007/s11897-021-00521-2.

[3] M. Born e E. Wolf: "Principles of Optics", Cambridge University Press, 2019. ISBN: 9781108477437.

[4] A. Beer: "Bestimmung der Absorption des rothen Lichts in farbigen Flüssigkeiten", German. *Annalen der Physik* **162**(5), 78–88 (1852). DOI: 10.1002/andp.18521620505.

[5] J. H. Lambert: "Photometria sive de mensura et gradibus luminis, colorum et umbrae", Latin. Viduae Eberhardi Klett, 1760.

[6] L. Wang e H. Wu: "Biomedical Optics: Principles and Imaging", Wiley, 2007. ISBN: 9780471743040.

[7] L. Scolaro et al.: "Parametric Imaging of the Local Attenuation Coefficient in Human Axillary Lymph Nodes Assessed Using Optical Coherence Tomography", *Biomedical Optics Express* **3**(2), 366 (2012). DOI: 10.1364/BOE.3.000366.

[8] L. Chin et al.: "En face parametric imaging of tissue birefringence using polarization-sensitive optical coherence tomography ", *Journal of Biomedical Optics* **18**(6), 066005 (2013). DOI: 10.1117/1.jbo.18.6.066005.

[9] P. Kubelka e F. Munk: "Ein Beitrag Zur Optik Der Farbanstriche.", *Zeitschrift für Technische Physik* **15**(12), 593–601 (1931).

[10] S. L. Jacques: "Tissue Optics", inf. téc. 2020.

[11] V. Krishnaswamy et al.: "Quantitative imaging of scattering changes associated with epithelial proliferation, necrosis, and fibrosis in tumors using microsampling reflectance spectroscopy", *Journal of Biomedical Optics* **14**(1), 014004 (2009). DOI: 10.1117/1.3065540.

[12] K. A. Schenkman et al.: "Myoglobin oxygen dissociation by multiwavelength spectroscopy", *Journal of Applied Physiology*, 86–92 (1997). DOI: 10.1152/jappl.1997.82.1.86.

[13] S. L. Jacques: "Optical Properties of Biological Tissues: A Review", *Physics in Medicine and Biology* **58**(11), R37–R61 (2013). DOI: 10.1088/0031-9155/58/11/R37.

[14] S. K. V. Sekar et al.: "Diffuse optical characterization of collagen absorption from 500 to 1700 nm", *Journal of Biomedical Optics* **22**(1), 015006 (2017). DOI: 10.1117/1.jbo.22.1.015006.

[15] S. Konugolu Venkata Sekar et al.: "Broadband diffuse optical characterization of elastin for biomedical applications", *Biophysical Chemistry* **229**, 130–134 (2017). DOI: 10.1016/j.bpc.2017.07.004.

[16] R. Nachabé et al.: "Estimation of biological chromophores using diffuse optical spectroscopy: benefit of extending the UV-VIS wavelength range to include 1000 to 1600 nm", *Biomedical Optics Express* **1**(6), 1432–1442 (2010). DOI: 10.1364/BOE.1.001432.

[17] L. Kou, D. Labrie e P. Chylek: "Refractive indices of water and ice in the 065- to 25-μm spectral range", *Applied Optics* **32**(19), 3531 (1993). DOI: 10.1364/AO.32.003531.

[18] E. Compain, S. Poirier e B. Drevillon: "General and self-consistent method for the calibration of polarization modulators, polarimeters, and Mueller-matrix ellipsometers", *Applied Optics* **38**(16), 3490–3502 (1999). DOI: 10.1364/AO.38.003490.

List of Publications

Journal articles

Published

1. José A. Gutiérrez-Gutiérrez, Verónica Mieites, José M. López-Higuera, and Olga M. Conde, "**Rotating mirror short-wave infrared hyperspectral imaging system**", *Sensors and Actuators B: Chemical*. Accepted for publication (2025). Preprint DOI: 10.2139/ssrn.4961885.
2. Verónica Mieites, Giulio Anichini, Ji Qi, Kevin O'Neill, Olga M. Conde, and Daniel S. Elson, "**PoLambRimetry: a multispectral polarimetric atlas of lamb brain**", *Journal of Biomedical Optics*, 29(9); pp. 096002 (2024). DOI: 10.1117/1.JBO.29.9.096002.
3. Verónica Mieites, José A. Gutiérrez-Gutiérrez, Arturo Pardo, José M. López-Higuera, and Olga M. Conde, "**Revealing stress-induced changes equivalence between polarization-sensitive optical coherence tomography and polarimetric camera measurements**", *Optics and Lasers in Engineering*, 175; pp. 107985 (2024). DOI: 10.1016/j.optlaseng.2023.107985.
4. Verónica Mieites, José A. Gutiérrez-Gutiérrez, José M. López-Higuera, and Olga M. Conde, "**Single-Image Multi-Parametric Representation of Optical Properties through Encodings to the HSV Color Space**", *Applied Sciences*, 14(1); pp. 155 (2024). DOI: 10.3390/app14010155.

Under review

1. Verónica Mieites, María Gabriela Fernández Manteca, Inés Santiuste Torcida, Fidel Madrazo Toca, María José Marín Vidalled, and Olga M. Conde "**Assessment of blood serum stability with Raman spectroscopy and explanatory AI.**", *Spectrochimica Acta Part A: Molecular and Biomolecular Spectroscopy*, (2025).
2. David Maestro, Ana Palanca, Irantzu Llarena, Alisa Nicole DeGrave, Gabriela Guedes, Guilherme Henrique de Oliveira, André Luiz Coelho Conceição, Verónica Mieites, Jose M. Icardo, Carlos Sanchez-Cano, Olga M. Conde, Susanne Lutz, Aitziber L. Cortajarena, and Ana V. Villar, "**Cardiac fibrosis inhibitor CTPR390 prevents structural and morphological changes in collagen and fibroblasts of human engineered cardiac connective tissue**", *iScience*, (2025). Preprint DOI: 10.1101/2025.01.15.633162.

International oral presentations

1. Olga M. Conde, José A. Gutiérrez-Gutiérrez, and Verónica Mieites, "**Explainable AI (XAI) Applied to Laser Applications in Life Sciences**" *17th International Conference on Laser Applications in Life Sciences (LALS 2024)*, Muğla (Turkey), 11-14 October 2024 (invited).
2. Verónica Mieites, Talía Lazuén, Jesús González-Urquijo, and Olga M. Conde, "**Optical Coherence Tomography for the Non-Invasive Exploration of Prehistoric Samples**", *Technoheritage 2024*, Technoheritage network, Santiago de Compostela (Spain), 25-27 September 2024 (best oral presentation award).
3. Verónica Mieites, José A. Gutiérrez, José Miguel López-Higuera, and Olga M. Conde, "**Hyperspectral Imaging for non-invasive applications: Technology, methodology and opportunities.**", *XXVIII National Spectroscopy Meeting - XII Iberian Spectroscopy Meeting*, Comité de espectroscopía de SEDOPITCA, Sociedad Española de química analítica, Sociedade Portuguesa de química , Granada (Spain), 26-28 June 2024 (invited).
4. Verónica Mieites, Giulio Anichini, Ji Qi, Kevin O'Neill, Olga M. Conde, and Daniel S. Elson "**Multispectral Mueller-Matrix Imaging: a potential tool to visualize white matter tracts**, *Photonics Europe 2024*, SPIE, Strasbourg (France), 7-11 April 2024. DOI: 10.1117/12.3017499.
5. José A. Gutiérrez Gutiérrez, Verónica Mieites, Alejandro Pontón, Inmaculada García Montesinos, José M. López Higuera, and Olga M. Conde, "**Evaluation of multiple cardiovascular pathologies in human aortas with Hyperspectral imaging and Optical Coherence Tomography**, *Photonics Europe 2024*, SPIE, Strasbourg (France), 7-11 April 2024. DOI: 10.1117/12.3022425.
6. Verónica Mieites, Arturo Pardo, José Alberto Gutiérrez-Gutiérrez, Xavier Suárez-Calvet, José Miguel López-Higuera, Jordi Díaz-Manera, and Olga M. Conde, "**Colorimetric fusion of attenuation and**

birefringence in OCT signatures: a screening tool for evaluating muscular degradation in alpha-sarcoglican murine models", *European Conferences on Biomedical Optics (ECBO)*, SPIE, Munich (Germany), 25-29 June 2023. DOI: 10.1117/12.2670555.

7. José Alberto Gutiérrez-Gutiérrez, Verónica Mieites, Arturo Pardo, José Miguel López Higuera, and Olga M. Conde, "**Comparison between optical coherence tomography and phase shifting profilometry for surface estimation**", *European Conferences on Biomedical Optics (ECBO)*, SPIE, Munich (Germany), 25-29 June 2023. DOI: 10.1117/12.2670564.
8. Verónica Mieites, Arturo Pardo, José Alberto Gutierrez Gutierrez, Jordi Díaz-Manera, Xavier Suárez-Calvet, Jose Miguel López Higuera, and Olga M. Conde, "**Hyperspectral infrared imaging of dystrophic mice muscles**", *XXVII National Spectroscopy Meeting - XI Iberian Spectroscopy Meeting*, Comité de espectroscopía de SEDOPITCA, Sociedad Española de Química Analítica, Sociedade Portuguesa de Química , Málaga (Spain), 5-8 July 2022 (best oral presentation award).
9. Alba Martín de la Torre, Verónica Mieites, Arturo Pardo, José A. Gutiérrez, Lorena García-Hevia, Mónica L. Fanarraga, José Miguel López-Higuera, and Olga M. Conde, "**Hyperspectral characterization of head and neck cancer in mice**", *XXVII National Spectroscopy Meeting - XI Iberian Spectroscopy Meeting*, Comité de espectroscopía de SEDOPITCA, Sociedad Española de Química Analítica, Sociedade Portuguesa de Química , Málaga (Spain), 5-8 July 2022.
10. Olga M. Conde, Arturo Pardo, Eusebio Real, José A. Gutiérrez-Gutiérrez, and Verónica Mieites, "**Machine learning fusion of hyperspectral and OCT imaging for tissue diagnosis and assessment**" *16th International Conference on Laser Applications in Life Sciences (LALS 2022)*, Nancy (France), 01-02 April 2022 (invited).

International posters

1. Verónica Mieites, Shayamita Ghosh, José A. Gutiérrez-Gutiérrez, Mónica L. Fanarraga, and Olga M. Conde, "**Melanoma Fixation for OCT Imaging: How Long is Too Long?**", *European Conferences on Biomedical Optics (ECBO)*. Accepted. SPIE, Munich (Germany), 22-26 June 2025.
2. José Alberto Gutiérrez-Gutiérrez, Verónica Mieites, and Olga M. Conde, "**Influence of Substrate Selection for Thin ex-vivo Specimens on Hyperspectral Imaging Measurements of Silicone Phantoms**", *European Conferences on Biomedical Optics (ECBO)*. Accepted. SPIE, Munich (Germany), 22-26 June 2025.
3. Verónica Mieites, María Gabriela Fernández Manteca, Inés Santiuste Torcida, Fidel Madrazo Toca, María José Marín Vidalled, and Olga M. Conde, "**Quality Assessment of Blood Samples with Raman Spectroscopy**", *ISBER 2023 Regional Symposium*, Instituto de Salud Carlos III, Granada (Spain) 24-25 October 2023.
4. María Gabriela Fernández Manteca, Verónica Mieites, Elena Sanz Piña, Inés Santiuste Torcida, Fidel Madrazo Toca, Olga M. Conde, and María José Marín Vidalled, "**Measurement Protocol for Quality Assessment Studies of Blood Samples Using Raman Spectroscopy**", *ISBER 2023 Regional Symposium*, Instituto de Salud Carlos III, Granada (Spain) 24-25 October 2023.
5. Verónica Mieites, José Alberto Gutiérrez-Gutiérrez, Arturo Pardo, Xavier Suárez-Calvet, José Miguel López-Higuera, Jordi Díaz-Manera, and Olga M. Conde, "**Wide-field optical properties estimation of whole limbs in muscle dystrophy murine models via SFDI: A case study**", *European Conferences on Biomedical Optics (ECBO)*, SPIE, Munich (Germany), 25-29 June 2023. DOI: 10.1117/12.2670573.

National oral presentations

1. José A. Gutiérrez, Verónica Mieites, Rosa Fabregat Borras, Rodrigo Astudillo Olalla, Noelia Suárez Álvarez, Marina Gutiérrez Ruiz, and Olga M. Conde, "**HSI assessment of radiochromic films for dosimetric evaluation**", *XIV Reunión Nacional de Óptica*, SEDOPTICA, Murcia (Spain), 3-5 July 2024.
2. Olga M. Conde, Antonio Quintela, M. Angeles Quintela, Francisco J. Madruga, Verónica Mieites, M. Gabriela Fernández-Manteca, Celia Gómez-Galdós, J.Francisco Algorri, Borja García, Andrea Pérez, and José M. López-Higuera, "**Una década de Óptica y Fotónica en las aulas: lecciones aprendidas por el Grupo de Ingeniería Fotónica de la UC**", *XIV Reunión Nacional de Óptica*, SEDOPTICA, Murcia (Spain), 3-5 July 2024.

National poster presentations

1. Verónica Mieites, María Gabriela Fernández Manteca, Inés Santiuste Torcida, Fidel Madrazo Toca, María José Marín Vidalled, and Olga M. Conde, "**Método de control de calidad para muestras de suero y plasma sanguíneo por medio de espectroscopía Raman**", *I Jornadas de la Plataforma ISCIII de Biobancos y Biomodelos*, Instituto de Salud Carlos III (ISCIII), Santander (Spain), 27-28 October 2022.
2. Mariola Garayo, Verónica Mieites, Lorena García Hevia, Mónica L. Fanarraga, José M. López Higuera, and Olga M. Conde, "**Tomografía de coherencia óptica aplicada a la evaluación de metástasis de melanoma en pulmón en modelos preclínicos**", *I Jornadas de la Plataforma ISCIII de Biobancos y Biomodelos*, Instituto de Salud Carlos III (ISCIII), Santander (Spain), 27-28 October 2022.
3. Alba Martín de la Torre, Verónica Mieites, Arturo Pardo, José A. Gutiérrez, Lorena García Hevia, Mónica L. Fanarraga, José Miguel López Higuera, and Olga M. Conde "**Análisis hiperespectral y colorimétrico del cáncer de cabeza y cuello en ratones para delineación de tumores**", *I Jornadas de la Plataforma ISCIII de Biobancos y Biomodelos*, Instituto de Salud Carlos III (ISCIII), Santander (Spain), 27-28 October 2022.

National posters

1. Verónica Mieites Alonso, José A. Gutiérrez, Arturo Pardo Franco, Jordi Díaz-Manera, Xavier Suárez-Calvet, José Miguel López-Higuera, and Olga M. Conde, "**Multimodal imaging for structural and chemical analysis of muscular dystrophies**", *XVI Jornadas Anuales CIBER-BBN*, Ciber de Biomédica en Red en Bioingeniería, Biomateriales y Nanomedicina (CIBER-BBN). Instituto de Salud Carlos III (ISCIII). A Coruña (Spain), 07-08 November 2022.
2. María Gabriela Fernández Manteca, Verónica Mieites, Inés Santiuste Torcida, Fidel Madrazo Toca, María José Marín Vidalled, and Olga M. Conde, "**Definición del Protocolo de medida para el desarrollo de un método de control de calidad de suero y plasma sanguíneo por medio de espectroscopía Raman**", *I Jornadas de la Plataforma ISCIII de Biobancos y Biomodelos*, Instituto de Salud Carlos III (ISCIII), Santander (Spain), 27-28 October 2022.
3. Verónica Mieites, Gonzalo Santos, Eusebio Real, Rosalía Demetrio, Alfonso Casado, José M. Lopez-Higuera, and Olga M. Conde, "**Conteo automatizado de agregados celulares en procesos de uveítis mediante tomografía de coherencia óptica**", *XIII Reunión Nacional de Óptica*, SEDOPTICA, Online, 22-24 November 2021.
4. Alba Martin de la Torre, Verónica Mieites, José A. Gutiérrez, Arturo Pardo, Francisco J. Madruga, Jaime Viera, Carmelo Morales, José M. López-Higuera, and Olga M. Conde, "**Evaluación de fugas de aerosoles en mascarillas sanitarias mediante un sistema óptico**", *XIII Reunión Nacional de Óptica*, SEDOPTICA, Online, 22-24 November 2021.

Datasets

1. Verónica Mieites, Giulio Anichini, Ji Qi, Kevin O'Neill, Olga M. Conde, and Daniel S. Elson, "**PoLambRimetry dataset: Multispectral Mueller matrices of lamb brain [dataset]**", *Zenodo*, 7 May 2024. DOI: 10.5281/zenodo.11127947.

Notation

The next list describes several symbols that are used within the body of the document.

α	Angle that defines the diagonal of the rectangle that describes the polarization ellipse
$\alpha_{L,C}$	Linear and circular anisotropy coefficients
χ	Ellipticity angle of the polarization ellipse
$\Delta\lambda$	Bandwidth
Δn	Birefringence
δ	Penetration depth (in the context of Ch. 2) or phase delay between components of the field amplitude (in the context of Ch. 3)
δ_{eff}	Penetration depth of the modulated light
ϵ	Electric permittivity of a medium (in the context of Ch. 2 and phase delay in a Michelson interferometer (in the context of Ch. 4)
ϵ_0	Vacuum permittivity
$\hat{M}$	Measured mueller matrix of a sample
κ	Complex part of the refractive index of a medium
λ	Wavelength
μ	Magnetic permeability of a medium
μ_0	Vacuum permeability
μ_a	Absorption coefficient
μ_s	Scattering coefficient
μ_s'	Reduced scattering coefficient
μ_t	Attenuation coefficient
μ_{eff}	Effective coefficient
μ_{tr}	Transport coefficient
ω	Angular frequency of a harmonic field
ϕ	Phase of a harmonic field
Φ_E	Electric flux
Φ_M	Magnetic flux
Ψ	Angle of rotation of the polarization ellipse

ρ Charge density

σ Conductivity (in the context of Ch. 2)

σ_a Absorption cross section

σ_g Geometrical cross-section

σ_i Pauli matrix

σ_s Scattering cross-section

τ Time-dependent phase (in the context of Ch. 3

θ Angle between the propagation vector and normal to a surface (in the context of Ch. 2) or rotation angle of an optical element with respect to the x axis of the system (in the context of Ch. 3; see M_R)

$\tilde{n}$ Refractive index of a medium

ε Decaic molar extinction coefficient

ε_λ Molar extinction coefficient

$\varphi(\vec{r},\vec{t})$ Space-time dependent phase of a harmonic field

$\vec{B}$ Magnetic induction

$\vec{dl}$ Line differential

$\vec{dS}$ Surface differential

$\vec{D}$ Electric displacement (in the context of Ch. 2) or Diattenuation (in the context of Ch. 3)

$\vec{E}$ Electric field

$\vec{F}_B$ Force applied by a magnetic field

$\vec{F}_E$ Force applied by an electric field

$\vec{H}$ Magnetic field

$\vec{J}$ Charge current density (in the context of Ch. 2) or Jones matrix (in the context of Ch. 3)

$\vec{k}$ Propagation vector (in the context of Ch. 2)

$\vec{P}$ Electric polarization (in the context of Ch. 2) or Polarizance (in the context of Ch. 3)

$\vec{S}$ Poynting's vector (in the context of Ch. 2) or Stokes vector (in the context of Ch. 3)

$\vec{v}$ Speed

$\{m_{ij}\}$ Components of the Mueller matrix

A Absorbance

a Radius of a scatterer (in the context of Ch. 2)

C Molar concentration of absorbers

c	Speed of light in vacuum
CB	Circular birefringence
CD	Circular dichroism
$d\Omega$	Solid angle
g	Anisotropy coefficient
H	Magnitude of the magnetic field (in the context of Ch. 2 or covariance matrix of a Mueller matrix (in the context of Ch. 3)
h	Planck constant
I	Irradiance (in the context of Ch. 2), intensity of the Stokes vector (in the context of Ch. 3) or total intensity (in the remaining chapters)
I_{bg}	Measurement of the background intensity
j	Charge current
L	Mueller matrix logarithm
l	Mean free path length
$L(\lambda)$	Optical path length
l_a	Absorption mean free path
L_m, L_u	G-symmetric and G-Antisymmetric components of the matrix logarithm
l_s	Scattering mean free path
LB	Linear birefringence
LD	Linear dichroism
M	Mueller matrix
M_Δ	Mueller matrix of a depolarizer
M_A	Mueller matrix of the polarization state analyzer
M_D	Mueller matrix of a diattenuator
m_D	Lower 3×3 block of the Mueller matrix of a diattenuator
M_G	Mueller matrix of the polarization state generator
M_R	Mueller matrix of a retarder
m_R	Lower 3×3 block of the Mueller matrix of a retarder
$m_{3\times3}$	Lower 3×3 block of a Mueller matrix
$M_{\Delta P}$	Mueller matrix of a depolarizer with polarizance
M_{AC}	Modulated component of light

M_{DC} Constant component of light

M_{HP} Mueller matrix of a horizontal linear polarizer

M_{LP} Mueller matrix of linear polarizer

M_{ND} Mueller matrix of a neutral density filter

M_{Rot} Mueller matrix of a rotator

M_{VP} Mueller matrix of a vertical linear polarizer

n Real part of the refractive index of a medium

OD Optical density

p_x, p_y Transmittance of a diattenuator along its x and y axes

$P_{1,2,3}$ Indices of polarimetric purity

P_α Degree of polarimetric purity

P_Δ Degree of polarimetric purity

Q Total charge

q Punctual charge

Q_s Scattering efficiency

R Reflectance

r Distance to a particle (in the context of Ch. 2)

R_d Diffuse reflectance

r_s Fresnel amplitude coefficient for the s-polarized portion of the reflected wave

R_{eff} Effective reflectance

$r_{s,p}$ Fresnel amplitude coefficients for the s- and p-polarized portions of the reflected wave

S_0 (or I), S_1 (or Q), S_2 (or U), S_3 (or V) Components of the Stokes vector

T Transmittance

t Time

$t_{s,p}$ Fresnel amplitude coefficients for the s- and p-polarized portions of the transmitted wave

X_i Volume fraction of a chemical component

dV Volume differential

List of abbreviations

A
ADC Apparent diffusion coefficient. 24
AD-EDMD Autosomal dominant Emery-Dreifuss muscular dystrophy. 14
AD-LGMD Autosomal dominant limb-girdle muscular dystrophy. 15
AEI Absolute echo intensity. 22
AR-LGMD Autosomal recessive limb-girdle muscular dystrophy. 15

B
BMD Becker muscular dystrophy. 13, 14, 18, 20, 23, 24

C
CK Creatine Kinase. 19
CMD Congenital muscular dystrophy. 16, 18, 19
CMF Color-matching functions. 141

D
DC Direct Current (electricity). 125, 126
DM Myotonic Dystrophy (from the Latin name *dystrophia myotonica*). 16, 17, 20–22, 26, 27
DM2 Myotonic dystrophy type II. xxvi, 173, 189
DMD Duchenne muscular dystrophy. 13, 14, 18, 20–26, 28, 163
DOP Degree of polarization. 114
DOPU Degree of polarization uniformity. 114
DTI Diffusion tensor imaging. 22–24
DWI Diffusion weighted imaging. 22, 23

E
ECG Electrocardiography. 21
ECM Eigenvalue Calibration Method. 130, 131, 133, 134, 257, 284, 303
ECT Engineered connective tissue. xxx, 263–265
EDMD Emery-Dreifuss muscular dystrophy. 14, 18, 22
EMG Electromyography. 20, 21

F
FDR Fisher's discriminant ratio. xxxii, 234, 235
FoV Field of View. 27, 129
FSHMD Fascioscapulohumeral muscular dystrophy. 14, 15, 18, 20, 22, 23
FTIR Fourier transform infrared spectroscopy. 26, 27

G
GSL Gray scale level. 21

H
H&E Hematoxylin and eosin (stain). 25, 163
HLP Horizontal linearly polarized light. 77
HSI Hyperspectral imaging. xxv, xxvi, xxxi–xxxiii, 4, 5, 7, 27, 101, 116–118, 121, 124, 126, 127, 141, 147, 177–180, 182, 187, 195, 196, 198, 200–202, 230, 231, 238, 239, 241, 273–275, 279, 281–283, 286–289, 291, 293, 299, 301, 305–307, 310, 312
HSV Hue-Saturation-Value. xxviii, xxxi, xxxii, 142, 225–227, 230, 231, 291, 310

I
IR Infrared (wavelength range). 24–26, 28, 168

Isomap Isometric Feature Mapping. xxix, xxxii, 149, 235, 236, 242, 291, 310

K

KDE Kernel density estimation. 263

KNN K-Nearest Neighbors (classification). xxvii, xxviii, 149, 214–216, 218, 219, 221–223, 290, 291, 309

KO Knock-out (referring to dystrophic mice). xxiv–xxix, xxxii, 159, 161, 163–166, 170, 171, 173, 183, 198–200, 228–230, 234, 236, 237, 239, 285, 303

KO-1mo Knock-out samples from one-month-old mice. 159, 173

KO-3mo Knock-out samples from three-month-old mice. xxiv, xxv, 163, 167, 168, 174

KO-6mo Knock-out samples from six-month-old mice. xxiv, 163, 167

KS Kolmogorov-Smirnov (test). xxxii, 234, 235

L

LD Mice leg dataset (see Tab. 6.2). xxiv, xxvii, xxviii, xxxii, 159, 160, 205–209, 211, 212, 217, 221, 289, 308

LED Light emitting diode. xxiii, xxvi, xxxi, xxxii, 124, 126, 129, 130, 193, 194, 196, 201, 284, 288, 303, 307

LGMD Limb-girdle muscular dystrophy. 15, 16, 18–20, 22, 24, 28, 159, 284, 303

LUT Lookup table. xxiv, 126, 146, 147, 191, 197

M

MCML Monte Carlo Multi-Layer. 143

MD Muscular dystrophy. xxi, 3, 4, 14, 16–27, 279, 299

MD1 Mice muscle dataset 1 (see Tab. 6.1). xxiv, xxv, xxviii, 159–164, 166, 168–170, 172–175, 225, 227, 228, 284–286, 303–305

MD2 Mice muscle dataset 2 (see Tab. 6.2). xxiv–xxix, xxxi–xxxiii, 159, 163, 165, 169, 171–175, 177, 178, 180, 181, 183–186, 191–196, 198–200, 225–227, 229, 231, 232, 234, 236, 239, 284–286, 288, 291, 303–305, 307, 310

MFM Myofibrillar myopathy. 17, 18, 20, 159, 284, 303

MIP Maximum intensity projection. xxiv, 106, 140, 161

MLP Multi-layer perceptron. xxix, 150, 237–242, 291, 310

MMI Mueller matrix imaging. xxiii, xxvii, xxxii, 5, 7, 127–130, 134, 135, 205, 206, 221–223, 257, 261, 273–275, 279, 283, 284, 289–293, 299, 302, 303, 308, 309, 311, 312

MRI Magnetic resonance imaging. xxi, 16, 21–23, 25, 201

MRS Magnetic resonance spectroscopy. 22, 23

MSE Mean squared error. 110, 140, 162

MSI Multispectral imaging. 27, 116

MTF Modulation Transfer Function. 122–125, 282, 283

MUP Motor unit potential. 20

N

NGS Next generation sequencing. 19

NIR Near-Infrared (wavelength range). 178

O

OCT Optical coherence tomography. xxiii, 4, 5, 7, 25, 29, 101, 103–110, 112, 114, 121, 139–141, 159–163, 168, 173–175, 177, 230, 231, 235, 239, 241, 242, 247–253, 273–276, 279, 280, 282, 284–286, 291–293, 299, 300, 303, 305, 310–312

OPMD Oculopharingeal muscular dystrophy. 17, 18, 20, 22

P

PCA Principal component analysis. xxix, xxxii, 148, 235, 236, 241, 291, 310

PSA Polarization State Analyzer. 128–130, 134, 257, 283, 284, 302, 303

PSF Point spread function. xxiii, 110, 111, 124, 280, 300

PSG Polarization State Generator. 128, 130, 134, 205, 257, 283, 284, 302, 303

PS-OCT Polarization sensitive optical coherence tomography. xxx, 4, 5, 7, 29, 101, 112, 113, 115, 127, 159, 169, 241, 242, 263–265, 273–275, 279, 280, 284, 286, 291–293, 299, 300, 303–305, 310–312

PSP Phase-shifting profilometry. 126

Q
QBA Quantitative backscattering analysis. 21

R
ReLU Rectified linear unit. 150
RGB Red-Green-Blue (referring to color channels on a camera). xxiv, xxv, 117, 124, 126, 141, 142, 167, 168, 174
RMSE Root mean squared error. xxv, 110, 140, 141, 184, 185
RoI Region of Interest. 174, 223

S
SAE Supervised autoencoder. xxviii, 151, 152, 217–221, 223, 290, 291, 309
SD-OCT Spectral-domain Optical coherence tomography. 107
SFDI Spatial frequency domain imaging. xxvi, xxxi, xxxii, 5, 7, 25, 101, 121, 122, 124–127, 147, 191, 193, 195–198, 200, 201, 231, 235, 239, 241, 242, 273–275, 279, 282, 283, 286, 288, 291–293, 299, 305–307, 310, 312
SHG Second harmonic generation. 28
SLED Superluminescent diode. 107
SMC Smooth muscle cell. 12
SNR Signal-to-noise ratio. xxvi, xxvii, xxxi, xxxii, 108, 112, 124, 139, 169, 181, 184, 185, 193, 194, 196, 198–201, 206, 287, 288, 306, 307
STE Speckle-tracking echocardiography. 22
SVD Singular value decomposition. 93, 94, 209
SVM Support Vector Machine. 163
SWIR Short-wave Infrared (wavelength range). xxv, xxvi, xxxiii, 5, 117, 177–179, 182, 183, 187–189, 200, 201, 231, 233, 239, 274, 279, 286–288, 299, 305–307

T
TD-OCT Time-Domain Optical coherence tomography. 104
THG Third harmonic generation. 28
TIR Total internal reflection. 58
t-SNE t-Distributed stochastic neighbor embedding. xxix, xxxii, 148, 149, 235, 236, 241, 291, 310

U
US Ultrasound. xxi, 21, 22
UV Ultraviolet (wavelength range). 24, 26

V
VIS Visible (wavelength range). 26
VISNIR Visible-Near infrared (wavelength range). xxv, 5, 117, 124, 141, 177–180, 182–185, 195, 200, 231, 274, 279, 286, 299, 305
VLP Vertical linearly polarized light. 77

W
WT Wild-Type (referring to healthy mice). xxiv–xxix, xxxii, 159, 161, 163–167, 169–171, 183, 198–200, 228–230, 232, 234, 236, 237, 239, 285, 303

X
XAI Explainable AI. 152
X-EDMD X-linked Emery-Dreifuss muscular dystrophy. 14, 20

All models are wrong,
but some are useful.

GEORGE E. P. BOX